

Electrowetting-based Actuation of Model Biological Fluids

Niyusha Samadi

A Thesis

In the Department

of

Mechanical and Industrial Engineering

Presented in Partial Fulfillment of the Requirements

for the Degree of

Doctor of Philosophy (Mechanical Engineering) at

Concordia University

Montreal, Quebec, Canada

September 2016

Copyright © Niyusha Samadi, 2016

CONCORDIA UNIVERSITY
SCHOOL OF GRADUATE STUDIES

This is to certify that the thesis prepared

By: **Niyusha Samadi**

Entitled: **Electrowetting-based Actuation of Model Biological Fluids**

and submitted in partial fulfillment of the requirements for the degree of

Doctor of Philosophy (Mechanical Engineering)

Complies with the regulations of the University and meets the accepted standards with respect to originality and quality.

Signed by final examining committee

<u>Dr. Nematollaah Shiri</u>	Chair
<u>Dr. Mina Hoorfar</u>	External Examiner
<u>Dr. Christopher Trueman</u>	External to Program
<u>Dr. Marius Paraschivoiu</u>	Examiner
<u>Dr. Rolf Wuthrich</u>	Examiner
<u>Dr. Paula M. Wood-Adams</u>	Thesis Supervisor
<u>Dr. Ali Dolatabadi</u>	Thesis Supervisor

Approved by

Chair of Department or Graduate Program Director

_____ 2016

_____ Dean of Faculty

ABSTRACT

Electrowetting-based Actuation of Model Biological Fluids

Niyusha Samadi, Ph.D.

Concordia University, 2016

In the past two decades, microfluidics-based lab-on-a-chip devices have received growing interest, and researchers have been developing chemical and biological analysis systems on very small scales. In Lab-on-a-chip systems, the goal is reducing chemical laboratory procedures and using miniaturized rapid, portable, inexpensive and reliable equipment which can be applied in medical diagnostics, and basic scientific research. The driving force behind the Lab-on-a-chip concept is “microfluidics” where contrary to bulk flows; surface tension is a dominant force for liquid handling and actuation. One method of actuation involves applying an external electric field which changes the surface tension between the solid-liquid interface reducing the meniscus contact angle and inducing motion of a droplet in a microchannel. This phenomenon is called “electrowetting”.

In this research, the effect of electrowetting on the behavior of biopolymer solutions such as DNA is experimentally investigated. To better assess the electrowetting phenomenon of such complex solutions, the physics of electrowetting of aqueous biopolymer solutions should be completely understood. Such a fundamental understanding currently does not exist. For this purpose, the effect of fluid composition (*i.e.* different concentrations of DNA solutions and the type of buffer solution) on the static response of the droplet to electric field variables such as applied voltage is identified.

In the transient response, the time and voltage dependency of the parameters such as droplet speed, total displacement, and elongation of the droplets of distilled water, Tris-HCl buffer and the DNA solutions is studied. Among these parameters, the droplet speed is a key factor which controls the rate of microfluidics-based lab-on-a-chip devices. It is found that the negatively charged oxygen ions on the DNA chain will affect the dynamic behaviour of DNA solutions significantly, and the electrophoretic velocity increases with voltage. Besides, it appears that the higher the DNA concentration is, the higher the DNA droplet velocity will be; as

the ionic strength and the total effective charge increase with DNA concentration. Therefore, both electrowetting and electrophoretic forces contribute to the movement of the negatively charged droplets of DNA solutions.

Overall, the results of this study will help us to better understand, analyze, design and prototype the microfluidic-based systems for DNA solutions.

Dedication

In memory of my father, Alireza, a sophisticated kind person whom I still miss every day;

I dedicate this work:

to my incredible loving mother, Ashraf;

to my wonderful caring husband, Shahab;

&

to the joy of my life, my sweet precious daughter, Rozhina.

Acknowledgements

First and foremost, I would like to take the opportunity to express my sincere appreciation to my supervisors, Dr. Paula Wood-Adams and Dr. Ali Dolatabadi for their continuous guidance, support, patience, and kindness throughout this entire research. I was very fortunate to have them as my supervisors during my Ph.D., as the completion of this work would not have been possible without their insightful leadership and continuous technical and moral support.

Also, I would like to express my deepest appreciation to the distinguished researchers of my thesis committee, Dr. Mina Hoorfar, Dr. Christopher W. Trueman, Dr. Marius Paraschivoiu, and Dr. Rolf Wuthrich, for accepting to be a member of my Ph.D. defense committee. I am profoundly grateful to them who were always more than generous with their expertise and precious time; above all, their patience throughout the entire doctorate program.

I would also like to thank Concordia University and the staff of the Department of Mechanical and Industrial Engineering for their support; especially, Leslie Hossein who was always welcoming and answered all my questions with thoughtful care and support; and also Maureen Thuringer, Arlene Zimmerman, and Sophie Méryneau for their dedication to supporting students.

My sincere acknowledgements go to the research and technical staff of the Department of Mechanical and Industrial Engineering – Concordia University: Dan Juras, Gilles Huard, Henry Szczawinski, and Dominic Ng for their assistance and valuable support in the development of my experimental set-up and conducting the experiments.

I am also deeply grateful to Charles Dolan and the staff of the machine shop at the Department of Chemical Engineering - McGill University for their meticulous work in the development of my contact angle measurement apparatus and camera support.

I would like to appreciate the help of McGill Nanotools Microfab Laboratory staff; especially Dr. Matthieu Nannini, for providing useful training and their meticulous work during the microfabrication procedure.

I would like to thank Dr. Suong Van Hoa for giving me the permission to use his lab facilities at the Department of Mechanical and Industrial Engineering - Concordia University, and also his friendly staff who always provided me with help. Special thanks and gratitude is owed to Heng Wang for his constant assistance and support in conducting the required experiments for this research and his trainings on certain experimental set-ups.

I am also very grateful to Dr. Mojtaba Kahrizi for giving me the permission to use the facilities of his MEMS laboratory at the Department of Electrical and Computer Engineering – Concordia University, and Sheilesh Prasad who provided me with support to use the spin coater.

I owe special gratitude to Dr. Mamoun Medraj for his very stimulating and fundamental discussion on how to use his TMRL research facilities at the Department of Mechanical and Industrial Engineering – Concordia University, and Mazen Samara, and Ahmad Omar Mostafa for their technical assistance while working on EDS elemental mapping experiments.

Special heartfelt thanks go to all my friends, colleagues, and officemates for their moral and emotional support during this period and also for providing a friendly environment to work in.

I have been blessed with the greatest parents who raised me and my siblings in a culturally enriching environment. They not only gave us unconditional love and support, but also they always stressed the importance of education and installed in us a tireless work ethic and persistent determination. To them I owe all that I have ever achieved. My father was with me when I started this journey, but he is really missed now.... with no doubt, his love will always be in my heart.

My deepest admiration is owed to my family; my amazing caring sisters and brother: Pershia, Parisa, and Hamidreza, and their wonderful families, for their continuous love, support and encouragements; and also to my family-in-law for being a great source of motivation; I am very grateful to each and every one of them.

I am tremendously thankful to my incredible husband, Shahab, who always believed in me, and supportively stood by me during this entire thesis. His unconditional love, support, and patience are the greatest gifts of my life.

And last, but not least, many thanks to my little sunshine, Rozhina, for her patience over the course of this time consuming work regardless of her absolute right to my attention. She has been my true inspiration and strength during stormy days and will always be a continual source of pride and enlightenment.

Table of Contents

List of Figures.....	xii
List of Tables.....	xxiv
Nomenclature	xxix
Chapter1	1
Background and Motivations	1
1.1) Introduction.....	1
1.2) Surface Tension Driven Flow	4
1.2.1) Actuation Principles.....	4
1.2.2) Methods of Actuation	7
1.2.2.1) Chemical Methods.....	8
1.2.2.2) Thermal Methods.....	9
1.2.2.3) Electrical Methods.....	10
1.3) Electrowetting Effect.....	11
1.3.1) Electrical Double Layer (EDL).....	13
1.3.2) Capacitance Model	15
1.3.3) Types of EWOD Microsystems.....	17
1.4) Contact Angle Saturation	19
1.5) State of the Art	22
1.6) Research Objectives	28
1.6.1) Thesis Structure	29
Chapter2.....	31
Design of Materials and Experimental Methodology	31
2.1) Determination of Droplet Volume Range	31
2.2) System Configuration.....	33
2.2.1) Material Design.....	36
2.3) Experimental Apparatus.....	39
2.4) Humidity Control	43
2.5) Microfabrication of Control Electrodes	44
2.6) Electrode Shapes and Wiring	46
2.7) Design of Switching Controller.....	50
Chapter3.....	51
Characterization of DNA-based Solutions	51

3.1) DNA Concentration Regimes.....	52
3.2) Preparation of DNA Solutions	53
3.3) Rheological Properties of DNA solutions.....	55
3.3.1) Rheological Experiments.....	61
3.3.2) SALS Experiments	64
3.4) Discussion of Results	67
Chapter4.....	69
Contact Angle Measurements.....	69
4.1) Contact Angle Measurement.....	70
4.1.1) Image Analysis Using AutoCAD for Measuring Apparent Contact Angle.	70
4.2) Selecting the appropriate Buffer solution.....	73
4.3) The Effect of Voltage on Contact Angle on Planar Electrodes.....	75
4.3.1) Sessile Droplets.....	75
4.3.2) Sandwiched Droplets	82
4.3.2.1) Microchannel Gap of 600 μm	82
4.3.2.2) Microchannel Gap of 300 μm	93
4.3.3) Comparison of Results and Discussion	104
Chapter5.....	114
Moving Droplets using Electrowetting	114
5.1) Fundamental Studies of Actuating Droplets on Single Square Electrodes	114
5.1.1) Droplet Transport.....	115
5.1.2) Definitions	118
5.1.2.1) Specifications for All Experiments:	121
5.1.2.2) Experimental Conditions	122
5.1.2.3) Onset of Actuation.....	123
5.1.3) Time Series Results	128
5.1.3.1) Distilled Water.....	131
5.1.3.2) Tris-HCl Buffer Solution.....	133
5.1.3.3) 4 $\mu\text{g/ml}$ DNA Solutions.....	135
5.1.3.4) 20 $\mu\text{g/ml}$ DNA Solution	137
5.1.3.5) Comparison of Time Series Results	139
5.1.4) Voltage Series Results	146
5.2) Comparison of Results for all solutions and Discussion.....	156
5.2.1) Minimum Actuation Voltage.....	156

5.2.2) Maximum Instantaneous Velocity	159
5.2.2.1) Velocity and Voltage	159
5.2.2.2) Velocity and Electrowetting Number	164
5.2.3) Actuation Force and the Opposing Forces.....	167
5.2.4) Total Displacement and Electrode Coverage.....	175
5.2.5) Droplet Elongation and Droplet Average Velocity	176
5.3) Summary	179
Chapter6.....	180
Conclusions, Contributions and Recommendations for Future Work.....	180
6.1) Summary of Conclusions	180
6.2) Contributions.....	182
6.3) Recommendations for Future Work.....	183
References	185
Appendix A.....	210
Appendix B.....	219
Appendix C.....	226
Appendix D.....	230
Appendix E.....	246
Appendix F.....	261
Appendix G.....	311
Appendix H.....	372
Appendix I.....	430
Appendix J.....	470

List of Figures

Figure 1-1: A continuous flow microfluidic device (Taken from reference: Wang <i>et al.</i>).....	2
Figure 1-2: A digital microfluidic device showing the creation, motion, splitting and.....	3
Figure 1-3: Equilibrium of forces acting on a droplet resting on a solid surface, (a) hydrophilic surface, wetting ($\theta_0 < 90^\circ$) and (b) hydrophobic surface, non-wetting ($\theta_0 > 90^\circ$).....	5
Figure 1-4: Illustration of a capillary tube immersed in a liquid risen to a	6
Figure 1-5: Schematic of a water droplet in a non-uniform electric field.	10
Figure 1-6: Continuous Electrowetting (CEW). (a) Electric Double Layer (EDL) and initial charge. (b) electrically induced surface tension gradient. (Taken from reference: Lee and Kim, IEEE Copyright line ©2000 IEEE).....	11
Figure 1-7: Wetting improves after applying voltage (dashed) to a droplet initially at rest on a solid surface (solid).....	12
Figure 1-8: Schematic of the Electric Double Layer (EDL).....	14
Figure 1-9: Effect of EDL on Total Capacitance with and without considering EDL, assuming a droplet of distilled water in a system with Parylene C (thickness of d) as the dielectric material.	17
Figure 1-10: The contact angle as a function of voltage for a sample with 1 μm SiO_2 insulator covered by 20 nm Teflon hydrophobic top coating. Electric breakdown strength $E_{bd} = 10^9$ V/m. Experimental data (symbols), model curve based on local dielectric breakdown (solid line), and Young-Lippmann equation (dashed line). (Reprinted with permission from Drygiannakis <i>et al.</i> , Copyright © 2009 American Chemical Society).....	21
Figure 2-1: Changes of Bond Number with droplet diameter for choosing the appropriate droplet volume to neglect the effect of gravity	32
Figure 2-2: Sandwiched droplet on a planar electrode	33
Figure 2-3: Sequence of events when applying voltage	34

Figure 2-4: Schematic diagrams of a parallel plate microchannel; definitions of contact angle (θ) and surface tension at different interfaces; γ_{lv} , γ_{sv} and γ_{sl} which are the surface tensions at the liquid-vapour, solid-vapour, and solid-liquid interfaces respectively, (a) with no voltage applied (b) voltage is applied on the first electrode which has reduced the surface tension γ_{sl} causing the droplet deformation. (c) Detail A, as shown in (b), an example of interdigitated electrode shape..... 35

Figure 2-5: Chemical structure of Parylene N,C. 37

Figure 2-6: (a) Breakdown voltage of Parylene N and C vs. polymer film thickness, (b) electrical properties of Parylene N and C. (Taken from specification sheet, Specialty Coating Systems (SCS), *Clear Lake, USA*). 38

Figure 2-7: (a) Isometric front view of contact angle measurement apparatus (design details in Appendix A), (b) positioning the top and bottom plates as used in the experiments. 41

Figure 2-8: Camera support, the arrows show the directions of movement. 41

Figure 2-9: Experimental set-up at the early stages of the experiments 42

Figure 2-10: The experimental set-up with the humidity chamber..... 43

Figure 2-11: Designed patterns of electrodes on Photomask..... 45

Figure 2-12: (a) Schematic of a bottom plate substrate, (b) schematic detail of a single square electrode, (c) schematic detail of an array of square electrodes, (d) positioning a droplet of distilled water with diameter “D” next to a single square electrode. The units are all in μm 47

Figure 2-13: (a) Schematic of a bottom plate substrate, (b) schematic detail of an array of interdigitated electrode. The units are all in μm 48

Figure 2-14: Schematic of the wirings..... 49

Figure 3-1: DNA structure: Chemical structure (Source: Wikipedia, Credit: Madeleine Price Ball)..... 52

Figure 3-2: Characterization of Standard flows..... 56

Figure 3-3: Shear flow velocity profile.....	57
Figure 3-4: Rheo-SALS device, the laser passes through the solutions of DNA in Couette geometry while being under shear rate	60
Figure 3-5: Comparison of results with those of <i>Sun et al.</i> in frequency domain for (a) $G'(\omega)$ Storage modulus, $G''(\omega)$ Loss modulus, (b) η^* Complex viscosity.....	61
Figure 3-6: Shear stress growth coefficient, the transient response in viscosity following a sudden inception of shear flow to DNA (3000 $\mu\text{g/ml}$) in a start-up test. Different curves represent different shear rates.	62
Figure 3-7: Crossover frequency of storage and loss modulus as a function of DNA concentration with the scaling power of -2.4. (Reprinted with permission from Reference Sun <i>et al.</i> . Copyright © 2005 American Chemical Society). The filled square shows the experimental result obtained in this research at 25 °C.....	63
Figure 3-8: The schematic of a basic SALS set-up for an unpolarized scattering. (Adapted from Reference: Lauger <i>et al.</i>).....	64
Figure 3-9: The axes x, y in the Couette geometry represent the direction of shear flow and shear gradient respectively, and z axis to the neutral direction. The propagation of the incident beam is along the z -axis (normal to the xy plane). (Adapted from Reference: Lauger <i>et al.</i>).....	65
Figure 3-10: Small angle light scattering (SALS) patterns and the plots of intensity as a function of distance obtained from SALS analysis software for DNA solution (3000 $\mu\text{g/ml}$).....	66
Figure 4-1: Image analysis using AutoCAD for a 1.6 μl water droplet sandwiched in a 580 μm microchannel gap, (a) detail of procedure, (b) reference scale, (c) droplet profile and measured contact angles and microchannel gap height and droplet maximum diameter.	71
Figure 4-2: Image analysis of a 1.6 μl sessile droplet of water on Teflon coated substrate by using AutoCAD.	72

Figure 4-3: Comparison of average contact angle as a function of DNA concentration for the droplets of Tris-HCl buffer solution (pH = 8.0), buffer solution (pH =7.0), and 4, 8, 350 and 1000 $\mu\text{g/ml}$ DNA solutions. The error bars indicate standard deviation. 74

Figure 4-4: Droplet morphology of Tris-HCl buffer solution with an average volume of $1.32 \pm 0.05 \mu\text{l}$ at: (a) 0 V, (b) 35 V, (c) 100 V. 76

Figure 4-5: The contact angle (θ) as a function of voltage for sessile droplets of 4 $\mu\text{g/ml}$ DNA solution with an average volume of $1.34 \pm 0.01 \mu\text{l}$. The saturation contact angle is shown on the graph (dashed line), and the error bars indicate standard deviation. Error bars are smaller than symbols in all cases where not visible. 77

Figure 4-6: Comparison of contact angle (θ) as a function of voltage for sessile droplets of Tris-HCl buffer solution and different concentrations of DNA solutions with an average volume of $1.35 \pm 0.08 \mu\text{l}$. The error bars indicate standard deviation. Error bars are smaller than symbols in all cases where not visible. 79

Figure 4-7: Comparison of $\Delta\theta_v$ (*i.e.* the difference between the contact angle in the absence of an electric field (θ_0) and the contact angle when the voltage is applied (θ)) as a function of voltage for all solutions with an average volume of $1.35 \pm 0.08 \mu\text{l}$ 80

Figure 4-8: Comparison of $\Delta\theta_s$ (*i.e.* the difference between the contact angle in the absence of an electric field (θ_0) and the saturation contact angle (θ_s)) as a function of DNA concentration for DNA solutions with an average volume of $1.35 \pm 0.08 (\mu\text{l})$ 81

Figure 4-9: The contact angle (θ) as a function of voltage for sandwiched droplets of distilled water with an average volume of $1.56 \pm 0.03 \mu\text{l}$ in a microchannel gap of $580 \pm 6 \mu\text{m}$ at the top and bottom interfaces; the solid line is based on the theory of Young-Lippmann's relation. The saturation contact angle is also shown on the graph (dashed line). The error bars indicate standard deviation. Error bars are smaller than symbols in all cases where not visible. 83

Figure 4-10: Droplet morphology of distilled water at various voltages: (a) 0 V, (b) 35 V, (c) 90 V. 84

Figure 4-11: The contact angle (θ) as a function of voltage for sandwiched droplets of 4 $\mu\text{g/ml}$ DNA solution with an average volume of $1.47 \pm 0.02 \mu\text{l}$ in a microchannel gap of $604 \pm 3 \mu\text{m}$ at the top and bottom interfaces. The saturation contact angle is shown on the graph (dashed line), and the error bars indicate standard deviation. Error bars are smaller than symbols in all cases where not visible. 85

Figure 4-12: Comparison of contact angle (θ) as a function of voltage for sandwiched droplets of distilled water, Tris-HCl buffer solution and different concentrations of DNA solutions with an average volume of $1.52 \pm 0.03 (\mu\text{l})$ and microchannel gap of $602 \pm 10 (\mu\text{m})$. The data are for the contact angle at the bottom interface, and the error bars indicate the standard deviations. Error bars are smaller than symbols in all cases where not visible. 87

Figure 4-13: Comparison of the average contact angle at the top interface, θ_T , as a function of DNA concentration in Tris-HCl buffer for sandwiched droplets of different concentrations of DNA solutions. The average volume of the droplets is $1.52 \pm 0.03 (\mu\text{l})$ for the average microchannel gap of $602 \pm 10 (\mu\text{m})$. The error bars indicate standard deviation. Error bars are smaller than symbols in all cases where not visible. 88

Figure 4-14: Comparison of $\Delta\theta_v$ (*i.e.* the difference between the contact angle in the absence of an electric field (θ_0) and the contact angle when the voltage is applied (θ)) as a function of voltage for sandwiched droplets of distilled water, Tris-HCl buffer solution and different concentrations of DNA solutions with an average volume of $1.52 \pm 0.03 (\mu\text{l})$ and microchannel gap of $602 \pm 10 (\mu\text{m})$. The data are for the contact angle at the bottom interface. 89

Figure 4-15: Comparison of $\Delta\theta_s$ (*i.e.* the difference between the contact angle at the bottom interface in the absence of an electric field (θ_0) and the average contact angle when the droplet reaches saturation (θ_s)) as a function of DNA concentration in Tris-HCl buffer for sandwiched droplets of DNA solutions. The average volume of the droplets and the microchannel gaps are $1.52 \pm 0.03 (\mu\text{l})$ and $602 \pm 10 (\mu\text{m})$ respectively. 91

Figure 4-16: Droplet morphology of: (a) distilled water, (b) Tris-HCl buffer solution, (c), (d), (e) 4, 350 1000 $\mu\text{g/ml}$ DNA solutions respectively. The average volume of the droplets is $1.52 \pm 0.03 (\mu\text{l})$ and the average microchannel gap is $602 \pm 10 (\mu\text{m})$. The numbers indicate the contact angles at the bottom interfaces. 92

Figure 4-17: The contact angle (θ) as a function of voltage for sandwiched droplets of distilled water with an average volume of $0.86 \pm 0.02 \mu\text{l}$ in a microchannel gap of $295 \pm 5 \mu\text{m}$ at the top and bottom interfaces; the solid line is based on the theory of Young-Lippmann's relation. The saturation contact angle is also shown on the graph (dashed line). The error bars indicate standard deviation. Error bars are smaller than symbols in all cases where not visible. 94

Figure 4-18: Morphology of distilled water droplets at various voltages: (a) 0 V, (b) 35 V, (c) 90 V. 95

Figure 4-19: The contact angle (θ) as a function of voltage for sandwiched droplets of 4 $\mu\text{g/ml}$ DNA solution with an average volume of $0.85 \pm 0.01 \mu\text{l}$ in a microchannel gap of $306 \pm 3 \mu\text{m}$ at the top and bottom interfaces. The saturation contact angle is shown on the graph (dashed line), and the error bars indicate standard deviation. Error bars are smaller than symbols in all cases where not visible. 96

Figure 4-20: Comparison of contact angle (θ) as a function of voltage for sandwiched droplets of distilled water, Tris-HCl buffer solution and different concentrations of DNA solutions with an average volume of $0.89 \pm 0.05 (\mu\text{l})$ and microchannel gap of $304 \pm 4 (\mu\text{m})$. The data are for the contact angle at the bottom interface, and the error bars indicate the standard deviation. Error bars are smaller than symbols in all cases where not visible. 98

Figure 4-21: Comparison of the average contact angle at the top interface, (θ_T), as a function of DNA concentration for sandwiched droplets of Tris-HCl buffer solution and different concentrations of DNA solutions with an average volume of $0.89 \pm 0.05 (\mu\text{l})$ for the average microchannel gap of $304 \pm 4 (\mu\text{m})$. The error bars indicate standard deviation. Error bars are smaller than symbols in all cases where not visible. 99

Figure 4-22: Comparison of $\Delta\theta_v$ (*i.e.* the difference between the contact angle in the absence of an electric field (θ_0) and the contact angle when the voltage is applied (θ)) as a function of voltage for sandwiched droplets of distilled water, Tris-HCl buffer solution and different concentrations of DNA solutions with an average volume of $0.89 \pm 0.05 (\mu\text{l})$ and microchannel gap of $304 \pm 4 (\mu\text{m})$. The data are for the contact angle at the bottom interface. 100

Figure 4-23: Comparison of $\Delta\theta_s$ (*i.e.* the difference between the contact angle at the bottom interface in the absence of an electric field (θ_0) and the average contact angle when the droplet reaches saturation (θ_s)) as a function of DNA concentration for sandwiched droplets of Tris-HCl buffer solution and different concentrations of DNA solutions. The average volume of the droplets and the microchannel gaps are 0.89 ± 0.05 (μl) and 304 ± 4 (μm) respectively. 102

Figure 4-24: Droplet morphology for: (a) distilled water, (b) Tris-HCl buffer solution, (c), (d), (e) 4, 20, 150 $\mu\text{g/ml}$ DNA solutions respectively. The average volume of the droplets is 0.89 ± 0.05 (μl) and the average microchannel gap is 304 ± 4 (μm). The numbers indicate the contact angles at the bottom interfaces. 103

Figure 4-25: The comparison of the average contact angle at the top interface, (θ_T), as a function of DNA concentration with average volumes of 1.52 ± 0.027 (μl) and 0.89 ± 0.052 (μl) for microchannel gaps of (602 ± 10) and (300 ± 4) μm respectively. 108

Figure 4-26: The effect of microchannel gap on $\Delta\theta_s$ (*i.e.* the difference between the contact angle at the bottom interface in the absence of an electric field (θ_0) and the average contact angle when the droplet reaches saturation (θ_s)) as a function of DNA concentration. The average volume is: 1.35 ± 0.08 (μl) for sessile droplets and 1.52 ± 0.027 (μl) and 0.89 ± 0.052 (μl) for sandwiched droplets in microchannel gaps of (602 ± 10) and (300 ± 4) μm respectively. 109

Figure 4-27: Schematic diagram of the advancing and receding contact angles at the onset of droplet motion. For the droplet to move: $\theta + \alpha \leq \theta_0 - \alpha$ (Adapted from reference: Barber and Emerson). 110

Figure 4-28: $\Delta\text{Cos } \theta$ as a function of $CV^2/2$ for the solutions of distilled water, Tris-HCl buffer, 4 $\mu\text{g/ml}$ and 20 $\mu\text{g/ml}$ DNA solutions. The obtained values of γ_{lv} are also shown. 112

Figure 5-1: Schematic of a droplet transport model showing sources of energy dissipation (F_{dd}, F_f). Here, F_m is the electrostatic driving force per unit length of the electrode (L_0). (Adapted from reference: Ren *et al.*). 116

Figure 5-2: The coordinate system specified according to the electrode edge, and the definitions of the: droplet start point, droplet initial diameter, electrode length, offset and overlap. 119

Figure 5-3: Droplet morphology corresponding to an applied voltage of 90 V for a 0.9 μl droplet of distilled water in a microchannel gap of 314 μm . The overlap and offset values are 60 μm and 314 μm respectively. A sudden inception of voltage is applied at $t = 0$ s, and remains constant until the droplet stops moving..... 124

Figure 5-4: Comparison of the average curves: (a) instantaneous displacement, (b) instantaneous velocity, (c) total displacement, and (d) acceleration as a function of time for the leading and trailing edges of distilled water droplets at 90 V..... 125

Figure 5-5: (a) Droplet elongation as a function of time, and (c) comparison of the average curves for the instantaneous velocity as a function of droplet position as shown in (b) for the leading and trailing edges of distilled water droplets at 90 V. The arrows in graph (c) indicate the changes of velocity along the direction of movement. 126

Figure 5-6: Droplet morphology corresponding to an applied potential of 65V voltage to a 0.82 μl droplet of distilled water in a microchannel gap of 370 μm . The overlap and offset values are 72 μm and 33 μm respectively. A sudden inception of voltage is applied at $t = 0$ s, and remains constant until the droplet stops moving..... 127

Figure 5-7: The instantaneous velocity of the distilled water droplets as a function of time for the applied voltages of 60 to 90V. Comparison of the average curves: (a) leading edge, (b) trailing edge. 131

Figure 5-8: The total displacement of the distilled water droplets as a function of time for the applied voltages of 60 to 90V. Comparison of the average curves: (a) leading edge, (b) trailing edge. 131

Figure 5-9: The comparison of the average curves for the elongation as a function of time for distilled water droplets..... 132

Figure 5-10: The instantaneous velocity of Tris-HCl buffer droplets as a function of time for the voltages of 50 to 90V. Comparison of the average curves: (a) leading edge, (b) trailing edge. 133

Figure 5-11: The total displacement of Tris-HCl buffer droplets as a function of time for the voltages of 50 to 90V. Comparison of the average curves: (a) leading edge, (b) trailing edge. 133

Figure 5-12: The comparison of the average curves for the elongation as a function of time for Tris-HCl buffer droplets. 134

Figure 5-13: The instantaneous velocity of the droplets of 4 $\mu\text{g/ml}$ DNA solutions as a function of time for the voltages of 50 to 90V. Comparison of the average curves: (a) leading edge, (b) trailing edge..... 135

Figure 5-14: The total displacement of the droplets of 4 $\mu\text{g/ml}$ DNA solutions as a function of time for the voltages of 50 to 90V. Comparison of the average curves: (a) leading edge, (b) trailing edge..... 135

Figure 5-15: The comparison of the average curves for the elongation as a function of time for 4 $\mu\text{g/ml}$ DNA solutions..... 136

Figure 5-16: The instantaneous velocity of the droplets of 20 $\mu\text{g/ml}$ DNA solutions as a function of time for the voltages of 50 to 90 V. Comparison of the average curves: (a) leading edge, (b) trailing edge..... 137

Figure 5-17: The total displacement of the droplets of 20 $\mu\text{g/ml}$ DNA solutions as a function of time for the voltages of 50 to 90 V. Comparison of the average curves: (a) leading edge, (b) trailing edge..... 137

Figure 5-18: The comparison of the average curves for the elongation as a function of time for 20 $\mu\text{g/ml}$ DNA solutions..... 138

Figure 5-19: The instantaneous velocity as a function of time for the droplets of distilled water, Tris-HCl buffer, 4 $\mu\text{g/ml}$ and 20 $\mu\text{g/ml}$ DNA solutions at the voltage of 90 V. Comparison of the average curves: (a) leading edge, (b) trailing edge..... 140

Figure 5-20: The total displacement as a function of time for the droplets of distilled water, Tris-HCl buffer, 4 $\mu\text{g/ml}$ and 20 $\mu\text{g/ml}$ DNA solutions at the voltage of 90 V. Comparison of the average curves: (a) leading edge, (b) trailing edge..... 140

Figure 5-21: The comparison of the average curves for the elongation as a function of time, for the droplets of distilled water, Tris-HCl buffer, 4 $\mu\text{g/ml}$ and 20 $\mu\text{g/ml}$ DNA solutions at the voltage of 90 V..... 141

Figure 5-22: The instantaneous velocity as a function of time for the droplets of distilled water, Tris-HCl buffer, 4 $\mu\text{g/ml}$ and 20 $\mu\text{g/ml}$ DNA solutions at the voltage of 80 V. Comparison of the average curves: (a) leading edge, (b) trailing edge. 142

Figure 5-23: The total displacement as a function of time for the droplets of distilled water, Tris-HCl buffer, 4 $\mu\text{g/ml}$ and 20 $\mu\text{g/ml}$ DNA solutions at the voltage of 80 V. Comparison of the average curves: (a) leading edge, (b) trailing edge. 142

Figure 5-24: The comparison of the average curves for the elongation as a function of time, for the droplets of distilled water, Tris-HCl buffer, 4 $\mu\text{g/ml}$ and 20 $\mu\text{g/ml}$ DNA solutions at the voltage of 80 V..... 143

Figure 5-25: The instantaneous velocity as a function of time for the droplets of distilled water, Tris-HCl buffer, 4 $\mu\text{g/ml}$ and 20 $\mu\text{g/ml}$ DNA solutions at the voltage of 75 V. Comparison of the average curves: (a) leading edge, (b) trailing edge. 144

Figure 5-26: The total displacement as a function of time for the droplets of distilled water, Tris-HCl buffer, 4 $\mu\text{g/ml}$ and 20 $\mu\text{g/ml}$ DNA solutions at the voltage of 75 V. Comparison of the average curves: (a) leading edge, (b) trailing edge. 144

Figure 5-27: The comparison of the average curves for the elongation as a function of time, for the droplets of distilled water, Tris-HCl buffer, 4 $\mu\text{g/ml}$ and 20 $\mu\text{g/ml}$ DNA solutions at the voltage of 75 V..... 145

Figure 5-28: An example showing the instantaneous velocity of the leading edge instantaneous velocity of distilled water droplets as a function of time (applied voltage of 85 V); (a) peaks of the individual experiments at point 1: (t_1, v_1) , point 2: (t_2, v_2) , and point 3: (t_3, v_3) , (b) peak of the average curve. 147

Figure 5-29: The average of maximum instantaneous velocity as a function of voltage for the leading and trailing edges of the droplets of (a) distilled water droplets, (b) Tris-HCl buffer,

(c) 4 $\mu\text{g/ml}$ DNA solution, (d) 20 $\mu\text{g/ml}$ DNA solution. The error bars indicate standard deviation..... 150

Figure 5-30: The average of maximum total displacement as a function of voltage for the leading and trailing edges of the droplets of (a) distilled water droplets, (b) Tris-HCl buffer, (c) 4 $\mu\text{g/ml}$ DNA solution, (d) 20 $\mu\text{g/ml}$ DNA solution. The error bars indicate standard deviation..... 153

Figure 5-31: The average of peak time for maximum total displacement as a function of voltage for the leading and trailing edges of the droplets of (a) distilled water droplets, (b) Tris-HCl buffer, (c) 4 $\mu\text{g/ml}$ DNA solution, (d) 20 $\mu\text{g/ml}$ DNA solution. The error bars indicate standard deviation..... 154

Figure 5-32: The average of maximum instantaneous velocity as a function of voltage, for the droplets of distilled water, Tris-HCl buffer, 4 $\mu\text{g/ml}$ and 20 $\mu\text{g/ml}$ DNA solutions: (a) leading edge, (b) trailing edge. The error bars indicate standard deviation. 160

Figure 5-33: The average of maximum instantaneous velocity as a function of voltage for the leading edges of the droplets of (a) distilled water, (b) Tris-HCl buffer, (c) 4 $\mu\text{g/ml}$ DNA solution and (d) 20 $\mu\text{g/ml}$ DNA solutions. The error bars indicate standard deviation..... 162

Figure 5-34: The average of maximum instantaneous velocity as a function of electrowetting number (η_{EW}), for the leading edges of the droplets of (a) distilled water, (b) Tris-HCl buffer, (c) 4 $\mu\text{g/ml}$ DNA solution and (d) 20 $\mu\text{g/ml}$ DNA solutions..... 165

Figure 5-35: The magnitudes of F_m , F_{dd} , F_f , F_{th} and the total force, F_{net} , and the average of the maximum leading edge instantaneous velocity as a function of voltage for the droplets of (a) distilled water, (b) Tris-HCl buffer, (c) 4 $\mu\text{g/ml}$ DNA solution and (d) 20 $\mu\text{g/ml}$ DNA solutions..... 170

Figure 5-36: The average peak time for maximum instantaneous velocity as a function of voltage, for the droplets of distilled water, Tris-HCl buffer, 4 $\mu\text{g/ml}$ and 20 $\mu\text{g/ml}$ DNA solutions: (a) leading edge, (b) trailing edge. The error bars indicate standard deviation..... 172

Figure 5-37: The average of the maximum leading edge instantaneous velocity as a function of total force, F_{net} for the droplets of (a) distilled water, (b) Tris-HCl buffer, (c) 4 $\mu\text{g/ml}$ DNA solution and (d) 20 $\mu\text{g/ml}$ DNA solutions. 174

Figure 5-38: The average of maximum total displacement as a function of voltage for the leading edges of the droplets of distilled water, Tris-HCl buffer, 4 $\mu\text{g/ml}$ and 20 $\mu\text{g/ml}$ DNA solutions. The error bars indicate standard deviation. 175

Figure 5-39: The average of maximum elongation as a function of voltage for the droplets of distilled water, Tris-HCl buffer, 4 $\mu\text{g/ml}$ and 20 $\mu\text{g/ml}$ DNA solutions. The error bars indicate standard deviation. 176

Figure 5-40: The average velocity, (a) leading edge, and (b) trailing edge, as a function of voltage for the droplets of distilled water, Tris-HCl buffer, 4 $\mu\text{g/ml}$ and 20 $\mu\text{g/ml}$ DNA solutions. The error bars indicate standard deviation. 178

List of Tables

Table 4-1: A comparison of saturation contact angles of sessile and sandwiched droplets of distilled water, Tris-HCl buffer solution and DNA solutions.....	104
Table 5-1: The experimental conditions for the droplets of distilled water, Tris-HCl buffer, 4 $\mu\text{g/ml}$ and 20 $\mu\text{g/ml}$ DNA solution. The standard deviations are also indicated.....	123
Table 5-2: the average of the maximum instantaneous velocity, and the average peak time for the experiment shown in Figure 5-28.	147
Table 5-3: The experimental conditions for the droplets of all solutions. The standard deviations are also indicated.....	156
Table 5-4: The comparison of minimum actuation voltage, and contact angle hysteresis, for the droplets of distilled water, Tris-HCl buffer, 4 $\mu\text{g/ml}$ and 20 $\mu\text{g/ml}$ DNA solutions.	157
Table 5-5: The average of maximum instantaneous velocity of the leading edge.....	161
Table 5-6: Electrowetting number (η_{EW}); the yellow highlights indicate the upper limits of the two linear sections in Figure 5-34	164
Table 5-7: The droplet effective contact line length for maximum leading edge instantaneous velocity.....	167
Table 5-8: Electrowetting force, F_m	167
Table 5-9: Shear force, F_{dd}	168
Table 5-10: Contact line friction force, F_f	168
Table 5-11: Contact angle hysteresis related static friction force, F_{th}	169

Abbreviations

AFM	Atomic force microscopy
CCD	Charged coupled device
CEW	Continuous electrowetting
CMOS	Complementary metal-oxide semiconductor
D4	4 $\mu\text{g/ml}$ DNA solution
D20	20 $\mu\text{g/ml}$ DNA solution
DEP	Dielectrophoresis
DI	Deionized water
DLC	Diamond-like-carbon
DMF	Digital microfluidics
DNA	Deoxyribonucleic acid
DNT	Dinitrotoluene
DW	Distilled water
EDL	Electric double layer
EDS	Energy dispersive spectroscopy
EDTA	Ethylenediaminetetraacetic acid
EHD	Electrohydrodynamic
EICE	Electrowetting on insulator coated electrode
EP	Electrophoresis
EW	Electrowetting
EWOD	Electrowetting on dielectric
fps	Frame per second

IPA	Isopropyl alcohol
ITO	Indium-tin-oxide
LOC	Lab-on-a-chip
LHE	Left hand electrode
MALDI-MS	Matrix assisted laser deposition/ionization mass spectrometry
PCB	Printed circuit board
PCR	Polymerase chain reaction
PECVD	Plasma-enhanced chemical vapor deposition
PVD	Physical vapour deposition
RHE	Right hand electrode
RPM	Round per minute
SALS	Small angle light scattering
SAOS	Small-amplitude oscillatory shear
SAW	Surface acoustic wave
SEM	Scanning electron microscopy
SOG	Spin-on-glass
T	Tris-HCl buffer solution
TGA	Thermogravimetric analyzer
TNT	Trinitrotoluene
TPL	Tri-phase-line
UCLA	University of California, Los Angeles
UV	Ultraviolet (radiation)

VOF	Volume-of-Fluid
BSA	Bovine serum albumin
BST	Barium strontium titanate
BZN	Bismuth zinc niobate
Ca	Calcium
CaO	Calcium oxide
Cl	Chlorine
CO ₂	Carbon dioxide
Cr	Chromium
Cr ⁺³	Chromium (III)
F	Fluorine
H ₂ CO ₃	Carbonic acid
HCl	Hydrochloric acid
H ₂ O	Regular water
KCl	Potassium chloride
Mg	Magnesium
MgCl ₂	Magnesium chloride
MgO	Magnesium oxide (magnesia)
N ₂	Nitrogen gas
Na	Sodium
NaCl	Sodium chloride
Na ₂ O	Sodium oxide

O	Oxygen
OH ⁻	Hydroxyl ions
Si	Silicon
SiN	Silicon Nitride
SiO ₂	Silicon dioxide
SiOC	Silicon oxycarbide

Nomenclature

γ_{lv}	Liquid-vapour interfacial tension
γ_{sv}	Solid-vapour interfacial tension
γ_{sl}	Solid-liquid interfacial tension
θ_0	Equilibrium contact angle (contact angle at no voltage)
θ	Contact angle after applying voltage / scattering angle
θ_{adv}	Advancing contact angle
θ_{rec}	Receding contact angle
r	Capillary radius
H	Capillary rise height
R	Radius of curvature / droplet radius
ΔP	Pressure difference
R_1, R_2	Principal radii of curvature
d_{stern}	Thickness of Stern layer
ϵ_{stern}	Permittivity of Stern layer
C_{stern}	Capacitance of Stern layer
d_{diff}	Thickness of diffuse layer
ϵ_{diff}	Permittivity of diffuse layer
C_{diff}	Capacitance of diffuse layer
ϵ	Permittivity
ϵ_r	Relative permittivity
$1/\kappa$	Debye length

q	Elementary charge (Coulombos)
n	Concentration of ions
K	Boltzmann's constant
T	Temperature
V	Applied voltage
C_{ins}	Capacitance of the insulator
C_{EDL}	Capacitance of EDL
ϵ_s	Permittivity of the dielectric layer (insulator)
d	Dielectric thickness
η_{EW}	Electrowetting number
C_{wEDL}	Total capacitance considering EDL
$C_{w/oEDL}$	Total capacitance without considering EDL
ϑ	Droplet volume
E	Energy
ρ	Density
m	Mass
h	Microchannel gap (μm)
B	Bond number
\vec{E}	Electric field
ϵ_a	Permittivity of the ambient fluid
\vec{F}_{el}	Electric force

F_m	Electrowetting force
E_{bd}	Electric breakdown strength
D	Diameter of sandwiched droplet
C^*	Overlap concentration
C_e	Entangled concentration
C	Concentration of ions / Electrical capacitance
∇	Nabla, Vector differential operator
\underline{v}	Velocity vector
μ / μ_l	Newtonian shear viscosity / droplet viscosity
$\underline{\underline{\tau}}$	Stress tensor related to the deformation of the fluid
\underline{g} / g	Acceleration vector / acceleration due to gravity
$\dot{\zeta}(t)$	Shear flow function
$\dot{\gamma}$	Shear rate
$\dot{\gamma}_0$	Constant shear rate
v_1	Velocity in the direction of flow/droplet instantaneous velocity at point 1
v_2	Velocity in the gradient direction /droplet instantaneous velocity at point 2
v_3	Velocity in the neutral direction / droplet instantaneous velocity at point 3
x_1, x	Cartesian coordinate system, direction of flow
x_2, y	Cartesian coordinate system, shear gradient direction
x_3, z	Cartesian coordinate system, neutral direction

t	Total time / $\sum \Delta t$
η	Steady state shear viscosity
η^+	Shear-stress growth coefficient
η^*	Complex viscosity
$G'(\omega)$	Storage modulus - elastic response
$G''(\omega)$	Loss modulus - viscous response
ω	Angular velocity
ω_c	Crossover frequency
δ	Phase difference between the strain wave and the stress response (phase lag)
$G'(p)$	Plateau modulus
\vec{q}	Scattering vector
λ	Light beam wavelength
$I(\vec{q})$	Intensity of the scattered light
$F(\vec{q})$	Form factor
$S(\vec{q})$	Structure factor
q_x	Component of \vec{q} along the x -axis
q_z	Component of \vec{q} along the z -axis
ϕ_l	The azimuthal angle between the x -axis and \vec{q}
$\Delta\rho$	Density difference
p	Perimeter of the sample plate (Wilhelmy balance method)

$\Delta\theta_v$	The difference between the contact angle in the absence of an electric field (θ_0) and the contact angle when the voltage is applied (θ)
$\Delta\theta_s$	The difference between the contact angle in the absence of an electric field (θ_0) and the saturation contact angle (θ_s)
θ_T	Contact angle at the top interface
θ_s	Saturation contact angle
I	Ionic strength
c_i	Molar concentration of ion i
z_i	Charge number of ion i
σ	Excess free energy of a drop on a solid surface
V_{min}	Minimum actuation voltage (threshold voltage)
α	Contact angle hysteresis
F_{dd}	Viscous flow force within the droplet
F_f	Contact line friction force
F_{ac}	Actuation force
v	Droplet velocity
ξ	Contact line friction coefficient
$A_1(x)$	Area of the droplet covering the actuated electrode
F_T	Threshold initiation force per unit length
F_{TH}	Contact line hysteresis related threshold initiation force per unit length
F_{th}	Contact line hysteresis related threshold initiation force

F_{TA}	Adsorption related threshold initiation force per unit length
F_{ta}	Adsorption related threshold initiation force
F_{net}	Total force
X	Axis perpendicular to the electrode edge
X_0	Overlap: position of the leading edge in the direction of X axis relative to the electrode edge before voltage is applied.
Y	Axis parallel to the electrode edge
Y_0	Offset: distance in the Y direction of the droplet center to the middle of the electrode before voltage is applied.
X_0, Y_0	Droplet start point
L_0	Length of the square electrode
ΔX_n	Instantaneous displacement
X_n	Total displacement
$X_n + X_0$	Droplet position
Δt	Time step (1/fps)
$\Delta X_n / \Delta t$	Instantaneous velocity
X_n / t	Average velocity, where $t = \sum \Delta t$
D_0	Initial diameter of sandwiched droplet (at no voltage)
ΔD	Droplet elongation
μ_l	Viscosity of a liquid
μ_{DW}	Viscosity of distilled water droplet
μ_T	Viscosity of Tris-HCl buffer droplet
μ_{D4}	Viscosity of 4 $\mu\text{g/ml}$ DNA solution

μ_{D20}	Viscosity of 20 $\mu\text{g/ml}$ DNA solution
v_{DW}	Instantaneous velocity of distilled water droplet
v_T	Instantaneous velocity of Tris-HCl buffer droplet
v_{D4}	Instantaneous velocity of 4 $\mu\text{g/ml}$ DNA solution
v_{D20}	Instantaneous velocity of 20 $\mu\text{g/ml}$ DNA solution
h_{DW}	Microchannel gap for the experiments on the droplets of distilled water
h_T	Microchannel gap for the experiments on the droplets of Tris-HCl buffer
h_{D4}	Microchannel gap for the experiments on the droplets of 4 $\mu\text{g/ml}$ DNA solution
h_{D20}	Microchannel gap for the experiments on the droplets of 20 $\mu\text{g/ml}$ DNA solution
F_{EP}	Electrophoretic force
f_f	Friction coefficient
η_{EP}	Electrophoretic mobility
\vec{v}_{EP}	Velocity of charged ions
h_x	Net projection of the string of DNA blobs in the direction of the electric force
L	Contour length of DNA chain
V_{ssat}	Static saturation voltage
V_{dsat}	Dynamic saturation voltage

Chapter 1

Background and Motivations

1.1) Introduction

Miniaturization of fluidic devices has become a technological trend^{1,2,3}. The most important consequence of this is an increase in the surface-to-volume ratio, which makes the control of the surface energies as one of the main challenges in microfluidics⁴. In the past two decades microfluidics-based lab-on-a-chip devices have received growing interest. Such systems are expected to revolutionize clinical diagnostics, DNA and protein analysis and many other laboratory procedures involving molecular biology^{5,6,7,8}.

Microfluidic systems can be classified into either continuous fluid flow or droplet-based systems. In the continuous flow systems, the movement of fluid through closed microchannels is made possible by different methods of manipulating such as external pressure sources, external mechanical pumps^{9,10,11}, integrated mechanical micropumps¹² or the electrokinetic mechanisms¹³. These systems are suitable for certain applications such as chemical separation and simple biochemical applications with predetermined tasks and functions; however, are less suitable for complex applications where a high degree of flexibility, scalability or complicated fluid manipulation is needed. In addition, these systems face challenges, such as low mixing efficiency, complex flow regulation in multichannel systems¹⁴, sample cross-contamination and diffusional dilution⁸. Figure 1-1 shows a continuous flow microfluidic device¹⁵.

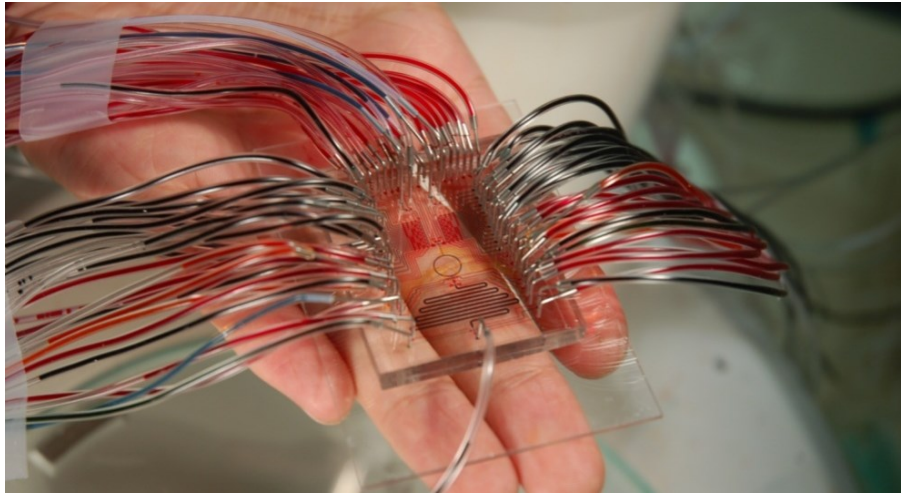


Figure 1-1: A continuous flow microfluidic device (Taken from reference: Wang *et al.*¹⁵)

However, an alternative approach, which is rapidly gaining popularity, is digital microfluidics - DMF^{16,17,18,19,20,21} where the liquid is manipulated in the form of discrete, unit-sized microdroplets⁸. In small scale droplet-based systems, capillary forces dominate²², thus the control of interfacial energies becomes an important role of manipulating droplets on surfaces.

There are several actuation mechanisms applied for DMF systems including electrowetting^{4,23,24,25,26,27}, dielectrophoresis^{28,29,30}, thermocapillarity^{31,32,33}, and optoelectrowetting^{34,35,36,37,38}. The other droplet handling technique is surface acoustic wave (SAW)^{39,40,41,42} where the droplet movement is achieved via the creation of acoustic waves rather than by changing the wettability of the surface⁸. The benefits of DMF systems are well documented and include sequential performance of the reactions or assays in a similar manner to traditional macroscale laboratory techniques where an extensive range of established chemical and biological protocols can be transformed to the microscale without the need to establish continuous flow protocols for the same reaction⁸. The other advantages include reduced reagent consumption, smaller analysis volumes, faster analysis, higher level of automation and increased instrument reliability²⁵. Among all the actuation techniques used for this purpose, electrowetting is particularly promising due to its simplicity (*i.e.* no pumps or valves) and reconfigurability (*i.e.* no hardwired fluid pathways)⁴³. Electrowetting can be combined with other actuation

mechanisms such as dielectrophoresis/electrophoresis to provide a technique for particle separation, sample enrichment^{44,45,46,47}, or collecting and separating magnetic particles^{8,48,49,50}. The application of electrowetting ranges from microfluidics-based biochips, also known as lab-on-a-chip or bio-MEMS, areas of optics (e.g. adjustable liquid lenses^{51,52,53} and fiber optics^{4,54}), various beam steering devices⁵⁵, area-tunable micromirrors⁵⁶ to electrowetting-based display screens and electronic papers (e-papers)^{27,57,58,59}.

Lab-on-a-chip applications of electrowetting were mostly initiated by the group of Fair at Duke University and that of Kim at UCLA. The idea behind these devices is to provide a substrate with an array of individually addressable electrodes that manipulate liquid microdroplets along arbitrary paths, depending on the programmable activation sequence of the electrodes⁴. In these systems, unit-sized droplets of a chemical sample such as DNA and protein solutions are dispensed from a source and transported through a network with discrete operations such as mixing, reaction, and splitting along the way^{4,60} (Figure 1-2).

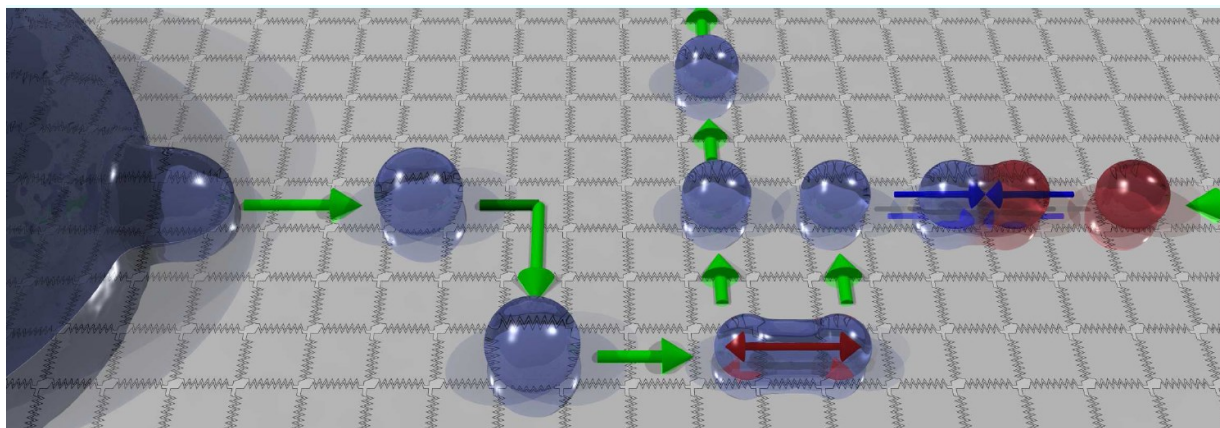


Figure 1-2: A digital microfluidic device showing the creation, motion, splitting and merging of the droplets (Taken from reference: Lienemann *et al.*⁶¹)

Within just a few years, a fast growing number of researchers has been working on the concept of electrowetting from the fundamental research stage to application-based digital microfluidic devices for chemical and biological assays^{8,62,63,64}.

In the present work, the ultimate goal is to identify the effect of fluid composition on the response of the droplet to electric field variables. This research will also enable us to configure the changes of characteristic parameters such as maximum velocity, average velocity, total displacement and droplet elongation with the applied voltage for droplets of DNA in solutions in order to improve the electrowetting-based microfluidic technologies for biological fluids.

1.2) Surface Tension Driven Flow

The force acting on the surface of a liquid, tending to minimize both the free energy and surface area is called “surface tension”. Gradients at a surface, such as in surface energy or temperature, can produce a bulk flow of liquid films or droplets. The oldest example is “tears of wine” which is most noticeable in wine that has a high alcohol content. This phenomenon, also called “wine legs” is a ring of clear liquid, near the top of a glass of wine, from which droplets are spontaneously formed and driven back into the wine due to surface tension imbalance arising from the evaporation of alcohol⁶⁵.

This mass transfer on, or in, a liquid layer due to a surface tension gradient, is called the “Maragoni effect” (or Gibbs-Maragoni effect) which was first explained by physicist James Thomson in 1855. Although the Maragoni effect is a surface flow with bulk flow being a secondary result, surface tension gradients can be also used to drive the bulk flow of liquid droplets on solid surfaces or within channels⁶⁶.

1.2.1) Actuation Principles

Consider a liquid drop resting on a solid surface (smooth, planar, rigid, and homogeneous) in the absence of the external electric field and gravity⁶⁷ (Figure 1-3). There is an equilibrium among the forces at the solid-liquid-vapour interface which is described by Young’s equation⁶⁸:

$$\gamma_{sv} - \gamma_{sl} = \gamma_{lv} \cdot \cos \theta_0 \quad \text{Equation 1-1}$$

where γ_{lv} , γ_{sv} and γ_{sl} are liquid-vapour, solid-vapour and solid-liquid interfacial tensions respectively. The angle between the solid-liquid, liquid-vapour interfaces at the three phase contact line is called the equilibrium contact angle (θ_0)^{8,69} where there is no applied voltage.

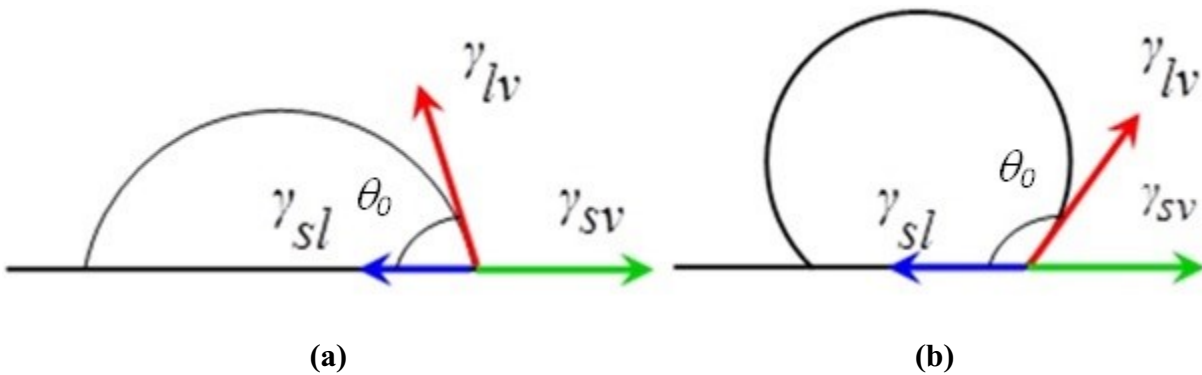


Figure 1-3: Equilibrium of forces acting on a droplet resting on a solid surface, (a) hydrophilic surface, wetting ($\theta_0 < 90^\circ$) and (b) hydrophobic surface, non-wetting ($\theta_0 > 90^\circ$)

By placing a small capillary of radius, r , in a liquid container exposed to the atmosphere, many liquids rise up to a certain height (H) (capillary rise) and wet the walls of capillary tube; forming a curvature (radius R) at the top (Figure 1-4). When the liquid rises up, the total energy reduction is equal to $(\gamma_{sv} - \gamma_{sl})2\pi rH$. This reduction is balanced by the work done to raise the column of the liquid, $\Delta P \pi r^2 H$, where ΔP is the pressure difference between the ends of the liquid column⁶⁶.

Balancing the energies gives:

$$\Delta P = \frac{2(\gamma_{sv} - \gamma_{sl})}{r} = \frac{2\gamma_{lv} \cos \theta_0}{r} \quad \text{Equation 1-2}$$

By minimizing the overall free energy of a liquid in contact with a solid, the general form of the fluid pressure across an arbitrarily curved surface is obtained.

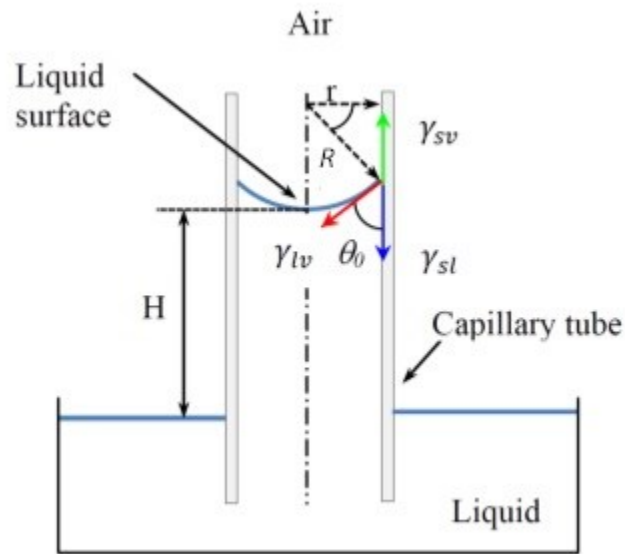


Figure 1-4: Illustration of a capillary tube immersed in a liquid risen to a height of H ($\theta_0 < 90^\circ$)

This is called the Laplace equation of capillarity or the Young-Laplace equation⁷⁰ :

$$\Delta P = \gamma_{lv} \left(\frac{1}{R_1} + \frac{1}{R_2} \right) \quad \text{Equation 1-3}$$

where γ_{lv} is the liquid-vapour interfacial tension, R_1 , R_2 , are the principal radii of curvature at the point of liquid surface in a 3D space, and ΔP is the capillary pressure.

The Laplace equation of capillarity (or the Young-Laplace equation) and Young's equation are two basic equations of surface tension and capillary phenomena.

The static value of the equilibrium contact angle, θ_0 which is a unique function of the interfacial tensions, is calculated by using Young's equation (Equation 1-1) ; however, experimentally observed contact angles are not uniquely determined by solid and liquid surface tensions, and usually there is a range of contact angles⁶⁹. It is common to record the largest contact angle as advancing (θ_{adv}) and the smallest contact angle as receding (θ_{rec}). The former is defined as the contact angle of the tri-phase line when the droplet is spreading over and wetting the surface, whilst the latter is the contact angle when the tri-phase is withdrawn over a pre-wetted surface as it happens in electrowetting and thermocapillary actuation processes^{4,8,67,71,72}. Contact angle hysteresis is the difference between these two angles which can be as small as 1.5 - 2° (e.g. de-ionized water droplet surrounded by silicone oil on an SiOC substrate⁸). The equilibrium contact angle, θ_0 , is within the range of advancing and receding contact angles and can be estimated from them. The origins of contact angle hysteresis are not well understood; however, the experiments show that with increasing roughness, advancing contact angle always increases, and receding contact angle decreases⁷³. Material heterogeneity is another issue associated with contact angle hysteresis^{66,69}. Therefore, understanding dynamic contact angle hysteresis is an important factor on electrowetting-based droplet manipulation⁷⁴.

To induce bulk flow of the droplet on a surface or within a channel, a surface energy gradient should exist at the vicinity of the droplet resulting to a net force which is calculated using the Laplace equation (Equation 1-3). However, if there is significant contact angle hysteresis, a surface tension gradient alone is not always adequate to induce motion of the droplets⁶⁶.

1.2.2) Methods of Actuation

As indicated before, in small scale droplet-based systems, capillary forces dominate²², thus the control of the interfacial energies plays an important role for manipulating droplets on surfaces. The manipulation of surface tension gradients, leading to a net mass transport of

liquids, can be controlled by chemical, thermal and electrical approaches. These methods are briefly described below.

1.2.2.1) Chemical Methods

A gradient in surface energy is generated using an external stimulus such as light (photochemical) or electrical potential (electrochemical). Generally, the surface energy of a solid substrate is specified by the atomic level composition of their outermost layer. In the photochemical approach, light-driven motion of liquids is achieved by alteration of chemical structures at the outermost atomic layer of solid substrates⁷⁵.

Ichimura *et al.*⁷⁶ investigated the macroscopic motion of liquids on a photosensitive surface by manipulation of UV light. They measured advancing (θ_{adv}) and receding (θ_{rec}) contact angles for various liquid droplets on a CRA-CM surface (a photoresponsive substrate). Based on Young's equation, changes in equilibrium thermodynamics properties cause a driving force for the motion of the droplets⁷⁶. Their observation showed that due to contact angle hysteresis, there was no motion generated for some liquids, even though θ_{adv} and θ_{rec} were altered after UV light irradiation. In this method, intensity and gradient of the light, droplet volume, surface tension and viscosity of the droplet all affect the velocity of the droplet. A very low maximum reported velocity of 0.05 mm/s exists for this method. For many liquids like water, moving the droplets was not possible due to contact angle hysteresis⁷⁶.

Electrochemical actuation is another technique used to create gradients in surface pressure, leading to fluid motion. The principle behind this method is that the gradients in concentrations of molecules can lead to changes in surface tension in the same manner that osmotic swelling is led by changes in bulk solute concentration⁷⁷. Generally, in a redox reaction, an atom's oxidation state changes as a result of electron transfer. The loss of electrons of a substance is oxidation, and the gain of electrons is reduction. Gallardo *et al.*⁷⁷ combined the electrochemical method with redox-active molecules (surfactants) to actively control the motion of aqueous and organic liquids in a channel. By application of potentials as low as +0.3 V and -0.3 V between two electrodes, surfactant was oxidized at one electrode and reduced at another, and thereby,

liquid drops were pumped in a fluidic network in the direction of decreasing surface pressure with an average velocity of 2 mm/s. No measurable liquid motion was observed in the absence of redox-surfactants. Unlike the other techniques which will be discussed in the following sections, this method does not offer independent control of multiple droplets since the electrochemical gradient must be formed along the full length of the electrode⁶⁶.

1.2.2.2) Thermal Methods

Thermocapillary pumping (TCP) is another mechanism used to transport liquids in a microchannel. Sammarco and Burns⁷⁸ developed a surface-tension driven pumping system to move liquid drops at the nanoliter and picoliter scale within a microfabricated channel. In this method, by heating the vicinity of a single drop at one side, a surface tension gradient across the diameter of the drop is obtained, resulting in a capillary pressure difference between the two sides of the droplet and finally droplet motion. Sammarco and Burns⁷⁸ observed velocities up to 0.33 mm/s for temperature differences between 10 °C and 70 °C. Their observations show that due to contact angle hysteresis, this method requires temperatures above the boiling point to induce motion. In order to overcome this problem, they used several strategies including surface treatments to reduce contact angle hysteresis, converging channels and the application of a small external pressure to assist in movement.

Although this system seems to be more promising than the previously mentioned techniques, complexity in design in addition to rapid evaporation, high power consumption, and heating of the liquid which is not desirable for many biological applications are factors that encourage researchers to explore other techniques.

1.2.2.3) Electrical Methods

The droplet-based lab-on-a-chip systems controlled by electrical methods operate under the principles of electrocapillarity and dielectrophoresis⁷⁹. Electrocapillarity⁸⁰ involves the changes of the interfacial tension at a liquid-liquid boundary by the application of electrical charges⁸¹. In 1875, the Nobel Prize winner, Gabriel Lippmann⁸², first studied electrocapillary effects, by applying voltage V to a mercury-electrode meniscus in a capillary tube⁴. The work of Lippmann and his followers became the basis of recent developments in the continuous electrowetting (CEW), electrowetting, and electrowetting on dielectric (EWOD) methods described in the following section.

In dielectrophoresis (DEP)^{83,84,85}, an electromechanical force is exerted on an electrically neutral particle subjected to a non-uniform electric field resulting to the motion of the particle⁷⁹ as shown in (Figure 1-5). The difference between electrocapillarity and dielectrophoresis is that the first is due to the presence of free charge at the interfaces while the latter is due to particle polarization⁷⁹. The term, dielectrophoresis, was first created by Pohl⁸⁶ in 1978, in order to clarify the differences between this effect and electrophoresis (EP)⁷⁹ as electrophoresis happens when a uniform field is exerted on a particle with a net charge and moves due to the Coulombic forces⁸⁷. In this instance, the particle will move in the direction of the field or against it, depending on the polarity of the charge on the particle. This phenomenon was first observed by Reuss⁸⁸ in 1809.

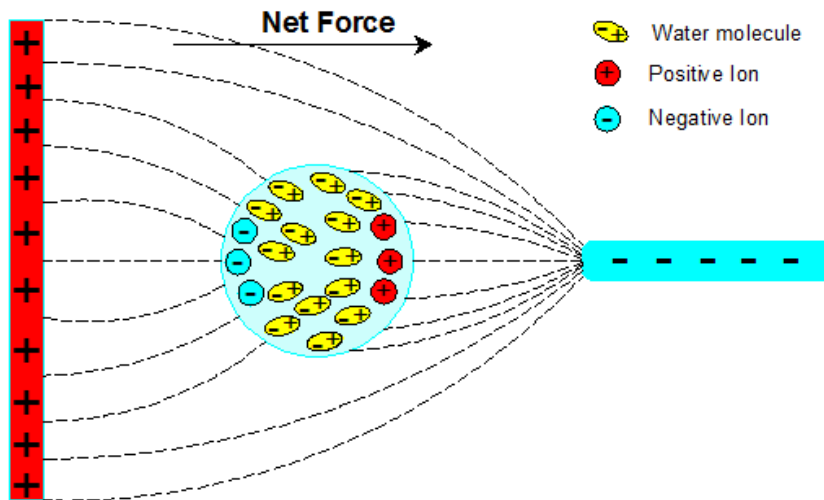


Figure 1-5: Schematic of a water droplet in a non-uniform electric field.

1.3) Electrowetting Effect

It is believed that the most feasible approach effectively creating a surface tension gradient is electrocapillarity⁸⁹. As mentioned before, continuous electrowetting (CEW), electrowetting on dielectric (EWOD) or electrowetting are electrocapillarity-based methods to modulate the interfacial tension forces and manipulate droplets⁷⁹. Continuous electrowetting (CEW) creates a non-uniform interface at the fluid-fluid interface (e.g. Mercury and electrolyte)⁷⁹. Lee and Kim⁸⁹ explored this phenomenon by placing a drop of liquid metal (mercury) in an electrolyte filled microchannel or capillary. By applying an electric potential across the length of the channel (electrodes), an electrostatic gradient was produced which resulted in a surface tension gradient and finally droplet motion (Figure 1-6). A rather high speed of 100 mm/s was achieved in this system; however, electrolysis (*i.e.* the electrolytic decomposition of water beyond a few hundred millivolts⁸) occurs.

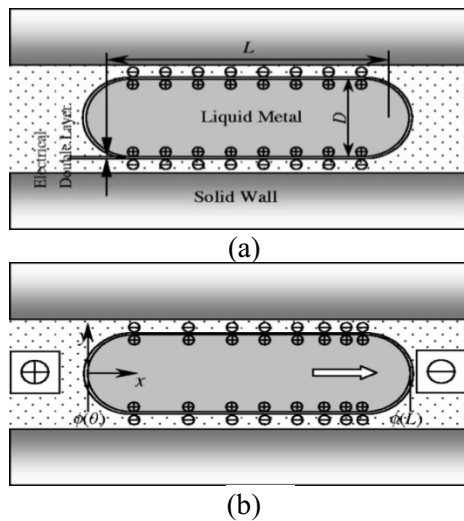


Figure 1-6: Continuous Electrowetting (CEW). (a) Electric Double Layer (EDL) and initial charge. (b) electrically induced surface tension gradient. (Taken from reference: Lee and Kim⁸⁹, IEEE Copyright line ©2000 IEEE)

Electrowetting on dielectric (EWOD) or electrowetting are methods where a thin layer of insulating solid material is placed between the droplet and the electrode to overcome electrolysis and accommodate the application of higher potentials^{4,79} (e.g. 100's of Volts in the early days^{90,91} and 15-80 V in air nowadays⁴³). This method which is also called electrowetting on insulator coated electrode (EICE)⁷⁹ was first introduced by Berge⁹² and Vallet *et al.*⁹⁰ in the 1990s. Berge experimentally showed that the voltage-induced contact angle reduction which was previously

observed for a droplet on a conducting surface (i.e. by applying electrowetting concept⁹³) could also be obtained by using an insulating surface covering a conductor⁴³.

To better understand electrowetting, consider Figure 1-7, where a conductive liquid droplet is initially at rest on a hydrophobic surface (θ_0). When an electrical potential is applied between the droplet and an insulated electrode, the solid-liquid interfacial energy decreases and consequently the contact angle (θ) decreases and wetting improves. It has been reported that the contact angle variations of more than 40° can be achieved by electrowetting⁸.

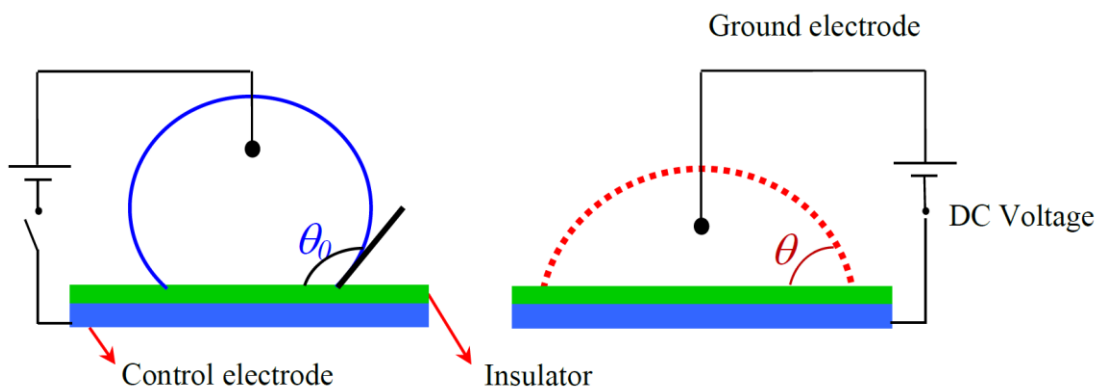


Figure 1-7: Wetting improves after applying voltage (dashed) to a droplet initially at rest on a solid surface (solid)

Electrowetting is very similar to, but distinct from continuous electrowetting (CEW), as it uses electric field to directly control interfacial tension between a solid-liquid interface instead of two liquid interfaces. This way, the energy may be controlled in a more precise manner through fixed solid structures rather than through an energized liquid medium; therefore, electrowetting can independently control multiple droplets⁶⁶. This system has become one of the most promising methods for digital microfluidics^{60,79}. Since Berge⁹², various configuration and platforms of EWOD have been reported. Mugele and Baret⁴, Berthier⁶⁷, Berthier and Silberzan⁹⁴ have thoroughly described electrowetting in their work whilst Pollack⁶⁶, Srinivasan⁹⁵ and Chatterjee *et al.*⁹⁶ have investigated the types of liquids that can be transported by this method⁸. Nelson and Kim⁴³ have created a table listing the benchmark achievements in technology development towards EWOD digital microfluidics during the early proof-of-concept era.

1.3.1) Electrical Double Layer (EDL)

In the absence of an electric field, the liquid is electrically neutral meaning that the amount of ions and counter ions are the same. However, under an electric field, the charges at the solid substrate attract the ions in the liquid increasing the charge concentration at the contact line of the droplet. Adjacent to the charged solid surface (Figure 1-8), there is a layer of ions which are strongly attracted to the solid surface; this layer is called Stern layer. For water, the Stern layer has a thickness (d_{stern}) comparable to the size of the ions at the solid/liquid interface with values between 0.1 nm^{97,98} and 0.5 nm^{97,99} and relative permittivity, ϵ_r , with estimated values between 5 and 10^{97, 98} which are lower than the bulk liquid because of the orientation of the water molecules⁹⁷. Depending on the applied voltage, the surface charges on this layer could be either positive or negative. From the Stern layer to the electrically neutral bulk fluid, there is another layer where the charge density gradually decreases to zero. This layer is called the diffuse layer which is composed of the ions attracted to the Stern layer because of the Coulombic force. The Stern layer and diffuse layer could be considered as two parallel-plate capacitors in series, each with the capacitances of $C_{stern} = \frac{\epsilon_{stern}}{d_{stern}}$ and $C_{diff} = \frac{\epsilon_{diff}}{d_{diff}}$ where C , ϵ and d are the capacitance, permittivity and the thickness of the relative layers respectively. The Electric Double Layer (EDL) consists of these two Stern and Diffuse layers. The capacitance of the EDL (C_{EDL}) is given by as Equation 1-4:

$$C = \frac{1}{\frac{1}{C_{stern}} + \frac{1}{C_{diff}}} \quad \text{Equation 1-4}$$

In order to know the value of d_{diff} , the effective thickness of EDL is defined as the Debye Length, $1/\kappa$ ⁹⁹:

$$\kappa = \sqrt{\frac{2q^2n}{\epsilon KT}} \quad \text{Equation 1-5}$$

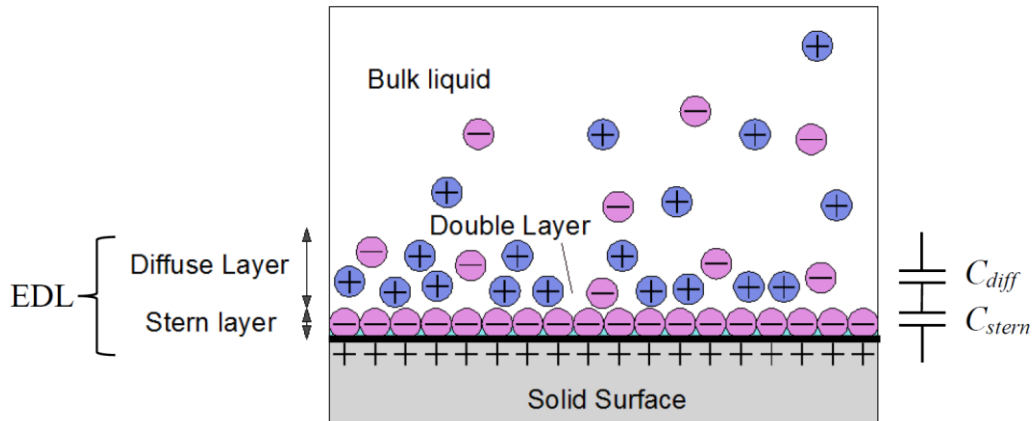


Figure 1-8: Schematic of the Electric Double Layer (EDL)

Where q is the elementary charge (Coulombs), n is the concentration of ions in the liquid ($1/m^3$), ϵ is the permittivity of the liquid (F/m), K is Boltzmann's constant ($1.38 \times 10^{-23} \text{ m}^2 \cdot \text{kg/s}^2 \cdot \text{K}$) and T is the temperature (K). This length decreases when the number of ions in the liquid increases. For instance, for distilled water, where the number of the ions in the solution is the least, this length is at its maximum value⁹⁷. Inserting values for water at 25 °C gives us the diffuse layer thickness of 0.964 μm , which is in agreement with the previously reported numbers for DI water with almost 1 μm thickness^{97,100}. Considering the relative permittivity of the Stern layer equal to 5 and the thickness of 0.5 nm, and the relative permittivity of the diffuse layer as that of the DI water, the total capacitance of double layer will be $7.15 \times 10^{-4} \text{ (F/m}^2\text{)}$. The values of d_{stern} and ϵ_{stern} are selected to give the minimal estimate of the EDL capacitance density. In section 1.3.2, this number will be used in comparison with the capacitance of the insulating layer and the effect of EDL on modeling electrowetting will be discussed.

Three different ways have been suggested to model the electrowetting phenomenon: The capacitance model, the energy minimization method^{101,102}, and the electromechanical approach^{103,79}. The capacitance model is discussed in detail in the following section.

1.3.2) Capacitance Model

In this thesis, the capacitance model is used for modeling the EWOD phenomenon¹⁰⁴. In this model, the energy stored in a capacitor is added to the Young's equation (Equation 1-1). The presence of an external electric field affects the free charges in the liquid which leads to their rearrangement. The resultant Coulombic force in the interface is the driving force for the liquid.

According to Young's equation, the solid-liquid interfacial energy γ_{sl} , and the contact angle (θ) are functions of the electrical potential while γ_{lv} and γ_{sv} remain constant with a good approximation. Based on this, Sondag-Huethorst and Fokkink proposed^{105,106}:

$$\gamma_{sl}(V) = \gamma_{sl}^0 + \gamma_{sl}^{el} = \gamma_{sl}^0 - \int \int C dV dV \quad \text{Equation 1-6}$$

where γ_{sl}^0 , γ_{sl}^{el} are the contributions from the chemical and electrical (potential-dependent) components to γ_{sl} respectively¹⁰⁷. C is the capacitance per unit area of the solid-liquid interface and V is the applied voltage. This interface can be considered of two layers: insulator and Electric Double Layer (EDL). Considering the dielectric layer and the EDL as two parallel-plate capacitors in series (C_{ins} and C_{EDL} respectively)^{106, 107} the total capacitance is calculated as:

$$\frac{1}{C} = \frac{1}{C_{ins}} + \frac{1}{C_{EDL}} \quad \text{Equation 1-7}$$

By inserting $C = \frac{\epsilon_s}{d}$ in Equation 1-6 where ϵ_s and d are the permittivity and the thickness of the solid-liquid interface:

$$\gamma_{sl}(V) = \gamma_{sl}(0) - \frac{1}{2} C V^2 = \gamma_{sl}(0) - \frac{\epsilon_s V^2}{2 d} \quad \text{Equation 1-8}$$

and finally, by using Young's relation (Equation 1-1), Young-Lippmann's relation between the applied voltage and the contact angle is obtained:

$$\cos \theta = \cos \theta_0 + \frac{\epsilon_s V^2}{2 \gamma_{lv} d} \quad \text{Equation 1-9}$$

Thus, by increasing voltage, the contact angle reduces and the droplet spreads or wets the surface. Note that γ_{lv} and γ_{sv} are independent of the applied voltage and are considered constant⁸⁰. The last term on the right-hand side of Equation 1-9 is sometimes called $\eta_{EW} = \frac{\epsilon_s V^2}{2 \gamma_{lv} d}$ or the dimensionless electrowetting number⁴. At low electric potentials, this theory explains the change between the wettability very well; though, it fails at high potentials because of contact angle saturation¹⁰⁸ (more detail in section 1.4).

In this thesis, Parylene C with an average thickness of 1.79 μm and relative permittivity of 3.15 is used as the insulator layer (the experimental condition design will be discussed in detail in the following chapter). The calculated capacitance for this layer is 1.56×10^{-5} (F/m²) which is approximately equal to 2 % of the minimum value of the EDL capacitance. By applying voltage to a droplet of distilled water in a system as shown in Figure 1-7 with Parylene C as the insulator, the total capacitance C (Equation 1-7) will be equal to 1.52×10^{-5} (F/m²). The calculated numbers for the capacitance of the insulation layer, C_{ins} and that of the EDL, C_{EDL} , show that $C_{ins} \ll C_{EDL}$, therefore the total capacitance $C \approx C_{ins}$ ⁴. Consequently, the effect of Electric Double Layer can be neglected in modeling the electrowetting phenomenon.

Figure 1-9 shows the effect of EDL on total capacitance with and without considering EDL, *i.e.* C_{wEDL} and $C_{w/oEDL}$ respectively. As it is shown, by decreasing the dielectric thickness d , C_{wEDL} will also decrease which means that the systems with thinner dielectric layers are more affected by EDL.

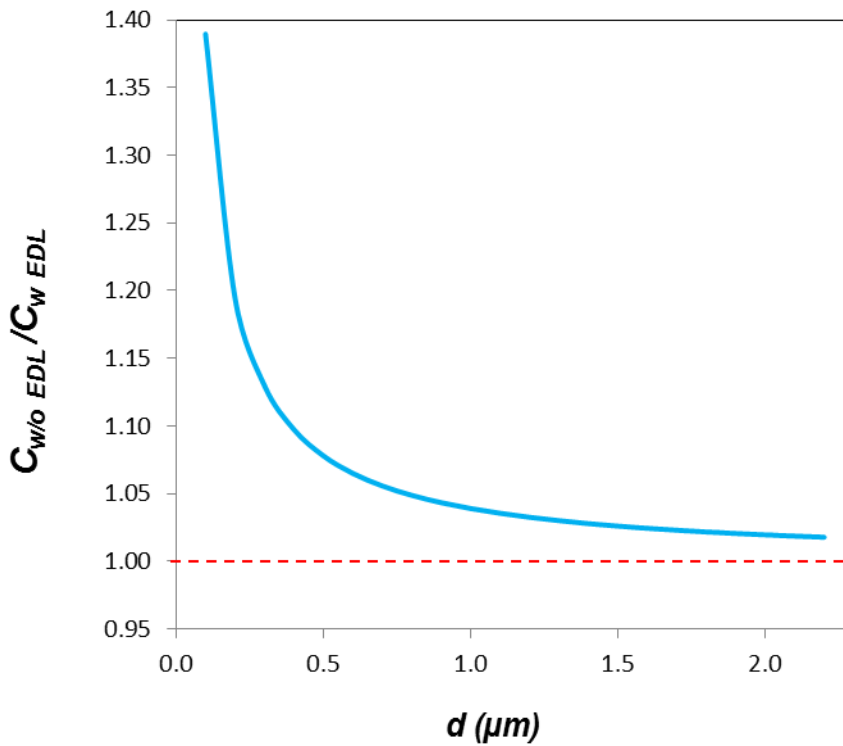


Figure 1-9: Effect of EDL on Total Capacitance with and without considering EDL, assuming a droplet of distilled water in a system with Parylene C (thickness of d) as the dielectric material.

1.3.3) Types of EWOD Microsystems

EWOD-based microfluidic systems can be divided into two distinct categories: open and covered⁸. The covered EWOD-based system is the most commonly used structure comprising two parallel plates typically separated by a distance of between 50 and 600 μm ^{8,14}. The experiments are usually done in air; however, the gap can be filled with a filler fluid such as silicon oil to prevent droplet evaporation and to reduce surface contamination²³. The ground electrode is located at the top plate and the bottom plate consists of either a planar electrode or an array of individually controllable electrodes. Each of these covered and open systems has advantages and disadvantages, e.g. dispensing, transporting and splitting of droplets are best performed in covered EWOD-based systems, while mixing and evaporation (*i.e.* in order to increase the sample concentration) are best performed in open systems^{8,67}.

In open EWOD systems, the electrical potential for droplet actuation is applied through the use of a conducting wire electrode (catenae, *i.e.* usually metallic wires often made of gold with a hydrophilic contact with the aqueous solutions⁶⁷) which are often placed on top of the hydrophobic surface or horizontally located at a specific distance parallel to that allowing the droplet to move from one electrode to the next alongside the catena^{8,67,109}; or via the use of a co-planar configuration where the bottom plate contains both the control and ground electrode^{8,17,110,111,112,113,114}.

In the systems with catenae located horizontally at a distance from the surface of the hydrophobic layer, it is very important that the catenae be carefully located parallel to the surface, aligned and centered with the electrode row; otherwise it will interfere with droplet motion⁶⁷. In this design, the droplet deforms at the region where the catena passes; however, the deformation stays localized to a small area close to the wire⁶⁷.

In co-planar designs, both the activation electrode and the ground electrode are located at the lower plate^{8,17}. The top plate is not required for this configuration as it is not responsible for droplet actuation, therefore the EWOD system becomes simpler and the effect of biomolecular adsorption will be minimized¹⁴.

1.4) Contact Angle Saturation

An important observation that is common in all EWOD studies is that the parabolic relation between the measured contact angle and the applied electric potential (*i.e.* Young-Lippmann's relation, Equation 1-9) is only valid below a critical threshold voltage, after which the contact angle saturates and becomes independent of the applied voltage^{4,8}. This phenomenon is called "Contact Angle Saturation". The saturation contact angle can be as high as 70-80° which is a serious limitation in electrowetting applications¹¹⁵, implying that it is impossible to achieve complete wetting⁸. However, in 2004, Krupenkin *et al.*¹¹⁶ showed that by using superhydrophobic nanostructured surfaces, it is possible to reach perfect wetting at voltages as low as 22 V^{8,116}. Despite various interpretations proposed to explain the saturation phenomenon, its origins have not yet been fully understood^{26,67,117}. In 1999, Verheijen and Prins¹¹⁸ related that to the charge trapped in or on the dielectric surface which has a stronger interaction with the dielectric layer than with the liquid. In other words, charge trapping could happen due to the attractive electrostatic force between ions in the liquid and the solid metal electrode. When this electrostatic force exceeds the force between the liquid and the ions, it moves toward the dielectric layer and remains in or at that layer¹¹⁸. They suggested that the trapped charge was uniformly distributed at a constant depth from the solid-vapour interface, extending past the tri-phase-line (TPL) to a length scale of at least the dielectric thickness, reducing the density of the charges at the solid-liquid interface, weakening the electrowetting force and eventually causing the contact angle saturation^{8,119}.

Vallet *et al.*¹²⁰ observed two other phenomena related to contact angle saturation. First, they proposed that air ionization at the TPL plays a key role in the contact angle saturation at high voltages. Although, they assumed that that droplet was surrounded by air; therefore, it fails to explain the occurrence of contact angle saturation when the droplet is surrounded by another liquid (e.g. silicon oil)⁸. They were also the first to observe the ejection of satellite droplets when the TPL becomes unstable at high voltages¹²⁰. This instability is due to the mutual repulsion of like charges at the vicinity of the contact line⁴. When the applied voltage exceeds a certain value, surface tension can no longer balance the electrostatic repulsion and ejection of the satellites droplets occurs creating a growing lateral space around the mother droplet⁴. Their finding was later reproduced by Mugele and Herminghaus¹²¹ who applied voltages on the order

of 600 V to droplets of deionized water, glycerol, and their mixtures. They noted that while many of these satellite droplets (also called daughter droplets) are stable for few seconds, some of the small ones are consumed by the bigger ones creating a new generation of bigger droplets due to the difference in Laplace pressure¹²².

Quinn *et al.*¹²³ called the saturation a natural thermodynamic limit. In 2009, Drygiannakis *et al.*¹¹⁷, proposed the transformation of dielectric material to a conductor where the electric field strength surpasses the material breakdown strength as a cause of contact angle saturation. In their hypothesis, it was stated that in the vicinity of the three-phase contact line (TPL) and when the critical voltage is reached, any increase of the applied voltage would not increase the electric field (*i.e.* consequently decreasing the contact angle); however, it would cause the conductive region to grow ahead of the contact line which also moves as the droplet deforms¹¹⁷ (Figure 1-10). This transition from a dielectric region to a conductive one is related to the charge trapping phenomenon which Verheijen and Prins¹¹⁸ had previously proposed¹¹⁷. The computational approach which Drygiannakis *et al.*¹¹⁷ presented is capable of modeling electrowetting beyond the saturation regime and the results are in good agreement with experimental data^{115,117}.

In 2011, Park *et al.*¹²⁴ proposed a dynamic phase field model of the electrowetting process and the corresponding morphology evolution. Their numerical approach revealed that at high voltages, instability is preceded by ejection of satellite droplets from the edge of the mother droplet. However, this instability can be avoided by increasing the surface energy of the droplet, like by adding salt. They explained that when the salt is added to a droplet, the ion-dipole bond formed between the water molecule and ion becomes stronger than the hydrogen bond formed between the water molecules; therefore an additional energy is needed to break the stronger bond raising the surface energy and consequently suppressing the instability¹²⁴.

Despite the diversity of explanations for contact angle saturation, it is not yet well understood^{26,117} and has been and remains the biggest challenge in electrowetting applications¹²⁵. It is probable that there is no unique explanation; however, it is clear that the divergence of electric fields at the TPL can induce several distinct non-linear effects⁴. Depending on the

specific experimental condition, each of these effects can dominate and may independently cause saturation⁴. In future, more work is required to identify these experimental conditions⁴.

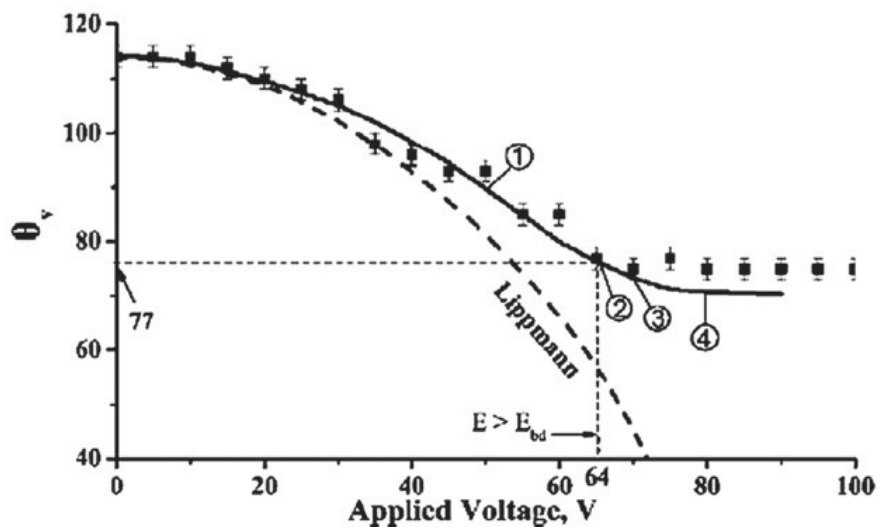


Figure 1-10: The contact angle as a function of voltage for a sample with 1 μm SiO_2 insulator covered by 20 nm Teflon hydrophobic top coating. Electric breakdown strength $E_{bd} = 10^9$ V/m. Experimental data (symbols), model curve based on local dielectric breakdown (solid line), and Young-Lippmann equation (dashed line). (Reprinted with permission from Drygiannakis *et al.*¹¹⁷, Copyright © 2009 American Chemical Society).

1.5) State of the Art

It was over 60 years ago when the earliest investigations on electrowetting with metal electrodes directly in contact with the electrolyte solutions occurred¹²⁶. Classical electrowetting first attracted practical attention in the early 1980's. Batchelder¹²⁷ demonstrated that water droplets can be transported on planar electrodes in a narrow gap filled with insulating fluid. In the 1990's, Vallet *et al.*⁹⁰ achieved large, yet irreversible contact angle variation on 12 μm thick polyethylene terephthalate (PET) films. They showed that solid insulation withstands higher electric fields (voltages up to 1000 V).

Following their investigation, Welters and Fokkink¹⁰⁷, and Verheijen and Prins^{118,128} produced reversible effects using high dielectric strength polymers such as polyimide and parylene for insulation and a fluoropolymer (Teflon AF) coating to increase the hydrophobicity and reduce contact angle hysteresis. They used 10 μm thick films and voltages up to 300 volts. In 1998, Washizu¹²⁹ fabricated a network of individually polarizable electrodes covered by an insulation layer and a hydrophobic Teflon film, and demonstrated transport, deflection and mixing of water droplets. Later in 2001, Pollack⁶⁶ demonstrated the feasibility of droplet actuation in a digital microfluidics (DMF) system in both silicon and air filled mediums using Teflon AF as the hydrophobic surface. By means of a top planar electrode used as a cover, Washizu's work was improved and a maximum speed of 30 mm/s was achieved.

In 2002, Pollack *et al.*²⁵ used the electrowetting technique for droplet generation, mixing and splitting over the volume range of nanoliter to microliter. Pollack's work was soon followed by many other researchers and became the basics for EWOD-based microfluidic systems. Some of the earliest demonstrations of these systems were reported by⁸ Lee *et al.*¹³⁰, Moon *et al.*¹³¹, Cho *et al.*⁸⁰, and later by Paik *et al.*^{132,133}, Yoon and Garrell¹³⁴ and Srinivasan *et al.*^{135,136}. Srinivasan *et al.*¹³⁵ presented a fully automated and integrated EWOD-based microfluidic Lab-on-a-chip (LOC) assay for *in vitro* glucose measurement used in the clinical applications⁸.

Another application of the EWOD-based systems is multiplexed proteomic sample preparation for MALDI-MS (matrix assisted laser desorption / ionisation mass spectrometry)⁸

which is a soft ionization technique allowing the analysis of biomolecules and large molecules which tend to be fragile when ionized by more conventional methods. This application was first introduced by Srinivasan *et al.*¹³⁷ and subsequently by Wheeler *et al.*¹³⁸ and Moon *et al.*¹³⁹. Generally, in these systems, the sample droplets are transported to target areas where they are dried and their impurities are removed by rinsing droplets. Afterwards, the matrix-containing droplets are delivered and dried and the samples are analyzed *in situ* by MALDI-MS¹³⁹. One of the advantages of these systems is that these functions are integrated into a single chip for parallel processing of multiple samples¹³⁹; however, devising suitable protocols for the activation of the control electrodes is challenging⁸. Some of these challenges have been addressed by Böhringer¹⁴⁰ and Griffith *et al.*¹⁴¹.

One of the other practical difficulties in EWOD-based actuations is to address each of the electrodes individually⁸. In 2004, Gascoyne *et al.*¹⁴², individually addressed a large number of electrodes with a 32×32 programmable element dielectrophoresis chip based on CMOS (complementary metal-oxidesemiconductor) technology (*i.e.* a technology used for constructing integrated circuits)⁸. Their work was then followed by Li *et al.*¹⁴³ with the integration of EWOD actuation on CMOS chips⁸. Recently, Gong and Kim¹⁴⁴, and Abdelgawad and Wheeler^{145,146}, have investigated the application of multilayer PCB (printed circuit boards) substrates for EWOD-based devices. These PCB-EWOD devices are suitable for low-cost / disposable applications and have shown to be comparable to those EWOD-based systems traditionally fabricated on polished glass or silicon⁸.

The required control voltage to manipulate the droplets in EWOD devices is also one of the most important parameters which has recently attracted the attention of researchers. Therefore, by carefully selecting a dielectric layer with a high relative permittivity (ϵ_s) and appropriate thickness, the control voltage can be significantly reduced^{8,143}. In this respect, Dielectric materials such as barium strontium titanate (BST) or bismuth zinc niobate (BZN) appear to be very promising materials⁸.

Improving the properties of the hydrophobic layer which plays a significant role in creating the equilibrium contact angle is another important factor in EWOD devices, and currently considerable effort is being directed towards that⁸. One of the most promising techniques to

create as large an equilibrium contact angle is using superhydrophobic surfaces and patterning the substrate with nanostructured pillars^{8,147,148,149}. However, electrowetting on superhydrophobic surfaces still suffers from a number of problems associated with the non-reversibility of the contact angle⁶⁷.

Recently, a wide range of EWOD-based technologies have been developed for chemical, biological and biomedical procedures where the highly flexible and reconfigurable nature of EWOD microfluidics has been demonstrated to possess the desired features for these applications^{8,64}. These applications range from⁶⁴:

- EWOD-based glucose arrays^{8,17,135,136}
- EWOD-based enzyme assays^{64,150, 151,152}
- EWOD-based immunoassays^{49,63,64}
- EWOD-cell-based assays^{47,64,153,154}
- EWOD-based TNT assays^{8,155} (*i.e.* the use of EWOD-based microfluidics for detecting nitroaromatic compounds such as commercial-grade 2,4,6-trinitrotoluene (TNT) or 2,4-dinitrotoluene (DNT))

- EWOD-based PCR systems (*i.e.* polymerase chain reaction (PCR) devices based on EWOD)^{8,14,156,157}
- EWOD-based DNA sequencing^{8,64,158}, hybridization^{14,64,159}, and cloning techniques^{14,64,160}

- EWOD-based proteomics^{64,137,138,139,161,162,163,164}
- EWOD-based tissue engineering^{64,165}

Along with the experimental studies, numerous analytical and numerical investigations have been also performed in order to clarify and support the empirical results. Namely the dynamics of EWOD-based actuations of droplet transport have been studied by a number of researchers. In 2002, Ren *et al.*¹⁶⁶ formulated a model to describe the dynamics of electrowetting-induced transport of liquid droplets as a function of applied voltage and relevant

physical parameters including viscosity, contact-line friction, geometric factors and surface tension¹⁶⁶.

Bahadur and Garimella¹⁰⁴ developed an energy-based analytical model to estimate the actuation force on a droplet moving between two electrodes. Their results show the effect of operating voltage, fluid properties and droplet geometry on droplet motion disclosing that contact-line friction is the dominant opposing force for the electrowetting-induced droplet movement¹⁰⁴.

Numerical investigation of electrowetting in microchannels was also conducted by Dolatabadi *et al.*¹⁶⁷. By employing Volume-of-Fluid (VOF) technique, the droplet flow under electrowetting actuation was characterized by parameters such as applied voltage, channel dimension, electrode size and the resultant velocity¹⁶⁷. Arzpeyma *et al.*^{168,169} conducted another numerical study to model droplet behavior under the electrowetting actuation. Their simulation included an algorithm to simultaneously calculate the space and time dependent electric field in the domain considering static contact angle¹⁶⁹.

In 2007, Chakraborty and Mittal¹⁷⁰ devised a theoretical approach to analyze the droplet dynamics in a parallel plate microchannel under the electrocapillary actuation. They concluded that there exists a threshold limit on the value of the interelectrode pitch beyond which the overall droplet transfer rate can be lowered to a significant extent. Furthermore, their investigations revealed that the optimal interelectrode spacings are strong functions of the applied voltage and the dielectric layer thickness¹⁷⁰.

An electromechanical model was then presented by Chatterjee *et al.*¹⁷¹ for calculating the forces on insulating and conducting liquids in two-plate devices. Their findings show that for conductive liquids, the electrowetting (EW) force dominates, while for dielectric liquids, both electrowetting (EW) and dielectrophoretic (DEP) forces contribute, and in some cases, the DEP force may dominate¹⁷¹.

Another numerical study was carried out by Keshavarz *et al.*⁷⁴ introducing a dynamic contact angle model which showed a significant improvement in the numerical results in comparison with the experimental data from literature⁷⁴. A new crescent shape electrode was

then proposed by Rajabi and Dolatabadi¹⁷² which is expected to facilitate device fabrication and droplet actuation in electrowetting though it suffers from the movement irreversibility¹⁷³. To resolve this problem, a two-way crescent array of electrodes was introduced¹⁷³.

In 2008, Bavière *et al.*¹⁷⁴ experimentally investigated the influence of viscosity on the dynamics of sessile droplets in the capillary regime induced by EWOD actuation, and compared their results with Brochard's theoretical model¹⁷⁵. Their findings revealed that the transport velocity is very sensitive to the droplet viscosity, and higher droplet velocities are achieved at lower viscosities¹⁷⁵. They also showed that the droplet transport velocity is also limited by dynamic saturation¹⁷⁵.

In 2009, Sen and Kim¹⁷⁶ reported the contact line dynamics of sessile water droplets. They also developed a model providing a good match to their experimental results indicating a linear relationship between the maximum droplet velocity and the applied voltage. Their finding was then contradicted by the model presented by Annapragada *et al.*¹⁷⁷ predicting a quadratic dependence of the maximum velocity on the applied voltage¹⁷⁷.

A new analytical model on the actuation force was then developed by Schertzer *et al.*¹⁷⁸ predicting the droplet transient position and velocity. They modeled the opposing forces (*i.e.* viscous shear forces in the droplet from the wall and the surrounding medium, and contact line friction; for more detail refer to Chapter 5) based on the models presented by Berthier⁶⁷, Bahadur and Garimella¹⁰⁴, and Bavière *et al.*¹⁷⁴. They also empirically validated their analytical model (voltage of 110 V) showing the dependency of the droplet transient position and velocity on the EWOD device geometry and droplet fluid properties¹⁷⁸. Their analytical model provides an argument for neglecting the effect of microchannel gap on the capillary force in practical EWOD devices¹⁷⁸.

Modeling the dynamics of electrowetting droplet motion was subsequently further explored by Oprins *et al.*¹⁷⁹ in 2012; where the dynamic droplet motion was modeled by a linearized equivalent damped mass-spring system; and it was shown that the optimal switching frequency (*i.e.* the inverse of the time that the droplet leading edge requires to travel from the beginning to the end of a single electrode^{168,180}) can be estimated by twice the natural frequency of the linearized damped mass-spring system¹⁷⁹.

In 2013, Hong *et al.*¹⁸¹ investigated the effect of drop size and viscosity on spreading dynamics of sessile droplets of water and glycerol mixtures and found out that a smaller drop reaches its maximum base radius faster than a large drop¹⁸¹. They also empirically determined that the maximum droplet velocity is slightly dependent on drop size but linearly proportional to the electrowetting number (section 1.3.2) combined with a weak effect from drop viscosity¹⁸¹.

At the same time, a review of fundamentals and applications of contact angle hysteresis was published by Eral *et al.*¹⁸² as there is still a lack of consensus on how to incorporate a description of contact angle hysteresis into physical models. Their study introduces the formalism and models for implementing contact angle hysteresis into relevant physical phenomena such as electrowetting¹⁸².

In 2015, Cui *et al.*¹⁸³ presented a dynamic saturation model of droplet motion on an EWOD-actuated sessile droplet showing the effect of device physical properties (*e.g.* dielectric thickness, dielectric constant, electrode length,...), hydrophobic surface material, and interface conditions on the dynamics of EWOD-based droplet transport¹⁸³.

Ni *et al.*¹⁸⁴ further investigated the electrowetting phenomenon by measuring the actuation force and showed that lowering the fluid surface energy can induce larger contact angle change and higher droplet speeds under the same voltage¹⁸⁴.

Recently, Guan and Tong¹⁸⁵ numerically investigated the fluid dynamics of water droplet transport in a parallel-plate EWOD device. Their findings revealed that hysteresis has only slight effects on both droplet shape and timescale of the transport process as hysteresis angle is much smaller than static contact angle; however, the transport time reduces as the microchannel gap increases¹⁸⁵. Moreover, the droplet shape experiences a larger deformation when the gap height is reduced¹⁸⁵.

From the early proof of electrowetting concept up until present, the growing number of publications in the EWOD field is a good indication of the popularity of this exciting diverse field⁶⁴. Although numerous numerical models and microfluidic prototypes based on electrowetting technique have been proposed and developed, there are still certain fundamental aspects of electrowetting-based droplet transport which are poorly understood¹⁷⁴. The efforts in

furthering the understanding of electrowetting phenomenon along with the work exploring the applications, novel device structures, and computer-aided design methods are all necessary to put the field on a solid footing and to find the unique place that the technology can fill¹⁷.

The behaviour of transient droplet shape when a voltage is suddenly applied has received less attention than that of static droplet shape; since the latter is well characterized by the Young-Lippmann's relation on the basis of the balance of surface tension and electrowetting force, while additional dynamic forces are at play during the transient process¹⁷⁷. Droplet motion is a complex physical phenomenon, and due to the great difficulty of conducting experiments at such small scales, it is still a subject of research⁶⁷ numerically and experimentally.

1.6) Research Objectives

Although the study of EWOD systems has been conducted for many years, the physics of droplet transport is not yet fully understood. It is perhaps a reflection of the fact that it is technically difficult to experimentally analyze the droplet motion due to the complexity of the transport process occurring at the microscale¹⁸⁵, specifically for the biological fluids such as DNA solutions. To better assess the electrowetting phenomenon of such complex solutions, the physics of electrowetting of aqueous biopolymer solutions should be completely understood. Such a fundamental understanding currently does not exist. For this purpose, the effect of fluid composition (*i.e.* different concentrations of DNA solutions and the type of buffer solution) on the static response of the droplet to electric field variables such as applied voltage has to be identified.

In the transient response, the time and voltage dependency of the parameters such as droplet speed, total displacement, and elongation of the droplets of distilled water, Tris-HCl buffer and the DNA solutions will be studied. Among these parameters, the droplet speed is a key factor which controls the rate of microfluidic operations in lab-on-chip systems¹⁰⁴. Our ultimate goal is to investigate the effect of electrophoresis on the dynamics of DNA solutions.

Accomplishing the objectives of this research was not possible without overcoming the material limitations in the experiments such as dielectric material breakdown and electrolysis. For this purpose, the failure mechanism of the samples which exhibited electrolysis will also be analyzed and characterized (Appendix J).

Overall, the results of this study will help us to better understand, analyze, design and prototype the microfluidic-based systems for DNA solutions.

1.6.1) Thesis Structure

In current chapter, the theory behind the electrowetting effect and the achievements in the development of EWOD systems from the early proof-of-concept era until recent years was presented; and it was discussed that the contact angle saturation still remains as one of the biggest challenges in electrowetting applications.

The next chapter gives a complete explanation on system configuration and material design, design and fabrication of the experimental set-up, and the microfabrication of control electrodes. In chapter 3, in order to get more familiar with DNA solutions, some limited rheological and SALS experiments are performed on 3000 $\mu\text{g/ml}$ DNA solutions to investigate their macroscopic and microscopic structures under the application of a shear flow with and without the application of an electric potential.

The experimental studies in chapter 4 will help us to verify the effect of the type of buffer solution on the contact angle of DNA solutions. It also includes the static contact angle measurements of sessile and sandwiched droplets of DNA solutions on planar electrodes by means of an in-house developed contact angle measurement apparatus and obtaining their saturation contact angles; in the case of sandwiched droplets, the experiments will be performed in two different microchannel gaps of 300 and 600 μm .

In chapter 5, we will move the droplets of DNA solutions on single square electrodes using electrowetting. Image analyses on droplet transport will help us to configure the changes of characteristic parameters such as maximum velocity, average velocity, acceleration and droplet

elongation with time and voltage, and compare the behavior of different concentrations of DNA solutions with that of distilled water and the selected buffer solution.

In the last chapter, the conclusions will highlight the importance of the obtained experimental results in this study.

Chapter2

Design of Materials and Experimental Methodology

2.1) Determination of Droplet Volume Range

In order to design and control any application of EWOD devices such as microfluidics systems, we need to decide which physical mechanisms are dominant in the device and which physical effects are negligible¹⁰². At equilibrium, a droplet of water deposited onto a solid surface will assume a spherical cap to minimize its free energy. This energy $E(R, \theta; p)$ is due to liquid-vapour, solid-liquid and solid-vapour interfaces plus the energy stored in the bulk due to external fields such as gravity and imposed electric potentials. It is dependent on the drop radius R , the contact angle θ , and p which is any relevant system field such as applied voltage V , dielectric constant ε and nominal liquid ion concentration C_0 . At equilibrium the energy is minimized subject to the constraint that the liquid volume must remain constant¹⁰².

In the case when the total potential energy includes only the interfacial energies, minimizing $E(R, \theta; p)$ will define an equation which is exactly Young's equation (Equation 1-1). If other additional effects such as electrical energy in the solid dielectric layer, electrical energy in the liquid, gravitational terms, or ion concentration effects are also included, then additional terms will be added to Young's equation. In this section, our concern is to evaluate the effect of

gravity; using the underlying non-dimensional number, called the “Bond Number” which determines the magnitude of gravity effects compared to surface tension effects.

The Bond number can be defined as $B \equiv R^2 \rho g / \gamma_{lv}$, which means that it scales with the drop radius squared. When this number is very small, the gravity is negligible compared to the interfacial term. For small drops of liquid, for example 1 to 3 μl , this ratio will be below 0.1 and gravity can be easily neglected. Therefore, if we want to neglect the effect of gravity in our calculations and achieve a good simulation of a microchannel, the droplet volume is considered to be less than 3 μl (Figure 2-1).

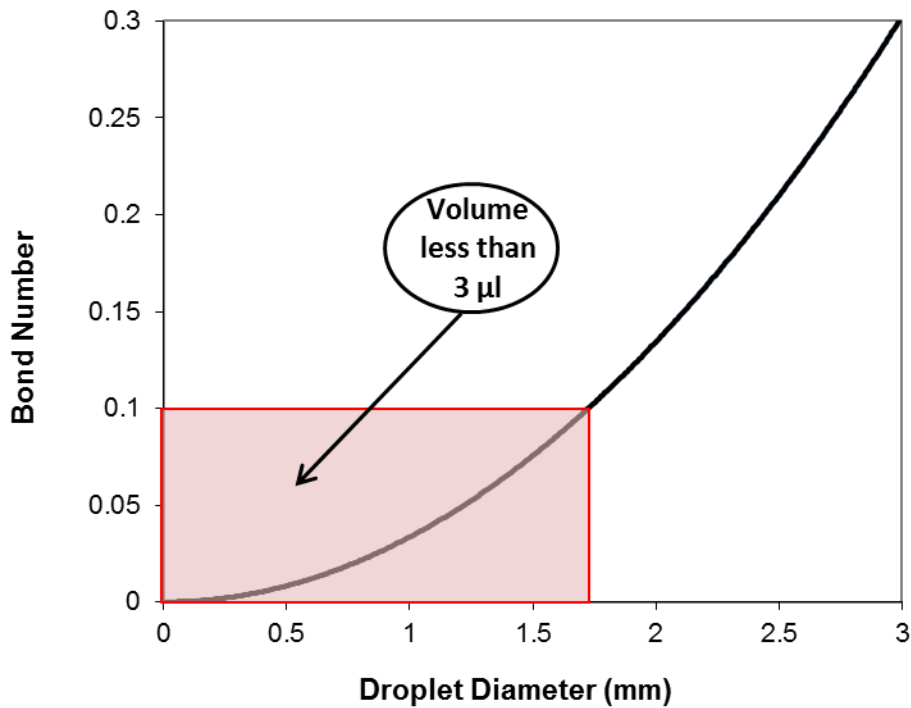


Figure 2-1: Changes of Bond Number with droplet diameter for choosing the appropriate droplet volume to neglect the effect of gravity

2.2) System Configuration

Electrowetting is a technique which provides potential control of the solid-liquid interfacial energy; though, droplet microactuation also depends on asymmetrical energization of this interface⁶⁶. As explained in section 1.3.3, the covered EWOD-based system is the most commonly used structure comprising two parallel plates typically separated by a distance of between 50 and 600 μm ^{8,14}. This asymmetry can be obtained by dividing the planar electrode in Figure 2-2 into an array of multiple independently controlled electrodes as shown in Figure 2-4. Depending on the type of the experiments, one or the other of these configurations has been used in this research. Studying the effect of electrical potential on static contact angle was done in the configuration with a planar electrode on the bottom plate, while the study of droplet motion has been performed in the microchannels with individually addressable electrodes.

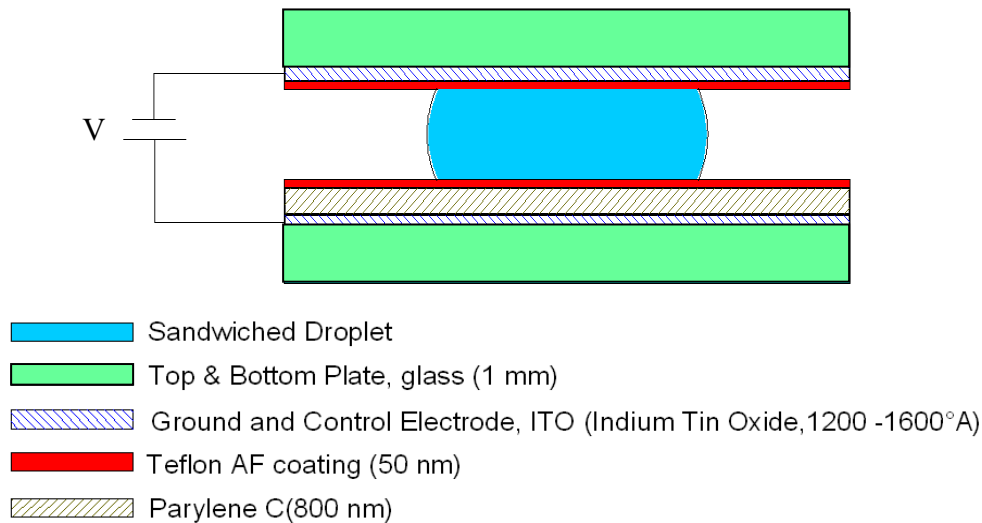


Figure 2-2: Sandwiched droplet on a planar electrode

As shown in Figure 2-2 and Figure 2-4, a polarizable and conductive liquid drop is sandwiched between two plates, and the surrounding filler is air. The bottom planar electrode or discrete control electrodes are covered by an electrically insulating coating and both top and bottom plates are coated by a hydrophobic layer of Teflon AF (for more details on material design, refer to section 2.2.1). The voltage is applied to the control and ground electrodes;

however, there is a voltage drop in the actual value of the voltage reached to the sandwiched droplet. The contact area of the droplet and bottom plate should be slightly larger than the pitch of the electrodes to create an overlap between the droplet and adjacent electrodes. This overlap may be increased through use of interdigitated electrodes illustrated in Figure 2-4 (c). This design with zigzag sides helps to increase the dynamic range of transported droplet volumes and reduce the sensitivity of the system to the position of the droplet with respect to the electrode⁶⁶. Although the interdigitated electrode shapes have been widely used in EWOD systems, they have their own shortcomings. Not only is this electrode shape very difficult to layout, fabricate and model due to its complex shape, but also the insulator between the gaps is easily subject to voltage breakdown because of the sharp voltage contours created¹⁷². Therefore, in this research, fundamental electrowetting actuation studies on single electrodes have been mainly performed on non-interdigitated square electrodes. The detail of these electrode shapes is given in section 2.6.

Digital microfluidics is a mechanism which is being used for transporting, cutting, and merging of liquid droplets. This can be done by switching the electrodes on and off sequentially. When all the electrodes are at the same potential, the shape of the droplet remains unchanged; however, by applying a potential difference between the electrode underneath the droplet and the other electrodes, a surface tension gradient is created which causes the droplet to move onto the charged electrode. By referring to the Young's governing equation (Equation 1-1), the sequence of events can be summarized as:



Figure 2-3: Sequence of events when applying voltage

However, the droplet shape does not return to a sphere even after all electrodes are turned off which is likely an effect of contact angle hysteresis.

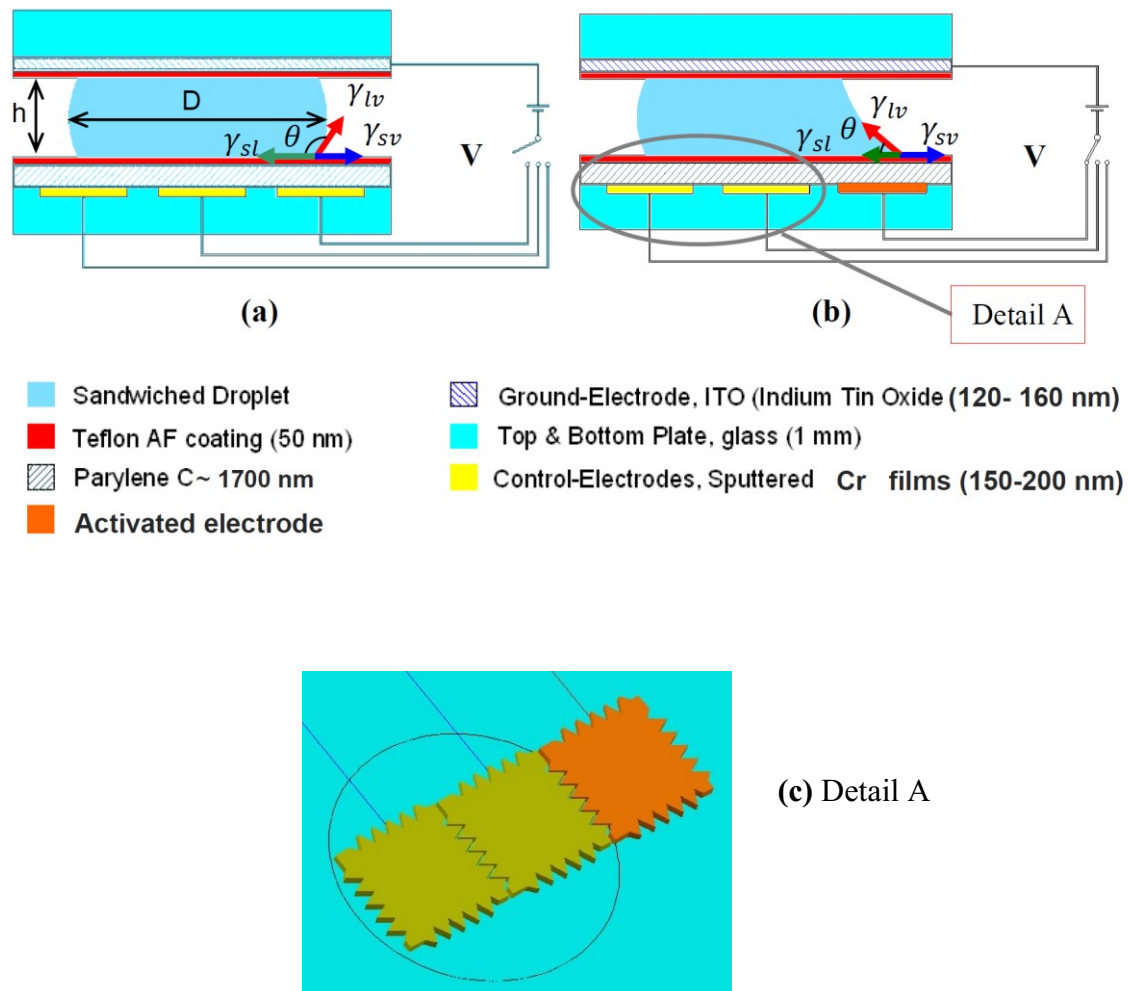


Figure 2-4: Schematic diagrams of a parallel plate microchannel; definitions of contact angle (θ) and surface tension at different interfaces; γ_{lv} , γ_{sv} and γ_{sl} which are the surface tensions at the liquid-vapour, solid-vapour, and solid-liquid interfaces respectively, (a) with no voltage applied (b) voltage is applied on the first electrode which has reduced the surface tension γ_{sl} causing the droplet deformation. (c) Detail A, as shown in (b), an example of interdigitated electrode shape.

2.2.1) Material Design

Choosing the best materials for each component is one of the challenges in fabrication of microchannels. In this section, material issues related to the covered EWOD-based microfluidic systems used in this research are discussed. As shown in Figure 2-2 and Figure 2-4, there are three types of materials required for an operable device: a dielectric material to provide the capacitance between the liquid and conductor, a conductive material to form the electrodes, and finally a hydrophobic coating at the interface of the insulator and the liquid. The material design in this section is based on the research done by Polack⁶⁶ which has been adapted in most published studies.

Substrate:

The top plates are glass microscope slides (75×25×1 mm, pre-coated with ITO (Sigma Aldrich). The bottom plates are glass microscope slides (50×25×1 mm, pre-coated with ITO (Sigma-Aldrich) for the experiments on planar electrodes, or glass or silicon wafers (50×25×0.5 mm - McGill Nanotools Microfab center¹⁸⁶) for the experiments on patterned electrodes.

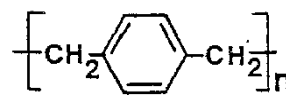
Insulator:

The insulation for the electrodes should ideally possess: high dielectric constant, high dielectric strength, low intrinsic charge, good mechanical stability, and good solvent resistance.

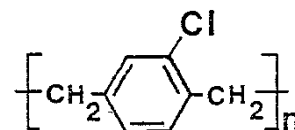
There are several options for the insulator (Silicon Dioxide (SiO₂), PECVD of (SiO₂), Silicon Nitride (SiN), Diamond-Like-Carbon (DLC), Spin-on-Glass (SOG), Polyimide, and Parylene); however, most literatures suggest that Parylene is the best choice⁶⁶. In this section, the information related to Parylene has been adapted from the website of Specialty Coating Systems company (SCS, *Clear Lake, USA*)¹⁸⁷.

Parylene is a generic name for a family of crystalline para-xylylene polymers that are deposited from the vapor phase at room temperature under moderate vacuum. This material can

provide a conformal, uniform and pinhole-free coating and has an excellent combination of chemical, electrical and mechanical properties. Most commonly used are Parylene C and Parylene N. Parylene C is produced from a similar monomer as Parylene N but modified only by the substitution of a chlorine atom for one of the aromatic hydrogens. Parylene C has a higher dielectric constant at sub-micron thickness and has a higher breakdown voltage than Parylene N, while Parylene N has superior thermal properties. One of the properties of Parylene N and C is that they can be formed in extremely thin films that withstand high voltages (Figure 2-6) before a portion of the dielectric layer degrades and becomes an electrically conductive layer.



Parylene N



Parylene C

Figure 2-5: Chemical structure of Parylene N,C.

Thus, Parylene C which is an excellent choice for EWOD-based systems has been chosen for this research. The samples are coated at Specialty Coating Systems (SCS, *Clear Lake, USA*). The samples with planar electrodes are coated with 800 nm thickness Parylene C, while the samples with patterned electrodes are coated with Parylene C with an average of 1.79 μm thickness.

Electrode Conductor:

The control electrode on the bottom plate can be made of any thin metal film; however, it needs to be a conductor with good adhesion to glass. Cr films and Indium-tin-oxide (ITO) are two conductors widely used in EWOD-based research. Sputtered Cr films (150-200 nm) have unacceptably low light transmission⁶⁶. In comparison, ITO coated microscope slides (Sigma-Aldrich) have typically more than 80% transmission and can be easily purchased.

In this research, the electrowetting actuation of the droplets is viewed from both top and side views. For this reason, the top plate (ground electrode) for both types of experiments (with planar or patterned electrodes) is ITO coated glass to allow for a clear image of the droplet in the

microchannel. As shown in Figure 2-2 and Figure 2-4 , the material of the control electrodes on the bottom plate may be either sputtered Cr films (thickness of 150-200 nm) or ITO.

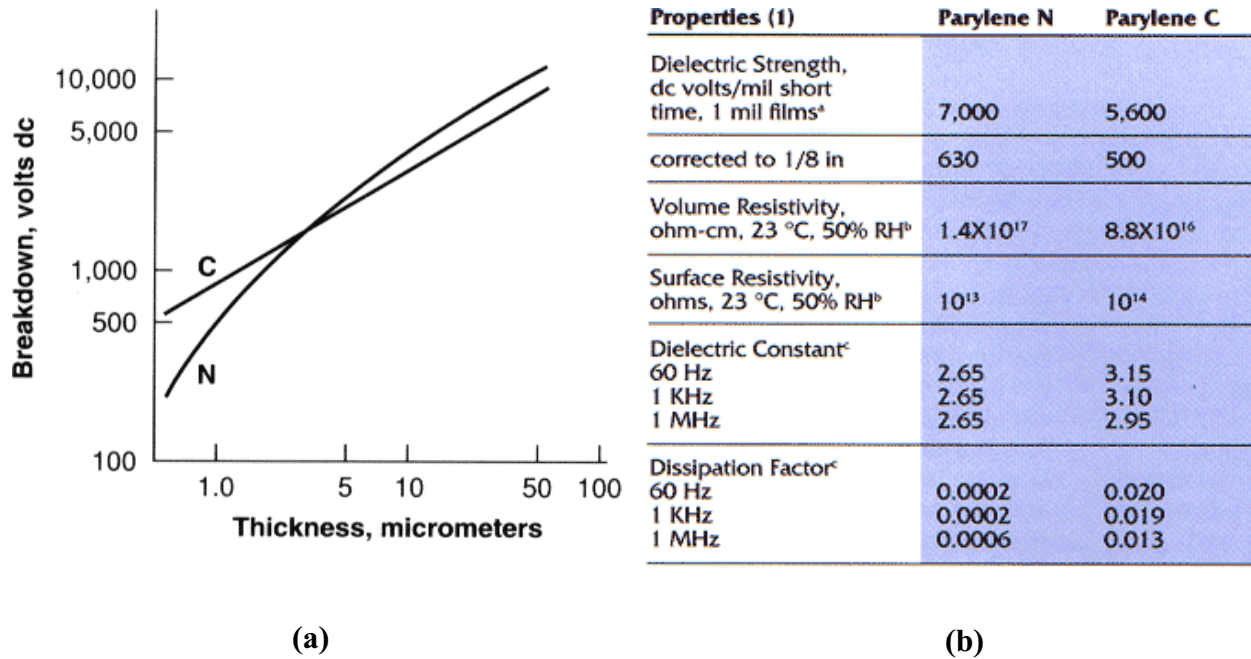


Figure 2-6: (a) Breakdown voltage of Parylene N and C vs. polymer film thickness, (b) electrical properties of Parylene N and C¹⁸⁸. (Taken from specification sheet, Specialty Coating Systems (SCS), Clear Lake, USA).

Hydrophobic Surface:

Bare parylene C has relatively small and irreversible electrowetting properties under an electric potential, so it requires the use of a hydrophobic top-layer to permit large reversible effects (less contact angle hysteresis)⁶⁶. Teflon AF (DuPont Company), which is a family of amorphous fluoropolymers, has been chosen based on the fact that it has an excellent chemical resistance, low surface energy, high temperature stability, and the ability to be coated as a thin layer. As the contact angle measurement is dependent on the history and processing conditions of the Teflon AF films, the coating procedure has to be optimized.

It was found that by spin coating (3000 RPM – 25 sec.) a 1% solution of Teflon AF in Fluorinert FC-77 (or FC- 40) (Sigma-Aldrich), the appropriate thickness could be obtained. Spin coating was carried out in cleanroom facilities, and the samples were dried in small closed containers for 3 days followed by curing in a vacuum oven: bake at 110 °C for 10 min., bake at 170 °C for 10 min., and bake at 285 °C for 10 min. In this way, the solvent evaporates gradually and a good surface with film thickness on the order of 50 nm can be obtained. When the Teflon coating was applied over Parylene, the final 285 °C curing step was replaced with an additional 10 minutes at 170 °C to avoid thermal degradation of Parylene.

The thickness of the Teflon layer was measured using an Atomic Force Microscope (AFM). AFM is a very high resolution type of scanning probe microscopy for imaging, measuring, and manipulating matter at the nanoscale. To measure the thickness, a scratch is made on the coated Teflon layer and the profile is measured at several different spots across the scratch. The results confirmed a uniform thickness of 50 ± 5 nm.

2.3) Experimental Apparatus

The contact angle studies are performed in an in-house developed apparatus, where a droplet of the desired solution, less than 2 μ l in volume dispensed by a digital syringe (Hamilton Co., USA, 7002 KH, 2 μ l), is sandwiched between two surfaces as shown in Figure 2-2 and Figure 2-4. By using a micropositioner (Luminos I3005, Canada.), the gap can be manually controlled with a resolution of 50 nm. A range of gaps between the two plates (300-600 μ m) was studied to provide results relevant to microchannels.

The images are recorded from the top and side using two CCD cameras equipped with optical microscopes. The cameras used in the experiments are from EO series (Edmunds Optics, USA) and can capture up to 25 fps with a resolution of 2560×1920 pixels.

The contact angle apparatus is also shown in Figure 2-7. Due to the precision needed with respect to the microchannel gap measurements, this contact angle device was precisely designed

with durable materials and then manufactured at McGill University (*Chemical Engineering Department, Machine Shop*).

To minimize the effect of vibration, the camera support was mounted on the same bread board (Newport, *USA*) where the experimental set-up was installed. Figure 2-8 shows the camera support which provides an accurate control over the translation of camera in x, y, and z directions. The manufacturing of this camera support was also done at McGill University (*Chemical Engineering Department, Machine Shop*). At the early stages of the experiments, the top camera was supported by assembled parts (Edmund Optics, *USA*) as shown in Figure 2-9. A 120 VDC power supply (Agilent 3612 A) was used to apply voltages up to 100 V to the droplets.

The experimental set-up is shown in Figure 2-9 where droplet movements are recorded simultaneously from both top and side views. At the later stages of the experiments, more items such as top and back lights, humidity chamber, and Arduino Nano microcontroller were added to the set-up to be able to record high quality images, control the humidity and finally to switch the electrodes in a sequential mode with a variable frequency.

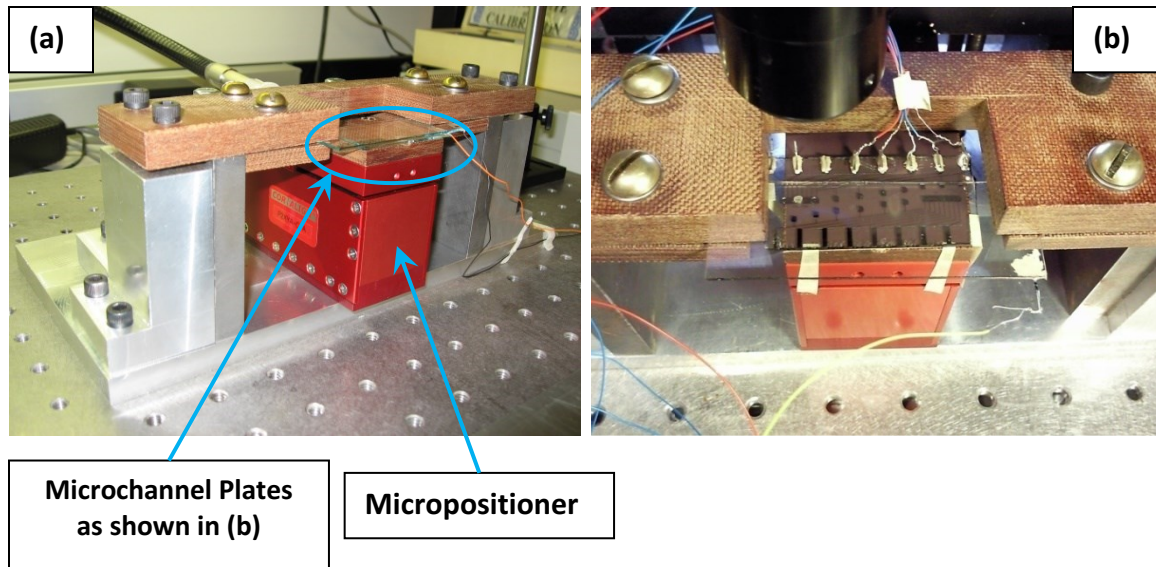


Figure 2-7: (a) Isometric front view of contact angle measurement apparatus (design details in Appendix A), (b) positioning the top and bottom plates as used in the experiments.

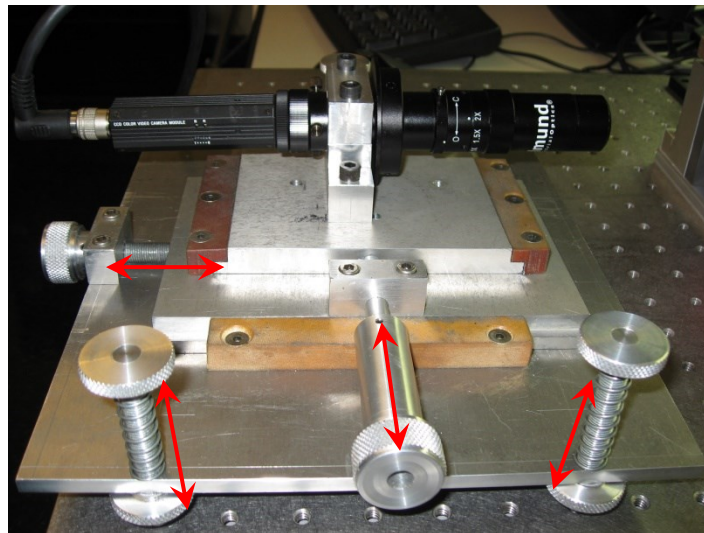
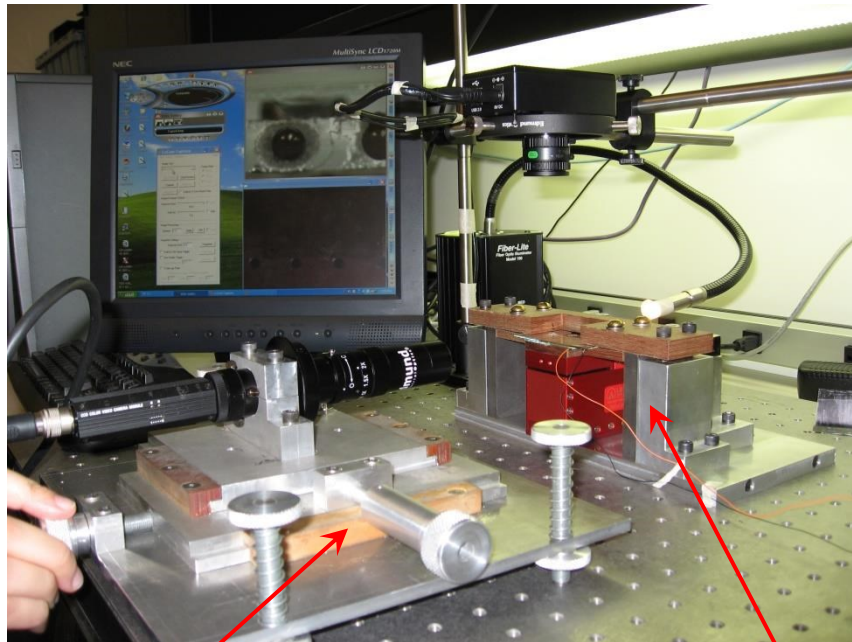


Figure 2-8: Camera support, the arrows show the directions of movement.



Side camera support

Top camera support

**Contact angle
measurement
apparatus**

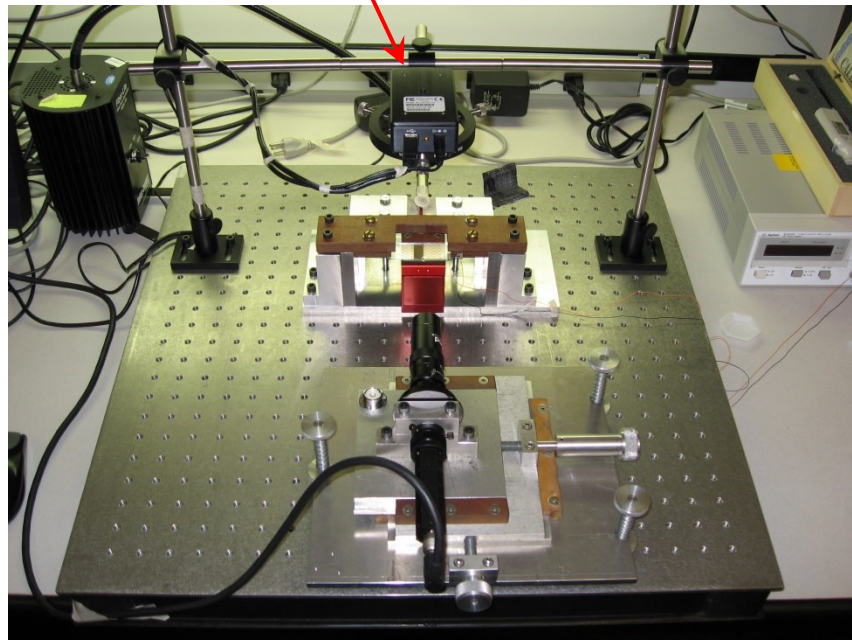


Figure 2-9: Experimental set-up at the early stages of the experiments

2.4) Humidity Control

One of the challenges was to avoid the rapid evaporation of the small 2 μl droplets. It was therefore necessary to control the humidity of the air around the droplet. For this purpose, a humidity chamber made of 3/16" Plexiglas of dimensions 32 \times 17 \times 11 cm with a clear view for the cameras was designed and manufactured at the Concordia Machine Shop (*Department of Mechanical and Industrial Engineering*). The chamber has a removable top to facilitate the dispensing of the droplets. For adding the humidity to the chamber, a small humidifier, which is usually used in cigar boxes, was obtained. The goal was to perform the experiments at room temperature with humidity of 70-80 %. The humidity chamber is shown in Figure 2-10.

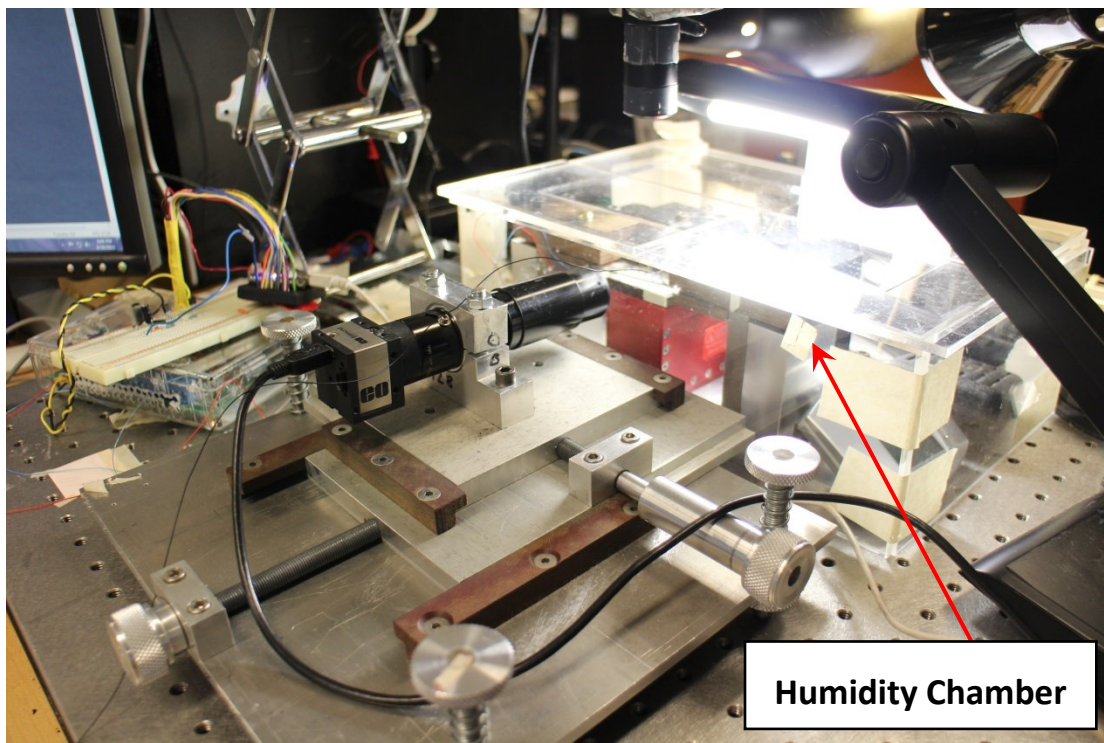


Figure 2-10: The experimental set-up with the humidity chamber

2.5) Microfabrication of Control Electrodes

Microfabrication which is the process of fabrication of miniaturized structures such as semiconductors is used in microelectromechanical systems (MEMS). Although microfabrication is a broad general term, it is actually a collection of technologies used in making microdevices which must be performed one after the other, many times repeatedly. The procedure typically includes depositing a film, patterning the film and etching portions of the film on substrates made of silicon wafers, glass or plastics.

For the experiments with bottom planar electrodes as shown in Figure 2-2, no special microfabrication procedure was needed. In order to fit the bottom plates in the contact angle measurement apparatus, the slides were cut to 50×25×1 mm. The cut samples were then sent to Specialty Coating System (SCS) to be coated with Parylene C at a thickness of 800 nm. The samples were then spin-coated with a layer of 50 nm Teflon AF.

The substrates with individually addressable electrodes as shown in Figure 2-4 had to be microfabricated in cleanroom facilities (McGill Nanotools Microfab center^{186,186}). Microfabrication of the patterned electrodes required the design (done by Rajabi¹⁷³) and fabrication (FineLine Imaging Company- *Colorado, USA*) of a photomask¹⁸⁹. With this mask, simultaneous microlithography of 6 samples each with the size of 50×25×1 mm is possible (Figure 2-11). Generally, photomasks are transparent glass plates that allow light to shine through a defined pattern of specific chrome metal-absorbing film. The microfabrication of the patterned control electrodes is explained in detail in below.

As clean photomasks and substrates are needed for microfabrication procedure, the mask and all the glass and silicon wafers were first cleaned by acetone followed by isopropanol (IPA) in an ultrasonic bath set at 40 °C, each for 5-10 min.; and then were rinsed with deionized water¹⁹⁰. This process removes all the remaining residues on the substrates as well as any traces of organic, ionic, and metallic impurities; and consequently, increases the quality and adhesion of the subsequent coating layers.

The chromium control electrodes were deposited with a sputtering machine (MRC 603¹⁹¹). This technique is a physical vapour deposition (PVD) method where atoms are ejected from

a solid target material and deposited on a substrate in a chamber filled with an inert gas. By adjusting the parameters of the machine, a chromium thickness of 150 nm was achieved. This thickness was measured by a Tencor P1 Profilometer¹⁹². This measuring instrument has a diamond stylus which moves vertically in contact with the sample and then laterally across the sample for a specified distance measuring the height variations across the surface.

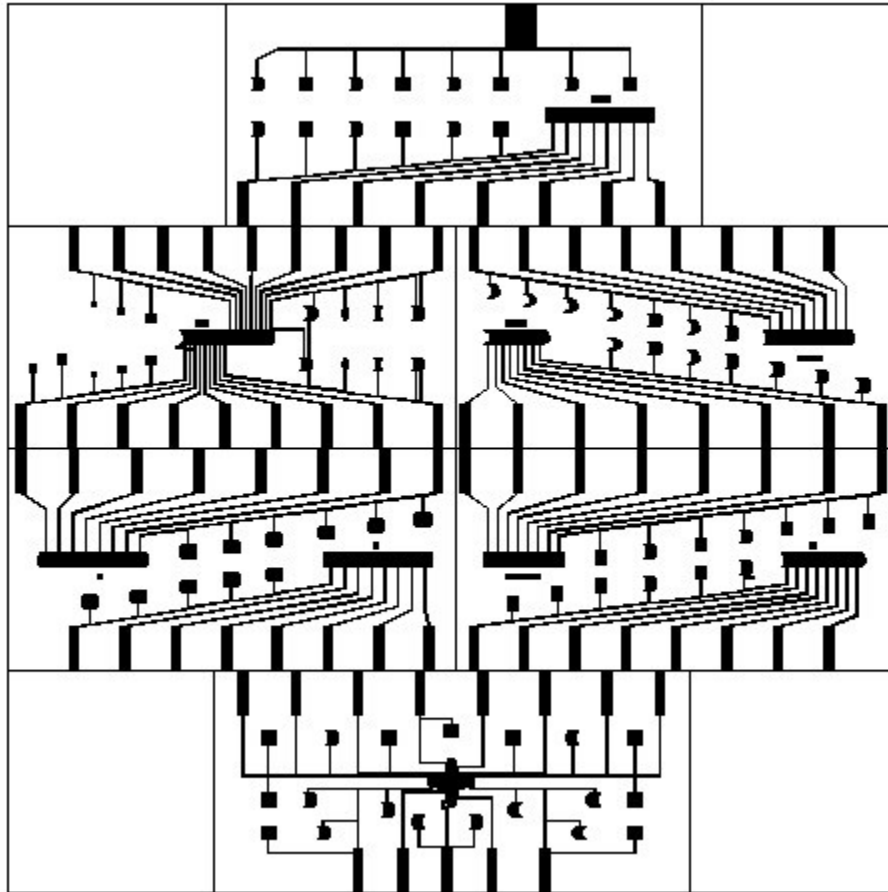


Figure 2-11: Designed patterns of electrodes on Photomask

Subsequently, the photolithographic process started which included sample cleaning, photoresist application, soft baking, mask alignment, exposure and development, and hard baking. First, the chromium-coated samples were cleaned with IPA solvent followed by rinsing with deionized water and drying with pressurized N₂ gas. Then, a spin-coater was used to coat the samples with a thin uniform layer of S1813 positive photoresist of 1.4 μm. Spin coating was done at 500 rpm for 5 sec. to spread and 3950 rpm for 30 sec. to spin the photoresist¹⁹³.

In order to drive off excess photoresist solvent so that it would not stick to the mask during the lithographic process, the samples were “soft-baked” in vacuum oven at 115 °C for 1 min.

For lithography, a top-side aligner (EVG620^{194,195}) was used. In these machines, the mask is aligned with the silicon wafer or glass substrate coated with chromium, so that the pattern can be transferred. After the alignment, the photoresist is exposed through the pattern on the mask with a high intensity UV light by the contact exposure method allowing for high resolution. The exposure to light causes a chemical reaction in the positive photoresist that later allows some of the photoresist to be removed with a developer solution.

The development of the exposed photoresist is one of the last steps in the lithographic process. At this stage, the samples were soaked in the developer MF319 for 45 sec. followed by rinsing with deionized water and drying with pressurized N₂ gas. At the final step in the lithography, the samples were “hard-baked” in vacuum oven at 90 °C for 10 min. This step hardens the remaining positive photoresist making it a more durable protecting layer for the chromium electrodes to resist the wet chemical etching.

In wet etching, a liquid agent called chromium etchant type 1020 was used with an etch rate of 40 angstroms/s at 40 °C removing the topmost layer in the areas not protected by photoresist. The thickness of the chromium electrode layer determines the etching time. To ensure that the removal of the unwanted chromium was successful, the samples were studied with an Olympus microscope with high magnification.

Finally, the photoresist was removed using the same procedure as for cleaning the photomask and substrates. At the end, the sample were rinsed with deionized water and dried by N₂ gas.

2.6) Electrode Shapes and Wiring

In this research, the study of actuating droplets is mainly done on single square electrodes, and the droplet motion is carried out on an array of interdigitated electrodes. The schematic details of these patterned substrates are given in Figure 2-12 and Figure 2-13. As shown, the square electrodes have a pitch with the length of 1500 μm.

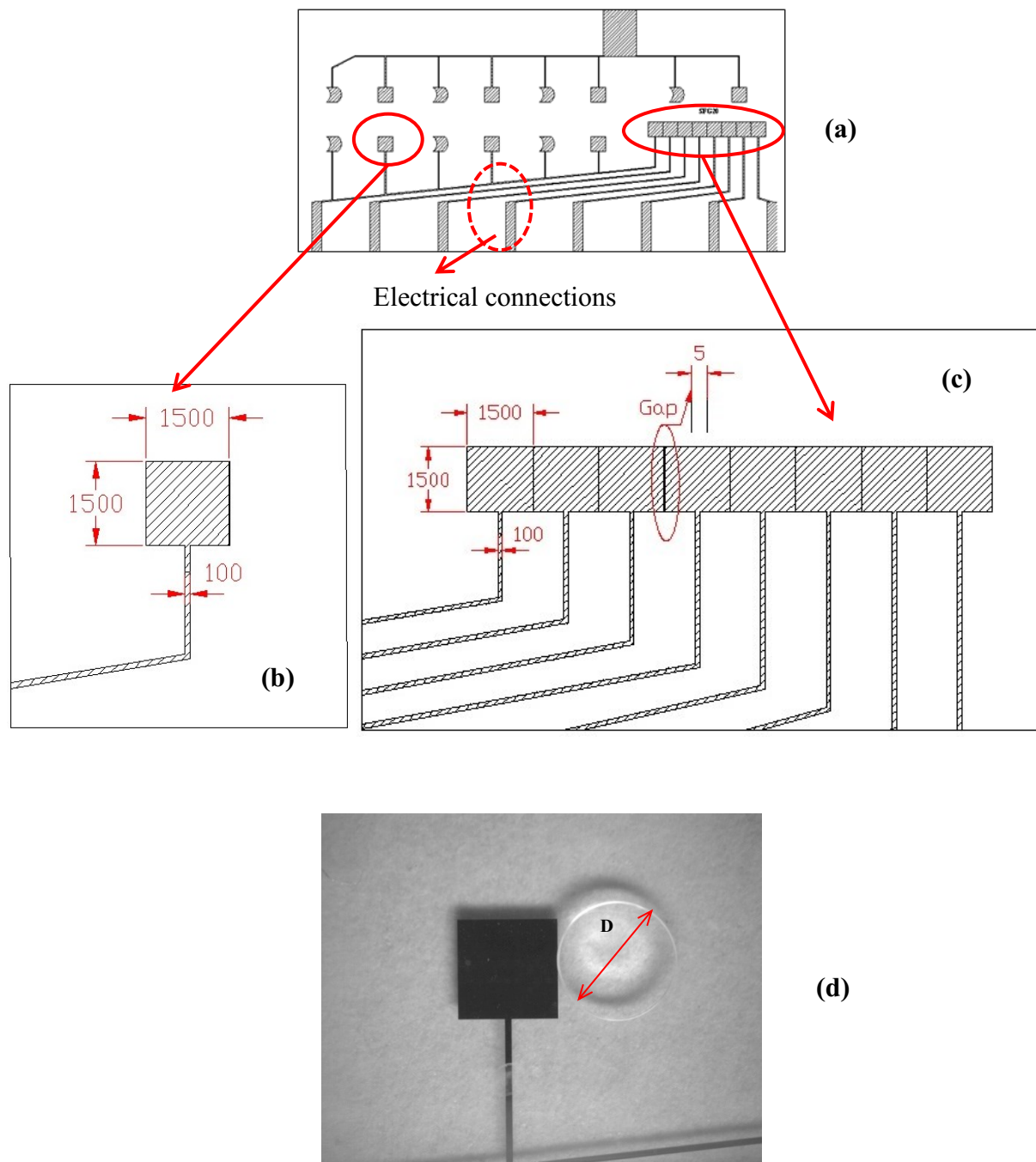


Figure 2-12: (a) Schematic of a bottom plate substrate, (b) schematic detail of a single square electrode, (c) schematic detail of an array of square electrodes, (d) positioning a droplet of distilled water with diameter "D" next to a single square electrode. The units are all in μm .

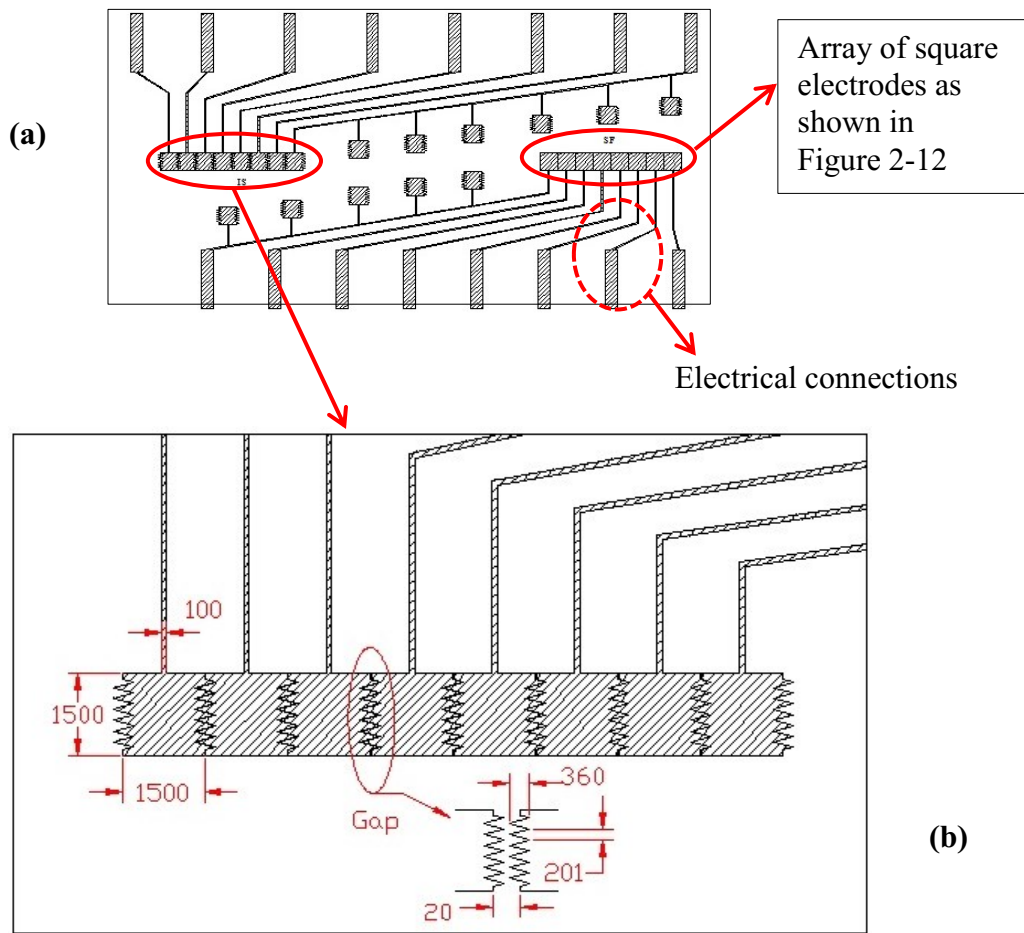


Figure 2-13: (a) Schematic of a bottom plate substrate, (b) schematic detail of an array of interdigitated electrode. The units are all in μm .

Through the course of this study, in order to achieve repeatable experimental results, an effort was made to position the droplets touching the edge of the electrode (shown in Figure 2-12), which was very challenging, while keeping the microchannel gap and the droplet volume constant (*i.e.* 300 or 600 μm and 1 or 2 μl respectively, depending on the type of the experiments).

Thus, in order to accurately measure the microchannel gap, it was necessary to have a scale with a pre-known precise size. For this purpose, a metal bead of $690 \pm 10 \mu\text{m}$ diameter was glued to the edge of the primary slides and was used as a reference scale in the image processing.

Not only is the microfabrication of the electrodes important, but also it is very crucial to make sure that there are no electrical disconnections on the other sections, especially on the parts of 100 μm width connecting the wires to the electrodes (*i.e.* detail (b) of Figure 2-12 and Figure 2-13). In many cases, the circuit failure was due to poor fabrication of these electrical connections.

To obtain accurate microchannel gaps and avoid electrical shortcuts, a secondary microscope slide was glued to the primary sample one from below and was used as a plate to connect the electrical connections on the sample slide to the wires through a thin layer of conductive epoxy (Electro Sonic Inc., *Canada*) as shown in Figure 2-14.

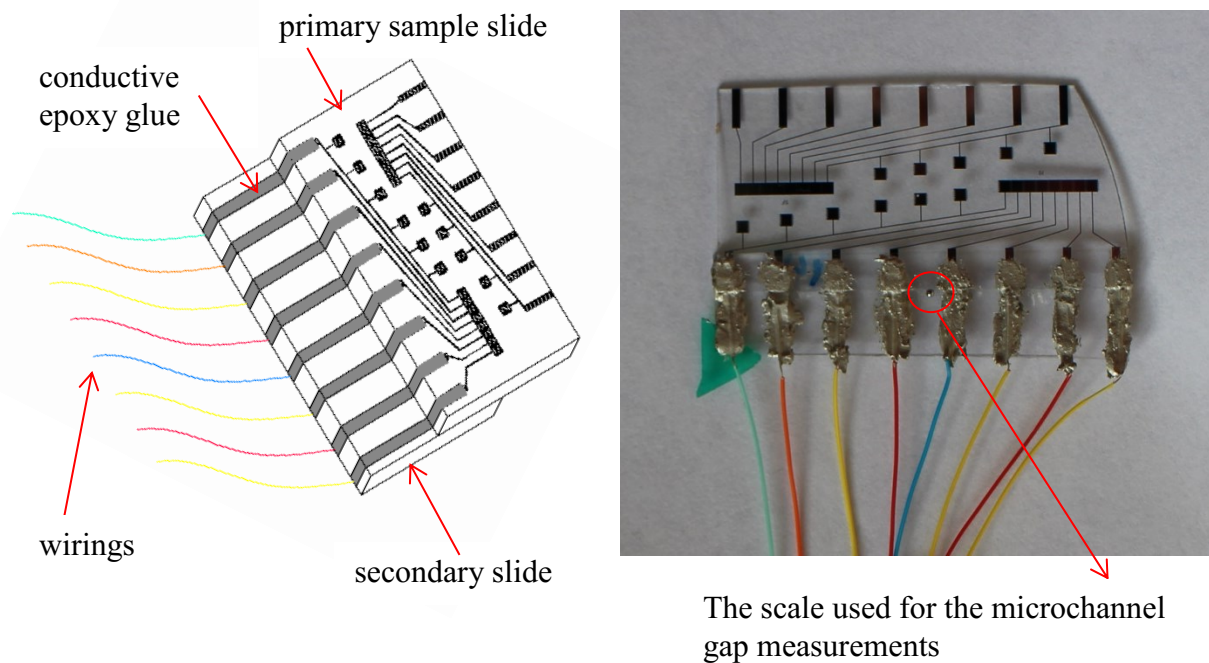


Figure 2-14: Schematic of the wirings

2.7) Design of Switching Controller

In order to move the droplets on an array of electrodes, a controller system was designed with the ability to switch the electrodes sequentially with a variable frequency. This controller system consisted of an Arduino Nano microcontroller (Gravitech, USA) powered via a Mini-B USB connection to the computer with an input DC voltage of 12 V, a Velleman K8044 light effect generator kit with 10 outputs and an ON-OFF button (ABRA Electronics, *Canada*), a discharging circuit and Arduino software. The Arduino environment is an open-source physical computing platform based on a simple microcontroller board, and a development environment for writing software (with a C derived programming language) for the board¹⁹⁶. A code was written to turn the electrodes ON and OFF on a sequential pattern with a variable switching frequency (Appendix B). The system was also used for the fundamental studies on single square electrodes where only one channel on the Velleman kit was used. In this system, the application of the voltage was synchronized with the reset button of the microcontroller and was controlled by a push ON-OFF button.

A discharging circuit was needed in the experiments involving the solutions of DNA in order to discharge the electrical system after each voltage application. By adding this circuit to the electrical system, we could minimize the attraction of the negatively charged droplets of DNA solutions to the positively charged electrode at the bottom plate.

In Appendix B, the computer program written for this system, the controller system, the discharging circuit, and the diagram of the controller system and its connections to the other components in the experimental set-up are shown in Table B-1, Figure B-1, Figure B-2, and Figure B-3 respectively.

Chapter3

Characterization of DNA-based Solutions

Deoxyribonucleic acid (DNA) is an important biopolymer that contains and transmits genetic information and is found in all living cells^{197,198}. In its native state, DNA has a double stranded (*i.e.* double-helical) conformation which is composed of building blocks called nucleotides consisting of deoxyribose sugar, a phosphate group and four nitrogenous bases: adenine, thymine, guanine and cytosine (Figure 3-1). However, in its denatured state, it has a random coil structure with separated strands¹⁹⁹. These base pairs can be separated by breaking the hydrogen bonds between them by using heat or chemical agents such as urea or formamide¹⁹⁹. As shown in Figure 3-1, DNA is negatively charged because of its phosphate backbone. These charges have important effects on the solution properties particularly in the presence of an external electric field.

Commercially, there are several deoxyribonucleic acid sodium salts available extracted from either herring testes or calf-thymus. In this research, D4522 deoxyribonucleic acid sodium salt from calf-thymus was purchased from Sigma Aldrich (Canada). This type of DNA is primarily double stranded and has been used by Bandyopdhyay and Sood¹⁹⁸, and Sun *et al.*¹⁹⁹ in rheological studies. In this macromolecule, the average number of base pairs will range between 13 and 115 kilobases and the molecular weight is reported to be between 10-15 million Daltons

prior to denaturation or nicking which means before separating the strands. This product is lyophilized (dehydrated by freeze drying) from a DNA solution containing 1mM Tris-HCl, pH 7.5, with 1 mM NaCl and 1 mM EDTA. The storage temperature for this product is recommended to be -20 °C.

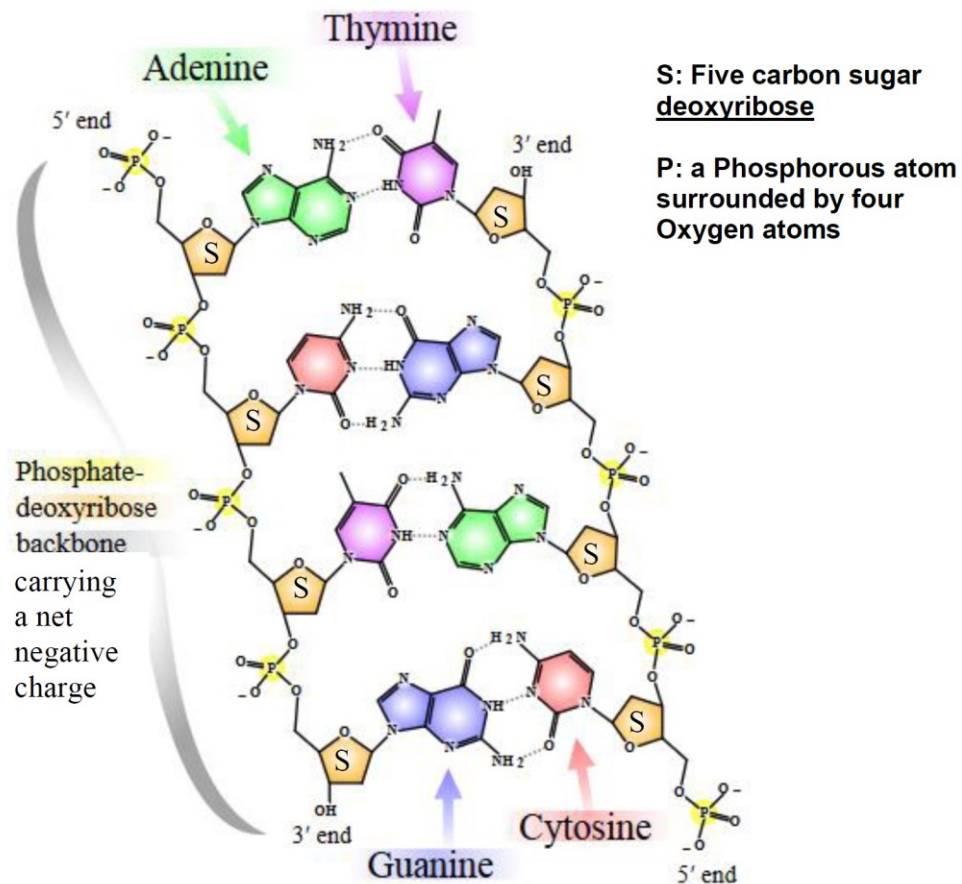


Figure 3-1: DNA structure: Chemical structure (Source: Wikipedia, Credit: Madeleine Price Ball)

3.1) DNA Concentration Regimes

In general, there are four important concentration regimes for solutions of polymers such as DNA: dilute, semi-dilute, overlap and entangled^{200,201}. In the dilute regime, the polymer concentration is low and the chains are very far apart such that they do not interact with one

another, but primarily interact with a good solvent (in a good solvent, the polymer chain segments prefer to be in contact with solvent molecules rather than in contact with other chain sections²⁰¹).

In the semi-dilute regime, the chains overlap each other and form some entanglements. The concentration at which the polymer coils begin to just touch each other is the overlap concentration (C^*) which is a transition from dilute to semi-dilute conditions. Therefore, in the dilute regime, the concentration C is less than the overlap concentration (*i.e.* $C < C^*$), and in semi-dilute regime, the concentration is greater than the overlap concentration (*i.e.* $C > C^*$). However, the overlap does not directly correspond to an entanglement and the entangled concentration, C_e , could be considerably larger than the overlap concentration¹⁹⁷. For calf-thymus DNA, Mason *et al.*¹⁹⁷ found that $C^* = 350 \mu\text{g/ml}$, and the entangled concentration $C_e \approx 2000 \mu\text{g/ml}$ (recently, Bravo-Anaya *et al.*²⁰² reported the value of $\approx 2400 \mu\text{g/ml}$).

Hence, in this research, for the specified calf thymus DNA, any concentration less than $350 \mu\text{g/ml}$ has been considered as dilute. For this purpose and in order to comply with the DNA concentrations often used in microfluidics¹³⁴, concentrations of 4, 8, 20, 50, 100 and $150 \mu\text{g/ml}$ have been chosen for the dilute regime experiments. Also, solutions of DNA with concentrations of $350 \mu\text{g/ml}$, $1000 \mu\text{g/ml}$ and $C \geq 3000 \mu\text{g/ml}$ have been prepared corresponding to overlap, semi-dilute and entangled regimes respectively.

3.2) Preparation of DNA Solutions

Based on the literature, the solutions of DNA can be made by dispersing the dehydrated DNA powder into:

- pure deionized water and equilibrating overnight (the pH of pure water is very close to 7.0)¹⁹⁹
- aqueous buffer solutions consisting of 10 mM Tris, 100 mM NaCl, 50 mM each of NaCl and KCl and 5 mM MgCl_2 , then allowing the samples to equilibrate for a day at 4°C to inhibit degradation¹⁹⁸

- aqueous buffer solutions containing 10 mM (Tris-HCl) with pH = 7.9, 50 mM NaCl, 50 mM KCl, 5 mM MgCl₂, 15 µg/ml BSA (bovine serum albumin), and 0.1 mM. EDTA¹⁹⁷

If using water for dissolving DNA, the water needs to be purified meaning that it should be RNase and DNase free (*i.e.* the enzymes which depolymerize or break a polymer into constituent monomers) and sterile if used for microbiology experiments. As purifying requires special additional treatments or functional testing to maintain pH, it was decided to dissolve DNA in aqueous buffer solutions.

The purpose of adding EDTA (ethylenediaminetetraacetic acid), which is a synthetic amino acid, to the buffer solution is to prevent DNA degradation, as EDTA removes the metal cofactors (typically Mg²⁺ and Ca²⁺ required for the activity of DNases and other DNA damaging enzymes). In this research, depending on the type of experiments, a specific buffer was prepared as follows:

- DNA suspension buffer containing 10 mM Tris-HCl and 0.1 mM EDTA with pH = 8.0, RNase/DNase-Free and sterile, readily purchased in 1 ml tubes from Teknova (USA), used for contact angle measurement studies (Chapter 4 and 5)
- buffer solution with pH =7.0, readily purchased from Fisher Scientific (Canada), used for contact angle measurement studies in order to compare the results with the solutions prepared in the DNA suspension buffer of Tris-HCl (mentioned above) and to verify the effect of the type of buffer on the contact angle (Chapter 4)
- buffer solutions containing 10 mM (Tris-HCl) with pH = 7.9, 50 mM NaCl, 50 mM KCl, 5 mM MgCl₂, 15 µg/ml BSA, and 0.1 mM. EDTA for bulk rheological studies (Section 3.3)). The preparation of this buffer is explained in detail in Appendix C.

Subsequently, stock solutions of DNA in buffer with the concentration of 1000 µg/ml (3000 µg/ml for rheological experiments) were prepared. Due to the precision needed in this study, for weighing DNA samples, a TGA thermogravimetric analyzer machine was used. In order to avoid any mechanical heating due to stirring, the solutions were gently inverted several times followed by an equilibration period of 1 day at 4 °C. Afterwards, the lower concentrations

of DNA in solution were prepared by diluting the concentrated stock solution and were used in a 2-3 months interval to minimize degradation and bacterial growth.

3.3) Rheological Properties of DNA solutions

For incompressible Newtonian fluids such as water and honey, the governing equations for flow properties are²⁰³:

1) Continuity equation: $\nabla \cdot \underline{v} = 0$ Equation 3-1

2) Conservation of Momentum: $\rho \left(\frac{\partial v}{\partial t} + \underline{v} \cdot \nabla v \right) = -\nabla p - \mu \nabla \cdot \nabla \underline{v} + \rho \underline{g}$ Equation 3-2

3) Newtonian constitutive equation: $\underline{\tau} = -\mu [\nabla \underline{v} + (\nabla \underline{v})^T]$ Equation 3-3

where ∇ is a vector differential operator called nebla, and \underline{v} , ρ , μ , \underline{g} and $\underline{\tau}$ are the velocity vector, fluid density, Newtonian shear viscosity, acceleration vector due to gravity, and extra stress tensor related to the deformation of the fluid respectively. The superscript T also stands for the transpose of a matrix.

The density ρ and the viscosity μ are two material constants that are needed to predict the behaviour of the incompressible Newtonian fluids. For incompressible, non-Newtonian fluids, the Continuity equation and the equation of the Conservation of Momentum remain the same; however, for the stress tensor a different equation is needed which is a much more complicated function of material properties than for Newtonian fluids. In the field of rheology, an important challenge is to find the appropriate Constitutive equation for non-Newtonian fluids. For this purpose, experiments are performed on materials using standard flows. Standard flows are categorized in two main groups; shear flows and elongational flows, and each can be subdivided into steady and unsteady (transient) flows (Figure 3-2). Biopolymer solutions are non-Newtonian fluids which have fading memory meaning that they remember past

deformations, but slowly forget about them. Thus, their behaviour in steady shear is different than in unsteady shear. In this research, we are interested in unsteady shear flows. A two dimensional schematic of the velocity profile in simple shear flow is shown in Figure 3-3.

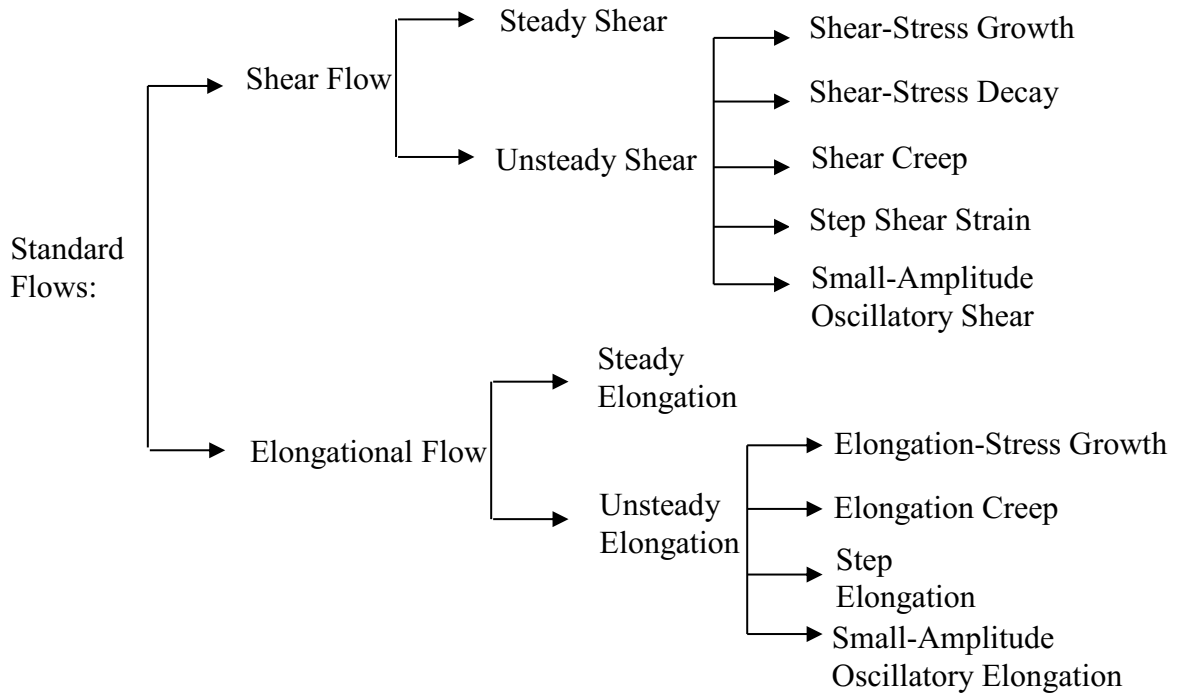


Figure 3-2: Characterization of Standard flows

The most common type of flow in rheology is simple shear flow where layers of fluid slide past each other, but do not mix and the velocity only varies in one direction²⁰³. Shear flow can be mathematically defined as²⁰³:

$$\underline{v} = \begin{pmatrix} v_1 \\ v_2 \\ v_3 \end{pmatrix}_{123} = \begin{pmatrix} \dot{\gamma}(t) x_2 \\ 0 \\ 0 \end{pmatrix} \quad \text{Equation 3-4}$$

where :

$$\dot{\gamma}(t) = \frac{\partial v_1}{\partial x_2} = \dot{\gamma}_{21}(t) \quad \text{Equation 3-5}$$

In Cartesian coordinate system, the standard directions are:

- direction 1 is the direction of flow
- direction 2 is the gradient direction
- direction 3 is the neutral direction

Depending on how the function $\dot{\zeta}(t)$ is described, we can have different types of the standard shear flows, and for each type, different material functions are defined. Among all the standard flows shown in Figure 3-2 we are interested in shear-stress growth (start-up) and small-amplitude oscillatory shear (SAOS).

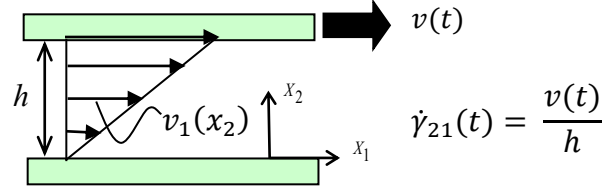


Figure 3-3: Shear flow velocity profile in between two plates

Shear stress growth or start-up experiment is a time-dependent shear flow experiment²⁰³. The kinematics for start-up and shear-stress growth coefficient can be written as Equation 3-6 and Equation 3-7 respectively:

$$\dot{\zeta}(t) = \begin{cases} 0 & t < 0 \\ \dot{\gamma}_0 & t \geq 0 \end{cases} \quad \text{Equation 3-6}$$

$$\eta^+(t, \dot{\gamma}) \equiv \frac{-\tau_{21}(t, \dot{\gamma})}{\dot{\gamma}_0} \quad \text{Equation 3-7}$$

where $\dot{\gamma}_0$ is constant shear rate. At steady state, the shear stress growth coefficient becomes only a function of shear rate, and if the magnitude of the shear rate goes to zero, this coefficient becomes zero-shear viscosity.

Another set of unsteady shear flow which is very widely used to characterize complex fluids is small-amplitude oscillatory shear (SAOS)²⁰³. The kinematics and the material functions for this flow can be written as Equation 3-8 to Equation 3-12:

Kinematics for SAOS:
$$\underline{v} = \begin{pmatrix} \dot{\zeta}(t)x_2 \\ 0 \\ 0 \end{pmatrix}_{123} \quad \text{Equation 3-8}$$

where;

$$\dot{\zeta}(t) = \dot{\gamma}_0 \cos \omega t \quad \text{Equation 3-9}$$

SAOS material functions:
$$\frac{-\tau_{21}(t, \dot{\gamma})}{\dot{\gamma}_0} = G' \sin \omega t + G'' \cos \omega t \quad \text{Equation 3-10}$$

where

$$G'(\omega) \equiv \frac{\tau_0}{\dot{\gamma}_0} \cos \delta \quad \text{Equation 3-11}$$

$$G''(\omega) \equiv \frac{\tau_0}{\dot{\gamma}_0} \sin \delta \quad \text{Equation 3-12}$$

In these equations, $G'(\omega)$ and $G''(\omega)$ are storage modulus (*i.e.* elastic response, in phase with strain) and loss modulus (*i.e.* viscous response, out of phase with strain) respectively; and δ is the phase difference between the strain wave and the stress response. The complex viscosity magnitude can be then defined as:

$$|\eta^*| = \frac{\sqrt{(G'(\omega))^2 + (G''(\omega))^2}}{\omega} \quad \text{Equation 3-13}$$

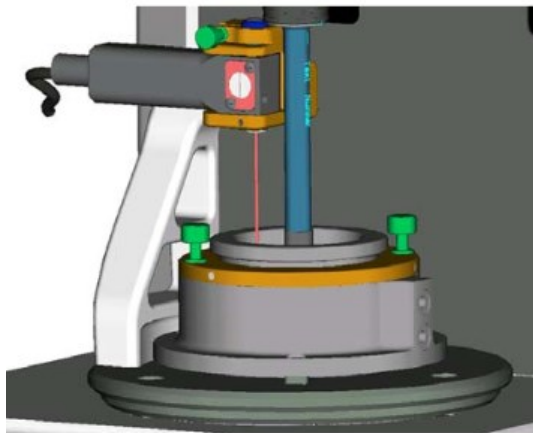
For bulk flow studies, the experiments were performed on 3000 $\mu\text{g/ml}$ of DNA solution in a rotational rheometer (Anton Paar, MCR 502), equipped with a small angle light scattering (Rheo-SALS) device and an electro-rheological cell (Figure 3-4). As the viscosity of DNA is low, the experiments were done in Couette geometry. The SALS device is a modular accessory

which can be mounted on a commercially available rheometer, and is used for detailed investigations of micrometer-sized structures. Macroscopic material functions of a substance can be provided by purely rheological methods. The macroscopic behaviour of a material is strongly dependent on its microscopic structure parameters which are very useful for a better understanding of the material rheological behaviour²⁰⁴. The Rheo-SALS set-up allows us to obtain structural information simultaneously to the rheological data. If there are concentration or orientation fluctuations existing in the sample, the polarized light will be scattered by the sample. A CCD camera records the scattering patterns from the screen. The information collected from the Rheo-SALS experiments is analyzed by the SALS-software version 1.1.²⁰⁴

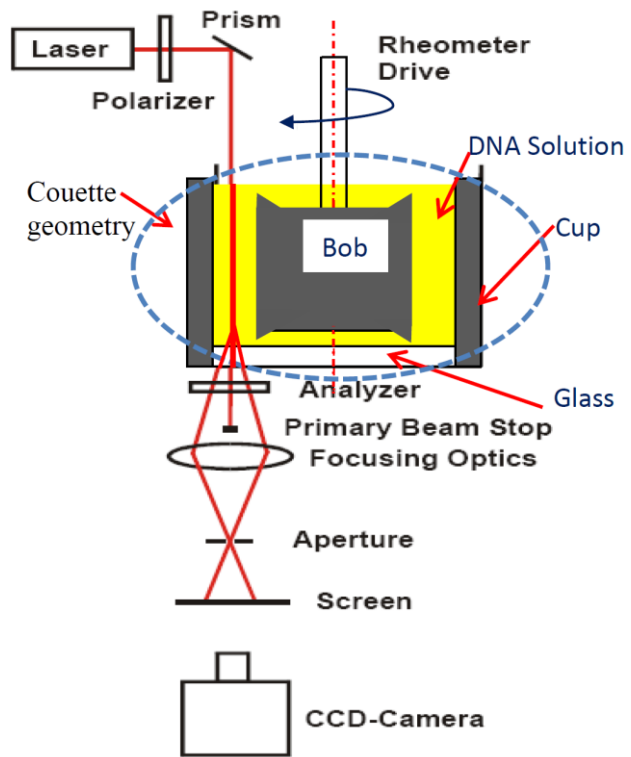
The purpose of this study was to measure shear viscoelastic properties of aqueous solutions of DNA under the application of a shear flow (with different shear rates) with and without the application of an electric potential. In order to bring electrical potential to the system, (after several unsuccessful attempts) a specific device was designed consisting of thin strands of carbon fiber. The goal was to avoid applying an external force to the rotating rheometer shaft, though the rheometer had to be calibrated each time this device was mounted. Passing an electric current through the solutions of DNA was not desired, therefore, the bob part of the Couette geometry (as shown in Figure 3-4) which was already coated with anodized aluminum had to be further coated with an insulation layer of Parylene C with a thickness of 7 μm (SCS, Clear Lake, USA).

Evaporation during the experiments was minimized by filling the top of the DNA solutions with a thin layer of silicon oil with the viscosity of 5 cSt, (Sigma Aldrich). As the viscosity of the aqueous solutions of calf thymus DNA increases with increasing DNA concentration¹⁹⁹, the experiments were conducted on sufficiently high concentration of 3000 $\mu\text{g/ml}$ due to the minimum torque required to do the rheological measurements. Although, at this concentration, the viscosity of the solution is still low and performing the rheological experiments on this low viscous solution was challenging. As it will be shown in the following section, this viscoelastic material will become even less viscous at higher shear rates. It was desired to do the experiments on higher concentrations of DNA (such as 10000 $\mu\text{g/ml}$); however, while doing the SALS experiments, electrolysis happened and the bob part of the system was severely damaged. It was due to the fact that under these experimental conditions (DNA dissolved in a solution with

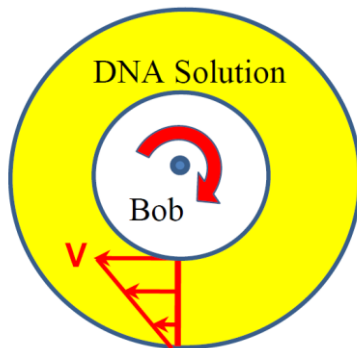
different added salts), the 7 μm layer of Parylene C was still very susceptible to dielectric breakdown. Thus, doing more experiments under the application of shear flow and electric field was impossible, and the reliable data obtained was limited. These results are shown in the following sections.



(a): Rheo-SALS Device
(Taken from Reference: Lauger *et al.*²⁰⁴)



(b): Schematic presentation of the Physica Rheo-SALS system
(Adapted from Reference: Lauger *et al.*²⁰⁴)



(c): Velocity profile for a solution in a Couette geometry, Top view

Figure 3-4: Rheo-SALS device, the laser passes through the solutions of DNA in Couette geometry while being under shear rate

3.3.1) Rheological Experiments

The results of the rheological experiments on 3000 $\mu\text{g/ml}$ DNA solutions under SAOS and start-up tests are presented in Figure 3-5 and Figure 3-6.

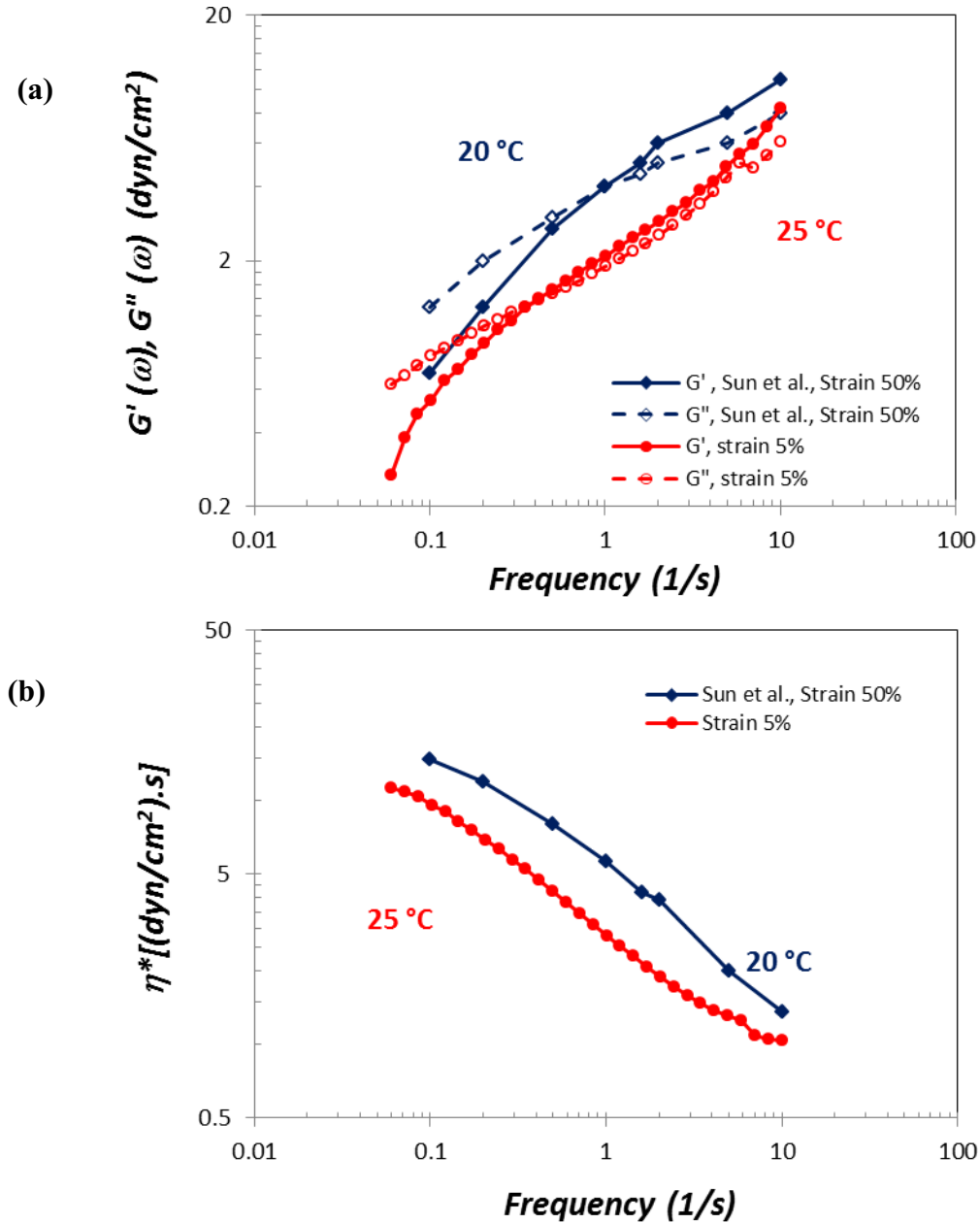


Figure 3-5: Comparison of results with those of *Sun et al.*¹⁹⁹ in frequency domain for
 (a) $G'(\omega)$ Storage modulus, $G''(\omega)$ Loss modulus, (b) η^* Complex viscosity

In Figure 3-5, the comparison results for complex viscosity are also shown in. The complex viscosity for this research has lower values than that of Sun *et al.*¹⁹⁹ due to the difference in temperature. As the Rheo-SALS system in an open assembly (as shown in Figure 3-4), there was no control over the temperature and the experiments were performed at 25°C (room temperature).

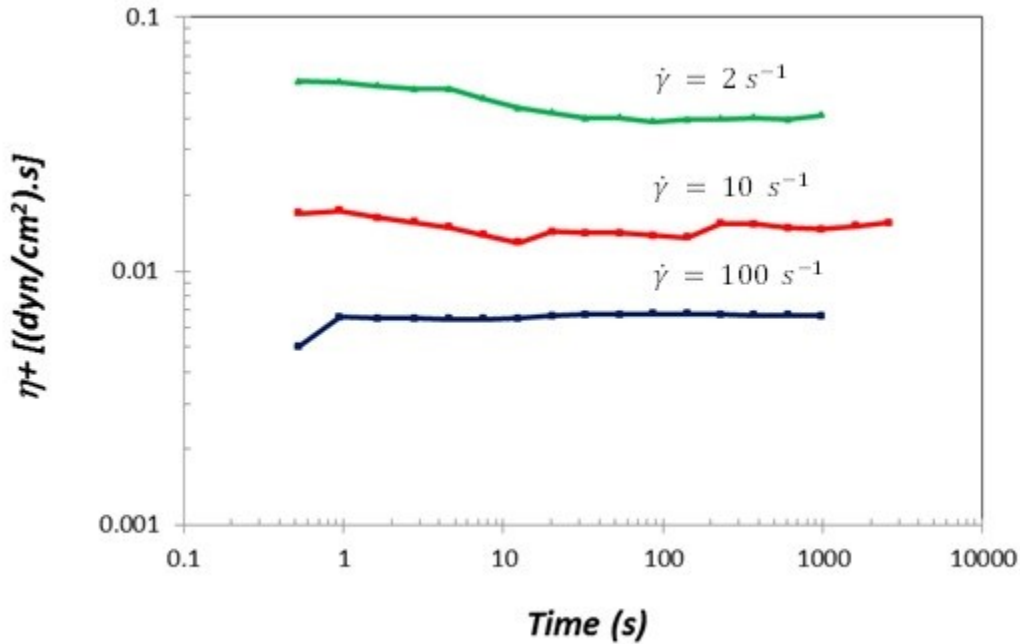


Figure 3-6: Shear stress growth coefficient, the transient response in viscosity following a sudden inception of shear flow to DNA (3000 $\mu\text{g/ml}$) in a start-up test. Different curves represent different shear rates.

Figure 3-6 shows the shear stress growth coefficient in a start-up test. These results are for the steady-state portion of the experiment when the material functions are only dependent on the magnitude of shear rate (*i.e.*: $\lim_{t \rightarrow \infty} \eta^+(t, \dot{\gamma}) = \eta(\dot{\gamma})$). As shown, by increasing the shear rate, the shear stress growth coefficient decreases implying that the viscoelastic fluids such as DNA are less viscous at higher shear rates.

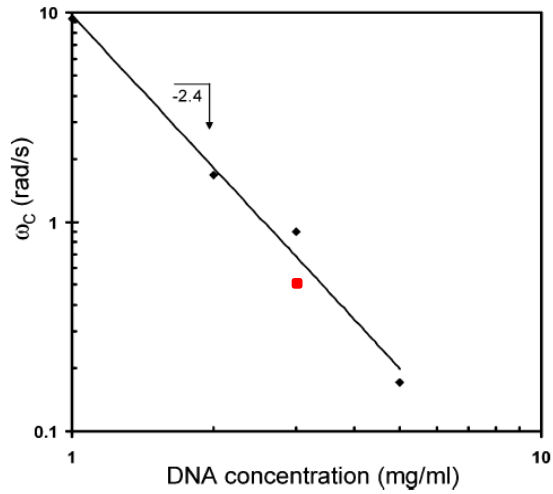


Figure 3-7: Crossover frequency of storage and loss modulus as a function of DNA concentration with the scaling power of -2.4. (Reprinted with permission from Reference Sun *et al.*¹⁹⁹. Copyright © 2005 American Chemical Society). The filled square shows the experimental result obtained in this research at 25 °C.

The linear viscoelastic limit is determined by measuring storage modulus $G'(\omega)$ and loss modulus $G''(\omega)$ as a function of strain. For the experimental results shown in Figure 3-5 and Figure 3-6, a strain of 5% has been chosen, as $G'(\omega)$ and $G''(\omega)$ are independent of strain at strains below 70%¹⁹⁹. In these figures, the experimental results obtained in this study are compared with those of Sun *et al.*¹⁹⁹ though at a higher temperature. Based on the literature^{197,199}, synthetic semiflexible polymers in a good solvent follow two empirical correlations that relate the plateau modulus $G'(p)$ and viscosity η to concentration: $G'(p) \sim C^{2.3}$ and $\eta \sim C^{4.7}$. Therefore, the viscosity and plateau storage modulus are also related by^{197,199}: $G'(p) = \eta \omega_c$. The temperature dependant, ω_c , is the crossover frequency where the storage and loss modulus cross-over and is equal to the reciprocal main relaxation time. These relations result in scaling the crossover frequency with concentration $\omega_c \sim C^{-2.4}$. Figure 3-7 shows the crossover frequency of storage and loss modulus as a function of DNA concentration with the scaling power of -2.4 taken from reference Sun *et al.*¹⁹⁹. The experimental result obtained in this research at 25 °C, with $\omega_c \sim 0.5$ (s⁻¹), is also shown in this figure which fits well to the reference line with crossover frequency of 0.7 (s⁻¹) for DNA concentration of 3000 $\mu\text{g/ml}$. The data from Sun *et al.*¹⁹⁹ in Figure 3-7 is at 20 °C.

3.3.2) SALS Experiments

Figure 3-8 shows the basic SALS set-up for an unpolarized scattering. The absolute value of the scattering vector, \vec{q} , is calculated by the following equation:

$$\vec{q} = (4\pi/\lambda) \sin (\theta/2) \quad \text{Equation 3-14}$$

where, λ is the wavelength of the light beam and θ represents the scattering angle.

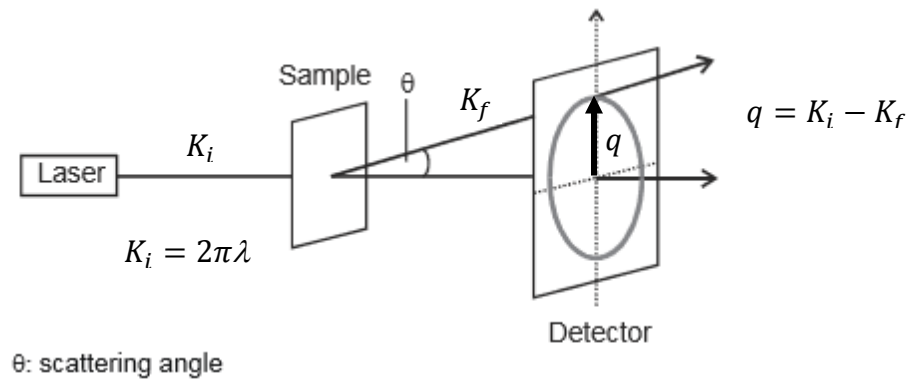


Figure 3-8: The schematic of a basic SALS set-up for an unpolarized scattering.

(Adapted from Reference: Lauger *et al.* ²⁰⁴)

The intensity of the scattered light, $I(\vec{q})$, is then calculated based on the scattering vector, \vec{q} , and is defined as: $I(\vec{q}) = F(\vec{q}) * S(\vec{q})$, where $F(\vec{q})$ represents “form factor” which describes interparticle interactions such as size and shape, and $S(\vec{q})$ or “structure factor” defines interparticle interactions such as repulsion and attraction. The definition of the coordinate system in a Couette geometry as used in our study is given in Figure 3-9.

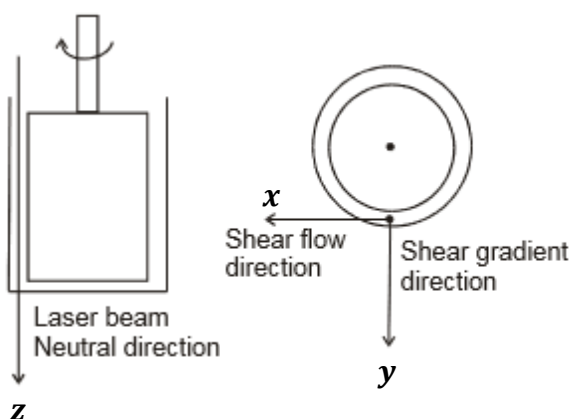


Figure 3-9: The axes x, y in the Couette geometry represent the direction of shear flow and shear gradient respectively, and z axis to the neutral direction. The propagation of the incident beam is along the z -axis (normal to the xy plane). (Adapted from Reference: Lauger *et al.* ²⁰⁴)

Figure 3-10 shows the small-angle light scattering (SALS) patterns and plots of intensity along the x and y axes for 3000 $\mu\text{g/ml}$ DNA solution under the application of: a start-up shear rate of $10 \text{ (s}^{-1}\text{)}$, a start-up shear rate of $10 \text{ (s}^{-1}\text{)}$ and a voltage of $+0.1 \text{ V}$ simultaneously, and at the end, only an applied voltage of $+0.1 \text{ V}$. The red colour represents the high intensity regions. Generally, at low shear rates, the light scattering patterns have circular shapes (the green circle as shown in Figure 3-10 (a)). By increasing the shear rate, the scattering images begin to change from a circular to an elliptical shape, and become more oriented perpendicular to the shear flow direction. The more the shear rate is, the more elliptical the scattering images are, as the light scattering shows an inverse reproduction of the structure present²⁰⁴. This change of shape is observable to some extent in Figure 3-10 (b) where the shear rate of 10 (1/s) is applied. No significant differences in intensity are observed in the graphs (a), (b), and (c), and the values of peak intensity are the same. However, in graph (b), the high intensity areas are concentrated in a narrower region along both axes due to the orientation of DNA molecules under the application of shear rate. When the voltage of 0.1 V is applied simultaneously to the shear rate of 10 (1/s) as shown in Figure 3-10 (c), no significant differences in shape are observed; however, it seems that the DNA molecules are more oriented compared to pattern (a) where they are distributed all over the solution. Finally, by removing the shear rate and applying the electric potential as low as $+0.1 \text{ V}$ solely, the DNA molecules move to a direction perpendicular to the shear flow (*i.e.* parallel to the shear gradient direction) due to electrophoresis. Whilst, no peak intensity along x -axis is observable, there is a remarkable increase in peak intensity along y -axis due to the attraction of DNA molecules to the electrical source.

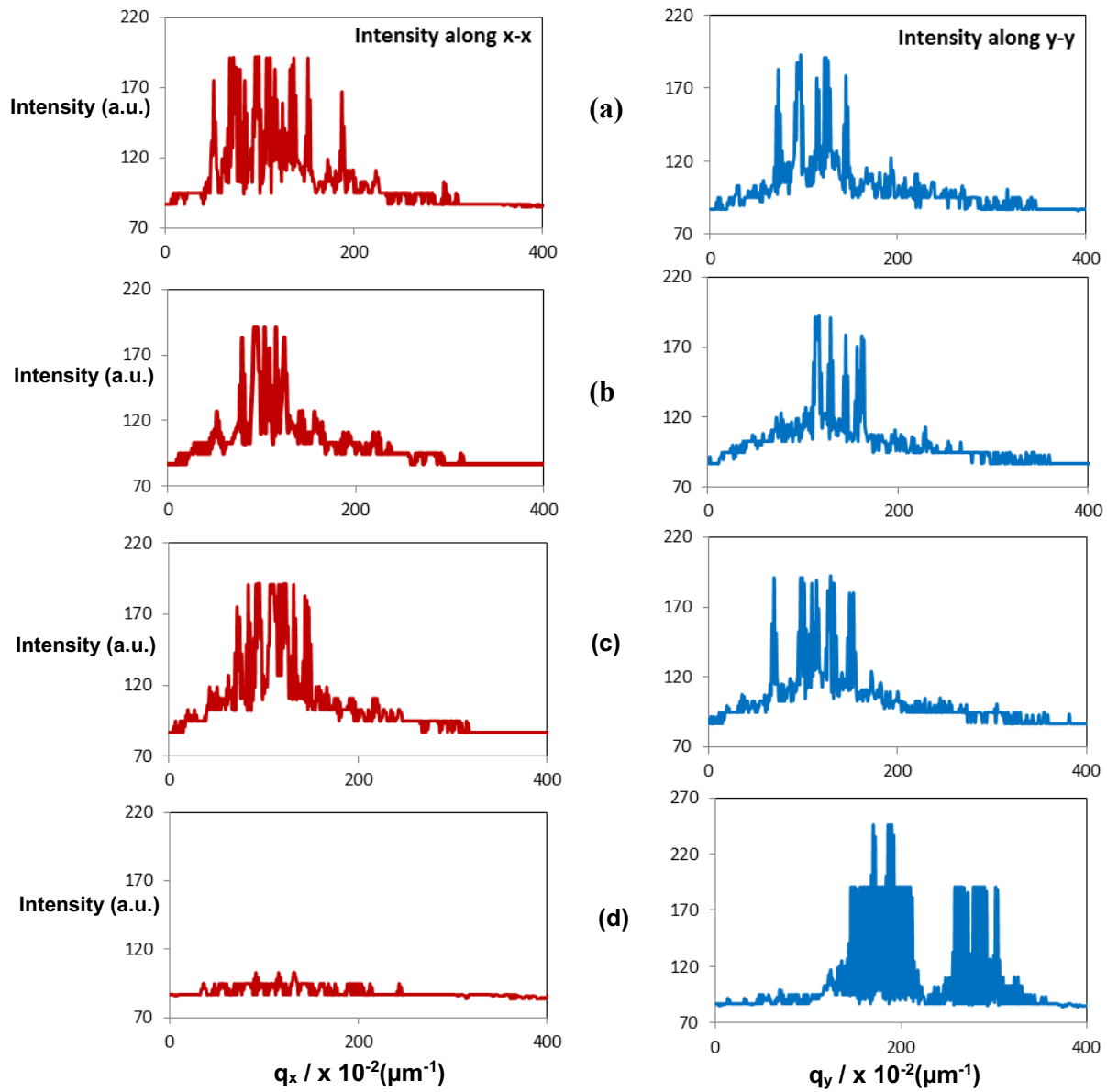
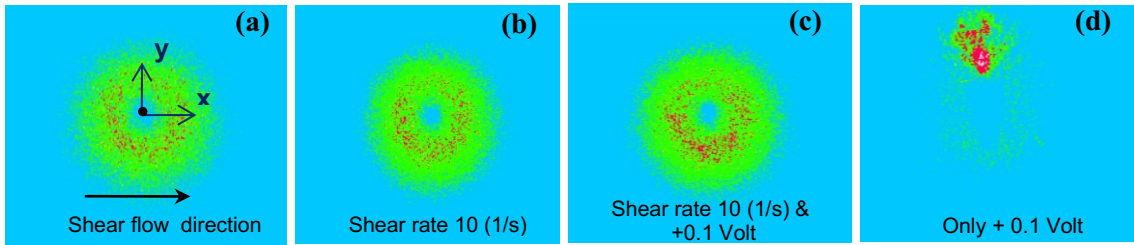


Figure 3-10: Small angle light scattering (SALS) patterns and the plots of intensity as a function of distance obtained from SALS analysis software for DNA solution (3000 $\mu\text{g/ml}$).

3.4) Discussion of Results

In this chapter, we were able to investigate the macroscopic and microscopic structures of 3000 $\mu\text{g/ml}$ DNA solution to some extent. Obtaining substantial results at lower concentrations of DNA was not possible due to the minimum torque required to do the rheological experiments. In general, for bulk flow studies on DNA solutions, it is desired to perform the rheological experiments at higher concentrations of DNA (5000 to 10000 $\mu\text{g/ml}$) for the following reason: the viscosity of DNA solutions increases with increasing DNA concentration¹⁹⁹, and the higher concentrations of DNA yield to higher signal to noise²⁰⁵; therefore, more reliable data is obtainable. In our study, while doing the SALS experiments, electrolysis happened and the bob part of the system was severely damaged; thus, performing the experiments at higher concentrations of DNA was not possible.

At the concentration of 3000 $\mu\text{g/ml}$ (entangled regime), the graphs attained for the storage modulus $G'(\omega)$, loss modulus $G''(\omega)$, and complex viscosity, η^* , in frequency domain are in good agreement with the literature¹⁹⁹; however, the comparable lower values of these parameters at our higher experimental temperatures are good indications of their temperature dependencies. These results reveal a $G'(\omega) / G''(\omega)$ crossover point whose frequency, $\omega_c \sim 0.5 \text{ (s}^{-1}\text{)}$, scales with concentration as $\omega_c \sim C^{-2.4}$. It implicates that the DNA molecules behave as semiflexible polymers when dissolved in an aqueous solution¹⁹⁹; in other words, they behave like isotropic rods which are continuously flexible. This information is useful while modeling DNA as a biopolymer.

The transient response in viscosity following a sudden inception of shear flow in a start-up test was also presented implying that the viscoelastic fluids such as DNA are less viscous at higher shear rates.

Limited results on SALS experiments were also obtained. Whilst, the changes of scattering images from a circular to an elliptical shape were observed to some extent at shear rate of 10 (1/s), no significant differences in scattering intensities were perceived while applying shear rate of 10 (1/s) and voltage of 0.1 V simultaneously. However, under the application of

electric field solely, the DNA molecules moved to a direction perpendicular to the shear flow due to electrophoresis.

It can be concluded that in bulk flow studies on DNA solutions, the charged oxygen groups play a significant role when the electric field is applied. In the following chapters, we will further investigate the behaviour of DNA solutions as discrete droplets under the application of voltage. Based on the results attained by far, it can be predicted that the negatively charged oxygen molecules will affect the dynamic behaviour of DNA solutions significantly.

In bulk flow studies, the reliable rheological results are obtainable at high concentrations of DNA in entangled regime ($C \geq 3000 \mu\text{g/ml}$). It will be compelling to know the effect of DNA concentration in small scale droplets where the capillary forces dominate, and determine which concentration regime (dilute, semidilute, overlap or entangled) is preferable in electrowetting applications.

Chapter4

Contact Angle Measurements

In this chapter, the effect of electrowetting on contact angle in the absence of motion is investigated. As mentioned in Section 1.2.1, if a liquid droplet is deposited onto a solid surface (smooth, planar, rigid, and homogeneous) in the absence of an external electric field and gravity⁶⁷, there is an equilibrium among the forces at the solid-liquid-vapour interface which is described by Young's equation⁶⁸ (Equation 1-1). When no voltage is applied, the static value of the angle between the solid-liquid, liquid-vapour interfaces at the three phase contact line is called the equilibrium contact angle (θ_0)^{8,69}. At a specific temperature and pressure, this angle is unique for a given system of solid, liquid and vapour. However, experimentally observed contact angles are not uniquely determined by solid and liquid surface tensions, and usually there is a range of contact angles; where the largest and the smallest are referred to advancing (θ_{adv}) and receding (θ_{rec}) contact angles respectively. Contact angle hysteresis is the difference between these two angles, and the equilibrium contact angle, θ_0 , is within the range of these values.

However, in electrowetting, when an electrical potential is applied between the droplet and an insulated electrode (section 1.3), the solid-liquid interfacial energy decreases and consequently the contact angle (θ) decreases and wetting improves (Figure 1-7). This angle is obtained by Young-Lippmann relation (Equation 1-9). Typically, there are several methods for measuring the contact angle which will be described in the next section.

4.1) Contact Angle Measurement

Different techniques have been developed with the aim of measuring contact angle²⁰⁶. The most common methods are: the static sessile drop method using a goniometer^{207,208,209,210}, the capillary rise method^{208,211}, the Wilhelmy balance method^{208,212,213} and drop shape methods^{214,215,216,217}.

In this chapter, AutoCAD is used for measuring the apparent or measured contact angle which is simply called contact angle.

4.1.1) Image Analysis Using AutoCAD for Measuring Apparent Contact Angle

In this research, not only is it important to measure the apparent contact angle accurately, but also to obtain as much information as possible from the captured images of the sandwiched droplets such as: droplet maximum diameter, droplet volume, and microchannel gap height. For this purpose, AutoCAD software is used in this study. Image analysis using this software is very straightforward. In a similar manner to the DropSnake method^{218,219} (a drop shape method), few knots are placed on the drop contour with close inspection of the tri-phase point. The connecting curve fitted by the software defines the droplet profile. By specifying the center of the curves at each side of the droplet and aligning a tangent with the drop profile at the solid-liquid interface, the apparent contact angles are obtained. By scaling the measured dimensions with the metal bead (reference scale shown in section 2.6), the real values of the droplet maximum diameter and

microchannel gap height are determined. The volume of the droplet is then attained by rotating the droplet profile along its axis (an available tool in AutoCAD).

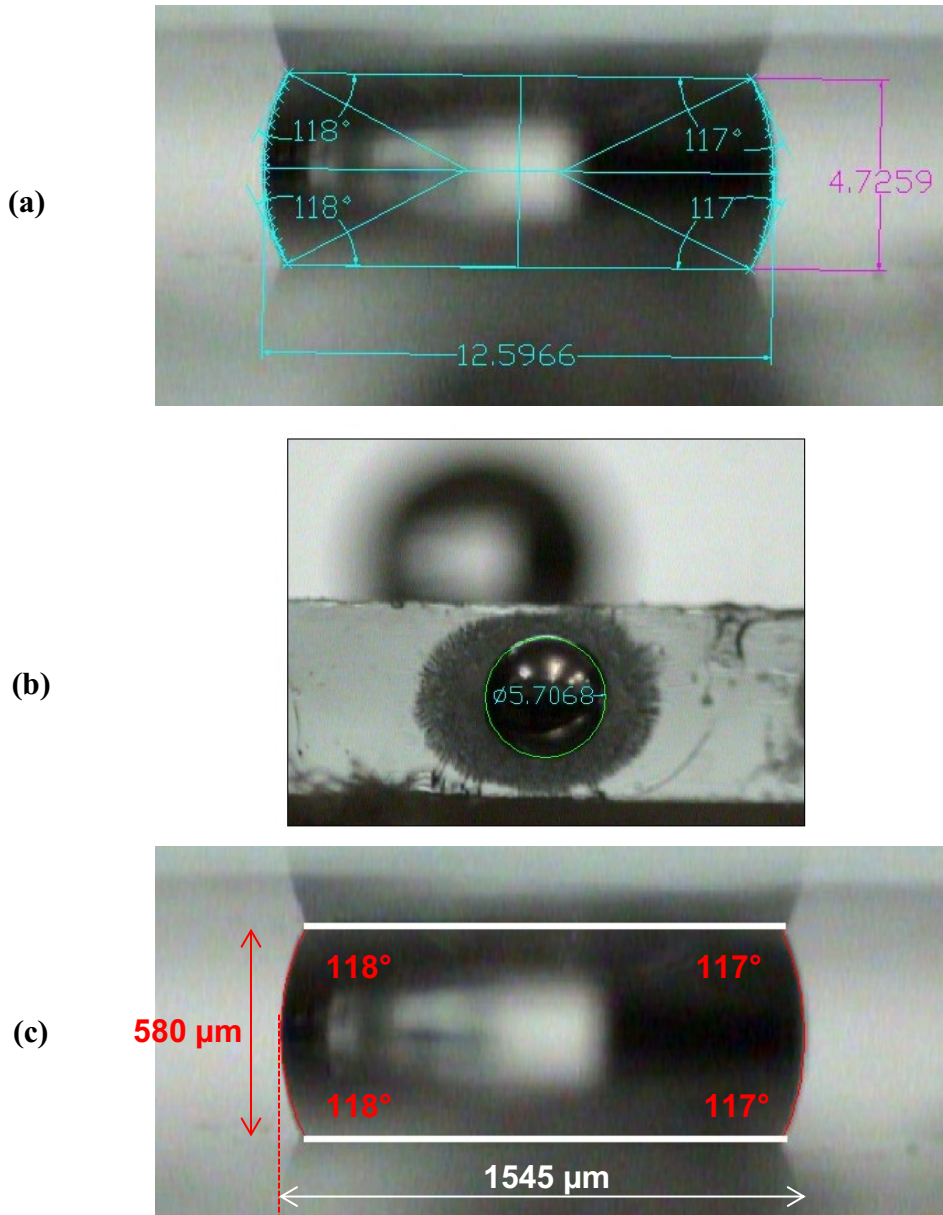


Figure 4-1: Image analysis using AutoCAD for a 1.6 μl water droplet sandwiched in a 580 μm microchannel gap, (a) detail of procedure, (b) reference scale, (c) droplet profile and measured contact angles and microchannel gap height and droplet maximum diameter.

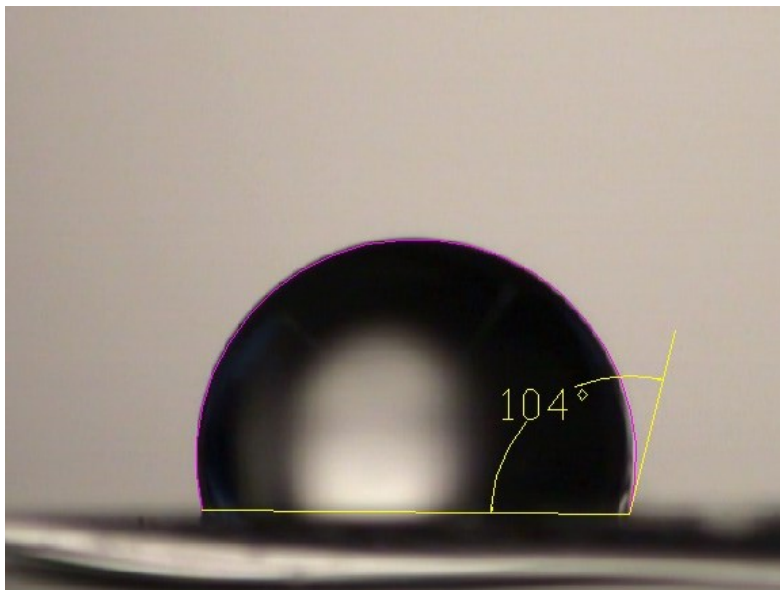
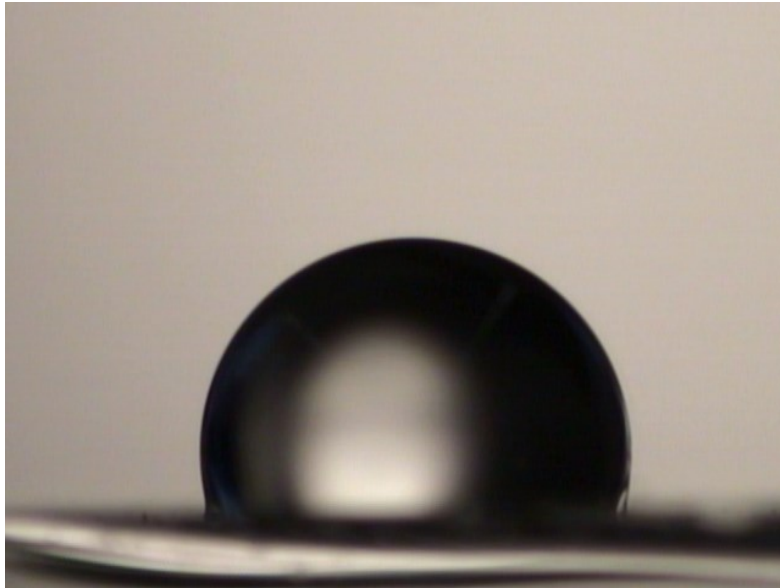


Figure 4-2: Image analysis of a 1.6 μl sessile droplet of water on Teflon coated substrate by using AutoCAD.

One of the challenges in contact angle measurement experiments is preparing the surfaces, as surface roughness largely depends on the surface preparation, and surfaces with small-scale roughness can be a major cause of variability⁶⁹. Contaminated surfaces also inhibit wetting and thus produce higher contact angles than clean surfaces. Acetone is often used to clean Teflon; however, previous findings have shown that acetone can increase the roughness of Teflon. Therefore, the surface of the samples has to be very carefully cleaned. Based on the recommendations received from Sigma-Aldrich, Advanced Coating Systems (SCS), and DuPont companies, the Teflon coated samples need to be first cleaned with IPA solvent followed by rinsing with deionized water, and then air dried (filtered air) before dispensing the droplets of the desired solution and taking images for contact angle measurements.

In addition to contamination, many other environmental conditions such as temperature, relative humidity, surface roughness, material homogeneity, and static electricity can affect contact angle.

4.2) Selecting the appropriate Buffer solution

In order to verify the effect of the type of buffer solution on the contact angle, the DNA samples were prepared in two commonly used buffer solutions as below:

- DNA suspension buffer containing 10 mM Tris-HCl and 0.1 mM EDTA with pH = 8.0, RNase/DNase-Free and sterile, readily purchased in 1 ml tubes from Teknova (USA)
- buffer solution with pH =7.0, readily purchased from Fisher Scientific (Canada)

The DNA samples with concentrations of 4 and 8 $\mu\text{g/ml}$ (the dilute regime), 350 $\mu\text{g/ml}$ (the overlap regime) and 1000 $\mu\text{g/ml}$ (the semi-dilute) were dissolved in the above mentioned buffer solutions. For measuring the contact angle, five separate droplets of each concentration and the corresponding buffer solutions were dispensed on a Teflon coated substrate (Figure 2-2 – only the bottom plate), and the contact angles were measured. In order to minimize the effect of evaporation, all the experiments were done in the humidity chamber

(shown in Figure 2-10) and the droplets volumes and the experimental conditions were kept the same. In this study, no voltage is applied and the behaviour of the sample solutions on Teflon surface is investigated.

The average contact angles of all solutions of Tris-HCl buffer (pH = 8.0) and buffer solution with pH = 7.0 are compared in Figure 4-3.

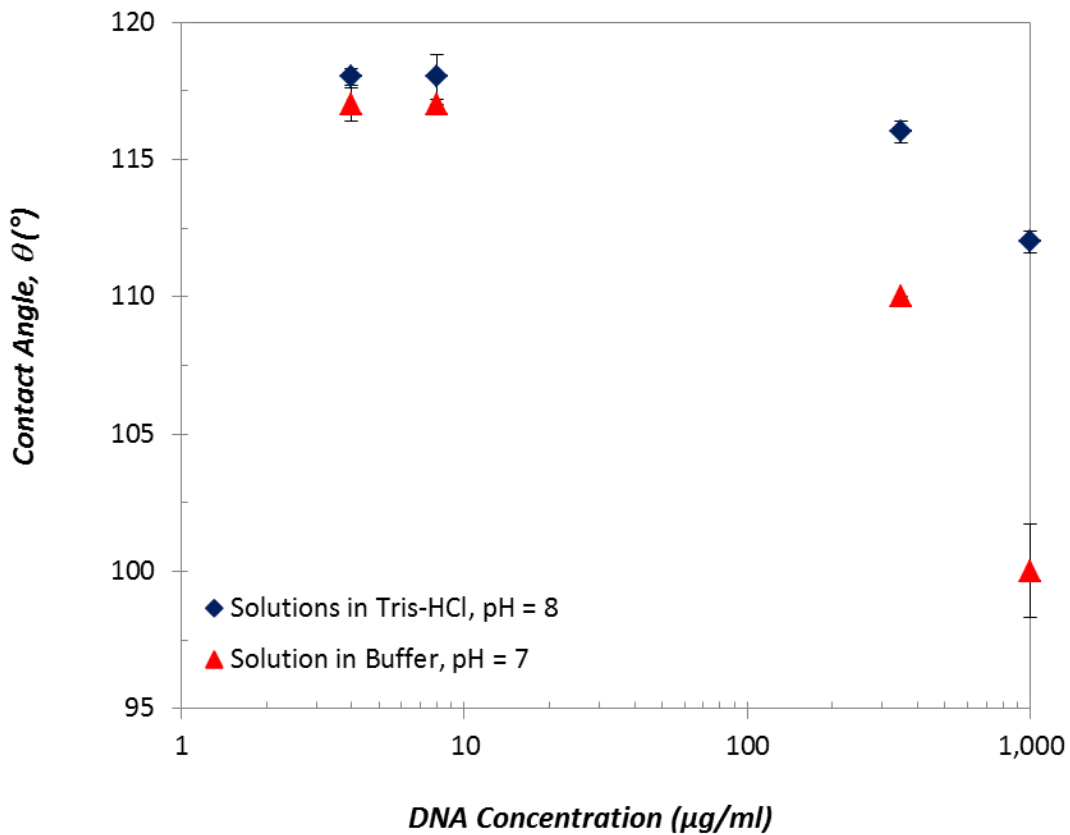


Figure 4-3: Comparison of average contact angle as a function of DNA concentration for the droplets of Tris-HCl buffer solution (pH = 8.0), buffer solution (pH =7.0), and 4, 8, 350 and 1000 µg/ml DNA solutions. The error bars indicate standard deviation.

Overall, the DNA solutions in Tris-HCl buffer (the average volume of $1.41 \pm 0.01 \mu\text{l}$) have higher contact angles (especially at higher concentrations of DNA) indicating that the Tris-HCl buffer solution is a more appropriate buffer solution for dissolving the DNA samples; since in electrowetting, higher contact angles before applying voltage are desirable. The differences in contact angle between the base buffer solutions and the DNA solutions with concentration of 4-8 $\mu\text{g/ml}$ are negligible; however, with increasing DNA concentration, the contact angle decreases. This reduction is more apparent for the buffer solution with $\text{pH} = 7.0$ (the average volume of $1.35 \pm 0.01 \mu\text{l}$) which could be related to the differences in pH 's and/or the elements present in Tris-HCl buffer solution. Based on literature, the adsorption at solid-liquid interface which plays a significant role on the contact angle is also dependent on the buffer type²²⁰. Therefore, all the experimental results presented in the rest of this chapter and chapter 5 are for the DNA solutions in Tris-HCl buffer with $\text{pH} = 8.0$.

4.3) The Effect of Voltage on Contact Angle on Planar Electrodes

In this section, the effect of voltage on contact angle on planar electrodes, as shown in Figure 2-2 is investigated. The details of these experiments are explained in the following sections.

4.3.1) Sessile Droplets

In this section, sessile droplets of Tris-HCl buffer solution and DNA solutions in Tris-HCl buffer with concentrations of 4, 8, 350 and 1000 $\mu\text{g/ml}$ are dispensed on Teflon coated substrates with 800 nm thick Parylene C coating. The configuration of the system is the same as in Figure 2-2; however, instead of the top plate, 0.25 mm thick silver wires are used to apply voltage to the sessile droplets. Starting from 0 V and the contact angle in the absence of an electric field (θ_0), the voltage is increased at a 10 V interval to 80-100 V. At each applied voltage, the images are recorded from the side and are processed using AutoCAD. The experiments are repeated for 3-5 different droplets of each fluid.

In Figure 4-4, droplet morphology of Tris-HCl buffer solution at various voltages is presented.

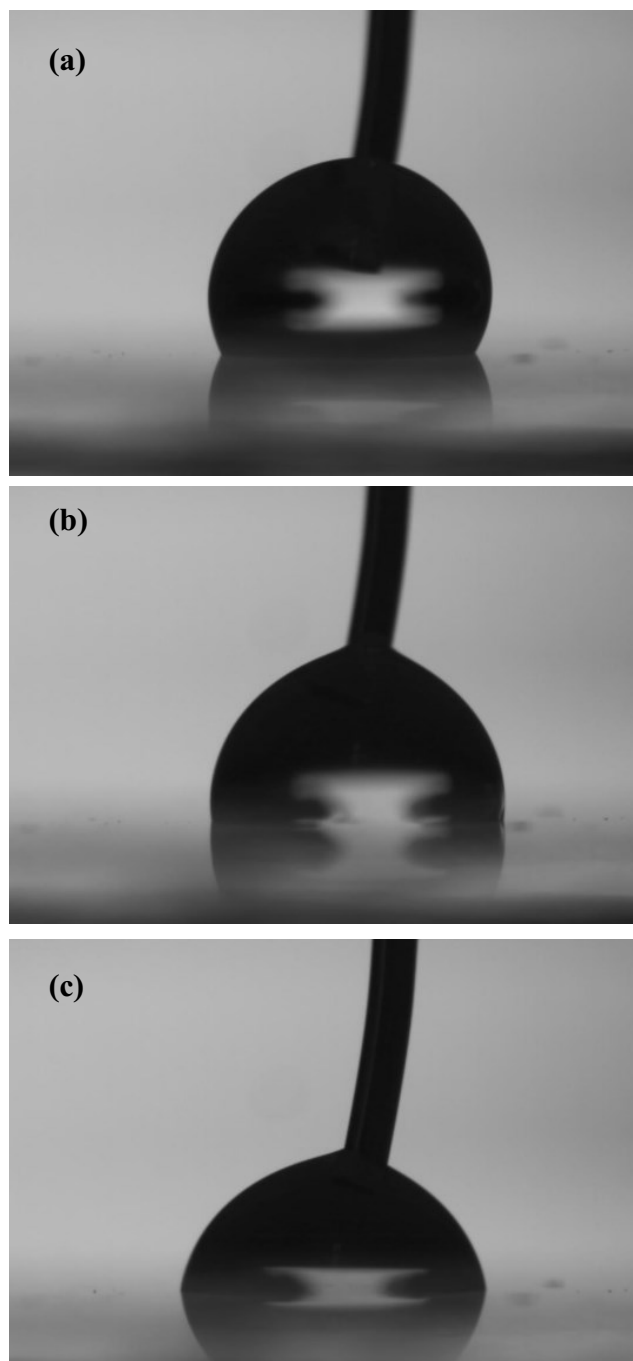


Figure 4-4: Droplet morphology of Tris-HCl buffer solution with an average volume of $1.32 \pm 0.05 \mu\text{l}$ at: (a) 0 V, (b) 35 V, (c) 100 V.

For all fluids, the contact angle (θ) decreases with increasing voltage; however, after reaching a critical threshold voltage, the contact angle saturates and becomes independent of the applied voltage. The change of contact angle with voltage is shown in Figure 4-5 for 4 $\mu\text{g/ml}$ DNA solution. The contact angle as a function of voltage for sessile droplets of Tris-HCl buffer solution, 8, 350 and 1000 $\mu\text{g/ml}$ DNA solutions are presented in Appendix D (Figure D-1 through Figure D-4). The observed differences in the contact angles from the contact angles shown in Figure 4-3 at higher concentrations of DNA solution is due to the fact that the experiments were done on different coated surfaces where the heterogeneity of the surfaces affected the results. In average, the volume of all fluids is $1.35 \pm 0.08 \mu\text{l}$.

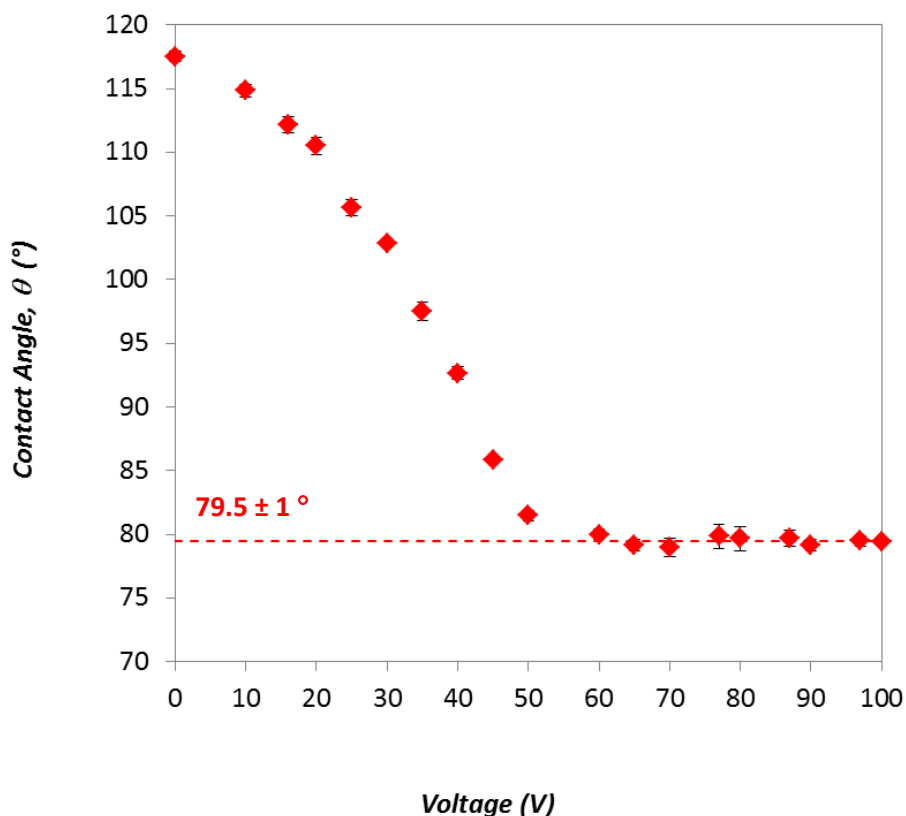


Figure 4-5: The contact angle (θ) as a function of voltage for sessile droplets of 4 $\mu\text{g/ml}$ DNA solution with an average volume of $1.34 \pm 0.01 \mu\text{l}$. The saturation contact angle is shown on the graph (dashed line), and the error bars indicate standard deviation. Error bars are smaller than symbols in all cases where not visible.

Figure 4-6 shows the contact angle (θ) as a function of voltage for all fluids. No significant difference in saturation contact angle (θ_s) is observed between the droplets of Tris-HCl buffer solution and the 4 $\mu\text{g/ml}$ DNA solution. For the 8 $\mu\text{g/ml}$ DNA solution, the divergence from the base buffer solution is more apparent. With increasing of DNA concentration to 350 and 1000 $\mu\text{g/ml}$, the contact angle in the absence of an electric field (θ_0) decreases to a greater extent, and the contact angle saturates at significantly higher contact angles.

Figure 4-7 shows the comparison of $\Delta\theta_v$ (*i.e.* the difference between the contact angle in the absence of an electric field (θ_0) and the contact angle when the voltage is applied (θ)) as a function of voltage. With increasing voltage, the curves start to diverge and finally reach a plateau at saturation. From this graph, it is concluded that the saturation potential is reduced when DNA concentration increases. After the saturation potential, any further increase of voltage will not change the contact angle, and the interface will only show instabilities.

In Figure 4-8, the effect of DNA concentration on the contact angle saturation is shown indicating that with increasing of DNA concentration, the contact angle saturates at higher values. While the saturation voltage reduces from ~ 60 V for sessile droplets of 4 $\mu\text{g/ml}$ DNA solution to ~ 50 V for 1000 $\mu\text{g/ml}$ DNA solution (Figure 4-7), the value of $\Delta\theta_s$ decreases from 38° to 15° (Figure 4-8).

The results of the experiments on sessile droplets are finally compared with those of sandwiched droplets (microchannel gaps of 300 and 600 μm) in section 4.3.3; where the expected impact of $\Delta\theta_v$ on droplet movement will be further discussed.

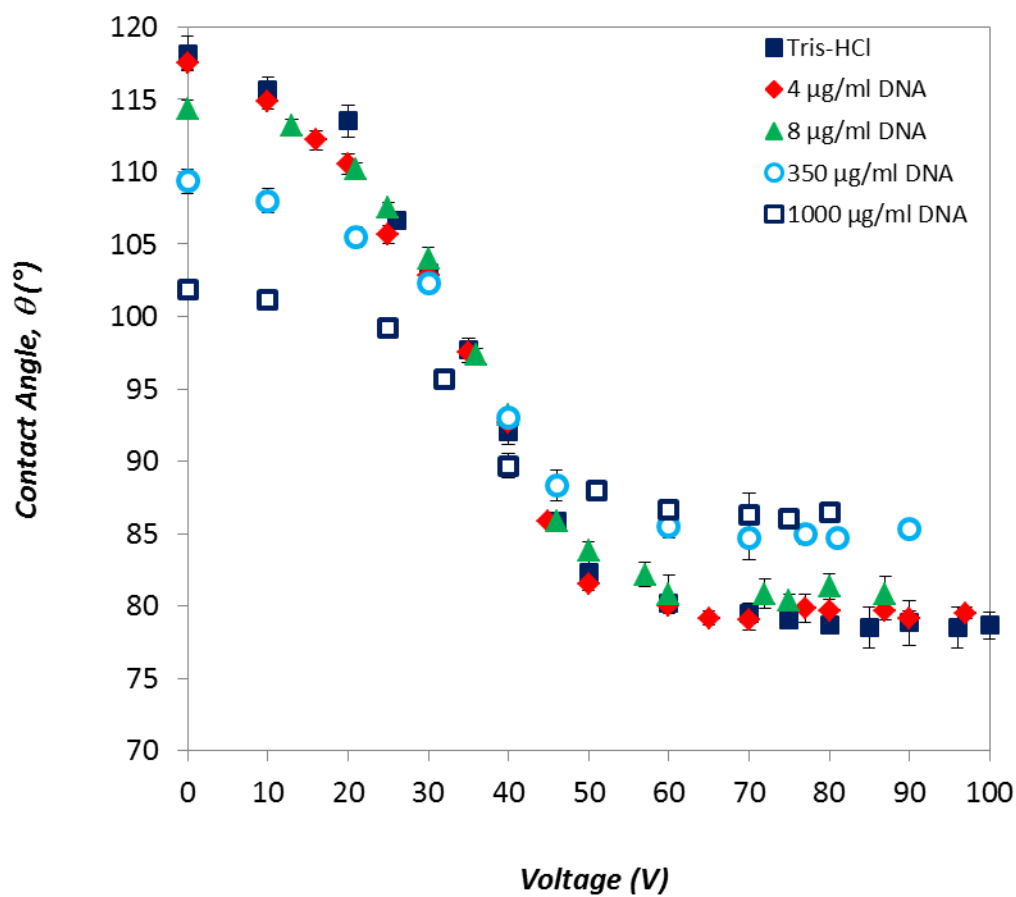


Figure 4-6: Comparison of contact angle (θ) as a function of voltage for sessile droplets of Tris-HCl buffer solution and different concentrations of DNA solutions with an average volume of $1.35 \pm 0.08 \mu\text{l}$. The error bars indicate standard deviation. Error bars are smaller than symbols in all cases where not visible.

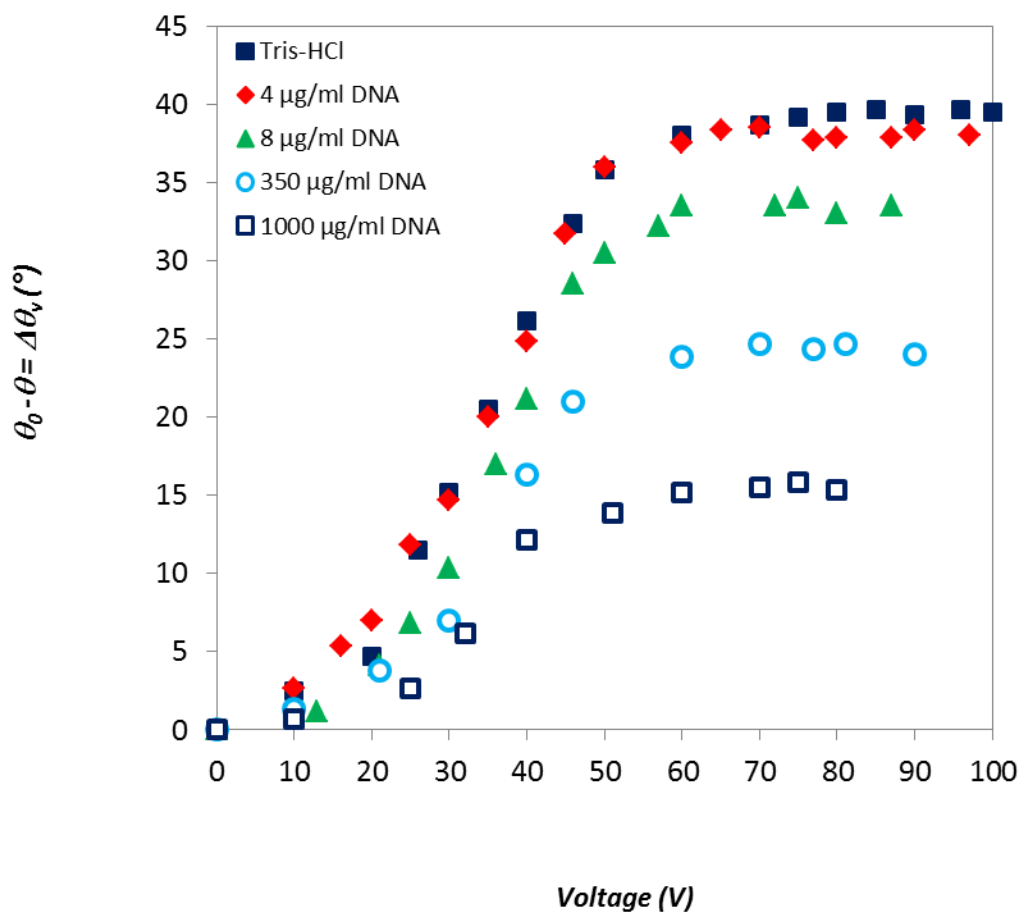


Figure 4-7: Comparison of $\Delta\theta_v$ (*i.e.* the difference between the contact angle in the absence of an electric field (θ_0) and the contact angle when the voltage is applied (θ)) as a function of voltage for all solutions with an average volume of $1.35 \pm 0.08 \mu\text{l}$.

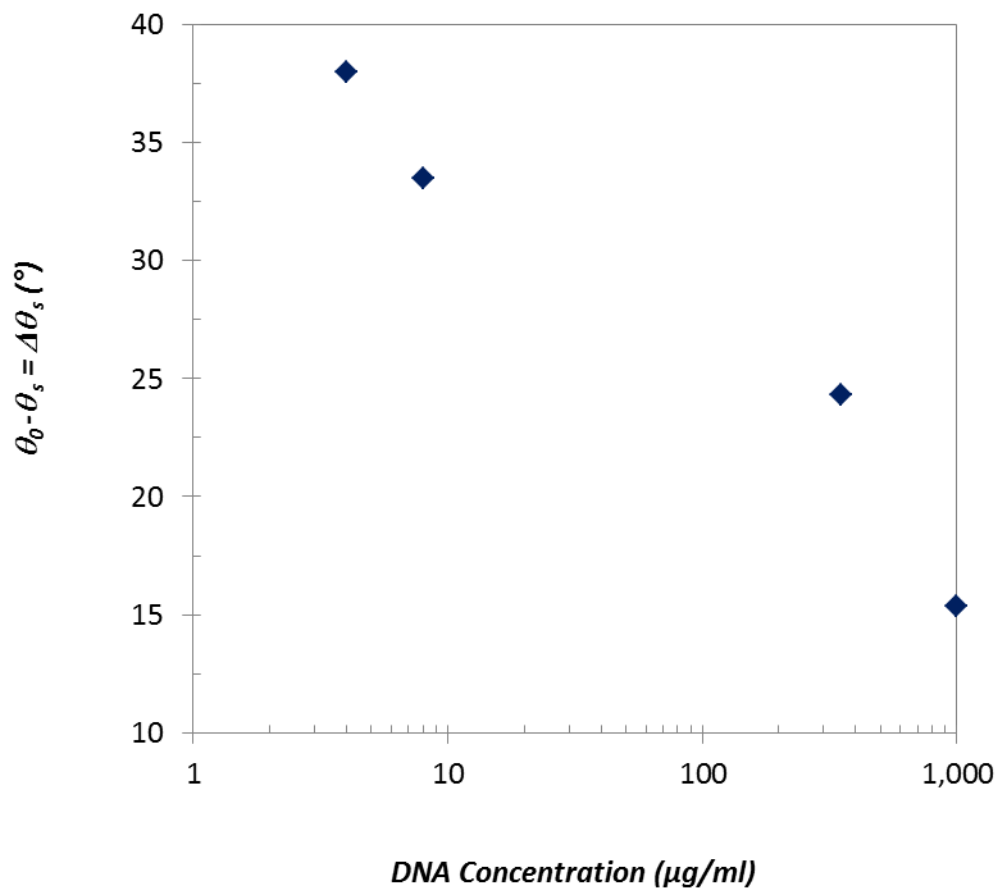


Figure 4-8: Comparison of $\Delta\theta_s$ (*i.e.* the difference between the contact angle in the absence of an electric field (θ_0) and the saturation contact angle (θ_s)) as a function of DNA concentration for DNA solutions with an average volume of 1.35 ± 0.08 (μl).

4.3.2) Sandwiched Droplets

In this section, the effect of voltage on the contact angle of sandwiched droplets in a microchannel gap with planar electrodes, as shown in Figure 2-2, is investigated. The details of these experiments are explained in the following sections.

4.3.2.1) Microchannel Gap of 600 μm

In this section, sessile droplets of Tris-HCl buffer solution and DNA solution with concentrations of 4, 8, 100, 150, 350 and 1000 $\mu\text{g/ml}$ are first dispensed on Teflon coated substrates with 800 nm thick Parylene C coating. The droplets are sandwiched in a microchannel gap with an average value of $602 \pm 10 \mu\text{m}$. The configuration of the system is the same as in Figure 2-2. Starting from 0 V and the contact angle in the absence of an electric field (θ_0), the voltage is increased at a 10 V interval to 90 V. At each applied voltage, the images are recorded from the side and are processed using AutoCAD. The experiments are repeated for 3-5 different droplets of each fluid. In order to compare with literature, droplets of distilled water are also studied. The average volume of all fluids is $1.52 \pm 0.03 \mu\text{l}$.

For distilled water, the change of contact angle (at the top and bottom interfaces) with voltage is shown in Figure 4-9. The contact angle at the top interface stays the same with an average value of $115.5 \pm 1^\circ$. For the bottom plate, the contact angle (θ) decreases with increasing voltage and saturates at $\sim 72^\circ$ after. The divergence of the curve from the theory of Young-Lippmann's relation (Equation 1-9) is also shown.

In Figure 4-10, droplet morphology of distilled water (the top and side views) at various voltages are presented which are in good agreement with the experimental results of Cho *et al.*⁸⁰.

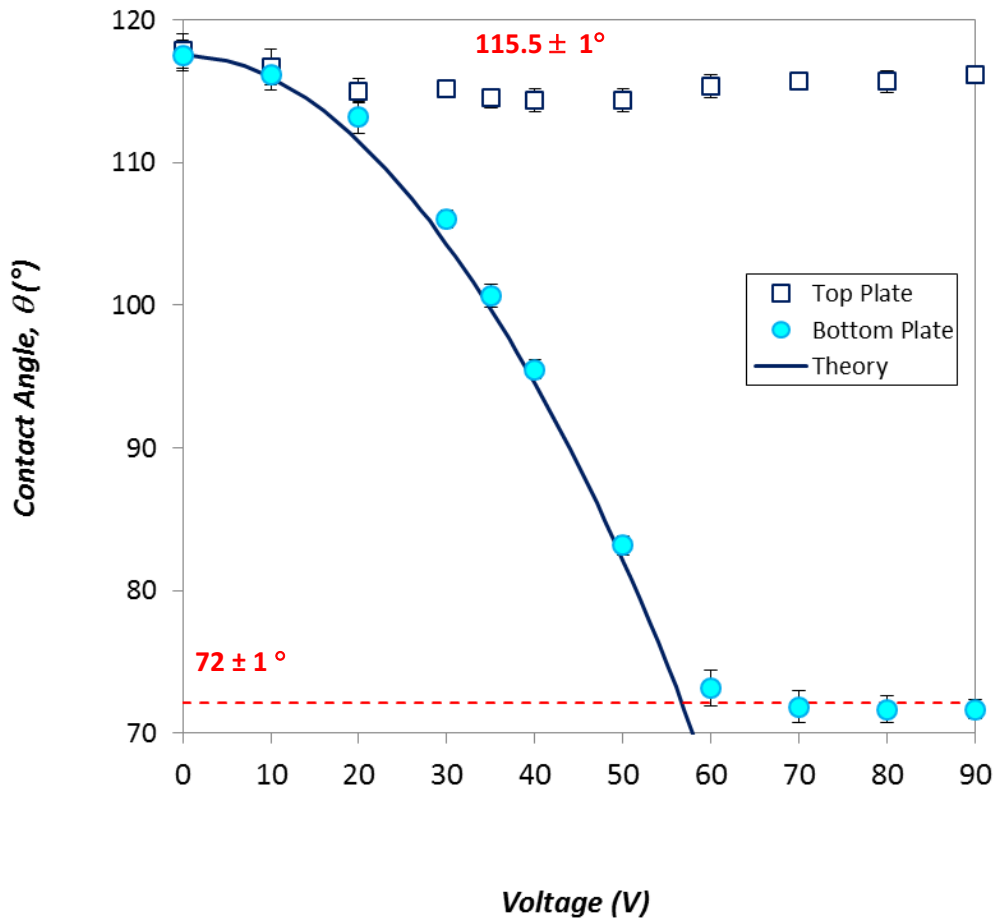


Figure 4-9: The contact angle (θ) as a function of voltage for sandwiched droplets of distilled water with an average volume of $1.56 \pm 0.03 \mu\text{l}$ in a microchannel gap of $580 \pm 6 \mu\text{m}$ at the top and bottom interfaces; the solid line is based on the theory of Young-Lippmann's relation. The saturation contact angle is also shown on the graph (dashed line). The error bars indicate standard deviation. Error bars are smaller than symbols in all cases where not visible.

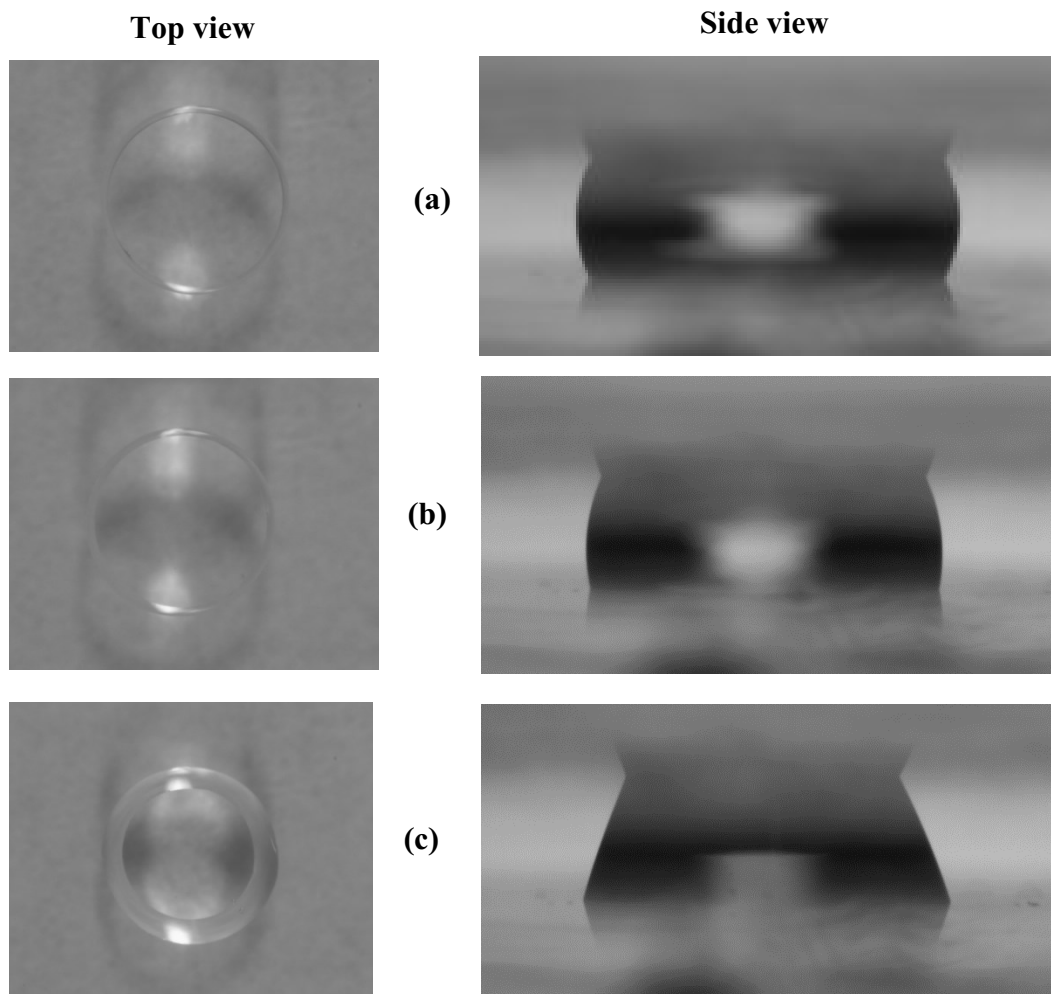


Figure 4-10: Droplet morphology of distilled water at various voltages: (a) 0 V, (b) 35 V, (c) 90 V.

Figure 4-11 shows the contact angle at the top and bottom interfaces as a function of voltage for sandwiched droplets of 4 $\mu\text{g/ml}$ DNA solutions. Figure D-5 through Figure D-10 in Appendix D present the contact angle as a function of voltage for Tris-HCl buffer solution and DNA solutions with concentrations of 8, 100, 150, 350 and 1000 $\mu\text{g/ml}$.

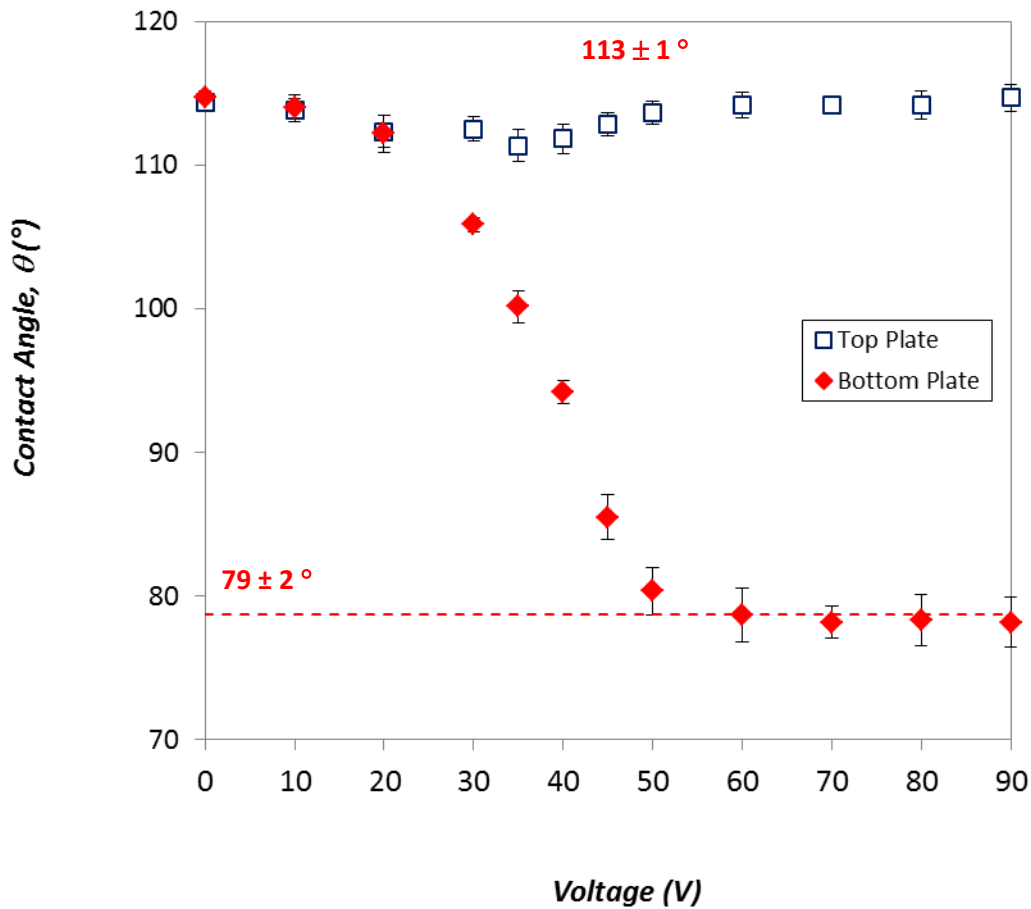


Figure 4-11: The contact angle (θ) as a function of voltage for sandwiched droplets of 4 $\mu\text{g/ml}$ DNA solution with an average volume of $1.47 \pm 0.02 \mu\text{l}$ in a microchannel gap of $604 \pm 3 \mu\text{m}$ at the top and bottom interfaces. The saturation contact angle is shown on the graph (dashed line), and the error bars indicate standard deviation. Error bars are smaller than symbols in all cases where not visible.

As shown in Figure 4-12 and Figure 4-16, in comparison to the other fluids investigated in this section, distilled water has a higher contact angle in the absence of an electric field, (θ_0) and a lower saturation angle (θ_s) than all other solutions. Despite the fact that in the absence of an electric field, there is merely a 3° difference among the contact angles of distilled water, Tris-HCl buffer solution and DNA solutions with concentrations of 4-8 $\mu\text{g/ml}$, the saturation contact angles change to a greater extent of 11° . It means that in a microchannel gap of $600\ \mu\text{m}$, increasing DNA concentration by a few $\mu\text{g/ml}$ causes the droplets to saturate at significantly higher contact angles. Finally, with increasing DNA concentration to $1000\ \mu\text{g/ml}$, the contact angle in the absence of an electric field reduces to 105° , and the saturation contact angle increases to 93° .

A comparison of the average contact angle at the top interface, (θ_T), as a function of DNA concentration is presented in Figure 4-13. It shows that with increasing DNA concentration, the contact angle at the top interface decreases. The reduction of contact angle from $4\ \mu\text{g/ml}$ DNA solution to $1000\ \mu\text{g/ml}$ DNA solution is around 16° . Depending on the contact angle hysteresis, (θ_T) can be equivalent to the contact angle in the absence of an electric field.

Figure 4-14 shows a comparison of $\Delta\theta_v$ (*i.e.* the difference between the contact angle in the absence of an electric field (θ_0) and the contact angle when the voltage is applied (θ)) as a function of voltage for sandwiched droplets. The same in Figure 4-7 for sessile droplets, with increasing voltage, the curves start to diverge and finally at saturation, each curve reaches a plateau. From this graph, it is concluded that the saturation potential is reduced when DNA concentration increases. After the saturation potential, any further increase of voltage will not change the contact angle, and the interface will only show instabilities. At saturation, the value of $\Delta\theta_v$ decreases from 38° for Tris-HCl buffer solution to 12° for $1000\ \mu\text{g/ml}$ DNA solution while the saturation potential decreases from $\sim 60\ \text{V}$ to $\sim 35\ \text{V}$. This indicates the significant effect of DNA on the change in contact angle in response to a voltage. The expected effect of $\Delta\theta_v$ on droplet movement will be discussed in section 4.3.3.

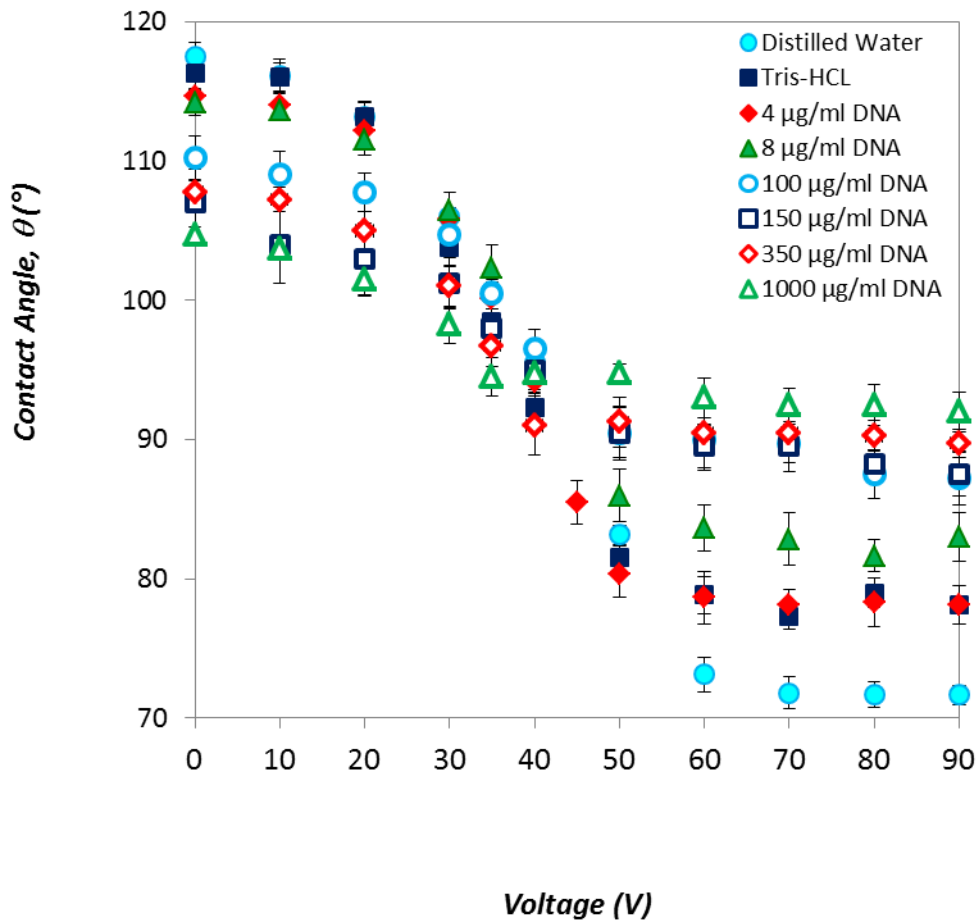


Figure 4-12: Comparison of contact angle (θ) as a function of voltage for sandwiched droplets of distilled water, Tris-HCl buffer solution and different concentrations of DNA solutions with an average volume of 1.52 ± 0.03 (μl) and microchannel gap of 602 ± 10 (μm). The data are for the contact angle at the bottom interface, and the error bars indicate the standard deviations. Error bars are smaller than symbols in all cases where not visible.

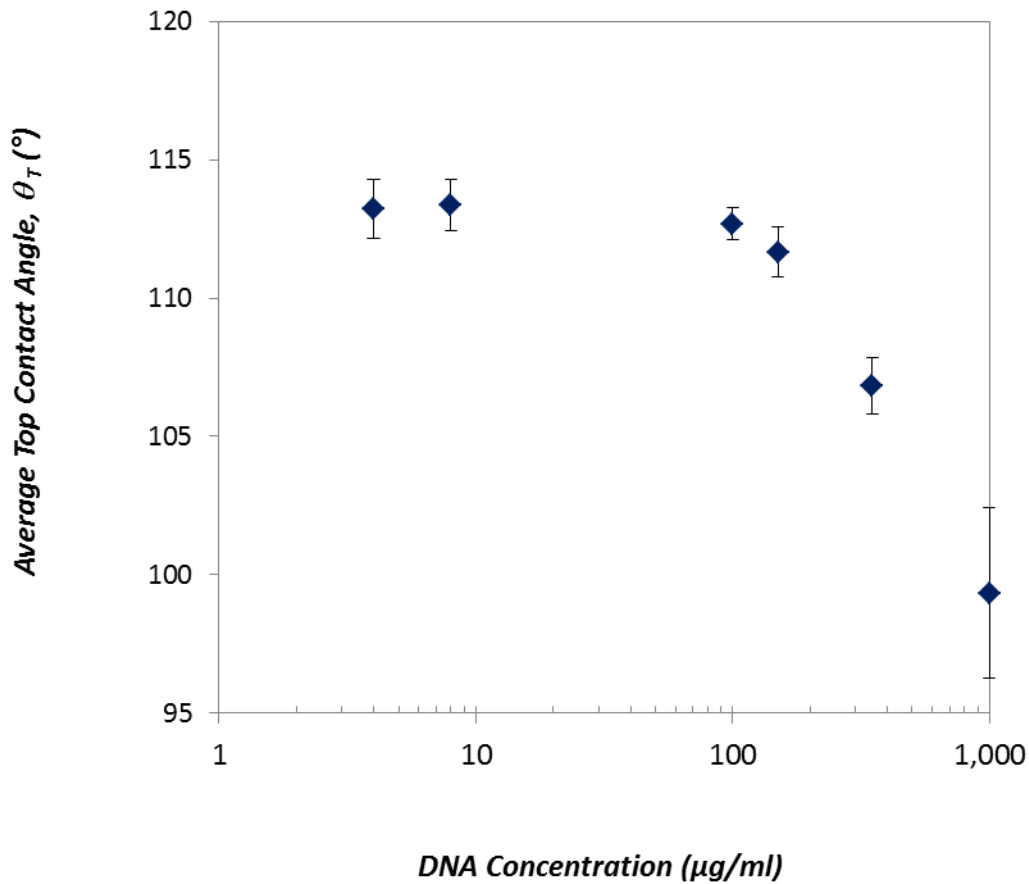


Figure 4-13: Comparison of the average contact angle at the top interface, θ_T , as a function of DNA concentration in Tris-HCl buffer for sandwiched droplets of different concentrations of DNA solutions. The average volume of the droplets is 1.52 ± 0.03 (μl) for the average microchannel gap of 602 ± 10 (μm). The error bars indicate standard deviation. Error bars are smaller than symbols in all cases where not visible.

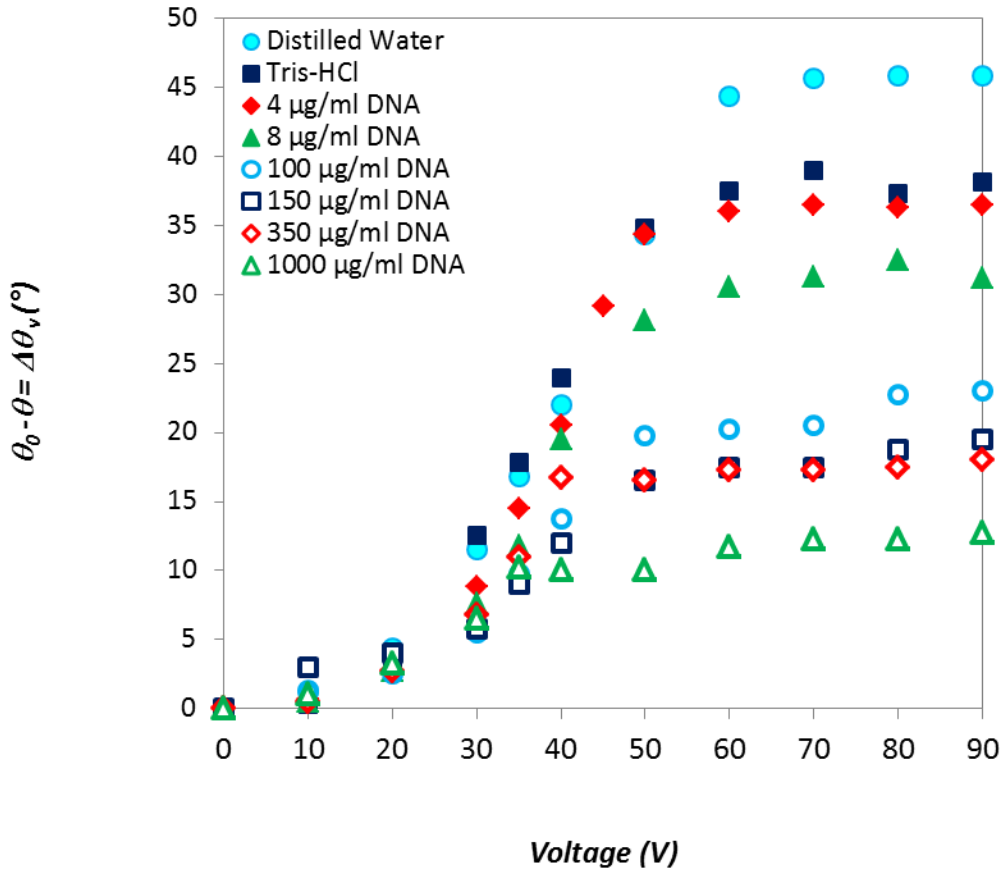


Figure 4-14: Comparison of $\Delta\theta_v$ (*i.e.* the difference between the contact angle in the absence of an electric field (θ_0) and the contact angle when the voltage is applied (θ)) as a function of voltage for sandwiched droplets of distilled water, Tris-HCl buffer solution and different concentrations of DNA solutions with an average volume of 1.52 ± 0.03 (μl) and microchannel gap of 602 ± 10 (μm). The data are for the contact angle at the bottom interface.

In Figure 4-15, the effect of DNA concentration on $\Delta\theta_s$ (*i.e.* the difference between the contact angle in the absence of an electric field (θ_0) and the contact angle when the droplet reaches saturation (θ_s)) is displayed. From this graph and Figure 4-12, it is concluded that the saturation contact angle increases with DNA concentration. As shown, $\Delta\theta_s$ decreases from 36° to 11° with increase of DNA concentration from $4 \mu\text{g/ml}$ to $1000 \mu\text{g/ml}$.

Droplet morphology of distilled water, Tris-HCl buffer solution, and DNA solutions are shown in Figure 4-16. With increasing DNA concentration, the sandwiched droplets become more cylindrical (*i.e.* in the absence of an electric field, the contact angles are smaller), and the tri-phase contact angles decrease only a few degrees before reaching saturation.

In section 4.3.3, the results of the experiments presented in this section are compared with those of sessile droplets and sandwiched droplets in a microchannel gap of $300 \mu\text{m}$.

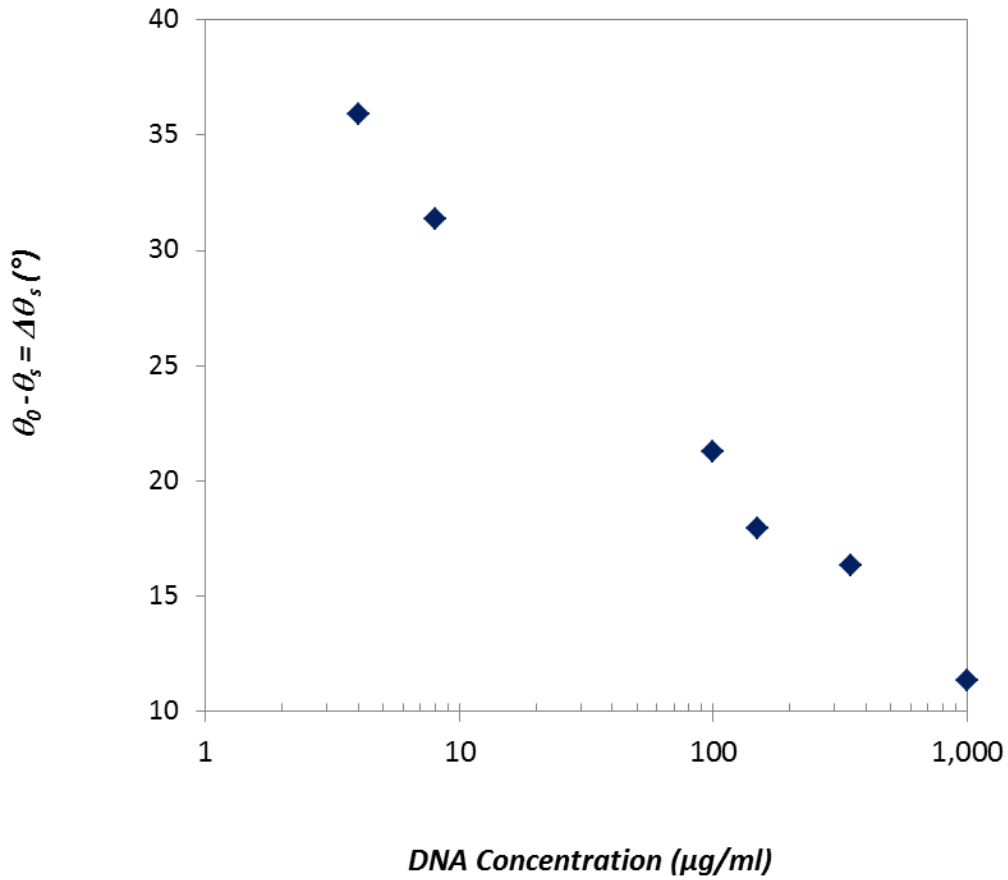


Figure 4-15: Comparison of $\Delta\theta_s$ (*i.e.* the difference between the contact angle at the bottom interface in the absence of an electric field (θ_0) and the average contact angle when the droplet reaches saturation (θ_s)) as a function of DNA concentration in Tris-HCl buffer for sandwiched droplets of DNA solutions. The average volume of the droplets and the microchannel gaps are 1.52 ± 0.03 (μl) and 602 ± 10 (μm) respectively.

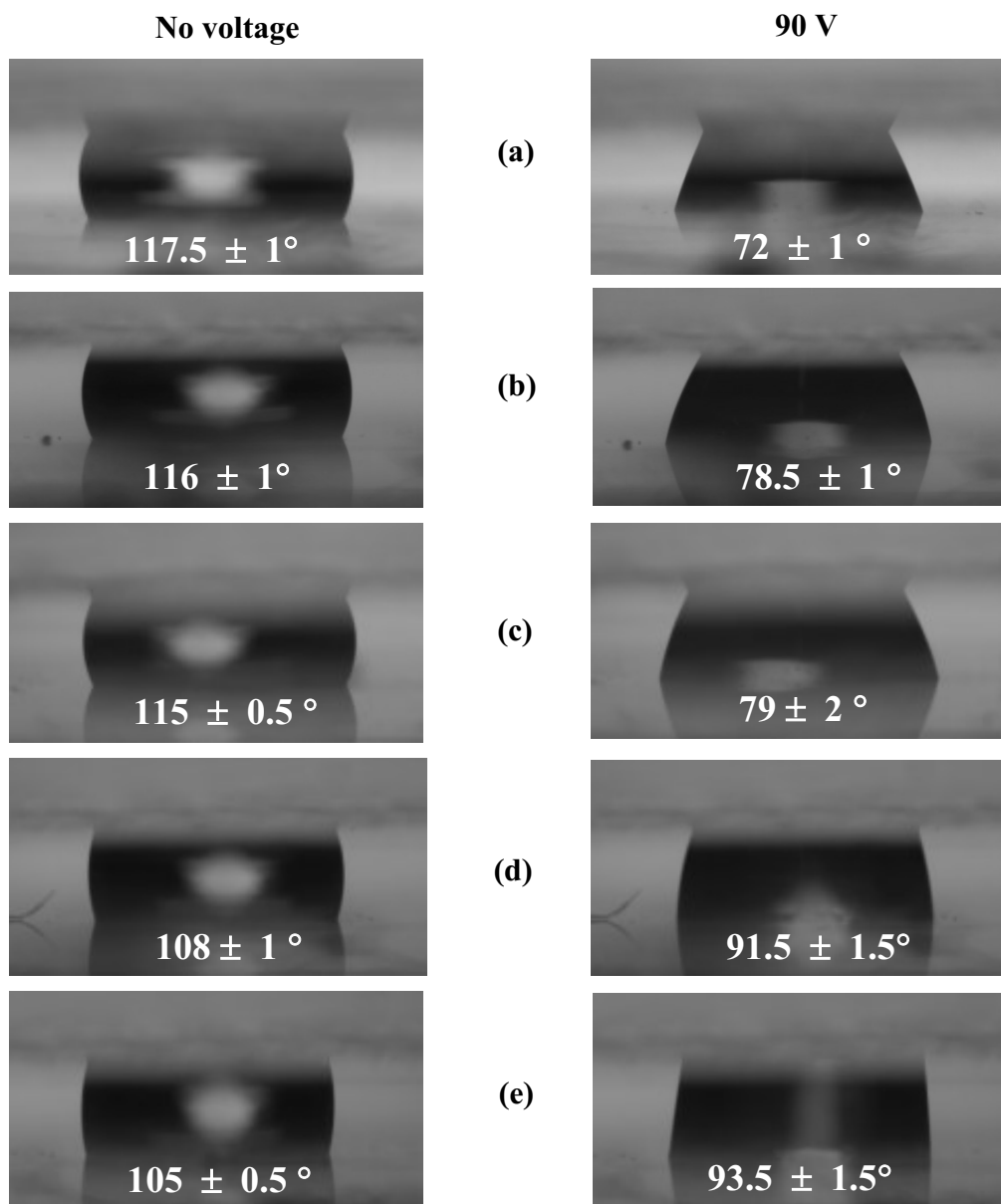


Figure 4-16: Droplet morphology of: (a) distilled water, (b) Tris-HCl buffer solution, (c), (d), (e) 4, 350 1000 $\mu\text{g/ml}$ DNA solutions respectively. The average volume of the droplets is 1.52 ± 0.03 (μl) and the average microchannel gap is 602 ± 10 (μm). The numbers indicate the contact angles at the bottom interfaces.

4.3.2.2) Microchannel Gap of 300 μm

In this section, sessile droplets of Tris-HCl buffer solution and DNA solution with concentrations of 4, 8, 20, 50, 100 and 150 $\mu\text{g/ml}$ are first dispensed on Teflon coated substrates with 800 nm thick Parylene C coating. The droplets are sandwiched in a microchannel gap with the average value of 304 ± 4 (μm). The configuration of the system is the same as in Figure 2-2. Starting from 0 V and the contact angle in the absence of an electric field (θ_0), the voltage is increased at a 10 V interval to 90 V. At each applied voltage, the images are recorded from the side and are processed using AutoCAD. The experiments are repeated for 3-5 different droplets of each fluid. The same as in section 4.3.2.1), droplets of distilled water are also studied. The average volume of all fluids is 0.89 ± 0.052 (μl).

For distilled water, the change of contact angle (at the top and bottom interfaces) with voltage is shown in Figure 4-17. The contact angle at the top interface stays the same with an average value of $116 \pm 1^\circ$. For the bottom plate, the contact angle (θ) decreases with increasing voltage and saturates at $\sim 74^\circ$ after. The divergence of the curve from the theory of Young-Lippmann's relation (Equation 1-9) is also shown.

In Figure 4-18, droplet morphology of distilled water (the top and side views) at various voltages are presented which are in good agreement with the experimental results of Cho *et al.*⁸⁰.

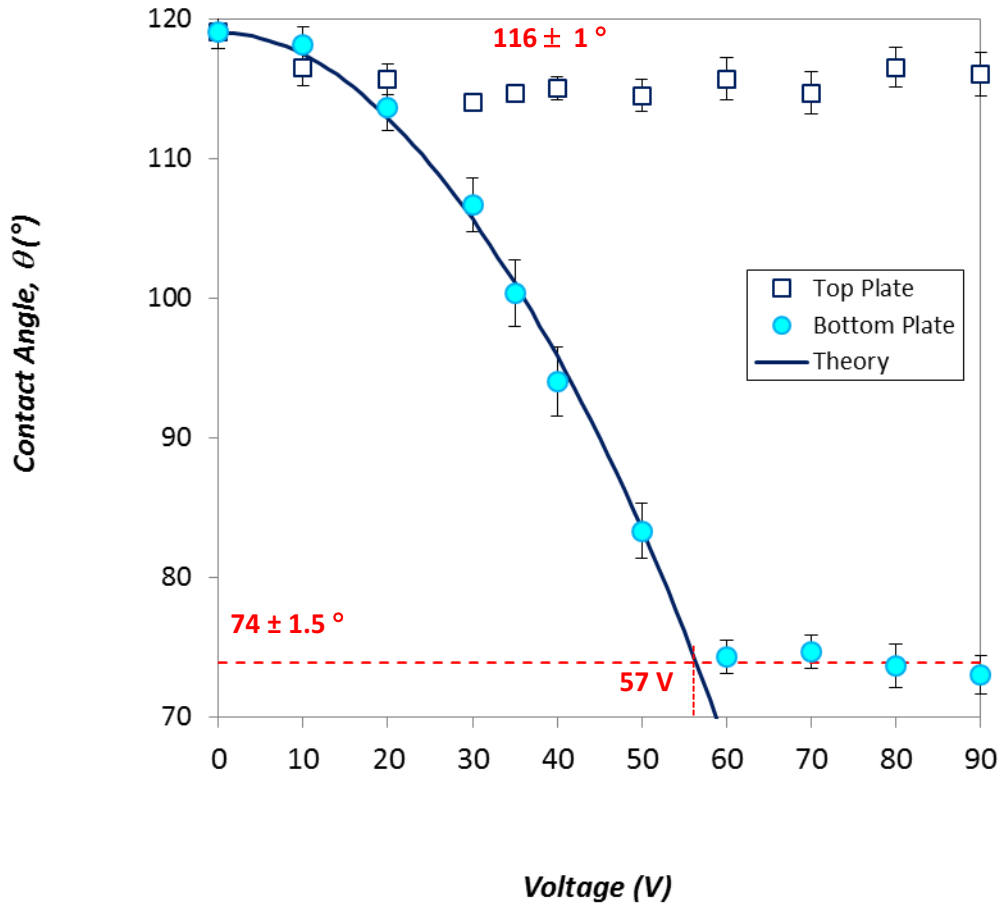


Figure 4-17: The contact angle (θ) as a function of voltage for sandwiched droplets of distilled water with an average volume of $0.86 \pm 0.02 \mu\text{l}$ in a microchannel gap of $295 \pm 5 \mu\text{m}$ at the top and bottom interfaces; the solid line is based on the theory of Young-Lippmann's relation. The saturation contact angle is also shown on the graph (dashed line). The error bars indicate standard deviation. Error bars are smaller than symbols in all cases where not visible.

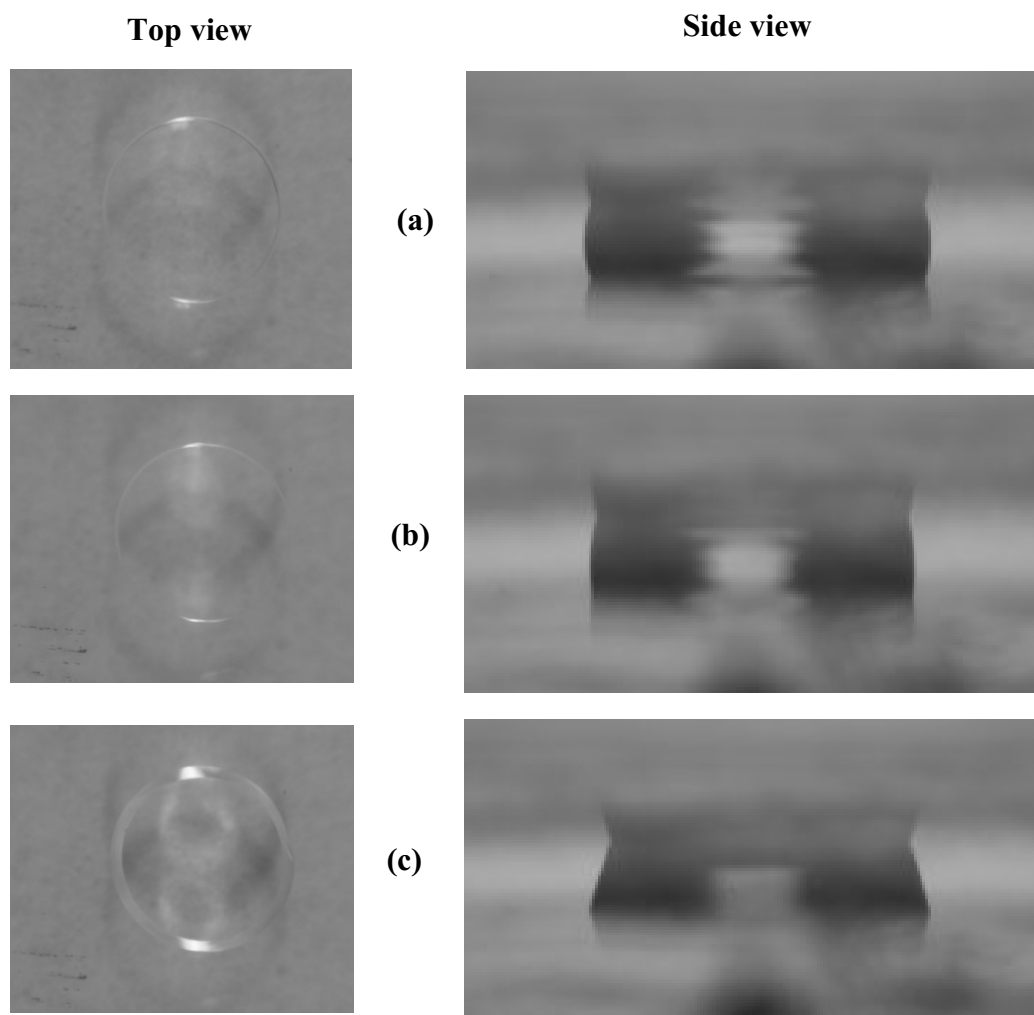


Figure 4-18: Morphology of distilled water droplets at various voltages: (a) 0 V, (b) 35 V, (c) 90 V.

Figure 4-19 shows the contact angle at the top and bottom interfaces as a function of voltage for sandwiched droplets of 4 $\mu\text{g/ml}$ DNA solutions. Figure D-11 through Figure D-16 in Appendix D present the contact angle as a function of voltage for Tris-HCl buffer solution and DNA solutions with concentrations of 8, 20, 50, 100 and 150 $\mu\text{g/ml}$.

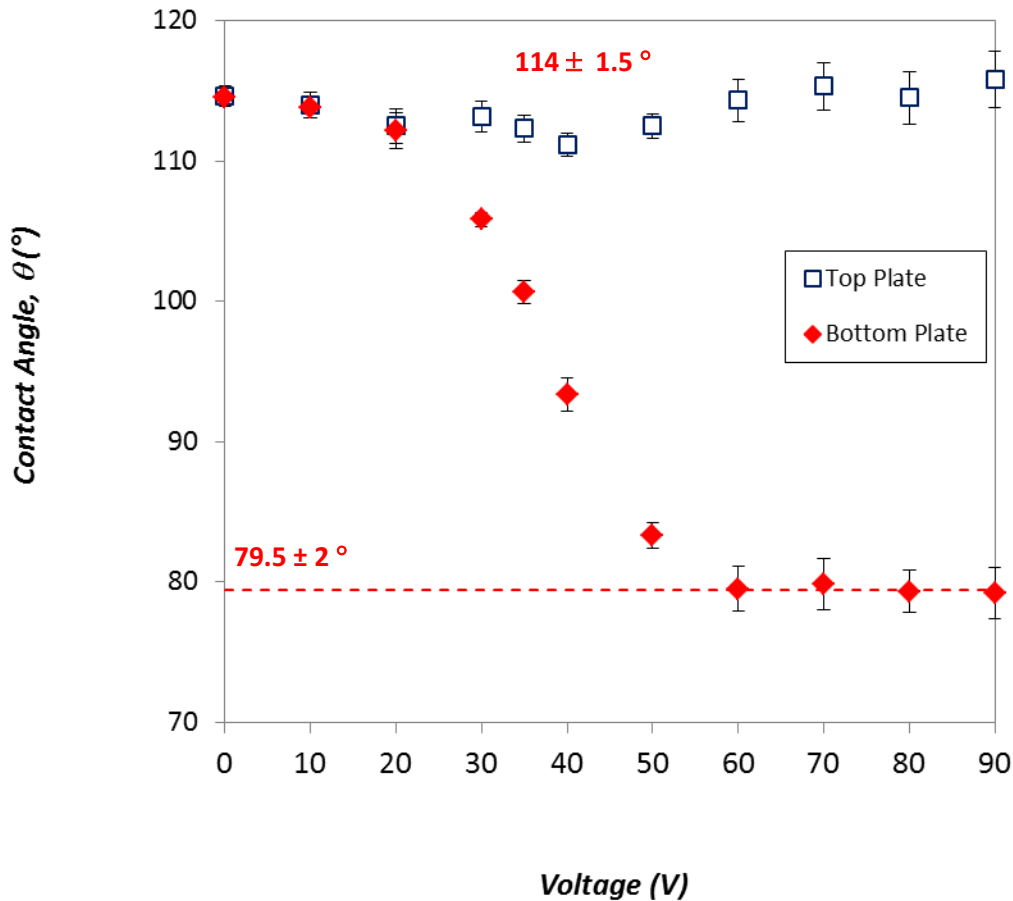


Figure 4-19: The contact angle (θ) as a function of voltage for sandwiched droplets of 4 $\mu\text{g/ml}$ DNA solution with an average volume of $0.85 \pm 0.01 \mu\text{l}$ in a microchannel gap of $306 \pm 3 \mu\text{m}$ at the top and bottom interfaces. The saturation contact angle is shown on the graph (dashed line), and the error bars indicate standard deviation. Error bars are smaller than symbols in all cases where not visible.

The same as in microchannel gap of 600 μm and as shown in Figure 4-20 and Figure 4-24, distilled water droplets have a higher contact angle in the absence of an electric field (θ_0) and a lower saturation angle (θ_s) than all other solutions. Despite the fact that in the absence of an electric field, there is a 5° difference among the contact angles of distilled water, Tris-HCl buffer solution and DNA solutions with concentrations of 4-8 $\mu\text{g/ml}$, the saturation contact angles change to a greater extent of 11° . It means that in a microchannel gap of 300 μm (the same as in microchannel gap of 600 μm), increasing DNA concentration by a few $\mu\text{g/ml}$ causes the droplets to saturate at significantly higher contact angles. Finally, with increasing DNA concentration to 150 $\mu\text{g/ml}$, the contact angle with no voltage reduces to 105° , and the saturation contact angle increases to 91° . Performing experiments with higher concentrations of DNA in microchannel gap of 300 μm was not possible due to electrolysis.

A comparison of the average contact angle at the top interface, (θ_T), as a function of DNA concentration is presented in Figure 4-21. It shows that for the DNA concentrations of 100 $\mu\text{g/ml}$ and lower, the contact angle at the top interface stays the same with an average value of $112 \pm 1^\circ$. This angle slightly decreases at 150 $\mu\text{g/ml}$ DNA concentration. Depending on the contact angle hysteresis, (θ_T) can be equivalent to the contact angle in the absence of an electric field.

Figure 4-22 shows a comparison of $\Delta\theta_v$ (*i.e.* the difference between the contact angle in the absence of an electric field (θ_0) and the contact angle when the voltage is applied (θ)) as a function of voltage for sandwiched droplets. The same as in Figure 4-7 for sessile droplets, and Figure 4-14 for microchannel gap of 600 μm , with increasing voltage, the curves start to diverge and finally at saturation, each curve reaches a plateau. From this graph, it is concluded that the saturation potential is reduced when DNA concentration increases. After the saturation potential, any further increase of voltage will not change the contact angle, and the interface will only show instabilities. At saturation, the value of $\Delta\theta_v$ decreases from 38° for Tris-HCl buffer solution to 13.5° for 150 $\mu\text{g/ml}$ DNA solution while the saturation potential decreases from ~ 60 V to ~ 50 V. This indicates the significant effect of DNA on the change in contact angle in response to a voltage. The expected effect of $\Delta\theta_v$ on droplet movement will be discussed in section 4.3.3.

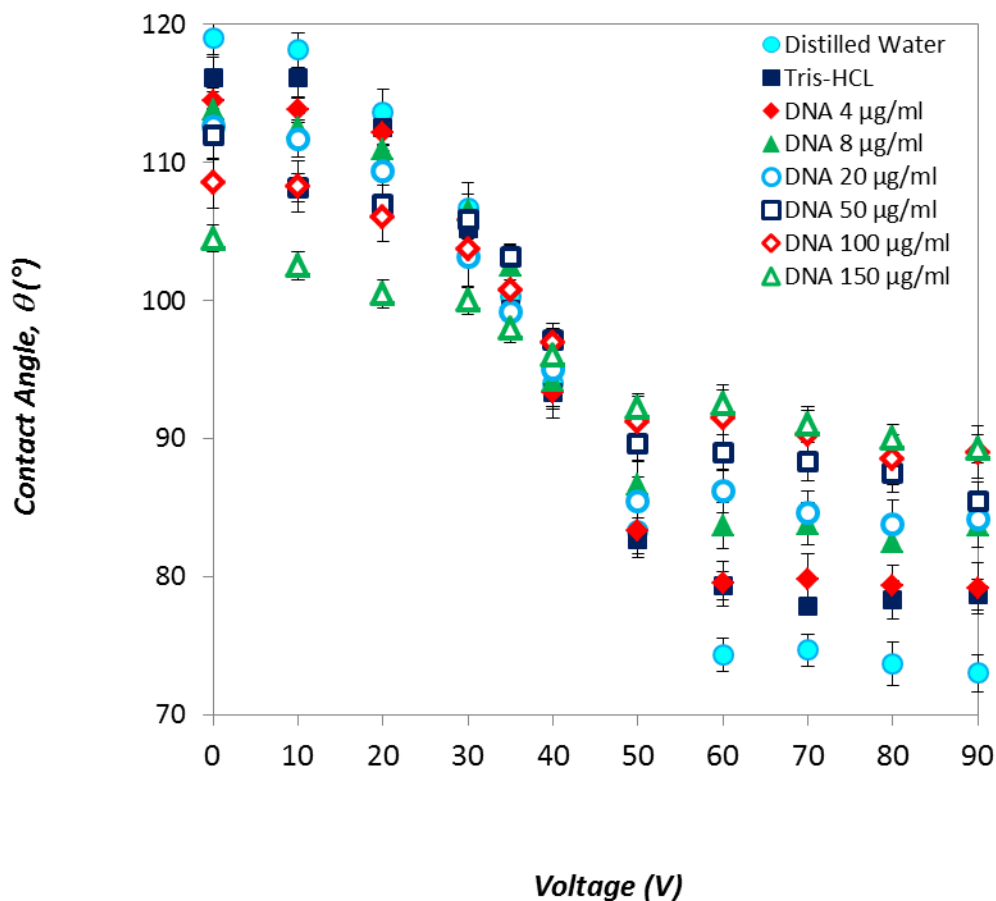


Figure 4-20: Comparison of contact angle (θ) as a function of voltage for sandwiched droplets of distilled water, Tris-HCl buffer solution and different concentrations of DNA solutions with an average volume of 0.89 ± 0.05 (μl) and microchannel gap of 304 ± 4 (μm). The data are for the contact angle at the bottom interface, and the error bars indicate the standard deviation. Error bars are smaller than symbols in all cases where not visible.

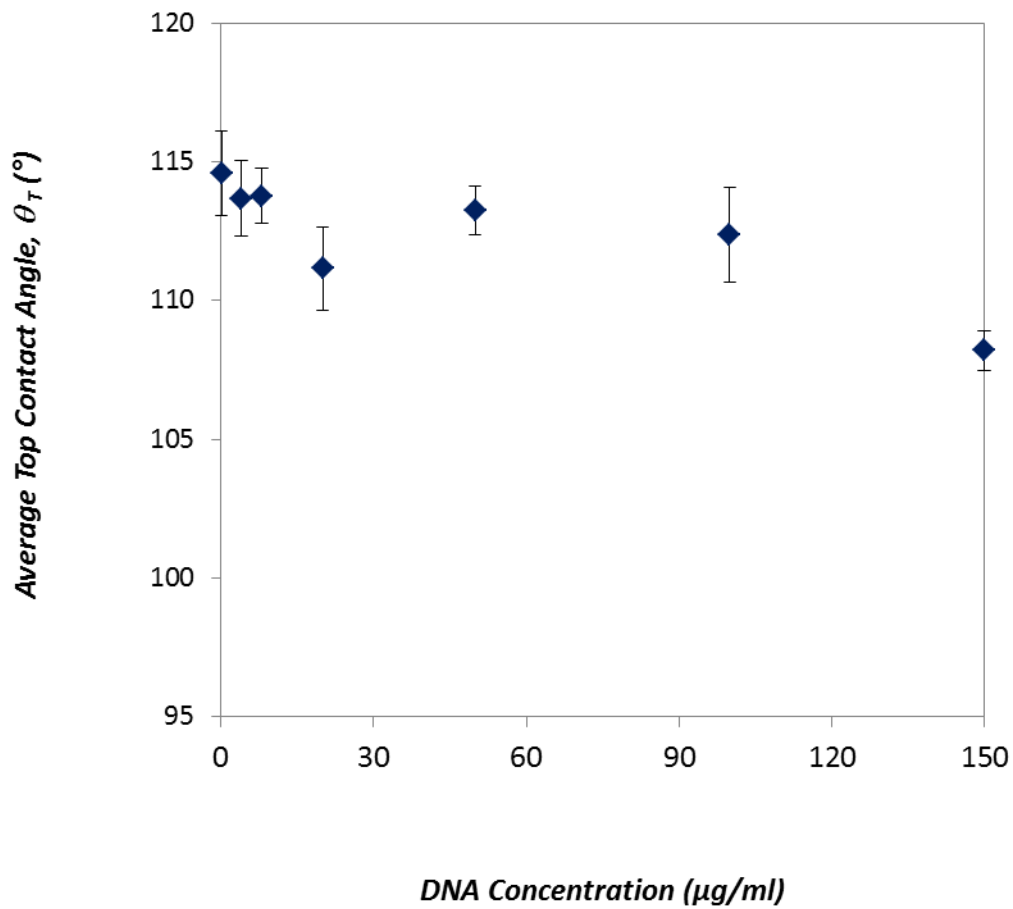


Figure 4-21: Comparison of the average contact angle at the top interface, (θ_T), as a function of DNA concentration for sandwiched droplets of Tris-HCl buffer solution and different concentrations of DNA solutions with an average volume of 0.89 ± 0.05 (μl) for the average microchannel gap of 304 ± 4 (μm). The error bars indicate standard deviation. Error bars are smaller than symbols in all cases where not visible.

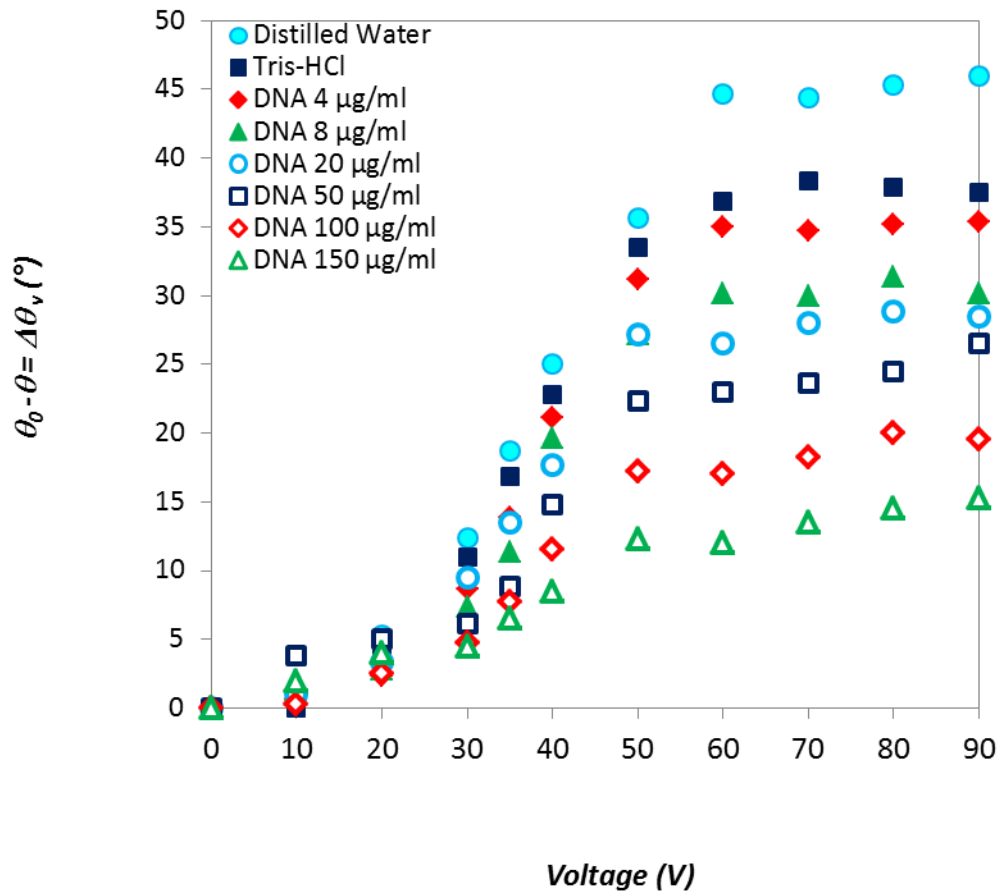


Figure 4-22: Comparison of $\Delta\theta_v$ (*i.e.* the difference between the contact angle in the absence of an electric field (θ_0) and the contact angle when the voltage is applied (θ)) as a function of voltage for sandwiched droplets of distilled water, Tris-HCl buffer solution and different concentrations of DNA solutions with an average volume of 0.89 ± 0.05 (μl) and microchannel gap of 304 ± 4 (μm). The data are for the contact angle at the bottom interface.

In Figure 4-23, the effect of DNA concentration on $\Delta\theta_s$ (*i.e.* the difference between the contact angle in the absence of an electric field (θ_0) and the contact angle when the droplet reaches saturation (θ_s)) is displayed. From this graph and Figure 4-20, it is concluded that the saturation contact angle increases with DNA concentration. As shown, $\Delta\theta_s$ decreases from 35° to 13.5° with increase of DNA concentration from $4\ \mu\text{g/ml}$ to $150\ \mu\text{g/ml}$.

Droplet morphology of distilled water, Tris-HCl buffer solution, and DNA solutions are shown in Figure 4-24. With increasing DNA concentration, the sandwiched droplets become more cylindrical (*i.e.* in the absence of an electric field, the contact angles are smaller), and the tri-phase contact angles decrease only a few degrees before reaching saturation.

In section 4.3.3, the results of these experiments are compared with those related to the sessile droplets and sandwiched droplets with microchannel gap of $600\ \mu\text{m}$.

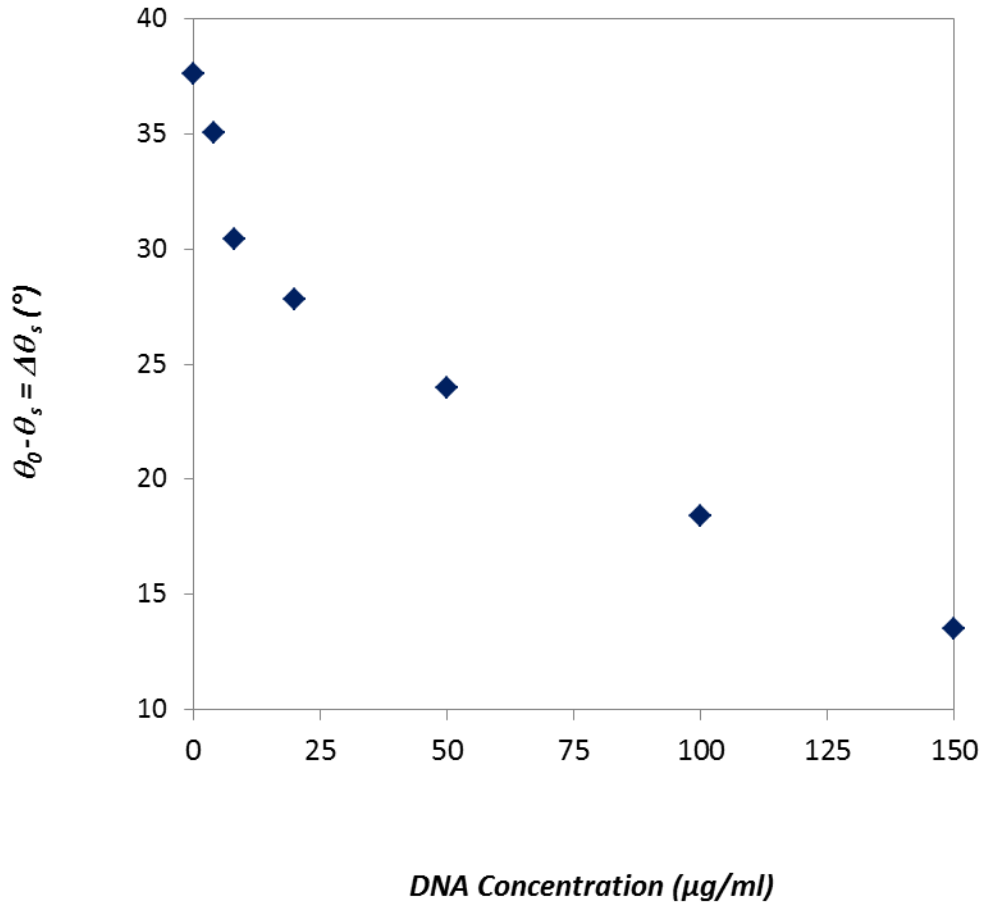


Figure 4-23: Comparison of $\Delta\theta_s$ (*i.e.* the difference between the contact angle at the bottom interface in the absence of an electric field (θ_0) and the average contact angle when the droplet reaches saturation (θ_s)) as a function of DNA concentration for sandwiched droplets of Tris-HCl buffer solution and different concentrations of DNA solutions. The average volume of the droplets and the microchannel gaps are 0.89 ± 0.05 (μl) and 304 ± 4 (μm) respectively.

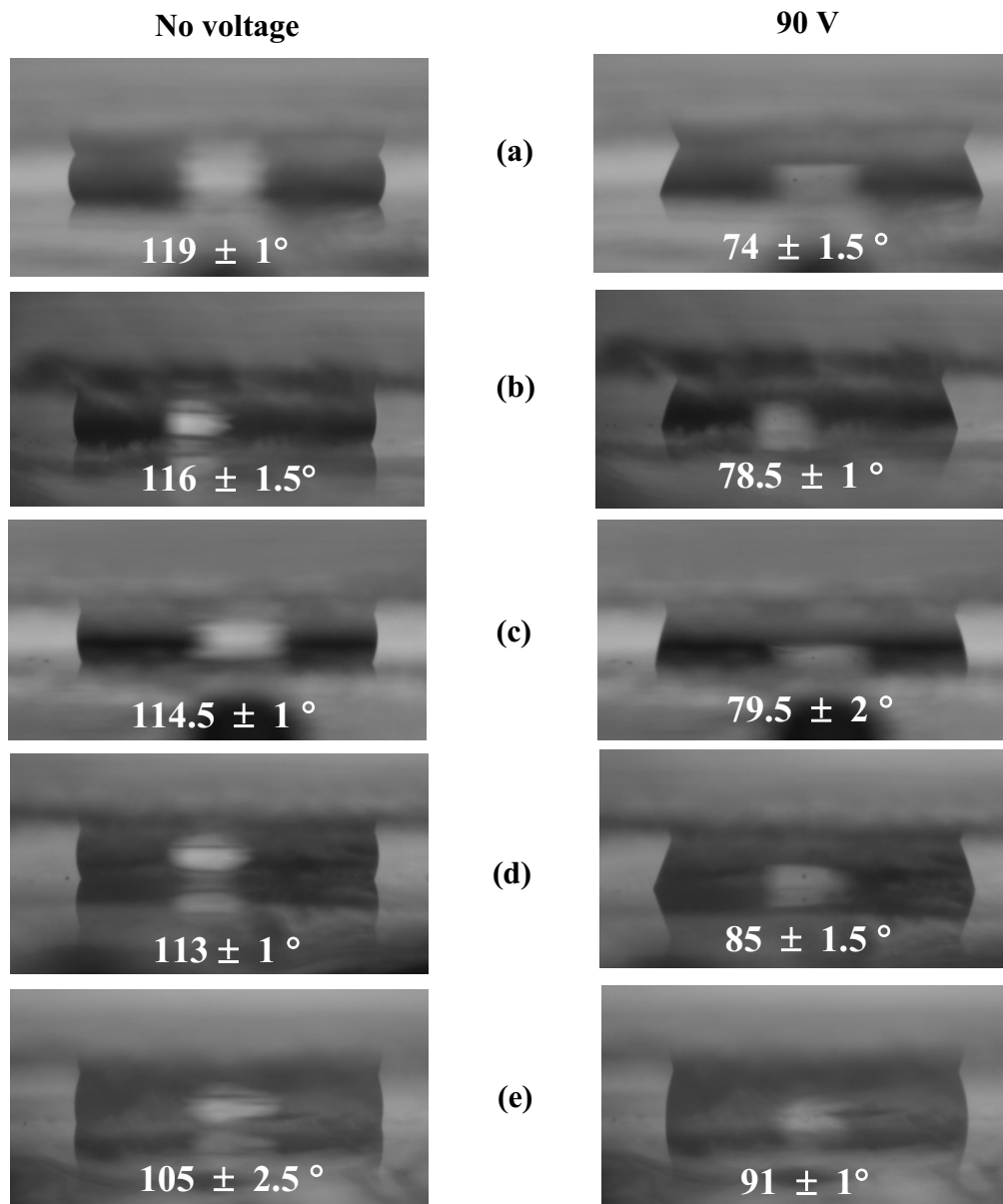


Figure 4-24: Droplet morphology for: (a) distilled water, (b) Tris-HCl buffer solution, (c), (d), (e) 4, 20, 150 $\mu\text{g/ml}$ DNA solutions respectively. The average volume of the droplets is 0.89 ± 0.05 (μl) and the average microchannel gap is 304 ± 4 (μm). The numbers indicate the contact angles at the bottom interfaces.

4.3.3) Comparison of Results and Discussion

In order to know the effect of DNA concentration and microchannel gap on saturation contact angle, the results obtained from the experiments performed on sessile and sandwiched droplets are compared (Table 4-1).

Solution Type	Saturation Contact Angle (θ_s)°		
	Sessile Droplets	Sandwiched Droplets	
		Gap = 600 μm	Gap = 300 μm
Distilled Water	-	72 \pm 1	74 \pm 1.5
Tris - HCl buffer Solution	79 \pm 1	78.5 \pm 1	78.5 \pm 1
DNA 4 $\mu\text{g/ml}$	79.5 \pm 1	79 \pm 2	79.5 \pm 2
DNA 8 $\mu\text{g/ml}$	81 \pm 1	83.5 \pm 2	83.5 \pm 1.5
DNA 20 $\mu\text{g/ml}$	-	-	85 \pm 1.5
DNA 50 $\mu\text{g/ml}$	-	-	88 \pm 1.5
DNA 100 $\mu\text{g/ml}$	-	89 \pm 2	90 \pm 2
DNA 150 $\mu\text{g/ml}$	-	89 \pm 1.5	91 \pm 1
DNA 350 $\mu\text{g/ml}$	85 \pm 1	91.5 \pm 1.5	-
DNA 1000 $\mu\text{g/ml}$	86.5 \pm 1	93.5 \pm 1.5	-

Table 4-1: A comparison of saturation contact angles of sessile and sandwiched droplets of distilled water, Tris-HCl buffer solution and DNA solutions.

These series of experiments were started with the sessile droplets and were finalized with the sandwiched droplets (gap of 300 μm). During the process of developing the experiments, several more concentrations of DNA along with distilled water (to compare with literature) were added to the experiments; therefore, regrettably, a complete comparison for all concentrations of DNA solutions is not available (blank sections in Table 4-1). As explained before, performing experiments with higher concentrations of DNA in microchannel gap of 300 μm was not possible due to electrolysis.

As shown, the saturation contact angle, (θ_s) , increases with DNA concentration. To explain the reasons behind these changes, the effect of ionic strength needs to be considered. The ionic strength of a solution is a function of the concentration of all ions in that solution, and is defined as:

$$I = \frac{1}{2} \sum_{i=1}^n c_i z_i^2 \quad \text{Equation 4-1}$$

where c_i is the molar concentration of ion i (M, mol/lit.), z_i is the charge number of that ion, and the sum is taken over all ions in the solution.

The ionic strength of distilled water is reported²²¹ to be less than 10^{-6} (M). The ionic strength of the buffer solution used in these experiments (a solution of 10 mM Tris-HCl and 0.1 mM EDTA, pH=8.0), is estimated to be 0.0108 (M) which is in agreement with the experimentally determined value of 0.01 M²⁰²; considering Tris with the chemical formula of $(\text{HOCH}_2)\text{CNH}_2$ and EDTA with four negatively charged oxygen atoms. Therefore, the ionic strength of Tris-HCl buffer solution is higher than that of distilled water. In this research, D4522 deoxyribonucleic acid sodium salt from calf-thymus is used (section 3.2) which is primarily double stranded. In this macromolecule, the average number of base pairs will range between 13 and 115 kilobases and the molecular weight is reported²⁰² to be between 8-15 million Daltons prior to separating the strands. The value of the ionic strength for the 4 $\mu\text{g}/\text{ml}$ DNA solution in Tris-HCl buffer is estimated to range between 0.1708 (M) (for 13 kbp) and 7.0641 (M) (for 115 kbp) considering two negatively charged oxygen atoms in each base pair. As shown in Figure 3-1, the base pairs with the 5' end have an extra terminal phosphate group (with one

negatively charged oxygen atom); therefore there will be three negatively charged oxygen atoms in these base pairs. Thus, the number of negative charges varies from two²⁰² to three depending on each individual repeating base pair and the DNA base sequence such as ATGCTAGC as shown in Figure 3-1. In either way, the negatively charged DNA solutions in Tris-HCl buffer have considerably higher ionic strengths than that of the base buffer. The ionic strength of DNA solutions increases with DNA concentration.

As explained in section 1.3.1, in the absence of an electric field, the liquid is electrically neutral meaning that the amount of ions and counter ions are the same at all locations. However, under an electric field, the charges at the solid substrate attract the ions in the liquid increasing the charge concentration at the contact line of the droplet. This charged surface and the resulting charge distribution in the solution is called the Electric Double Layer (EDL), where its effective thickness is defined as the Debye length (Equation 1-5). This length is proportional to the reciprocal square root of the solution concentration (or solution ionic strength). Thus, the larger the concentration of ions in solution is, the more they shield the charged surface and the thinner the Debye length is. As Verheijen and Prins¹¹⁸ suggested, some of the charges will be trapped in or on the dielectric surface due to the stronger attractive electrostatic force between the ions in the liquid and the solid metal electrode, and eventually cause contact angle saturation. Our observations in this experimental study indicate that as the ionic strength increases (from distilled water to high concentration DNA solution), and the EDL becomes thinner, the contact angle saturates at higher values.

The increase of saturation contact angle when DNA is added to the Tris-HCl buffer solution may also be related to DNA adsorption, as biomolecules have the tendency to adsorb unspecifically onto hydrophobic surfaces^{134,222}. A detailed investigation on DNA passive adsorption is presented in Appendix E (Figure E-6 through Figure E-8, and Figure E-10). As shown, there is significant reduction in contact angle over time for DNA solutions comparing to that of buffer solution which is a good indication of biomolecular adsorption on the Teflon coating. As a result, at the applied voltage of V , the effective thickness of the dielectric (d) increases and according to Equation 1-9, $\cos \theta$ decreases, and the contact angle, θ , increases¹³⁴ providing that ($0 \leq \theta \leq \pi/2$). Therefore, DNA solutions reach saturation at higher values than their base Tris-HCl buffer solution.

It is likely therefore that the effects of ionic strength in combination with biomolecular adsorption of DNA cause the observed changes in saturation contact angle.

As shown in Figure 4-6, Figure 4-12 and Figure 4-20, in the absence of an electric field, there is a decreasing trend in the contact angle from distilled water to Tris-HCl buffer solution and finally to DNA solutions. To clarify the reason behind this observation, the excess free energy of a drop on a solid surface (σ) is considered. This energy is defined as²²³:

$$\sigma = \gamma_{lv}S + P\vartheta + \pi R^2(\gamma_{sl} - \gamma_{sv}) \quad \text{Equation 4-2}$$

where, γ_{lv} , γ_{sv} and γ_{sl} are liquid-vapour, solid-vapour and solid-liquid interfacial tensions respectively; ϑ and S are the droplet volume and the area of the liquid-vapor interface, P is the excess pressure inside the droplet, and R is the droplet base radius. This energy is reduced when γ_{lv} decreases, γ_{sl} decreases or γ_{sv} increases.

At the end of this chapter, the values of γ_{lv} for the droplets of distilled water, Tris-HCl buffer, 4 $\mu\text{g/ml}$ and 20 $\mu\text{g/ml}$ DNA solutions are estimated and compared. As it will be shown, with increasing DNA concentration, γ_{lv} increases due to that fact that the larger the concentration of ions in solution is, the more they shield the charged surface resulting in an increase in γ_{lv} . Therefore, an increasing trend in the contact angle without voltage from distilled water to Tris-HCl buffer solution and finally to DNA solutions is expected. This is contrary to our observations as shown in Figure 4-6, Figure 4-12 and Figure 4-20. The rational can be explained by the fact that the adsorption at the tri-phase line strongly changes γ_{sl} ²²⁴. As explained in Appendix E, the significant reduction of contact angle for DNA solutions compared to that of buffer solution is a good indication of biomolecular adsorption. By referring to Equation 4-2, it is believed that the adsorption affects the amount of γ_{sl} to that extent that the overall excess free energy is lower for DNA solutions; which creates a significant reduction in contact angles of these solutions in the absence of a voltage.

Figure 4-25 compares the contact angle at the top interface, θ_T , as a function of DNA concentration for microchannel gaps of 300 and 600 μm . For the concentrations of 100 $\mu\text{g/ml}$ and lower, this angle stays the same; however, for the gap of 300 μm , it slightly decreases at the concentration of 150 $\mu\text{g/ml}$. For the microchannel gap of 600 μm , θ_T decreases strongly when the DNA concentration exceeds 150 $\mu\text{g/ml}$. In the microchannel gap of 300 μm , it was impossible to perform experiments with DNA concentrations above 150 $\mu\text{g/ml}$ due to electrolysis.

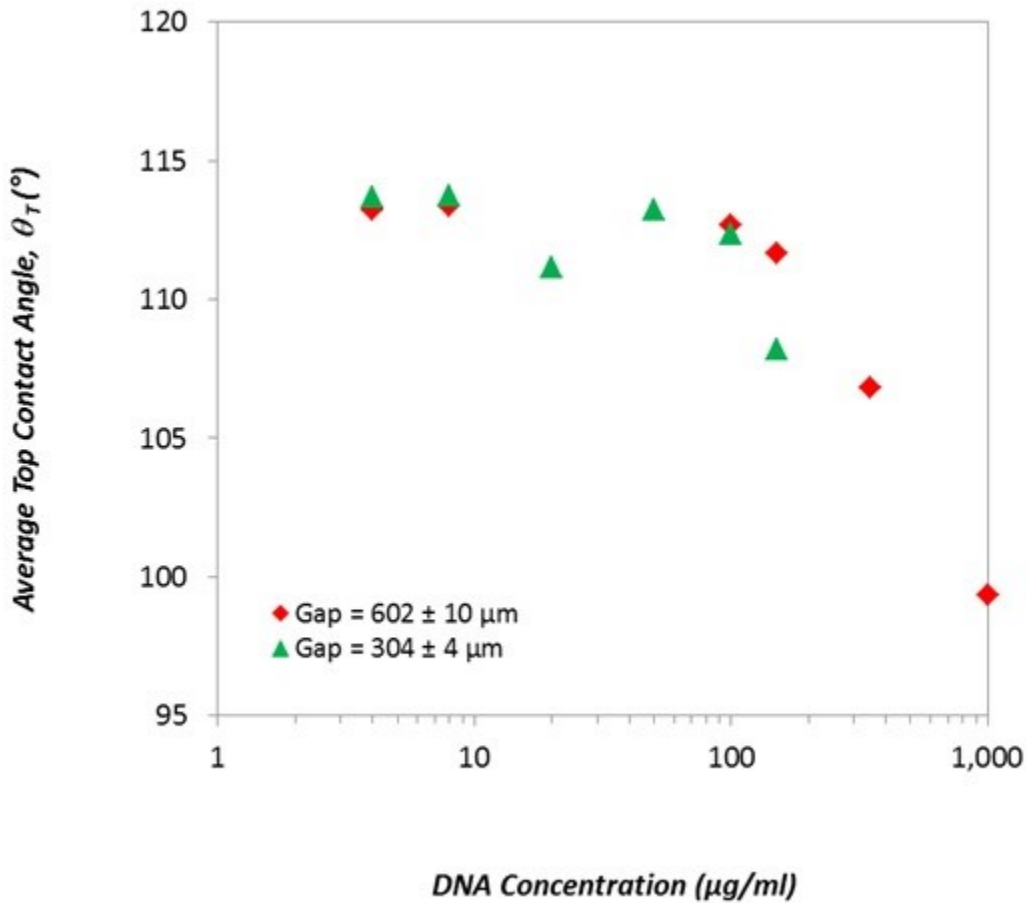


Figure 4-25: The comparison of the average contact angle at the top interface, (θ_T), as a function of DNA concentration with average volumes of 1.52 ± 0.027 (μl) and 0.89 ± 0.052 (μl) for microchannel gaps of (602 ± 10) and (300 ± 4) μm respectively.

$\Delta\theta_s$ as a function of DNA concentration is presented in Figure 4-26. This graph shows the combined effects of microchannel gap and DNA concentration on the contact angle when it reaches saturation. As shown, the upper, middle, and lower curves respectively represent the results for the sessile droplets, and sandwiched droplets in microchannel gaps of 600 μm and 300 μm ; and the divergence of the curves becomes more significant when DNA concentration exceeds 100 $\mu\text{g/ml}$.

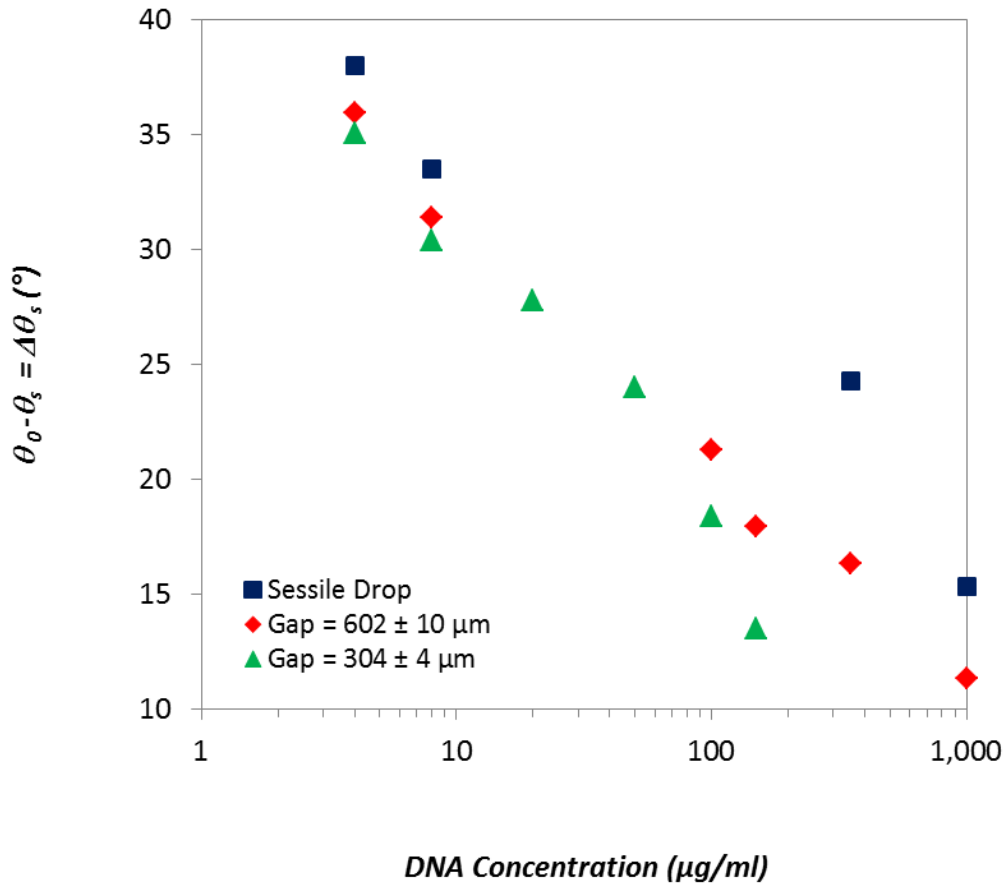


Figure 4-26: The effect of microchannel gap on $\Delta\theta_s$ (*i.e.* the difference between the contact angle at the bottom interface in the absence of an electric field (θ_0) and the average contact angle when the droplet reaches saturation (θ_s)) as a function of DNA concentration. The average volume is: 1.35 \pm 0.08 (μl) for sessile droplets and 1.52 \pm 0.027 (μl) and 0.89 \pm 0.052 (μl) for sandwiched droplets in microchannel gaps of (602 \pm 10) and (300 \pm 4) μm respectively.

In order to know the impact of the parameters studied in this chapter such as: the contact angle in the absence of an electric field (θ_0), the contact angle after applying voltage (θ), the difference between these contact angles ($\Delta\theta_v$), and the applied voltage (V), on droplet movement (which will be discussed in detail in the following chapter), the minimum actuation potential (V_{min} , *i.e.* the threshold voltage) needs to be defined.

Based on literature^{8,67}, contact angle hysteresis (see section 1.2.1) is responsible for the minimum actuation voltage (V_{min}), and the droplet will not begin to move until the electrical potential exceeds V_{min} . As shown in Figure 4-27, at the onset of droplet motion, the contact angle at the advancing contact line (*i.e.* leading edge) is $(\theta + \alpha)$ whereas the contact angle at the receding contact line (*i.e.* trailing edge) is $(\theta_0 - \alpha)$; where α is the contact angle hysteresis⁸.

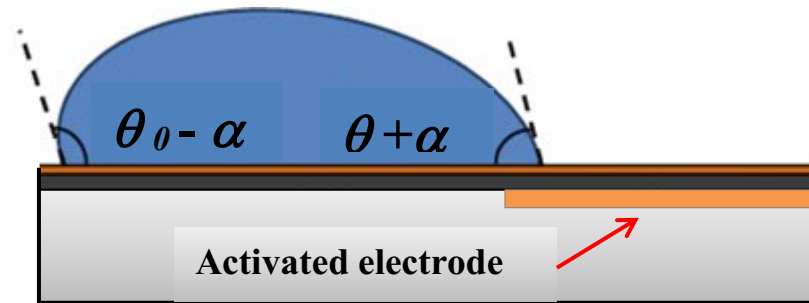


Figure 4-27: Schematic diagram of the advancing and receding contact angles at the onset of droplet motion. For the droplet to move: $\theta + \alpha \leq \theta_0 - \alpha$ (Adapted from reference: Barber and Emerson⁸).

Providing that there is a net positive electrowetting force towards the activated electrode, the droplet will begin to move and the V_{min} will be determined:

$$\theta + \alpha \leq \theta_0 - \alpha \quad \rightarrow \quad \Delta\theta_v \geq 2\alpha \quad \text{Equation 4-3}$$

Combining this expression with Young-Lippmann's relation (Equation 1-9), and assuming that α is small, a simplified equation for the minimum actuation potential is defined^{8,67}:

$$V_{\min} \approx 2 \sqrt{\frac{\alpha \sin \theta_0 \gamma_{lv}}{C}} \quad \text{Equation 4-4}$$

where α is expressed in radians.

In order to minimise the actuation potential of the droplets, a large dielectric capacitance (C), a large equilibrium contact angle (*i.e.* the contact angle in the absence of an electric field (θ_0)), a small hysteresis α , and a low surface tension γ_{lv} are desirable.

The solutions of interest which will be studied in the next chapter are: distilled water, Tris-HCl buffer solution, and 4 $\mu\text{g/ml}$ and 20 $\mu\text{g/ml}$ DNA solutions. The experiments will be performed in a microchannel of 300 μm where Parylene C is used as an insulation layer on all bottom substrates. By solving Equation 4-4 for a comparison between a sandwiched droplet of distilled water and 20 $\mu\text{g/ml}$ DNA solution:

$$\frac{V_{\min (DW)}}{V_{\min (D20)}} \approx \sqrt{\frac{\alpha_{DW} \sin \theta_{0(DW)} \gamma_{lv(DW)}}{\alpha_{D20} \sin \theta_{0(D20)} \gamma_{lv(D20)}}} \quad \text{Equation 4-5}$$

By inserting the values of θ_0 from Figure 4-24, the above equation is simplified as:

$$\frac{V_{\min (DW)}}{V_{\min (D20)}} \approx 0.975 \sqrt{\frac{\alpha_{DW} \gamma_{lv DW}}{\alpha_{D20} \gamma_{lv D20}}} \quad \text{Equation 4-6}$$

Since the DNA solutions were prepared in very small volumes of Tris-HCl buffer (readily purchased in 1 ml tubes from Teknova (USA), it was not possible to experimentally measure the surface tension with available tensiometers. However, based on Young-Lippmann's relation (Equation 1-9): $\cos \theta = \cos \theta_0 + \frac{\epsilon_s V^2}{2 \gamma_{lv} d}$, the surface or interfacial tension of very small volumes of solutions can be easily estimated. This method is called electrowetting-based microdrop tensiometry and has been recently used by Banpurkar *et al.*²²⁵ and Ni *et al.*¹⁸⁴. As

shown in Figure 4-28 for sandwiched droplets in a 300 μm gap, once the thickness of the dielectric layer is known, the absolute values of the interfacial tensions can be readily extracted from the values of φ (*i.e.* the slope of the curves at low voltages before contact angle saturation occurs²²⁵); where $C = \frac{\varepsilon_s}{d}$ and ε_s and d are the permittivity and the thickness of the solid-liquid interface (in these experiments: $d = 800$ nm), and V is the applied voltage. By using this method, the values of γ_{lv} for the solutions of distilled water, Tris-HCl buffer, 4 $\mu\text{g/ml}$ and 20 $\mu\text{g/ml}$ DNA solutions are obtained (as shown in Figure 4-28). The surface tension of ~ 71.4 mN/m for distilled water is within the reported range of 70 – 72 mN/m⁶⁷.

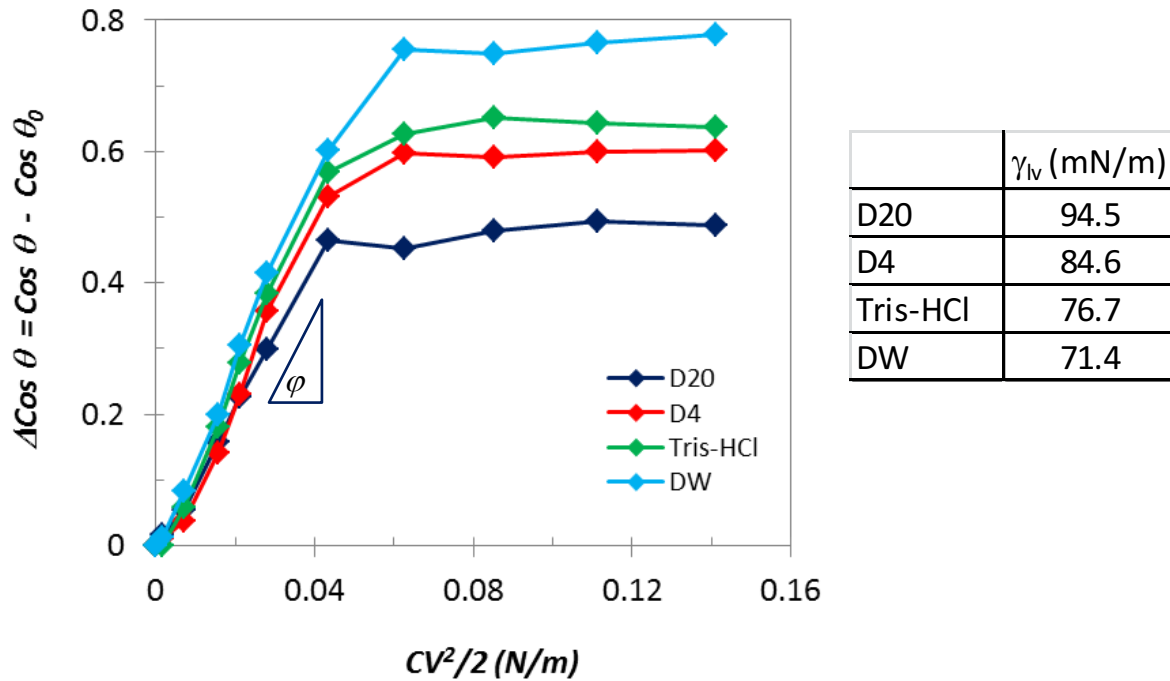


Figure 4-28: $\Delta\text{Cos } \theta$ as a function of $CV^2/2$ for the solutions of distilled water, Tris-HCl buffer, 4 $\mu\text{g/ml}$ and 20 $\mu\text{g/ml}$ DNA solutions. The obtained values of γ_{lv} are also shown.

From Figure 4-28, it can be concluded that with increasing the ionic strength of a droplet, the value of its γ_{lv} increases. Depending on the value of the contact angle hysteresis, we can determine which solution requires a lower actuation voltage. In the following chapter where the

dynamics of droplet transport will be studied in detail, the experimental values of the minimum actuation voltage for the solutions of interest will be reported.

Chapter5

Moving Droplets using Electrowetting

5.1) Fundamental Studies of Actuating Droplets on Single Square Electrodes

In this chapter, the objective is to study the dynamics of droplet transport on single square electrodes using electrowetting in terms of characteristic parameters such as maximum velocity, average velocity, acceleration, droplet position and droplet elongation varying with time and voltage.

For this purpose, sessile droplets of distilled water, Tris-HCl buffer solution, 4 $\mu\text{g/ml}$ and 20 $\mu\text{g/ml}$ DNA solutions in Tris-HCl buffer are first dispensed on Teflon coated substrates with 1.79 μm (on average) thick Parylene C coating. The droplets are then sandwiched in a microchannel while the leading edges are positioned at a certain distance on/from the edge of the electrode (see leading edge and overlap definitions in section 5.1.2). The configuration of the

system is the same as in Figure 2-4. The goal is to investigate the actuation dynamics of the sandwiched droplets when positioned next to an activated single square electrode as shown in Figure 2-12 (b) and (d). Subsequently, the droplets are actuated by the application of a voltage between 50 to 90 volts to the square electrodes. As shown in Figure 2-3, by applying voltage to an electrode, the surface energy and consequently the solid-liquid contact angle at the advancing side of the droplet reduces initiating the droplet movement onto the charged electrode. This movement is recorded from the top and the side in order to understand how the droplet is actuated and deformed while approaching the activated electrode. The images are then extracted from the recorded videos and are analyzed frame by frame using AutoCAD to determine the position and shape of the droplet as a function of time and voltage. At each applied voltage, the experiments are repeated for 3-7 different droplets of each solution.

5.1.1) Droplet Transport

The dynamics of EWOD-based actuations of droplet transport have been studied by a number of researchers. In 2002, Ren *et al.*¹⁶⁶ formulated a model to describe the dynamics of electrowetting-induced transport of liquid droplets as a function of applied voltage and relevant physical parameters including viscosity, contact-line friction, geometric factors and surface tension¹⁶⁶. This model is developed based on the principle of balancing the work done by the external capillary force (caused by the difference in solid-liquid interfacial tension created at the interface between the droplet and the dielectric layer following the application of voltage) with the energy transformed and dissipated during droplet movement¹⁶⁶. A schematic of this model is shown in Figure 5-1.

In 2006, Bahadur and Garimella¹⁰⁴ developed an energy-based analytical model to estimate the actuation force on a droplet moving between two electrodes. Their objective was to study the influence of each of the opposing forces represented by simplified algebraic expressions on the overall droplet motion¹⁰⁴. Their results show the effect of operating voltage, fluid properties and droplet geometry on droplet motion disclosing that contact-line friction is the dominant opposing force for the electrowetting-induced droplet movement¹⁰⁴. Their work was then followed by Schertzer *et al.*¹⁷⁸ Oprins *et al.*¹⁷⁹, and Cui *et al.*¹⁸³ (section 1.5).

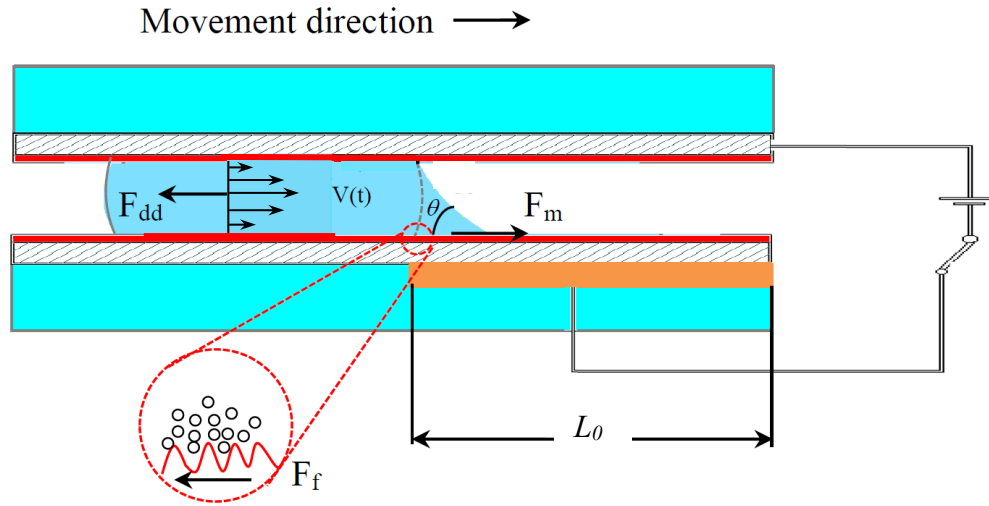


Figure 5-1: Schematic of a droplet transport model showing sources of energy dissipation (F_{dd}, F_f). Here, F_m is the electrostatic driving force per unit length of the electrode (L_0). (Adapted from reference: Ren *et al.*¹⁶⁶).

Based on these models and considering the droplet as a single mass (m , mass of the droplet) moving through the microchannel, the components of energy dissipation are:

- 1) the viscous flow within the droplet during transport (F_{dd} , *i.e.* the shear force due to the top and bottom plates, assuming a parabolic velocity profile with zero slip boundary conditions at the top and bottom plates¹⁰⁴) as shown in Figure 5-1,

$$F_{dd} = \left(\frac{3\pi\mu_l}{h} D^2 \right) (v) \quad \text{Equation 5-1}$$

where μ_l , D , h , v are the droplet viscosity, diameter of sandwiched droplet, microchannel gap and droplet velocity respectively.

- 2) the contact line friction force (F_f) which is proportional to the droplet velocity^{104,166}:

$$F_f = (2\pi\xi D) (v) \quad \text{Equation 5-2}$$

where ξ is the proportionally coefficient of contact line friction defined in molecular kinetics¹⁷⁹.

From the above equations, it is concluded that all the forces opposing F_m are proportionally related to the droplet velocity, v ¹⁰⁴.

Consequently, the balance of the forces acting on the droplet (Figure 5-1), projected on the actuation direction, can be written as^{166,179}:

$$m \frac{dv}{dt} = F_{ac} - F_{dd} - F_f \quad \text{Equation 5-3}$$

where F_{ac} is the actuation force (*i.e.* the electrostatic driving force) defined in Equation 5-4 indicating that the actuation force varies as the square of the applied voltage¹⁰⁴:

$$F_{ac} = \left(\frac{\varepsilon_s V^2}{2d} - F_T \right) \frac{dA_1(x)}{dx} \quad \text{Equation 5-4}$$

$$A_1(x) = \frac{D^2}{4} \cos^{-1} \left(1 - \frac{2x}{D} \right) - \left(\frac{D}{2} - x \right) \sqrt{\frac{D^2}{4} - \left(x - \frac{D}{2} \right)^2} \quad \text{Equation 5-5}$$

The term $\frac{\varepsilon_s V^2}{2d}$ is from the Young-Lippmann's relation (Equation 1-9), where ε_s and d are the permittivity and the thickness of dielectric layer respectively and V is the applied voltage. The position of the droplet leading edge is tracked by the coordinate x , and $A_1(x)$ (Equation 5-5) is the area of the droplet covering the actuated electrode at the bottom plate; subsequently, its derivative in Equation 5-4 is called the droplet effective contact line length which varies with the droplet position (x) when the droplet moves. Subsequently, the electrowetting force, F_m , can be expressed as¹⁸⁴:

$$F_m = \frac{\varepsilon_s V^2}{2d} \frac{dA_1(x)}{dx} \quad \text{Equation 5-6}$$

F_T is also a threshold initiation force per unit length taking into account the contact angle hysteresis between the leading and trailing edges of the droplet, F_{TH} , and/or any other static friction, such as friction from adsorption^{104,166,226}, F_{TA} ; and is added to signify the decrease in external force once transport is initiated¹⁶⁶, and overall $F_T = F_{TH} + F_{TA}$.

Chang and Pak²²⁷ have defined the maximum static friction related to the contact angle hysteresis (per unit length) as: $F_{TH} = \gamma_{lv} (\cos(\theta_0 - \alpha) - \cos\theta_0)$; where γ_{lv} , θ_0 and α are the liquid-vapour interfacial tension, contact angle in the absence of an electric field, and contact angle hysteresis respectively. The notion of contact angle hysteresis is a very approximate perception⁷²; therefore, it can be assumed that contact angle hysteresis (α) is small compared to θ and θ_0 ¹⁸⁵, and the related static force remains constant during droplet movement⁷² for any specific solution (γ_{lv} , θ_0 , α are constant for any type of solution which is in contact with a specific solid surface, Chapter 4). As the term defining the hysteresis related static force is always negative, it is concluded that hysteresis always reduces the electrowetting force⁷². Static friction per unit length can be also produced by adsorbed layers at the microscopic scale¹⁶⁶, F_{TA} , such as biomolecular adsorption or biofouling (as discussed in Appendix E) and can be substantial when droplets of biofluids such as DNA solutions are transported in the microchannel due to the effect of passive biomolecular adsorption. This matter will be discussed in section 5.2.

5.1.2) Definitions

The coordinate system specified according to the electrode edge, and the definitions of the droplet start point, droplet initial diameter, electrode length, offset and overlap are shown in Figure 5-2. As shown, the Y axis is parallel to the edge of the electrode and the X axis is perpendicular to the edge, pointing in the direction of movement. The center of the coordinate system is located at the middle of electrode edge.

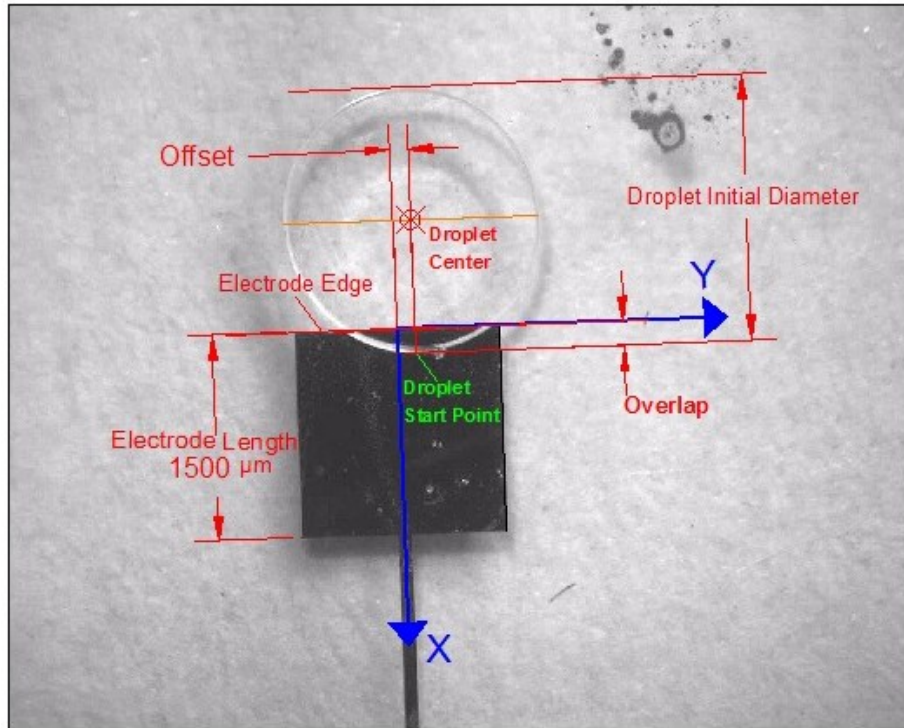


Figure 5-2: The coordinate system specified according to the electrode edge, and the definitions of the: droplet start point, droplet initial diameter, electrode length, offset and overlap.

Based on the coordinate system, the parameters are defined as:

- **Leading edge:** the front edge of the droplet that first contacts the electrode
- **Trailing edge:** the rear edge of the droplet
- **Electrode length (L_0):** the length of the square electrode (1500 μm)
- **Overlap (X_0):** the position of the leading edge in the direction of X axis relative to the electrode edge before voltage is applied.
- **Offset (Y_0):** the distance in the Y direction of the droplet center to the middle of the electrode before voltage is applied.

- **Droplet start point:** the initial position of the leading edge before voltage is applied defined by the overlap and offset: (X_0, Y_0) .
- **Instantaneous displacement (ΔX_n):** the displacement of each edge (leading or trailing) in each frame (n) relative to the previous frame (n-1) along the X direction. On the graphs, it is plotted as percent instantaneous displacement normalized by the electrode length (1500 μm).
- **Total displacement (X_n):** the total displacement of each edge (leading or trailing) in each frame (n), measured from the droplet start point along the X direction. On the graphs, it is plotted as percent total displacement normalized by the electrode length (1500 μm).
- **Position:** the total displacement of each edge (leading or trailing) in each frame (n), measured from the electrode edge along the X direction while considering the overlap; defined as $(X_n + X_0)$. On the graphs, it is plotted as percent position normalized by the electrode length (1500 μm).
- **Δt (s):** defined as $(1/\text{fps})$, where fps (*i.e.* frame per sec.) is a property of the CCD camera.
- **Instantaneous velocity (mm/s):** defined as $(\Delta X_n / \Delta t)$.
- **Maximum instantaneous velocity:** the maximum instantaneous velocity of the droplet measured during the course of movement until the leading edge stops moving.
- **Average velocity:** the total displacement from the start point divided by the total time until the leading edge stops moving; defined as (X_n / t) where $(t = \sum \Delta t)$.
- **Droplet elongation (ΔD):** the change of droplet diameter (stretching) along the X direction. On the graphs, it is plotted as percent elongation normalized by the initial diameter of the sandwiched droplet (D_0).

5.1.2.1) Specifications for All Experiments:

While sandwiching the droplets, it was very challenging to position the leading edges of the droplets exactly at the edge of the electrodes due to the hydrophobic surface of the Teflon coatings. Therefore, the experiments had to be repeated several times before having an overlap within the experimental limits.

In order to have comparable results for all solutions, these conditions need to be satisfied:

- the microchannel gap (h) is in the range of $330 \pm 50 \mu\text{m}$.
- without voltage, the droplet volume is in the range of $1 \pm 0.2 \mu\text{l}$.
- the maximum allowable overlap is $135 \mu\text{m}$.
- the minimum allowable overlap is $0 \mu\text{m}$.
- before applying voltage, the droplet must be circular in shape from the top view.

At each applied voltage, all experimental results (including the rejected data) are plotted in Appendices F, G, H, I for the droplets of distilled water, Tris-HCl buffer solution, $4 \mu\text{g/ml}$ and $20 \mu\text{g/ml}$ DNA solutions respectively. The average curves for the changes of the instantaneous displacement, instantaneous velocity, total displacement, acceleration, elongation, and position with time are also plotted. These curves are obtained by averaging the data at each point in time and are plotted as a function of time.

The changes of the instantaneous velocity as a function of droplet position along the X direction for the leading and trailing edges are also presented in the Appendices. Not only does the graph of velocity as a function of droplet position show the initial position of the leading and trailing edges at no voltage, but also it demonstrates how far the droplet has moved forward onto the electrode by the end of movement. At each voltage, the average curves for the leading and trailing edges are finally compared (see Appendices F, G, H, I).

5.1.2.2) Experimental Conditions

The experimental conditions for the droplets of distilled water, Tris-HCl buffer, 4 $\mu\text{g/ml}$ and 20 $\mu\text{g/ml}$ DNA solutions are summarized in Table 5-1. The experimental conditions for distilled water droplets (Table 5-1) are similar to those reported by Pollack *et al.*²⁵; however, they performed the experiments on microliter droplets of water with 0.1 M KCL in a microchannel with 0.8 μm thick Parylene C coating layer. Although, in electrowetting, there is no dependence on the salt concentration over the range of 10^{-6} -1 M²⁵, the difference in dielectric layer thickness has a major effect on the minimum voltage required to initiate droplet movement (section 4.3.3). Comparing to $V_{min} \sim 48$ V reported in literature²⁵, no droplet actuation was observed at the voltages of 50 and 55 volts (*i.e.* neither the leading nor the trailing edges moved), and the actuation started with a slight movement of the leading edge at ~ 60 volts. This can be explained by referring to the equation: $C = \frac{\epsilon_s}{d}$ where the total capacitance (C) of the dielectric layer and EDL has an inverse relation with the thickness of the dielectric layer (section 1.3.2). The greater the thickness of the dielectric layer, the weaker is the energizing effect¹⁷⁰ resulting in a lower actuation force per unit length $F_{ac} \approx \frac{\epsilon_s V^2}{2d}$ (assuming that the contact angle hysteresis is small in Equation 5-4). For a given actuation force, the mean electric field in the dielectric layer decreases as the thickness increases $\left(\frac{V}{d} \approx \sqrt{\frac{2F_{ac}}{d\epsilon_s}}\right)$; therefore, the minimum actuation voltage has increased in these experiments.

It should be noted that increasing the dielectric thickness was beneficial in our experiments as less electrolysis (more detail in Chapter 6) was observed compared to the experimental studies of static contact angle discussed in Chapter 4 with the dielectric thickness of 0.8 μm .

Table 5-1: The experimental conditions for the droplets of distilled water, Tris-HCl buffer, 4 $\mu\text{g/ml}$ and 20 $\mu\text{g/ml}$ DNA solution. The standard deviations are also indicated.

	Distilled water	Tris-HCl buffer	4 $\mu\text{g/ml}$ DNA solution	20 $\mu\text{g/ml}$ DNA solution
Microchannel gap (μm)	345 ± 22	327 ± 19	322 ± 17	310 ± 14
Initial volume of sandwiched droplets (μl)	0.92 ± 0.04	0.89 ± 0.06	0.88 ± 0.04	0.99 ± 0.10
Initial diameter of sandwiched droplets (μm)	1866 ± 63	1877 ± 83	1925 ± 53	1978 ± 59
Overlap (μm)	56 ± 25	62 ± 10	67 ± 10	59 ± 13
Offset (μm)	139 ± 69	136 ± 48	178 ± 54	219 ± 66

5.1.2.3) Onset of Actuation

In this section, the droplet morphology while advancing on an actuated electrode is investigated. As the droplet morphology of all solutions: distilled water, Tris-HCl buffer, 4 $\mu\text{g/ml}$ and 20 $\mu\text{g/ml}$ DNA solutions, corresponding to the applied voltages of 50 to 90 V (constant voltage) are similar, as an instance, only the sequences of droplet morphology for distilled water at 90 V and 65 V are presented in Figure 5-3 and Figure 5-6. The droplet morphology for distilled water at voltages of 60, and 70 to 85 V are shown in Appendix F.

In general, before the electrowetting deforms the droplet, the droplet is circular (top view). As time passes, the leading edge of the droplet will be drawn toward the electrode under the influence of electrowetting. With lowering voltage, the total time that the droplet needs to fully cover the electrode length increases. As the leading edge initially accelerates more rapidly than the trailing edge, the droplet stretches along its axis of motion and attains an ellipse-like shape²²⁸ to conserve the mass.

As an instance, at 90 V, the comparison of the average data for the leading and trailing edges of the distilled water droplets are presented in Figure 5-4 and Figure 5-5. At the time that the leading edge decelerates and finally stops moving, the trailing edge accelerates compensating for its delay in time. It results in a slight shrinkage (compression) in relative droplet diameter after the leading edge has stopped moving due to the inertial effect¹⁷⁸ as shown in Figure 5-5 (a). As observed in Figure 5-3, the droplet has finally assumed the shape of the lower electrode to minimize its surface energy in preference to its original circular shape¹⁰⁴.

As shown in Figure 5-4 (c), the percent total displacement, and in Figure 5-5 (c), the velocity as a function of droplet position, the droplet leading edge has reached to the end of the electrode meaning that the droplet has completely covered the electrode length. At the end, the droplet nearly recovers its original shape. For a complete set of experimental data for all solutions at the voltages of 50 to 90 V, refer to the Appendices F, G, H, and I.

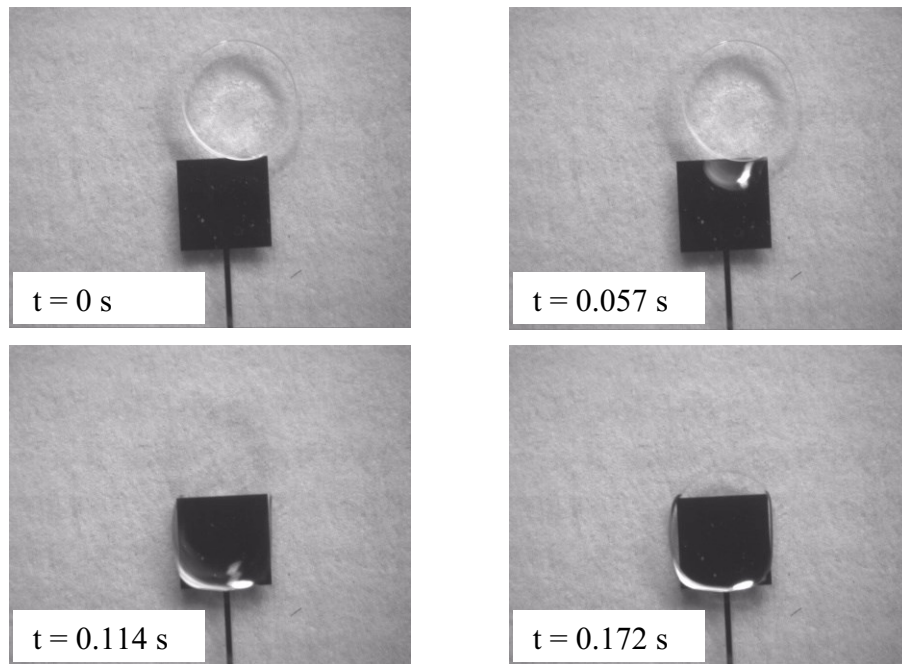


Figure 5-3: Droplet morphology corresponding to an applied voltage of 90 V for a 0.9 μl droplet of distilled water in a microchannel gap of 314 μm . The overlap and offset values are 60 μm and 314 μm respectively. A sudden inception of voltage is applied at $t = 0$ s, and remains constant until the droplet stops moving.

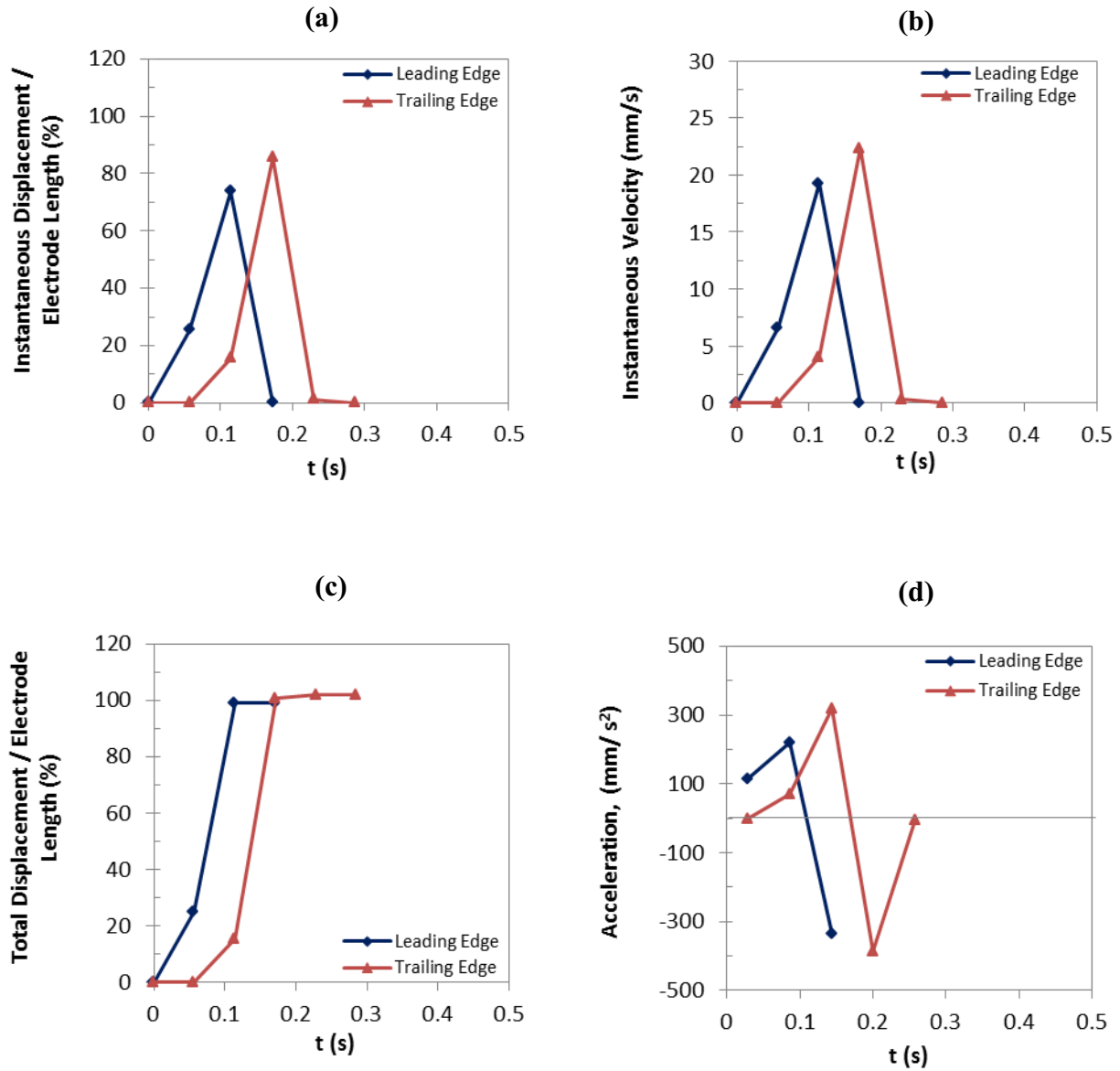


Figure 5-4: Comparison of the average curves: (a) instantaneous displacement, (b) instantaneous velocity, (c) total displacement, and (d) acceleration as a function of time for the leading and trailing edges of distilled water droplets at 90 V.

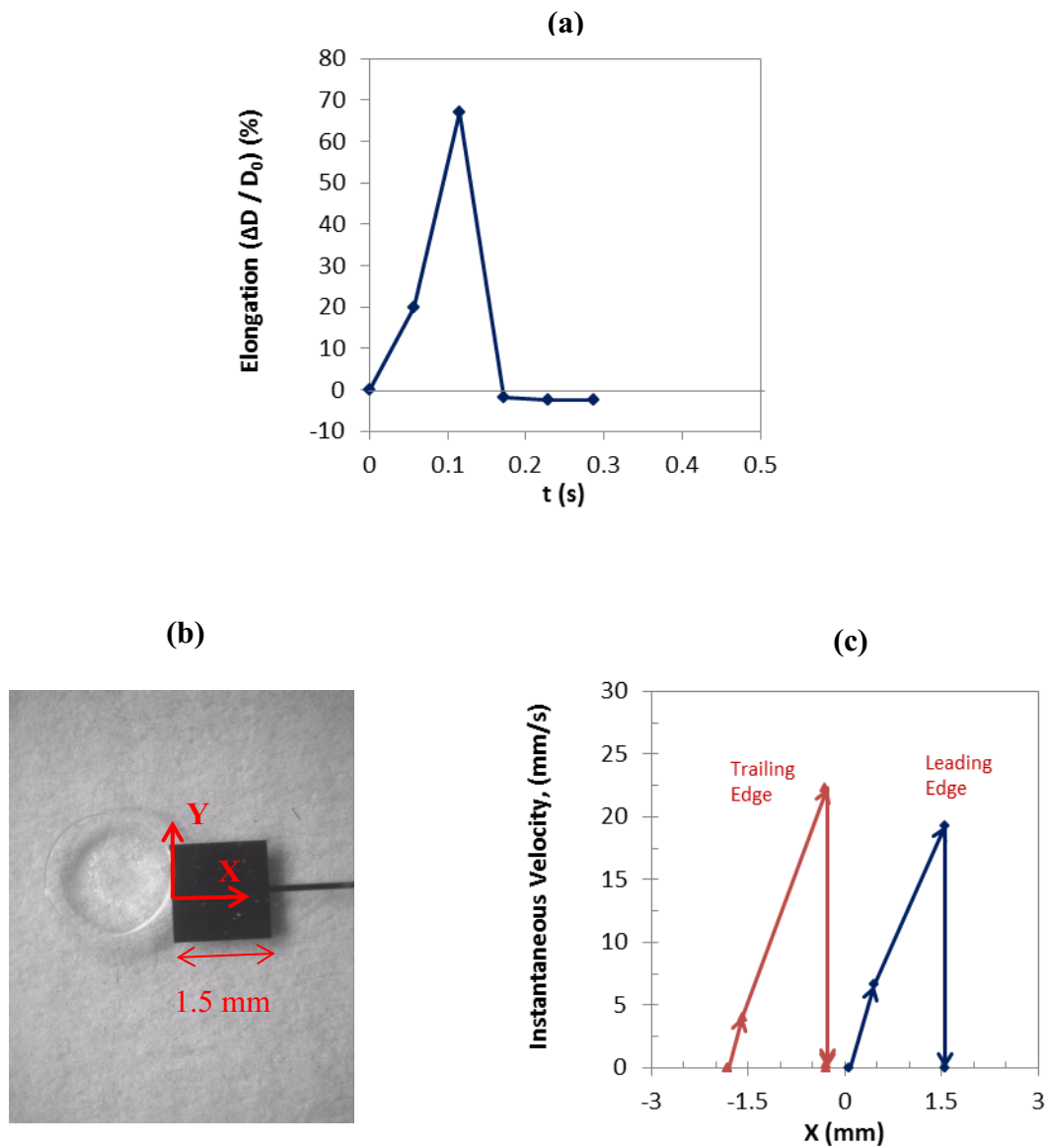


Figure 5-5: (a) Droplet elongation as a function of time, and (c) comparison of the average curves for the instantaneous velocity as a function of droplet position as shown in (b) for the leading and trailing edges of distilled water droplets at 90 V. The arrows in graph (c) indicate the changes of velocity along the direction of movement.

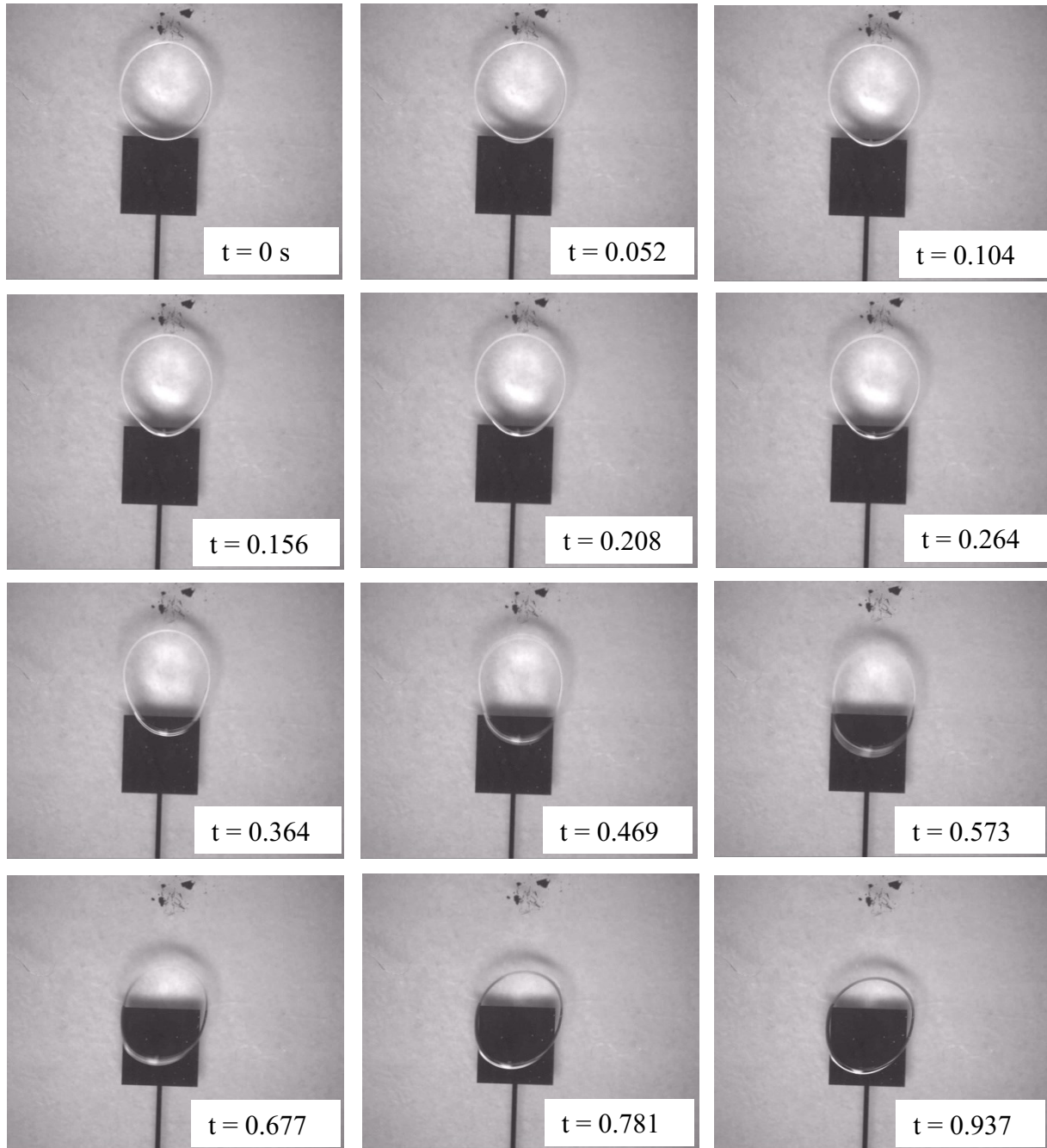


Figure 5-6: Droplet morphology corresponding to an applied potential of 65V voltage to a 0.82 μl droplet of distilled water in a microchannel gap of 370 μm . The overlap and offset values are 72 μm and 33 μm respectively. A sudden inception of voltage is applied at $t = 0$ s, and remains constant until the droplet stops moving.

5.1.3) Time Series Results

In this section, the instantaneous velocity, total displacement and elongation of the droplets of distilled water, Tris-HCl buffer, 4 $\mu\text{g/ml}$ and 20 $\mu\text{g/ml}$ DNA solutions as a function of time at the applied voltages of 50 to 90V, under the conditions outlined in Table 5-1, are presented. Refer to the Appendices F, G, H, I for the graphs of instantaneous displacement and acceleration with time, and the graphs of instantaneous velocity as a function of droplet position.

In each figure, the average curves which are obtained by averaging the data at each point in time, are plotted versus time and compared for the leading edge (a) and the trailing edge (b). As observed, in general, the higher the value of the applied voltage is, the higher the peaks of the curves of instantaneous velocity and elongation will be.

Exceptions:

- distilled water: the average curves of instantaneous velocity and elongation at 75 V;
- Tris-HCl buffer: the average curves of instantaneous velocity and elongation at 85 V, and the average curve of elongation at 75 V;
- 4 $\mu\text{g/ml}$ DNA solution: the average curve of elongation at 75 V;

Reason: by referring to the figures shown in Appendices F, G, H and I for the accepted experiments and the average curves, it is observed that the peak of each individual curve (the changes of instantaneous velocity, total displacement and elongation with time) happens at a specific time during the course of droplet movement toward the end of electrode which is not necessarily the peak time of the average curve; except for the applied voltages of 75 V for distilled water, and 85 V for Tris-HCl buffer where all the accepted experiments have their peaks happening at the same time. It is believed to be due to the similar yet different experimental conditions (*e.g.* different overlaps) and/or hysteresis which will all affect the actuation force, and consequently the time that the droplets reach their peak values in velocity, total displacement and elongation. At 75 V, the average curves of droplet elongation for Tris-HCl buffer and 4 $\mu\text{g/ml}$ DNA solution show higher values than

those of 80 V, due to hysteresis and/or another problem with the surface of the coating layer.

The comparison of results for the experiments with the highest leading edge instantaneous velocity for the leading trailing edges are shown in Appendix F (Figure F-54 through Figure F-56 for distilled water), Appendix G (Figure G-67 through Figure G-69 for Tris-HCl buffer), Appendix H (Figure H-70 through Figure H-72 for 4 $\mu\text{g/ml}$ DNA solution) and Appendix I (Figure I-43 through Figure I-45 for 20 $\mu\text{g/ml}$ DNA solution). As expected, the higher the value of the applied voltage is, the higher the value of the instantaneous velocity and elongation will be.

Exceptions:

- the droplet elongation of distilled water and Tris-HCl buffer at 75 V;
- the droplet elongation of 20 $\mu\text{g/ml}$ DNA solution at 85 V;

Reason: At 75 V, the average curves of droplet elongation for distilled water and Tris-HCl buffer solution show higher values than those of 80 V, due to hysteresis and/or another problem with the surface of the coating layer. For an unknown reason, at 85 V, the droplet of 20 $\mu\text{g/ml}$ DNA solution with the highest leading edge instantaneous velocity did not show any considerable elongation compared to those at lower voltages.

Overall, the higher the applied voltage is, the higher the droplet speed will be, as the actuation force, F_{ac} , scales with the applied voltage squared (Equation 5-4); although, with decreasing the applied voltage, the peaks of the curves are shifted in time. For all solutions, once the voltage is increased, the actuation force and the opposing forces of F_{dd} and F_f , (Equation 5-3) which are proportionally related to the droplet velocity¹⁰⁴, will all increase. Providing that the actuation force overcomes the opposing forces, the droplet movement will initiate. However, at the early stages of the droplet transport, it is required that the actuation force overcomes the resistance of the threshold initiation force of F_T (Equation 5-4) which takes into account the contact angle hysteresis between the leading and trailing edges of the droplet and/or any other static friction, such as friction from adsorption^{104,166,226}. As explained in section 5.1.1, it can be assumed that this resistant force remains constant during droplet movement⁷² for any specific solution (γ_{lv} , θ_0 , α are constant for any type of solution in contact

with a specific solid surface) as it is not directly affected by the amount of voltage. Therefore, with decreasing voltage and consequently the actuation force and all opposing forces, the effect of F_T will become more considerable. This will result in a time delay in the actuation response. This observation is contrary to the results obtained by the analytical model proposed by Chakraborty and Mittal¹⁷⁰, where no shift in time has been predicted as the effect of hysteresis is discounted in their approach. At 65 V, this time delay is more apparent for 20 $\mu\text{g/ml}$ DNA solutions due to the accumulative effect of hysteresis and DNA adsorption. The actuation force and the opposing forces will be empirically compared at the end of this chapter (section 5.2).

For all solutions, the figures of the instantaneous velocity (Figure 5-7, Figure 5-10, Figure 5-13 and Figure 5-16) and total displacement (Figure 5-8, Figure 5-11, Figure 5-14 and Figure 5-17) show that there is a time delay in the actuation response of the trailing edges and consequently the peaks of their related curves compared to those of the leading edges, as the leading edges accelerate more rapidly than the trailing edges under the influence of an electric field.

The total displacement curves are also good indications of the fact whether the droplets can reach to the end of the electrode under the application of a specific voltage which will be further discussed in the following sections (section 5.1.3.1 through 5.1.3.4).

In addition, in Appendices F, G, H and I, for the applied voltages of 50 to 90 V, the information related to the peaks of the average curves and the values of the average velocity for all experiments, and the peaks of the curves and the values of the average velocity for the experiments with the highest leading edge instantaneous velocity are summarized as:

- Appendix F (distilled water): Table F-1 through Table F-4
- Appendix G (Tris-HCl buffer): Table G-1 through Table G-4
- Appendix H (4 $\mu\text{g/ml}$ DNA solution): Table H-1 through Table H-4
- Appendix I (20 $\mu\text{g/ml}$ DNA solution): Table I-1 through Table I-4

5.1.3.1) Distilled Water

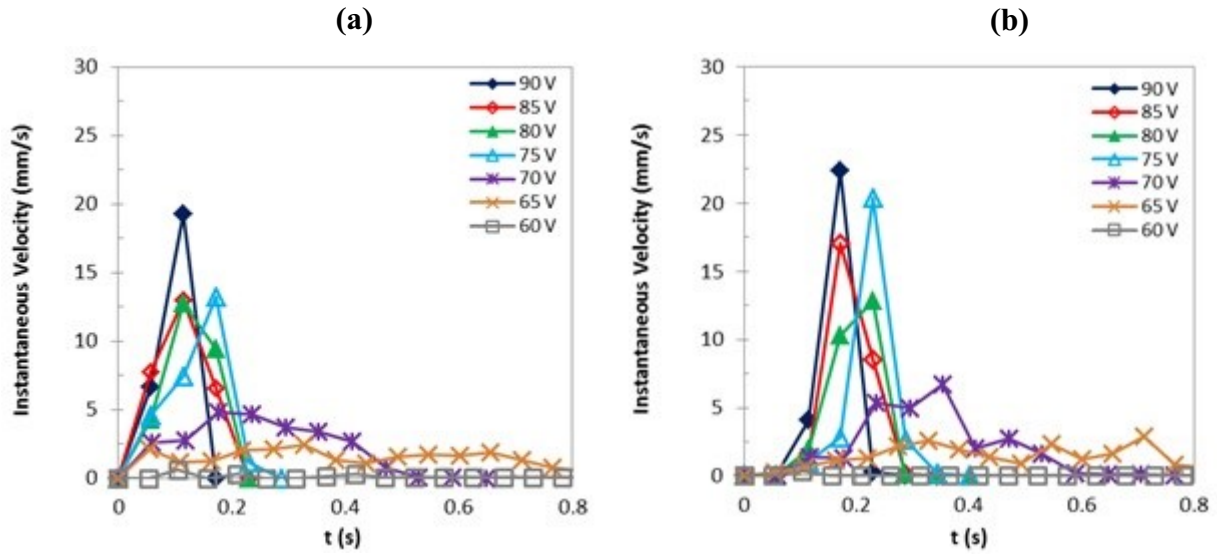


Figure 5-7: The instantaneous velocity of the distilled water droplets as a function of time for the applied voltages of 60 to 90V. Comparison of the average curves: (a) leading edge, (b) trailing edge.

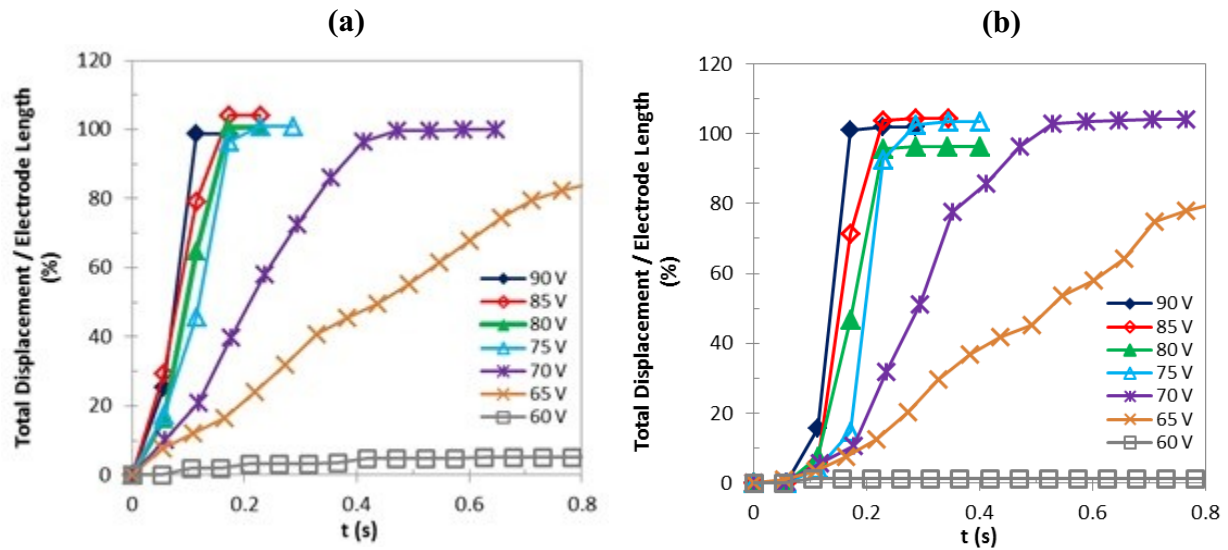


Figure 5-8: The total displacement of the distilled water droplets as a function of time for the applied voltages of 60 to 90V. Comparison of the average curves: (a) leading edge, (b) trailing edge.

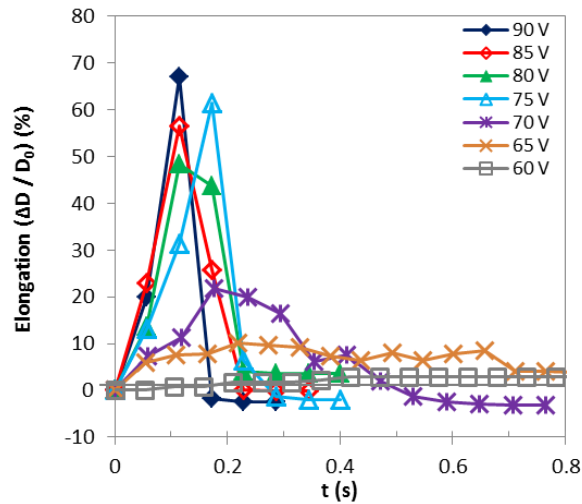


Figure 5-9: The comparison of the average curves for the elongation as a function of time for distilled water droplets.

Figure 5-8 shows that the distilled water droplets can reach to the end of the electrode at the applied voltages $V \geq 70\text{V}$; below which, the droplets partially cover the electrode length, denoting that the actuation force is not sufficient to draw the droplets of distilled water to the end of the electrode. The coverage abruptly decreases from 70 V to 60 V, where the leading edge of the droplet only covers 8.5% of the electrode length (Table F-1). At voltages below 55 V, no actuation was observed for the leading and trailing edges signifying the fact that the actuation force was not high enough to overcome the resistant forces (Equation 5-3 and Equation 5-4).

For the voltages of 60 to 90 V, Figure 5-9 shows that the droplets of distilled water nearly recover their original shapes at the end of movement where the elongation remains $< 10\%$.

5.1.3.2) Tris-HCl Buffer Solution

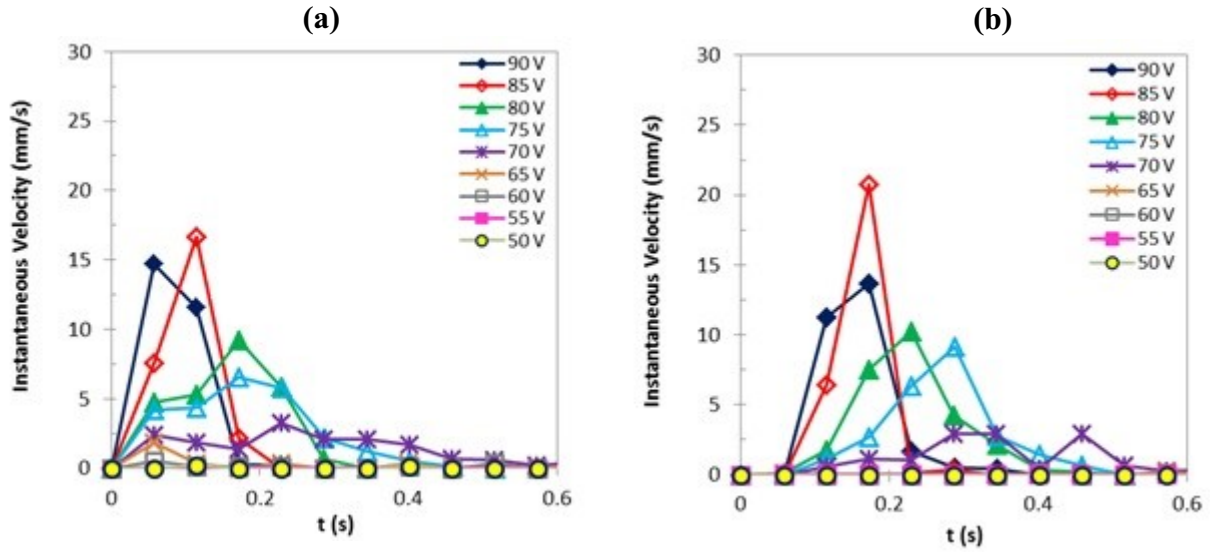


Figure 5-10: The instantaneous velocity of Tris-HCl buffer droplets as a function of time for the voltages of 50 to 90V. Comparison of the average curves: (a) leading edge, (b) trailing edge.

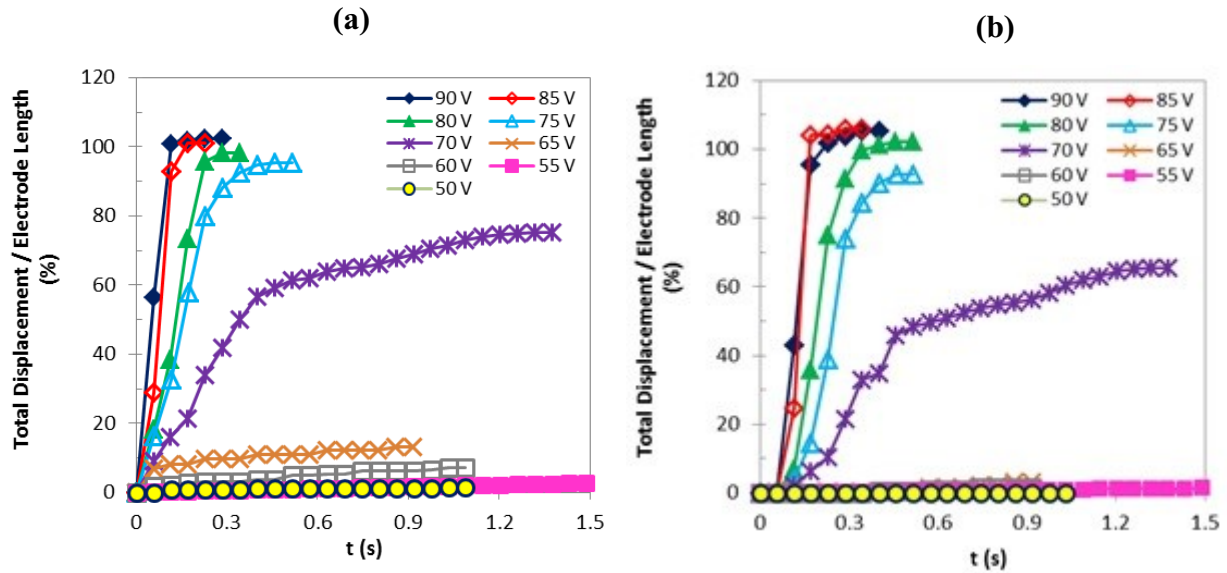


Figure 5-11: The total displacement of Tris-HCl buffer droplets as a function of time for the voltages of 50 to 90V. Comparison of the average curves: (a) leading edge, (b) trailing edge.

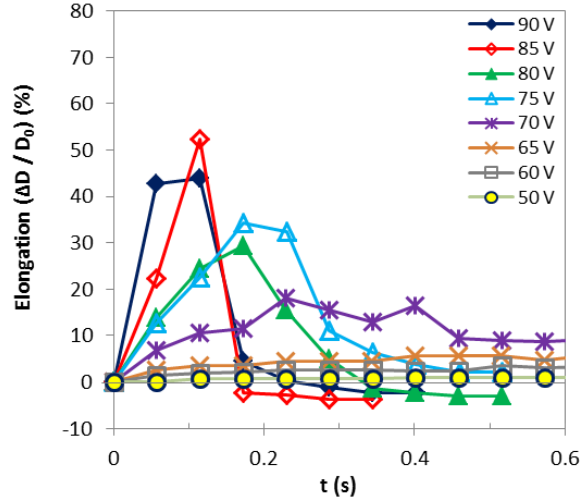


Figure 5-12: The comparison of the average curves for the elongation as a function of time for Tris-HCl buffer droplets.

Figure 5-11 shows that the droplets of Tris-HCl buffer can approximately reach to the end of the electrode at the applied $V \geq 80$ V; below which, the droplets partially cover the electrode length. This coverage decreases abruptly from 75 V to 50 V, where the leading edges of the droplets only cover 2% of the electrode length (Table G-1). At 50 V, no actuation was observed on the trailing edges of this solution.

For the voltages of 50 to 90 V, Figure 5-12 shows that the droplets of Tris-HCl buffer nearly recover their original shapes at the end of movement except for the voltage of 70 V where the elongation remains $\sim 10\%$.

5.1.3.3) 4 $\mu\text{g/ml}$ DNA Solutions

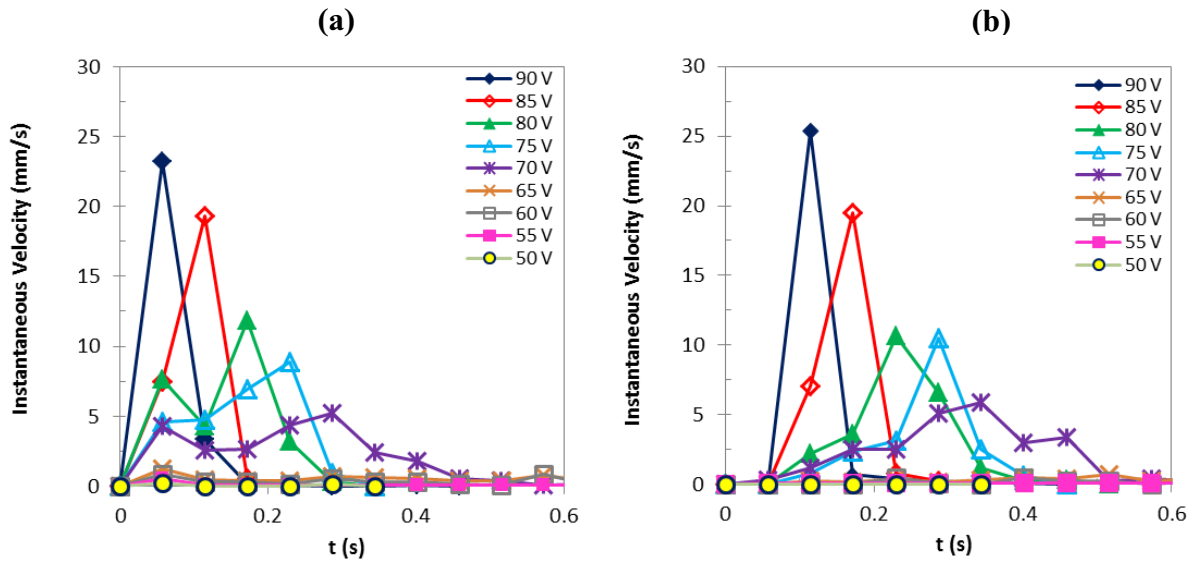


Figure 5-13: The instantaneous velocity of the droplets of 4 $\mu\text{g/ml}$ DNA solutions as a function of time for the voltages of 50 to 90V. Comparison of the average curves: (a) leading edge, (b) trailing edge.

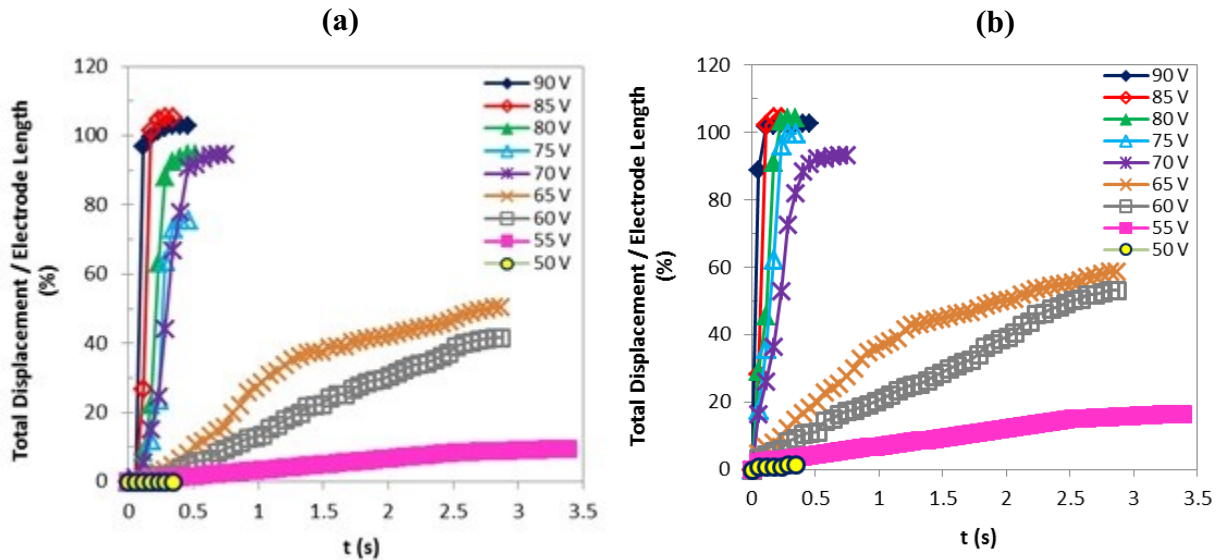


Figure 5-14: The total displacement of the droplets of 4 $\mu\text{g/ml}$ DNA solutions as a function of time for the voltages of 50 to 90V. Comparison of the average curves: (a) leading edge, (b) trailing edge.

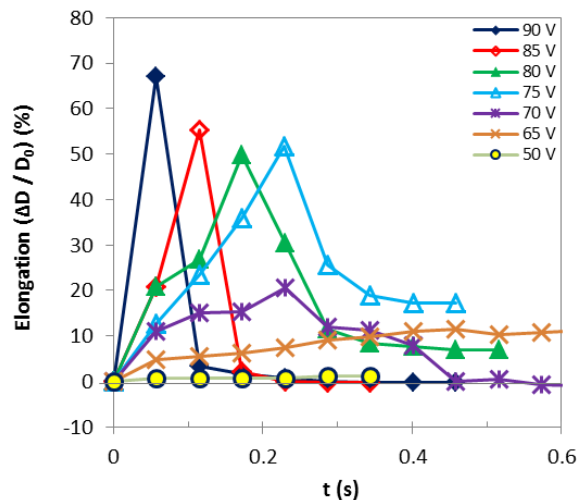


Figure 5-15: The comparison of the average curves for the elongation as a function of time for 4 $\mu\text{g/ml}$ DNA solutions.

Figure 5-14 shows that the droplets of 4 $\mu\text{g/ml}$ DNA solutions can reach to the end of the electrode at the applied voltages $V \geq 75$ V; below which, the droplets partially cover the electrode length. This coverage decreases from 75 V to 50 V, where the leading edges of the droplets only cover 2% of the electrode length (Table H-1). At 50 V, no actuation was observed on the trailing edges of this solution.

From Figure 5-15, it is observed that under the application of voltages of 65, 75 and 80 V, the droplets of 4 $\mu\text{g/ml}$ DNA solutions do not attain their original shape and remain elongated at the end of movement which seems to be due to the contact angle hysteresis and/or the effect of static friction caused by the adsorption of DNA solutions to the solid surface. Due to the excessive number of images to be analyzed (*e.g.* over 100 frames for the voltage of 55 V), the elongation curves at the voltages of 55 and 60 V are not shown.

5.1.3.4) 20 $\mu\text{g/ml}$ DNA Solution

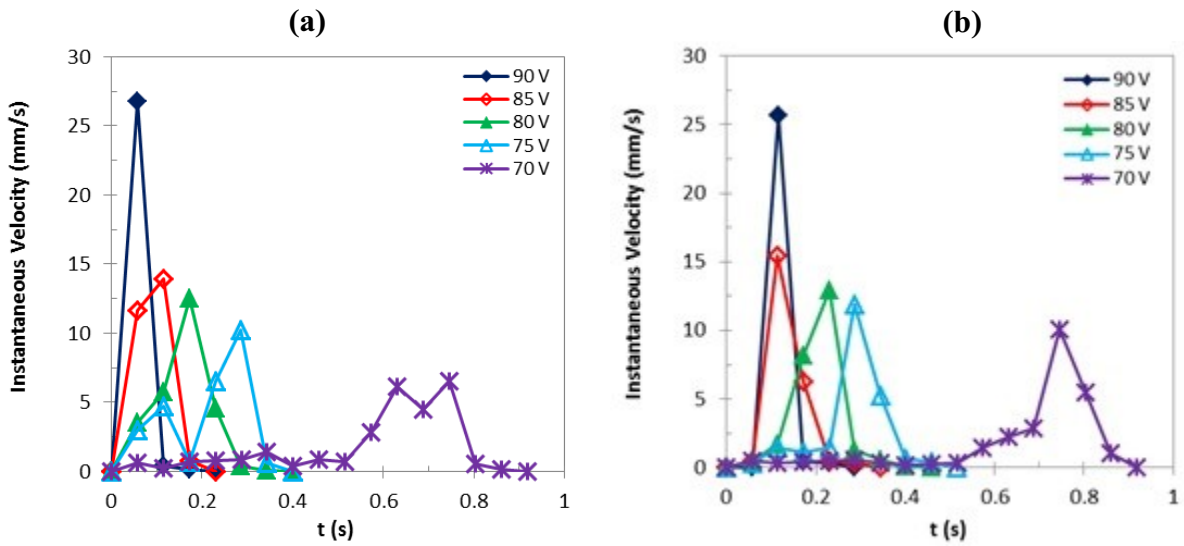


Figure 5-16: The instantaneous velocity of the droplets of 20 $\mu\text{g/ml}$ DNA solutions as a function of time for the voltages of 50 to 90 V. Comparison of the average curves: (a) leading edge, (b) trailing edge.

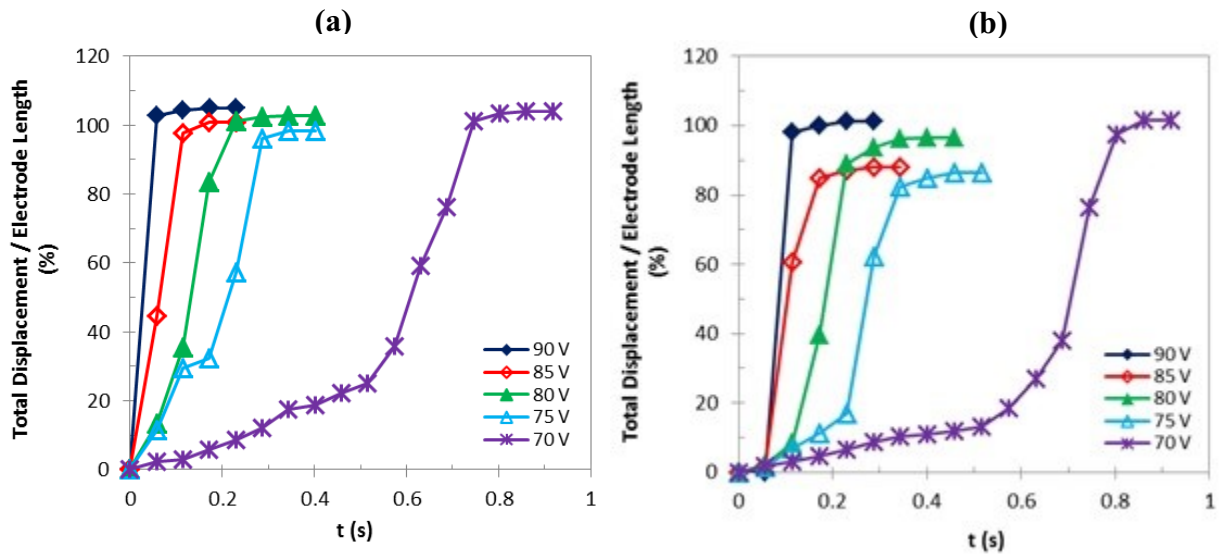


Figure 5-17: The total displacement of the droplets of 20 $\mu\text{g/ml}$ DNA solutions as a function of time for the voltages of 50 to 90 V. Comparison of the average curves: (a) leading edge, (b) trailing edge.

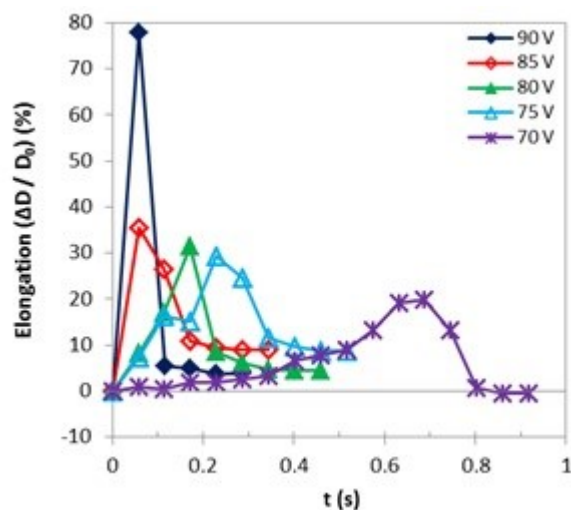


Figure 5-18: The comparison of the average curves for the elongation as a function of time for 20 $\mu\text{g/ml}$ DNA solutions.

In Figure 5-16, the instantaneous velocity of the droplets of 20 $\mu\text{g/ml}$ DNA solutions as a function of time for the voltages of 70 to 90 V is shown; where, similar to the other solutions, with decreasing the applied voltage, the peaks of the curves will decrease and will be shifted in time (as explained in section 5.1.3). Due to the huge number of images to be analyzed (*e.g.* over 1000 frames for the voltage of 60 V), the curves at the voltages of $V \leq 65\text{V}$ are not shown; however the related peak values are presented in Table I-1 through Table I-4 and also on the related curves of the voltage series experiments in section 5.1.4.

The total displacement curves for 20 $\mu\text{g/ml}$ DNA solutions (Figure 5-17, Table I-1 and Table I-3) are also good indications of the fact that these droplets can reach to the end of the electrode at the activation voltages $V \geq 65\text{V}$. At 65 V, this coverage is around 95 % compared to the coverage of 85%, 59% and 13% for the droplets of distilled water, 4 $\mu\text{g/ml}$ DNA solution and Tris-HCl buffer respectively. Below 65 V, the droplets partially cover the electrode length. This coverage decreases from 65 V to 60 V, where the leading edge of the droplet only covers 39% of the electrode length. Contrary to the other solutions, the trailing edges of the droplets were actuated at 50 V.

For the same reason, averaging the elongation data for the voltages of 50 to 65V was difficult, and the related curves are only presented for the voltages of $V \leq 70\text{ V}$ (Figure 5-18).

5.1.3.5) Comparison of Time Series Results

As an instance, in Figure 5-19 through Figure 5-21, Figure 5-22 through Figure 5-24, and Figure 5-25 through Figure 5-27, the comparison of results for the instantaneous velocity, total displacement and elongation for the droplets of distilled water, Tris-HCl buffer, 4 $\mu\text{g/ml}$ and 20 $\mu\text{g/ml}$ DNA solutions as a function of time respectively for the voltages of 90V, 80 V and 75 V are shown. As explained in section 5.1.3, in each figure, the average curves which are obtained by averaging the data at each point in time, are plotted versus time and compared for the leading edge (a) and the trailing edge (b) for all fluids.

At 90 V (Figure 5-19 through Figure 5-21), while the droplets of all fluids fully cover the entire length of electrode, the DNA solutions have the highest leading edge instantaneous velocity. The elongation curves show that the droplets nearly attain their original shape at the end of movement.

At 80 V (Figure 5-22 through Figure 5-24), the leading edge instantaneous velocity of the droplets of distilled water and DNA solutions have the same peak magnitudes; and all fluids cover the entire length of electrode. The elongation curves show that the droplets nearly attain their original shape at the end of movement.

At 75 V (Figure 5-25 through Figure 5-27), the differences in the peak magnitudes of the instantaneous velocity of the fluids are shown to become progressively more noticeable. As shown in Figure 5-26, the leading edges of all fluids nearly cover the entire length of electrode; however, compared to distilled water droplets, the related curves for the droplets of other solutions are shifted in time. The time delay is the highest for the droplets of 20 $\mu\text{g/ml}$ DNA solutions due to their higher static forces related to hysteresis and biomolecular adsorption (section 5.2.3). In Figure 5-26, the observed differences between the related graphs of the leading and trailing edges are also due to the contact angle hysteresis.

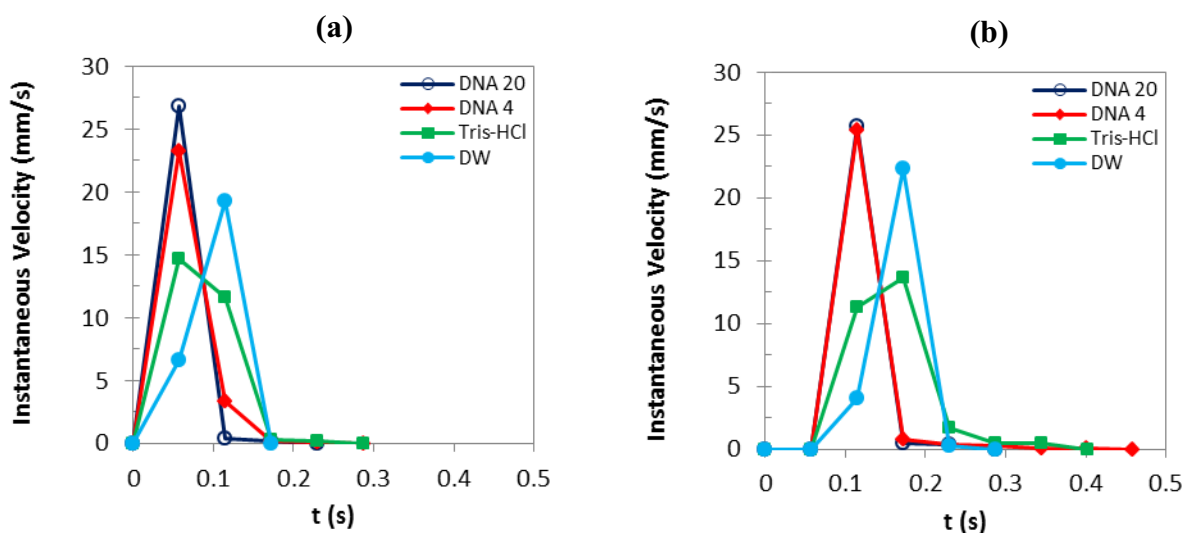


Figure 5-19: The instantaneous velocity as a function of time for the droplets of distilled water, Tris-HCl buffer, 4 $\mu\text{g/ml}$ and 20 $\mu\text{g/ml}$ DNA solutions at the voltage of 90 V. Comparison of the average curves: (a) leading edge, (b) trailing edge.

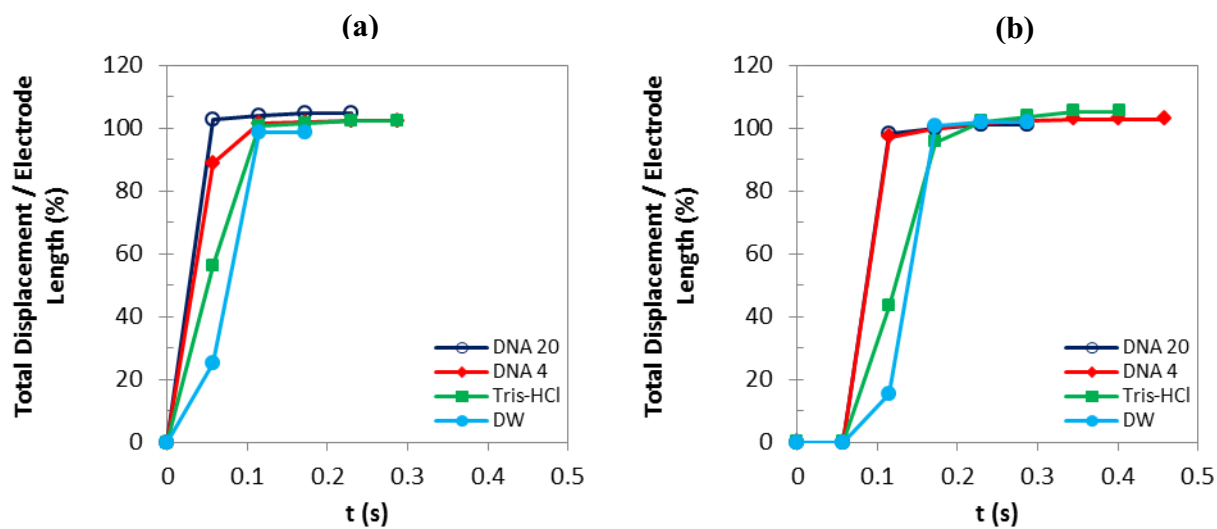


Figure 5-20: The total displacement as a function of time for the droplets of distilled water, Tris-HCl buffer, 4 $\mu\text{g/ml}$ and 20 $\mu\text{g/ml}$ DNA solutions at the voltage of 90 V. Comparison of the average curves: (a) leading edge, (b) trailing edge.

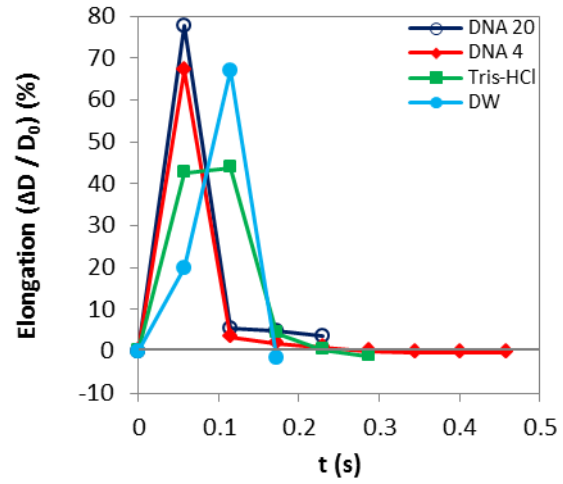


Figure 5-21: The comparison of the average curves for the elongation as a function of time, for the droplets of distilled water, Tris-HCl buffer, 4 $\mu\text{g/ml}$ and 20 $\mu\text{g/ml}$ DNA solutions at the voltage of 90 V.

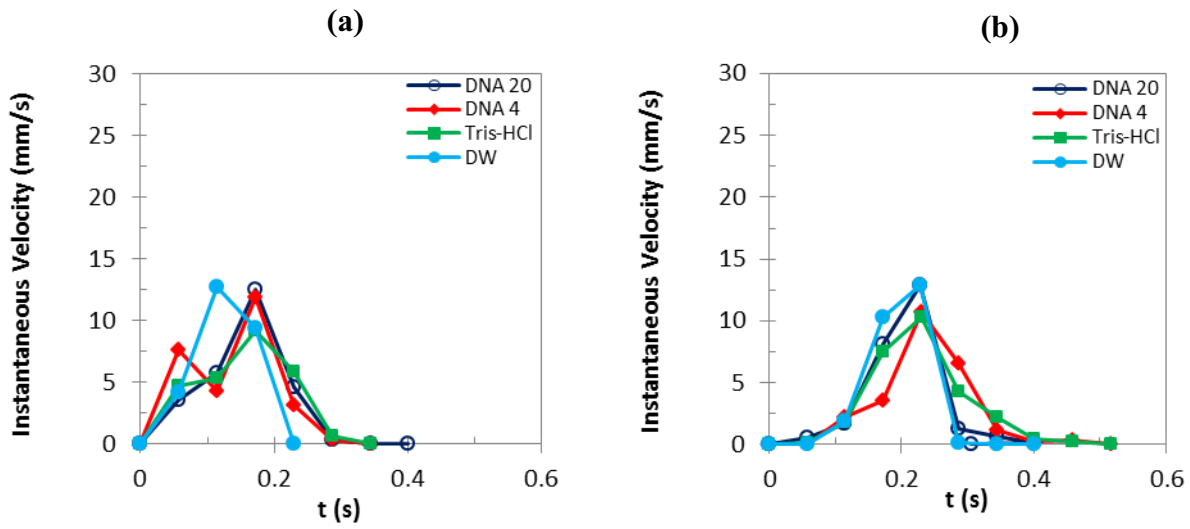


Figure 5-22: The instantaneous velocity as a function of time for the droplets of distilled water, Tris-HCl buffer, 4 $\mu\text{g/ml}$ and 20 $\mu\text{g/ml}$ DNA solutions at the voltage of 80 V. Comparison of the average curves: (a) leading edge, (b) trailing edge.

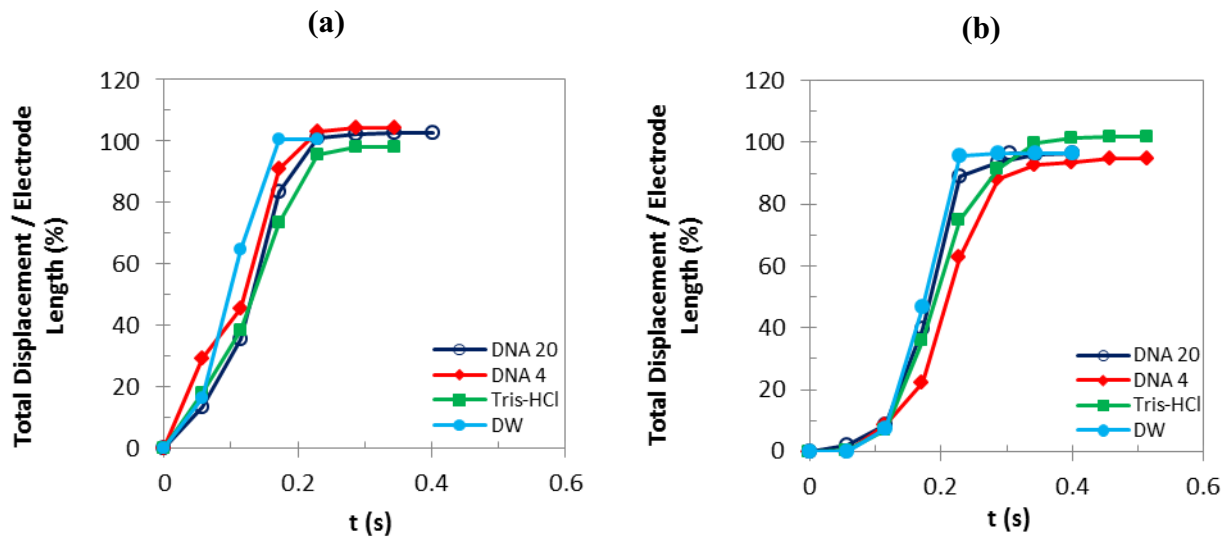


Figure 5-23: The total displacement as a function of time for the droplets of distilled water, Tris-HCl buffer, 4 $\mu\text{g/ml}$ and 20 $\mu\text{g/ml}$ DNA solutions at the voltage of 80 V. Comparison of the average curves: (a) leading edge, (b) trailing edge.

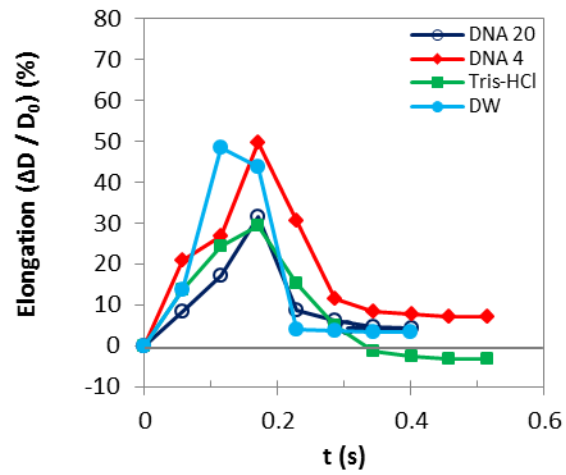


Figure 5-24: The comparison of the average curves for the elongation as a function of time, for the droplets of distilled water, Tris-HCl buffer, 4 $\mu\text{g/ml}$ and 20 $\mu\text{g/ml}$ DNA solutions at the voltage of 80 V.

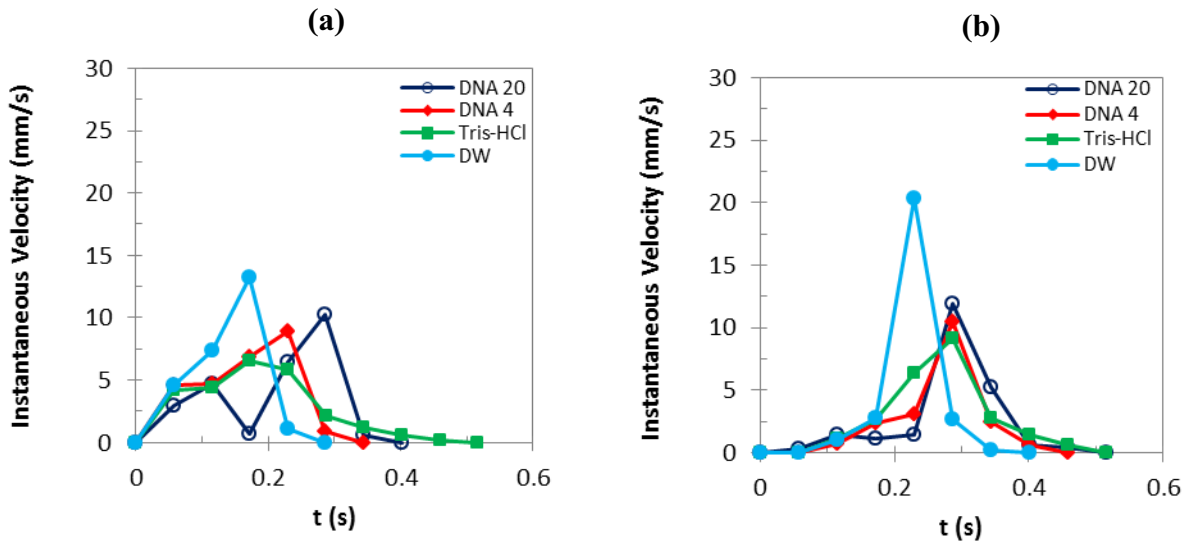


Figure 5-25: The instantaneous velocity as a function of time for the droplets of distilled water, Tris-HCl buffer, 4 $\mu\text{g/ml}$ and 20 $\mu\text{g/ml}$ DNA solutions at the voltage of 75 V. Comparison of the average curves: (a) leading edge, (b) trailing edge.

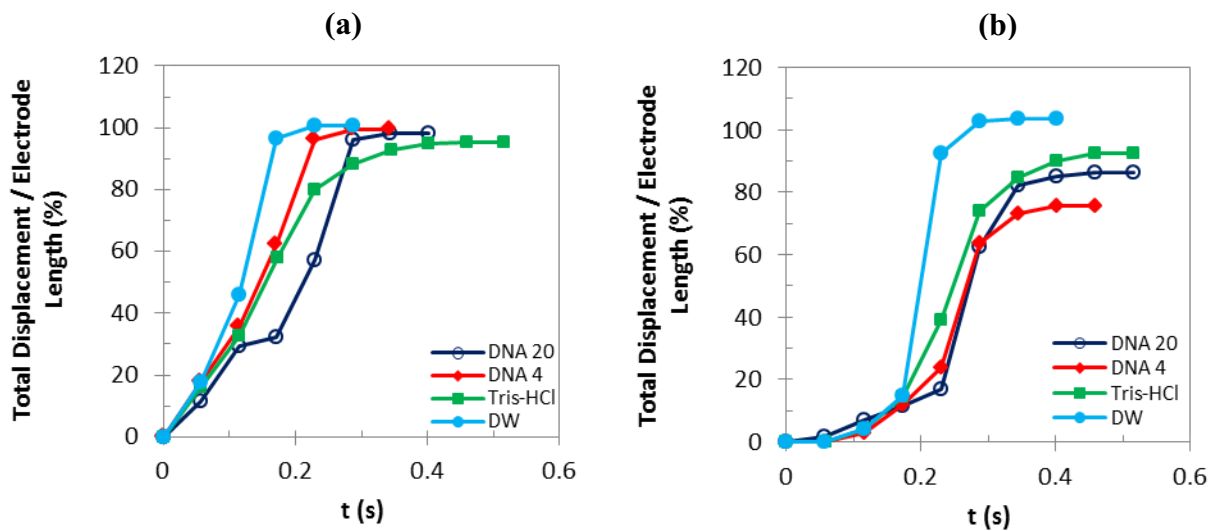


Figure 5-26: The total displacement as a function of time for the droplets of distilled water, Tris-HCl buffer, 4 $\mu\text{g/ml}$ and 20 $\mu\text{g/ml}$ DNA solutions at the voltage of 75 V. Comparison of the average curves: (a) leading edge, (b) trailing edge.

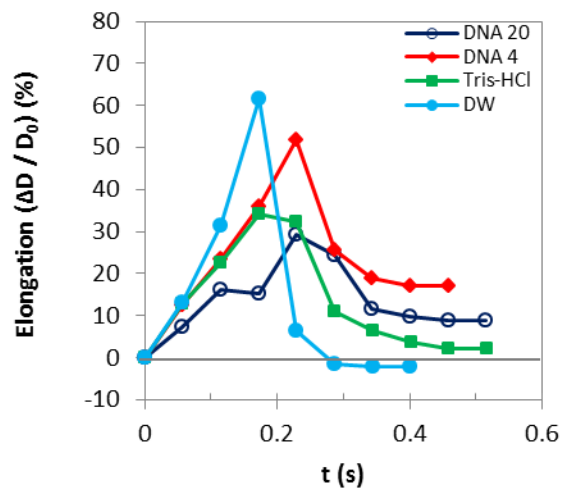


Figure 5-27: The comparison of the average curves for the elongation as a function of time, for the droplets of distilled water, Tris-HCl buffer, 4 $\mu\text{g/ml}$ and 20 $\mu\text{g/ml}$ DNA solutions at the voltage of 75 V.

5.1.4) Voltage Series Results

In this section, Figure 5-29 to Figure 5-31 show the results for the average values of the maximum instantaneous velocity, maximum total displacement, and average time for the maximum total displacement of the leading and trailing edges as a function of the applied voltage for all solutions. Figure 5-28 (a) is an example showing how these maximum values and the corresponding peak times (*i.e.* the time that the maximum instantaneous velocity is occurred) are obtained. As shown, at this specific voltage, there are three acceptable individual experimental peaks: point 1: (t_1, v_1) , point 2: (t_2, v_2) , and point 3: (t_3, v_3) . By averaging the values of v_1, v_2, v_3 and the corresponding times of t_1, t_2, t_3 , the average of the maximum instantaneous velocity, and the average peak time are obtained (Table 5-2 at 85 V, distilled water). The same procedure is followed to obtain the maximum values of the total displacement, droplet elongation and average velocity for the leading and trailing edges (for more detail, refer to Appendices F, G, H, I; *e.g.* for distilled water: Figure F-57 through Figure F-59 in Appendix F).

An alternate procedure can be followed where the maximum values correspond to the peaks of the average curves Figure 5-28 (b). These graphs are presented in Appendices F, G, H, I (*e.g.* for distilled water: Figure F-60 through Figure F-63 in Appendix F) for the same parameters as in Figure 5-29 to Figure 5-31.

Overall, the procedure described in Figure 5-28 (a) appears to be a better method to present the maximum values of the parameters studied in this section, as the experiments are performed on different individual droplets (not performing several experiments on the same droplet) under similar yet different experimental conditions (*e.g.* different overlaps) and/or hysteresis which will all affect the actuation force, and consequently the time that droplets reach their maximum velocity. By using this method, the real values of the maximum velocities achieved in the EWOD system will be averaged along with the corresponding real peak time. For instance, as shown in Table 5-2, the average of maximum values (18.5 mm/s) will better represent the velocities of 15.8, 19.9 and 19.7 mm/s achieved in the experiments than the peak of the average curve which is 13.0 mm/s. In other words, by doing more experiments, it is more probable to reach the value of 18.5 mm/s than 13.0 mm/s. Although the standard deviations for the latter

procedure (Appendices F, G, H, I) are still within the uncertainty of the experiments, but they are significantly higher (e.g. in Figure F-60 through Figure F-63 in Appendix F for distilled water) than the standard deviations calculated based on the procedure described in Figure 5-28 (a).

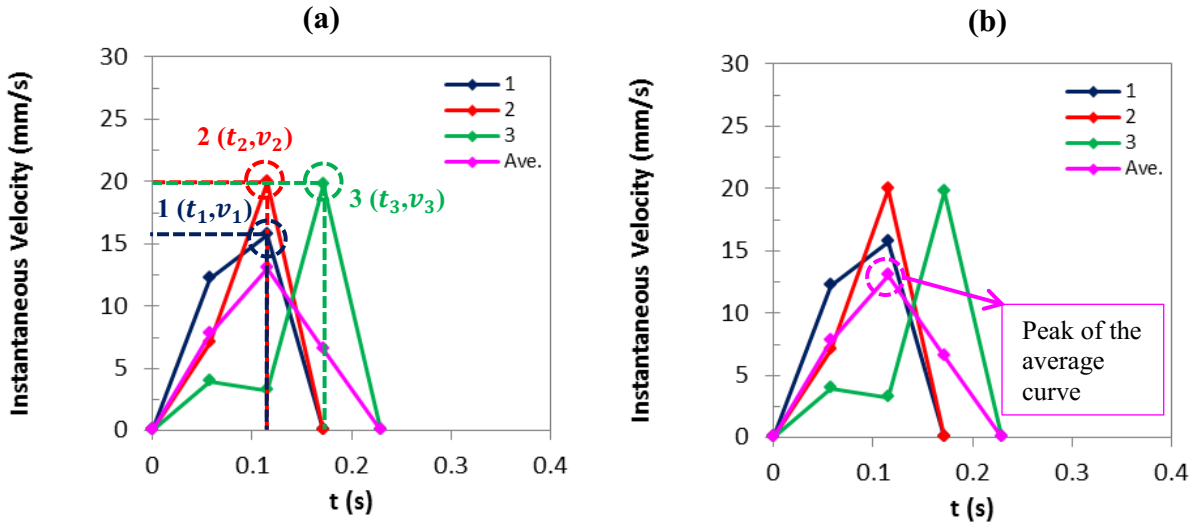


Figure 5-28: An example showing the instantaneous velocity of the leading edge instantaneous velocity of distilled water droplets as a function of time (applied voltage of 85 V); (a) peaks of the individual experiments at point 1: (t_1, v_1) , point 2: (t_2, v_2) , and point 3: (t_3, v_3) , (b) peak of the average curve.

	Actual value: (s, mm/s)
point 1: (t_1, v_1)	(0.1146, 15.8)
point 2: (t_2, v_2)	(0.1146, 19.9)
point 3: (t_3, v_3)	(0.1719, 19.7)
Average of maximum values	(0.1337, 18.5)
Peak of the average curve	(0.1146, 13.0)

Table 5-2: the average of the maximum instantaneous velocity, and the average peak time for the experiment shown in Figure 5-28.

Figure 5-29 shows the average of maximum instantaneous velocity as a function of voltage for the droplets of all fluids. From Figure 5-29 (a) for distilled water droplets, it is observed that at the voltages of $V \geq 80$ V, the droplet speed becomes less sensitive to the applied voltage indicating dynamic saturation^{174,183}, which was neither observed in the experimental results of Pollack *et al.*²⁵, nor the analytical models developed by Ren *et al.*¹⁶⁶, Bahadur and Garimella¹⁰⁴, Chakraborty and Mittal¹⁷⁰, and Oprins *et al.*¹⁷⁹ (section 5.1.1). Our experimental results, similarly to those of Bavière *et al.*¹⁷⁴, though in very different experimental configurations, reveal that the transport velocity induced by electrowetting is limited by dynamic saturation^{174,183}. In our case, static and dynamic saturations take place at different voltages: $V_{ssat} \sim 60$ V and $V_{dsat} \sim 80$ V; because of the thicker dielectric layer in the dynamic studies.

In accordance with Seyrat and Hayes²²⁹, the resistance to dielectric breakdown increased with dielectric thickness resulting in less electrolysis in the dynamic experiments compared to the static studies discussed in Chapter 4. It is believed that dynamic saturation originates from the same cause as the static saturation previously observed in our studies on the static contact angle possibly from the very high electric fields in the vicinity of the three-phase line^{120,174}.

As shown in Figure 5-29 (b) for Tris-HCl buffer droplets, at voltages of $V \geq 80$ V, contrary to distilled water, the curves of the average of maximum instantaneous velocity do not reach a plateau; denoting that dynamic saturation is not observed within our experimental region; however, the droplet speed becomes less sensitive to the applied voltage at $V \geq 85$ V which is a good indication that dynamic saturation will probably happen in the region of $V \geq 85$ V. This matter, can be attributed to the presence of negatively charged EDTA molecules in the buffer (sections 3.2 and 4.3.3).

From Figure 5-29 (c) and (d) for the droplets of 4 $\mu\text{g/ml}$ and 20 $\mu\text{g/ml}$ DNA solutions respectively, it is also observed that the instantaneous velocity incrementally increases with voltage and contrary to distilled water, dynamic saturation for DNA solutions is not observed (more detail in section 5.2).

Overall, for all solutions, the instantaneous velocity of the trailing edge is higher than that of the leading edge (Figure 5-29); however, the corresponding average velocity of the trailing edge is lower (refer to section 5.2.5, Figure 5-40) which is attributable to the fact that at the

beginning of the movement, there is a short period of time when the leading edge has started moving, while the trailing edge is still at rest. At the time that the leading edge decelerates and finally stops moving, the trailing edge accelerates compensating for its delay in time.

In Figure 5-29 through Figure 5-31 (and the following figures in section 5.2), wherever the data are not shown is either because the droplets were not actuated at that specific voltage (e.g. distilled water droplets at $V \leq 55$ V, and the average time for maximum total displacement of the trailing edges of Tris-HCl buffer and 4 $\mu\text{g/ml}$ DNA solutions at 50 V) or the information is missing due to the excessive number of images (~70 frames for Tris-HCl buffer and 4 $\mu\text{g/ml}$ DNA solutions or huge number of images ~1000 frames for 20 $\mu\text{g/ml}$ DNA solutions) to be analyzed.

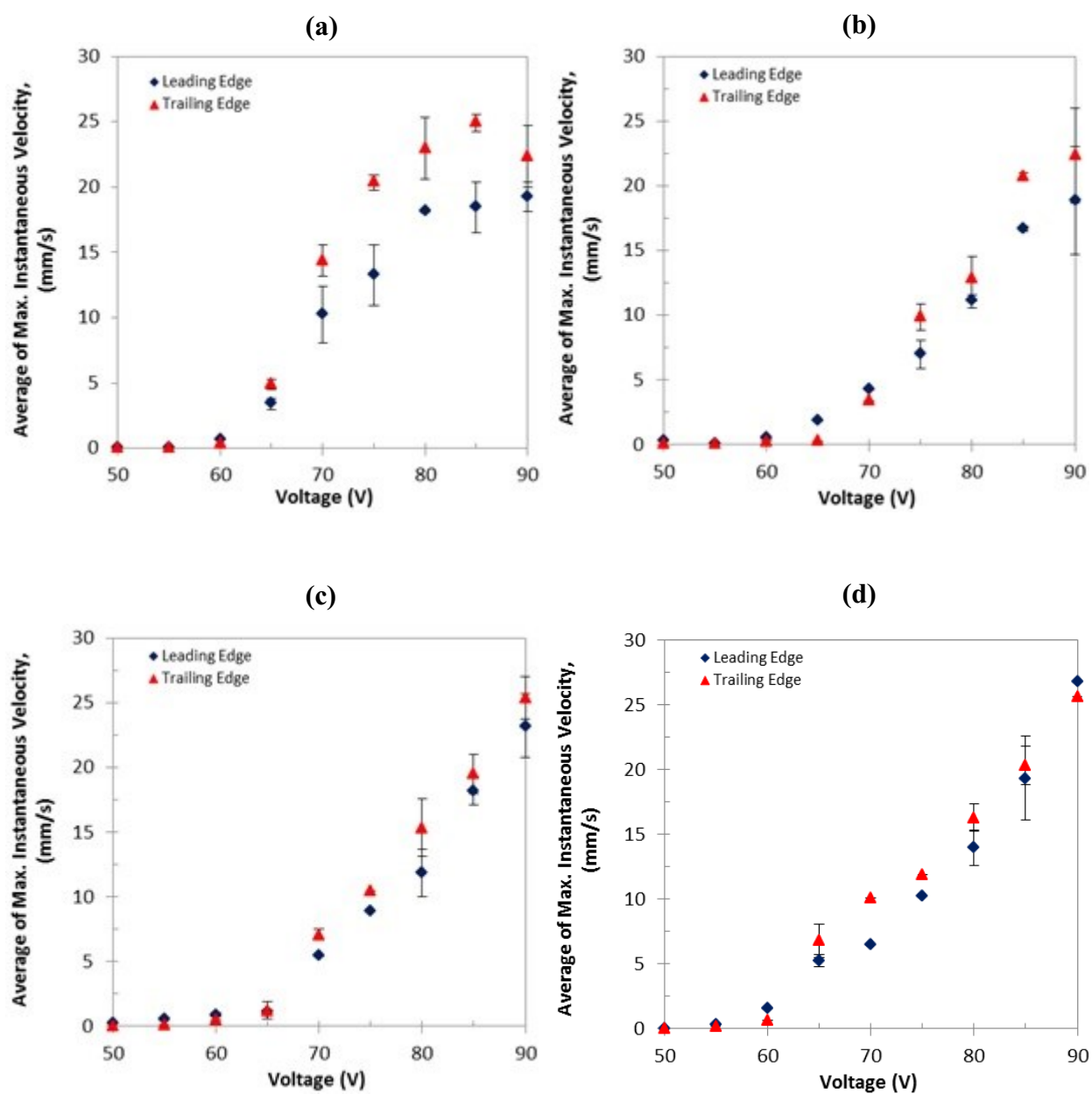


Figure 5-29: The average of maximum instantaneous velocity as a function of voltage for the leading and trailing edges of the droplets of (a) distilled water droplets, (b) Tris-HCl buffer, (c) 4 $\mu\text{g/ml}$ DNA solution, (d) 20 $\mu\text{g/ml}$ DNA solution. The error bars indicate standard deviation.

The same as in Figure 5-8, Figure 5-30 (a) shows that by applying voltages of 70 to 90 V, the droplets of distilled water will move to fully cover the length of the electrode. The voltages of 60 to 70 V will actuate the leading and the trailing edges; however, the droplets will partially cover the electrode length. At 65 V, the electrode coverage is around 83% compared to 100% at 70V within an average time which is three times longer (Figure 5-31 (a)). The 8.5% coverage at 60 V takes also an average time which is 10 times longer than the relevant time at 70V. Therefore, in this study, the applied voltage of 70 V is a critical voltage below which the droplets of distilled water need a much longer time to only partially cover the electrode length.

The same as distilled water droplets, time and voltage are two important factors for all fluids. The travel time (or cycle time) which is the time required by the droplet to reach to the end of the electrode (*i.e.* the inverse of switching frequency)^{168,180} is also an important factor which can be used to estimate the electrode switching frequencies needed to obtain a continuous droplet motion on arrays of electrodes¹⁰⁴. As observed in Figure 5-31, the average time for the maximum total displacement increases with a reduction in the applied voltage due to the fact that with lowering the voltage, the energy supplied to the system decreases¹⁷⁰. The regions that the droplets cover the entire electrode are marked on the related graphs in Figure 5-31. In order to compare the results of distilled water with the other solutions, the scale of Y axis for the transition time has been set to 1000 s.

As shown in Figure 5-30 (b), by applying voltages of 80 to 90 V, the droplets of Tris-HCl buffer will move to fully cover the entire length of the electrode which is in agreement with the results in Figure 5-11. The voltages of 55 to 75 V will actuate the leading and the trailing edges; however, the droplets will only partially cover the electrode length. At 70 V, the electrode coverage is around 75% comparing to 100% at 80 V within an average time which is three times longer (Figure 5-31 (b)).

As shown in Figure 5-30 (c) (the same as in Figure 5-14), by applying voltages of 75 to 90 V, the droplets of 4 $\mu\text{g/ml}$ DNA solutions will move to fully cover the length of the electrode. The voltages of 55 to 70 V will actuate the leading and the trailing edges; however, the droplets will partially cover the electrode length. At 65 V, the electrode coverage is around 60% comparing to 88% at 70 V within an average time which is five times longer (Figure 5-31 (c)).

Figure 5-30 (d) shows that by applying voltages of $V \geq 65$ V, the droplets of 20 $\mu\text{g/ml}$ DNA solutions will move to fully cover the length of the electrode which is in agreement with Figure 5-17. The voltages of 50 to 60 V will actuate both the leading and the trailing edges, however, the droplets will partially cover the electrode length. At 60 V, the electrode coverage is around 40% comparing to 98% at 65 V within an average time which is ten times longer (Figure 5-31 (d)).

Overall, at voltages of $V \leq 65$ V the electrode coverage for 20 $\mu\text{g/ml}$ DNA solutions has higher values compared to the other solutions; however the average time is longer due to the reduced electrowetting and electrophoretic forces (in the following section, this matter will be further discussed). Our experimental results are in good agreement with the analytical results of Bahadur and Garimella¹⁰⁴ asserting the substantial dependence of the average time for maximum total displacement on the voltage and the droplet viscosity. Therefore, the higher the concentration of DNA solutions is, the higher the viscosity of the solutions and the longer the average time for maximum total displacement will be.

The differences in microchannel gaps (Table 5-1) are also causing some of the differences in average time for maximum total displacement which is in agreement with the modeling results of Bahadur and Garimella¹⁰⁴ and recent findings of Guan *et al.*¹⁸⁵. Overall, it is concluded that the average time for maximum total displacement strongly depends on the applied voltage and the droplet viscosity in addition to the effect of gap height at lower voltages.

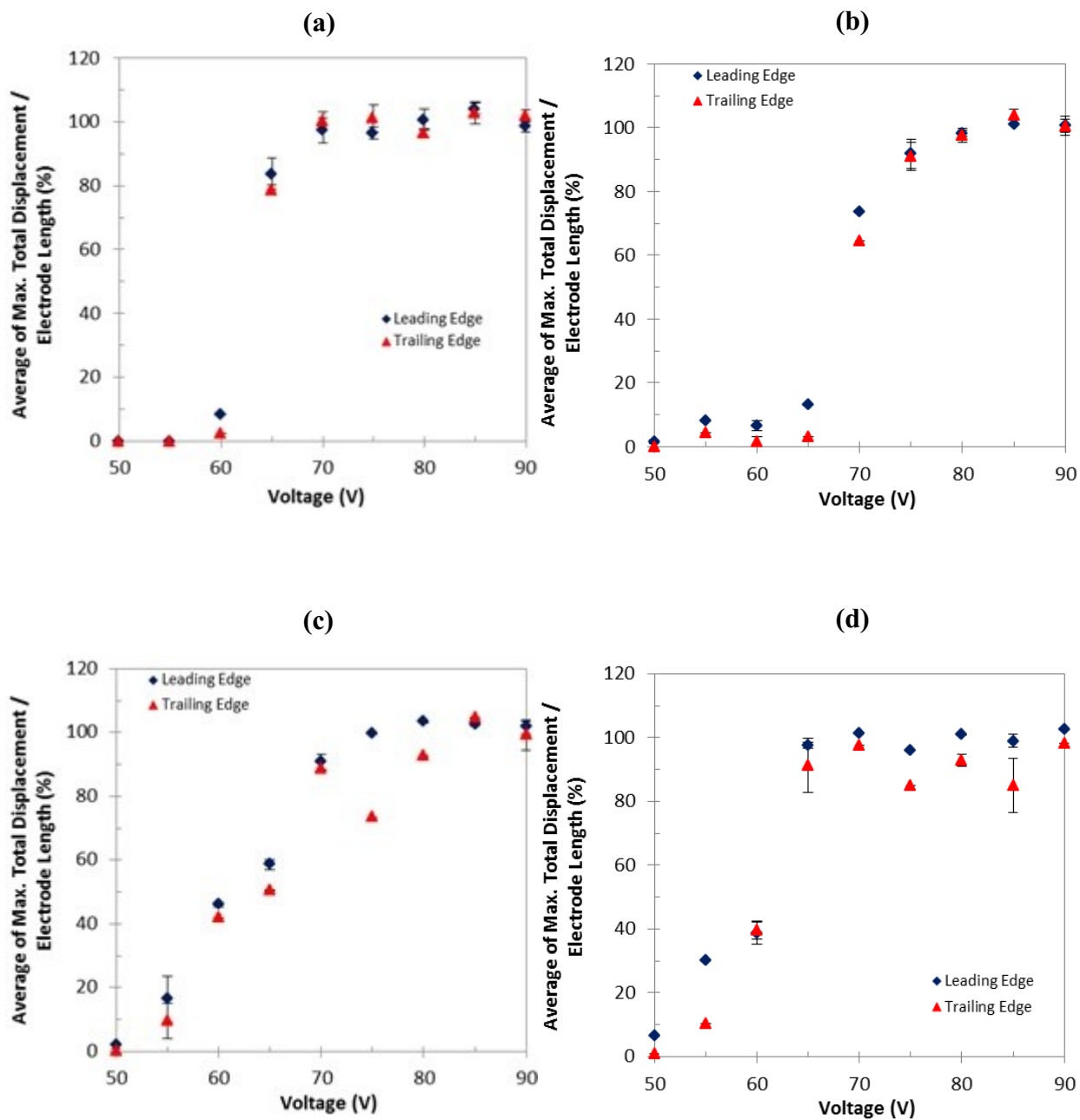


Figure 5-30: The average of maximum total displacement as a function of voltage for the leading and trailing edges of the droplets of (a) distilled water droplets, (b) Tris-HCl buffer, (c) 4 $\mu\text{g/ml}$ DNA solution, (d) 20 $\mu\text{g/ml}$ DNA solution. The error bars indicate standard deviation.

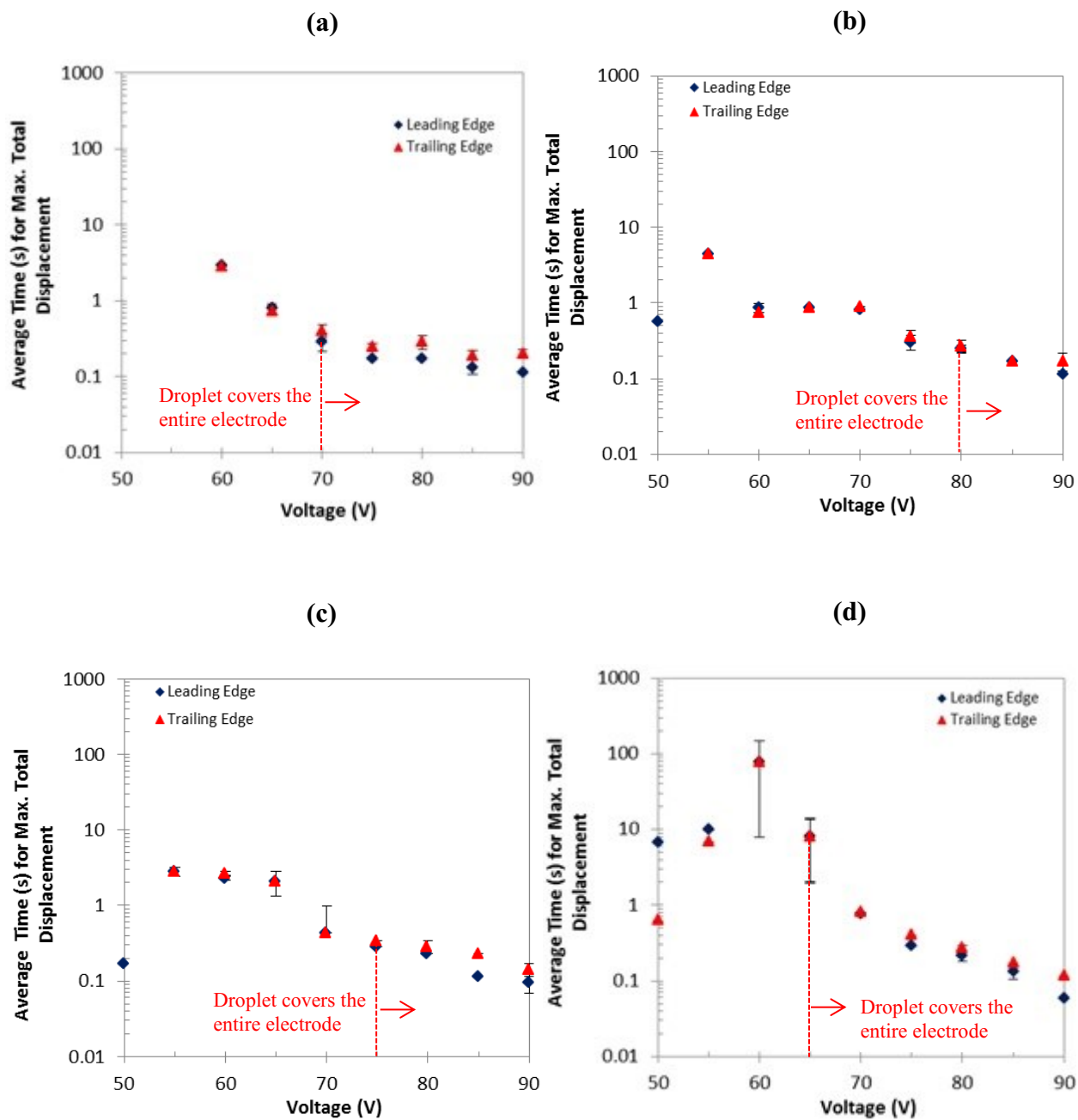


Figure 5-31: The average of peak time for maximum total displacement as a function of voltage for the leading and trailing edges of the droplets of (a) distilled water droplets, (b) Tris-HCl buffer, (c) 4 $\mu\text{g/ml}$ DNA solution, (d) 20 $\mu\text{g/ml}$ DNA solution. The error bars indicate standard deviation.

From Figure 5-29 to Figure 5-31, it is concluded that all parameters of interest in this chapter including the droplet instantaneous velocity and total displacement strongly depend on the applied voltage emphasizing the dominant influence of the voltage on the surface tension¹⁰⁴. Among these parameters, the droplet speed is a key factor which controls the rate of microfluidic operations in lab-on-a-chip systems¹⁰⁴.

The alternate procedure, which was described in Figure 5-28 (b), can be followed where the maximum values correspond to the peaks of the average curve. These graphs are presented in Appendices F, G, H, I (*e.g.* for distilled water: Figure F-60 through Figure F-63 in Appendix F) for the same parameters as in Figure 5-29 through Figure 5-31.

5.2) Comparison of Results for all solutions and Discussion

In this chapter, we were able to study the dynamics of droplet transport when positioned next to an activated single square electrode in terms of characteristic parameters such as maximum velocity, total displacement, elongation and average velocity varying with time and voltage. For this purpose, microliter droplets of distilled water, Tris-HCl buffer solution, 4 $\mu\text{g/ml}$ and 20 $\mu\text{g/ml}$ DNA solutions were studied. The experimental conditions for all solutions are summarized in Table 5-3.

Microchannel gap (μm)	326 ± 23
Droplets initial volume (μl)	0.91 ± 0.07
Droplets initial diameter (μm)	1900 ± 70
Overlap (μm)	65 ± 10
Offset (μm)	200 ± 60

5.2.1) Minimum Actuation Voltage

Based on literature^{8,67}, contact angle hysteresis (α , see section 1.2.1), is responsible for the minimum actuation voltage (V_{min} , *i.e.* the threshold voltage.) in EWOD applications, and the droplet will not begin to move until the electrical potential exceeds V_{min} . The notion of contact angle hysteresis is a very approximate perception⁷² and still needs additional studies to provide a complete understanding as many factors such as repetitively using the samples (top and bottom plates, Figure 2-4) and/or dispensing droplets on the same location in several experiments (consequently affecting the properties of coating layer), biomolecular adsorption and electrophoresis will affect that. As reported by Schertzer *et al.*¹⁷⁸, the hysteresis angle exponentially increases with applied voltage; however, they used AC voltage which may lead to different hysteresis from that exhibited under DC voltage²³⁰. The physical mechanism behind

dynamic contact angle hysteresis is beyond the scope of the present study for a quantitative consideration and additional studies are needed to provide a complete understanding.

In Chapter 4, the impact of the contact angle in the absence of an electric field (θ_0), the contact angle after applying voltage (θ), the difference between these contact angles ($\Delta\theta_v$), and the applied voltage (V), on the minimum actuation voltage was studied. Table 5-4 shows the experimental results for the minimum actuation voltage obtained in that chapter for the droplets of distilled water, Tris-HCl buffer, 4 $\mu\text{g/ml}$ and 20 $\mu\text{g/ml}$ DNA solutions. As explained in section 5.1.2.2, the actuation potential for distilled water droplets in our experiments ($V_{min} \sim 60$ V) is higher than that of Pollack *et al.*²⁵ ($V_{min} \sim 48$ V) due to the thicker dielectric layer.

Table 5-4: The comparison of minimum actuation voltage, and contact angle hysteresis, for the droplets of distilled water, Tris-HCl buffer, 4 $\mu\text{g/ml}$ and 20 $\mu\text{g/ml}$ DNA solutions.

	Minimum actuation voltage (V_{min} (V))		Contact angle hysteresis: α ($^\circ$)
	Leading edge	Trailing edge	
Distilled Water	60	60	7-9*
Tris-HCl buffer solution	50	55	5-7
DNA 4 $\mu\text{g/ml}$	50	55	5-6
DNA 20 $\mu\text{g/ml}$	50	50	3-5

* Reference: Berthier⁶⁷ and Berthier *et al.*⁷²

Table 5-4 indicates that with increasing DNA concentration, the minimum threshold voltage to actuate the trailing edges of the droplets decreases. At 50 V, the leading and trailing edges of the droplets of 20 $\mu\text{g/ml}$ DNA solutions will actuate, while this voltage is merely

sufficient to actuate the leading edges of the droplets of Tris-HCl buffer and 4 $\mu\text{g/ml}$ DNA solutions. In order to further investigate this observation, the values of contact angle hysteresis for all solutions need to be estimated.

Berthier⁶⁷ and Berthier *et al.*⁷² have reported the value of $7-9^\circ$ for the contact angle hysteresis of deionized water with a Teflon substrate in air. Simply, by substituting this number and the experimentally obtained values of minimum actuation voltage from Table 5-4 in Equation 4-6, the approximate values of contact angle hysteresis for Tris-HCl buffer, 4 $\mu\text{g/ml}$ and 20 $\mu\text{g/ml}$ DNA solutions are obtained (Table 5-4).

These results show that with increasing DNA concentration, contact angle hysteresis decreases (providing comparable experimental conditions); therefore, the droplets will start moving at lower voltages. However, this analysis is misleading as by referring to the graphs of elongation as a function of time for the droplets of distilled water (Figure 5-9), Tris-HCl buffer (Figure 5-12), 4 $\mu\text{g/ml}$ DNA solution (Figure 5-15), and 20 $\mu\text{g/ml}$ DNA solution (Figure 5-18), it is observed that contrary to distilled water, the droplets of Tris-HCl buffer and DNA solutions do not attain their original shape at the end of movement and stay elongated. In literature^{178,181,184}, this phenomenon is referred to as contact line pinning, originating from molecular adhesion at the contact line or hysteresis.

Overall, the reason that the minimum actuation voltage for 20 $\mu\text{g/ml}$ DNA solutions is the lowest amongst all solutions might be attributed to the contribution of electrophoresis to the movement of negatively charged DNA solutions in EWOD systems. In the following sections, the effect of electrophoresis will be further discussed.

5.2.2) Maximum Instantaneous Velocity

Droplet motion is a complex physical phenomenon and is still a subject of research⁶⁷. Due to the great difficulty of conducting experiments at such small scales to correlate physical properties with observable phenomena; theoretical models have been proposed for explaining droplet transport dynamics^{104,166,169,181,185}. However, there is no comprehensive model covering the entire range of physical properties for various conditions¹⁸¹. In this research, from the experimental results presented in this chapter, it is concluded that all parameters of interest in this chapter (droplet speed, total displacement, and elongation) strongly depend on the applied voltage emphasizing the dominant influence of the voltage on the surface tension¹⁰⁴. Among these parameters, the droplet speed is a key factor which controls the rate of microfluidic operations in lab-on-a-chip systems¹⁰⁴. According to the findings reported in literature^{25,104,166,169,185}, the droplet transport velocity increases with the applied voltage. Despite the fact that it is technically difficult to experimentally analyze the droplet motion due to the complexity of the transport process occurring at the microscale, the present study will further investigate the voltage dependency of the maximum instantaneous velocity of the droplets of distilled water, Tris-HCl buffer and the DNA solutions.

5.2.2.1) Velocity and Voltage

Figure 5-32 shows the comparison of results for the average of maximum instantaneous velocity for the leading and trailing edges of the droplets of distilled water, Tris-HCl buffer, 4 $\mu\text{g/ml}$ and 20 $\mu\text{g/ml}$ DNA solutions. As observed, for all solutions, with increasing voltage, the droplet instantaneous velocity prominently increases; except at the voltages of $V \geq 80 \text{ V}$ and $V \geq 85 \text{ V}$ for the droplets of distilled water and Tris-HCl buffer respectively; where the droplet speed becomes less sensitive to the applied voltage which is a good indication of dynamic saturation^{174,183} (section 5.1.4).

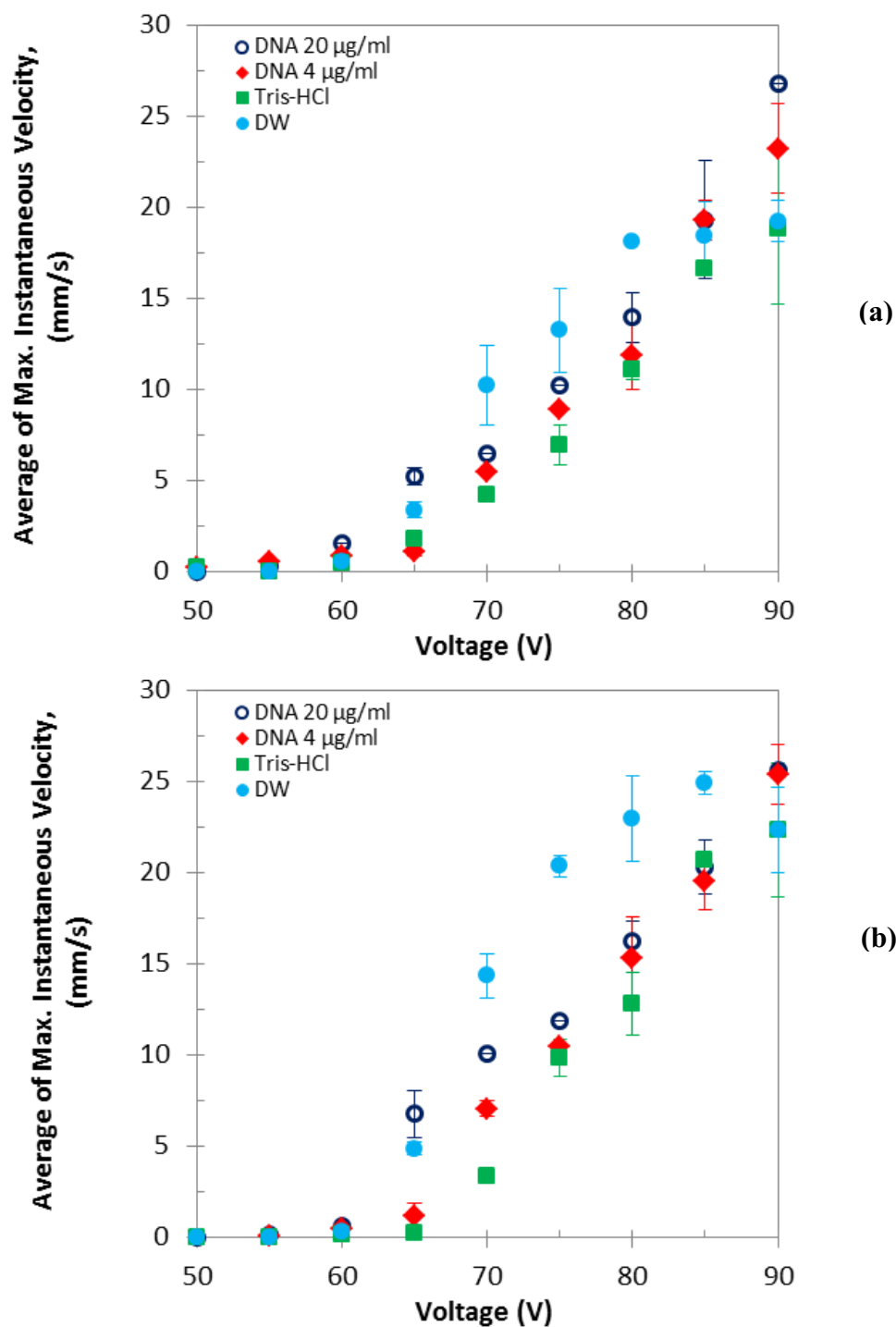


Figure 5-32: The average of maximum instantaneous velocity as a function of voltage, for the droplets of distilled water, Tris-HCl buffer, 4 µg/ml and 20 µg/ml DNA solutions: (a) leading edge, (b) trailing edge. The error bars indicate standard deviation.

The experimentally obtained instantaneous velocities of all solutions (the average of maximum instantaneous velocity of the leading edges) are summarized in Table 5-5.

Table 5-5: The average of maximum instantaneous velocity of the leading edge

	Applied Voltage (V)								
	90	85	80	75	70	65	60	55	50
	Leading edge, Average of maximum Instantaneous Velocity (mm/s)								
Distilled water	19.3	18.4	18.1	13.3	10.2	3.4	0.6	0	0
Tris-HCl	18.9	16.7	11.1	6.9	4.3	1.8	0.5	0.1	0.1
4 $\mu\text{g/ml}$ DNA	23.2	18.2	11.9	8.9	5.5	1.1	0.9	0.4	0.2
20 $\mu\text{g/ml}$ DNA	26.8	19.3	14.0	10.2	6.5	5.3	1.6	0.6	0.3

Based on theoretical analysis^{8,67}, providing that the applied voltage is less than the saturation voltage and assuming a small contact angle hysteresis, the droplet velocity is proportional to $\frac{h}{\mu D} CV^2$; where $C = \frac{\epsilon_s}{d}$ (section 1.3.2), and h, D, μ, V are the microchannel gap, diameter of sandwiched droplet, droplet viscosity and the applied voltage respectively. This relation indicates that the droplet velocity is proportional to the square of the applied voltage.

By inserting the values of h and D from Table 5-1, and knowing that $\mu_T < \mu_{D4} < \mu_{D20}$ (as the viscosity of calf thymus DNA solutions increases with increasing DNA concentration¹⁹⁹ (section 3.4) and the base for all solutions is Tris-HCl buffer); it is anticipated that $v_T > v_{D4} > v_{D20}$ (v is the droplet velocity). In this research, the annotations of $DW, T, D4$ and $D20$ represent distilled water, Tris-HCl buffer, 4 $\mu\text{g/ml}$ and 20 $\mu\text{g/ml}$ DNA solutions respectively. However, the experimental results shown in Figure 5-32 (a) do not completely follow this prediction and in general $v_{D20} > v_{D4} > v_T$.

In order to further investigate this observation, the graphs of the average of maximum instantaneous velocity of the leading edges for the droplets of distilled water, Tris-HCl, 4 $\mu\text{g/ml}$ and 20 $\mu\text{g/ml}$ DNA solutions as a function of voltage are shown individually along with fitted polynomials (Figure 5-33). These graphs show that there exists a quadratic dependence of the maximum instantaneous velocity on the applied voltage in our experimental results at least at lower voltages as expected^{8,67}. As a result of dynamic saturation, at the voltages of $V \geq 80$ V and

$V \geq 85$ V for the droplets of distilled water and Tris-HCl buffer respectively (Figure 5-33 (a) and (b)), the droplet speed becomes less sensitive to the applied voltage. This effect is not observed for DNA solutions which is believed to be due to electrophoresis.

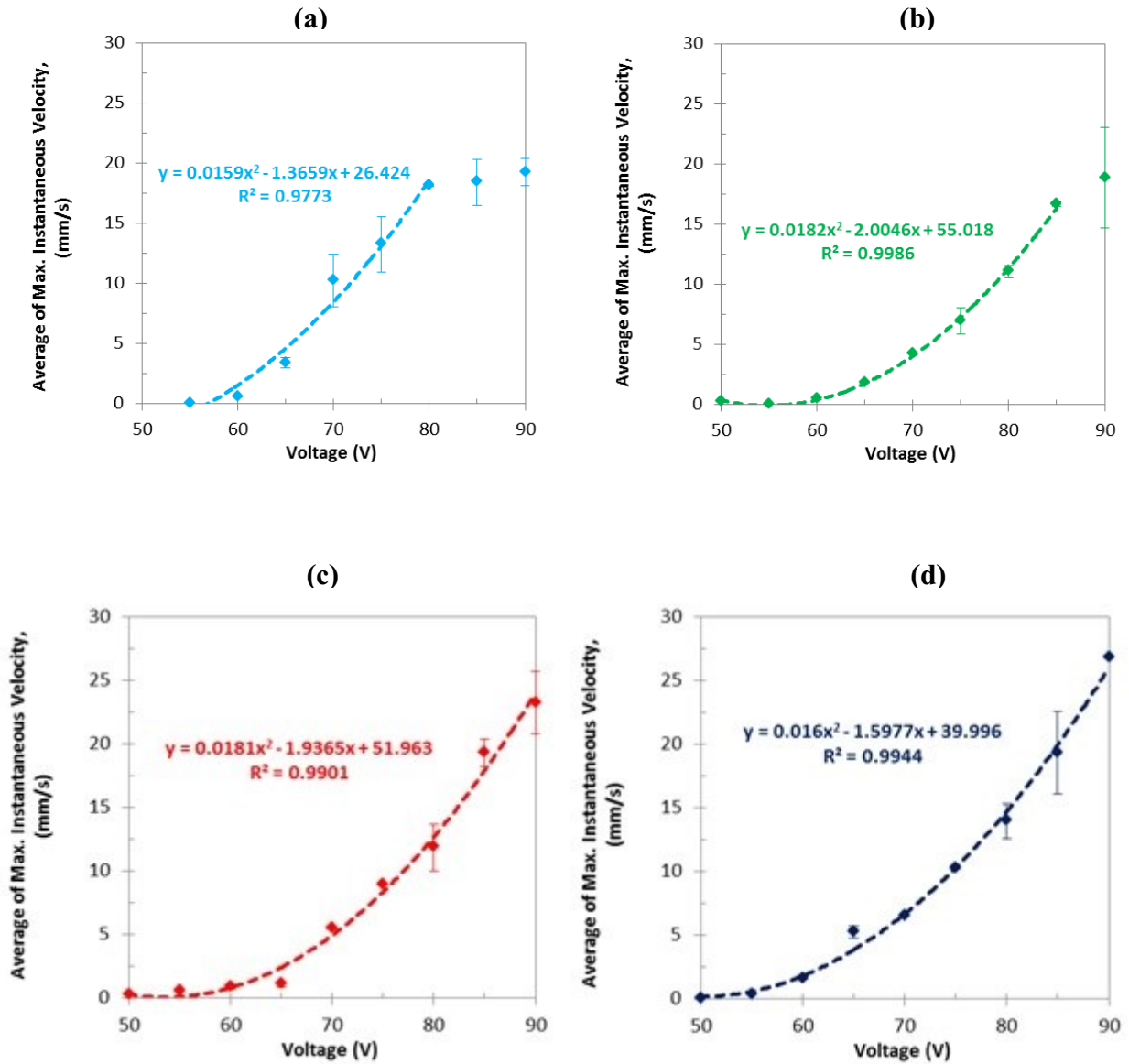


Figure 5-33: The average of maximum instantaneous velocity as a function of voltage for the leading edges of the droplets of (a) distilled water, (b) Tris-HCl buffer, (c) 4 $\mu\text{g/ml}$ DNA solution and (d) 20 $\mu\text{g/ml}$ DNA solutions. The error bars indicate standard deviation.

Electrophoresis is defined as the migration of charged ions under the effect of an electric field²³¹. The electrophoretic force ($\overrightarrow{F_{EP}}$) is proportional to the effective electrical charge, (q), and the electric field strength, $|\vec{E}| = V/h$ (here, V and h are the applied voltage and the distance between two oppositely parallel plates respectively). Therefore, $\overrightarrow{F_{EP}} = q \vec{E}$. However, the movement of the charged ions is opposed by a retarding frictional force²³¹: $F_{fEP} = f_f v_{EP}$; where, based on the theory of electrophoretic mobility, v_{EP} , the velocity of the charged ions such as negatively charged DNA molecules, is directly proportional to the electric field strength²³² and is defined as:

$$\overrightarrow{v_{EP}} = \eta_{EP} \vec{E} \quad \text{Equation 5-7}$$

here, η_{EP} is the electrophoretic mobility which is proportionally related to the DNA electric charge, and inversely proportional to the friction coefficient, f_f . When DNA is immersed in a buffer solution, it will form a 3D blob; therefore, many factors such as Kuhn length, Bjerrum length and the radius of gyration need to be defined²³³. The electrophoretic force acting on this complex elastic charged biopolymer is then modified as: $\overrightarrow{F_{EP}} = q \vec{E} \frac{h_x}{L}$; where h_x is a key parameter defined as the net projection of the string of blobs in the direction of electric field or against it depending on the polarity of the charge, and L is the contour length of the DNA chain²³³. It has to be noted that q is not uniform along a DNA molecule. Overall, additional studies are needed to understand the complex electrophoretic mobility of DNA chains which is beyond the scope of current study.

Nevertheless, Equation 5-7 clearly shows that the electrophoretic velocity increases with voltage. Besides, it appears that the higher the DNA concentration is, the higher the DNA droplet velocity will be; as the ionic strength and the total effective charge increase with DNA concentration (section 4.3.3). In our experimental set-up, the direction of electric field is along the microchannel height; except at the region where the droplet leading edge is slightly on the electrode¹⁶⁹. Therefore, our observations where $v_{D20} > v_{D4} > v_T$ can be explained by the fact that both electrowetting force and the effective component of electrophoretic force contribute to the movement of the negatively charged droplets of DNA solutions.

5.2.2.2) Velocity and Electrowetting Number

In Figure 5-34, the average of maximum instantaneous velocity is plotted against electrowetting number ($\eta_{EW} = \frac{\epsilon_s V^2}{2\gamma_{lv}d}$, (section 1.3.2)) for the leading edges of all solutions. The calculated values of electrowetting numbers are shown in Table 5-6. The results in Figure 5-34 reveal that the maximum instantaneous velocity of a sandwiched droplet is linearly proportional to the electrowetting number, which is in agreement with the findings of Hong *et al.*¹⁸¹ who empirically determined that the maximum spreading velocity of sessile droplets of water is linearly proportional to the electrowetting number. They also indicated that the maximum spreading velocity generally becomes saturated when $\eta_{EW} > 0.56$. Here, we will investigate whether such a criterion can be applied to sandwiched droplets of all fluids in this research.

Table 5-6: Electrowetting number (η_{EW}); the yellow highlights indicate the upper limits of the two linear sections in Figure 5-34

	Applied Voltage (V)								
	90	85	80	75	70	65	60	55	50
	η_{EW}								
Distilled water	0.89	0.79	0.70	0.61	0.54	0.46	0.39	0.33	0.27
Tris-HCl	0.82	0.73	0.65	0.57	0.50	0.43	0.37	0.31	0.25
4 $\mu\text{g/ml}$ DNA	0.75	0.67	0.59	0.52	0.45	0.39	0.33	0.28	0.23
20 $\mu\text{g/ml}$ DNA	0.67	0.60	0.53	0.46	0.40	0.35	0.30	0.25	0.21

As observed in Figure 5-34, based on the values of electrowetting number, each graph can be divided into three sections:

- $\eta_{EW} < 0.4$ (for 20 $\mu\text{g/ml}$ DNA solution, $\eta_{EW} \leq 0.3$); where, the velocity of the droplets linearly increases with voltage at a very low rate ($v < 2$ mm/s, when compared with Table 5-5 at $60 \text{ V} \leq V \leq 65\text{V}$). The slope of this linear region increases with DNA concentration due to electrophoresis.

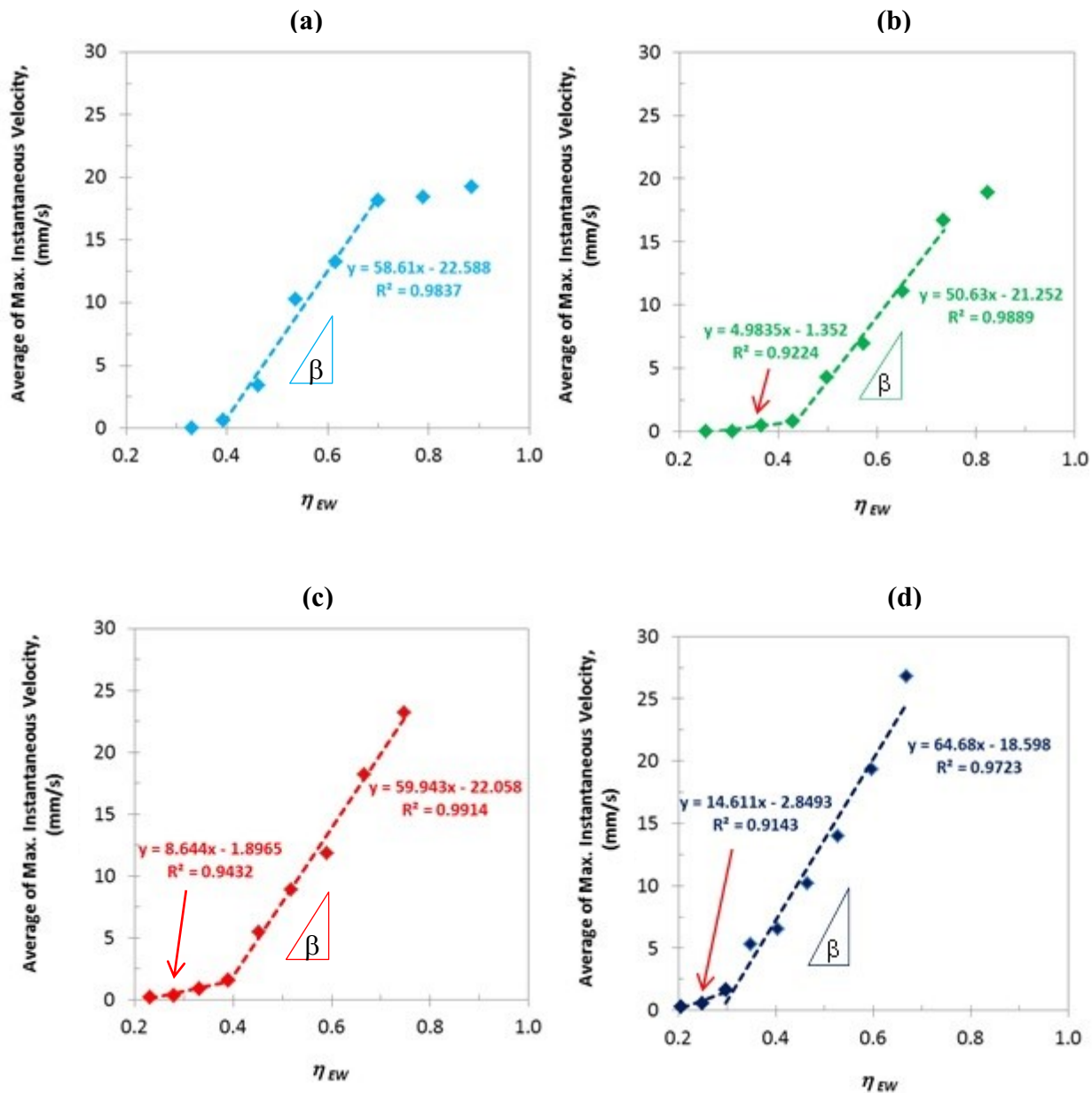


Figure 5-34: The average of maximum instantaneous velocity as a function of electrowetting number (η_{EW}), for the leading edges of the droplets of (a) distilled water, (b) Tris-HCl buffer, (c) 4 $\mu\text{g/ml}$ DNA solution and (d) 20 $\mu\text{g/ml}$ DNA solutions.

- $0.4 \leq \eta_{EW} \leq 0.7$ (for 20 $\mu\text{g/ml}$ DNA solution, $0.3 < \eta_{EW} \leq 0.7$); where, the velocity of the droplets linearly increases with voltage with a higher slope (β). The slope of this linear region also increases with DNA concentration due to electrophoresis.
- $\eta_{EW} > 0.7$; where, dynamic saturation occurs.

In Figure 5-34 at $\eta_{EW} \geq 0.7$ (the same as in Figure 5-32 (a) and Figure 5-33 for the voltages greater than 80 V), the velocity of distilled water droplets reaches a plateau as dynamic saturation occurs^{174,183}. The droplet velocity of other solutions monotonically increases with voltage, though, with a lower rate for the droplets of Tris-HCl buffer at the voltages of $85 \text{ V} \leq V_{dsat} \leq 90 \text{ V}$; denoting that the dynamic saturation voltage for Tris-HCl buffer is likely to be in this range. Compared with the static saturation voltages of the droplets of 4 $\mu\text{g/ml}$ DNA solutions ($V_{ssat} \sim 60 \text{ V}$) and 20 $\mu\text{g/ml}$ DNA solutions ($V_{ssat} \sim 50 \text{ V}$) in Figure 4-20, it is anticipated that their dynamic saturation voltages be greater than the static ones in a similar manner as the droplets of distilled water and Tris-HCl. However, for the DNA solutions, dynamic saturation is not observed. This can be explained by the fact that at the voltages greater than 80 V, it is likely that dynamic saturation occurs for the droplets of DNA solutions; however, the velocity of the droplets continues to increase due to electrophoresis.

Due to the presence of four negatively charged oxygen atoms on EDTA in the Tris-HCl buffer solution (section 3.2), the droplet movement of this solution is also affected by electrophoresis to some extent; therefore, the apparent dynamic saturation voltage of Tris-HCl buffer ($V_{dsat} \geq 85 \text{ V}$) is higher than that of distilled water ($V_{dsat} \sim 80 \text{ V}$).

Overall, these results indicate that dynamic EWOD systems involving higher concentrations of DNA solutions can be practically used in a wider range of voltages (Table 5-6) due to the combined effect of electrowetting and electrophoresis. This is contrary to our predictions based on the results in Chapter 4 for the 20 $\mu\text{g/ml}$ DNA solutions which had the lowest $\Delta\theta_v$, compared to the other solutions.

5.2.3) Actuation Force and the Opposing Forces

As explained in section 5.1.1, the electrowetting force, F_m , is expressed by Equation 5-6 as $F_m = \frac{\epsilon_s V^2}{2d} \frac{dA_1(x)}{dx}$; where $\frac{dA_1(x)}{dx}$ (the droplet effective contact line length) is the derivative of Equation 5-5. The opposing forces, F_{dd} and F_f , are also shown to be proportionally related to the droplet velocity¹⁰⁴ (Equation 5-1 and Equation 5-2). Therefore, the maximum of all opposing forces are obtained providing that the droplet velocity has reached its highest value (Table 5-5). By taking the derivative of Equation 5-5 and inserting the values of D , the diameter of sandwiched droplet, and x , the position of the droplet leading edge when it reaches its maximum leading edge instantaneous velocity from our experimental results, the droplet effective contact line length and the electrowetting force, F_m , are calculated. The results are shown in Table 5-7 and Table 5-8 respectively.

Table 5-7: The droplet effective contact line length for maximum leading edge instantaneous velocity

	Applied Voltage (V)								
	90	85	80	75	70	65	60	55	50
	dA_1/dx (μm)								
Distilled water	2074	2197	2030	1937	1406	1014	151	N/A	N/A
Tris-HCl	1867	1744	1564	1075	562	280	213	203	209
4 $\mu\text{g/ml}$ DNA	1561	2107	1647	1881	1378	523	240	233	210
20 $\mu\text{g/ml}$ DNA	1878	1705	1892	1824	1903	1608	697	581	295

Table 5-8: Electrowetting force, F_m

	Applied Voltage (V)								
	90	85	80	75	70	65	60	55	50
	F_m (μN)								
Distilled water	131	124	101	85	54	33	4	N/A	N/A
Tris-HCl	118	98	78	47	21	9	6	5	4
4 $\mu\text{g/ml}$ DNA	99	119	82	83	53	17	7	5	4
20 $\mu\text{g/ml}$ DNA	119	96	94	80	73	53	20	14	6

For all solutions, a comparison of the opposing forces, F_{dd} , and F_f is given in Table 5-9 and Table 5-10. Overall, the objective is to study the influence of each of the opposing forces on the dynamic of droplet motion, and identify the dominant forces¹⁰⁴. Here, the values of μ_l , ξ for distilled water in Equation 5-1 and Equation 5-2 are^{104,178} 0.001 N.s/m² and 0.04 N.s/m² ($\xi = 0.04$ N.s/m² in the experiments with oil as a filler; however, this value is also commonly used for air as a filler) respectively. As an approximation, in these tables, a comparable value as that of distilled water has been assumed for Tris-Hcl buffer and 4 μ g/ml DNA solutions²⁰². For 20 μ g/ml DNA solution, the values of μ_l and ξ are also estimated²⁰² as 0.0012 N.s/m² and 0.048 N.s/m² respectively.

Table 5-9: Shear force, F_{dd}

	Applied Voltage (V)								
	90	85	80	75	70	65	60	55	50
	F_{dd} (μN)								
Distilled water	1.84	1.76	1.72	1.26	0.98	0.32	0.05	N/A	N/A
Tris-HCl	1.92	1.69	1.12	0.71	0.43	0.19	0.05	0.003	0.002
4 μ g/ml DNA	2.52	1.98	1.29	0.96	0.59	0.12	0.09	0.04	0.026
20 μ g/ml DNA	4.06	2.93	2.12	1.55	0.99	0.80	0.24	0.09	0.04

Table 5-10: Contact line friction force, F_f

	Applied Voltage (V)								
	90	85	80	75	70	65	60	55	50
	F_f (μN)								
Distilled water	9.03	8.65	8.50	6.22	4.80	1.60	0.28	N/A	N/A
Tris-HCl	8.90	7.86	5.23	3.28	2.02	0.87	0.23	0.013	0.008
4 μ g/ml DNA	11.24	8.81	5.74	4.30	2.65	0.52	0.42	0.18	0.11
20 μ g/ml DNA	15.98	11.54	8.34	6.09	3.89	3.15	0.96	0.34	0.17

As mentioned in section 5.1.1, F_T is a threshold initiation force per unit length taking into account the contact angle hysteresis between the leading and trailing edges of the droplet, F_{TH} , and/or any other static friction, such as friction from adsorption^{104,166,226}, F_{TA} ; overall $F_T = F_{TH} + F_{TA}$.

The maximum static friction force per unit length related to the contact angle hysteresis is defined as²²⁷ : $F_{TH} = \gamma_{lv} (\cos(\theta_0 - \alpha) - \cos\theta_0)$; where γ_{lv} , θ_0 and α are the liquid-vapour interfacial tension, contact angle in the absence of an electric field, and contact angle hysteresis respectively. By considering $F_{th} = F_{TH} \cdot \frac{dA_1(x)}{dx}$, and inserting the values of θ_0 from Figure 4-24, γ_{lv} from Figure 4-28, α from Table 5-4, and $\frac{dA_1(x)}{dx}$ from Table 5-7, an estimation of the static friction force related to the contact angle hysteresis, F_{th} is obtained (Table 5-11). The empirical values of F_{dd} , F_f and F_{th} are in good agreement with literature¹⁷⁸ for distilled water.

Table 5-11: Contact angle hysteresis related static friction force, F_{th}

	Applied Voltage (V)								
	90	85	80	75	70	65	60	55	50
	$F_{th} (\mu N)$								
Distilled water	21.15	22.40	20.70	19.75	14.33	10.34	1.54	N/A	N/A
Tris-HCl	16.14	15.07	13.52	9.29	4.86	2.42	1.84	1.75	1.81
4 $\mu\text{g/ml}$ DNA	12.86	17.36	13.57	15.50	11.36	4.31	1.98	1.92	1.73
20 $\mu\text{g/ml}$ DNA	11.99	11.46	12.03	11.83	12.06	11.11	5.08	3.92	1.23

Static friction per unit length can also be produced by adsorbed layers at the microscopic scale¹⁶⁶, F_{TA} , and can be substantial when droplets of biofluids such as DNA solutions are transported in the microchannel due to the effect of passive biomolecular adsorption. With increasing DNA concentration (*i.e.* increasing the ionic strength), the DNA absorbance onto the substrate surface increases; although other factors such as: pH and type of the solution, substrate nature, time, temperature, the DNA concentration regime and the applied voltage will also affect the DNA adsorption^{234,235,236,237}. These factors are the same for all solutions in our experiments. Therefore, the higher the DNA concentration is, the higher the amount of absorbance will be which will directly affect F_{TA} . The physical mechanism behind DNA absorbance is beyond the scope of the present study for a quantitative consideration and additional studies are needed to provide a complete understanding.

For all solutions, the magnitudes of the electrowetting force and all opposing forces as a function of voltage are shown in Figure 5-35. For comparison, the related velocity curve (Table 5-5) is also presented. In this figure, due to the lack of information, the static force from

adsorption, F_{ta} , where $F_{ta} = F_{TA} \cdot \frac{dA_1(x)}{dx}$, is not shown; however, by including this force, the total force, F_{net} , for the DNA solutions will decrease.

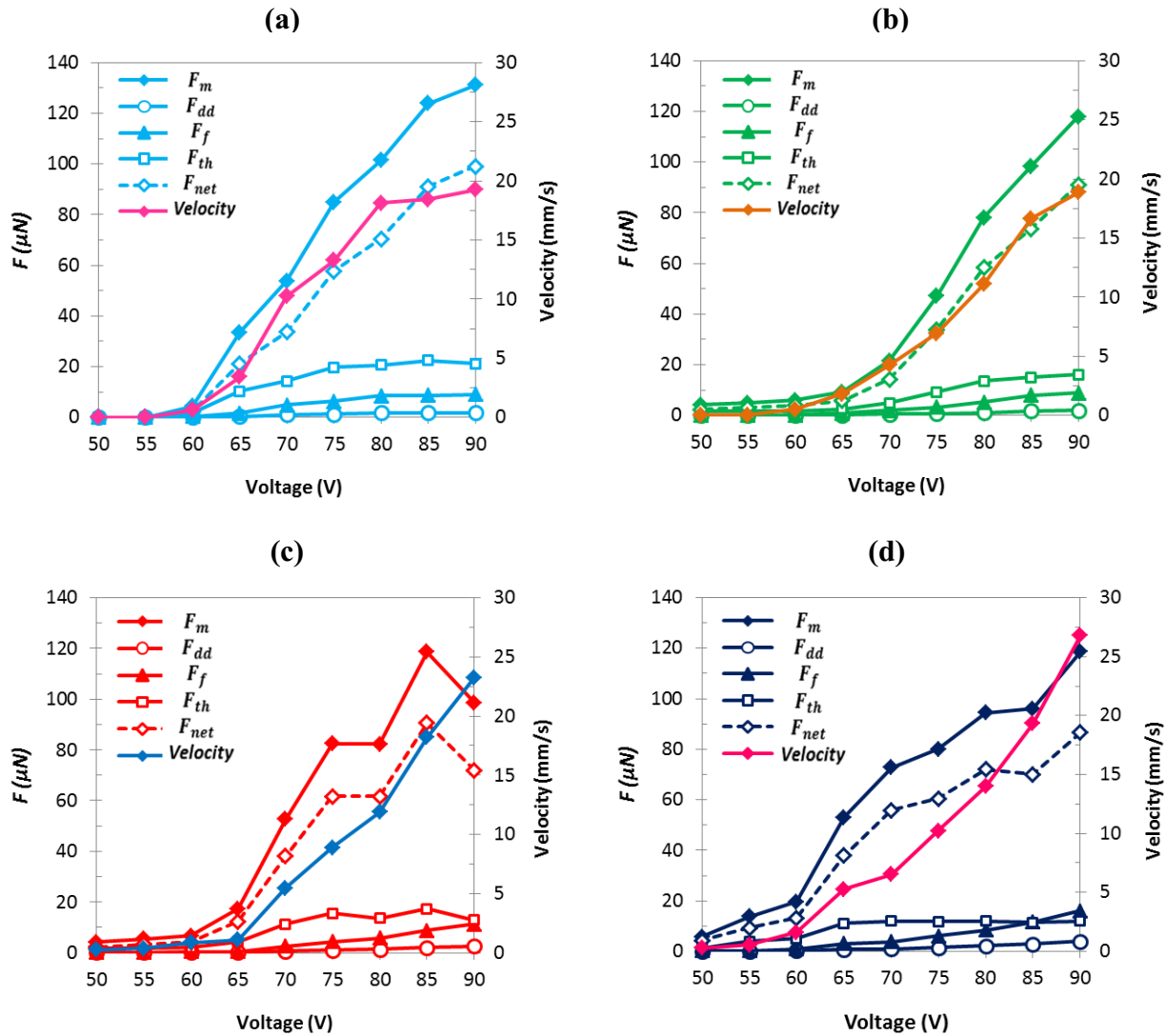


Figure 5-35: The magnitudes of F_m , F_{dd} , F_f , F_{th} and the total force, F_{net} , and the average of the maximum leading edge instantaneous velocity as a function of voltage for the droplets of (a) distilled water, (b) Tris-HCl buffer, (c) 4 $\mu\text{g/ml}$ DNA solution and (d) 20 $\mu\text{g/ml}$ DNA solutions.

Moreover, Figure 5-35 indicates that the contact angle hysteresis related static force plays a significant role on the dynamics of droplet transport. As discussed in section 5.1.3, with decreasing voltage to $\sim 60 - 65$ V and consequently the electrowetting force and all opposing forces, the effect of F_T becomes more important; specifically for the DNA solutions where the static force from adsorption is also expected to be substantial. This results in a time delay in the actuation response as observed in all time series experimental results in section 5.1.3. This observation is contrary to the results obtained by the analytical model proposed by Chakraborty and Mittal¹⁷⁰, where no time delay is predicted as they neglect hysteresis. Consequently, at voltages of 60 and 65 V, the average peak time for the 20 $\mu\text{g/ml}$ DNA solutions in Figure 5-36 is longer compared to the other solutions due to their higher static forces related to the hysteresis and biomolecular adsorptions. As the droplet moves further on the electrode length, its effective contact line length and subsequently the electrowetting force will increase; thus, the droplet abruptly accelerates and the electrode coverage increases (section 5.2.4).

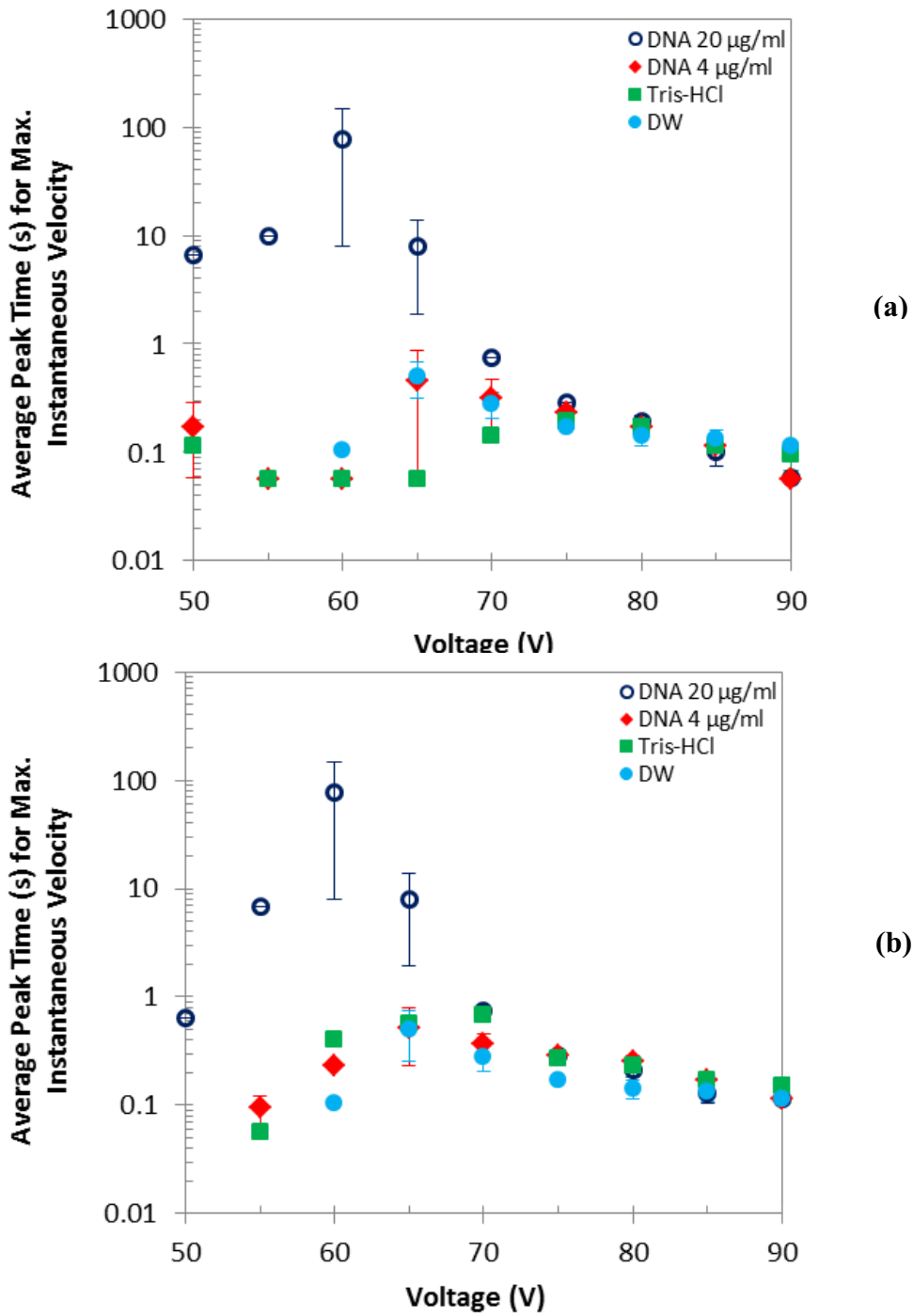


Figure 5-36: The average peak time for maximum instantaneous velocity as a function of voltage, for the droplets of distilled water, Tris-HCl buffer, 4 µg/ml and 20 µg/ml DNA solutions: (a) leading edge, (b) trailing edge. The error bars indicate standard deviation.

From another perspective, our observations in Figure 5-37 also indicate that the electrophoresis plays a significant role on the dynamics of charged DNA molecules. In this figure, the vertical axis (velocity) is the average of maximum leading edge instantaneous velocity from Table 5-5. As observed, at voltages below dynamic saturation, the total force, F_{net} , is proportional to the velocity for distilled water and Tris-HCl buffer. Then, at saturation, velocity is no longer affected by the total force. In contrast, the velocity of DNA solutions increases even though there is no significant change in the total force, which clearly shows the contribution of electrophoresis, F_{EP} , to the movement of charged particles specifically at higher concentrations of DNA solutions.

In general, for all solutions, Equation 5-3 is modified as:

$$M \frac{dv}{dt} = F_m + F_{EP} - F_{th} - F_{ta} - F_{dd} - F_f \quad \text{Equation 5-8}$$

where additional terms including: effective component of F_{EP} for charged molecules, F_{th} for the contact angle hysteresis related static force and F_{ta} for the adsorption related static force, have been considered. If the droplets are not charged and/or the effect of the absorbance is minimal, F_{EP} and F_{ta} will be disregarded. Our experimental results in Figure 5-35 and Figure 5-37 show that Equation 5-8 is a much better equation for modeling charged solutions.

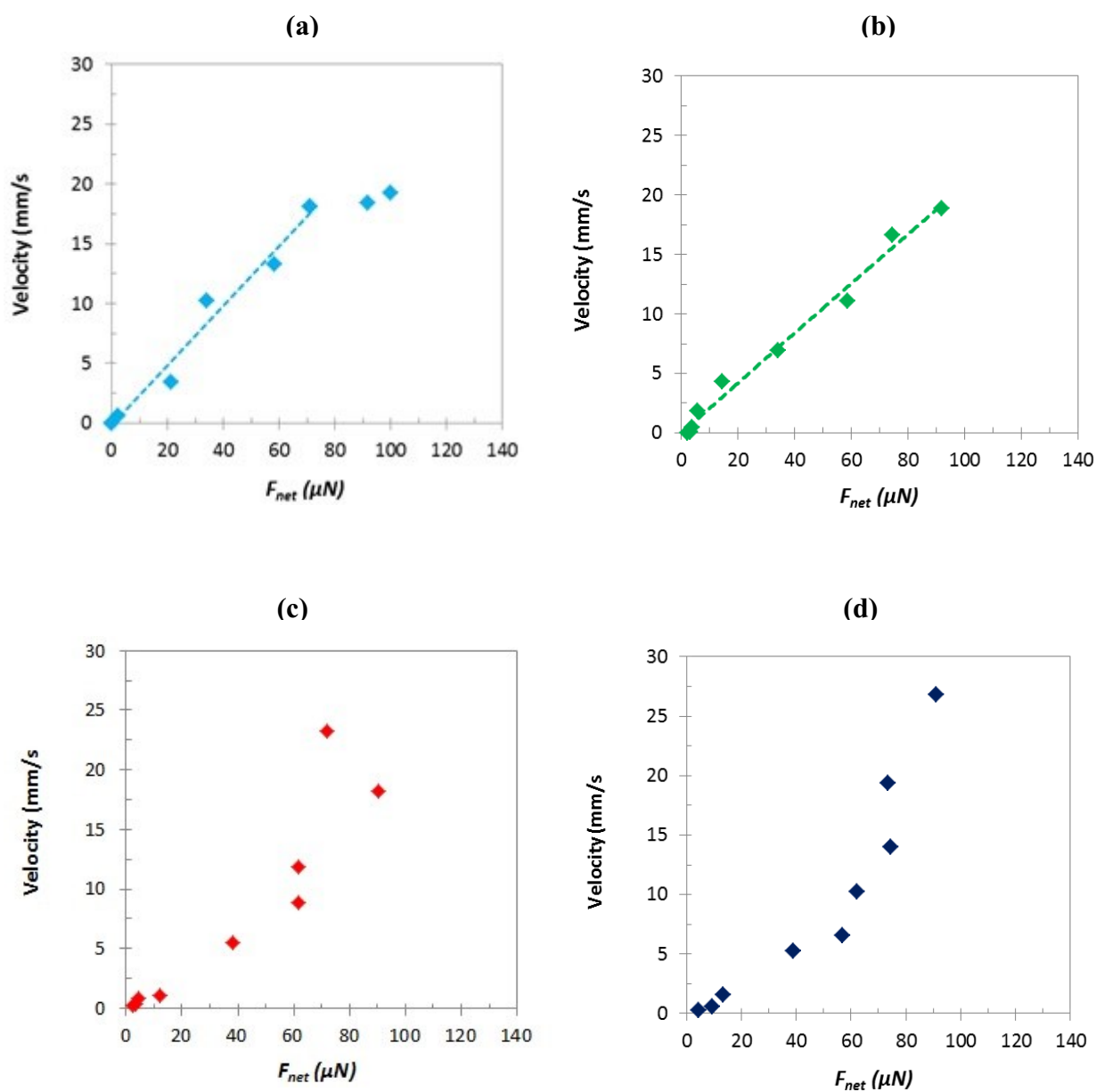


Figure 5-37: The average of the maximum leading edge instantaneous velocity as a function of total force, F_{net} for the droplets of (a) distilled water, (b) Tris-HCl buffer, (c) 4 $\mu g/ml$ DNA solution and (d) 20 $\mu g/ml$ DNA solutions.

5.2.4) Total Displacement and Electrode Coverage

As explained in Chapter 4, by increasing the concentration of DNA in solution, the number of negatively charged ions and consequently the ionic strength significantly increases. This will create a stronger response to the electrophoretic force pulling the droplets toward the positively charged electrode compensating for the lower electrowetting force at lower voltages. Consequently, at 65 V, the droplets of 20 $\mu\text{g/ml}$ DNA solutions will move to the end of the electrode under the influence of electrowetting and electrophoresis improving the electrode coverage to 95% compared to 59% and 13% coverage for 4 $\mu\text{g/ml}$ DNA solution and Tris-HCl buffer respectively (Figure 5-38). The combined effect of both forces will actuate the leading edges of the droplets of 20 $\mu\text{g/ml}$ DNA solutions under the application of a voltage as low as 50 V.

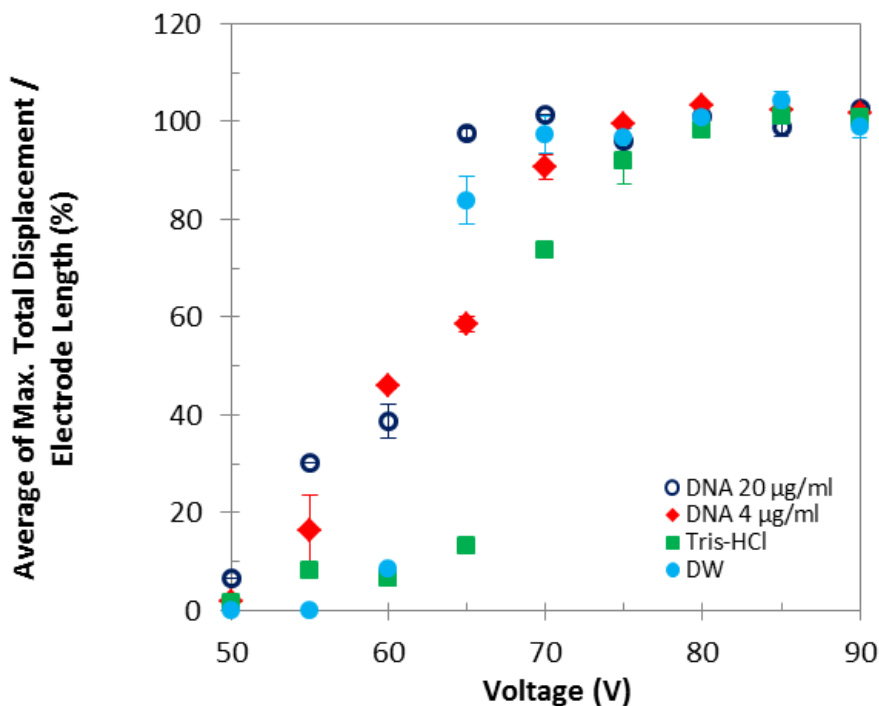


Figure 5-38: The average of maximum total displacement as a function of voltage for the leading edges of the droplets of distilled water, Tris-HCl buffer, 4 $\mu\text{g/ml}$ and 20 $\mu\text{g/ml}$ DNA solutions. The error bars indicate standard deviation.

5.2.5) Droplet Elongation and Droplet Average Velocity

The characterization of droplet elongation is complex, as many factors such as contact line friction, viscosity, contact angle hysteresis and in the case of DNA solutions, the viscoelasticity, all contribute to the droplet deformation¹⁸⁴. Although, the droplet elongation depends on the droplet initial diameter, it is an important parameter in dynamic transport showing to what extent the droplet stretches before moving due to the differences in the leading and trailing edges accelerations. If it exceeds a certain value because of hysteresis at the trailing edge, it may result in droplet breakup which is generally not desirable. However, by the application of voltage on both sides of a droplet, and thereby elongating it, the droplet may be split purposely which is one of the common operations performed in DMF's^{238,239}. The physical mechanism behind this application is beyond the scope of the present study for a quantitative consideration.

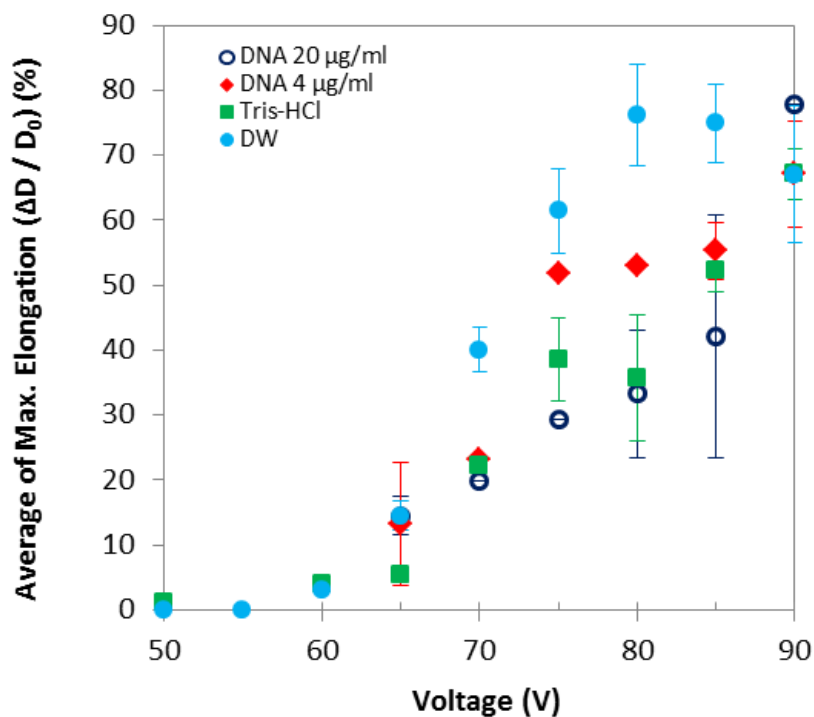


Figure 5-39: The average of maximum elongation as a function of voltage for the droplets of distilled water, Tris-HCl buffer, 4 $\mu\text{g/ml}$ and 20 $\mu\text{g/ml}$ DNA solutions. The error bars indicate standard deviation.

As shown in Figure 5-39, distilled water droplets with the lowest surface tension compared to Tris-HCl buffer and DNA solutions, deformed much more in a shorter period of time during actuation, and attained their original shape at the end of movement (Figure 5-9). However, with increasing surface tension from distilled water to 20 $\mu\text{g/ml}$ DNA solution, this deformation became minimal. These results are consistent with the results of Ni *et al.*¹⁸⁴ where the droplet elongation of high and low surface tension fluids were compared.

Figure 5-40 shows the average velocity of the leading and trailing edges as a function of voltage. As observed, at $V < 85$ V, with a good approximation, the average velocity of Tris-HCl buffer and DNA solutions can be considered the same. However, at $V \geq 85$ V; the velocity of the DNA solutions continuously increases with voltage due to electrophoresis. Amongst all solutions, distilled water droplets have the highest average velocity except at $V \geq 85$ V when dynamic saturation occurs.

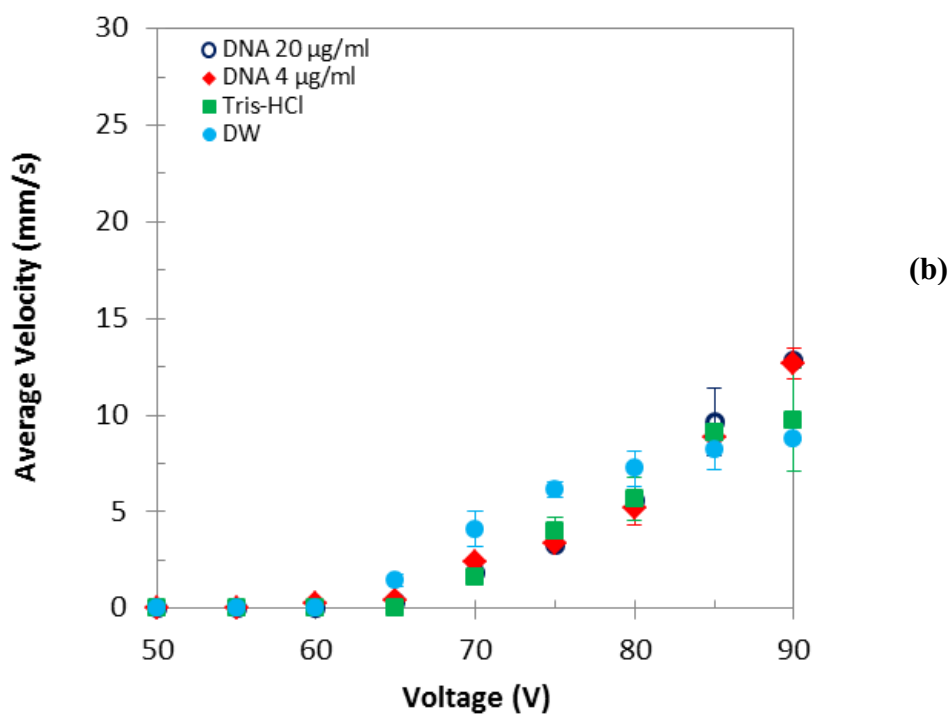
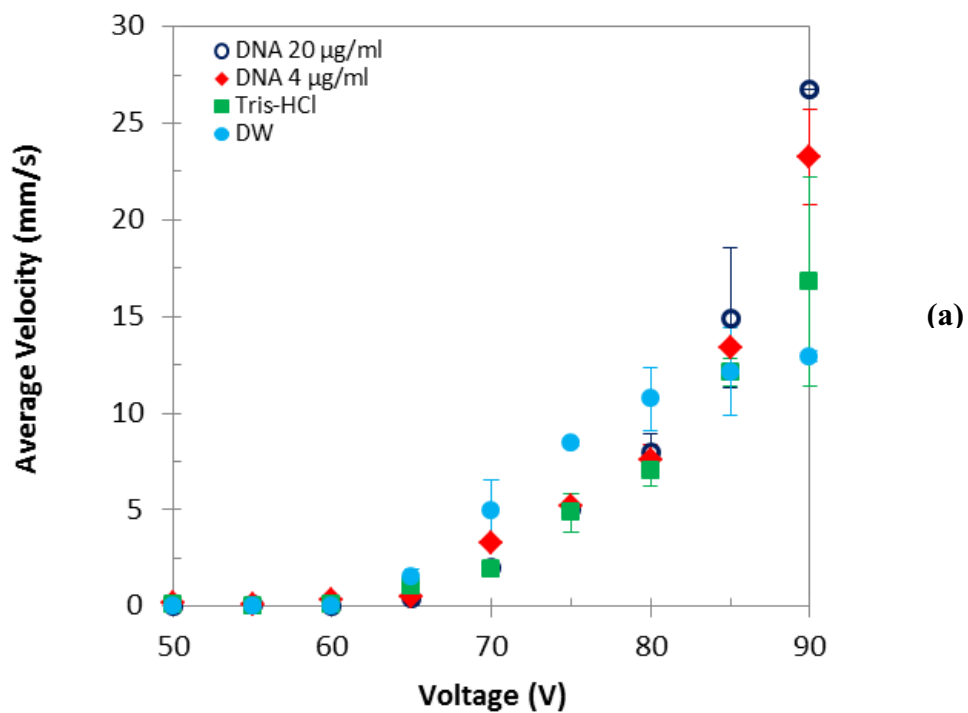


Figure 5-40: The average velocity, (a) leading edge, and (b) trailing edge, as a function of voltage for the droplets of distilled water, Tris-HCl buffer, 4 µg/ml and 20 µg/ml DNA solutions. The error bars indicate standard deviation.

5.3) Summary

In this chapter, it was concluded that the droplet instantaneous velocity, total displacement, elongation and average velocity strongly depend on the applied voltage. Before saturation, there exists a quadratic dependence of the maximum instantaneous velocity on voltage. Thereafter, the velocity becomes less sensitive to the applied voltage. Our findings also revealed that the maximum instantaneous velocity of sandwiched droplets is linearly proportional to the electrowetting number and generally becomes saturated when this number is greater than 0.7. We were also able to empirically compare the electrowetting and all opposing forces. Overall, it was shown that below saturation, the total force and droplet instantaneous velocity of the droplets of distilled water and Tris-HCl buffer are linearly proportional; then, at saturation, velocity is no longer affected by the total force. In contrast, the velocity of DNA solutions increases even when there is no significant change in the total force, which clearly shows the significant contribution of electrophoresis to the movement of negatively charged DNA solutions specifically at higher concentrations of DNA solutions.

Due to the combined effect of electrowetting and electrophoresis, the voltage required by the droplet to cover the entire length of the electrode decreases with DNA concentration. However, the travel time, which is the time required by the droplet to reach to the end of the electrode (inverse of switching frequency) increases with DNA concentration. These factors are important for designing the switching controller.

Dielectric failure is one of the most important and longstanding fundamental problems of the EWOD platform. In Appendix J, the breakdown spots on the substrates which exhibited electrolysis is investigated by means of optical microscopy and EDS elemental mapping, and the material failure mechanism is analyzed and characterized.

Chapter6

Conclusions, Contributions and Recommendations for Future Work

6.1) Summary of Conclusions

Experimentally analyzing the dynamic behaviour of a droplet in the presence of an electric field is a complex yet intriguing area of research. In this thesis, an investigation has been made concerning the implementation of electrowetting for actuating the DNA solutions in a microchannel. In order to characterize the DNA solutions, limited bulk flow rheological and SALS experiments were performed on 3000 $\mu\text{g/ml}$ DNA solutions. The transient response in viscosity following a sudden inception of shear flow in a start-up test was presented indicating that the viscoelastic fluids such as DNA are less viscous at higher shear rates. Our results on SALS experiments under the application of electric field solely showed that the DNA molecules moved to a direction perpendicular to the shear flow due to electrophoresis. Overall, in bulk flow studies on DNA solutions, it was concluded that the charged oxygen groups play a significant role when the electric field is applied.

However, in electrowetting applications where the capillary forces dominate, it is essential to know the effect of DNA concentration in small scale droplets. In order to better assess the physics of electrowetting of DNA solutions, the effect of fluid composition (*i.e.* different

concentrations of DNA solutions and the type of buffer solution) on the static response of the droplet to electric field variables such as applied voltage was studied. Since in electrowetting, higher contact angles before applying voltage are desirable, a buffer solution of 10 mM Tris-HCl and 0.1 mM EDTA with pH = 8.0 was selected as an appropriate buffer solution for dissolving the DNA samples. Subsequently, the effect of voltage on static contact angle in the absence of an electric field and after the application of voltage, and on the saturation contact angle was studied for the sessile and sandwiched droplets of distilled water, Tris-HCl buffer and DNA solutions with the concentrations ranging from 4 $\mu\text{g/ml}$ to 1000 $\mu\text{g/ml}$ on planar electrodes. The experiments were done in an in-house developed contact angle measurement experimental set-up. Our results revealed that the static contact angle in the absence of an electric field decreases with DNA concentration. On the contrary, there is an increase in the contact angle after the application of voltage and the saturation contact angle when the DNA concentration increases while the saturation voltage decreases. This means that the electrowetting susceptibility reduces with increasing DNA concentration. By following the method of electrowetting-based microdrop tensiometry, we were able to obtain the surface tension of all fluids studied in this research concluding that the value of surface tension of DNA solutions increases with DNA concentration.

In the next stage, the ultimate goal was to investigate the dynamic behaviour of DNA solutions as discrete droplets when actuated and deformed while advancing on an activated single square electrode in order to explore the effect of negatively charged oxygen molecules on droplet transport. It was found that the droplet instantaneous velocity, total displacement, elongation and average velocity strongly depend on the applied voltage. Before saturation, there exists a quadratic dependence of the maximum instantaneous velocity on voltage. Thereafter, the velocity becomes less sensitive to the applied voltage. Our findings also revealed that the maximum instantaneous velocity of sandwiched droplets is linearly proportional to the electrowetting number and generally becomes saturated when this number is greater than 0.7. We were also able to empirically compare the electrowetting and all opposing forces. Overall, it was shown that below saturation, the total force and droplet instantaneous velocity of the droplets of distilled water and Tris-HCl buffer are linearly proportional; then, at saturation, velocity is no longer affected by the total force. In contrast, the velocity of DNA solutions increases even when there is no significant change in the total force, which clearly shows the

significant contribution of electrophoresis to the movement of negatively charged DNA solutions specifically at higher concentrations of DNA solutions.

Due to the combined effect of electrowetting and electrophoresis, at 65 V, the droplets of 20 $\mu\text{g/ml}$ DNA solutions will move to the end of the electrode improving the electrode coverage to 95% compared to 59% and 13% coverage respectively for 4 $\mu\text{g/ml}$ DNA solution and Tris-HCl buffer; however, the higher the concentration of DNA solutions (higher viscosities) is, the longer it takes for the droplet to reach to the end of the electrode. Overall, it was concluded that the travel time strongly depends on the applied voltage and the droplet viscosity in addition to the effect of gap height at lower voltages.

6.2) Contributions

Although the study of the electrowetting-based systems has been conducted for many years, the physics of droplet transport is not yet fully understood; which is perhaps a reflection of the fact that performing and analyzing the experiments on droplet motion at the microscale is technically difficult; as many factors such as surface tension, viscosity, contact angle saturation, contact angle hysteresis, contact line friction, and adsorption all contribute to this complex phenomenon. In addition, achieving reliable experimental results is only possible providing that the experimental limitations such as dielectric breakdown and in many cases, the electrical circuit failure due to poor fabrication of the electrical connections at microscale can be prevailed. The complexity of DNA solutions will also affect the performance of the experiments.

As a result of our study, there are three main contributions to such a field of work. For the first time, the static response of DNA solutions to a variety of voltages was studied. This included the static contact angle in the absence of an electric field and after the application of voltage, and the saturation contact angle for the sessile and sandwiched droplets of DNA solutions; and the effect of buffer solution, DNA concentration, microchannel height on these parameters was determined. Our results revealed that higher DNA concentrations and smaller microchannel gaps both have a negative effect on the static response of DNA solutions to electrowetting.

Second, for the first time, the transient response of DNA solutions to a variety of voltages was studied. In the transient response, the time and voltage dependency of the parameters such as droplet speed, total displacement, and elongation of the droplets of DNA solutions was studied. It was found that the negatively charged oxygen groups in DNA will affect the dynamic behaviour of DNA solutions significantly. Both electrowetting and electrophoretic forces contribute to the movement of the negatively charged droplets of DNA solutions.

Overall, the results of this study will help us to better understand, analyze, design and prototype the microfluidic-based systems for DNA solutions.

6.3) Recommendations for Future Work

Most of the intended future work of this study has been already mentioned in the text; however, there are many opportunities to continue working in this field numerically and experimentally. Some suggestions are summarized in the following paragraphs:

- The static force produced by the adsorbed layers at the microscopic scale, F_{ta} , can be substantial when droplets of biofluids such as DNA solutions are transported in a microchannel due to the effect of passive biomolecular adsorption. Additional studies are needed for a quantitative consideration to provide complete understanding.
- As the electrophoretic mobility of DNA chains is complex, additional studies are needed to experimentally determine the electrophoretic force acting on complex charged biopolymers such as DNA solutions.
- The contact line coefficient, ξ , of DNA solutions need to be experimentally determined.
- There is the possibility to utilize the micro cantilever rheometry to measure the rheological properties of DNA solutions; such as their related viscosities; since, in this method, smaller quantities of the fluid (*i.e.* microliter) are sufficient compared to the commercially available rheometers.

- The viscous flow within the droplet during transport has been modeled under the assumption of a constant parabolic velocity profile in the droplet (section 5.1.1)¹⁰⁴, which is not correct for a discrete moving droplet; therefore, it is worth performing specific experiments showing the flow visualization inside the droplets to better model the opposing force related to the shear force due to the top and bottom plates.

The actuation of droplets by electrowetting under the transient conditions is complex; therefore, additional numerical studies along with the experiments will be beneficial for developing EWOD systems for biofluids.

References

- ¹ D. Janasek, J. Franzke, A. Manz, “Scaling and the Design of Miniaturized Chemical-analysis systems”, *Nature*, vol. 442 (7101), pp.374-380, 2006.
- ² G. Karniadakis, A. Beskok, N. Aluru, “Microflows and Nanoflows: Fundamentals and Simulation”, *Springer, New York*, 2005.
- ³ N. Kockmann, “Transport Phenomena in Micro Process Engineering”, *Springer, Berlin*, 2008.
- ⁴ F. Mugele, J.-Ch. Baret, “Electrowetting: From Basics to Applications”, *J. Phys: Condens. Matter*, vol. 17 (28), pp. R705-R774, 2005.
- ⁵ H. Craighead, “Future lab-on-a-chip technologies for interrogating individual molecules”, *Nature*, vol. 442 (7101), pp. 387–393, 2006.
- ⁶ H. Song, D. L. Chen, R. F. Ismagilov, “Reactions in droplets in microfluidic channels”, *Angew Chem Int Ed*, vol. 45, pp. 7336–7356, 2006.
- ⁷ S. Haeberle, R. Zengerle, “Microfluidic platforms for lab-on-a-chip applications”, *Lab Chip*, vol. 7 (9), pp. 1094–1110, 2007.
- ⁸ R. B. Barber, D. R. Emerson, “Recent Advances in Electrowetting Microdroplet Technologies”, Chapter 4 of Book: “Microdroplet Technology, Principles and Emerging Applications in Biology and Chemistry”, *Springer, New York*, pp. 77- 116, 2012.
- ⁹ H. Y. Huang, T. L. Wu, H. R. Huang, C. J. Li, H. T. Fu, Y. K. Soong, M. Y. Lee, D. J. Yao, “Isolation of motile spermatozoa with a microfluidic chip having a surface-modified microchannel”, *J. Lab. Autom*, vol. 19 (1), pp. 91-99, 2014.

-
- ¹⁰ X. Jiang, W. Jing, L. Zheng, S. Liu, W. Wu, G. Sui, “A continuous-flow high-throughput microfluidic device for airborne bacteria PCR detection”, *Lab on a Chip*, vol. 14 (4), pp. 671–676, 2014.
- ¹¹ D. P. Kise, D. Magana, M. J. Reddish, R. B. Dyer, “Submillisecond mixing in a continuous-flow, microfluidic mixer utilizing mid-infrared hyperspectral imaging detection”, *Lab on a Chip*, vol. 14 (3), pp. 584-591, 2014.
- ¹² P. Woias, “Micropumps - past, progress and future prospects”, *Sensors Actuators B:Chem*, vol. 105(1), pp. 28-38, 2005.
- ¹³ H-C. Chang, L. Y. Yeo, “Electrokinetically Driven Microfluidics and Nanofluidics”, *Cambridge University Press*, 2010.
- ¹⁴ H-H Shen, S.-K. Fan, C.-J. Kim, “EWOD microfluidic systems for biomedical application”, *Microfluid Nanofluid*, vol. 16 (5), pp. 965-987, 2014.
- ¹⁵ Y. Wang, W-Y. Lin, K. Liu, R. J. Lin, M. Selke, H. C. Kolb, N. Zhang, X.-Z. Zhao, M. E. Phelps, C. K. F. Shen, K. F. Faull, and H- R. Tseng, "An integrated microfluidic device for large-scale in situ click chemistry screening", *Lab on a Chip*, vol. 9 (16), pp. 2281-2285, 2009.
- ¹⁶ R. B. Fair, A. Khlystov, V. Srinivasan, V.K. Pamula, K.N. Weaver, “Integrated chemical/ biochemical sample collection, pre-concentration and analysis on a digital microfluidic lab-on-a-chip platform”, *Lab-on-a-chip: Platforms, Devices, And Applications, Proc. SPIE*, vol. 5591, pp. 113-124, 2004.
- ¹⁷ R. B. Fair, “Digital Microfluidics: Is a true Lab-on-a-chip possible?”, *Microfluid Nanofluid*, vol. 3 (3), pp. 245-281, 2007.
- ¹⁸ R. B. Fair, A. Khlystov, T.D. Taylor, V. Ivanov, R.D. Evans, V. Srinivasan, V. K. Pamula, M. G. Pollack, P. B. Griffin, J. Zhou, “Chemical and Biological Applications of Digital-Microfluidic Devices”, *IEEE Design Test Comput*, vol. 24 (1), pp. 10–24, 2007.

-
- ¹⁹ S-Y. Teh, R. Lin, L.-H. Hung, A. P. Lee, “Droplet microfluidics”, *Lab Chip*, vol. 8 (2), pp. 198–220, 2008.
- ²⁰ Y. Fouillet, D. Jary, C. Chabrol, P. Claustre, C. Peponnet, “Digital Microfluidic Design and Optimization of Classic and New Fluidic Functions for Lab on a Chip Systems”, *Microfluid Nanofluid*, vol. 4 (3), pp. 159–165, 2008.
- ²¹ M. Abdelgawad, A. R. Wheeler, “The Digital Revolution: A New Paradigm for Microfluidics”, *Adv. Mater*, vol. 21 (8), pp. 920–925, 2009.
- ²² P-G. de Gennes, F. Brochard-Wyart, D. Quéré, “Capillarity and wetting phenomena: drops, bubbles, pearls, waves”, *Springer, New York*, 2004.
- ²³ M. G. Pollack, R. B. Fair, A. D. Shenderov, “Electrowetting-based actuation of liquid droplets for microfluidic applications”, *Appl. Phys. Lett.*, vol. 77 (11), pp. 1725–1726, 2000.
- ²⁴ C. Quilliet, B. Berge, “Electrowetting: a recent outbreak”, *Curr. Opin. Colloid Interface Sci.*, vol. 6 (1), pp. 34-39, 2001.
- ²⁵ M. G. Pollack, A.D. Shenderov, R.B. Fair, “Electrowetting-based actuation of droplets for integrated microfluidics”, *Lab Chip*, vol. 2, pp. 96-101, 2002.
- ²⁶ F. Mugele, A. Klingner, J. Buehrle, D. Steinhauser, S. Herminghaus, “Electrowetting: a convenient way to switchable wettability patterns”, *J. Phys. Condens. Matter*, vol. 17 (9), pp. S559–S576.
- ²⁷ R. Shamaï, D. Andelman, B. Berge, R. Hayes, “Water, electricity, and between. . . On electrowetting and its applications”, *Soft Matter*, vol. 4 (1), pp. 38–45, 2008.
- ²⁸ J. A. Schwartz, J. V. Vykoukal, P. R. C. Gascoyne, “Droplet-based chemistry on a programmable micro-chip”, *Lab Chip*, vol. 4 (1), pp. 11–17, 2004.

-
- ²⁹ S.-K. Fan, T.-H. Hsieh, D.-Y. Lin, “General digital microfluidic platform manipulating dielectric and conductive droplets by dielectrophoresis and electrowetting”, *Lab Chip*, vol. 9 (9), pp. 1236–1242, 2009.
- ³⁰ K.-L. Wang, T. B. Jones, A. Raisanen, “DEP actuated nanoliter droplet dispensing using feedback control”, *Lab Chip*, vol. 9 (7), pp. 901–909, 2009.
- ³¹ A. A. Darhuber, J. P. Valentino, S. M. Troian, S. Wagner, “Thermocapillary actuation of droplets on chemically patterned surfaces by programmable microheater arrays”, *J. Microelectromech Syst.*, vol. 12 (6), pp. 873–879, 2003.
- ³² A. A. Darhuber, J. Z. Chen, J. M. Davis, S. M. Troian, “A study of mixing in thermocapillary flows on micropatterned surfaces”, *Philos. Trans. R. Soc. Lond. A*, vol. 362 (1818), pp. 1037–1058, 2004.
- ³³ A. A. Darhuber, J. P. Valentino, S. M. Troian, “Planar digital nanoliter dispensing system based on thermocapillary actuation”, *Lab Chip*, vol. 10 (8), pp. 1061–1071, 2010.
- ³⁴ P. Y. Chiou, H. Moon, H. Toshiyoshi, C.-J. Kim, M. C. Wu, “Light actuation of liquid by optoelectrowetting”, *Sens. Actuators A : Physical; Selected papers based on contributions revised from the Technical Digest of the 2002 Solid-State Sensors, Actuators and Microsystems workshop*, vol. 104 (3), pp. 222–228, 2003.
- ³⁵ H.-S. Chuang, A. Kumar, S. T. Wereley, “Open optoelectrowetting droplet actuation”, *Appl. Phys. Lett.*, vol. 93 (6), pp. (064104-1)-(064104-3), 2008.
- ³⁶ P. Y. Chiou, S.-Y. Park, M. C. Wu, “Continuous optoelectrowetting for picoliter droplet manipulation”, *Appl. Phys. Lett.*, vol. 93 (22), pp. (221109-1)-(221109-3), 2008.
- ³⁷ F. Krogmann, H. Qu, W. Mönch, H. Zappe, “Push/pull actuation using optoelectrowetting”, *Sens. Actuators A: Physical*, vol. 141 (2), pp. 499–505, 2008.

-
- ³⁸ P.-Y. Chiou, Z. Chang, M. C. Wu, “Droplet manipulation with light on optoelectrowetting device”, *J. Microelectromech. Syst.*, vol. 17 (1), pp. 133–138, 2008.
- ³⁹ Z. Guttenberg, H. Müller, H. Habermüller, A. Geisbauer, J. Pipper, J. Felbel, M. Kielpinski, J. Scriba, A. Wixforth, “Planar chip device for PCR and hybridization with surface acoustic wave pump”, *Lab Chip*, vol. 5 (3), pp. 308–317, 2005.
- ⁴⁰ D. Beyssen, L. Le Brizoual, O. Elmazria, P. Alnot, “Microfluidic device based on surface acoustic wave”, *Sens. Actuators B: Chemical*, vol. 118 (1), pp. 380–385, 2006.
- ⁴¹ J. K. Luo, Y. Q. Fu, Y. Li, X. Y. Du, A. J. Flewitt, A. J. Walton, W. I. Milne, “Moving-part-free microfluidic systems for lab-on-a-chip”, *J. Micromech. Microeng.*, vol. 19 (5), pp. 054001-14, 2009.
- ⁴² Y. Q. Fu, J. K. Luo, X. Y. Du, A. J. Flewitt, Y. Li, G. H. Markx, A. J. Walton, W. I. Milne, “Recent developments on ZnO films for acoustic wave based bio-sensing and microfluidic applications: a review”, *Sens. Actuators B: Chemical*, vol. 143 (2), pp. 606–619, 2010.
- ⁴³ W. C. Nelson, C.-J. Kim, “Droplet Actuation by Electrowetting-on-Dielectric (EWOD): A Review”, *J Adhes. Sci. Technol.*, vol. 26 (12-17), pp. 1747-1771, 2012.
- ⁴⁴ S. K. Cho, C.-J. Kim, “Particle separation and concentration control for digital microfluidic systems”, *16th. IEEE annual international conference on MEMS, Kyoto, Japan*, pp. 686–689, 2003.
- ⁴⁵ Y. Zhao, U-C. Yi, S. K. Cho, “Microparticle concentration and separation by traveling-wave dielectrophoresis (twDEP) for digital microfluidics”, *J. Microelectromech. Syst.*, vol. 16 (6), pp. 1472–1481, 2007.
- ⁴⁶ S. K. Cho, Y. Zhao, C.-J. Kim, “Concentration and binary separation of microparticles for droplet-based digital microfluidics”, *Lab Chip*, vol. 7 (4), pp. 490–498, 2007.

-
- ⁴⁷ S-K. Fan, P-W. Huang, T-T. Wang, Y-H. Peng, “Cross-scale electric manipulations of cells and droplets by frequency-modulated dielectrophoresis and electrowetting”, *Lab Chip*, vol. 8 (8), pp. 1325–1331, 2008.
- ⁴⁸ Y. Wang, Y. Zhao Y, S. K. Cho, “Efficient in-droplet separation of magnetic particles for digital microfluidics”, *J. Micromech. Microeng.*, vol. 17 (10), pp. 2148–2156, 2007.
- ⁴⁹ R. S. Sista, A. E. Eckhardt, V. Srinivasan, M. G. Pollack, S. Palanki, V. K. Pamula, “Heterogeneous immunoassays using magnetic beads on a digital microfluidic platform”, *Lab Chip*, vol. 8 (12), pp. 2188–2196, 2008.
- ⁵⁰ G. J. Shah, C.-J. Kim, “Meniscus-assisted high-efficiency magnetic collection and separation for EWOD droplet microfluidics”, *J. Microelectromech. Syst.*, vol. 18 (2), pp. 363–375, 2009.
- ⁵¹ B. H.W. Hendriks, S. Kuiper, M. A. J. Van As, C. A. Renders, T. W. Tukker, “Electrowetting-based variable-focus lens for miniature systems”, *Opt. Rev.*, vol. 12 (3), pp. 255–259, 2005.
- ⁵² S. Kuiper, B. H. W. Hendriks, “Variable-focus liquid lens for miniature cameras,” *Appl. Phys. Lett.*, vol. 85 (7), pp. 1128–1130, 2004.
- ⁵³ B. Berge, J. Peseux, “Variable focal lens controlled by an external voltage: An application of electrowetting”, *Eur. Phys. J. E*, vol. 3 (2), pp. 159-163, 2000.
- ⁵⁴ S. Yang, P. Mach, T. Krupenkin, J. A. Rogers, “Dynamic tuning of optical waveguides with electrowetting pumps and recirculating fluid channels”, *Appl. Phys. Lett.*, vol. 81 (2), pp. 202-204, 2002.
- ⁵⁵ N. R. Smith, D. C. Abeysinghe, J. W. Haus, J. Heikenfeld, “Agile wide-angle beam steering with electrowetting micropisms”, *Opt. Express*, vol. 14 (14), pp. 6557–6563, 2006.
- ⁵⁶ Z. Wan, H. Zeng, A. Feinerman, “Area-tunable micromirror based on electrowetting actuation of liquid-metal droplets”, *Appl. Phys. Lett.*, vol. 89 (20), pp. 201107, 2006.

-
- ⁵⁷ R. A. Hayes, B. J. Feenstra, “Video-speed electronic paper based on electrowetting”, *Nature*, vol. 425 (6956), pp. 383–385, 2003.
- ⁵⁸ K. Zhou, J. Heikenfeld, “Arrayed electrowetting microwells”, *Appl. Phys. Lett.*, vol. 92 (11), pp. 113515, 2008.
- ⁵⁹ J. Heikenfeld, P. Drzaic, J-S. Yeo, T. Koch, “Review paper: A critical review of the present and future prospects for electronic paper”, *J. Soc. Inf. Display*, vol. 19 (2), pp. 129-156, 2011.
- ⁶⁰ M. G. Pollack, A.D. Shenderov and R.B. Fair, “ Electrowetting-based actuation of droplets for integrated microfluidics”, *Lab Chip*, vol. 2, pp. 96-101, 2002.
- ⁶¹ J. Lienemann, A. Greiner, and J. G. Korvink, "Electrode Shapes for Electrowetting Arrays," *IEEE Transactions on Computer-Aided Design of Integrated Circuits and Systems*, vol. 25 (2), 2006.
- ⁶² N. Nashida, W. Satoh, J. Fukuda, H. Suzuki, “Electrochemical immunoassay on a microfluidic device with sequential injection and flushing functions”, *Biosens. Bioelectron.*, vol. 22 (12), pp.3167–3173, 2007.
- ⁶³ R. Sista, Z. Hua, P. Thwar, A. Sudarsan, V. Srinivasan, A. Eckhardt, M. Pollack, V. Pamula, “Development of a digital microfluidic platform for point of care testing”, *Lab Chip*, vol. 8 (12), pp. 2091–2104, 2008.
- ⁶⁴ L. Malic, D. Brassard, T. Veres, M. Tabrizian, “Integration and detection of biochemical assays in digital microfluidic LOC devices”, *Lab Chip*, vol. 10(4), pp. 418–431, 2010.
- ⁶⁵ M. K. Chaudhury, G. M. Whitesides, “How to make water run uphill”, *Science*, vol. 256 (5063), pp.1539-1541, 1992.
- ⁶⁶ M. Pollack, “Electrowetting-based microactuation of droplets for digital microfluidics” *Ph.D. thesis*, Duke University, 2001.

-
- ⁶⁷ J. Berthier, “Microdrops and digital microfluidics: Processing, development and applications”, *William Andrew, Norwich, NY*, 2008.
- ⁶⁸ T. Young, “Miscellaneous works”, *J. Murray*, London, vol. 1, (*G. Peacock, ed.*), 1855.
- ⁶⁹ D. Li, A. W. Neumann, “The thermodynamic status of contact angles” Chapter 3 in *Applied Surface Thermodynamics*, A.W. Neumann, ed., Marcel-Dekker, vol. 63, pp. 109-168, Anonymous 1996.
- ⁷⁰ R. J. Good, “A thermodynamic derivation of Wenzel's modification of Young's equation for contact angles; together with a theory of hysteresis”. *J. Am. Chem. Soc.*, vol. 74(20), pp. 5041-5042, 1952.
- ⁷¹ J. Z. Chen, S. M. Troian, A. A. Darhuber, S. Wagner, “Effect of contact angle hysteresis on thermocapillary droplet actuation”, *J. Appl. Phys.*, vol. 97 (1), pp. 014906 (1-9), 2005.
- ⁷² J. Berthier, P. Dubois, P. Clementz, P. Claustre, C. Peponnet, Y. Fouillet, “Actuation potentials and capillary forces in electrowetting based microsystems”, *Sens. Actuators A*, vol. 134 (2), pp. 471–479, 2007.
- ⁷³ J. J. Jasper, E. V. Kring. “The isobaric surface tensions and thermodynamic properties of the surfaces of a series of *n*-Alkanes, C₅ to C₁₈, 1-Alkenes, C₆ to C₁₆, and of *n*-Decylcyclopentane, *n*-Decylcyclohexane and *n* - Dcylbenzene”, *J. Phys. Chem.*, vol. 59(10), pp. 1019-1021, 1955.
- ⁷⁴ Z. Keshavarz-Motamed, L. Kadem, A. Dolatabadi, “Effects of dynamic contact angle on numerical modeling of electrowetting in parallel plate microchannels”, *Microfluid. Nanofluid.*, vol. 8 (1), pp.47–56, 2010.
- ⁷⁵ G. M. Whitesides, P.E.Laibinis, “Wet chemical approaches to the characterization of organic surfaces: self-assembled monolayers, wetting, and the physical-organic chemistry of the solid-liquid interface”, *Langmuir*, vol. 6 (1), pp. 87-96, 1990.

-
- ⁷⁶ K. Ichimura, S.-K. Oh, M. Nakagawa, “Light-driven motion of liquids on a photoresponsive surface”, *Science*, vol. 288 (5471), pp. 1624-1626, 2000.
- ⁷⁷ B., Gallardo, V. K. Gupta, F. D. Eagerton, L. I. Jong,, V. S. Craig,, R. R. Shah, N. L. Abbott, “Electrochemical principles for active control of liquids on submillimeter scales”, *Science*, vol. 283 (5398), pp. 57-60, 1999.
- ⁷⁸ T. S. Sammarco, M. A. Burns, “Thermocapillary pumping of discrete drops in microfabricated analysis devices ”, *AIChE .J.*, vol. 45 (2), pp. 350-366, 1999.
- ⁷⁹ J. Zeng, T. Korsmeyer, “Principles of droplet electrodynamics for Lab-on-a-chip”, *Lab Chip*, vol. 4 (4), pp. 265-277, 2004.
- ⁸⁰ S. K. Cho, H. Moon, C.-J. Kim, “Creating, transporting, cutting, and merging liquid droplets by electrowetting-based actuation for digital microfluidic circuits”, *J. Microelectromechanical Syst.*, vol. 12 (1), pp. 70-80, 2003.
- ⁸¹ A. A. Darhuber, S. M. Troian, “Principles of microfluidic actuation by modulation of surface stresses”, *Annu. Rev. Fluid Mech.*, vol. 37 (1), pp. 425-455, 2005.
- ⁸² G. Lippmann, “Relations entre les phenomenes electriques et capillaires”, *Ann. Chim. Phys.*, vol. 5, 494, 1875.
- ⁸³ J. A. Schwartz, J. V. Vykoukal, P. R. C. Gascoyne, “Droplet-based chemistry on a programmable micro-chip”, *Lab Chip*, vol. 4 (1), pp. 11-17, 2004.
- ⁸⁴ T. B. Jones, M. Gunji, M. Washizu, M. J. Feldman, “Dielectrophoretic liquid actuation and nanodroplet formation”, *J. Appl. Phys.*, vol. 89 (2), pp. 1441-1448, 2001.
- ⁸⁵ T. B. Jones, K. L. Wang, D. J. Yao, “Frequency-dependent electromechanics of aqueous liquids: Electrowetting and Dielectrophoresis”, *Langmuir*, vol. 20(7), pp. 2813-2818, 2004.

-
- ⁸⁶ H. A. Pohl, “Dielectrophoresis: The Behaviour of Neutral Matter in Nonuniform Electric Fields”, *Cambridge University Press*, Cambridge, 1978.
- ⁸⁷ T. B. Jones, G. W. Bliss, “Bubble dielectrophoresis”, *J. Appl. Phys.*, vol. 48 (4), pp. 1412-1417, 1977.
- ⁸⁸ F. F. Reuss, “Sur un nouvel effet de l'électricité galvanique”, *Mémoires de la Société Impériale des Naturalistes de Moscou*, vol. 2, pp. 327- 337, 1809.
- ⁸⁹ J. Lee and Ch.-J. Kim, “Surface-tension-driven microactuation based on continuous electrowetting”, *J. Microelectromech. Syst.*, vol. 9 (2), pp. 171-180, 2000.
- ⁹⁰ M. Vallet, B. Berge, L. Vovelle, “Electrowetting of water and aqueous solutions on poly (ethylene terephthalate) insulating films”, *Polymer*, vol. 37 (12), pp. 2465–2470, 1996.
- ⁹¹ H. Dahms, “Electrocapillary measurements at the interface insulator-electrolytic solution”, *J. Electrochem. Soc.*, vol. 116 (11), pp. 1532–1534, 1969.
- ⁹² B. Berge, “Electrocapillarity and wetting of insulator films by water”, *C. R. Acad. Sci. Paris, Série II*, vol. 317, pp. 157–163, 1993.
- ⁹³ G. Beni, S. Hackwood, “Electro-wetting displays”, *Appl. Phys. Lett.*, vol. 38 (4), pp. 207–209, 1981.
- ⁹⁴ J. Berthier, P. Silberzan, “Microfluidics for biotechnology”, 2nd Edition, *Artech House Inc.*, Boston, 2010.
- ⁹⁵ V. Srinivasan, “A digital microfluidic lab-on-a-chip for clinical applications”, *Ph.D. thesis*, Duke University, USA, 2005.
- ⁹⁶ D. Chatterjee, B. Hetayothin, A. R. Wheeler, D. J. King, R. L. Garrell, “Droplet-based microfluidics with nonaqueous solvents and solutions”, *Lab Chip*, vol. 6 (2), pp. 199–206, 2006.

-
- ⁹⁷ A. Torkkeli, "Droplet microfluidics on a planar surface", *Ph.D. Thesis*, Helsinki University, 2003.
- ⁹⁸ J.N. Israelachvili, "Intermolecular and surface forces", 3rd Edition, Academic Press, London, ISBN 0-12-375180-2, 1989.
- ⁹⁹ D. J. Shaw, "Introduction to Colloid and surface chemistry", 4th. Edition, Butterworth, London, ISBN 0-7506-1182-0, 1992.
- ¹⁰⁰ Ch-M. Ho , Y-Ch. Tai, "Micro-Electro-Mechanical-Systems (MEMS) and Fluid Flows, *J. Annu. Rev. Fluid Mech.*, vol. 30 (1), pp. 579-612, 1998.
- ¹⁰¹ R. Digilov, "Change-induced modification of Contact Angle: The secondary Electrocapillary Effect", *Langmuir*, vol. 16 (16), pp. 6719-6723, 2000.
- ¹⁰² B. Shapiro, H. Moon, R.L. Garrell, and C. J. Kim, "Equilibrium behavior of sessile drops under surface tension, applied external fields, and material variations", *J. Appl. Phys.*, vol. 93(9), pp. 5794-5811, 2003.
- ¹⁰³ J. R. Melcher, "Continuum electromechanics", Section 3.7, *The MIT Press*, 1981.
- ¹⁰⁴ V. Bahadur, S. V. Garimella, "An energy-based model for electrowetting- induced droplet actuation," *J. Micromech. Microengineering*, vol. 16 (8), pp. 1494-1503, 2006.
- ¹⁰⁵ J. A. M. Sondag-Huethorst, L. G. J. Fokkink, "Electrical double layers on thiol-modified polycrystalline gold electrodes", *J. Electroanal. Chem.*, vol. 367(1-2), 49, 1994.
- ¹⁰⁶ J. A. M. Sondag-Huethorst, L. G. J. Fokkink, "Potential-dependent wetting of electroactive Ferrocene-Terminated Alkanethiolate monolayers on gold", *Langmuir*, vol. 10 (11), pp. 4380-4387, 1994.
- ¹⁰⁷ W. J. J. Welters, L. G. J. Fokkink , "Fast electrically switchable capillary effects", *Langmuir*, vol.14 (7), pp. 1535-1538, 1998.

-
- ¹⁰⁸ V. Peykov, A. Quinn and J. Ralston, “Electrowetting: a model for contact-angle saturation”, *Colloid Polym. Sci.*, vol. 278 (8), pp. 789-793, 2000.
- ¹⁰⁹ J. Berthier, P. Clementz, O. Raccurt, D. Jary, P. Claustre, C. Peponnet, Y. Fouillet, “Computer aided design of an EWOD microdevice”, *Sens. Actuators A*, vol. 127 (2), pp. 283–294, 2006.
- ¹¹⁰ P. Y. Paik, V. K. Pamula, K. Chakrabarty, “Thermal effects on droplet transport in digital microfluidics with applications to chip cooling”, *In: Thermomechanical phenomena in electronic systems—proceedings of the intersociety conference, ITherm 2004—9th intersociety conference on thermal and thermomechanical phenomena in electronic systems*, vol. 1, pp. 649–654, 2004.
- ¹¹¹ M. Gong, C.-J. Kim, “Two-dimensional digital microfluidic system by multilayer printed circuit board”, *In: 18th IEEE international conference on micro electro mechanical systems*, pp. 726–729, 2005.
- ¹¹² V. K. Pamula, M. G. Pollack, P. Y. Paik, H. Ren, R. B. Fair, “Apparatus for manipulating droplets by electrowetting-based techniques”, *US Patent 6,911,132*, June 28, 2005.
- ¹¹³ C. G. Cooney, C.-Y. Chen, M. R. Emerling, A. Nadim, J. D. Sterling, “Electrowetting droplet microfluidics on a single planar surface”, *Microfluid Nanofluid*, vol. 2 (5), pp. 435–446, 2006.
- ¹¹⁴ U.-C. Yi, C.-J. Kim, “Characterization of electrowetting actuation on addressable single-side coplanar electrodes”, *J. Micromech. Microeng.*, vol. 16 (10), pp. 2053–2059, 2006.
- ¹¹⁵ F. Mugele, “Fundamental challenges in electrowetting: from equilibrium shapes to contact angle saturation and drop dynamics”, *Soft Matter*, vol. 5 (18), pp. 3377-3384, 2009.
- ¹¹⁶ T. N. Krupenkin, J. A. Taylor, T. M. Schneider, S. Yang, “From rolling ball to complete wetting: the dynamic tuning of liquids on nanostructured surfaces”, *Langmuir*, vol. 20 (10), pp. 3824–3827, 2004.

-
- ¹¹⁷ A. I. Drygiannakis, A. G. Papathanasiou, A. G. Boudouvis, “On the connection between dielectric breakdown strength, trapping of charge, and contact angle saturation in Electrowetting”, *Langmuir*, vol. 25(1), pp. 147-152, 2009.
- ¹¹⁸ H. J. J. Verheijen, M. W. J. Prins, “Reversible Electrowetting and Trapping of Charge: Model and Experiments”, *Langmuir*, vol. 15 (20), pp. 6616-6620, 1999.
- ¹¹⁹ P. W. Chudleigh, “Mechanism of charge transfer to a polymer surface by a conducting liquid contact”, *J. Appl. Phys.*, vol. 47 (10), pp. 4475-4483, 1976.
- ¹²⁰ M. Vallet, M. Vallade, B. Berge, “Limiting phenomena for the spreading of water on polymer films by electrowetting”. *The European Physical Journal B - Condensed Matter and Complex Systems*, vol. 11(4), pp. 583-591, 1999.
- ¹²¹ F. Mugele, S. Herminghaus, “Electrostatic stabilization of fluid microstructures”, *Appl. Phys. Lett.*, vol. 81 (12), pp. 2303-2305, 2002.
- ¹²² T. Pfohl, F. Mugele, R. Seemann, S. Herminghaus, “Trends in microfluidics with complex fluids”, *ChemPhysChem*, vol. 4 (12), pp. 1291-1298, 2003.
- ¹²³ A. Quinn, R. Sedev, J. Ralston, “Contact angle saturation in electrowetting”, *J. Phys. Chem. B*, vol. 109 (13), pp. 6268-6275, 2005.
- ¹²⁴ J. Park, X. Feng, W. Lu, “Instability of electrowetting on a dielectric substrate”, *J. Appl. Phys.*, vol. 109 (3), pp. 034309-6, 2011.
- ¹²⁵ R. Sedev, “Electrowetting: electrocapillary, saturation, and dynamics”, *Eur. Phys. J. Special Topics*, vol. 197 (1), pp. 307-3019, 2011.
- ¹²⁶ A.W. Adamson, A.P. Gast, “Physical chemistry of surfaces”, *John Wiley and Sons Inc.*, 6th. edition, 1997.

-
- ¹²⁷ J.S. Batchelder, “Dielectrophoretic manipulator”, *Rev. Sci. Instrum.*, vol. 54 (3), pp. 300-302, 1983.
- ¹²⁸ H. J. J. Verheijen, M.W. J. Prins, “Contact angles and wetting velocity measured electrically”, *Rev. Sci. Instrum.*, vol.70 (9), pp. 3668-3673, 1999.
- ¹²⁹ M. Washizu, “Electrostatic actuation of liquid droplets for micro-reactor applications”, *IEEE Trans. Ind. Appl.*, vol. 34 (4), pp. 732–737, 1998.
- ¹³⁰ J. Lee, H. Moon, J. Fowler, T. Schoellhammer, C.-J. Kim, “Electrowetting and electrowetting-on-dielectric for microscale liquid handling”, *Sensors Actuators A*, vol. 95 (2), pp. 259–268, 2002.
- ¹³¹ H. Moon, S.-K. Cho, R. L. Garrell and C.-J. Kim, “Low voltage electrowetting-on-dielectric”, *J. Appl. Phys.*, vol. 92 (7), pp. 4080–4087, 2002.
- ¹³² P. Paik, V. K. Pamula, M. G. Pollack, R. B. Fair RB, “Electrowetting-based droplet mixers for microfluidic systems”, *Lab Chip*, vol. 3 (1), pp. 28–33, 2003.
- ¹³³ P. Paik, V. K. Pamula, R. B. Fair RB, “Rapid droplet mixers for digital microfluidic systems”, *Lab Chip*, vol. 3 (4), pp. 253–259, 2003.
- ¹³⁴ J. Y. Yoon, R. L. Garrell, “Preventing biomolecular adsorption in electrowetting-based biofluid chips”, *Anal. Chem.*, vol. 75 (19), pp.5097-5102, 2003.
- ¹³⁵ V. Srinivasan, V. K. Pamula, R. B. Fair, “An integrated digital microfluidic lab-on-a-chip for clinical diagnostics on human physiological fluids”, *Lab Chip*, vol. 4 (4), pp. 310–315, 2004.
- ¹³⁶ V. Srinivasan, V. K. Pamula, R. B. Fair, “Droplet-based microfluidic lab-on-a-chip for glucose detection”, *Anal. Chim. Acta*, vol. 507 (1), pp.145–150, 2004.
- ¹³⁷ V. Srinivasan, V. Pamula, P. Paik, R. Fair, “Protein stamping for MALDI Mass Spectrometry using an electrowetting-based microfluidic platform”, *Lab-on-a-chip: platforms*,

devices, and applications. Proceedings of SPIE, Philadelphia, Pennsylvania (PA), USA, vol. 5591, pp. 26–32, 2004.

¹³⁸ A. R. Wheeler, H. Moon, C. A. Bird, R. R. O. Loo, C.-J. Kim, J. A. Loo, R. L. Garrell, “Digital microfluidics with in-line sample purification for proteomics analyses with MALDI-MS”, *Anal. Chem.*, vol. 77 (2), pp. 534–540, 2005.

¹³⁹ H. Moon, A. R. Wheeler, R. L. Garrell, J. A. Loo, C.-J. Kim, “An integrated digital microfluidic chip for multiplexed proteomic sample preparation and analysis by MALDI-MS”, *Lab Chip*, vol. 6 (9), pp. 1213–1219, 2006.

¹⁴⁰ K. F. Böhringer, “Modeling and controlling parallel tasks in droplet-based microfluidic systems”, *IEEE Trans. Comput. Aid Des. Integr. Circ. Syst.*, vol. 25 (2), pp. 334–344, 2006.

¹⁴¹ E. J. Griffith, S. Akella, M. K. Goldberg, “Performance characterization of a reconfigurable planar-array digital microfluidic system”, *IEEE Trans. Comput. Aid Des. Integr. Circ. Syst.*, vol. 25 (2), pp. 345–357, 2006.

¹⁴² P. R. C. Gascoyne, J. V. Vykoukal, J. A. Schwartz, T. J. Anderson, D. M. Vykoukal, K. W. Current, C. McConaghy, F. F. Becker, C. Andrews, “Dielectrophoresis-based programmable fluidic processors”, *Lab Chip*, vol. 4 (4), pp. 299–309, 2004.

¹⁴³ Y. Li, W. Parkes, L. I. Haworth, A. A. Stokes, K. R. Muir, P. Li, A. J. Collin, N. G. Hutcheon, R. Henderson, B. Rae, A. J. Walton, “Anodic Ta₂O₅ for CMOS compatible low voltage electrowetting-on-dielectric device fabrication”, *Solid State Electron.*, vol. 52 (9), pp. 1382–1387, 2008.

¹⁴⁴ J. Gong, C.-J. Kim, “Direct-referencing two-dimensional-array digital microfluidics using multilayer printed circuit board”. *J. Microelectromech. Syst.*, vol. 17 (2), pp.257–264, 2008.

¹⁴⁵ M. Abdelgawad, A. R. Wheeler, “Rapid prototyping in copper substrates for digital microfluidics”, *Adv. Mater.*, vol. 19(1), pp.133–137, 2007.

-
- ¹⁴⁶ M. Abdelgawad, A. R. Wheeler, “Low-cost, rapid-prototyping of digital microfluidics devices”. *Microfluid Nanofluid*, vol. 4 (4), pp.349–355, 2008.
- ¹⁴⁷ D. L. Herbertson, C. R. Evans, N. J. Shirtcliffe, G. McHale, M. I. Newton MI, “Electrowetting on superhydrophobic SU-8 patterned surfaces”, *Sens. Actuators A*, vol. 130–131, pp. 189–193, 2006.
- ¹⁴⁸ N. Verplanck, Y. Coffinier, V. Thomy, R. Boukherroub, “Wettability switching techniques on superhydrophobic surfaces”, *Nanoscale Res. Lett.*, vol. 2 (12), pp. 577–596, 2007.
- ¹⁴⁹ J. Heikenfeld, M. Dhindsa, "Electrowetting on Superhydrophobic Surfaces: Present Status and Prospects," *Journal of Adhesion Science and Technology*, vol. 22 (3-4), pp. 319-334, 2008.
- ¹⁵⁰ T. Taniguchi, T. Torii, T. Higuchi, “Chemical reactions in microdroplets by electrostatic manipulation of droplets in liquid media”, *Lab Chip*, vol. 2 (1), pp. 19–23, 2002.
- ¹⁵¹ K. P. Nichols, H. Gardeniers, “A digital microfluidic system for the investigation of pre-steady-state enzyme kinetics using rapid quenching with MALDI-TOF Mass Spectrometry”, *Anal. Chem.*, vol. 79 (22), 8699–8704, 2007.
- ¹⁵² E. M. Miller, A. R. Wheeler, “A Digital microfluidic approach to homogeneous enzyme assays”, *Anal. Chem.*, vol. 80 (5), pp. 1614–1619, 2008.
- ¹⁵³ P.-W. Huang, T.-T. Wang, S.-W. Lin, Y.-C. Chang, S.-K. Fa, “Dielectrophoretic cell concentrator on EWOD-based chips”, *Proceedings of the 1st IEEE International Conference on Nano/Micro Engineered and Molecular Systems*, pp. 1418–1421, 2006.
- ¹⁵⁴ I. Barbulovic-Nad, H. Yang, P. S. Park, A. R. Wheeler, “Digital Microfluidics for Cell-Based Assays”, *Lab Chip*, vol. 8 (4), pp. 519–526, 2008.
- ¹⁵⁵ V. K. Pamula, V. Srinivasan, H. Chakrapani, R. B. Fair, E. J. Toone, “A droplet-based lab-on-a-chip for colorimetric detection of nitroaromatic explosives”, *In: 18th IEEE international conference on MEMS, Miami Beach, FL, USA*, pp. 722–725, 2005.

-
- ¹⁵⁶ M. G. Pollack, P. Y. Paik, A. D. Shenderov, V. K. Pamula, F. S. Dietrich, R. B. Fair, “Investigation of electrowetting-based microfluidics for real-time PCR applications”, *Seventh international conference on miniaturized chemical and biochemical analysis systems—proceedings of the 2003 MicroTAS conference, Squaw Valley, CA*, pp. 619–622, 2003.
- ¹⁵⁷ Y.-H. Chang, G.-B. Lee, F.-C. Huang, Y.-Y. Chen, J.-L. Lin, “Integrated polymerase chain reaction chips utilizing digital microfluidics”, *Biomed. Microdevices*, vol. 8 (3), pp. 215–225, 2006.
- ¹⁵⁸ R. B. Fair, “Digital microfluidics: is a true lab-on-a-chip possible?”, *Microfluid Nanofluid*, vol. 3 (3), pp. 245–281, 2007.
- ¹⁵⁹ L. Malic, T. Veres, M. Tabrizian, “Biochip functionalization using electrowetting-on-dielectric digital microfluidics for surface plasmon resonance imaging detection of DNA hybridization”, *Biosens. Bioelectron.*, vol. 24 (7), pp. 2218–2224, 2009.
- ¹⁶⁰ H. C. Lin, Y. J. Liu, D. J. Yao, “Core-shell droplets for parallel DNA ligation of an ultra-micro volume using an EWOD microfluidic system”, *JALA*, vol. 15 (3), pp. 210–215, 2010.
- ¹⁶¹ M. J. Jebrail, A. R. Wheeler, “Digital microfluidic method for protein extraction by precipitation”, *Anal. Chem.*, vol. 81 (1), pp. 330–335, 2009.
- ¹⁶² V. N. Luk, G. C. Mo, A. R. Wheeler, “Pluronic additives: A solution to sticky problems in digital microfluidics”, *Langmuir*, vol. 24 (12), pp. 6382–6389, 2008.
- ¹⁶³ A. R. Wheeler, H. Moon, C. J. Kim, J. A. Loo, R. L. Garrell, “Electrowetting-based microfluidics for analysis of peptides and proteins by Matrix-Assisted Laser Desorption/Ionization Mass Spectrometry”, *Anal. Chem.*, vol. 76 (16), pp. 4833–4838, 2004.
- ¹⁶⁴ J. L. Poulos, W. C. Nelson, T.-J. Jeon, C.-J. C. J. Kim, J. J. Schmidt, “Electrowetting on dielectric-based microfluidics for integrated lipid bilayer formation and measurement”, *Appl. Phys. Lett.*, vol. 95 (1), pp. 013706 (1-3), 2009.

-
- ¹⁶⁵ J. Zhou, L. Lu, K. Byrapogu, D. M. Wootton, P. I. Lelkes, R. Fair, “Electrowetting-based multi-microfluidics array printing of high resolution tissue construct with embedded cells and growth factors”, *Virtual and Physical Prototyping*, vol. 2 (4), pp. 217–223, 2007.
- ¹⁶⁶ H. Ren, R. B. Fair, M. G. Pollack, E. J. Shaughnessy, “ Dynamics of electro-wetting droplet transport”, *Sens. Actuators B*, vol. 87 (1), pp. 201–206, 2002.
- ¹⁶⁷ A. Dolatabadi, K. Mohseni, A. Arzpeyma, "Behaviour of a moving droplet under electrowetting actuation: Numerical simulation," *Canadian Journal of Chemical Engineering*, vol. 84 (1), pp. 17-21, 2006.
- ¹⁶⁸ A. Arzpeyma, "Numerical investigation of droplet actuation via electrowetting in microchannels," *M.A.Sc. thesis*, Concordia University, Montreal, 2007.
- ¹⁶⁹ A. Arzpeyma, S. Bhaseen, A. Dolatabadi, P.M. Wood-Adams, "A coupled electro-hydrodynamic numerical modeling of droplet actuation by electrowetting," *Colloids and Surfaces A: Physicochemical and Engineering Aspects*, vol. 323 (1), p. 28–35, 2008.
- ¹⁷⁰ S. Chakraborty, R. Mittal, “Droplet dynamics in a microchannel subjected to electrocapillary actuation”, *J. Appl. Phys.*, vol. 101(10), pp. 104901, 2007.
- ¹⁷¹ D. Chatterjee, H. Shepherd, R. L. Garrell, “Electromechanical model for actuating liquids in a two-plate droplet microfluidic device”, *Lab Chip*, vol. 9 (9), pp. 1219–1229, 2009.
- ¹⁷² N. Rajabi, A. Dolatabadi, “A novel electrode shape for electrowetting-based microfluidics”, *Colloids and Surfaces A: Physicochemical and Engineering Aspects*, vol. 365 (1), pp. 230-236, 2010.
- ¹⁷³ N. Rajabi, "Droplet actuation on various electrode shapes in electrowetting-based microfluidics" *M.A.Sc. thesis*, Concordia University, Montreal, 2009.
- ¹⁷⁴ R. Bavière, J. Boutet, Y. Fouillet, “Dynamics of droplet transport induced by electrowetting actuation”, *Microfluid Nanofluid*, vol. 4 (4), pp. 287–294, 2008.

-
- 175 F. Brochard, “Motions of droplets on solid surfaces induced by chemical or thermal gradients”, *Langmuir*, vol. 5 (2), pp. 432–438, 1989.
- 176 P. Sen, C. J. Kim, “Capillary spreading dynamics of electrowetted sessile droplets in air”, *Langmuir*, vol. 25 (8), pp. 4302-4305, 2009.
- 177 S. R. Annapragada, S. Dash, S. V. Garimella, J. Y. Murthy, “Dynamics of droplet motion under electrowetting actuation”, *Langmuir*, vol. 27 (11), pp. 8198-8204, 2011.
- 178 M. J. Schertzer, S. I. Gubarenko, R. Ben-Mard, P. E. Sullivan, “An empirically validated analytical model of droplet dynamics in electrowetting on dielectric devices”, *Langmuir*, vol. 26 (24), pp. 19230-19238, 2010.
- 179 H. Oprins, B. Vandeveld, M. Baelmans, “Modeling and control of electrowetting induced droplet motion”, *Micromachines*, vol. 3 (1), pp. 150-167, 2012.
- 180 L. Leslie, J. friend, “Electrowetting applications”, *Encyclopedia of Microfluidics and Nanofluidics*, pp. 1-14, 2014.
- 181 J. Hong, Y. K. Kim, K. H. Kang, J. M. Oh, I. S. Kang, “Effects of drop size and viscosity on spreading dynamics in DC electrowetting”, *Langmuir*, vol. 29 (29), pp. 9118-9125, 2013.
- 182 H. B. Eral, D. J. C. M. ‘t Mannetje, J. M. Oh, “Contact angle hysteresis: a review of fundamentals and applications”, *Colloid Polym Sci*, vol. 291 (2), 247-260, 2012.
- 183 W. Cui, M. Zhang, X. Duan, W. Pang, D. Zhang, H. Zhang, “ Dynamics of electrowetting droplet motion in digital microfluidics systems: from dynamic saturation to device physics”, *Micromachines*, vol. 6 (6), pp. 778-789, 2015.
- 184 Q. Ni, D. E. Capecchi, N. B. Crane, “Electrowetting force and velocity dependence on fluid surface energy”, *Microfluid Nanofluid*, vol. 19 (1), pp. 181-189, 2015.

185 Y. Guan, A. Y. Tong, “A numerical study of microfluidic droplet transport in a parallel-plate electrowetting-on-dielectric (EWOD) device”, *Microfluidic Nanofluid*, vol. 19 (6), pp. 1477-1495, 2015.

186 <http://www.mcgill.ca/microfab/>

187 http://scscoatings.com/what_is_parylene/parylene_properties.aspx

188 <http://scscoatings.com/corporate/library.aspx>

189 “Mask design guide for the EVG620 aligner “, McGill Nanotools Microfab Documents, 2006.

190 “Standard operating procedure: Solvent Clean”, McGill Nanotools Microfab Documents, 2005.

191 “MRC 603 metal sputter operation”, McGill Nanotools Microfab Documents, 2006.

192 “Tencor P1 profilometer user manual”, McGill Nanotools Microfab Documents, 2005.

193 “Laurell spin-coater user manual”, McGill Nanotools Microfab Documents, 2006.

194 “Top and bottom side lithography – EVG620 user manual”, McGill Nanotools Microfab Documents, 2005.

195 “Lithography processes available in the photoroom”, McGill Nanotools Microfab Documents, 2005.

196 <http://arduino.cc/en/Guide/HomePage>

197 T. G. Mason, A. Dhople, D. Wirtz, “ Linear viscoelastic moduli of concentrated DNA solutions”, *Macromolecules*, vol. 31 (11), pp. 3600-3603, 1998.

-
- ¹⁹⁸ R. Bandyopdhyay, A. K. Sood, “Rheology of semi-dilute solutions of calf-thymus DNA”, *Pramana- Journal of Physics*, vol. 58 (4), pp. 685-694, 2002.
- ¹⁹⁹ M. Sun, S. Pejanovic and J. Mijovic, “Dynamics of deoxyribonucleic acids solutions as studied by dielectric relaxation spectroscopy and dynamic mechanical spectroscopy”, *Macromolecules*, vol. 38 (23), pp. 9854-9864, 2005.
- ²⁰⁰ L. H. Sperling, “Introduction to physical polymer science”, 3rd Edition, John Wiley and Sons, New York, 2001.
- ²⁰¹ Lecture Notes: Physical Chemistry of Polymers, Dr. Paula Wood-Adams, Concordia University, Fall 2006.
- ²⁰² L. M. Bravo-Anaya, M. Rinaudo, F. A. S. Martínez, “Conformation and Rheological Properties of Calf-Thymus DNA in Solution”, *Polymers (polym8020051)*, vol. 8 (2), 1-19, 2016.
- ²⁰³ F.A. Morrison, “Understanding Rheology”, *Oxford University Press*, 2001.
- ²⁰⁴ J. Lauger, P. Heyer, G. Pfeifer, “A new integrated Small Angle Light Scattering (Rheo-SALS) device”, *Annual Transactions of the Nordic Rheology Society*, vol. 12, pp. 137-140, 2004.
- ²⁰⁵ <https://www.youtube.com/watch?v=SevPRumWqsE>, SAXS Part 1: Introduction to Biological Small Angle Scattering.
- ²⁰⁶ A. Kalantarian, “Development of Axisymmetric Drop Shape Analysis – No Apex (ADSA-NA)” *Ph.D. thesis*, Toronto University, 2011.
- ²⁰⁷ A. W. Adamson, A. P. Gast, “Physical Chemistry of Surfaces”, *Wiley, New York*, 6th edition, 1997.
- ²⁰⁸ A. W. Neumann, R. J. Good, “Experimental methods in surface and colloid science”, *Plenum Press, New York*, Chapter 2, pp. 31–91, 1979.

-
- 209 S. Hartland, “Surface and interfacial tension: Measurement, Theory, and Applications”, *Marcel Dekker*, 2004.
- 210 C. W. Extrand, “Contact angles and their hysteresis as a measure of liquid-solid adhesion”, *Langmuir*, vol. 20 (10), pp. 4017–4021, 2004.
- 211 Y. Gu, D. Li, P. Cheng, “A novel contact angle measurement technique by analysis of capillary rise profile around a cylinder (acrpac)”, *Colloids and Surfaces A: Physicochemical and Engineering Aspects*, vol. 122 (1-3), pp. 135–149, 1997.
- 212 A. Mennella, N. R. Morrow, “Point-by-point method of determining contact angles from dynamic Wilhelmy plate data for oil / brine / solid systems”, *Journal of Colloid and Interface Science*, vol. 172 (1), pp. 48–55, 1995.
- 213 M.E.P. Walinder, I. Johansson, “Measurement of wood wettability by the Wilhelmy method - Part 2: Determination of apparent contact angles”, *Holzforschung*, vol. 55 (1), pp. 33–41, 2001.
- 214 M. Hoorfar, A. W. Neumann, “Recent progress in Axisymmetric Drop Shape Analysis (ADSA)”, *Advances in Colloid and Interface Science*, vol. 121 (1), pp.25–49, 2006.
- 215 N. M. Dingle, M. T. Harris, “A robust algorithm for the simultaneous parameter estimation of interfacial tension and contact angle from sessile drop profiles”, *Journal of Colloid and Interface Science*, vol. 286 (2), pp. 670–680, 2005.
- 216 M. G. Cabezas, A. Bateni, J. M. Montanero, A. W. Neumann, “Determination of surface tension and contact angle from the shapes of axisymmetric fluid interfaces without use of apex coordinates”, *Langmuir*, vol. 22, pp.10053–10060, 2006.
- 217 O. I. del Rio, A. W. Neumann, “Axisymmetric Drop Shape Analysis: Computational Methods for the Measurement of Interfacial Properties from the Shape and Dimensions of Pendant and Sessile Drops”, *Journal of Colloid and Interface Science*, vol. 196 (2), pp. 136-147, 1997.

-
- 218 A. F. Stadler, G. Kulik, D. Sage, L. Barbieri, P. Hoffmann, “ A snake-based approach to accurate determination of both contact points and contact angles”, *Colloids and Surfaces A: Physicochemical and Engineering Aspects*, vol. 286 (1), pp. 92-103, 2006.
- 219 A.F. Stalder, DropSnake, Biomedical Imaging Group, EPFL,
<http://bigwww.epfl.ch/demo/dropanalysis>
- 220 T. Wei, S. Kaewtathip, K. Shing, “Buffer effect on protein adsorption at liquid/solid interface”, *J. Phys. Chem.*, vol.113 (6), pp. 2053-2062, 2009.
- 221 H. L. Youmans, “Measurement of pH of distilled water”, *J. Chem. Educ.*, vol. 49(6), p. 429, 1972.
- 222 D. G. Castner, B.D. Ratner, “Biomedical surface science: Foundations to frontiers”, *Surf. Sci.*, vol.500 (1-3), pp. 28-60, 2002.
- 223 K.S. Lee, N. Ivanova, V. M. Starov, N. Hilal, V. Dustschk, “Kinetics of wetting and spreading by aqueous surfactant solutions”, *Adv. Colloid Interface Sci.*, vol. 144 (1), pp. 54-65, 2008.
- 224 C.A. Ward, Jiyu Wu, “Effect of adsorption on the surface tensions of solid-fluid interfaces”, *J. Phys. Chem. B*, vol. 111 (14), pp. 3685-3694, 2007.
- 225 A. G. Banpurkar, K. P. Nichols, F. Mugele, “Electrowetting-based microdrop tensiometer”, *Langmuir*, vol. 24 (19), pp. 10549-10551, 2008.
- 226 G. He, M. H. Muser, M. O. Robbins, “Adsorbed layers and the origin of static friction”, *Science*, vol. 284 (5420), pp. 1650-1652, 1999.
- 227 J.-H. Chang, J. J. Pak, “Effect of contact angle hysteresis on electrowetting threshold for droplet transport”, *J. Adhesion Science and Technology*, vol. 26 (2), pp. 2105-2111, 2012.

-
- 228 K. Mohseni, A. Dolatabadi, "Electrowetting droplet actuation in micro scale devices", *43th AIAA Aerospace Sciences Meeting and Exhibit*, AIAA paper 2005-0677, Reno, NV, January 10-13, 2005.
- 229 E. Seyrat, R. A. Hayes, "Amorphous fluoropolymer as insulators for reversible low-voltage electrowetting", *Journal of Applied Physics*, vol. 90 (3), pp. 1383-1386, 2001.
- 230 W. C. Nelson, P. Sen, C.-J. Kim, "Dynamic contact angles and hysteresis under electrowetting-on-dielectric", *Langmuir*, vol. 27 (16), pp. 10319-10326, 2011.
- 231 Y. Xu, "Tutorial: Capillary electrophoresis", *The technical educator*, vol. 1 (2), *Springer-Verlag Inc., New York*, 1996.
- 232 K. D. Altria, "Capillary electrophoresis guidebook: principles, operations and applications", *Humana Press, New York*, 1995.
- 233 G. B. Saleib-Beugelaar, K. D. Dorfman, A. van der Berg, J. C. T. Eijkel, "Electrophoretic separation of DNA in gels and nanostructures", *Lab Chip*, vol. 9 (17), pp. 2508-2523, 2009.
- 234 M. E. Çorman, N. Bereli, S. Özkara, L. Uzun, A. Denizli, "Hydrophobic cryogels for DNA adsorption: effect of embedding of monosize microbeads into cryogel network on their adsorptive performances", *Biomed. Chromatogr.*, vol. 27, pp. 1524-1531, 2013.
- 235 K. Saeki, T. Kunito, M. Sakai, "Effect of Tris-HCl buffer on DNA adsorption by a variety of soil constituents", *Microbes Environ.*, vol. 26 (1), pp. 88-91, 2011.
- 236 A. M. O. Brett, A-M. Chiorcea, "Effect of pH and applied potential on the adsorption of DNA on highly oriented pyrolytic graphite electrodes. Atomic force microscopy surface characterisation", *Electrochemistry Communications*, vol. 5, pp. 178-183, 2003.
- 237 B. Saoudi, N. Jammul, M.-L. Abel, M. Chehimi, G. Dodin, "DNA adsorption onto conducting polypyrrole", *Synthetic Metals*, Vol. 87, pp. 97-103, 1997.

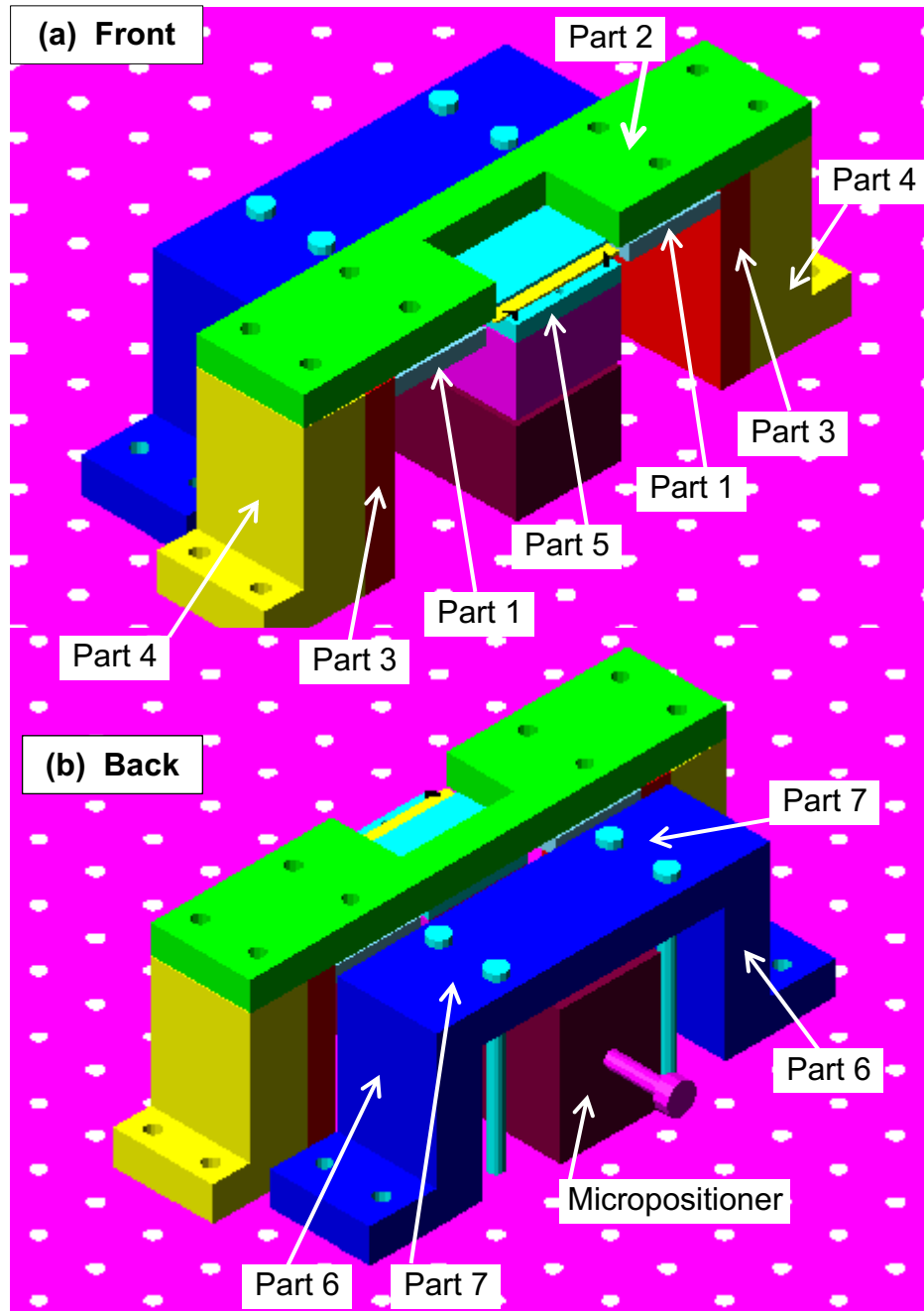
²³⁸ B. Bhattacharjee, “Study of droplet splitting in an electrowetting based digital microfluidic system” *Ph.D. thesis*, The university of British Columbia, 2012.

²³⁹ A. A. Pit, M. H. G. Duits, F. Mugele, “Droplet manipulations in two phase flow microfluidics”, *Micromachines*, vol. 6(11), pp. 1768-1793, 2015.

Appendix A

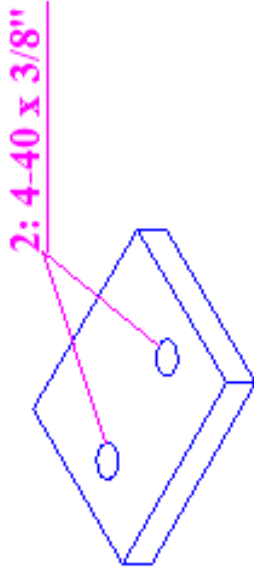
Design Details

Figure A-1: (a) to (i) design details - contact angle measurement apparatus

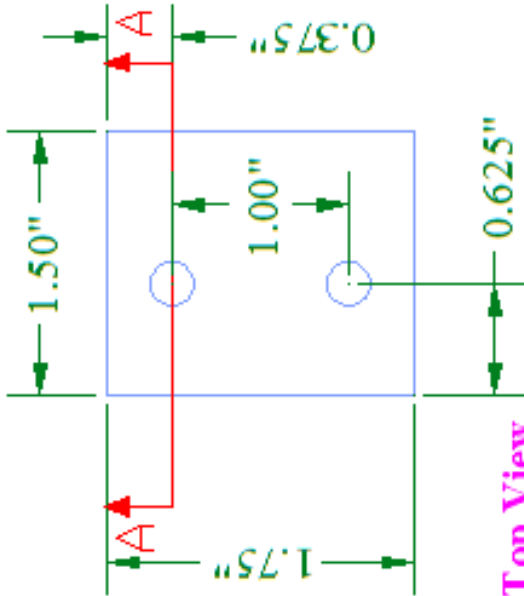


(C)

Isometric View

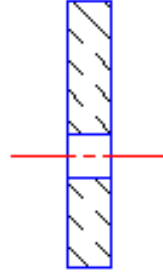
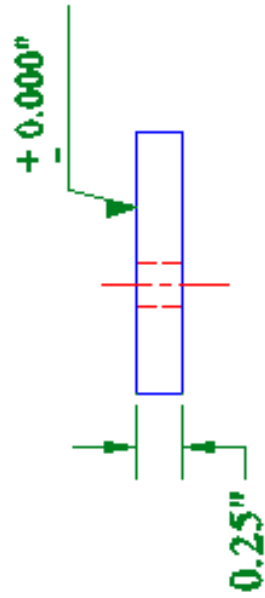


Part 1, non-conductive
Quantity: 2



Top View

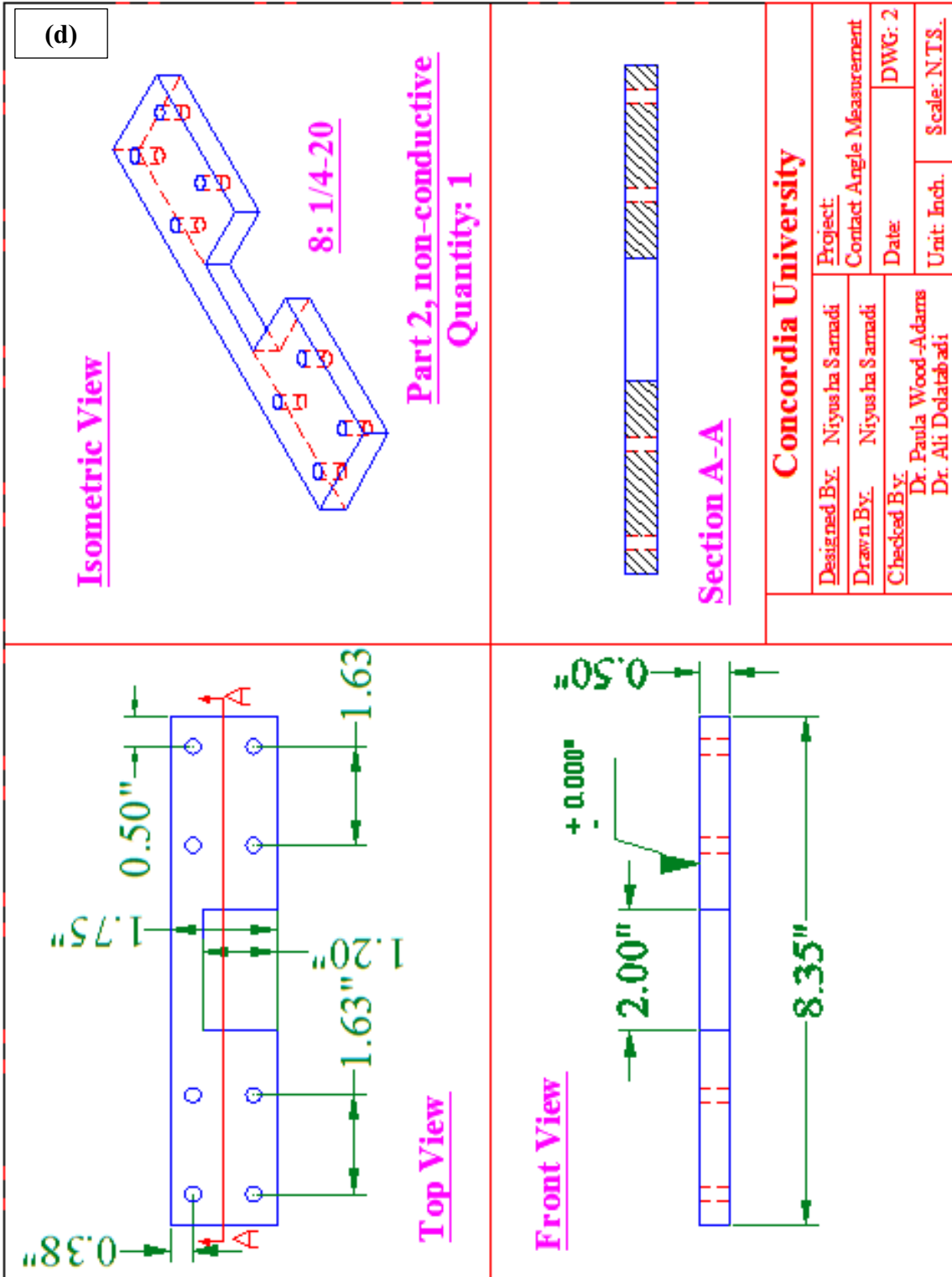
Front View



Section A-A

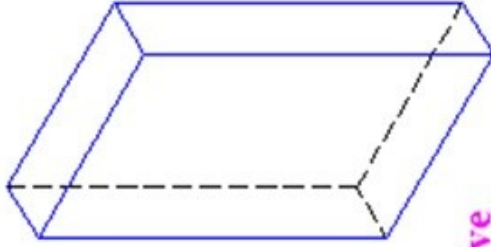
Concordia University

<u>Designed By:</u> Niyusha Samadi	<u>Project:</u> Contact Angle Measurement
<u>Drawn By:</u> Niyusha Samadi	<u>Date:</u> DWG: 1
<u>Checked By:</u> Dr. Paula Wood-Adams Dr. Ali Dolatabadi	<u>Unit:</u> Inch. <u>Scale:</u> N.T.S.



(e)

Isometric View

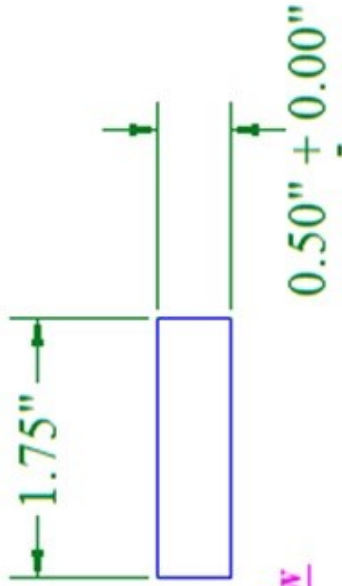


Part 3, conductive
Quantity: 2

Gauge Block

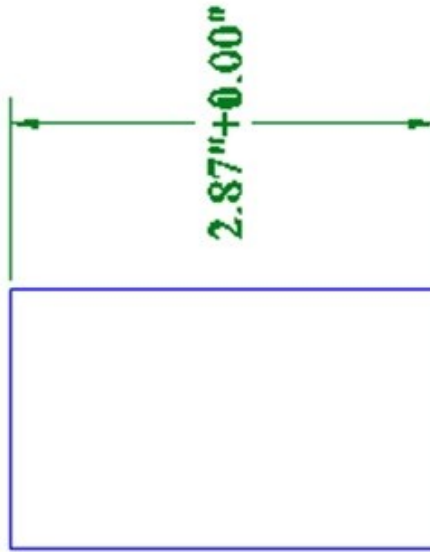
Concordia University

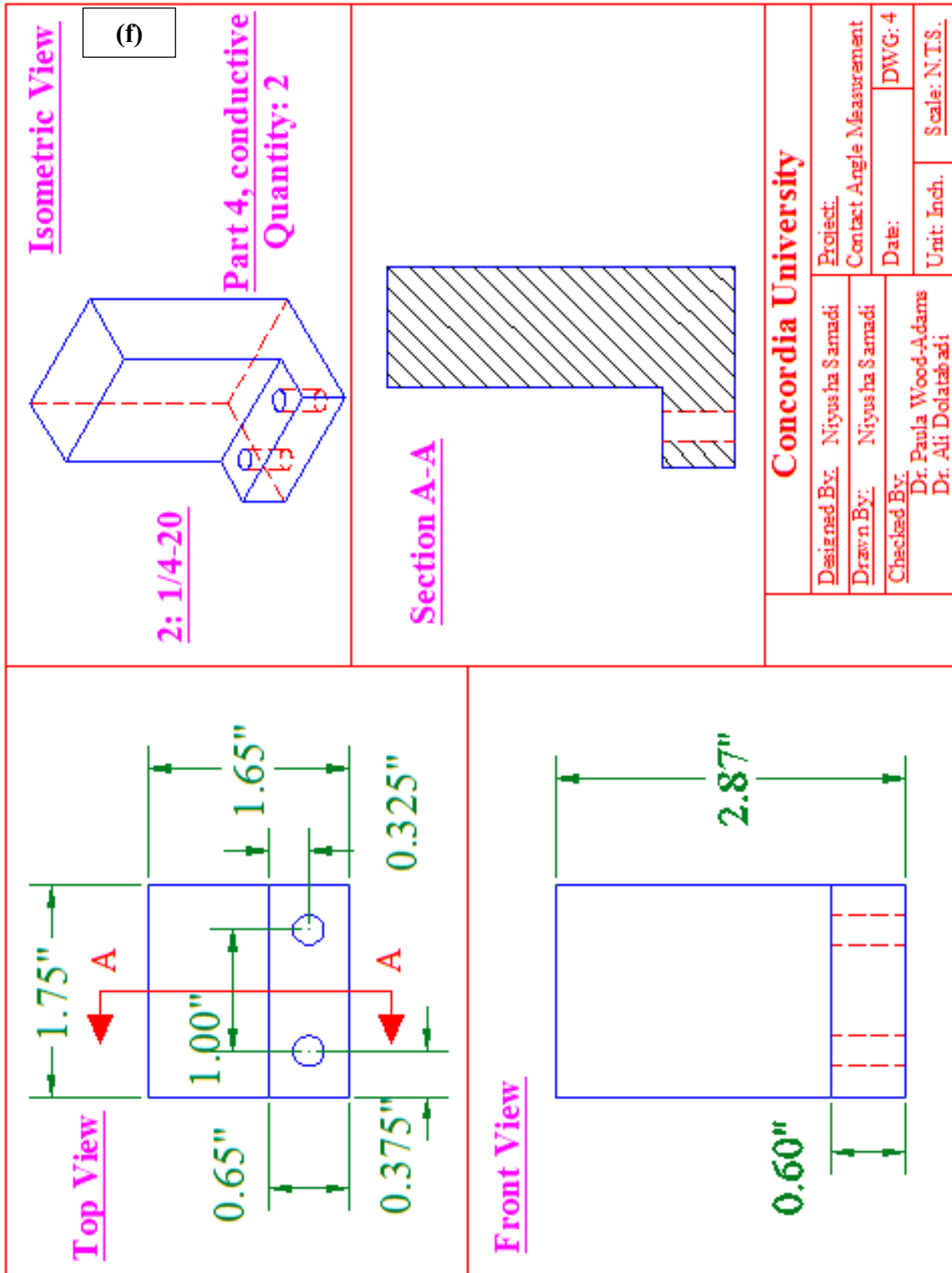
<u>Designed By:</u> Niyusha Samadi	<u>Project:</u>
<u>Drawn By:</u> Niyusha Samadi	<u>Contact Angle Measurement</u>
<u>Checked By:</u> Dr. Paula Wood-Adams Dr. Ali Dolatabadi	<u>Date:</u>
	<u>DWG:</u> 3
	<u>Unit:</u> Inch
	<u>Scale:</u> N.T.S.

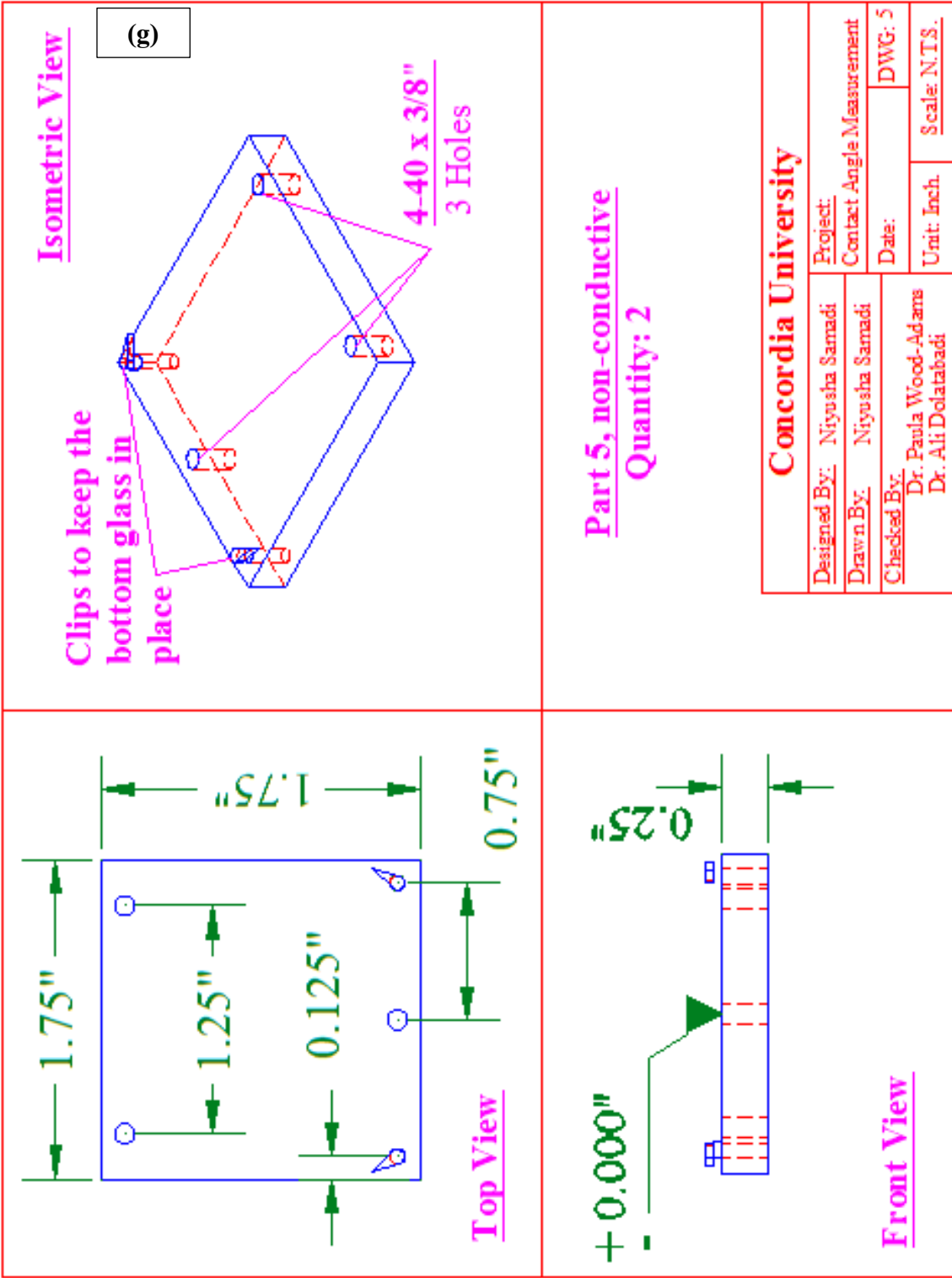


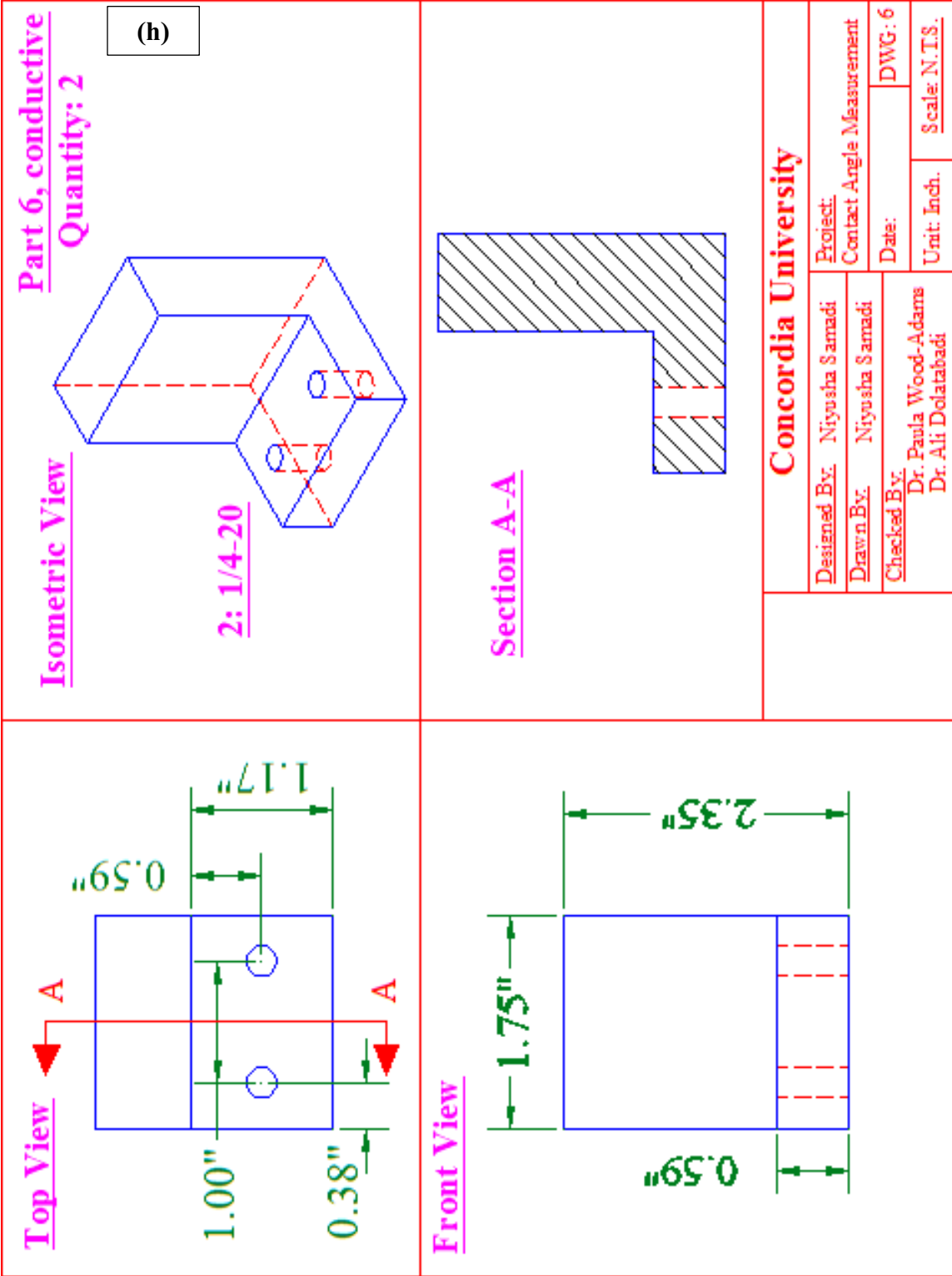
Top View

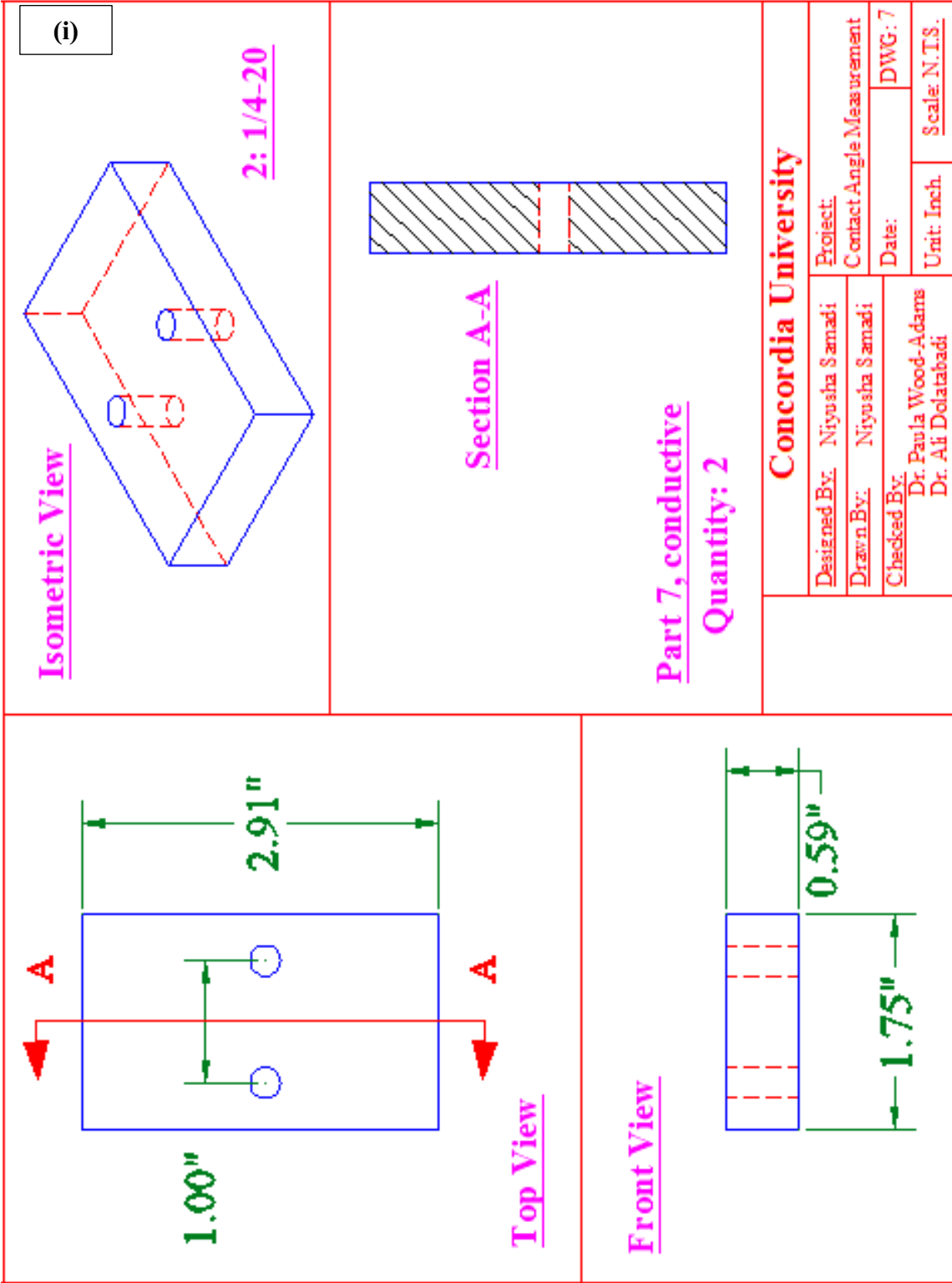
Front View











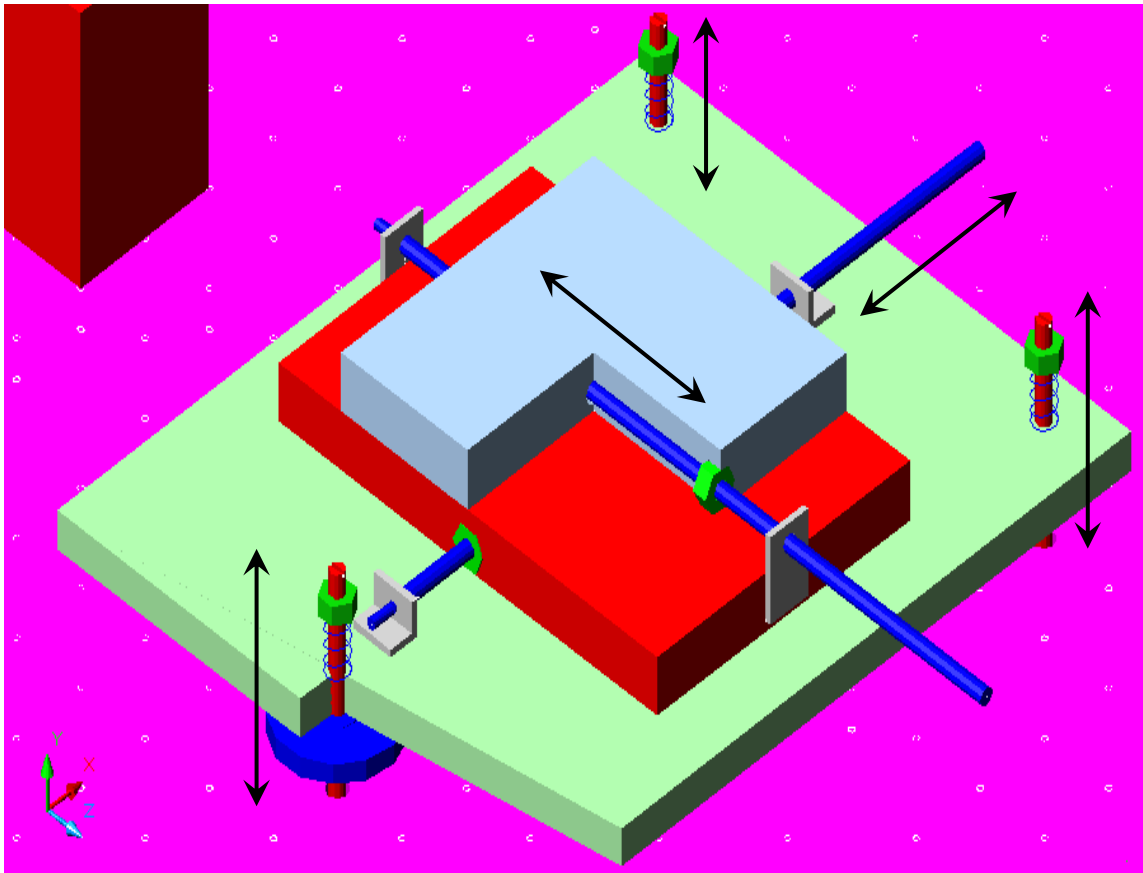


Figure A-2: Design detail – camera support

Appendix B

Programming, details of the controller system

Table B-1: Electrode sequencing control program written for Arduino Nano microcontroller with 10 outputs

```
/*  
  
*/  
int Button=12;  
const int delay_time =1000;  
void setup() {  
    // initialize the digital pin as an output.  
    // Pin 13 has an LED connected on most Arduino boards:  
  
    pinMode(2, OUTPUT);//to chaser out1  
    pinMode(3, OUTPUT);//to chaser out2  
    pinMode(4, OUTPUT);//to chaser out3  
    pinMode(5, OUTPUT);//to chaser out4  
    pinMode(6, OUTPUT);//to chaser out5  
    pinMode(7, OUTPUT);//to chaser out6  
    pinMode(8, OUTPUT);//to chaser out7  
    pinMode(9, OUTPUT);//to chaser out8  
    pinMode(10,OUTPUT);//to chaser out9  
    pinMode(11,OUTPUT);//to chaser out10  
    pinMode(12,INPUT);//to chaser from button  
    pinMode(13,OUTPUT);//to indicate the change in the output
```

```

}

void loop()
{
  if (digitalRead(Button) == LOW)

  {
    //chaser out1
    digitalWrite(13, HIGH);
    //outled 1
    digitalWrite(2, HIGH); // set the LED on
    delay(delay_time) ;    // wait for 1000 ms
    digitalWrite(2, LOW) ; // set the LED off

    digitalWrite(3, HIGH);
    delay(delay_time);
    digitalWrite(3, LOW) ;

    digitalWrite(4, HIGH);
    delay(delay_time);
    digitalWrite(4, LOW) ;

    digitalWrite(5, HIGH);
    delay(delay_time);
    digitalWrite(5, LOW) ;
  }
}

```

```
digitalWrite(6, HIGH);  
delay(delay_time);  
digitalWrite(6, LOW) ;
```

```
digitalWrite(7, HIGH);  
delay(delay_time);  
digitalWrite(7, LOW) ;
```

```
digitalWrite(8, HIGH);  
delay(delay_time);  
digitalWrite(8, LOW) ;
```

```
digitalWrite(9, HIGH);  
delay(delay_time);  
digitalWrite(9, LOW) ;
```

```
digitalWrite(10, HIGH);  
delay(delay_time);  
digitalWrite(10, LOW) ;
```

```
digitalWrite(11, HIGH);  
delay(delay_time);  
digitalWrite(11, LOW) ;
```

```
delay(delay_time); // wait for 1000 ms
```

```
//digitalWrite(13, LOW);  
  
//delay(delay_time);  
  
//chaser return  
//digitalWrite(13, HIGH);  
  
digitalWrite(11, HIGH); // set the LED on  
delay(delay_time);      // wait for 1000 ms  
digitalWrite(11, LOW); // set the LED off  
  
digitalWrite(10, HIGH);  
delay(delay_time);  
digitalWrite(10, LOW);  
  
digitalWrite(9, HIGH);  
delay(delay_time);  
digitalWrite(9, LOW);  
  
digitalWrite(8, HIGH);  
delay(delay_time) ;  
digitalWrite(8, LOW) ;  
  
digitalWrite(7, HIGH);  
delay(delay_time) ;  
digitalWrite(7, LOW) ;
```

```
digitalWrite(6, HIGH) ;  
delay(delay_time) ;  
digitalWrite(6, LOW) ;
```

```
digitalWrite(5, HIGH);  
delay(delay_time) ;  
digitalWrite(5, LOW) ;
```

```
digitalWrite(4, HIGH);  
delay(delay_time) ;  
digitalWrite(4, LOW) ;
```

```
digitalWrite(3, HIGH);  
delay(delay_time) ;  
digitalWrite(3, LOW) ;
```

```
digitalWrite(2, HIGH);  
delay(delay_time) ;  
digitalWrite(2, LOW) ;  
digitalWrite(13, LOW);
```

```
delay(delay_time); // wait for 1000 ms
```

```
}
```

```
}
```

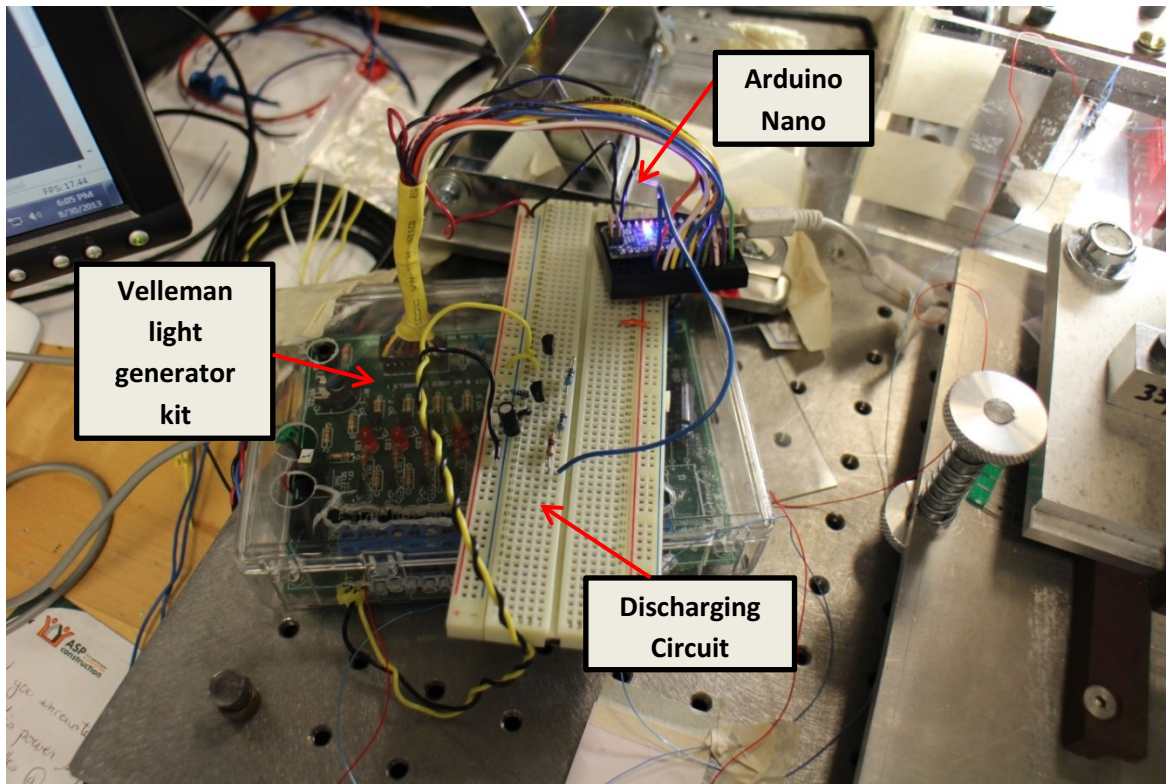


Figure B-1: The controller system

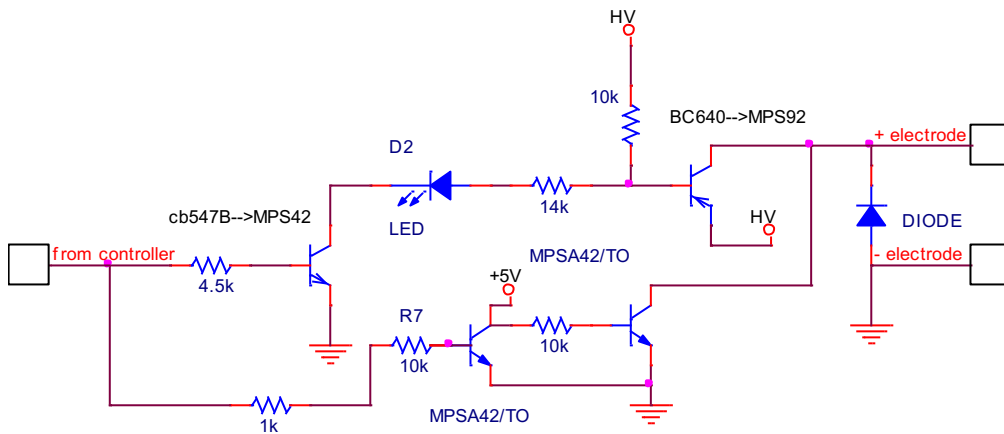


Figure B-2: Detail of the discharging circuit

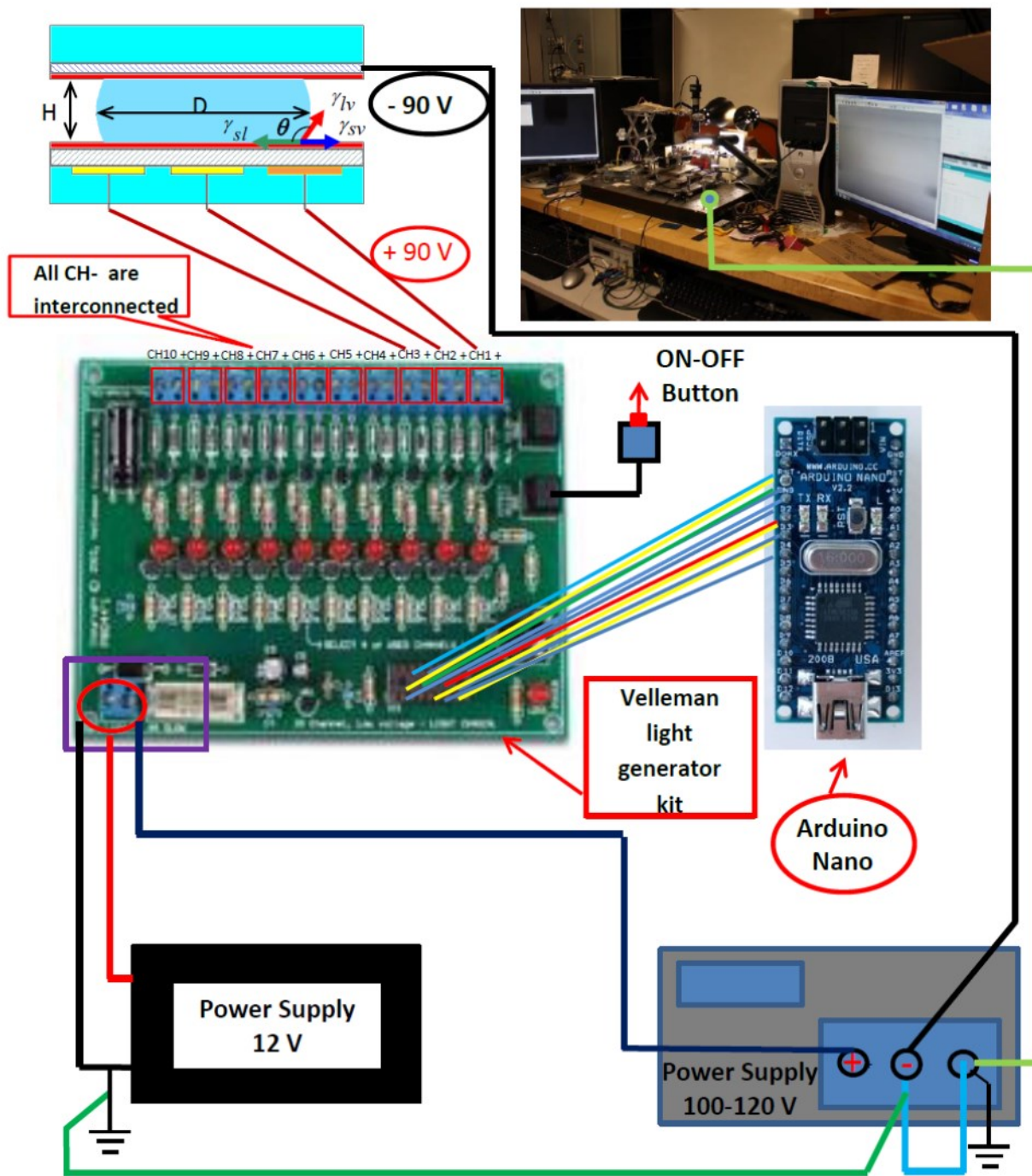


Figure B-3: The diagram of the controller system and its connections to the other components in the experimental set-up.

Appendix C

Preparation of the buffer solution containing 10 mM (Tris-HCl) with pH = 7.9, 50 mM NaCl, 50 mM KCl, 5 mM MgCl₂, 15 µg/ml BSA, and 0.1 mM EDTA

(With Special Thanks to Nithya Subramanian)

1) Preparation of 10 mM Tris:

Molecular weight of Tris = 121.135 g/mol

Therefore:

$$10 \text{ mM} = 10 \times 10^{-3} \text{ M} = 10 \times 10^{-3} \times 121.135 \text{ g/mol} = 1.2114 \text{ g}$$

This 1.2114 gr should be dissolved in 1000 ml of water, but we are adding much more things like HCl and EDTA, so this 1.2114 gr of Tris will be dissolved in 350 ml of distilled water (almost 1/3 of total Volume) and will be kept aside.

2) Preparation of 1 M HCl:

What we prepare will exactly depend on what we are starting with. Typically, we will start with a stock solution of more concentrated HCl which we will then dilute.

Concentrated solution of HCl is usually = 37.5 % (36-38.5 %)

Density of concentrated solution of HCl = 1.189 g/ml (~ 1.19 g/ml)

$$\left\{ \begin{array}{ll} 37.5 \text{ ml HCl} & 100 \text{ ml solution} \\ X & 1000 \text{ ml solution (water + HCl)} \end{array} \right.$$

Therefore: $X = 375 \text{ ml HCl} / 1000 \text{ ml solution}$

$$m = \rho \cdot v = 1.189 \text{ g/ml HCl} \times 375 \text{ ml HCl} / 1000 \text{ ml solution}$$
$$= 445.875 \text{ g HCl} / 1000 \text{ ml solution}$$

{	1M	36.46 g HCl / 1000 ml solution
	X	445.875 g HCl / 1000 ml solution

Therefore: $X = 12.229 \text{ M}$

So, the molarity of concentrated Solution = 12.229 M

For reaching 1 M HCl = 1 mole of HCl in 1000 ml of solution:

- Equation 1: moles of solute = Molarity * Liters of Solution
- Equation 2: liters of solution = moles of Solute / molarity

So, if we want to have 1 M HCl:

Then the liters of concentrated solution = $1/12.229 = 0.0818 \text{ lit.}$

$$= 81.8 \text{ ml of concentrated solution} \sim 82 \text{ ml}$$

This 81.8 ml of concentrated HCl solution will be taken from the stock and will be added to distilled water with the final volume of 1000 ml (total volume).

This prepared solution of 1M HCl will be kept in a separate flask as a stock solution.

3) Preparation of 10 mM Tris-HCl:

The 1 M HCl solution will be added (drop by drop) to the previously prepared 350 ml solution of (Tris + distilled water). HCl should be added drop by drop, stirred till reaching steady-state, and measuring pH with pH meter, it should be showing pH = 7.9.

Now, this prepared Tris-HCl Buffer solution (pH = 7.9) is ready and could be stored.

4) Preparation of 0.1 mM EDTA:

Molecular weight of EDTA = 292.2 *g/mol*

Therefore:

$$0.1 \times 10^{-3} \times 292.2 \text{ g/mol} = 0.02922 \text{ g}$$

If 1 mM EDTA is desired, then:

$$1 \times 10^{-3} \times 292.2 \text{ g/mol} = 0.2922 \text{ g}$$

5) Preparation of 50 mM NaCl:

Molecular weight of NaCl = 58.44 *g/mol*

Therefore:

$$50 \times 10^{-3} \times 58.44 \text{ g/mol} = 2.922 \text{ g}$$

6) Preparation of 5 mM MgCl₂:

Molecular weight of MgCl₂ = 95.2104 *g/mol*

Therefore:

$$5 \times 10^{-3} \times 95.2104 \text{ g/mol} = 0.476 \text{ g}$$

7) Preparation of 50 mM KCl:

$$\text{Molecular weight of KCl} = 74.551 \text{ g/mol}$$

Therefore:

$$50 \times 10^{-3} \times 74.551 \text{ g/mol} = 3.727 \text{ g}$$

8) Now, all of these materials will be added to the 350 ml of the prepared solution of Tris + HCl + Water (the volume is more than 350 ml as we added HCl drop by drop to keep its pH = 7.9).

9) Then, at the last step, in a 1 liter volumetric flask add distilled water until reaching to the volume of 1000 ml.

10) We have a buffer solution ready to be stored (1000 ml).

Appendix D

Sessile and Sandwiched droplets

Sessile Droplets:

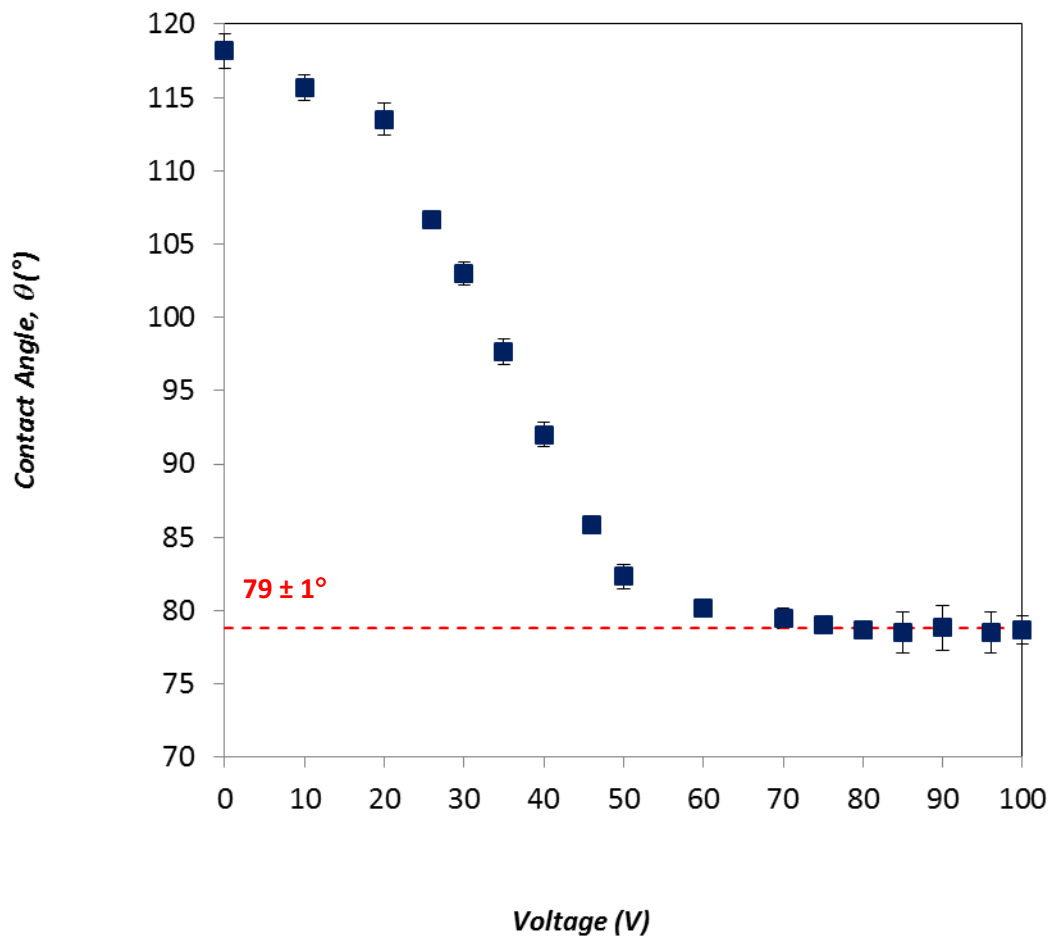


Figure D-1: The contact angle (θ) as a function of voltage for sessile droplets of Tris-HCl buffer solution with an average volume of $1.32 \pm 0.05 \mu\text{l}$. The saturation contact angle is shown on the graph (dashed line), and the error bars on the graph indicate standard deviation. Error bars are smaller than symbols in all cases where not visible.

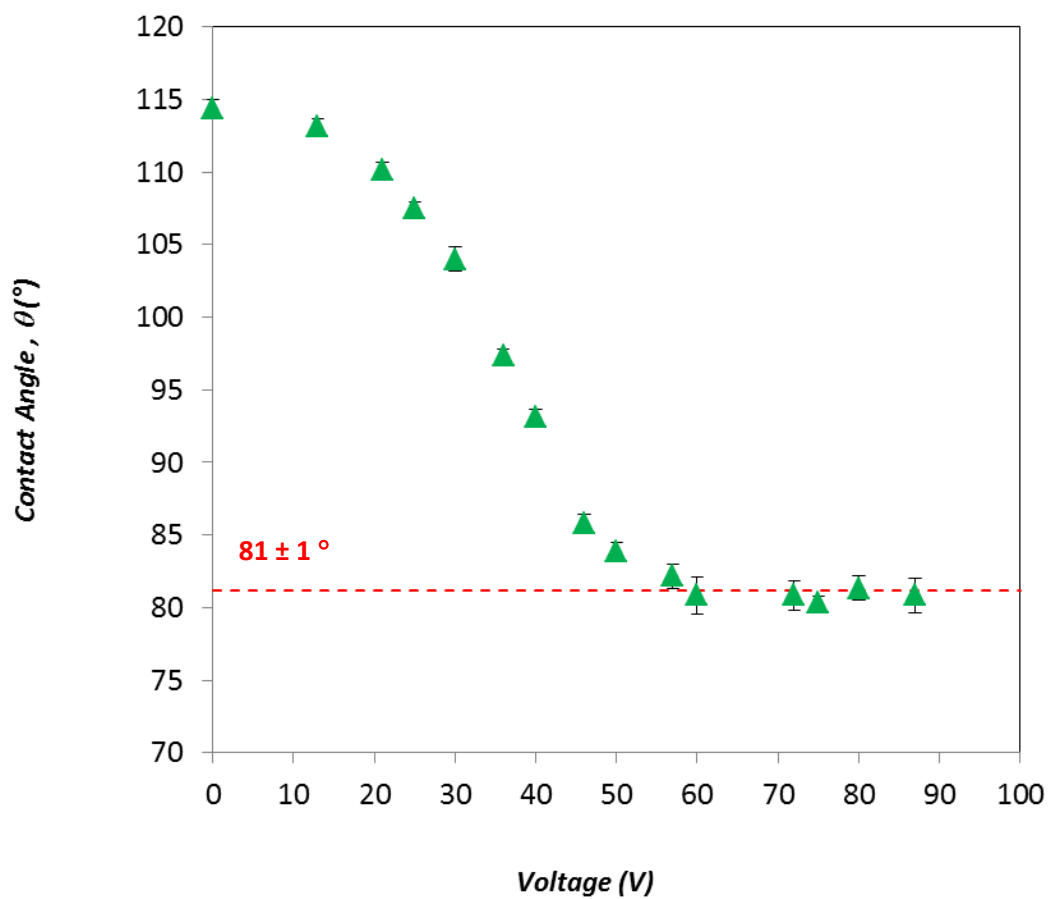


Figure D-2: The contact angle (θ) as a function of voltage for sessile droplets of 8 $\mu\text{g/ml}$ DNA solution with an average volume of $1.35 \pm 0.01 \mu\text{l}$. The saturation contact angle is shown on the graph (dashed line), and the error bars on the graph indicate standard deviation. Error bars are smaller than symbols in all cases where not visible.

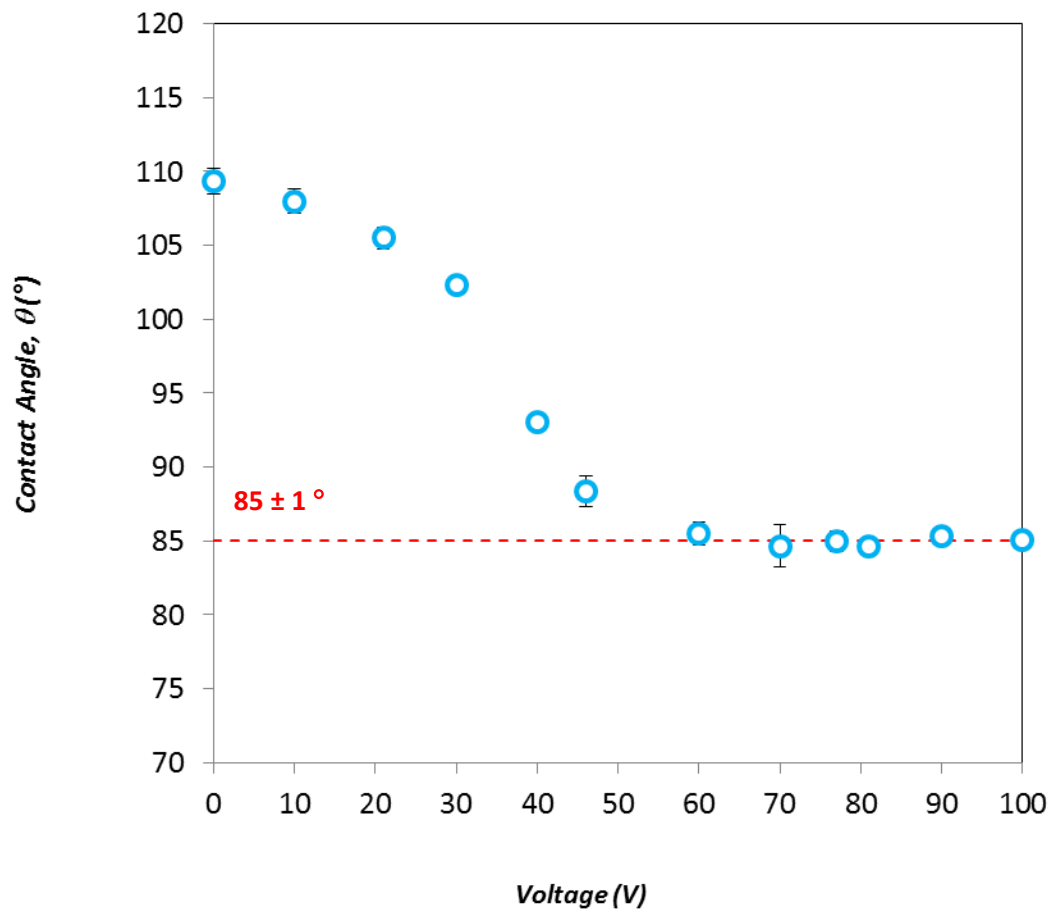


Figure D-3: The contact angle (θ) as a function of voltage for sessile droplets of 350 $\mu\text{g/ml}$ DNA in solution with an average volume of $1.37 \pm 0.05 \mu\text{l}$. The saturation contact angle is shown on the graph (dashed line), and the error bars indicate standard deviation. Error bars are smaller than symbols in all cases where not visible.

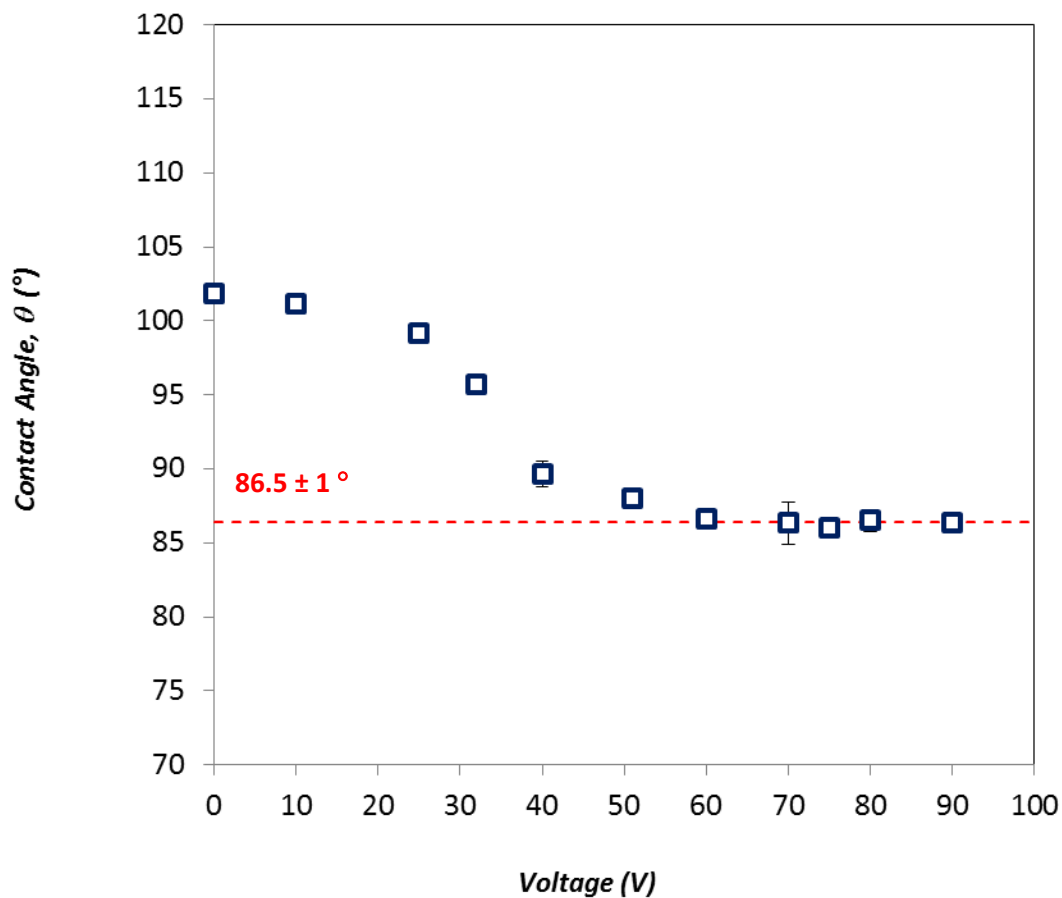


Figure D-4: The contact angle (θ) as a function of voltage for sessile droplets of 1000 $\mu\text{g/ml}$ DNA in solution with an average volume of $1.37 \pm 0.01 \mu\text{l}$. The saturation contact angle is shown on the graph (dashed line), and the error bars on the graph indicate standard deviation. Error bars are smaller than symbols in all cases where not visible.

Sandwiched Droplets (Gap of 600 μm)

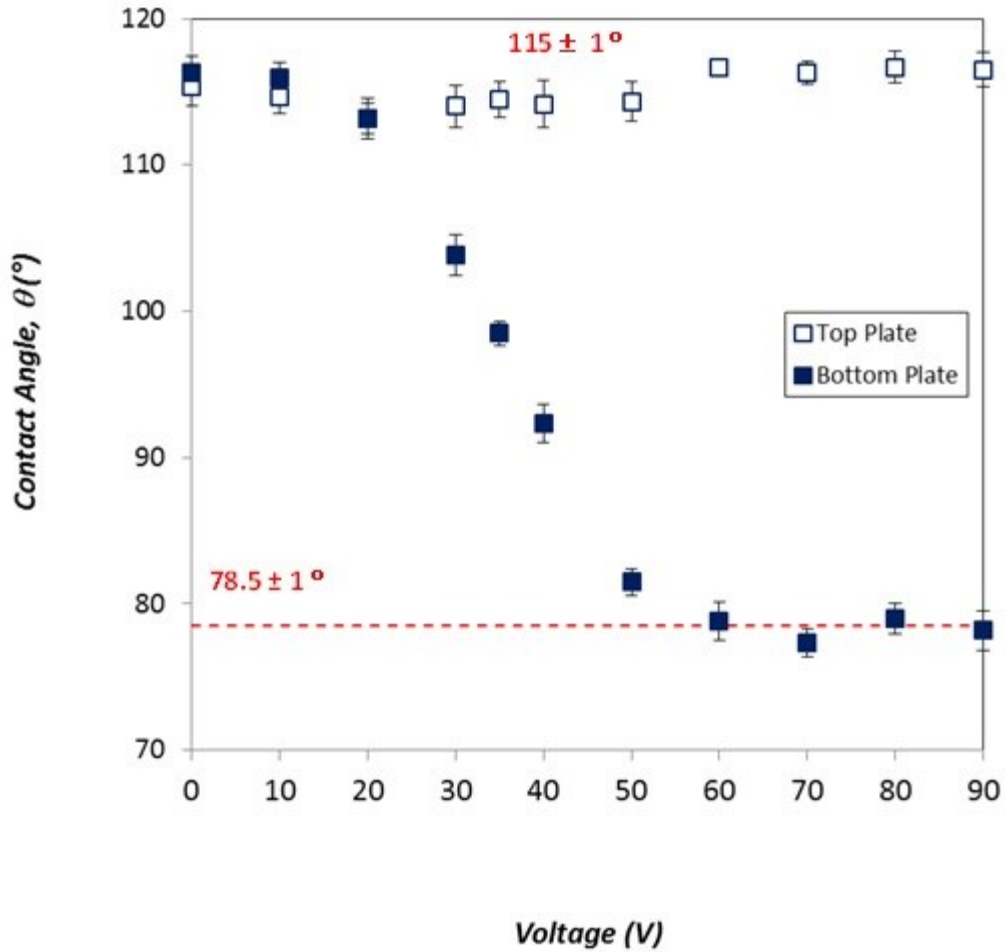


Figure D-5: The contact angle (θ) as a function of voltage for sandwiched droplets of Tris-HCl buffer solution with an average volume of $1.49 \pm 0.02 \mu\text{l}$ in a microchannel gap of $610 \pm 2 \mu\text{m}$ at the top and bottom interfaces. The saturation contact angle is shown on the graph (dashed line), and the error bars indicate standard deviation. Error bars are smaller than symbols in all cases where not visible.

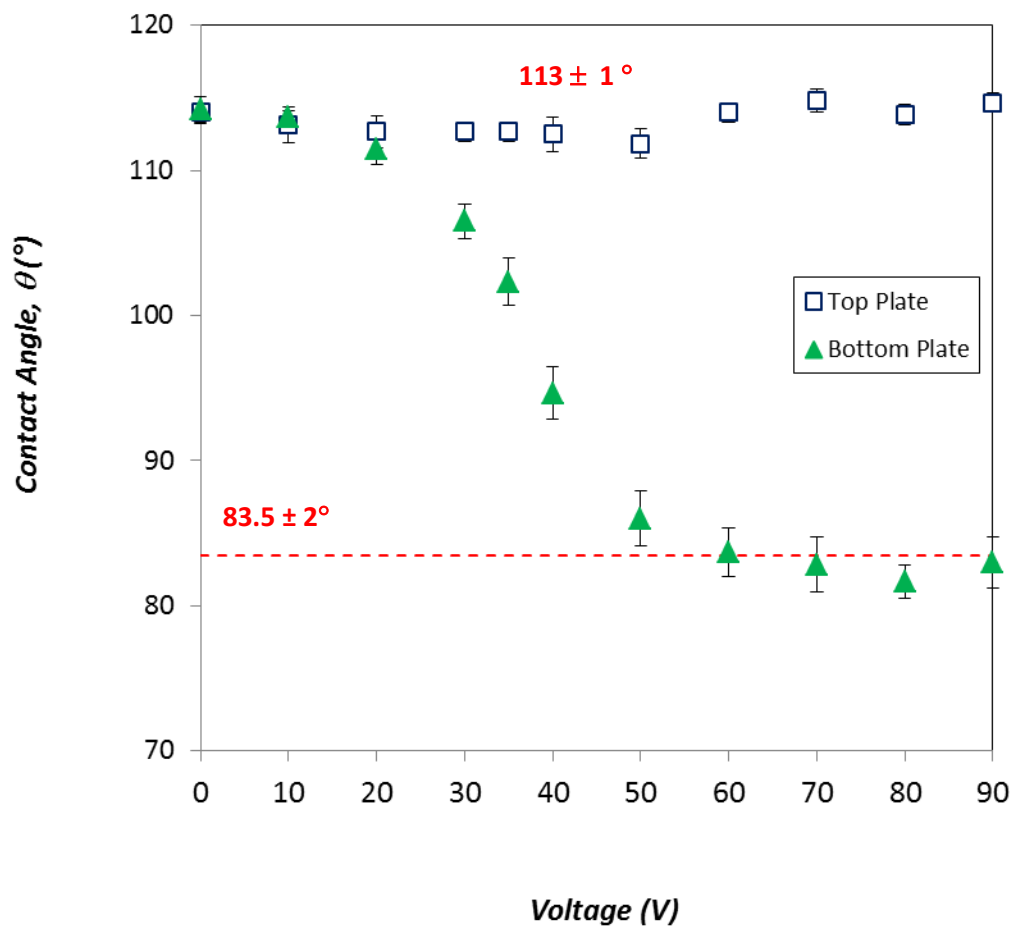


Figure D-6: The contact angle (θ) as a function of voltage for sandwiched droplets of $8 \mu\text{g/ml}$ DNA solution with an average volume of $1.54 \pm 0.06 \mu\text{l}$ in a microchannel gap of $602 \pm 2 \mu\text{m}$ at the top and bottom interfaces. The saturation contact angle is shown on the graph (dashed line), and the error bars indicate standard deviation. Error bars are smaller than symbols in all cases where not visible.

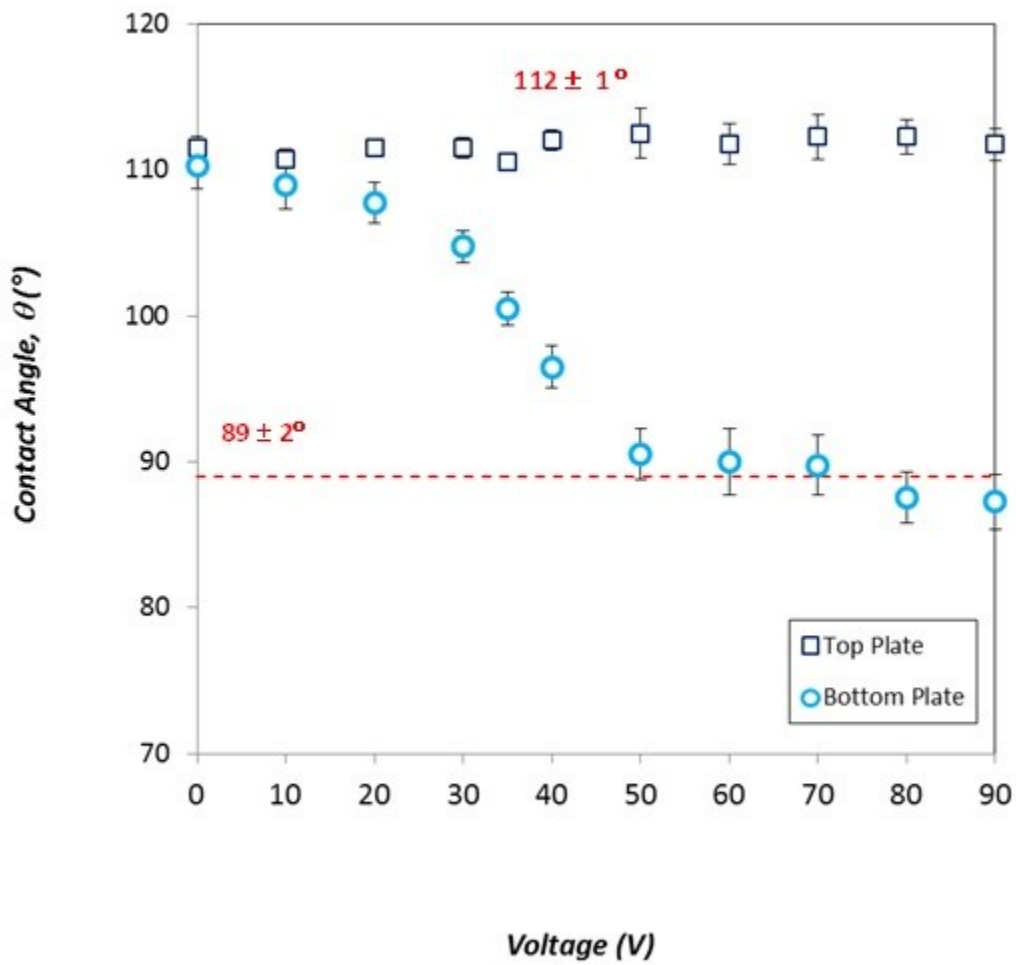


Figure D-7: The contact angle (θ) as a function of voltage for sandwiched droplets of 100 $\mu\text{g/ml}$ DNA solution with an average volume of $1.52 \pm 0.04 \mu\text{l}$ in a microchannel gap of $607 \pm 3 \mu\text{m}$ at the top and bottom interfaces. The saturation contact angle is shown on the graph (dashed line), and the error bars indicate standard deviation. Error bars are smaller than symbols in all cases where not visible.

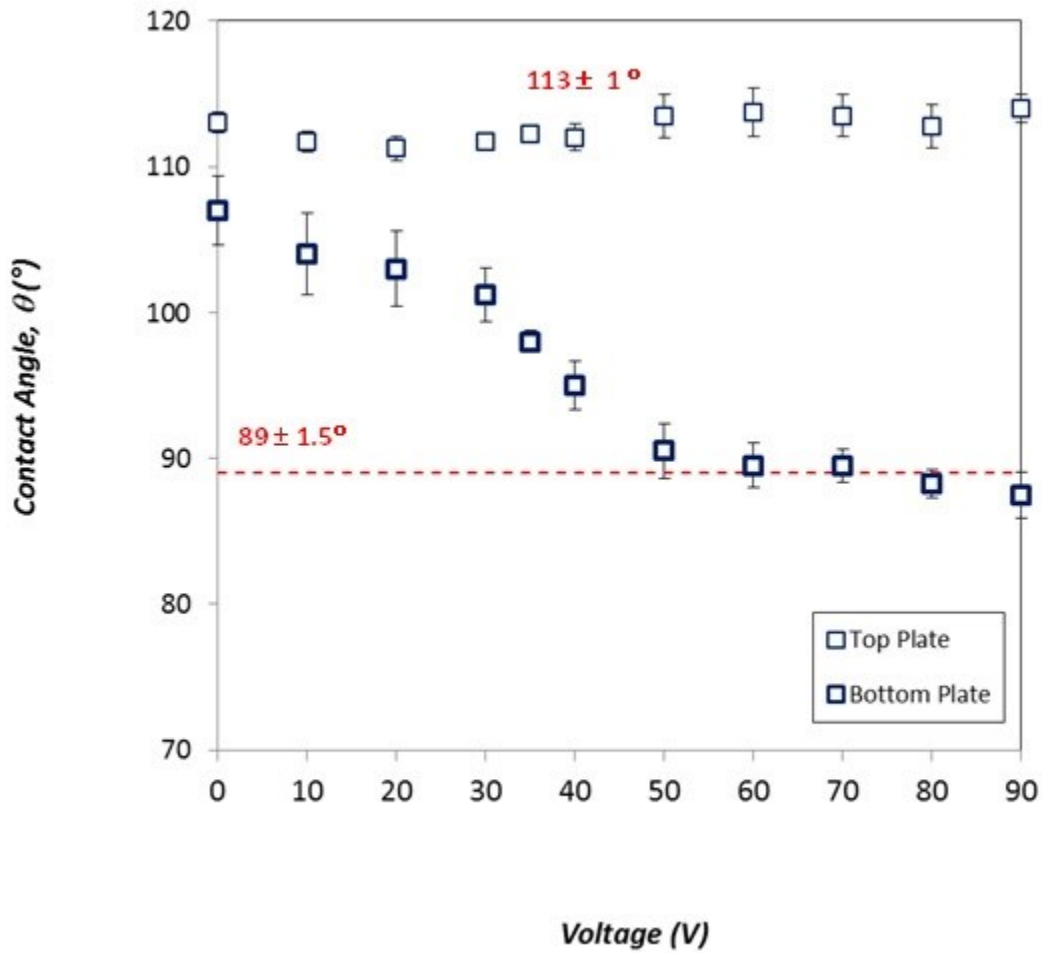


Figure D-8: The contact angle (θ) as a function of voltage for sandwiched droplets of 150 $\mu\text{g/ml}$ DNA solution with an average volume of $1.49 \pm 0.01 \mu\text{l}$ in a microchannel gap of $609 \pm 2 \mu\text{m}$ at the top and bottom interfaces. The saturation contact angle is shown on the graph (dashed line), and the error bars indicate standard deviation. Error bars are smaller than symbols in all cases where not visible.

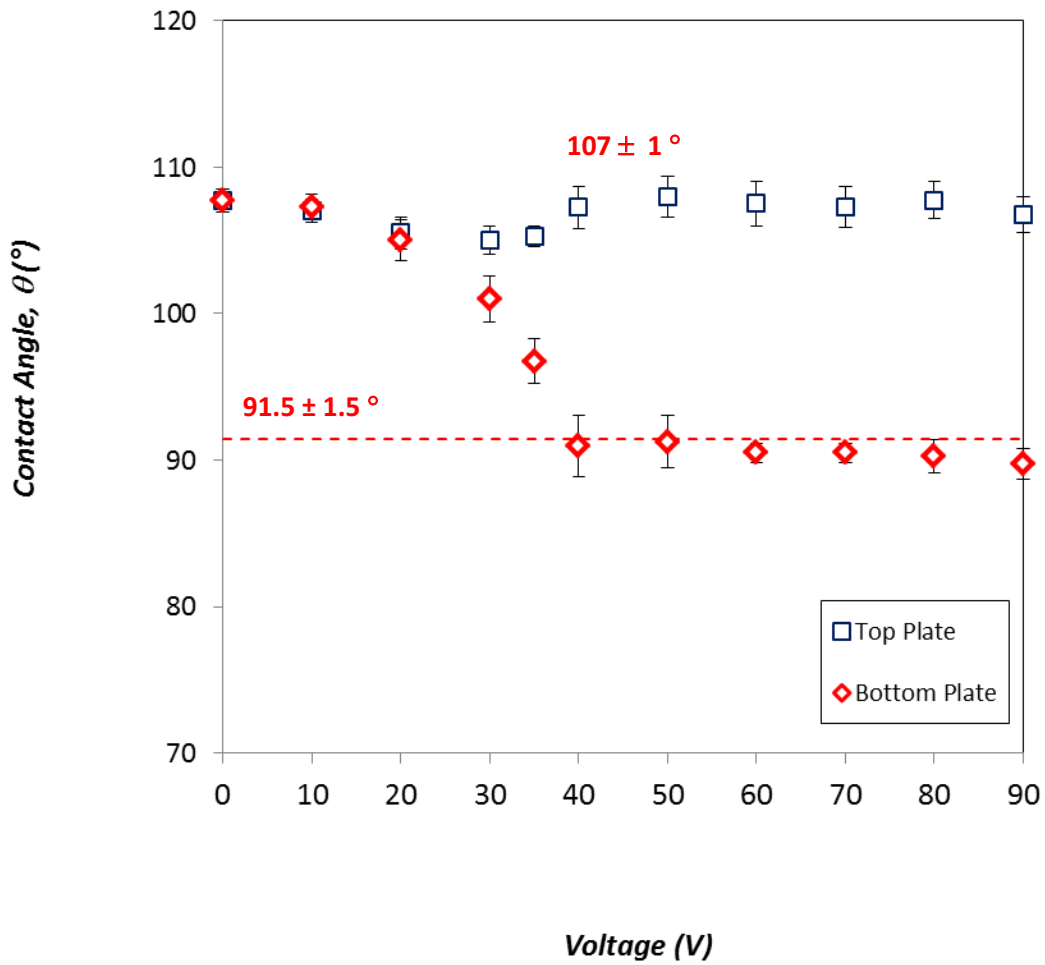


Figure D-9: The contact angle (θ) as a function of voltage for sandwiched droplets of 350 $\mu\text{g/ml}$ DNA solution with an average volume of $1.52 \pm 0.02 \mu\text{l}$ in a microchannel gap of $610 \pm 1 \mu\text{m}$ at the top and bottom interfaces. The saturation contact angle is shown on the graph (dashed line), and the error bars indicate standard deviation. Error bars are smaller than symbols in all cases where not visible.

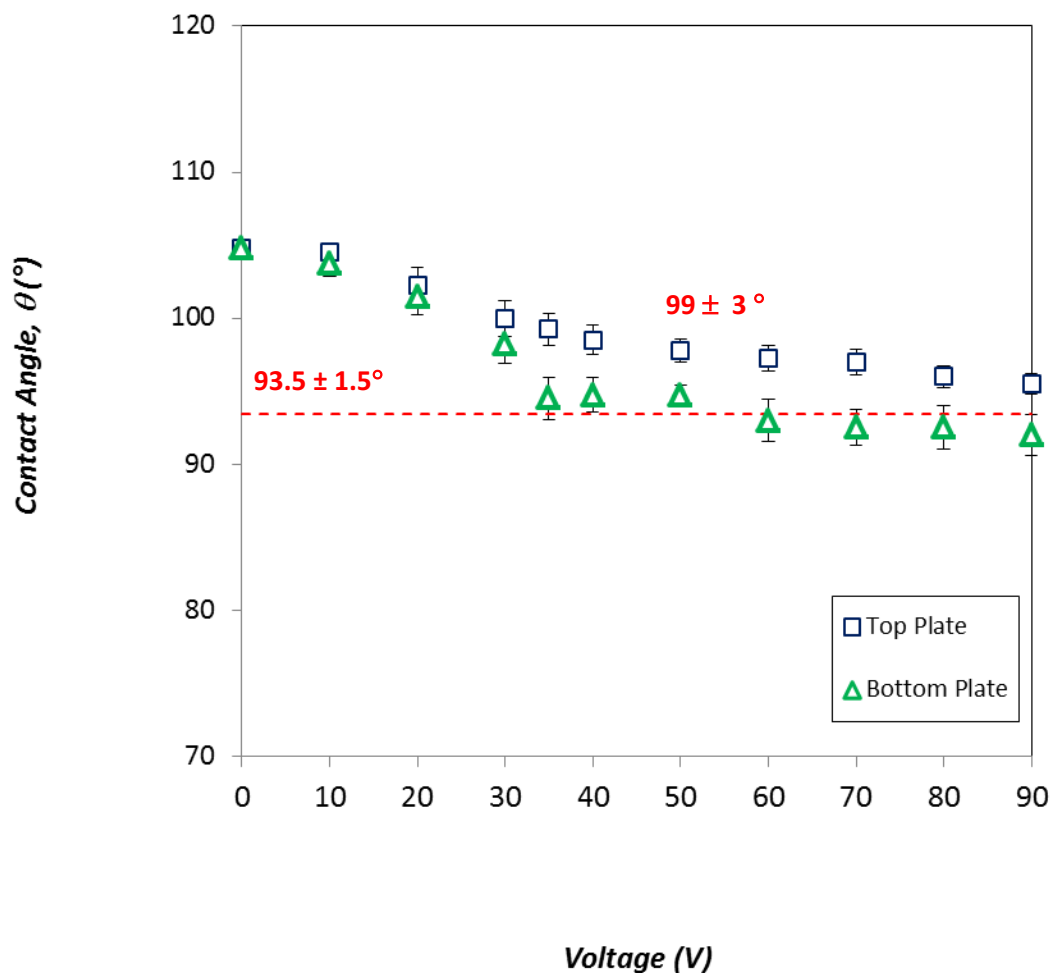


Figure D-10: The contact angle (θ) as a function of voltage for sandwiched droplets of 1000 $\mu\text{g/ml}$ DNA solution with an average volume of $1.52 \pm 0.02 \mu\text{l}$ in a microchannel gap of $596 \pm 5 \mu\text{m}$ at the top and bottom interfaces. The saturation contact angle is shown on the graph (dashed line), and the error bars indicate standard deviation. Error bars are smaller than symbols in all cases where not visible.

Sandwiched Droplets (Gap of 300 μm)

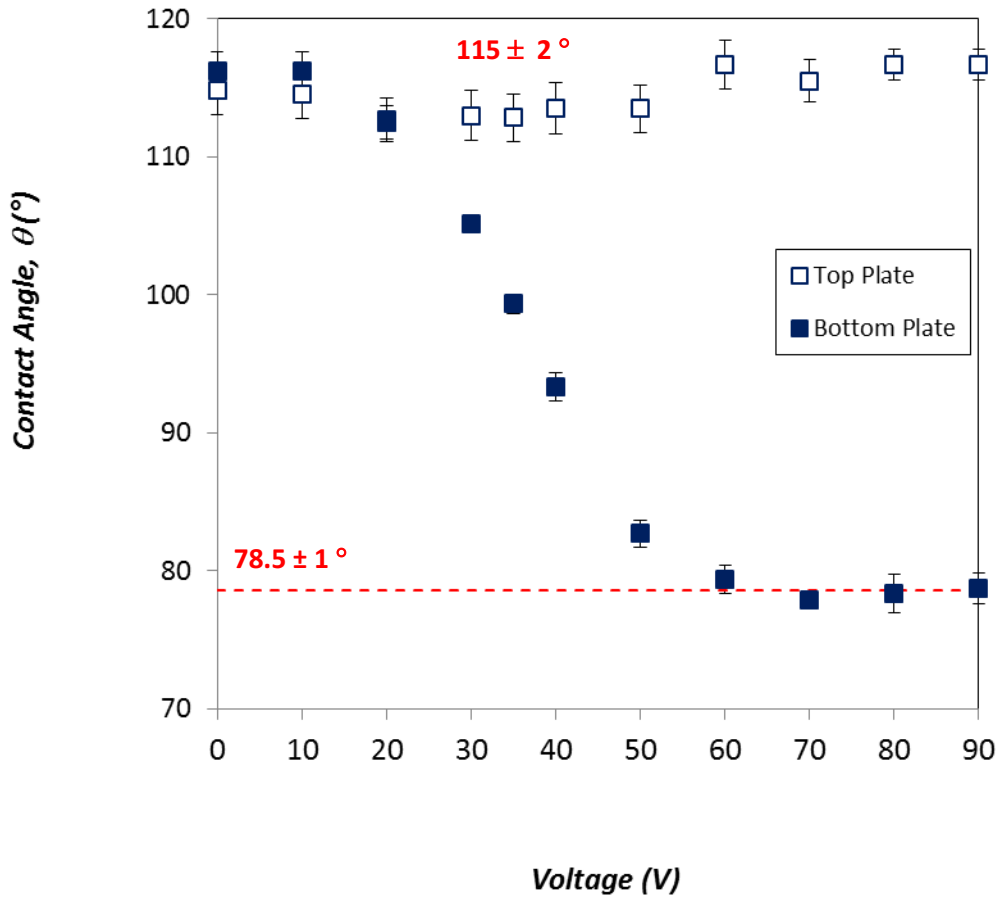


Figure D-11: The contact angle (θ) as a function of voltage for sandwiched droplets of Tris-HCl buffer solution with an average volume of $0.85 \pm 0.04 \mu\text{l}$ in a microchannel gap of $308 \pm 5 \mu\text{m}$ at the top and bottom interfaces. The saturation contact angle is shown on the graph (dashed line), and the error bars indicate standard deviation. Error bars are smaller than symbols in all cases where not visible.

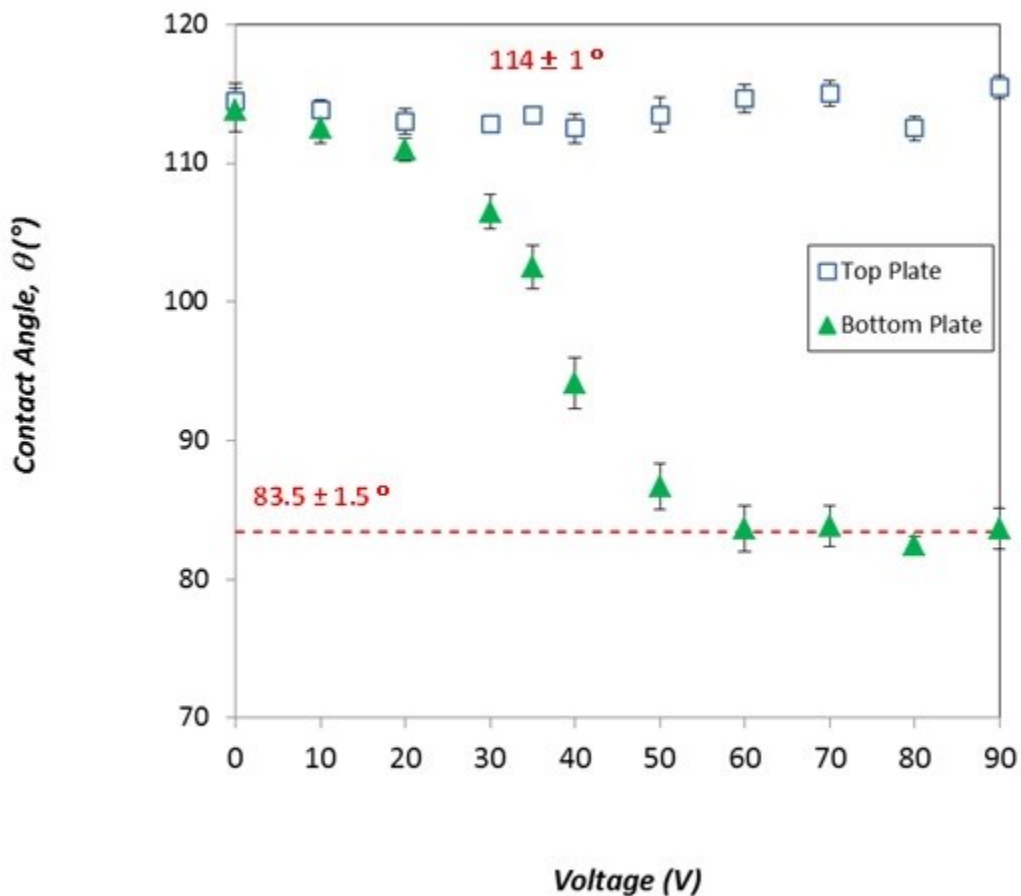


Figure D-12: The contact angle (θ) as a function of voltage for sandwiched droplets of 8 $\mu\text{g}/\text{ml}$ DNA solution with an average volume of $0.91 \pm 0.04 \mu\text{l}$ in a microchannel gap of $302 \pm 3 \mu\text{m}$ at the top and bottom interfaces. The saturation contact angle is shown on the graph (dashed line), and the error bars indicate standard deviation. Error bars are smaller than symbols in all cases where not visible.

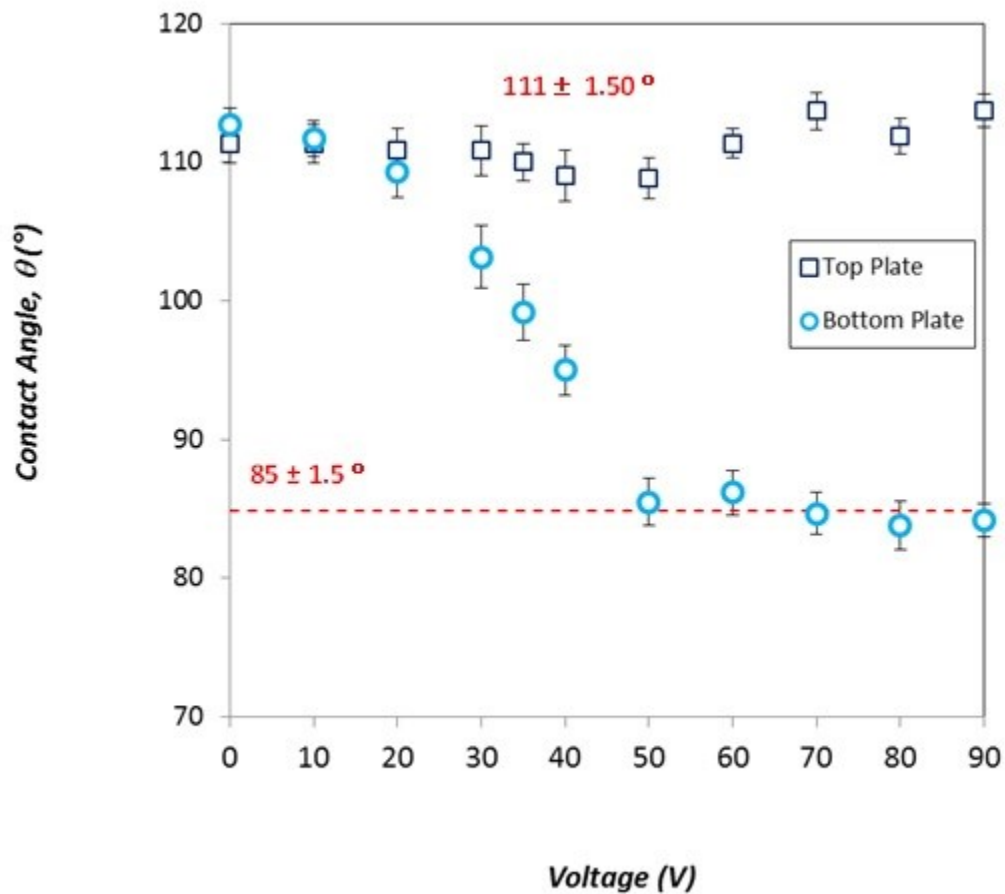


Figure D-13: The contact angle (θ) as a function of voltage for sandwiched droplets of 20 $\mu\text{g/ml}$ DNA solution with an average volume of $0.89 \pm 0.08 \mu\text{l}$ in a microchannel gap of $306 \pm 2 \mu\text{m}$ at the top and bottom interfaces. The saturation contact angle is shown on the graph (dashed line), and the error bars indicate standard deviation. Error bars are smaller than symbols in all cases where not visible.

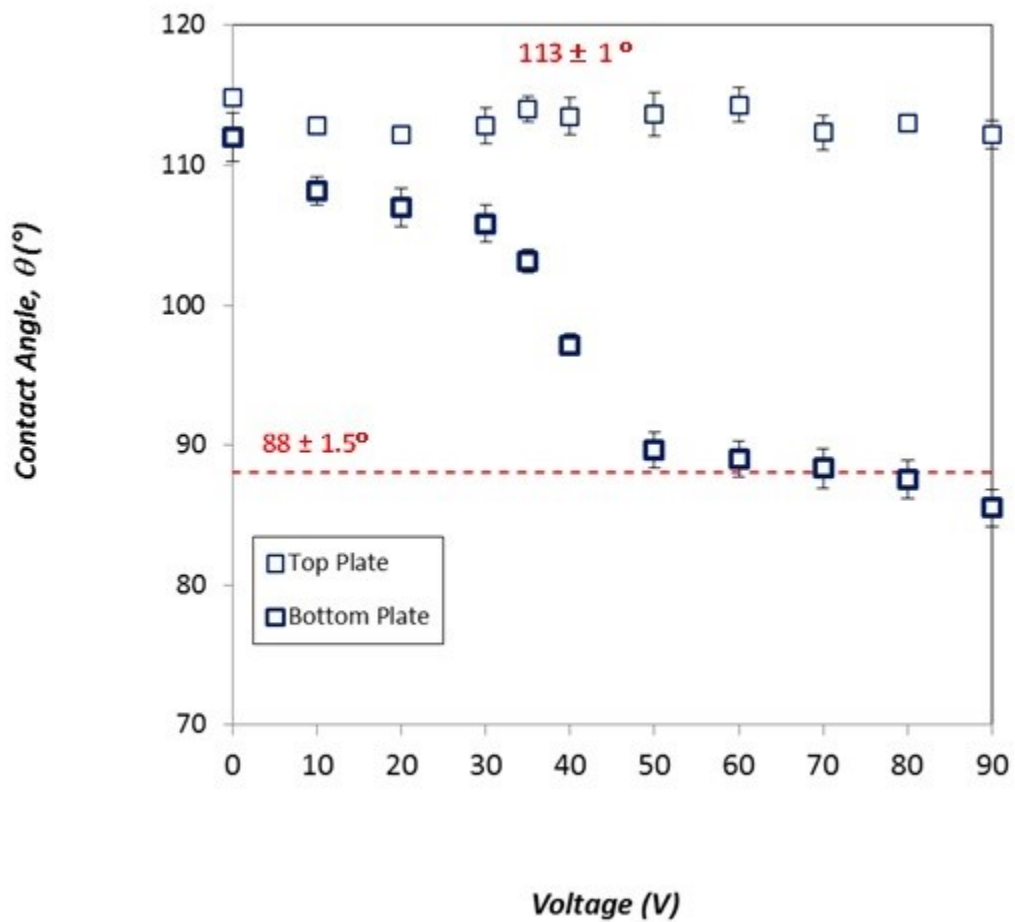


Figure D-14: The contact angle (θ) as a function of voltage for sandwiched droplets of 50 $\mu\text{g/ml}$ DNA solution with an average volume of $0.90 \pm 0.03 \mu\text{l}$ in a microchannel gap of $307 \pm 4 \mu\text{m}$ at the top and bottom interfaces. The saturation contact angle is shown on the graph (dashed line), and the error bars indicate standard deviation. Error bars are smaller than symbols in all cases where not visible.

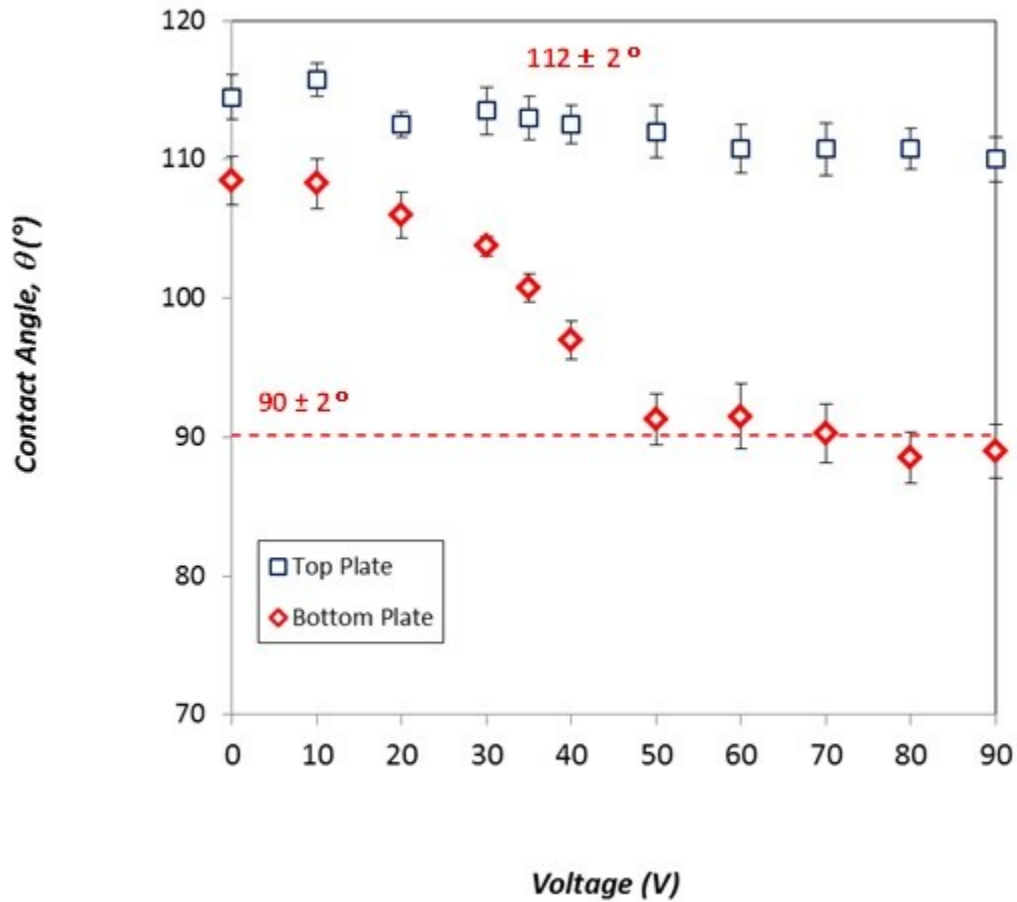


Figure D-15: The contact angle (θ) as a function of voltage for sandwiched droplets of 100 $\mu\text{g/ml}$ DNA solution with an average volume of $1.02 \pm 0.01 \mu\text{l}$ in a microchannel gap of $307 \pm 1 \mu\text{m}$ at the top and bottom interfaces. The saturation contact angle is shown on the graph (dashed line), and the error bars indicate standard deviation. Error bars are smaller than symbols in all cases where not visible.

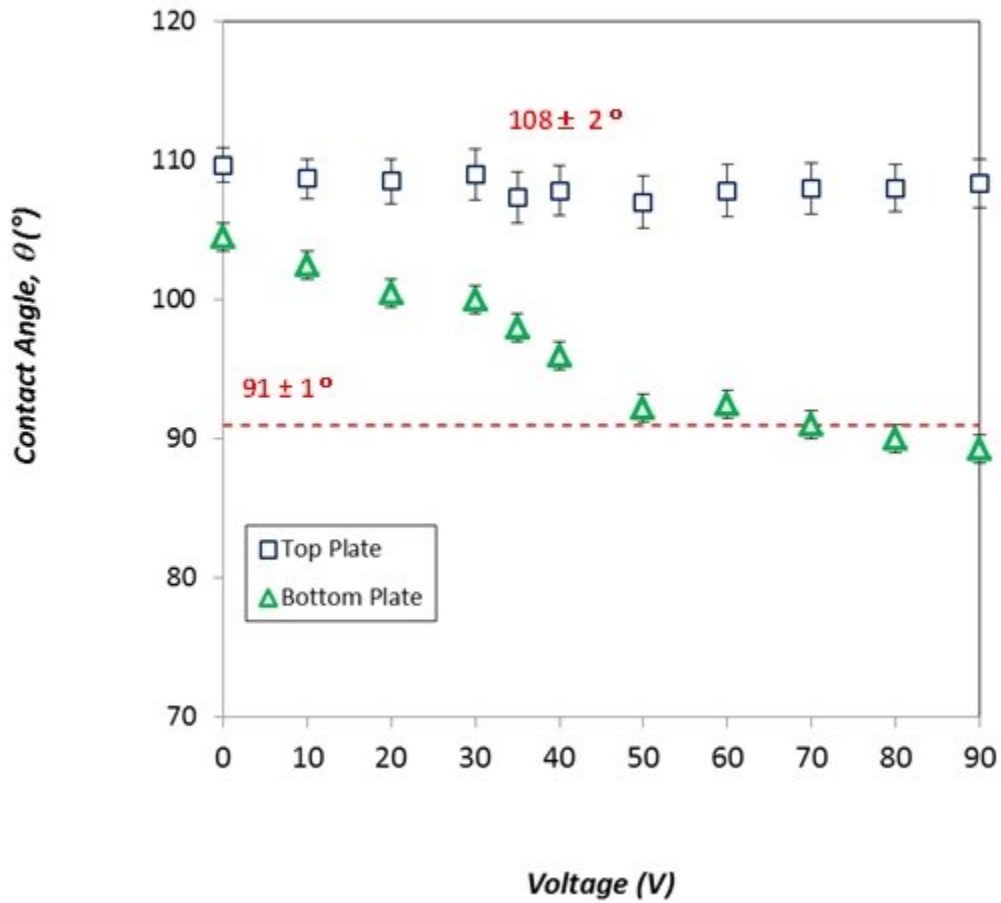


Figure D-16: The contact angle (θ) as a function of voltage for sandwiched droplets of 150 $\mu\text{g/ml}$ DNA solution with an average volume of $0.86 \pm 0.02 \mu\text{l}$ in a microchannel gap of $303 \pm 7 \mu\text{m}$ at the top and bottom interfaces. The saturation contact angle is shown on the graph (dashed line), and the error bars indicate standard deviation. Error bars are smaller than symbols in all cases where not visible.

Appendix E

DNA Adsorption

One of the issues investigated in this research was the effect of passive biomolecular adsorption or biofouling. The importance of this matter can be clearly understood from the studies done by Castner *et al*ⁱ. and also Yoon and Garrellⁱⁱ. They found out that biomolecules have the tendency to adsorb unspecifically onto hydrophobic surfaces. This irreversible adsorption reduces the contact angle permanently and therefore compromises the performance of the droplet actuation. To perform this investigation, experiments were done on 8 µg/ml DNA in buffer solution (pH =7). To determine the extent of this passive adsorption, the droplets of DNA solutions with volumes ≤ 2 µl were deposited on the Teflon AF substrates and the changes of contact angle over time with no applied potential were monitored. In one experiment, the dispensed droplets were left to evaporate in air, and the other time, the humidity chamber was used. In both cases, the concentration of DNA solution was 8 µg/ml. The last experiment was done on DNA solutions with the concentration of 1000 µg/ml.

Due to mass transfer, the contact angle of a sessile droplet deposited on a solid surface changes with evaporation. Typically, the global shape evolution of a sessile drop (drop base diameter, height, and contact angle) under saturated conditions has four distinct stagesⁱⁱⁱ. In stage 1, the contact diameter remains constant, whilst the drop height and contact angle decline slightly. In stage 2, the contact diameter remains initially constant, but the drop height

ⁱ D. G. Castner, B.D. Ratner, “Biomedical surface science: Foundations to frontiers”, *Surf. Sci.*, vol.500 (1-3), pp. 28-60, 2002.

ⁱⁱ J. Y. Yoon, R. L. Garrell, “Preventing biomolecular adsorption in electrowetting-based biofluid chips”, *Anal. Chem.*, vol. 75 (19), pp. 5097-5102, 2003.

ⁱⁱⁱ M. E. R. Shanahan, C. Bourges, “Effects of evaporation on contact angles on polymer surfaces”, *Int. J. Adhesion and Adhesives*, Vol. 14 (3), pp. 201-205, 1994.

and contact angle decrease more rapidly than the previous stage. In stage 3, both drop contact diameter and height diminish proportionally, and the contact angle stays approximately constant. In the final stage, the drop contact diameter, height and contact angle decline till the droplet completely disappears.

Cioulachjian *et al.*^{iv} investigated the drop evaporation under moist air, and reported two major stages. In stage 1, the drop contact diameter remains constant, while the drop height and contact angle decrease. This stage might last only a short period of time. The next stage, the drop diameter and height decrease progressively, and contact angle remains nearly constant for a period of time before it decreases until the drop disappears. Until the end of stage 2 (Figure E-6 to Figure E-8), our experimental conditions and the results obtained in section “Experiment 2” comply with the work done by Cioulachjian *et al.*^{iv}. Thereafter, the humidity in the chamber significantly increased (similar to a saturated atmosphere), thus, two more stages were observed. In stage 3, as the evaporation rate was very low, all the parameters (drop height, diameter, and contact angle) remained nearly constant, though the drop contact diameter and height declined to some extent. In stage 4, once more, a decreasing trend was observed in drop contact diameter, height and contact angle, most probably due to the opening of the humidity chamber and releasing the humidity to a degree. After six hours of experiment, the rate of evaporation was so slow that the experiment was not continued. The results of this experiment performed on buffer solution and 8 µg/ml DNA solution are compared in Figure E-8. In a period of time denoted as stage 2, the contact angles of DNA solution decreased in more extent which is as a good indication of DNA adsorption.

^{iv} S. Cioulachtjian, S. Launay, S. Boddaert, M. Lallemand, “Experimental investigation of water drop evaporation under moist air or saturated vapour conditions”, *Int. J. Therm. Sci.*, vol. 49 (6), pp. 859-866, 2010.

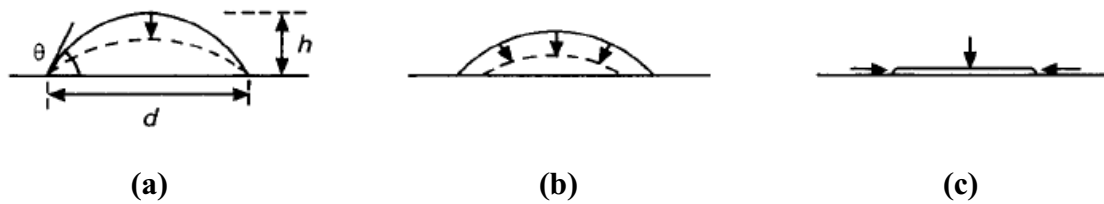


Figure E-1: The global shape evolution of a sessile drop, and the definitions of drop contact diameter d , height h and contact angle θ . (a) the contact diameter remains constant whilst the contact angle and drop height decrease, (b) the drop diameter and height decrease with no apparent change in the contact angle, (c) the contact diameter, height and contact angle decrease until the drop disappears. (Taken from Reference: *Shanahan and Bourges*ⁱⁱⁱ)

Experiment 1:

In this experiment, droplets of 8 $\mu\text{g/ml}$ DNA in buffer solution ($\text{pH} = 7$) and droplets of the same buffer solution used to dissolve DNA, are dispensed on Teflon substrates without using the humidity chamber. First, the images of both solutions are recorded simultaneously in every minute by a CCD camera over a 6 min. total time to minimize the effect of evaporation. The contact angles are then calculated in AutoCAD software (as explained in Chapter 4). At the end, the changes in contact angle are compared. It was found that the contact angle of DNA solution decreased about 55° in 6 min. comparing to 38° for buffer solution. It is a good indication of extensive passive adsorption of DNA on hydrophobic surfaces.

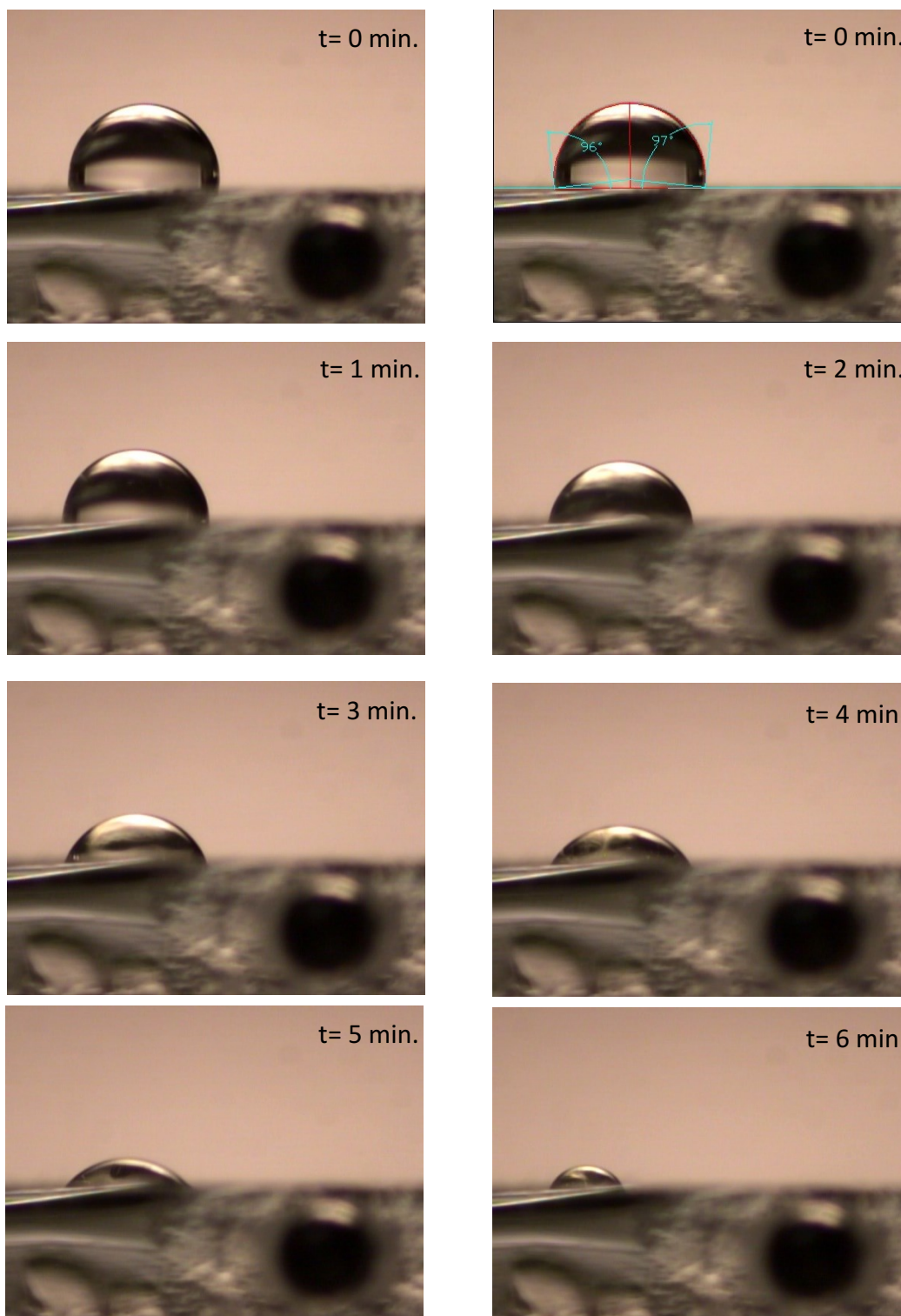


Figure E-2: Recorded images of droplets of DNA solution ($8 \mu\text{g/ml}$)

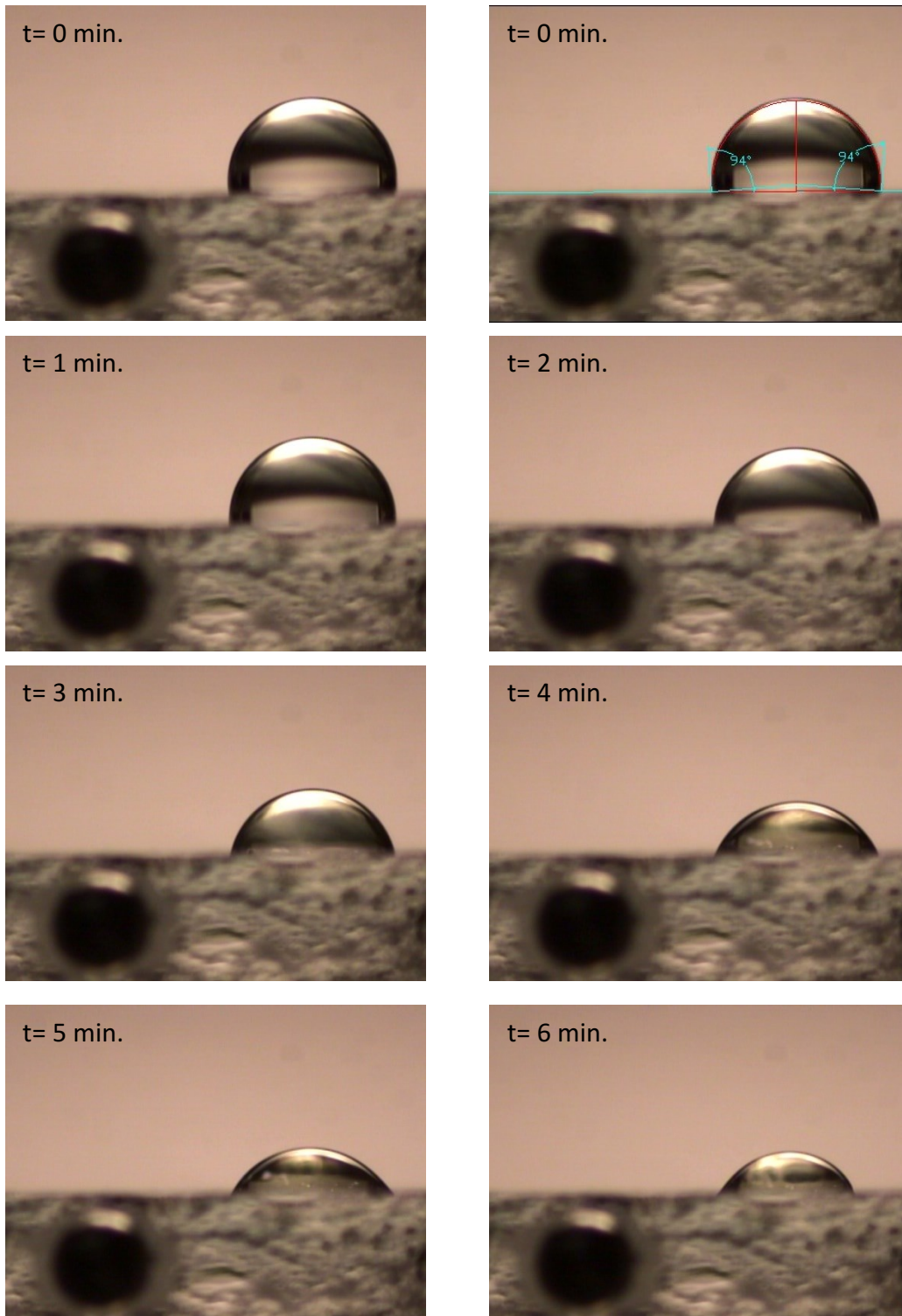


Figure E-3: Recorded images of droplets of Buffer solution

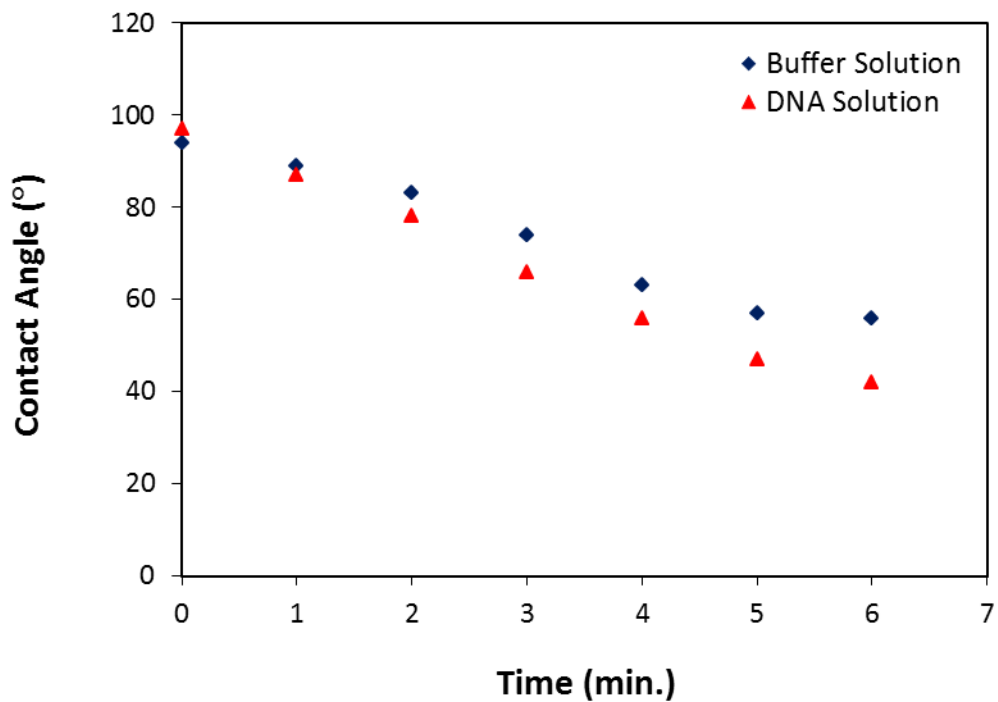


Figure E-4: Changes of contact angle with time in a passive experiment. The concentration of DNA solution is 8 $\mu\text{g/ml}$. The contact angle of DNA solution has decreased 55° in 6 min. comparing to 38° for buffer solution. The initial volume of the droplets for both solutions is around 1 μl .

Experiment 2:

In this experiment, droplets of 8 $\mu\text{g/ml}$ DNA in buffer solution ($\text{pH} = 7$) and droplets of the same buffer solution used to dissolve DNA, are dispensed on Teflon substrates in a humidity chamber. First, the images of both solutions are recorded simultaneously at every minute by a CCD camera over a 6 hour time interval. The contact angles are then calculated using AutoCAD (as explained in Chapter 4). At the end, the changes in contact angle are compared (Figure E-8). It was found that the contact angle of the DNA solution decreased about 33° in 3 hours comparing to 16° for the buffer solution. It is a good indication of extensive passive adsorption of DNA on hydrophobic surfaces. Towards the end of the experiment, the humidity nearly increased to saturation conditions; therefore, at the end of 6 hours, there were still small droplets of both solutions left.

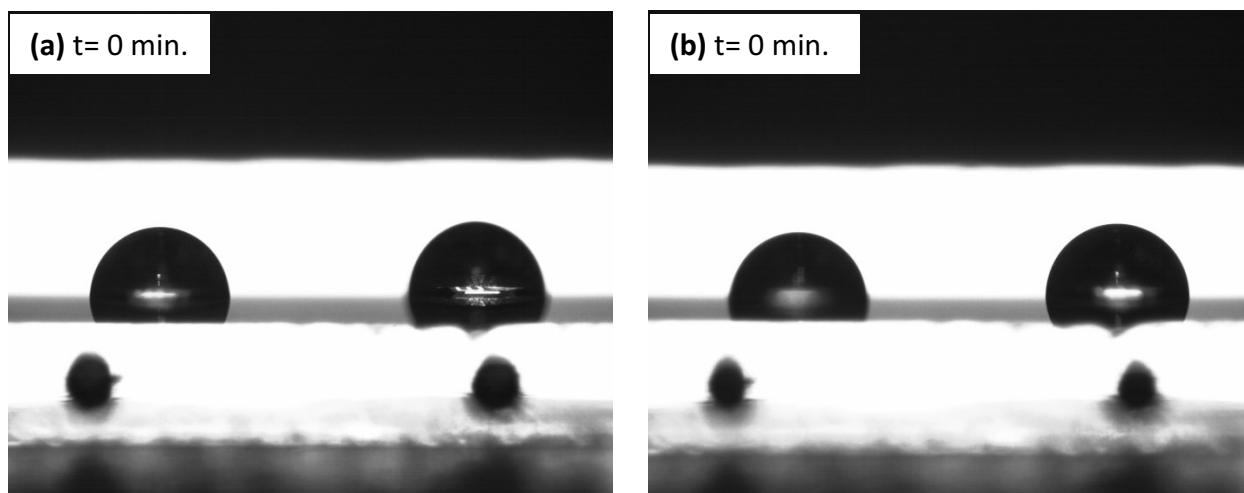


Figure E-5: Recorded images of droplets of: (a) buffer solution, (b) 8 $\mu\text{g/ml}$ DNA solution, at the beginning of the experiment. The initial volume of the droplets for both solutions is $1.35 \pm 0.05 \mu\text{l}$.

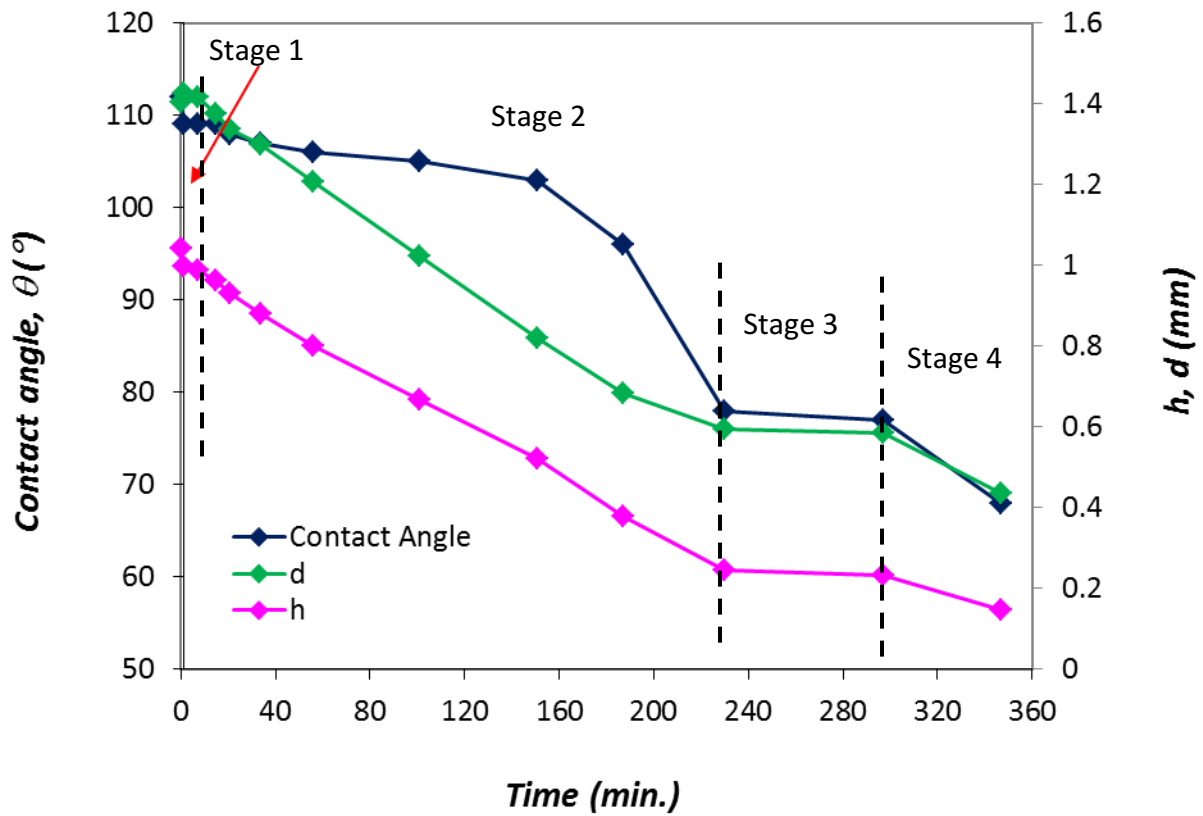


Figure E-6: Changes of contact angle θ , contact diameter d , and droplet height h , with time in a passive experiment on buffer solution. Stage 1 approximately lasts 10 minutes, whilst the major evaporation happens in stage 2. At the end of Stage 2, the drop did not evaporate significantly.

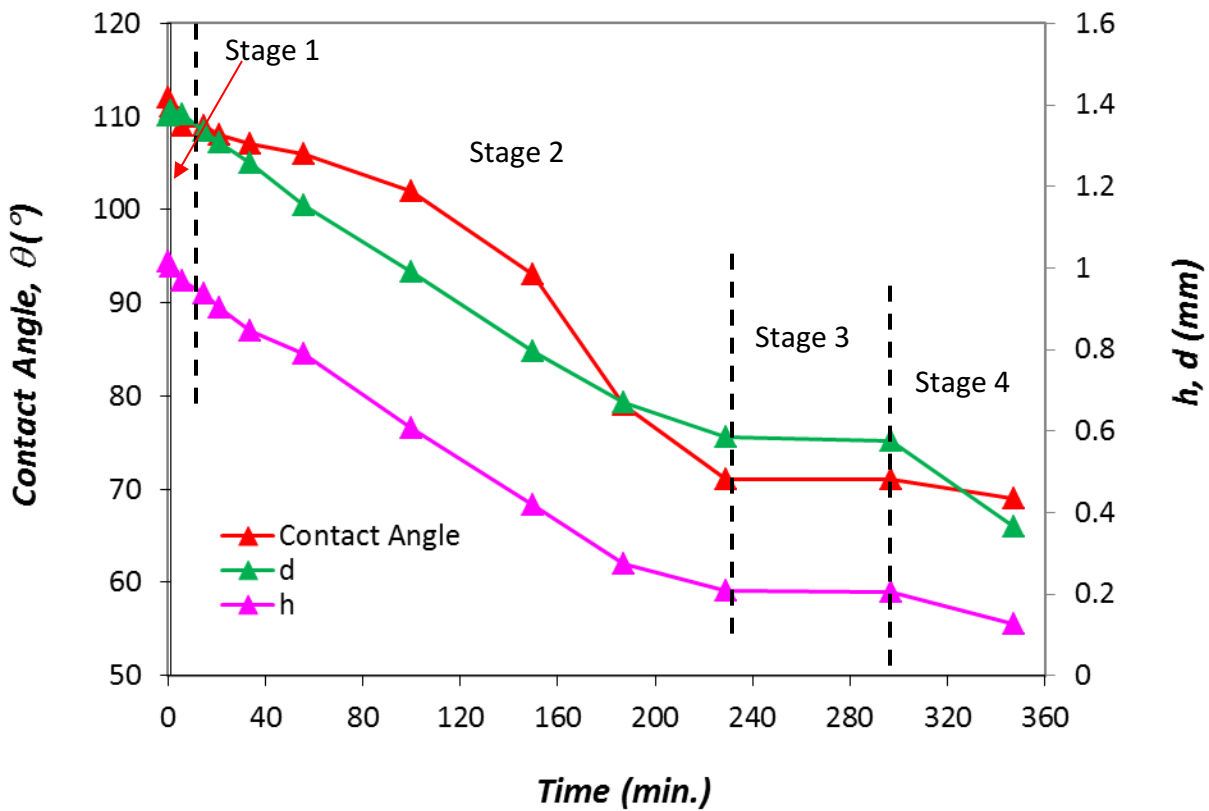


Figure E-7: Changes of contact angle θ , contact diameter d , and droplet height h , with time in a passive experiment on 8 $\mu\text{g/ml}$ DNA solution. Stage 1 approximately lasts 10 minutes, whilst the major evaporation happens in stage 2. At the end of Stage 2, the drop did not evaporate significantly.

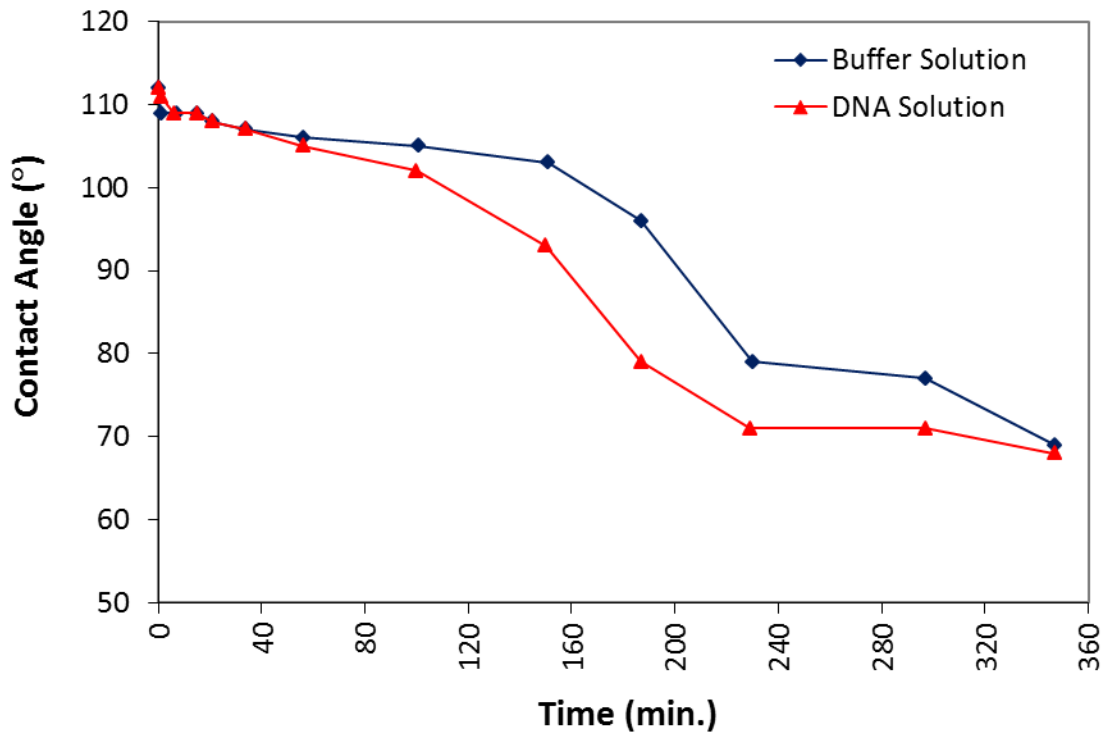


Figure E-8: Changes of contact angle with time in a passive experiment on 8 $\mu\text{g/ml}$ DNA solution and buffer solution.

Experiment 3:

In this experiment, droplets of 1000 $\mu\text{g/ml}$ DNA in buffer solution ($\text{pH} = 7$) and droplets of the same buffer solution used to dissolve DNA, are dispensed on Teflon substrates and left to evaporate in air. First, the images of both solutions are recorded simultaneously in every minute by a CCD camera over a 25 min. time interval. The contact angles are then calculated using AutoCAD (as explained in Chapter 4). At the end, the changes in contact angle are compared. It was found that the contact angle of DNA solution decreased about 35° in 10 min. comparing to 20° for buffer solution. It is another experiment proving the extensive passive adsorption of DNA on hydrophobic surfaces. As the concentration of DNA is very high, at the end of the experiment, the buffer solution that the DNA was dissolved in evaporated completely, but the DNA was left as a residue on the substrate, thus, the changes of contact angle over time reaches a plateau at 30° .

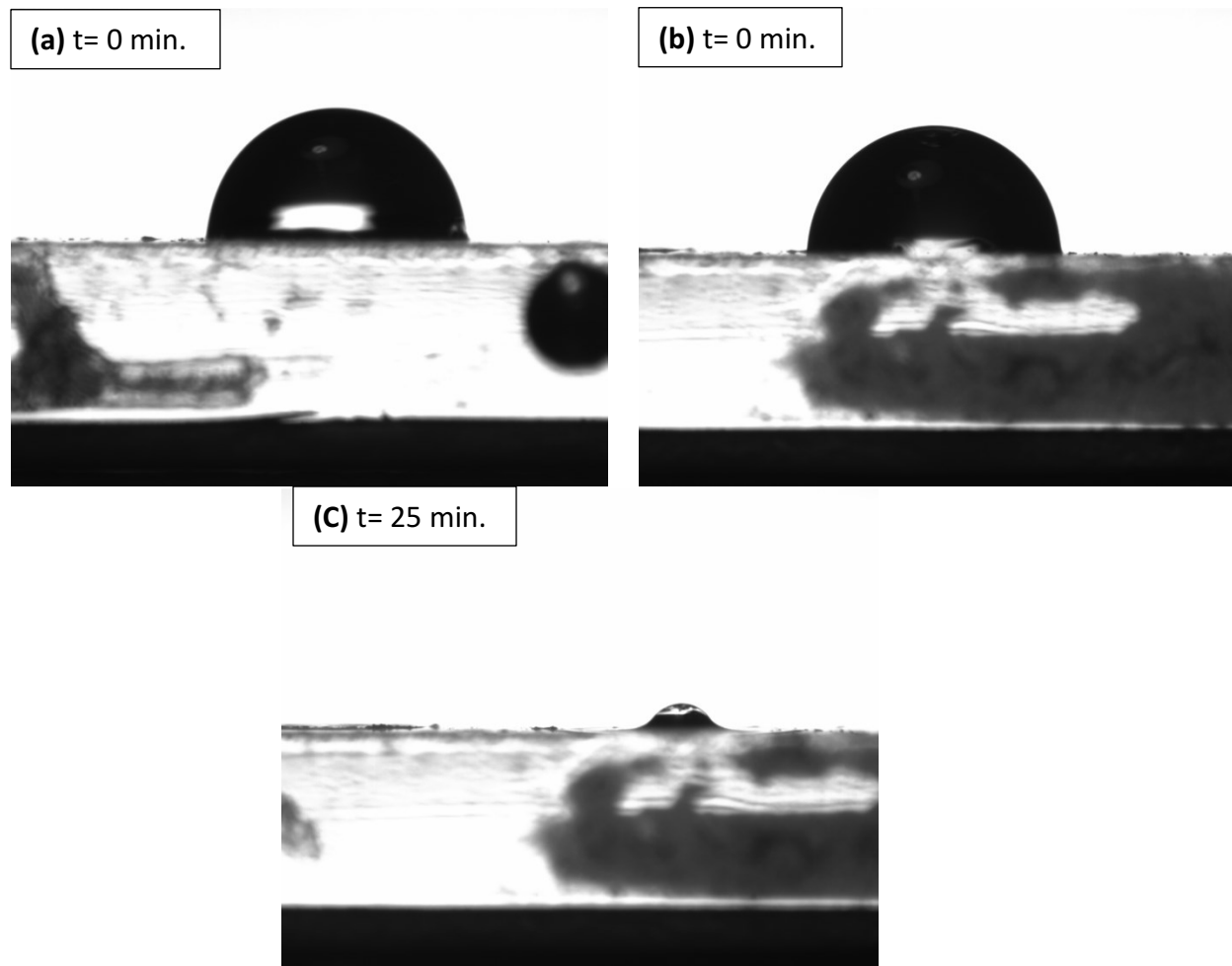


Figure E-9: Recorded images of droplets of: (a) buffer solution, (b) DNA solution, at the beginning of the experiment, (c) the residue left from DNA solution at the end of the experiment. The concentration of DNA is $1000 \mu\text{ mg/ml}$, and the initial volume of droplets for both solutions is around $1 \mu\text{l}$.

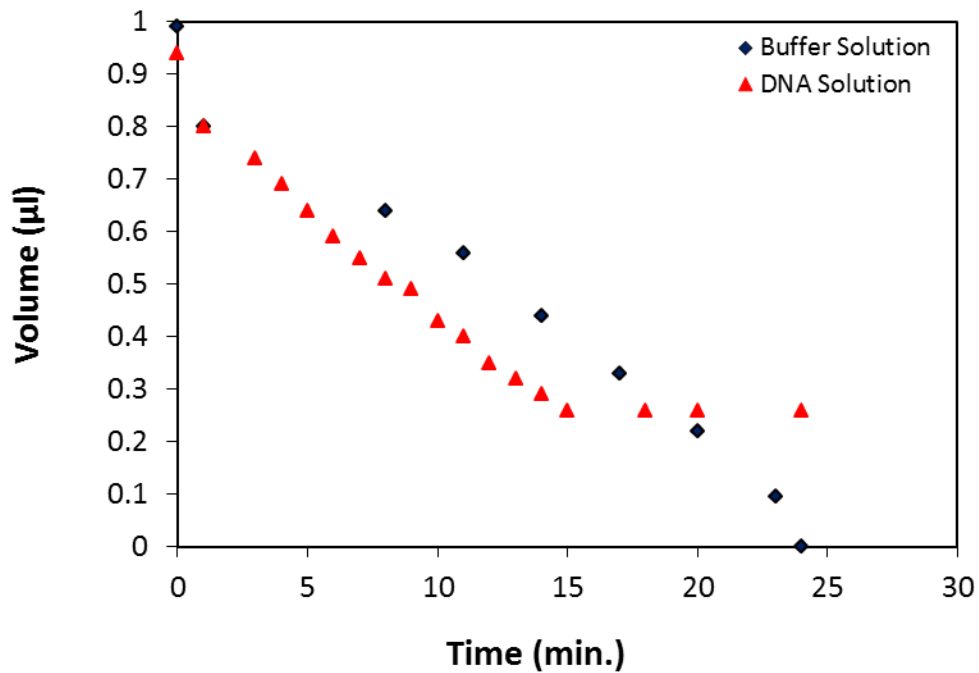
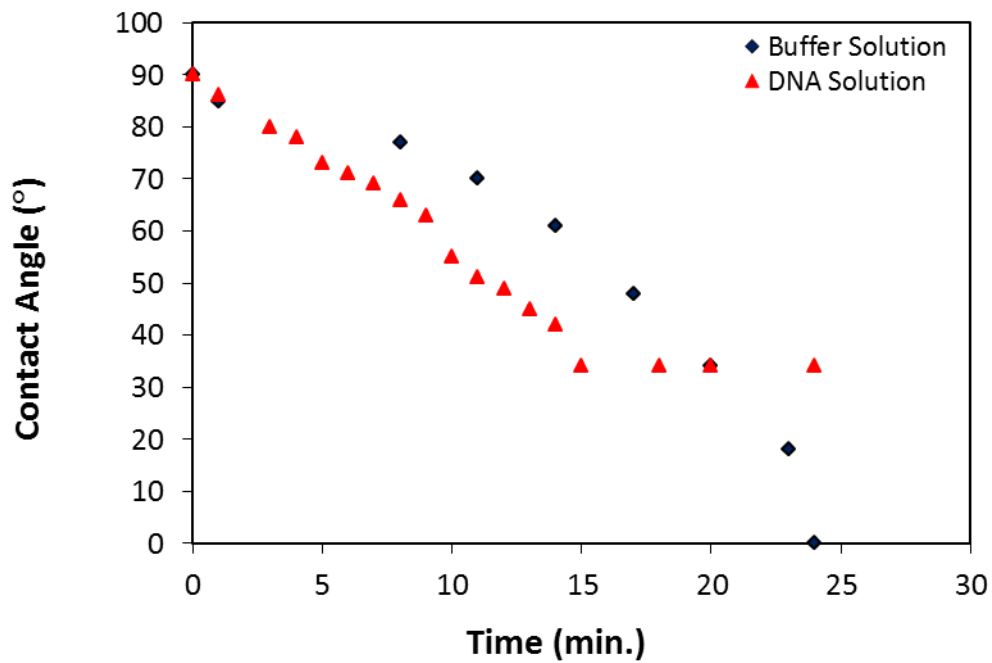


Figure E-10: Comparison of: (a) changes of contact angle with time, (b) changes of calculated volume for droplets of 1000 µg/ml DNA solution and buffer solution with time.

The volumes shown in have been calculated by rotating the recorded images of the droplets in AutoCAD software using the formula for a truncated sphere.

$$V = \frac{1}{3}\pi h^2(3r - h) \quad \text{Equation A-1}$$

where r is the radius of the sphere, and h is the height of the truncated part of the sphere.

From the last experiment, it is also concluded that using high concentrations of DNA solution could leave an amount of DNA residue on the surfaces which interferes with the movement of the droplets in EWOD and could cause blockages in the microchannels. Therefore, the concentrations of 4 $\mu\text{g/ml}$ and 8 $\mu\text{g/ml}$, which are commonly used in EWOD applications, are better choices.

Overall, in all these experiments, there have been significant reductions in contact angle for DNA solution comparing to those of buffer solution which is a good indication of the biomolecular adsorption. This adsorption could be minimized by:

- modifying the hydrophobic surface (*i.e.* using a surface which is less hydrophobic than Teflon AF), but it would make the EWOD-based actuation more difficultⁱⁱ.
- minimizing the time that the solution is in contact with the hydrophobic solution, which is usually the case in EWOD-based systems, as the droplets typically move very rapidly in the microchannels,
- using low concentrations of Pluronic additives such as F68, F127, P105^{v,vi} due to their interactions with the protein molecules (*i.e.* it is possible that the molecules of these additives coat the biomolecules such as DNA preventing them to be adsorbed by the

^v V. N. Luk, G. C. Mo, A. R. Wheeler, “Pluronic additives: A solution to sticky problems in digital microfluidics”, *Langmuir*, vol. 24 (12), pp. 6382–6389, 2008.

^{vi} S. H. Au, P. Kumar. A. R. Wheeler, “A New Angle on Pluronic Additives: Advancing Droplets and Understanding in Digital Microfluidics”, *Langmuir*, vol. 27 (11), pp.8586-8594, 2011.

hydrophobic surfaces^v). Generally, Pluronics are triblock copolymers of poly ethylene oxide (PEO) and poly propylene oxide (PPO)^{vi}. The longer is the PPO chain (such as P105), the better is the reduction of biofouling^{vi}.

Appendix F

F-1) Distilled Water, droplet morphology

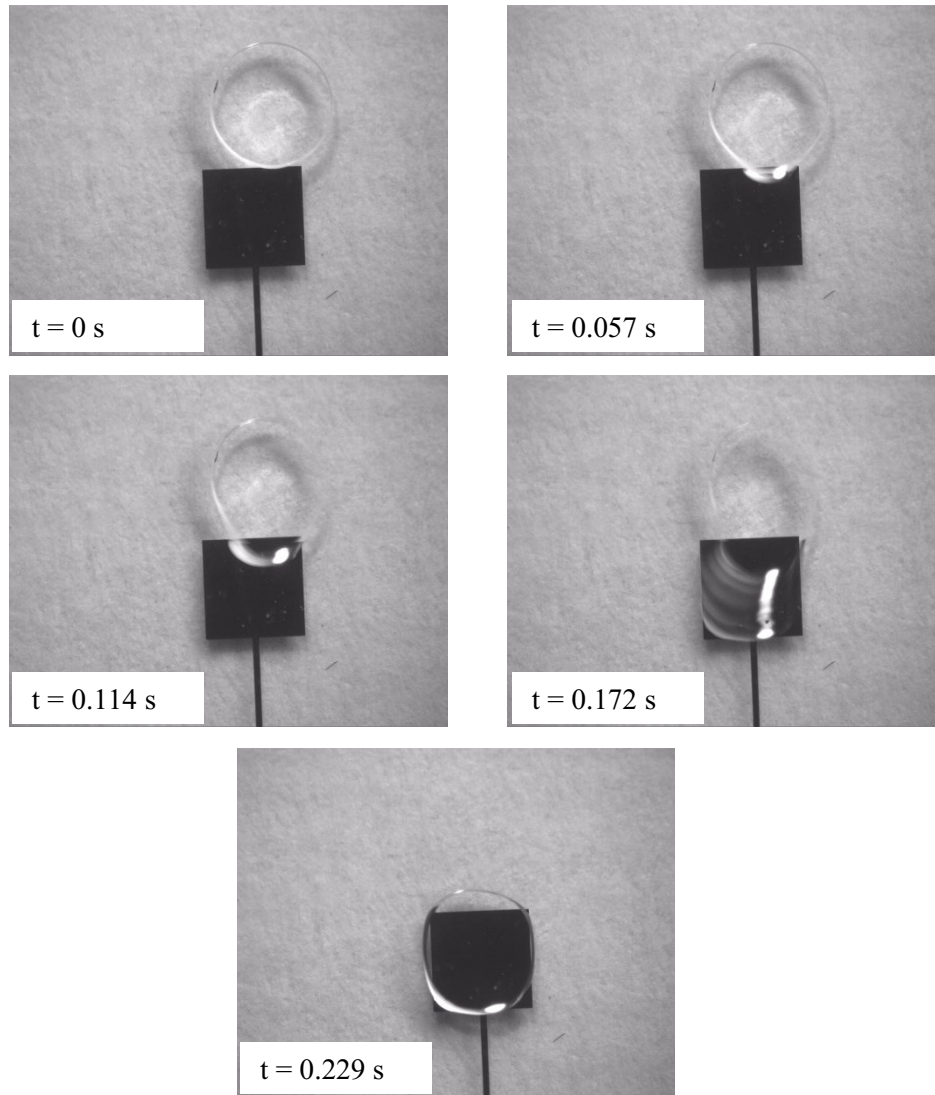


Figure F-1: Droplet morphology corresponding to an applied potential of 85V to a $0.94 \mu\text{l}$ droplet of distilled water in a microchannel gap of $352 \mu\text{m}$. The overlap and offset values are $26 \mu\text{m}$ and $296 \mu\text{m}$ respectively. A sudden inception of voltage is applied at $t = 0$ s, and remains constant until the droplet stops moving.

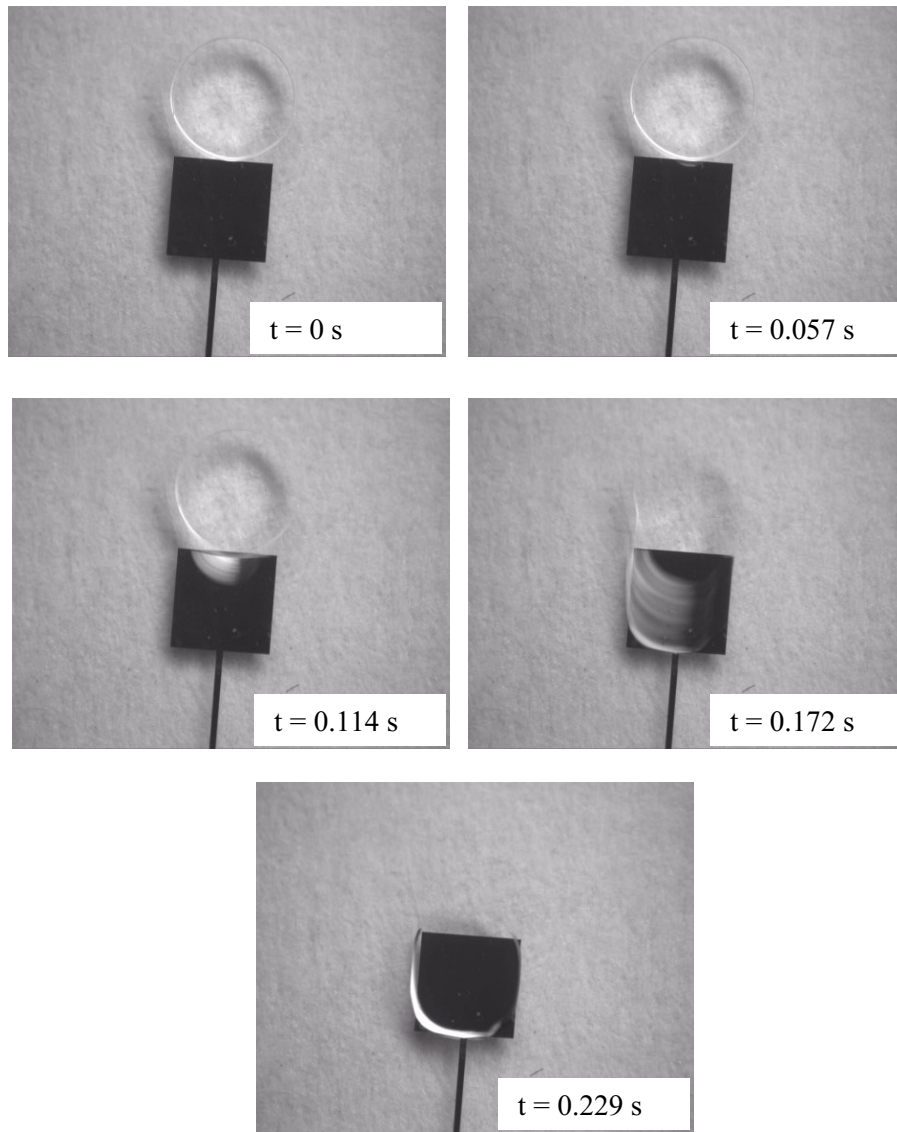


Figure F-2: Droplet morphology corresponding to an applied potential of 80V to a 0.92 μl droplet of distilled water in a microchannel gap of 330 μm . The overlap and offset values are 13 μm and 71 μm respectively. A sudden inception of voltage is applied at $t = 0$ s, and remains constant until the droplet stops moving.

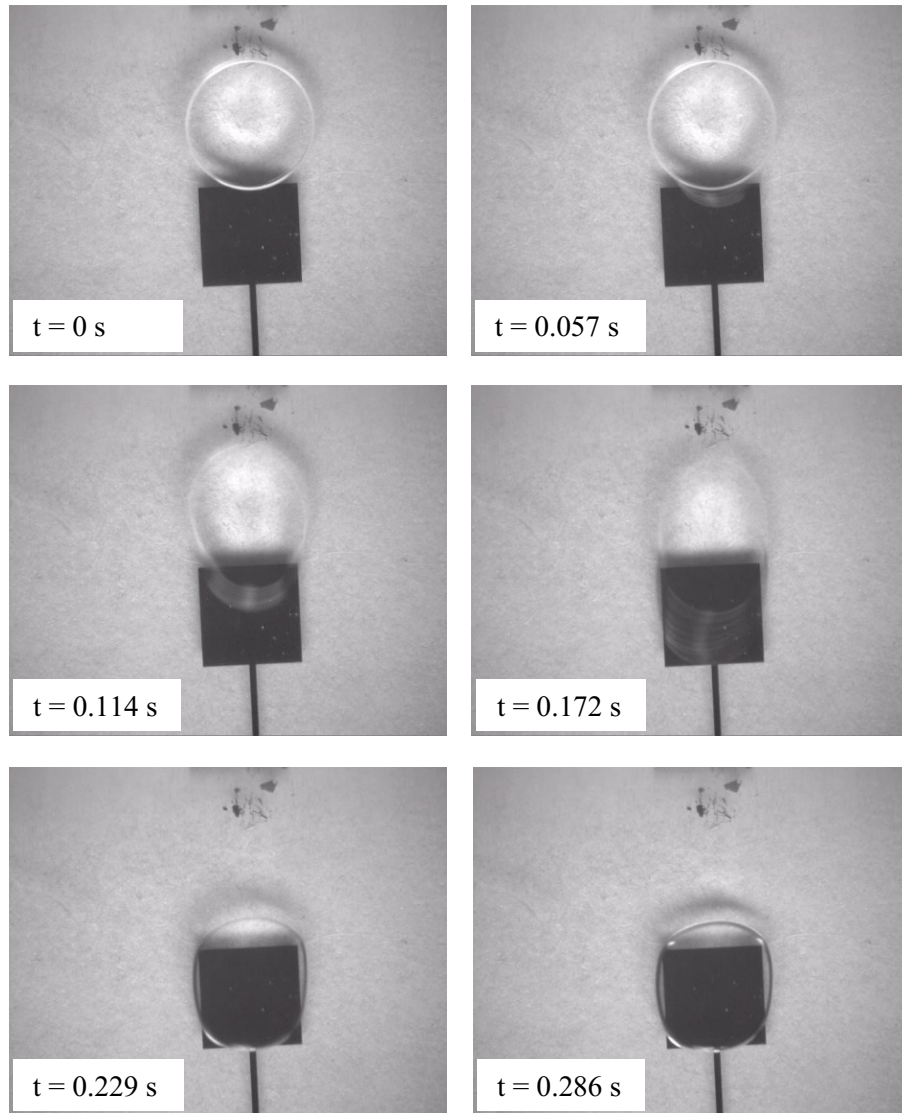


Figure F-3: Droplet morphology corresponding to an applied potential of 75V to a 0.98 μl droplet of distilled water in a microchannel gap of 338 μm . The overlap and offset values are 99 μm and 5 μm respectively. A sudden inception of voltage is applied at $t = 0$ s, and remains constant until the droplet stops moving. A sudden inception of voltage is applied at $t = 0$ s, and remains constant until the droplet stops moving. A sudden inception of voltage is applied at $t = 0$ s, and remains constant until the droplet stops moving.

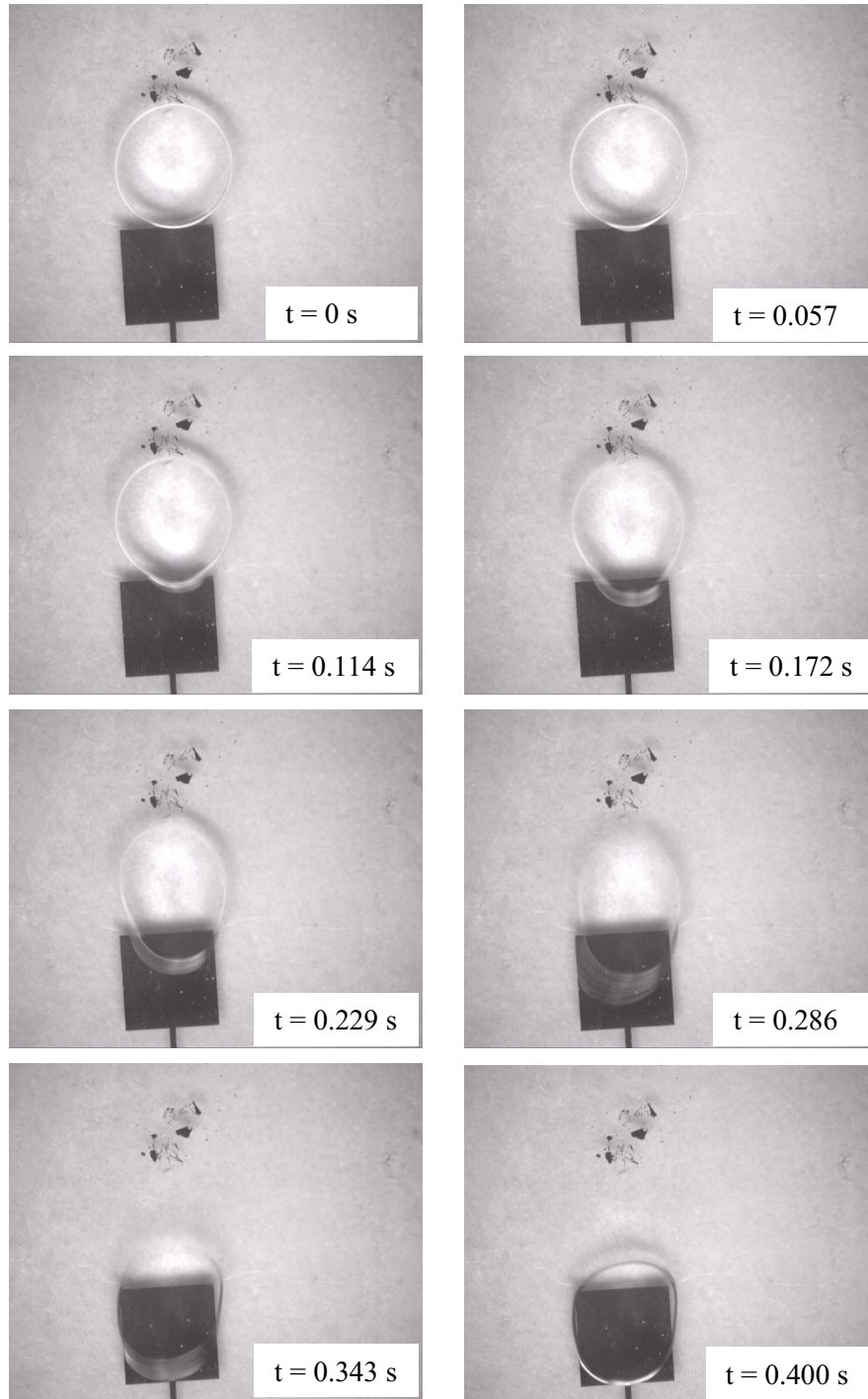


Figure F-4: Droplet morphology corresponding to an applied potential of 70V voltage to a 0.92 μl droplet of distilled water in a microchannel gap of 329 μm . The overlap and offset values are 25 μm and 145 μm respectively. A sudden inception of voltage is applied at $t = 0$ s, and remains constant until the droplet stops moving.

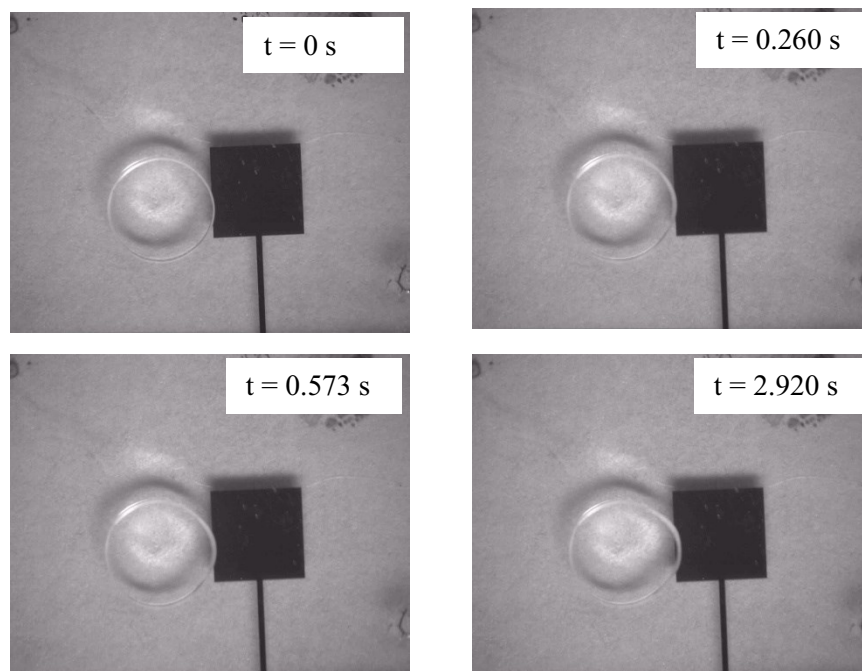


Figure F-5: Droplet morphology corresponding to an applied potential of 60V voltage to a 0.85 μl droplet of distilled water in a microchannel gap of 285 μm . The overlap and offset values are 13 μm and 196 μm respectively. As shown, the applied voltage of 60 V is only enough to actuate the leading and trailing edges of the droplet to some extent.

F-2) Distilled Water, 90 V

Distilled Water, 90 V, Leading edge

Accepted experiments and the average curves

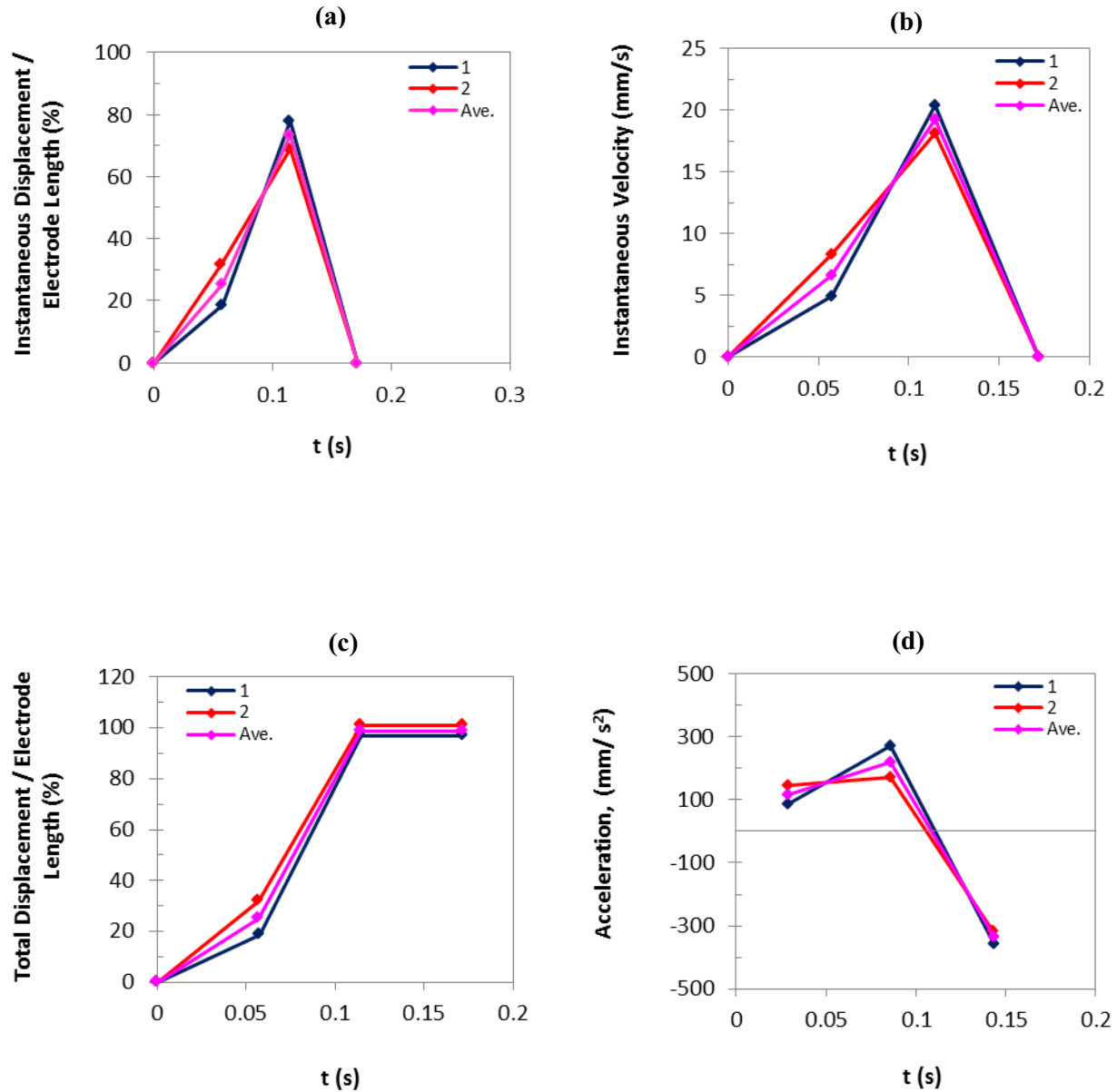


Figure F-6: (a) Instantaneous displacement, (b) instantaneous velocity, (c) total displacement, and (d) acceleration of the leading edges of distilled water droplets as a function of time at 90 V.

Distilled Water, 95 V, Trailing edge

Accepted experiments and the average curves

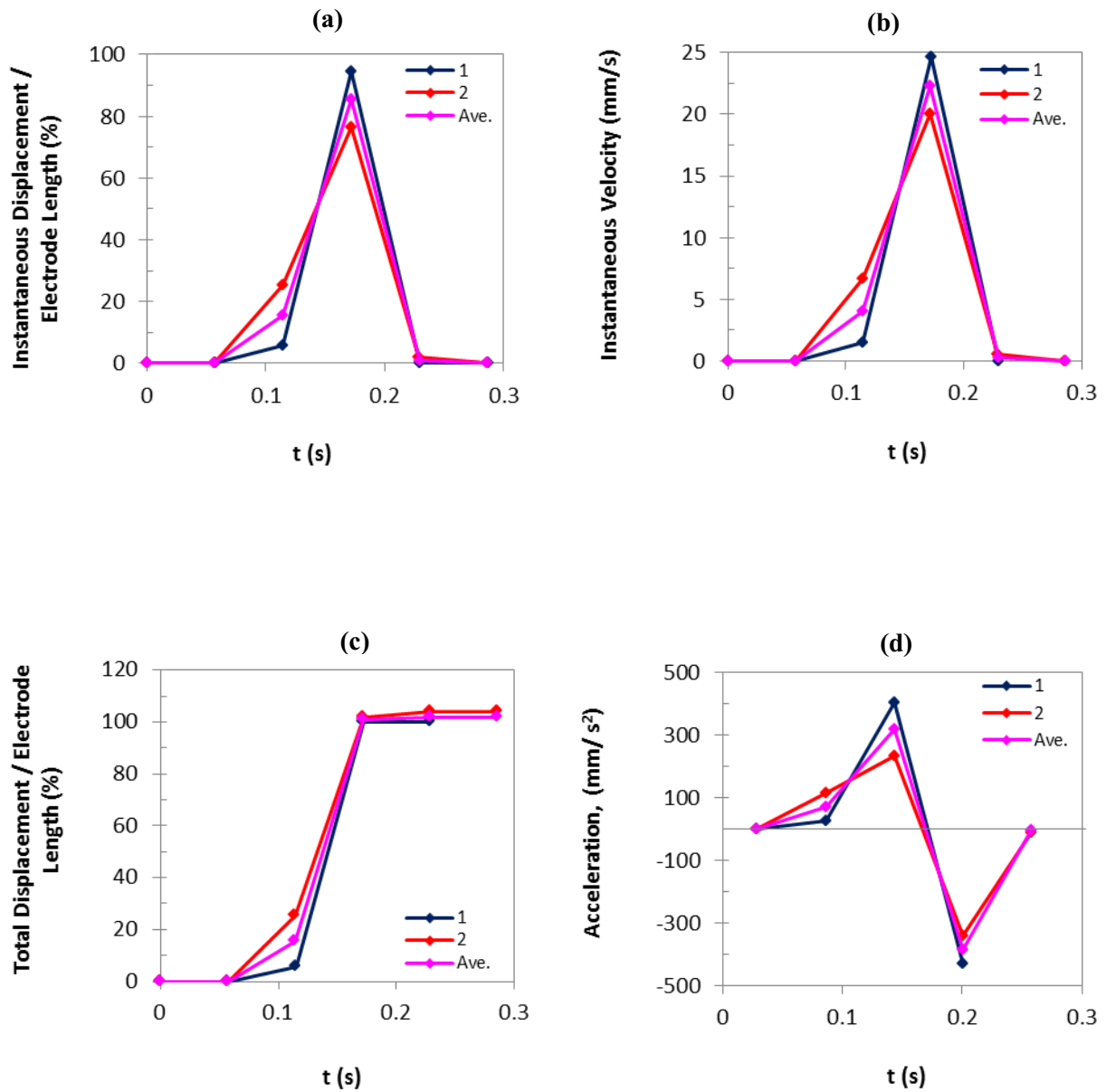


Figure F-7: (a) Instantaneous displacement, (b) instantaneous velocity, (c) total displacement, and (d) acceleration of the trailing edges of distilled water droplets as a function of time at 90 V.

Distilled Water, 90 V

Accepted experiments and the average curves

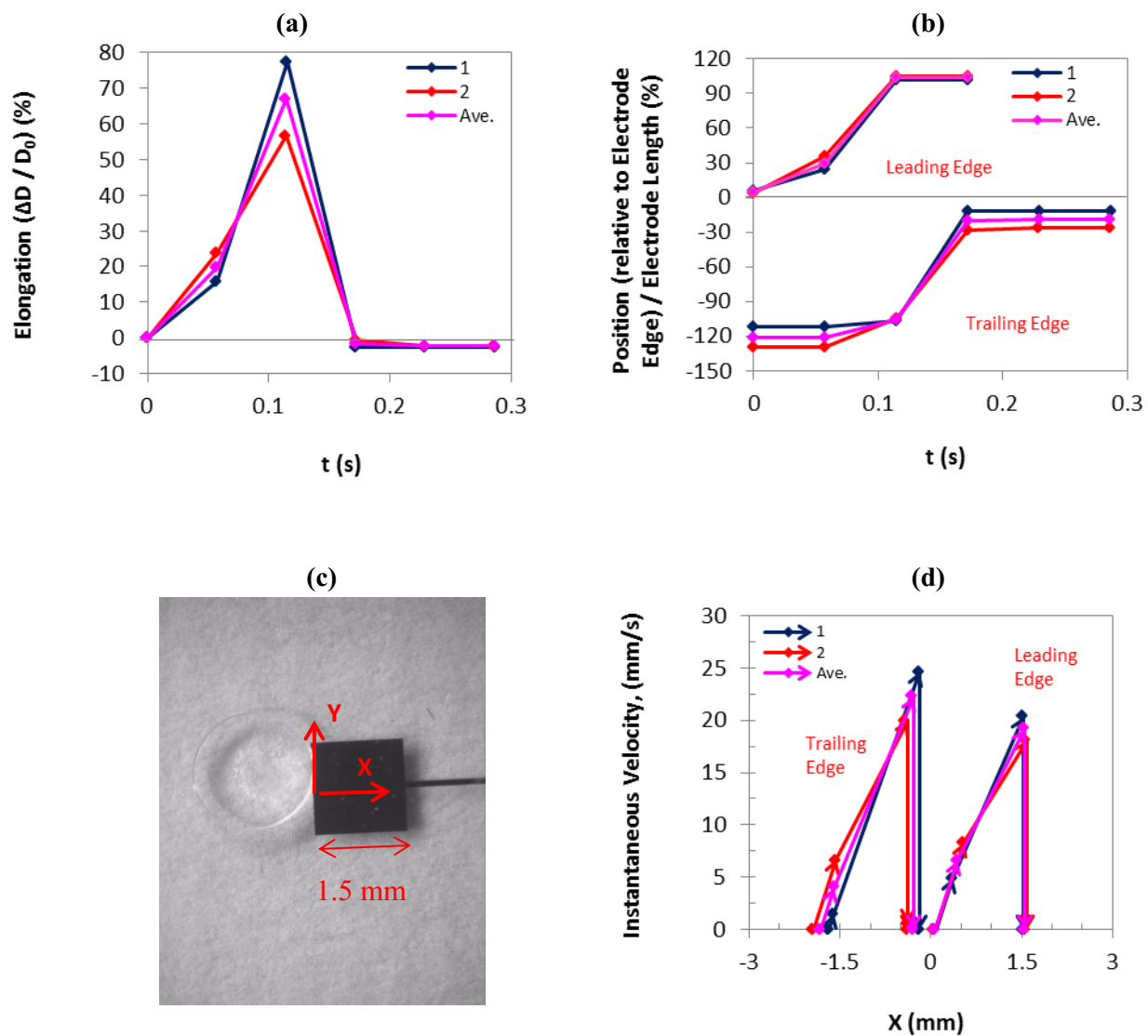


Figure F-8: (a) Droplet elongation and (b) droplet position as a function of time, and (d) instantaneous velocity as a function of droplet position as shown in (c) for the leading and trailing edges of distilled water droplets at 90 V. The arrows in (d) indicate the changes of velocity along the direction of movement.

F-3) Distilled Water, 85 V

Distilled Water, 85 V, Leading edge,

Accepted experiments and the average curves

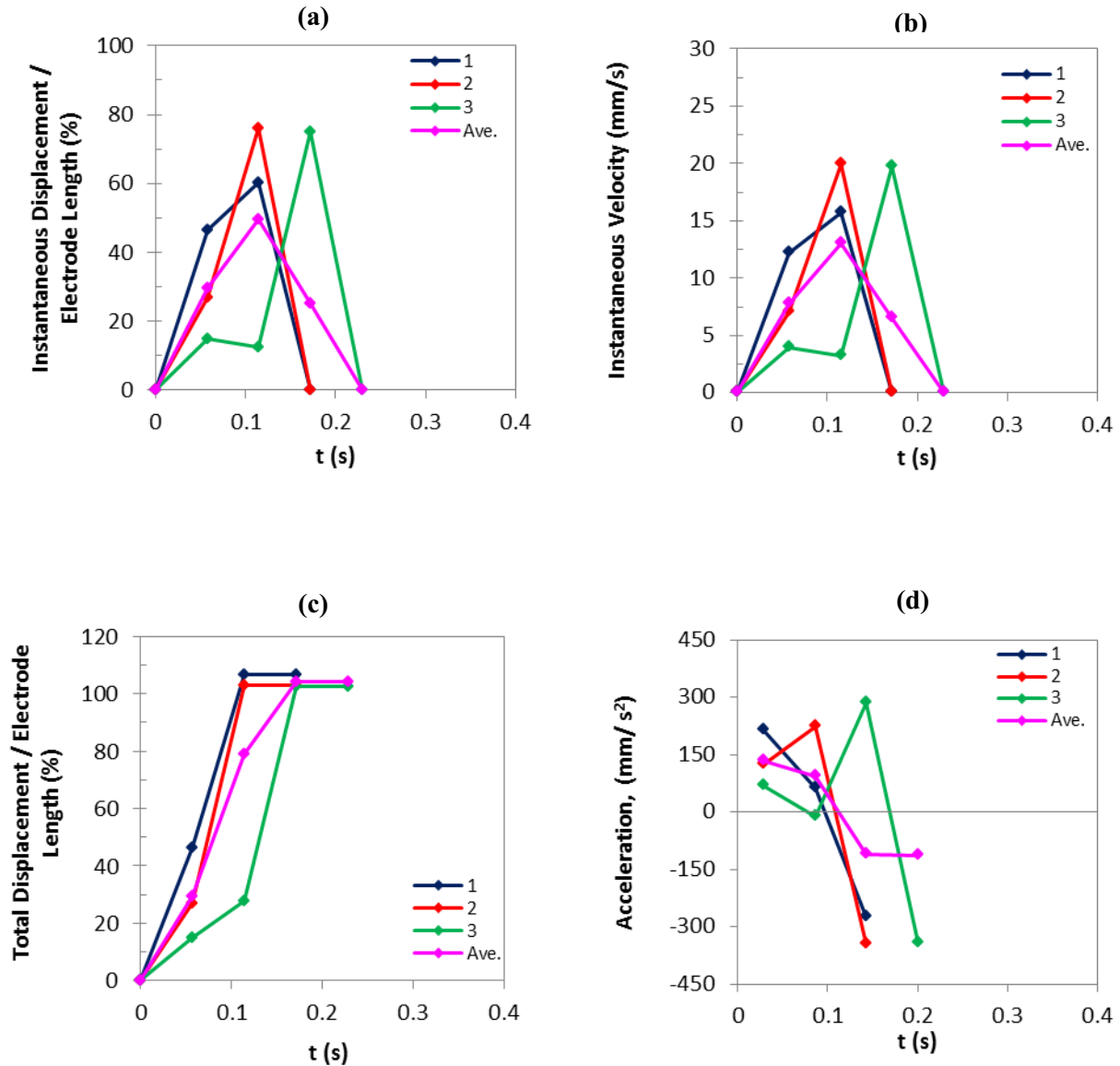


Figure F-9: (a) Instantaneous displacement, (b) instantaneous velocity, (c) total displacement, and (d) acceleration of the leading edges of distilled water droplets as a function of time at 85 V.

Distilled Water, 85 V, Trailing edge

Accepted experiments and the average curves

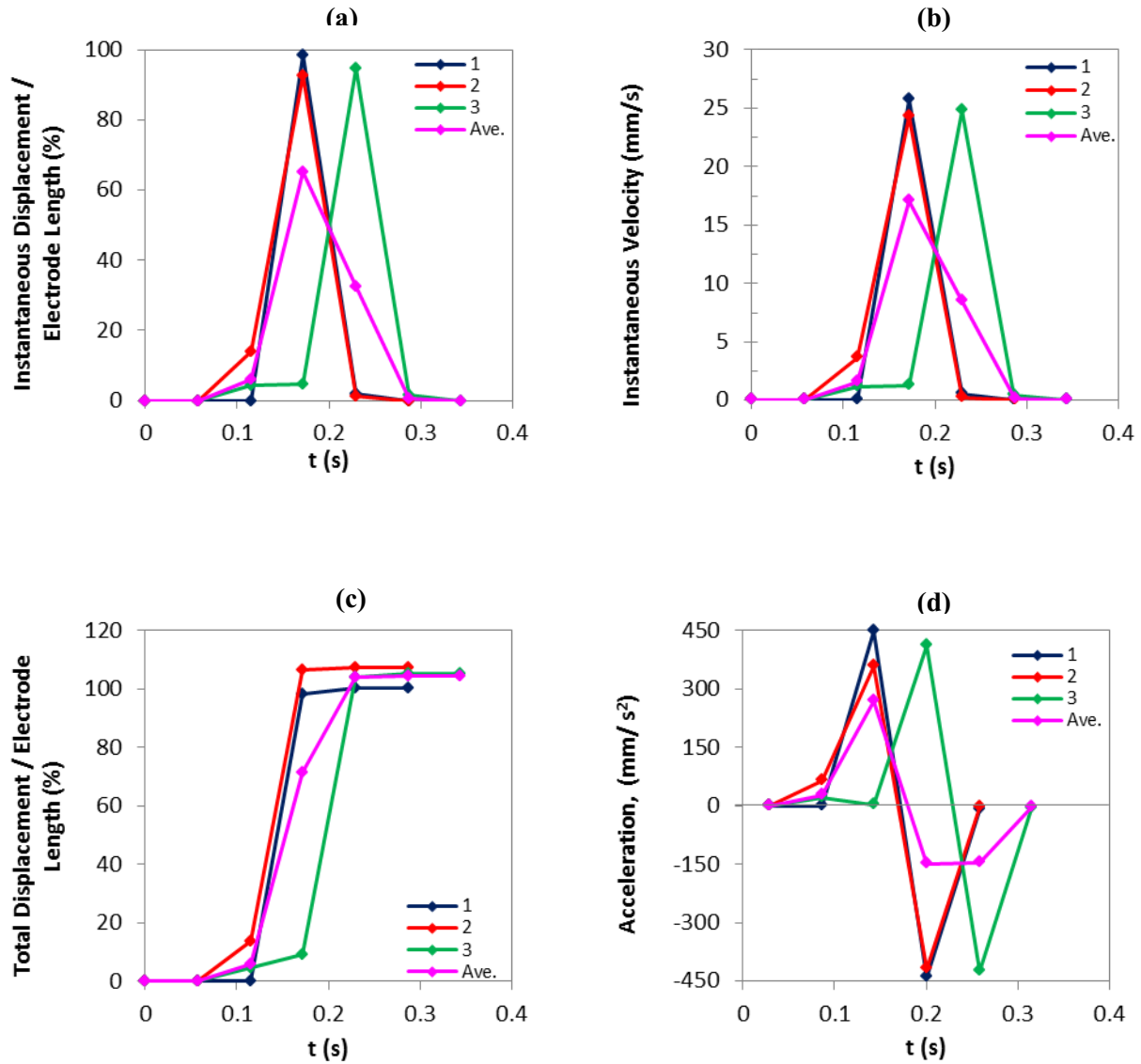


Figure F-10: (a) Instantaneous displacement, (b) instantaneous velocity, (c) total displacement, and (d) acceleration of the trailing edges of distilled water droplets as a function of time at 85 V.

Distilled Water, 85 V

Accepted experiments and the average curves

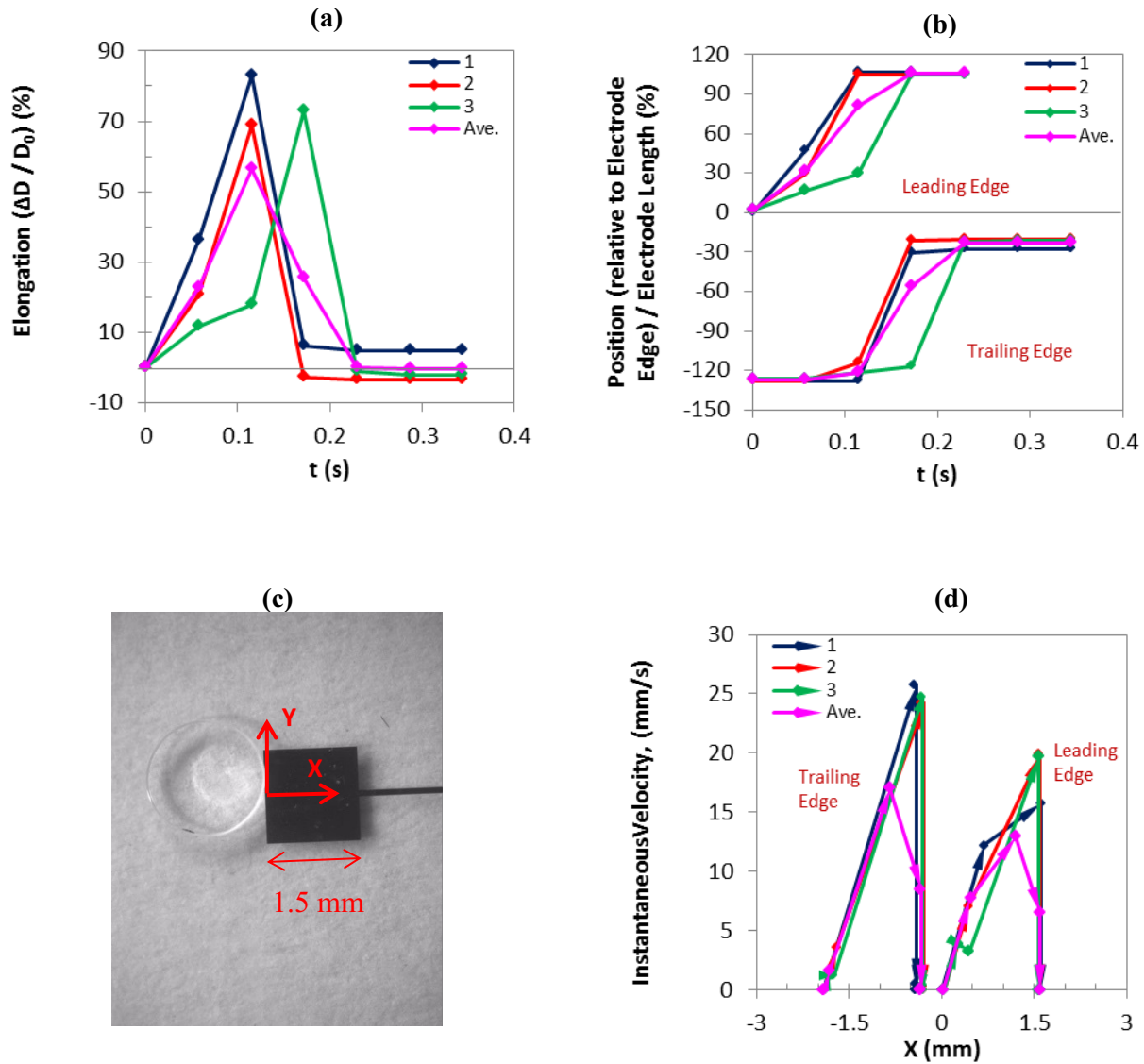


Figure F-11: (a) Droplet elongation and (b) droplet position as a function of time, (d) instantaneous velocity as a function of droplet position as shown in (c) for the leading and trailing edges of distilled water droplets at 85 V. The arrows in (d) indicate the changes of velocity along the direction of movement.

Distilled Water, 85 V, Average curves

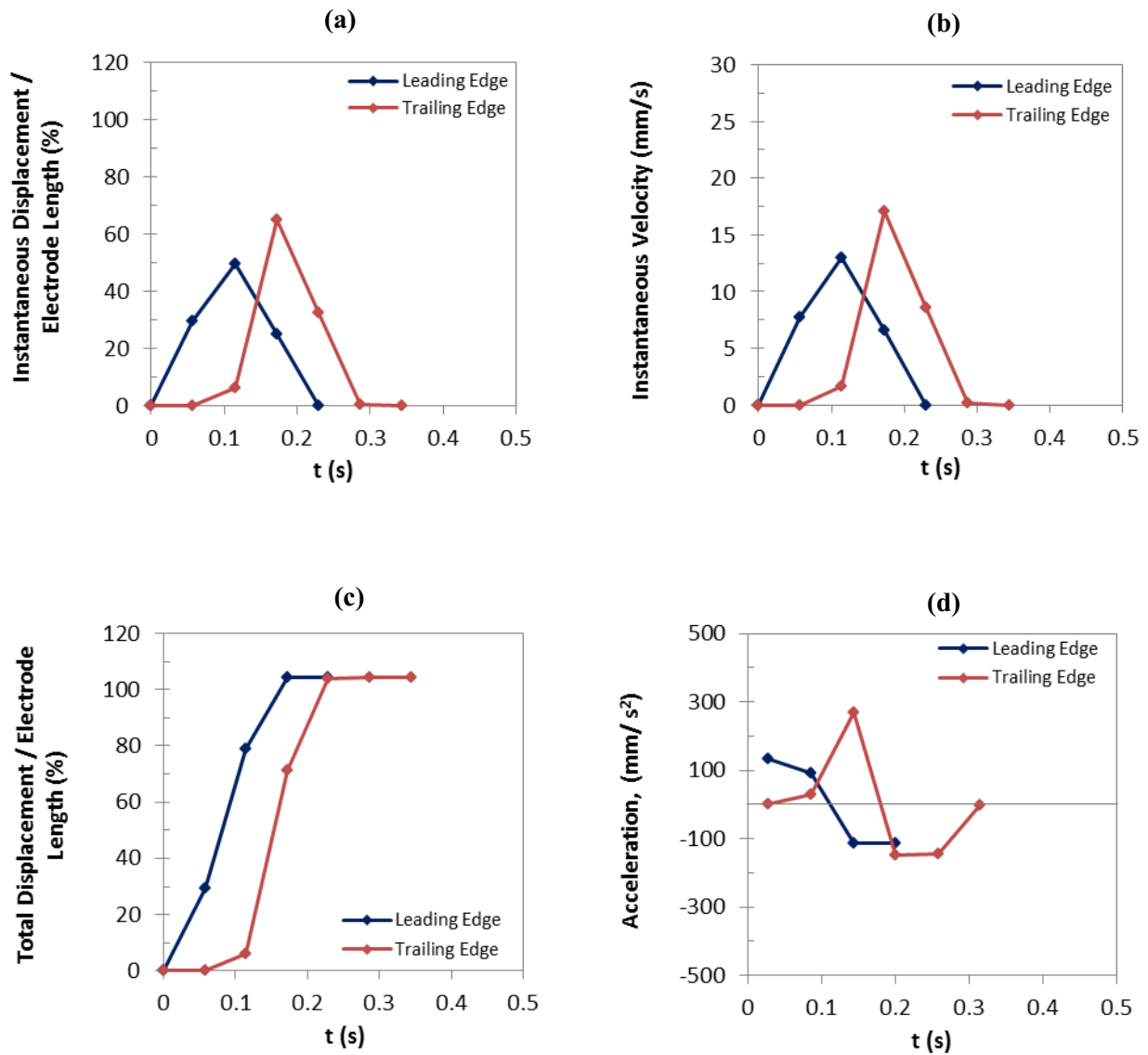


Figure F-12: Comparison of the average curves: (a) instantaneous displacement, (b) instantaneous velocity, (c) total displacement, and (d) acceleration, as a function of time for the leading and trailing edges of distilled water droplets at 85 V.

Distilled Water, 85 V, Average curves

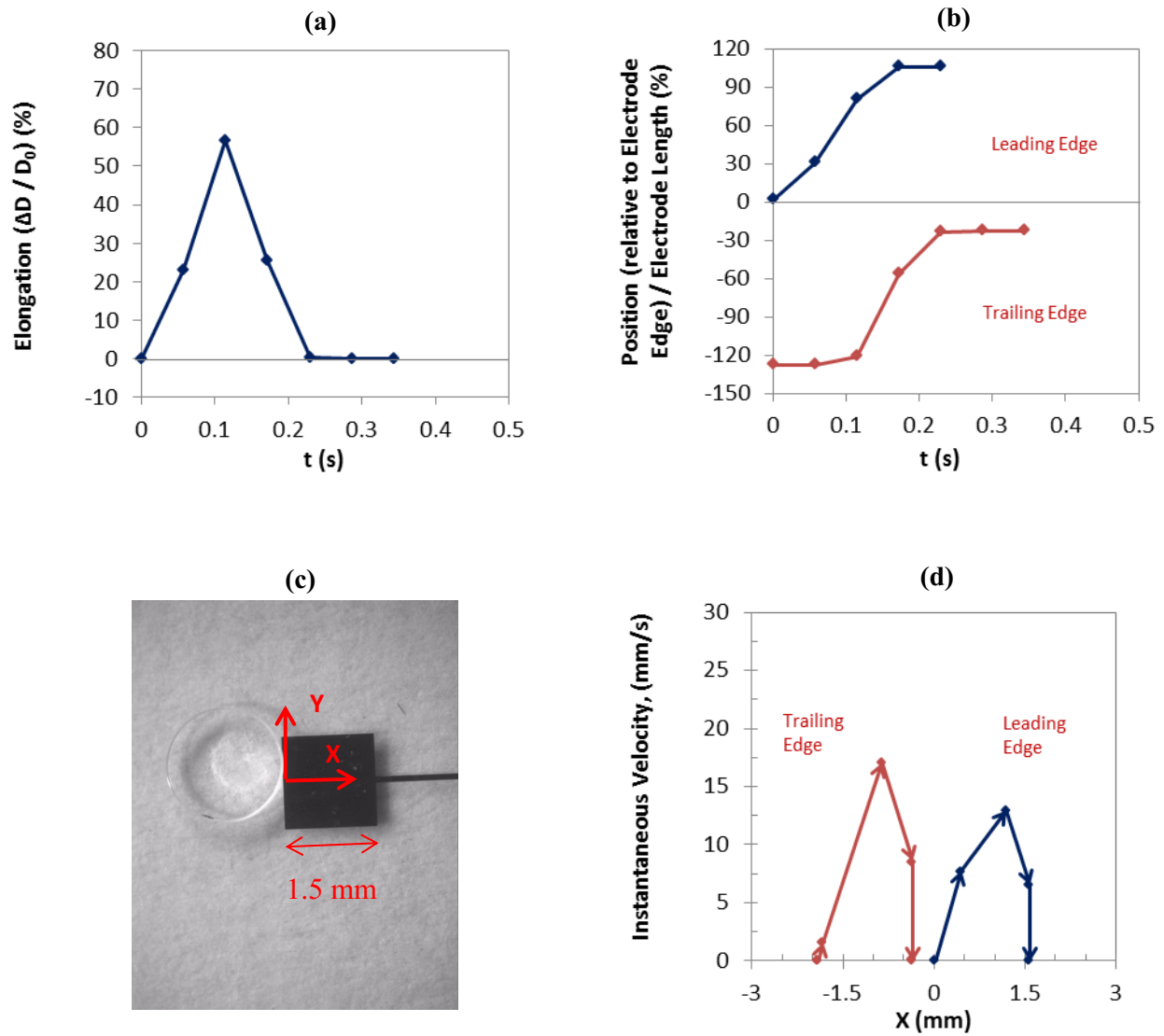


Figure F-13: Comparison of the average curves: (a) droplet elongation and (b) droplet position as a function of time, (d) instantaneous velocity as a function of droplet position as shown in (c) for the leading and trailing edges of distilled water droplets at 85 V. The arrows in graph (d) indicate the changes of velocity along the direction of movement.

F-4) Distilled Water, 80 V

Distilled Water, 80 V, Leading edge,

Accepted experiments and the average curves

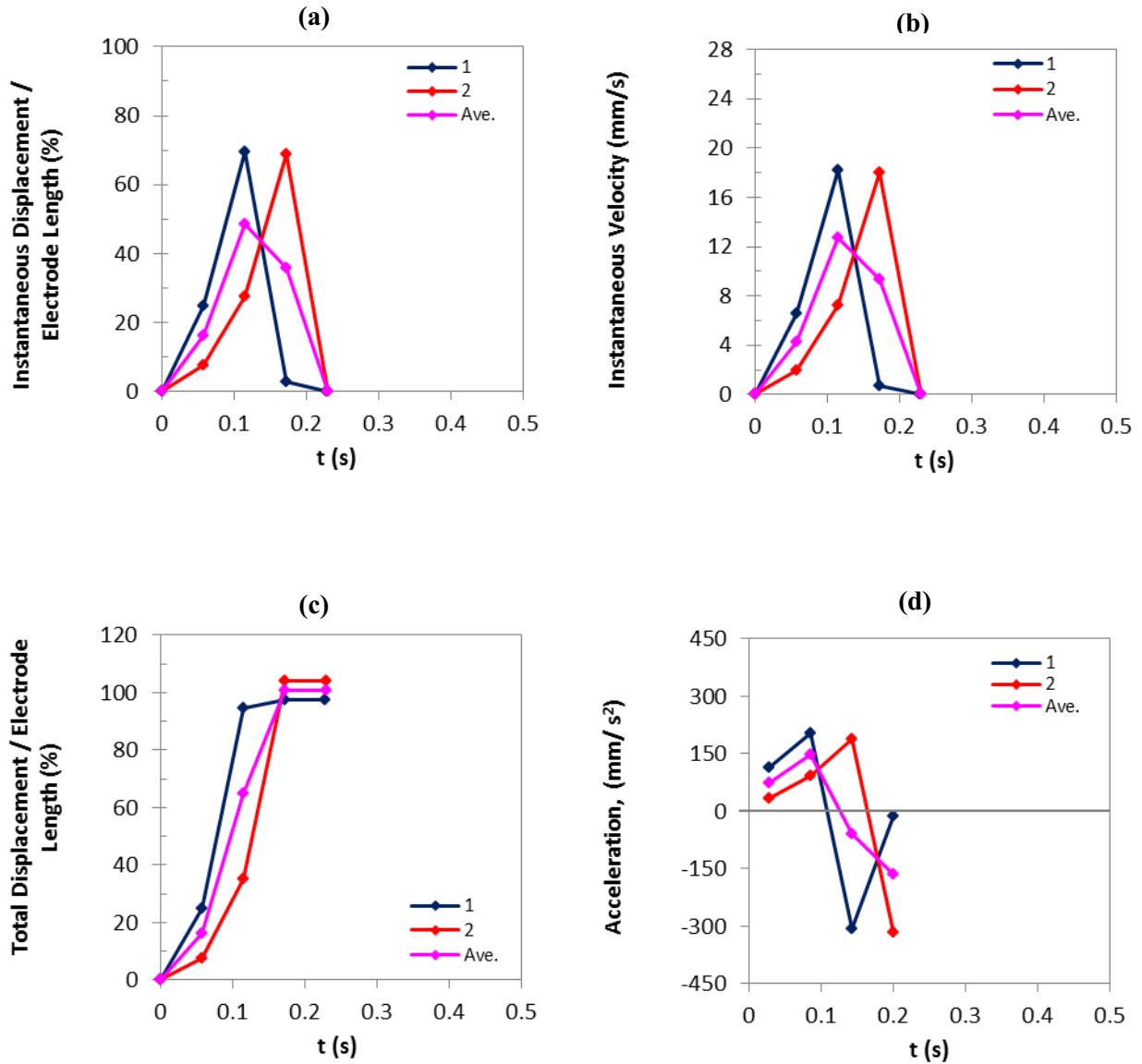


Figure F-14: (a) Instantaneous displacement, (b) instantaneous velocity, (c) total displacement, and (d) acceleration of the leading edges of distilled water droplets as a function of time at 80 V.

Distilled Water, 80 V, Trailing edge

Accepted experiments and the average curves

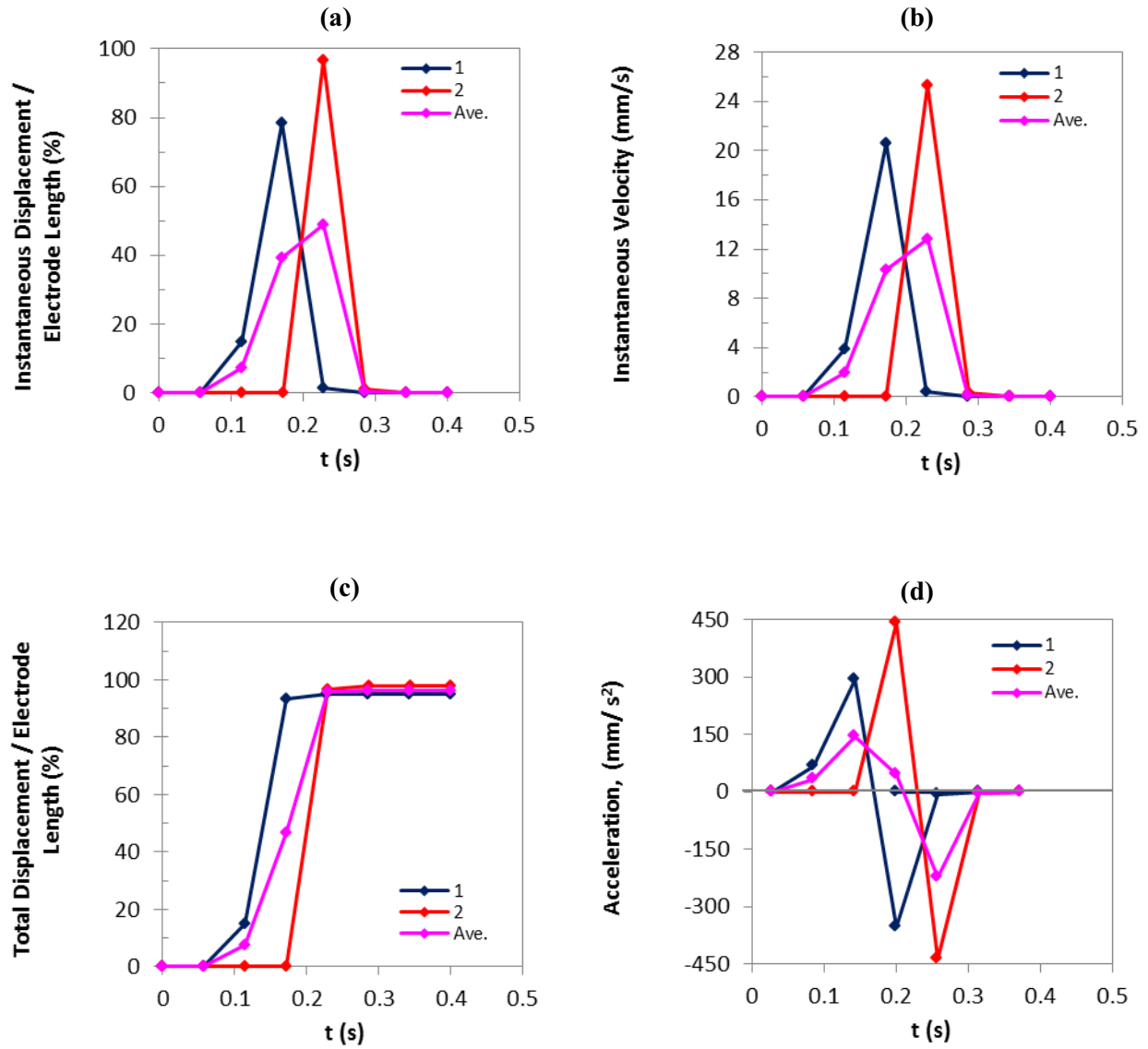


Figure F-15: (a) Instantaneous displacement, (b) instantaneous velocity, (c) total displacement, and (d) acceleration of the trailing edges of distilled water droplets as a function of time at 80 V.

Distilled Water, 80 V

Accepted experiments and the average curves

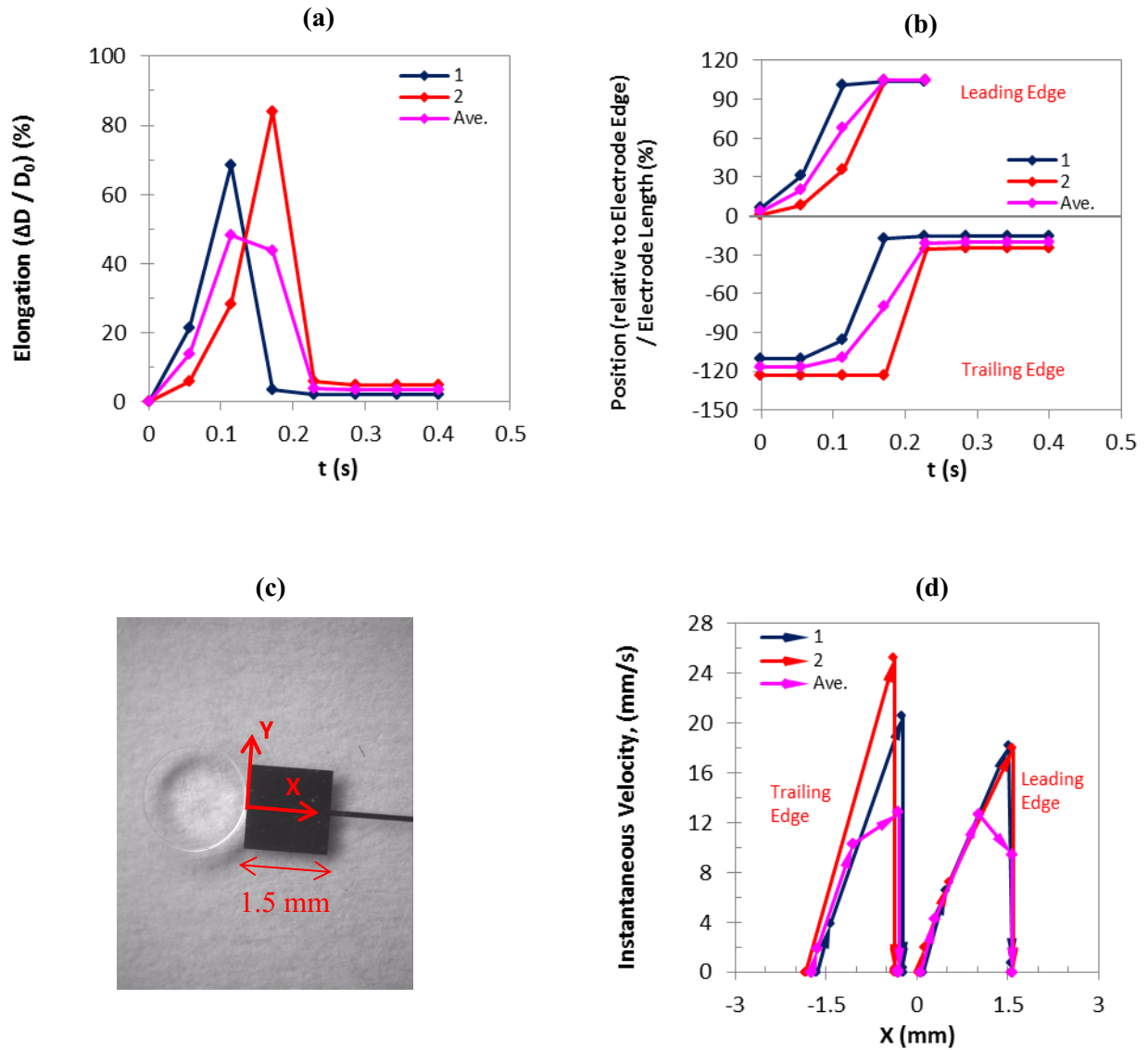


Figure F-16: (a) Droplet elongation and (b) droplet position as a function of time, (d) instantaneous velocity as a function of droplet position as shown in (c) for the leading and trailing edges of distilled water droplets at 80 V. The arrows in (d) indicate the changes of velocity along the direction of movement.

Distilled Water, 80 V, Average curves

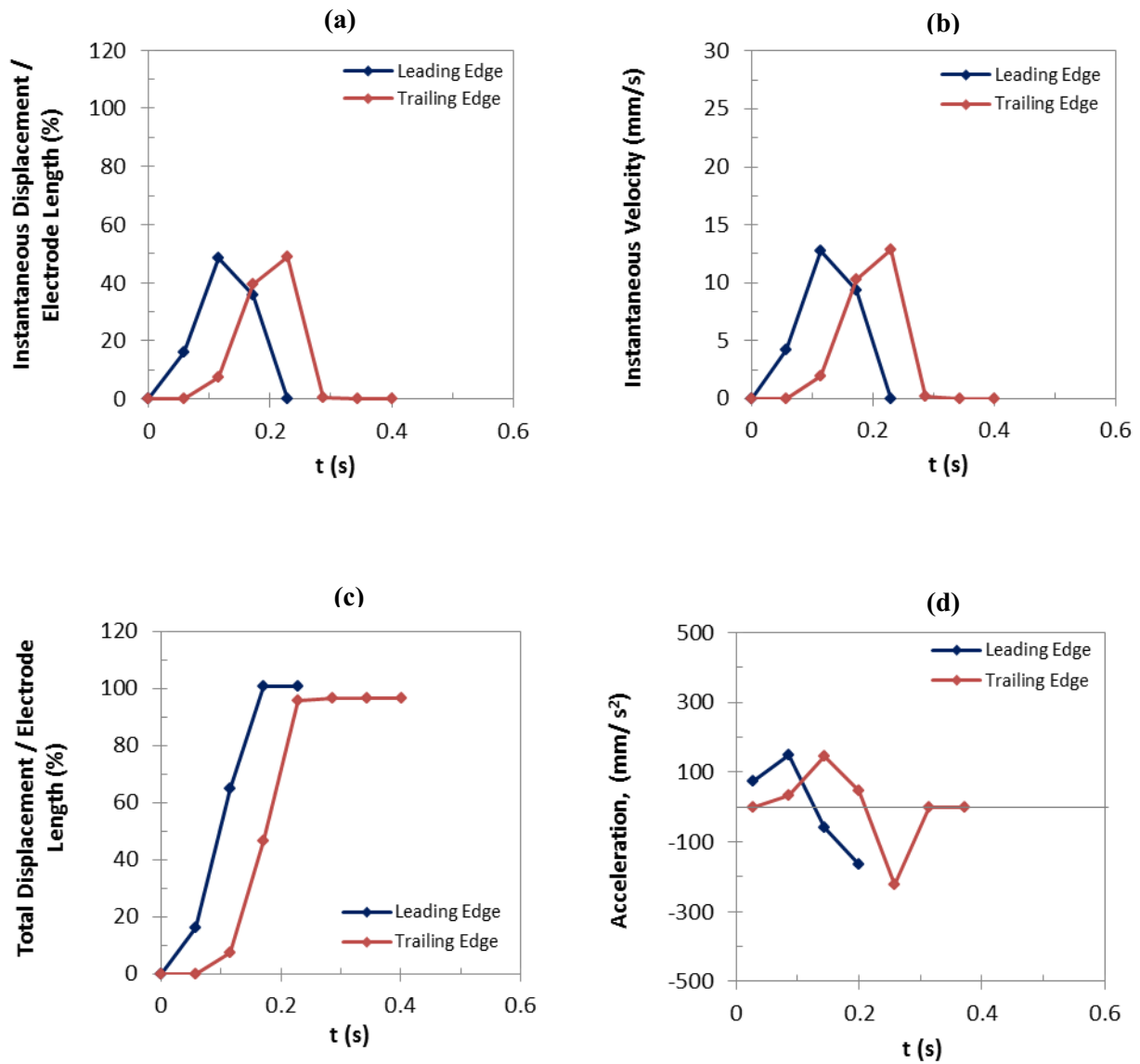


Figure F-17: Comparison of the average curves: (a) instantaneous displacement, (b) instantaneous velocity, (c) total displacement, and (d) acceleration, as a function of time for the leading and trailing edges of distilled water droplets at 80 V.

Distilled Water, 80 V, Average curves

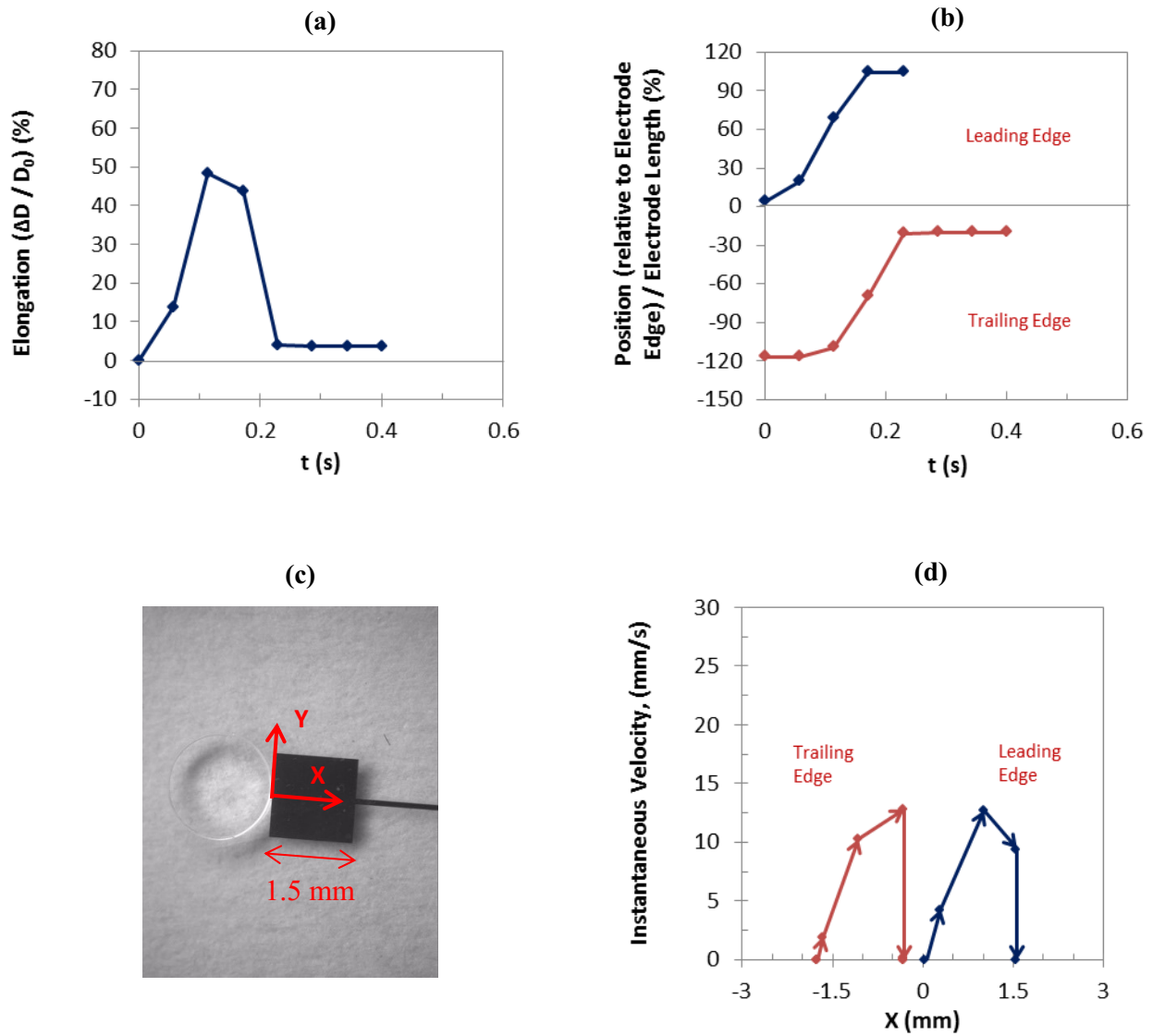


Figure F-18: Comparison of the average curves: (a) droplet elongation and (b) droplet position as a function of time, (d) instantaneous velocity as a function of droplet position as shown in (c) for the leading and trailing edges of distilled water droplets at 80 V. The arrows in graph (d) indicate the changes of velocity along the direction of movement.

F-5) Distilled Water, 75 V

Distilled Water, 75 V, Leading edge,

Accepted experiments and the average curves

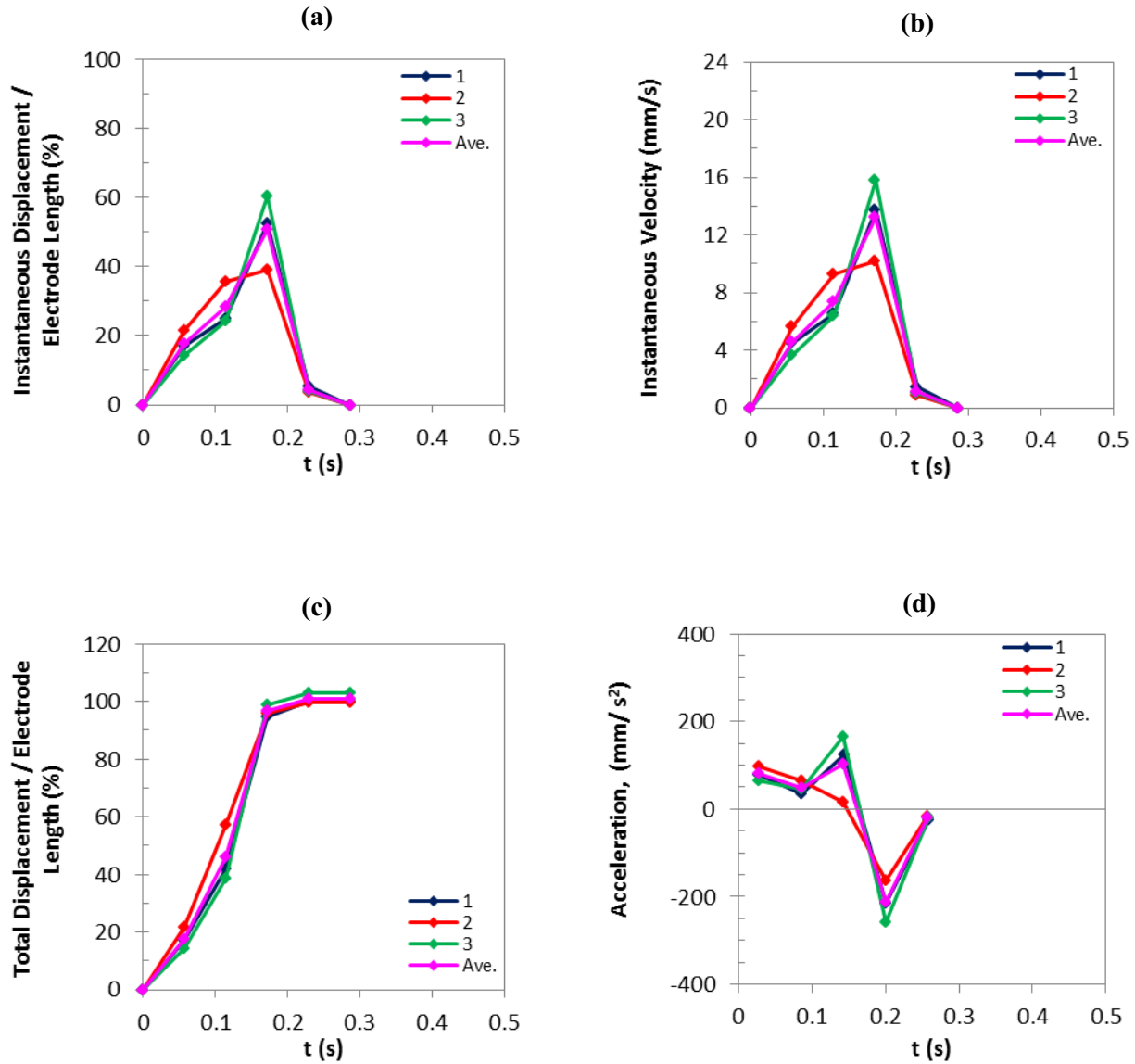


Figure F-19: (a) Instantaneous displacement, (b) instantaneous velocity, (c) total displacement, and (d) acceleration of the leading edges of distilled water droplets as a function of time at 75 V.

Distilled Water, 75 V, Trailing edge

Accepted experiments and the average curves

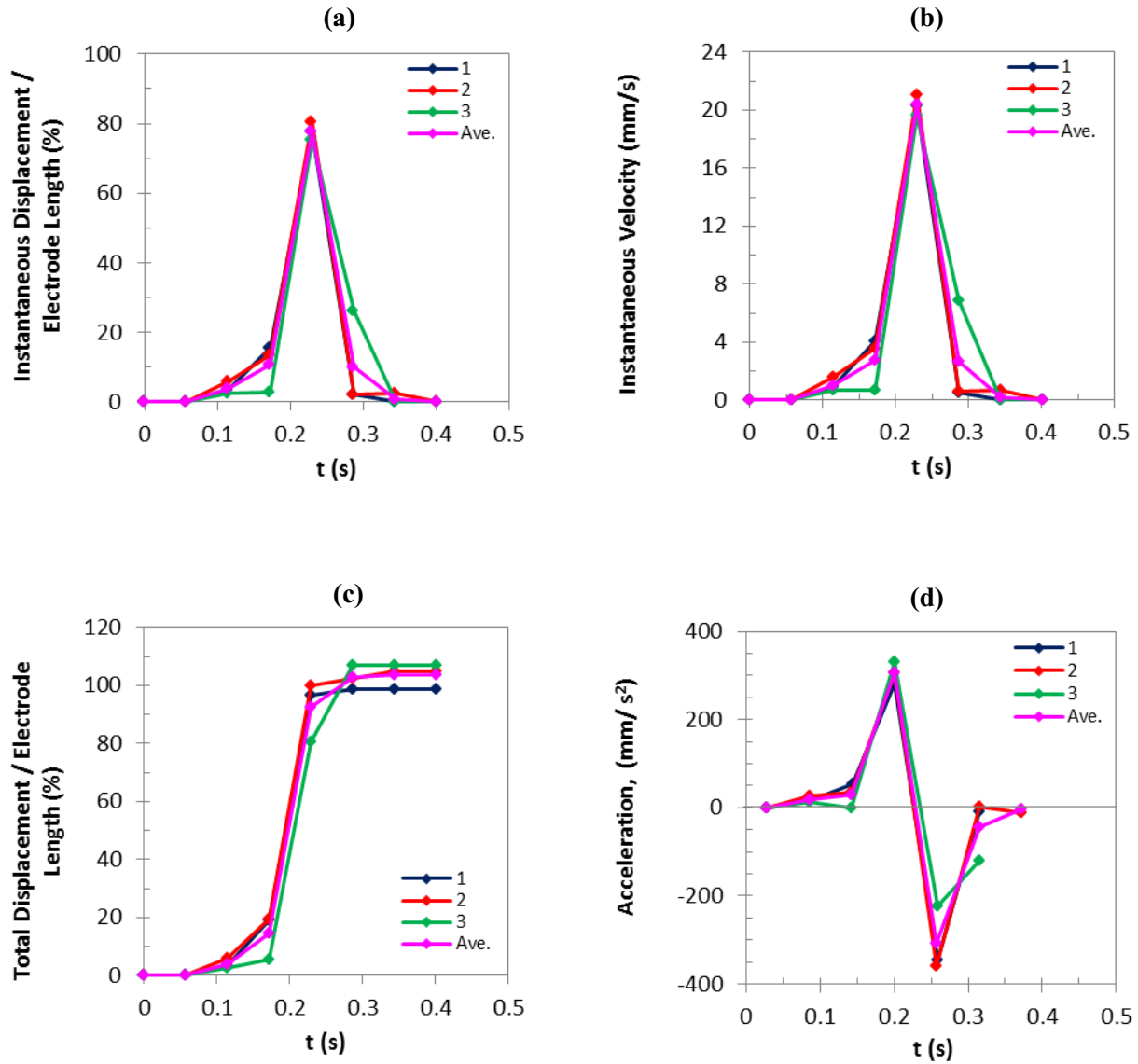


Figure F-20: (a) Instantaneous displacement, (b) instantaneous velocity, (c) total displacement, and (d) acceleration of the trailing edges of distilled water droplets as a function of time at 75 V.

Distilled Water, 75 V

Accepted experiments and the average curves

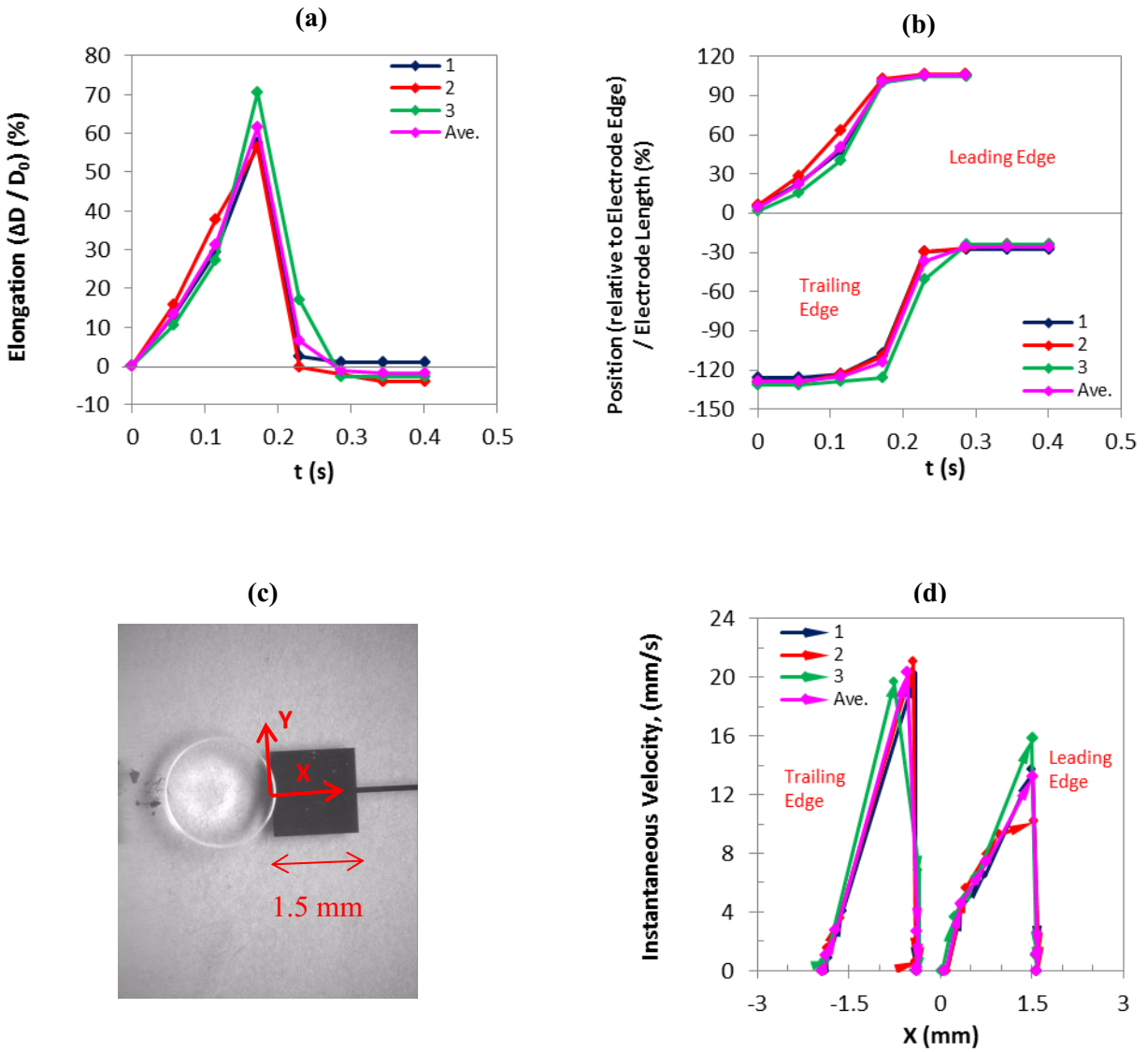


Figure F-21: (a) Droplet elongation and (b) droplet position as a function of time, (d) instantaneous velocity as a function of droplet position as shown in (c) for the leading and trailing edges of distilled water droplets at 75 V. The arrows in (d) indicate the changes of velocity along the direction of movement.

Distilled Water, 75 V, Average curves

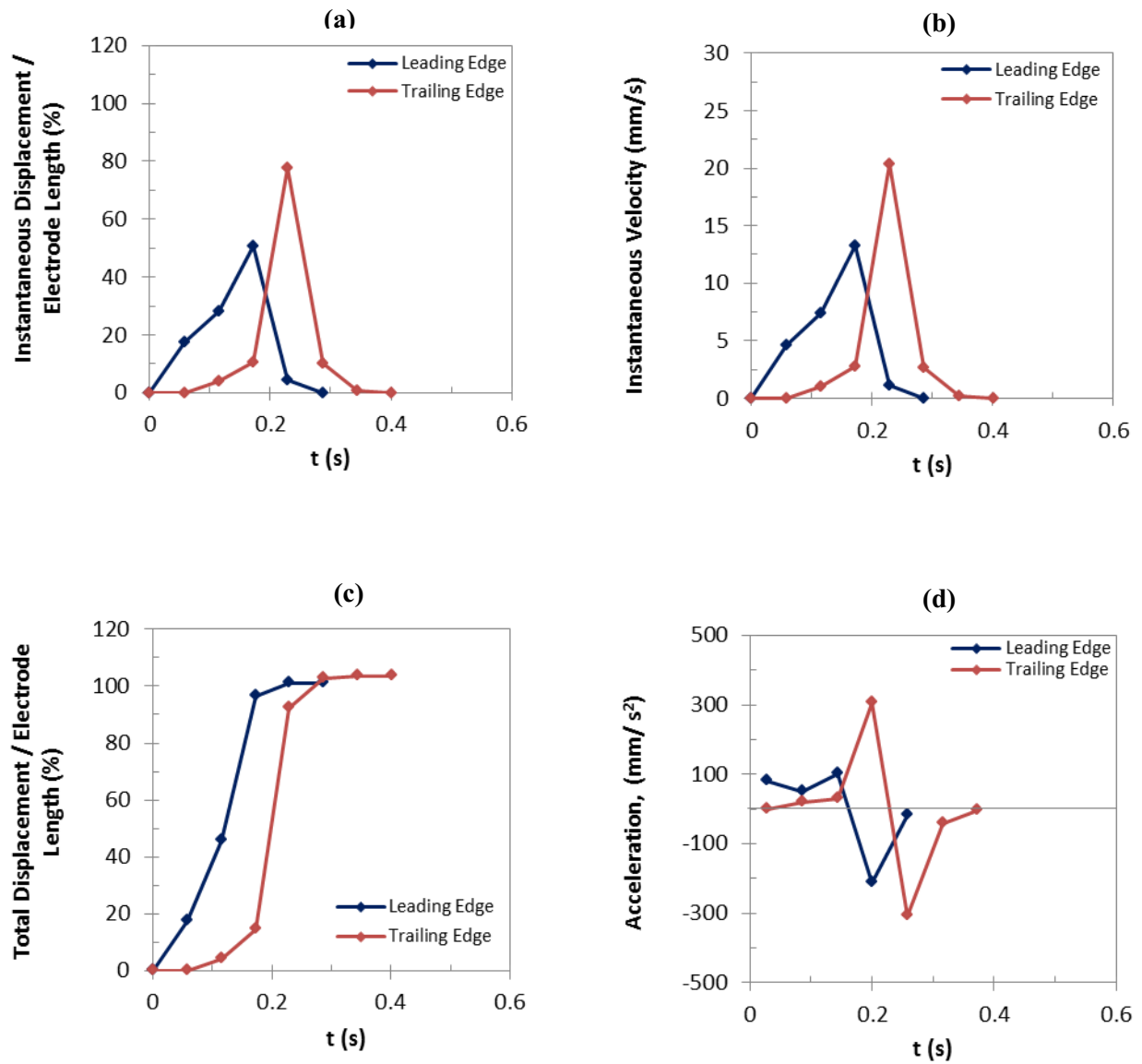


Figure F-22: Comparison of the average curves: (a) instantaneous displacement, (b) instantaneous velocity, (c) total displacement, and (d) acceleration, as a function of time for the leading and trailing edges of distilled water droplets at 75 V.

Distilled Water, 75 V, Average curves

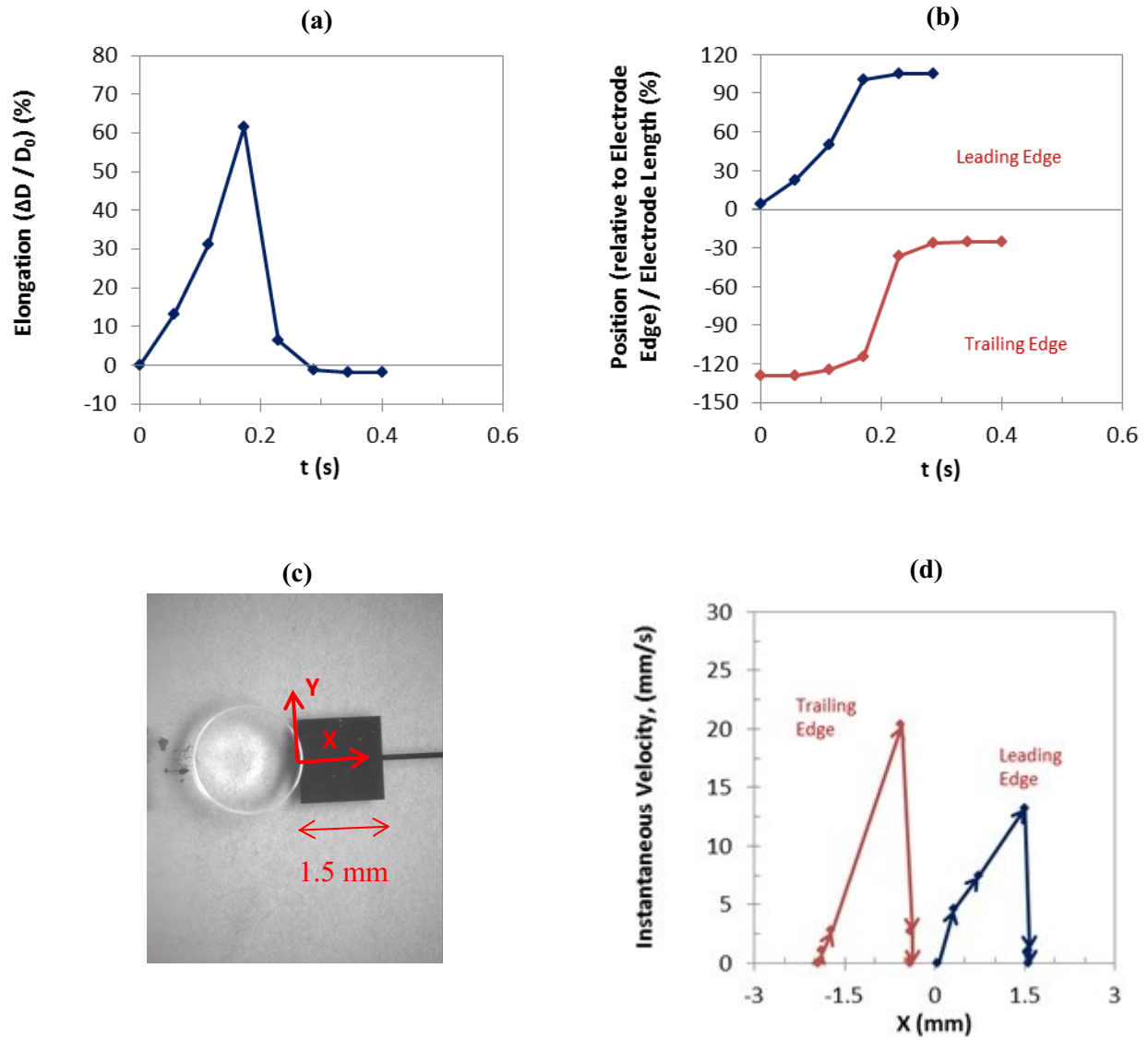


Figure F-23: Comparison of the average curves: (a) droplet elongation and (b) droplet position as a function of time, (d) instantaneous velocity as a function of droplet position as shown in (c) for the leading and trailing edges of distilled water droplets at 75 V. The arrows in graph (d) indicate the changes of velocity along the direction of movement.

F-6) Distilled Water, 70 V

Distilled Water, 70 V, Leading edge,

Accepted experiments and the average curves

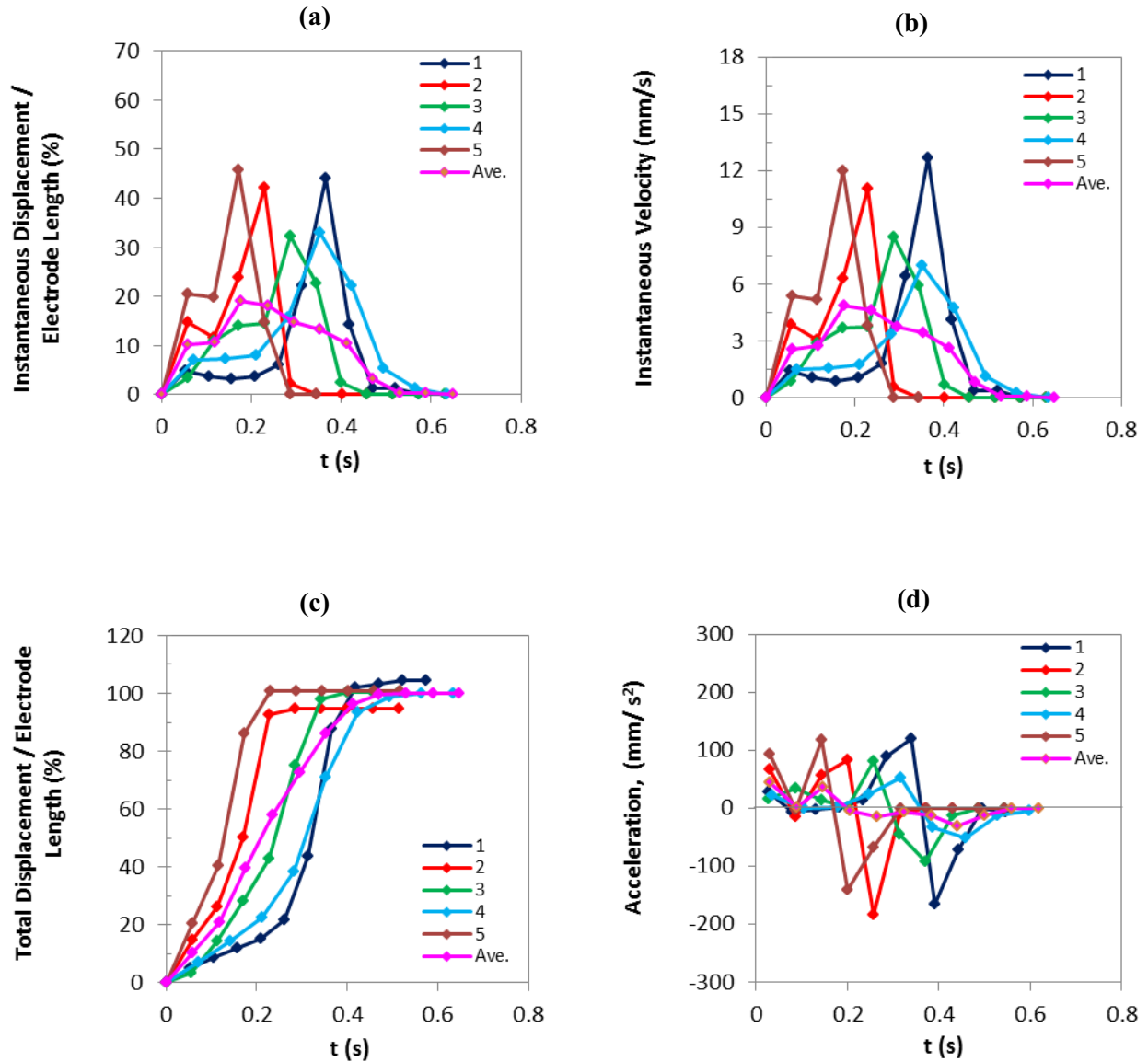


Figure F-24: (a) Instantaneous displacement, (b) instantaneous velocity, (c) total displacement, and (d) acceleration of the leading edges of distilled water droplets as a function of time at 70 V.

Distilled Water, 70 V, Trailing edge

Accepted experiments and the average curves

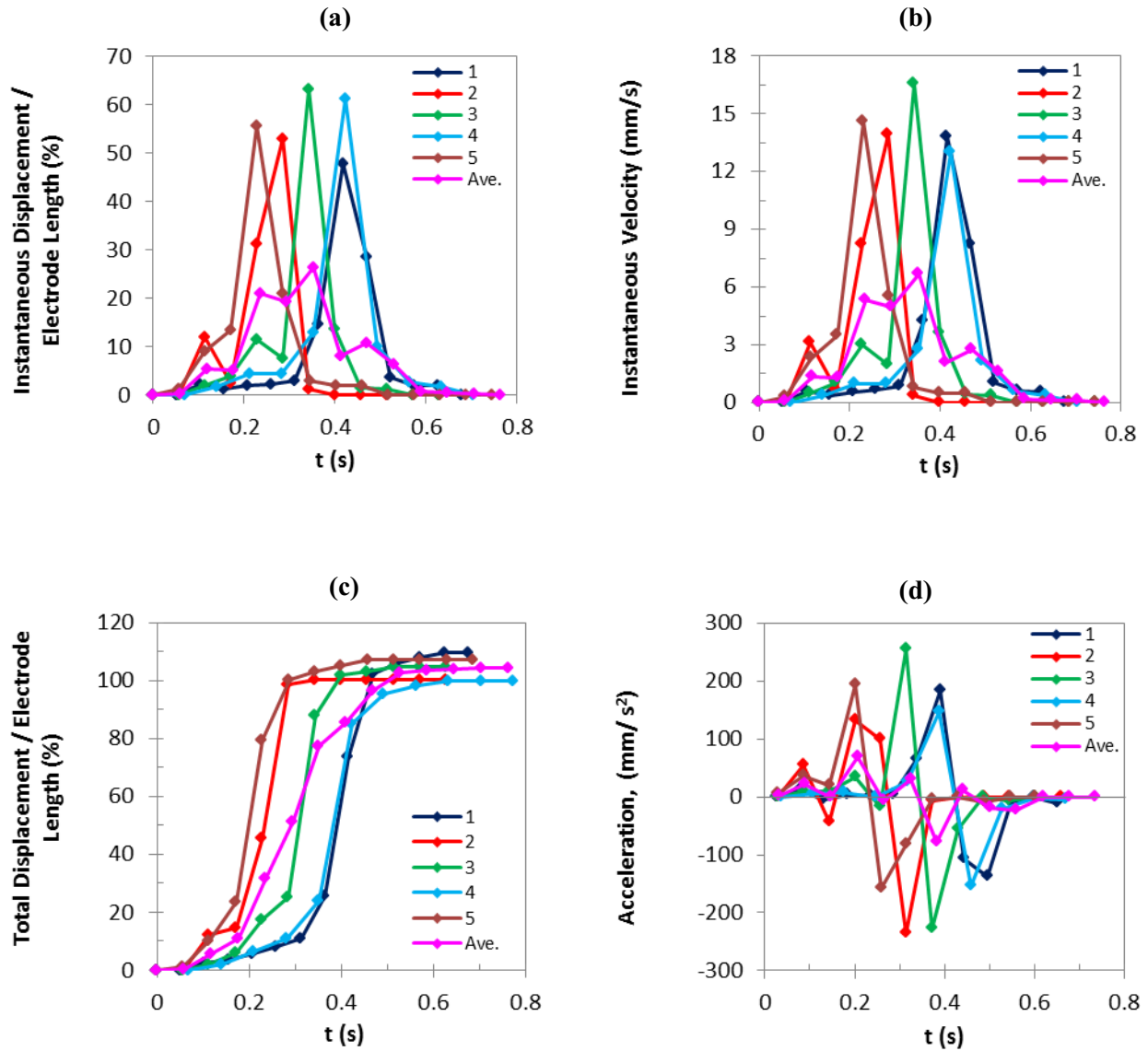


Figure F-25: (a) Instantaneous displacement, (b) instantaneous velocity, (c) total displacement, and (d) acceleration of the trailing edges of distilled water droplets as a function of time at 70 V.

Distilled Water, 70 V

Accepted experiments and the average curves

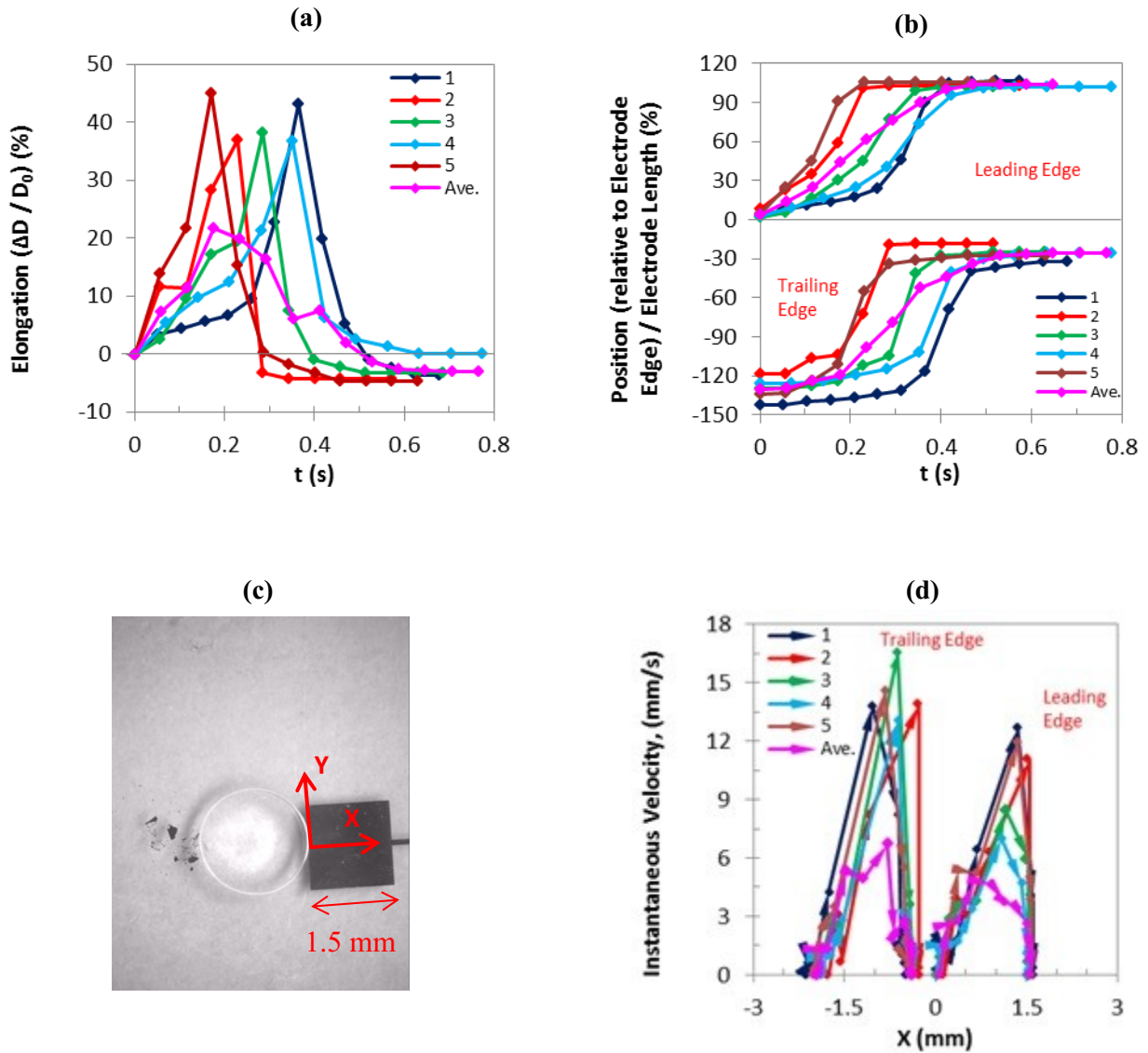


Figure F-26: (a) Droplet elongation and (b) droplet position as a function of time, (d) instantaneous velocity as a function of droplet position as shown in (c) for the leading and trailing edges of distilled water droplets at 70 V. The arrows in (d) indicate the changes of velocity along the direction of movement.

Distilled Water, 70 V, Average curves

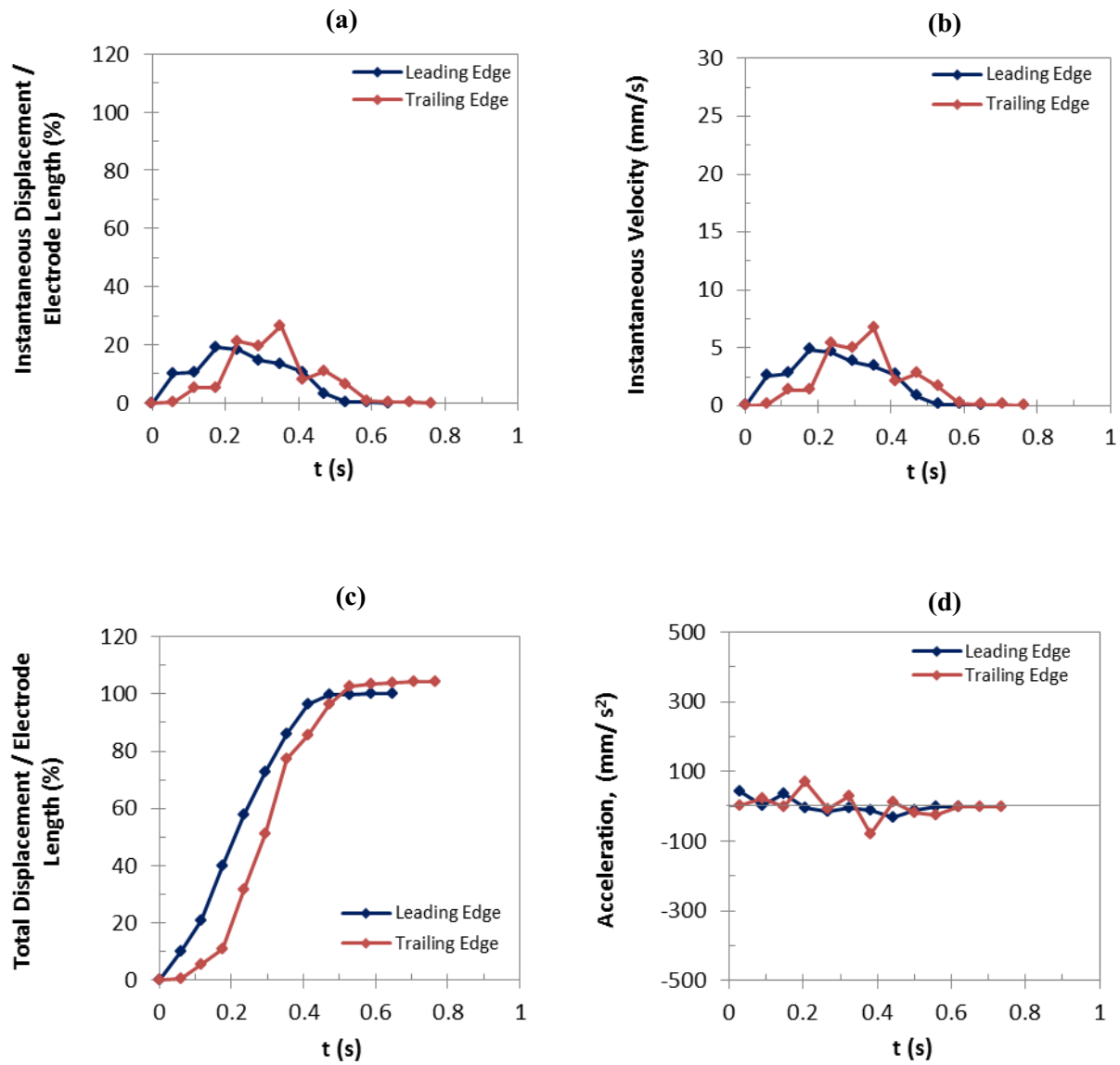


Figure F-27: Comparison of the average curves: (a) instantaneous displacement, (b) instantaneous velocity, (c) total displacement, and (d) acceleration, as a function of time for the leading and trailing edges of distilled water droplets at 70 V.

Distilled Water, 70 V, Average curves

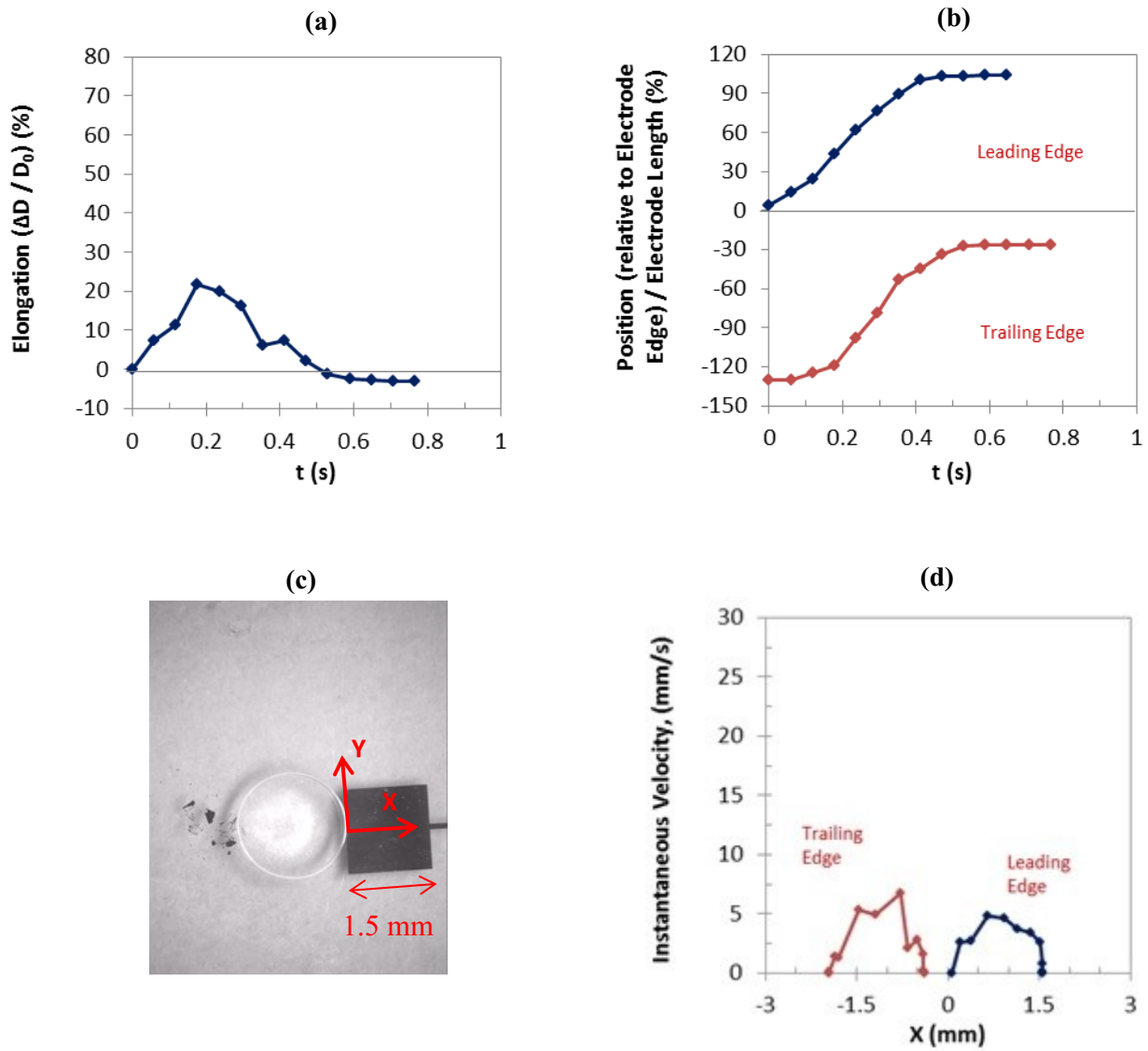


Figure F-28: Comparison of the average curves: (a) droplet elongation and (b) droplet position as a function of time, (d) instantaneous velocity as a function of droplet position as shown in (c) for the leading and trailing edges of distilled water droplets at 70 V.

F-7) Distilled Water, 65 V

Distilled Water, 65 V, Leading edge,

Accepted experiments and the average curves

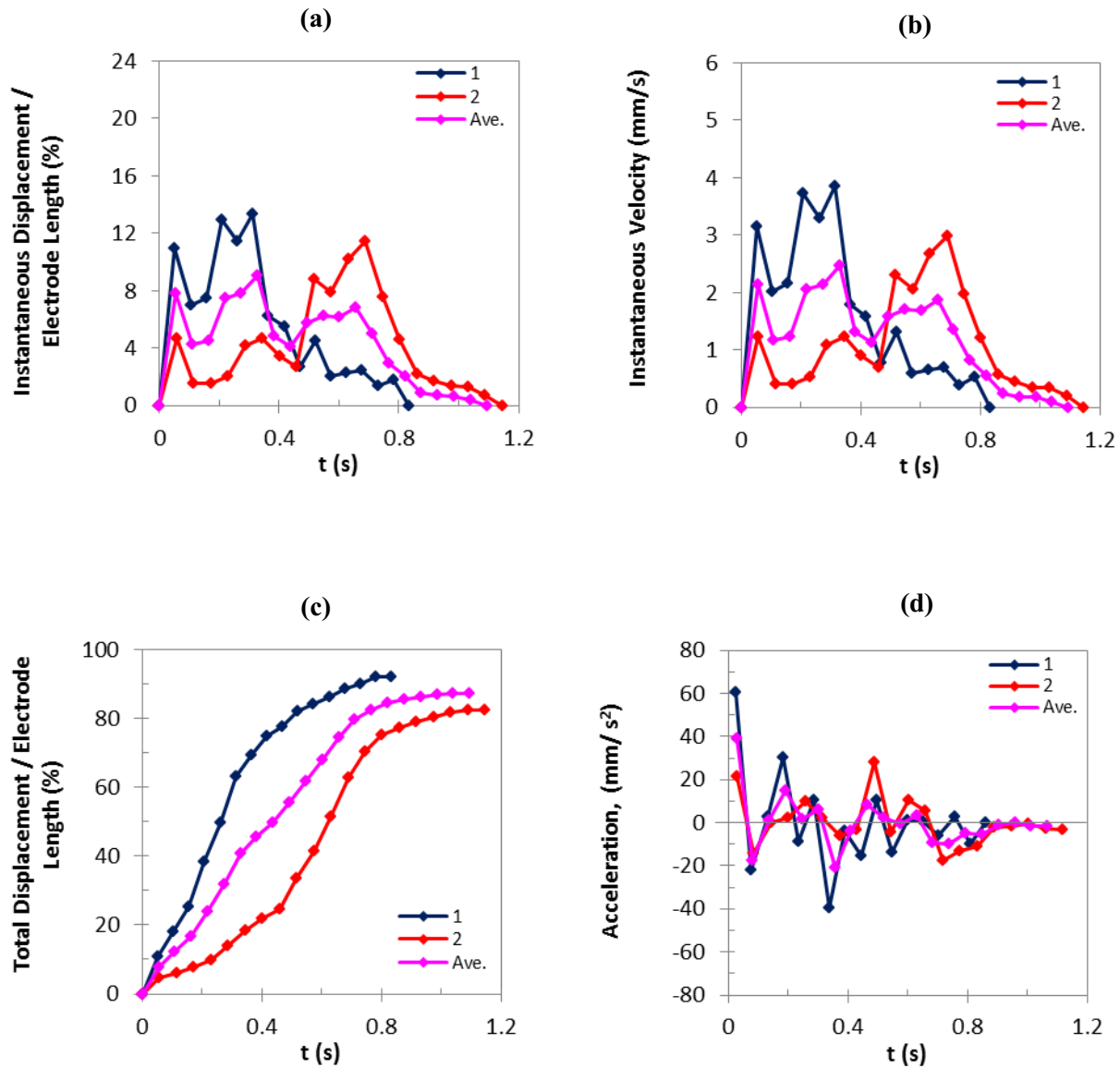


Figure F-29: (a) Instantaneous displacement, (b) instantaneous velocity, (c) total displacement, and (d) acceleration of the leading edges of distilled water droplets as a function of time at 65 V.

Distilled Water, 65 V, Trailing edge

Accepted experiments and the average curves

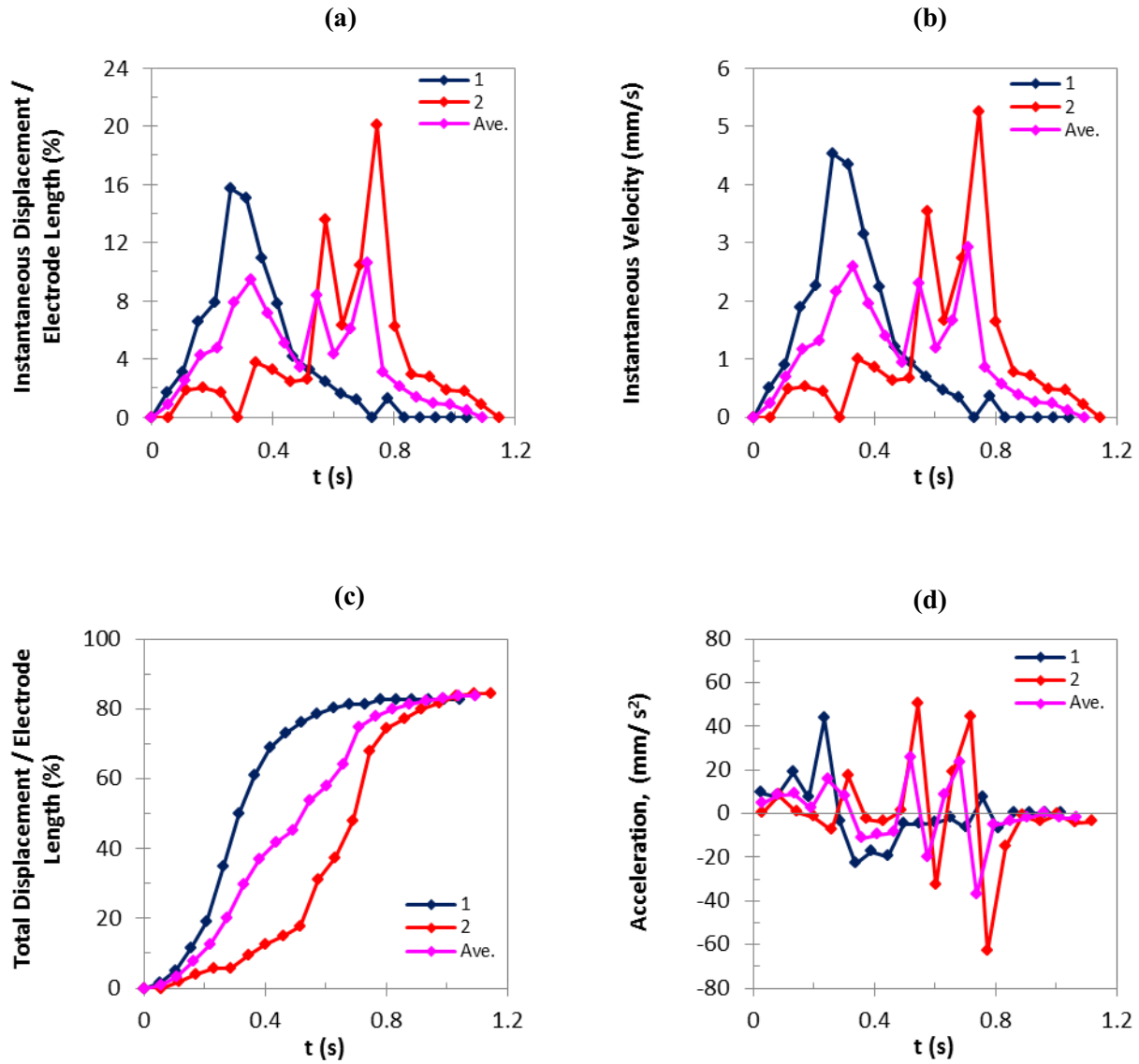


Figure F-30: (a) Instantaneous displacement, (b) instantaneous velocity, (c) total displacement, and (d) acceleration of the trailing edges of distilled water droplets as a function of time at 65 V.

Distilled Water, 65 V

Accepted experiments and the average curves

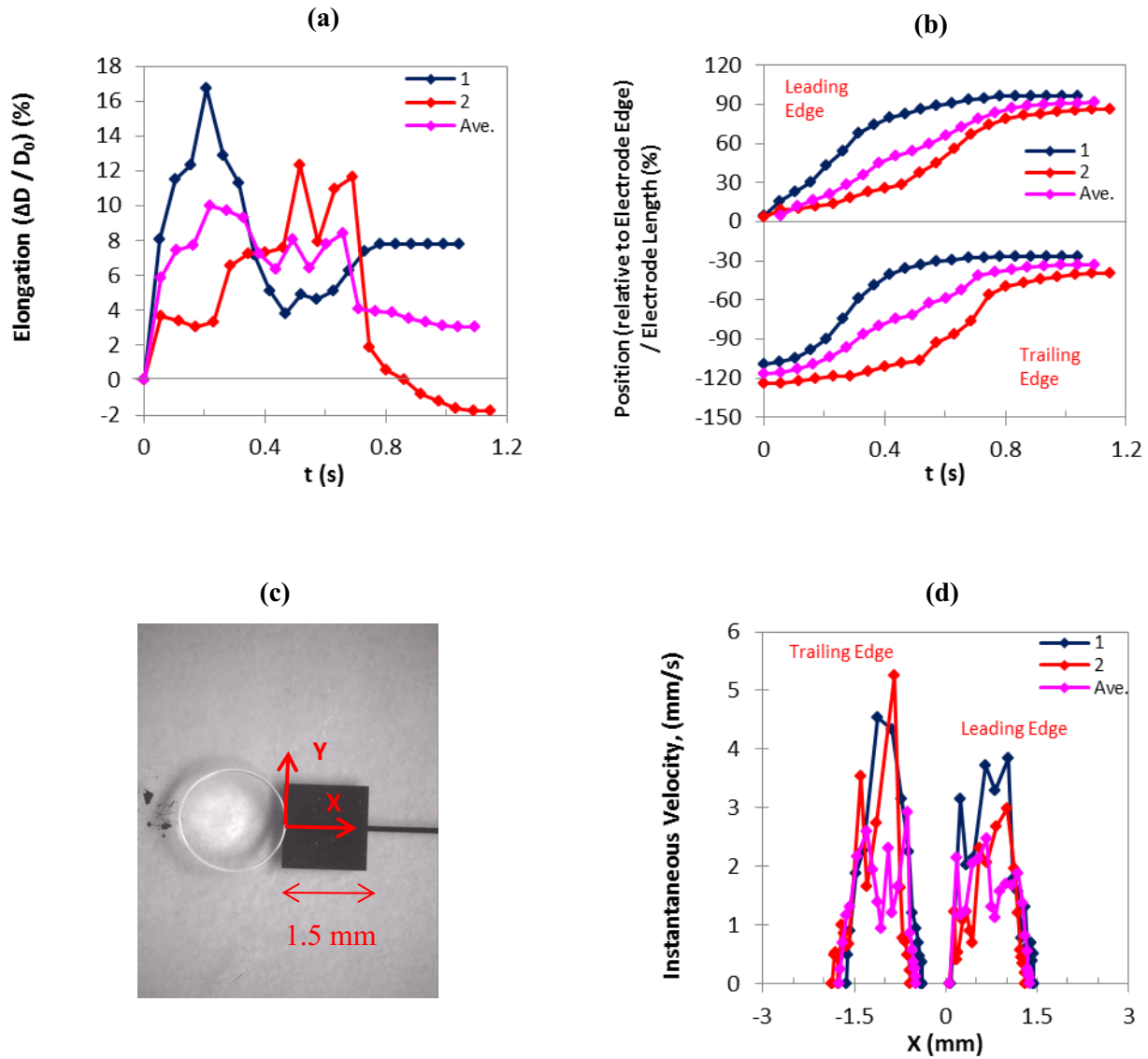


Figure F-31: (a) Droplet elongation and (b) droplet position as a function of time, (d) instantaneous velocity as a function of droplet position as shown in (c) for the leading and trailing edges of distilled water droplets at 65 V.

Distilled Water, 65 V, Average curves

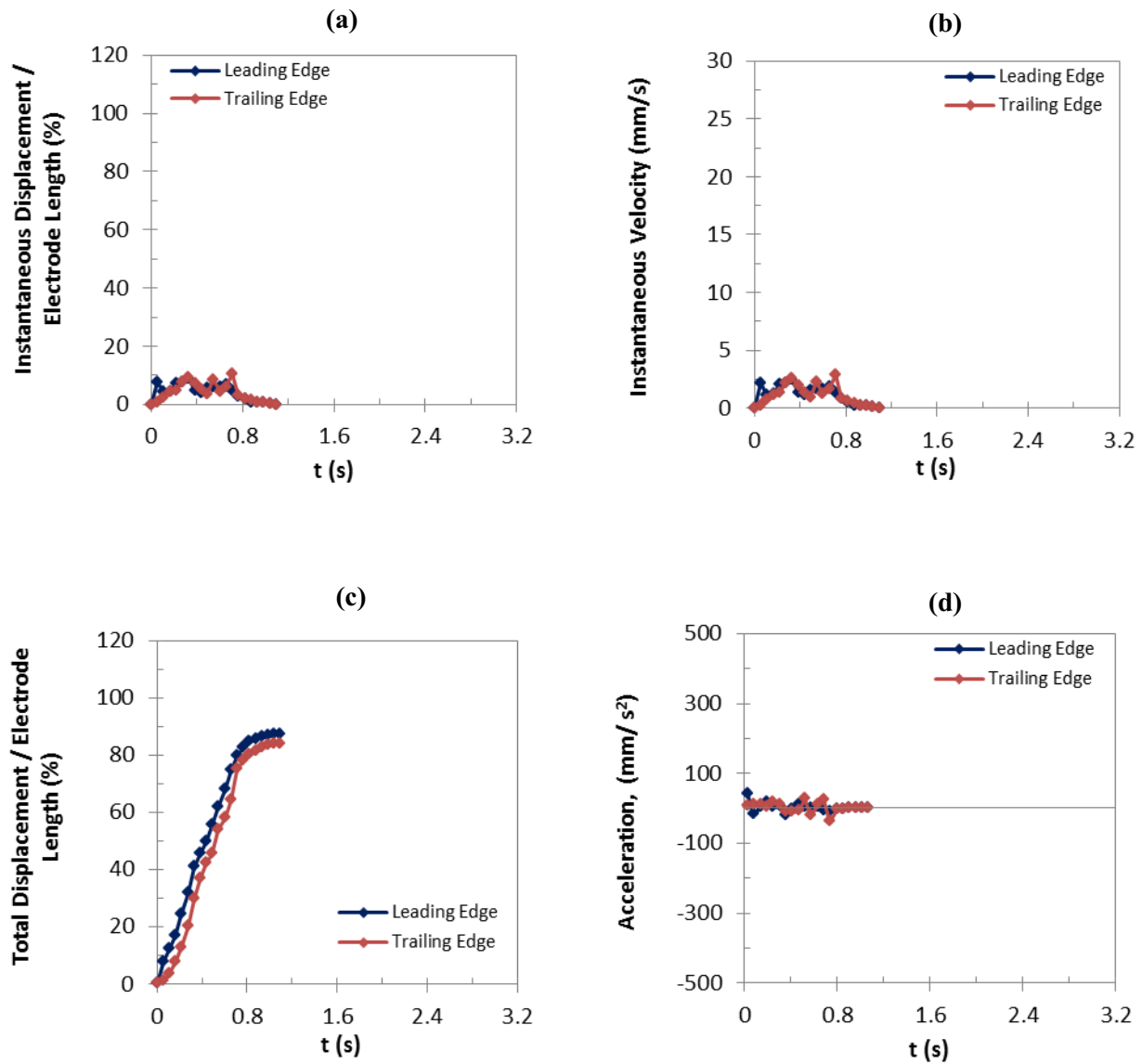


Figure F-32: Comparison of the average curves: (a) instantaneous displacement, (b) instantaneous velocity, (c) total displacement, and (d) acceleration, as a function of time for the leading and trailing edges of distilled water droplets at 65 V.

Distilled Water, 65 V, Average curves

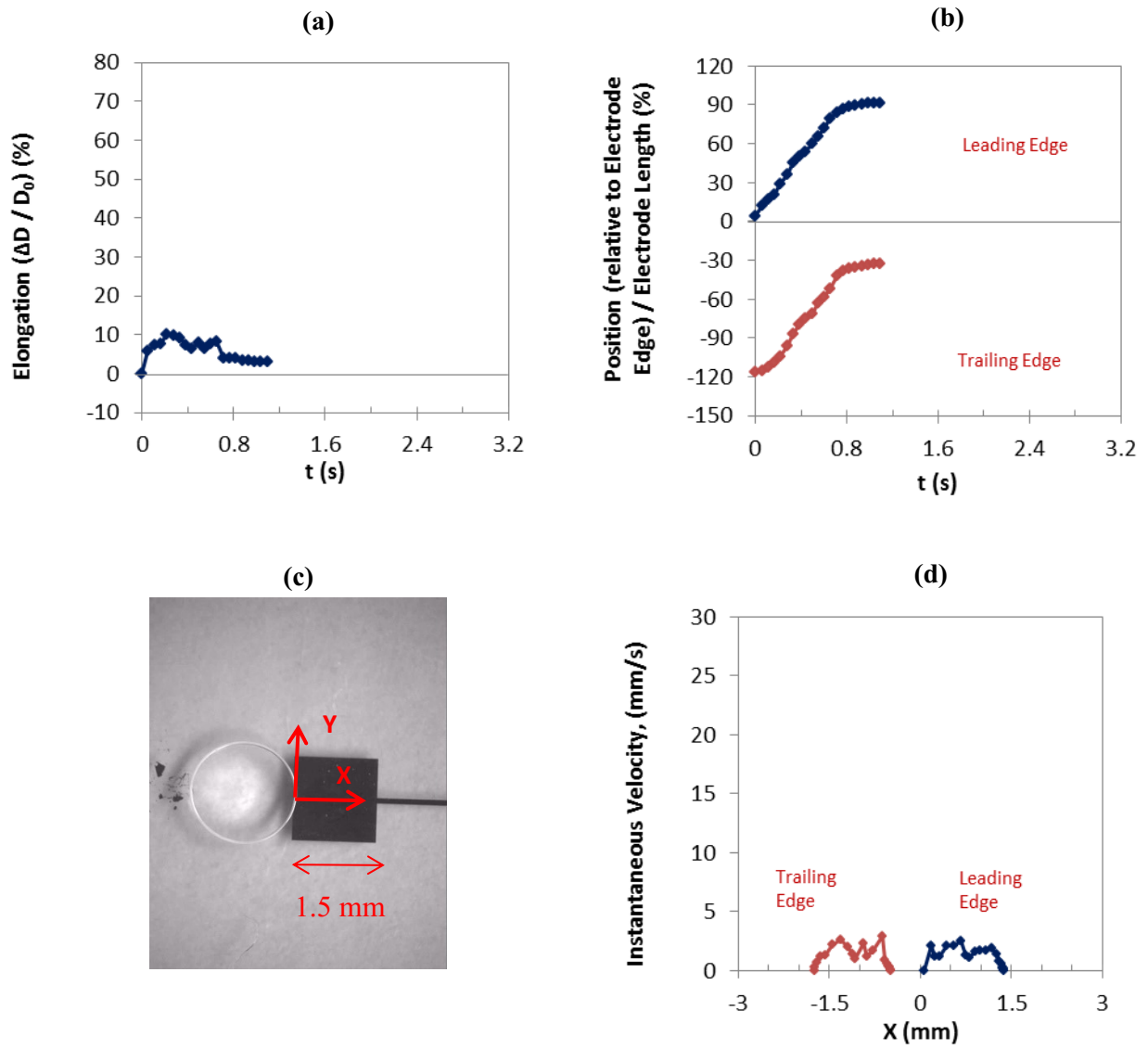


Figure F-33: Comparison of the average curves: (a) droplet elongation and (b) droplet position as a function of time, (d) instantaneous velocity as a function of droplet position as shown in (c) for the leading and trailing edges of distilled water droplets at 65 V.

F-8) Distilled Water, 60 V

Distilled Water, 60 V, Leading edge,

Accepted experiment

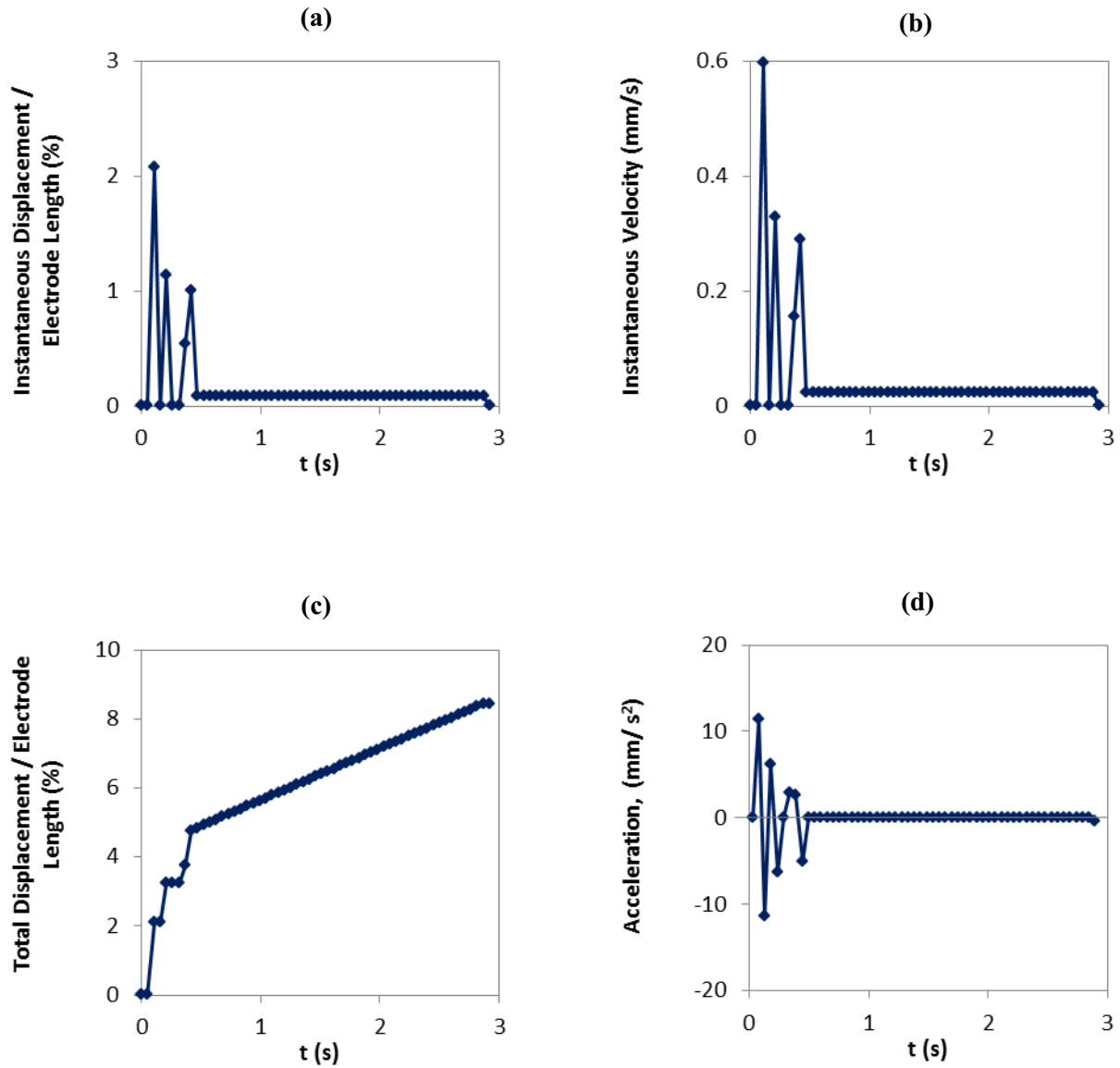


Figure F-34: (a) Instantaneous displacement, (b) instantaneous velocity, (c) total displacement, and (d) acceleration of the leading edges of distilled water droplets as a function of time at 60 V.

Distilled Water, 60 V, Trailing edge

Accepted experiment

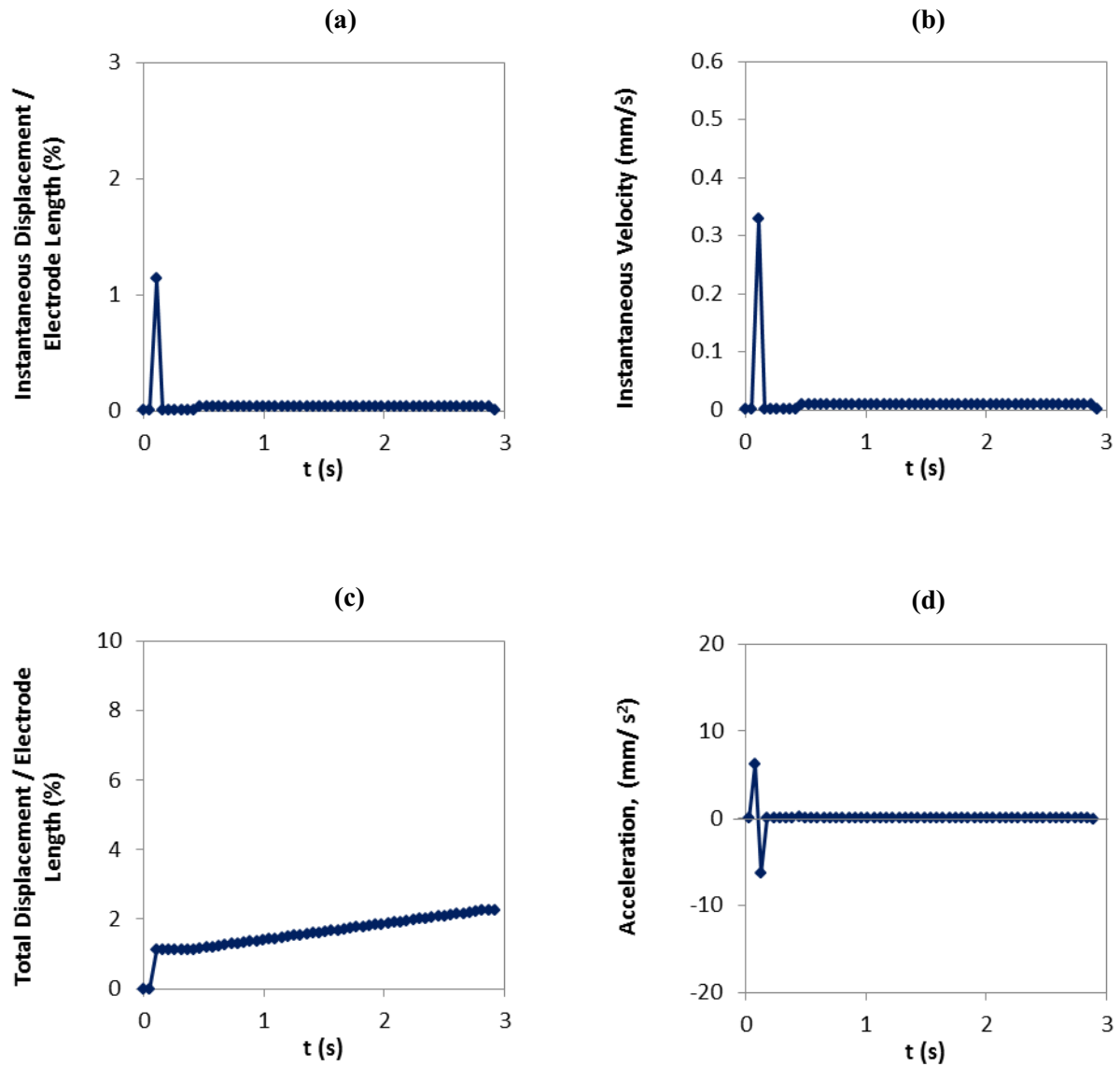


Figure F-35: (a) Instantaneous displacement, (b) instantaneous velocity, (c) total displacement, and (d) acceleration of the trailing edges of distilled water droplets as a function of time at 60 V.

Distilled Water, 60 V

Accepted experiment

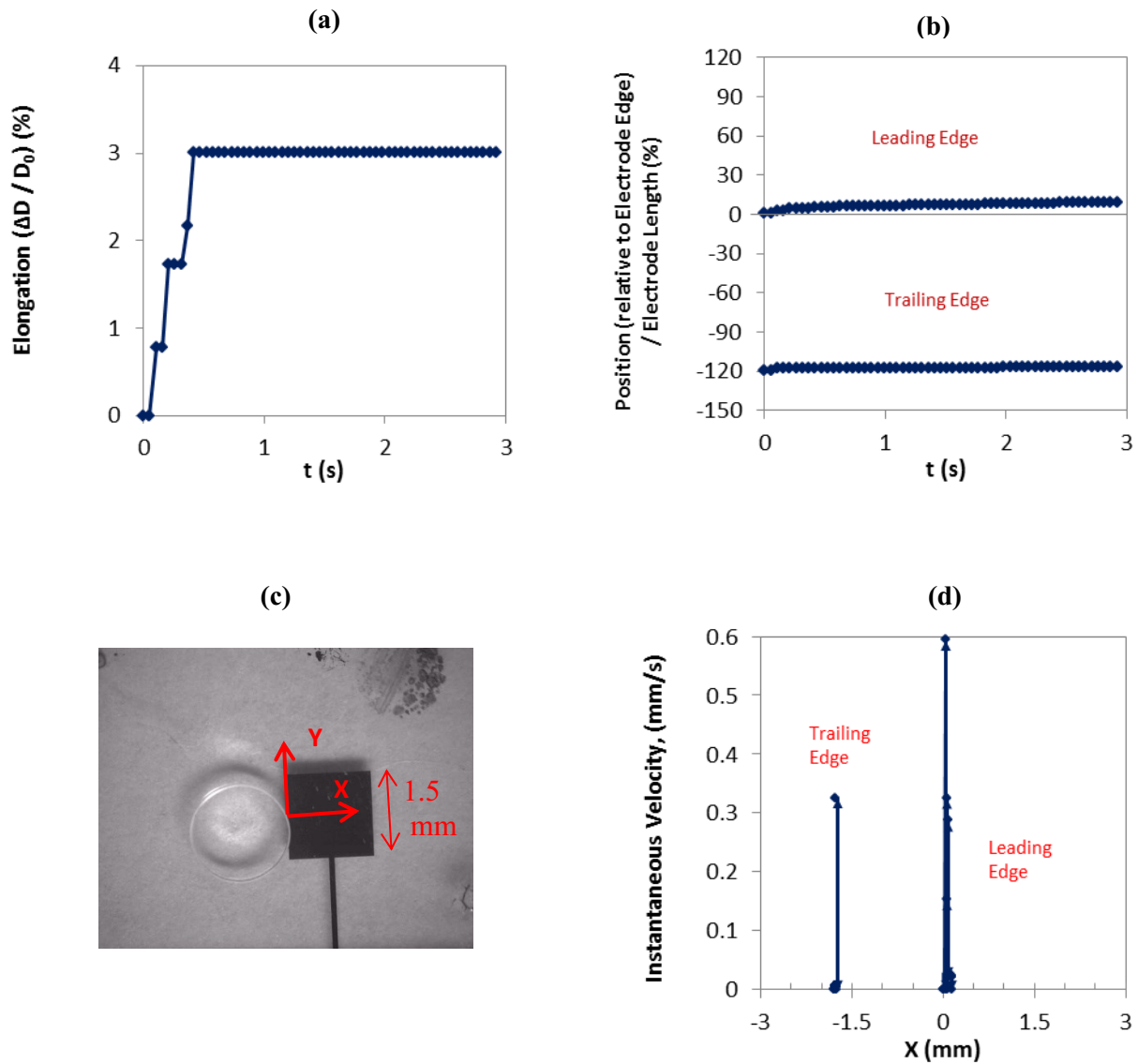


Figure F-36: (a) Droplet elongation and (b) droplet position as a function of time, (d) instantaneous velocity as a function of droplet position as shown in (c) for the leading and trailing edges of distilled water droplets at 60 V.

Distilled Water, 60 V, Average curves

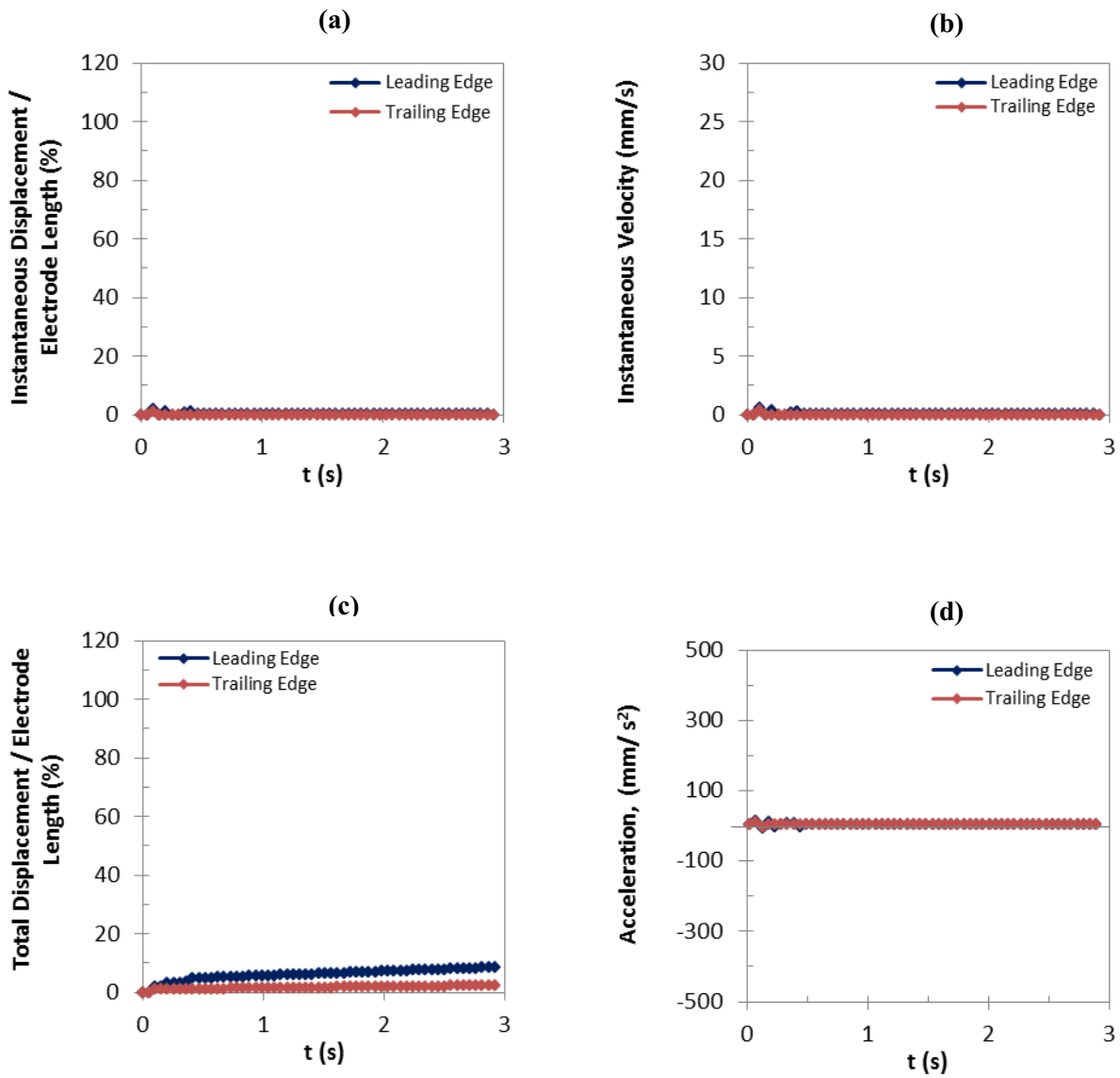


Figure F-37: Comparison of the average curves: (a) instantaneous displacement, (b) instantaneous velocity, (c) total displacement, and (d) acceleration, as a function of time for the leading and trailing edges of distilled water droplets at 60 V.

Distilled Water, 60 V, Average curves

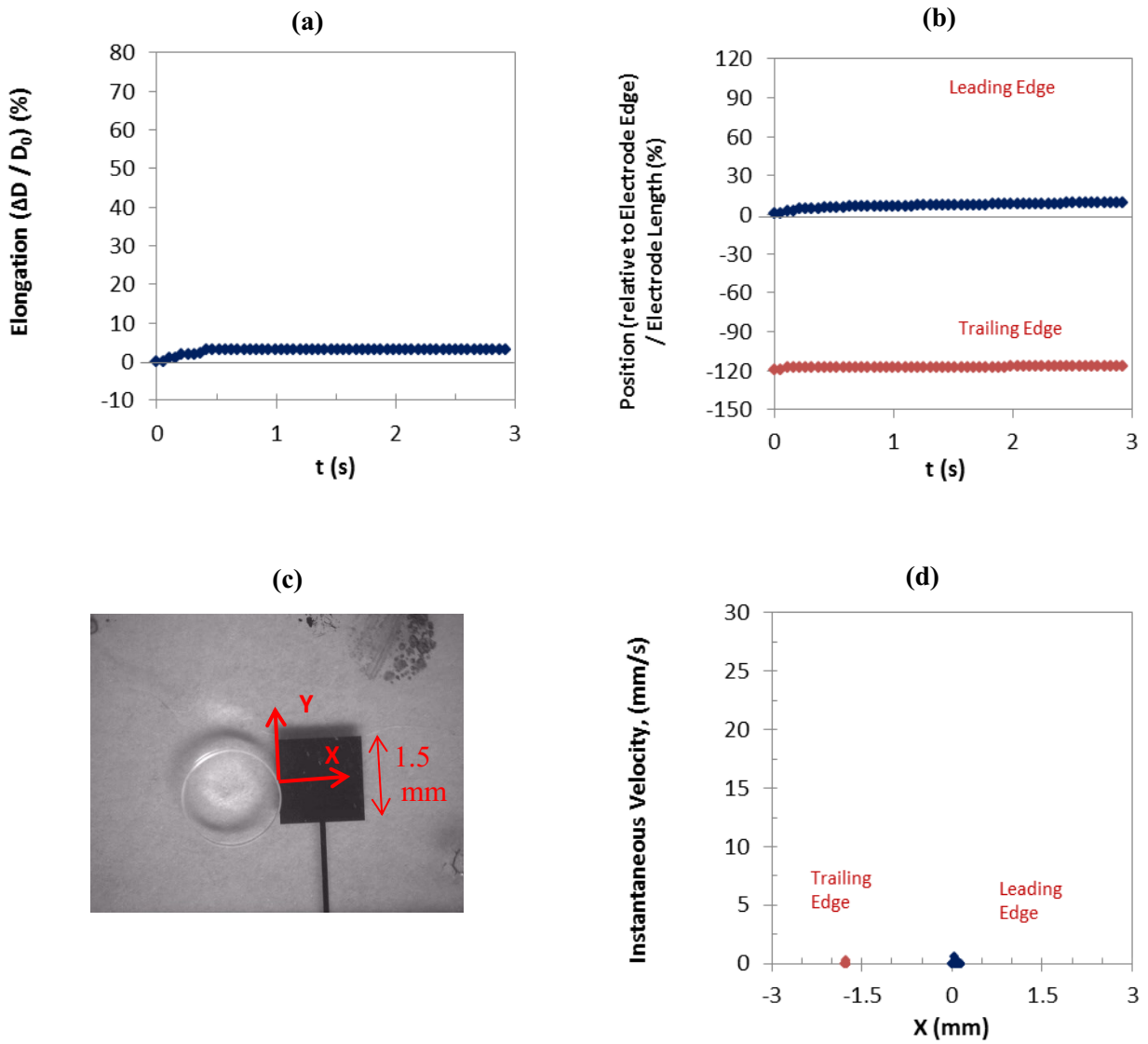


Figure F-38: Comparison of the average curves: (a) droplet elongation and (b) droplet position as a function of time, (d) instantaneous velocity as a function of droplet position as shown in (c) for the leading and trailing edges of distilled water droplets at 60 V.

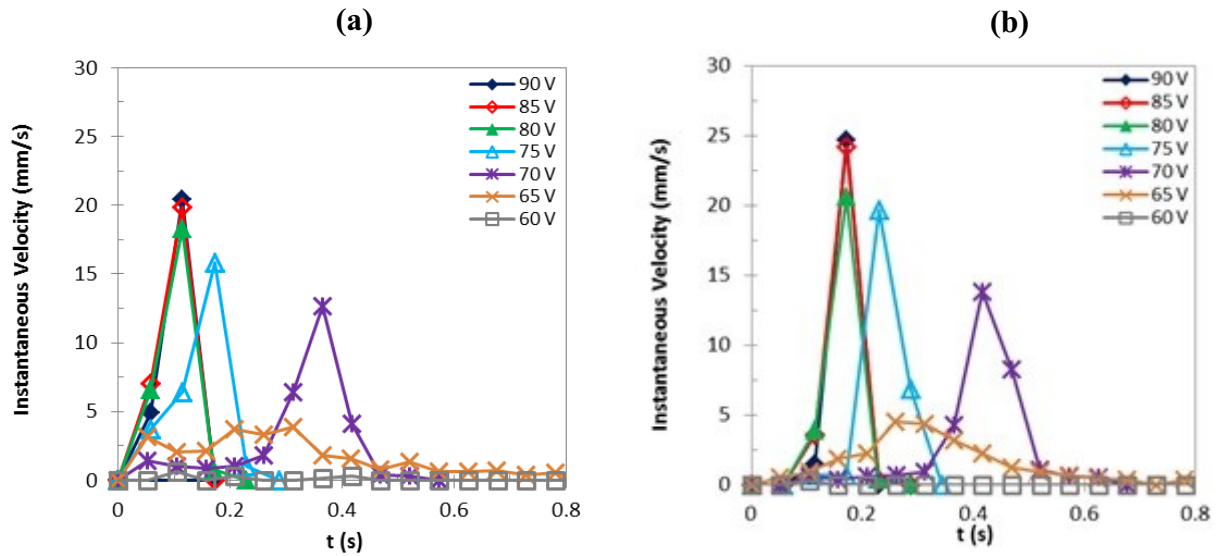


Figure F-39: The instantaneous velocity of the distilled water droplets as a function of time for the applied voltages of 60 to 90V. Comparison of results for the experiments with the highest leading edge instantaneous velocity: (a) leading edge, (b) trailing edge.

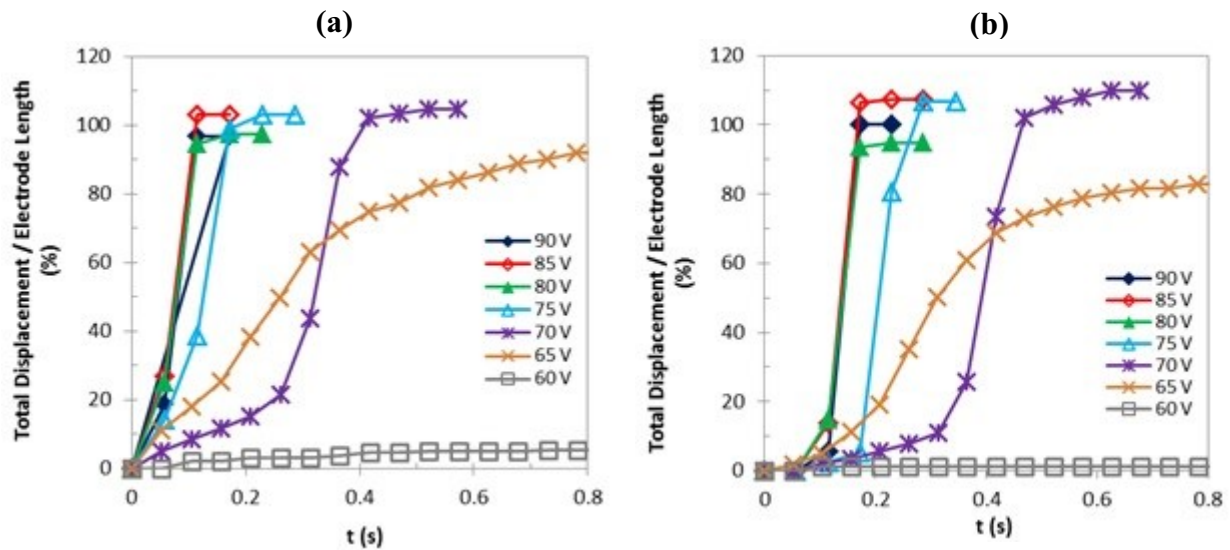


Figure F-40: The total displacement of the distilled water droplets as a function of time for the applied voltages of 60 to 90V. Comparison of results for the experiments with the highest leading edge instantaneous velocity: (a) leading edge, (b) trailing edge.

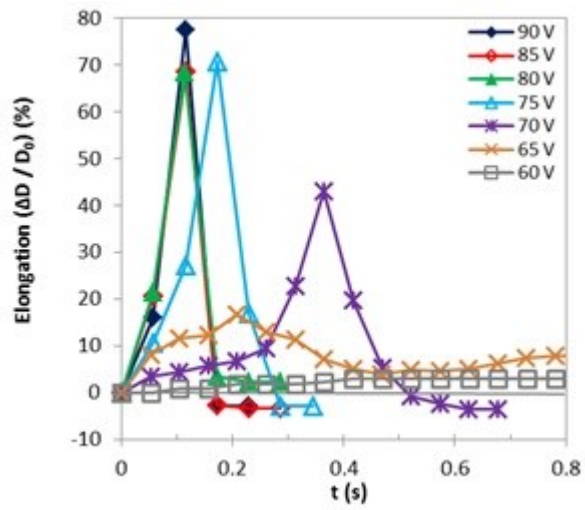


Figure F-41: The comparison of results for the elongation of distilled water droplets as a function of time for the experiments with the highest leading edge instantaneous velocity.

Table F-1: Peaks of the average curves, distilled water

Applied Voltage	90 V	85 V	80 V	75 V	70 V	65 V	60 V	55 V	50 V
Leading Edge									
Instantaneous Velocity (mm/s)	19.3	13.0	12.7	13.3	4.9	2.5	0.6	0	0
Total Displacement	99%	104%	101%	101%	100%	85%	8.5%	0	0
Trailing Edge									
Instantaneous Velocity (mm/s)	22.4	17.1	12.9	20.4	6.7	2.9	0.3	0	0
Total Displacement	101%	104%	96%	103%	103%	81%	2.3%	0	0
Elongation (normalized)	67%	57%	48%	61%	22%	10%	3%	0	0

Table F-2: Peaks of the curves for the experiments with the highest leading edge instantaneous velocity, distilled water

Applied Voltage	90 V	85 V	80 V	75 V	70 V	65 V	60 V	55 V	50 V
Leading Edge									
Instantaneous Velocity (mm/s)	20.4	19.9	18.2	15.8	12.7	3.90	0.6	0	0
Total Displacement (normalized)	97%	103%	97%	99%	102%	89%	8.5%	0	0
Trailing Edge									
Instantaneous Velocity (mm/s)	24.7	24.2	20.6	19.7	13.8	4.5	0.3	0	0
Total Displacement (normalized)	100%	106%	95%	107%	102%	80%	2.3%	0	0
Elongation (normalized)	78%	69%	68%	71%	43%	17%	3%	0	0

Table F-3: Average velocity for all experiments, distilled water

Leading Edge									
Average Velocity (mm/s)	13.0	12.2	10.7	8.4	5.0	1.6	0.1	0	0
Trailing Edge									
Average Velocity (mm/s)	8.8	8.2	7.2	6.2	4.1	1.5	0	0	0

Table F-4: Average velocity for the experiments with the highest leading edge instantaneous velocity, distilled water

Leading Edge									
Average Velocity (mm/s)	12.7	13.5	12.4	8.7	3.6	2.0	0.1	0	0
Trailing Edge									
Average Velocity (mm/s)	8.7	9.3	8.2	5.6	3.3	1.8	0	0	0

Distilled Water, Leading edge

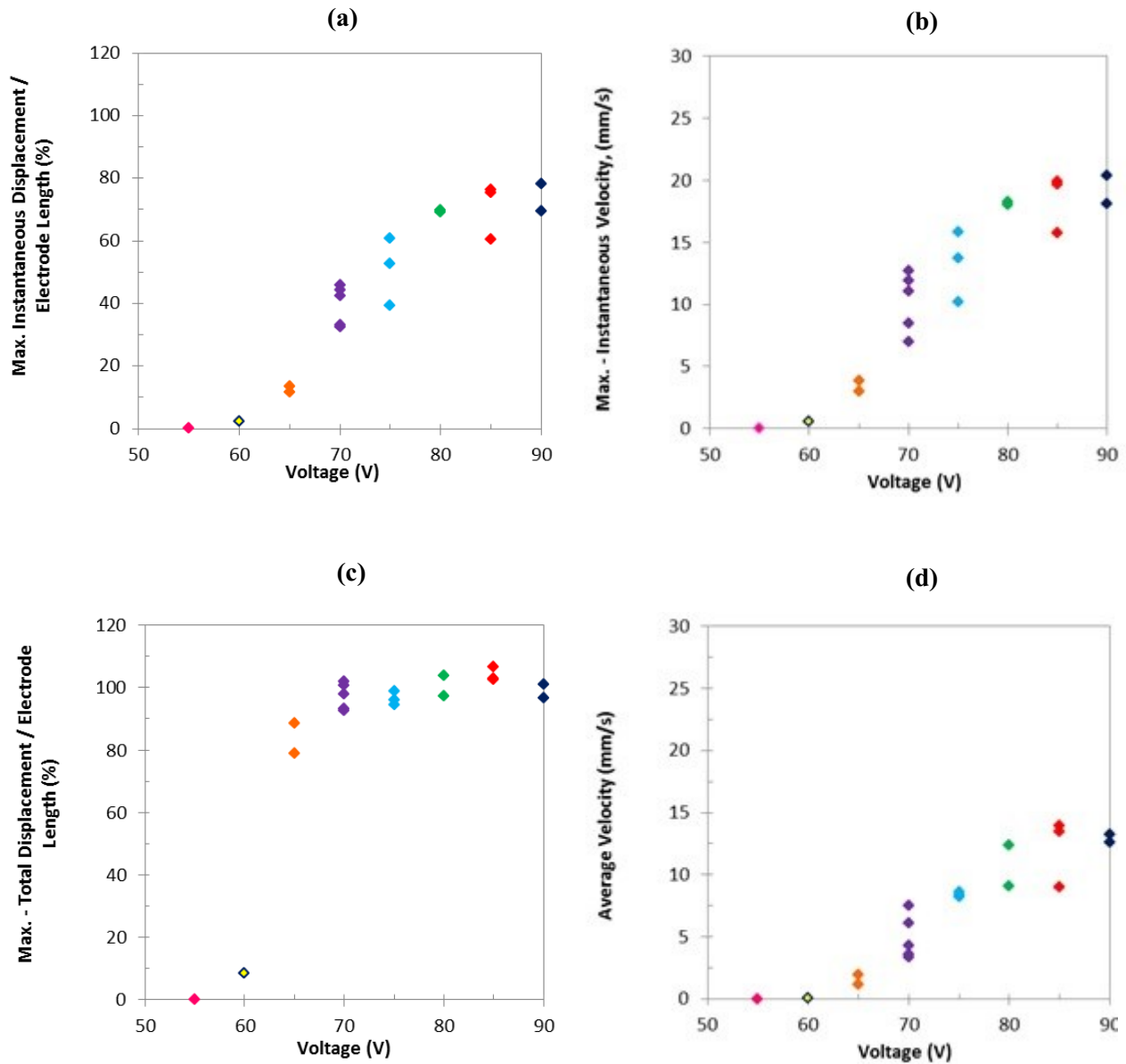


Figure F-42: Changes of the max.: (a) instantaneous displacement, (b) instantaneous velocity, (c) total displacement, and (d) average velocity with the applied voltage for the leading edges of distilled water droplets.

Distilled Water, Trailing edge

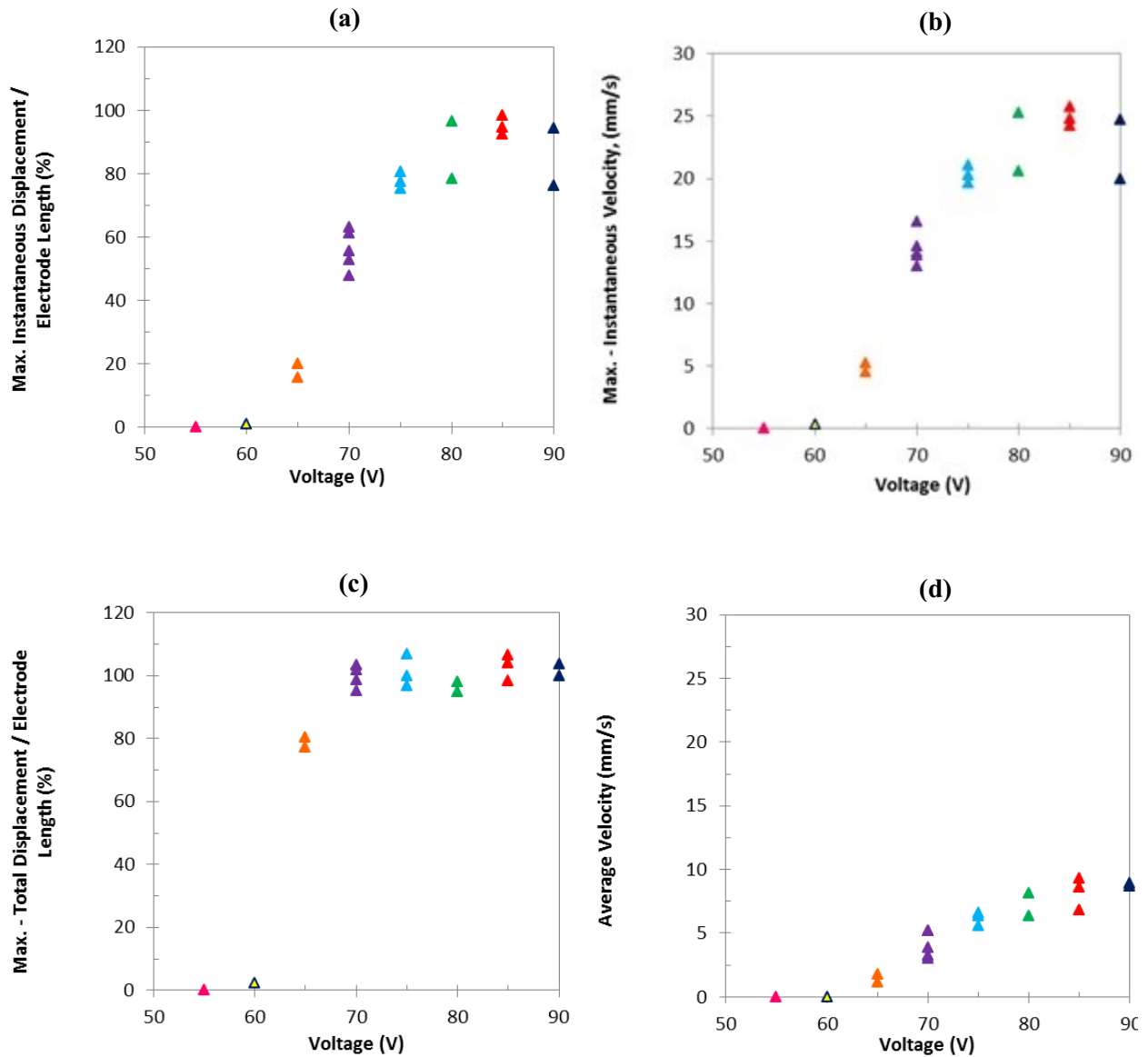


Figure F-43: Changes of the max.: (a) instantaneous displacement, (b) instantaneous velocity, (c) total displacement, and (d) average velocity with the applied voltage for the trailing edges of distilled water droplets.

Distilled Water

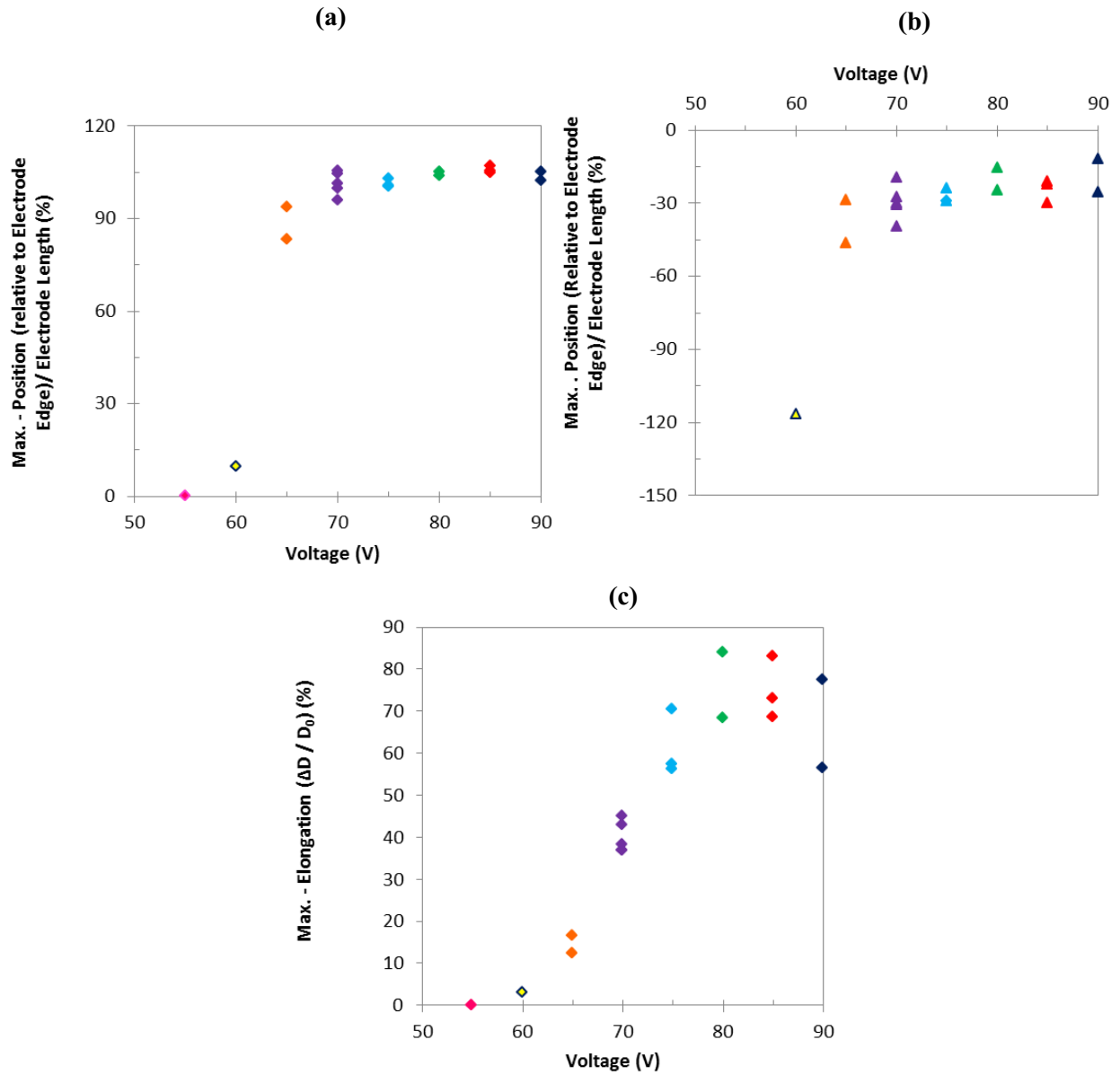


Figure F-44: Changes of the max.: (a) position of the leading edge, (b) position of the trailing edge, (c) elongation, with the applied voltage for distilled water droplets.

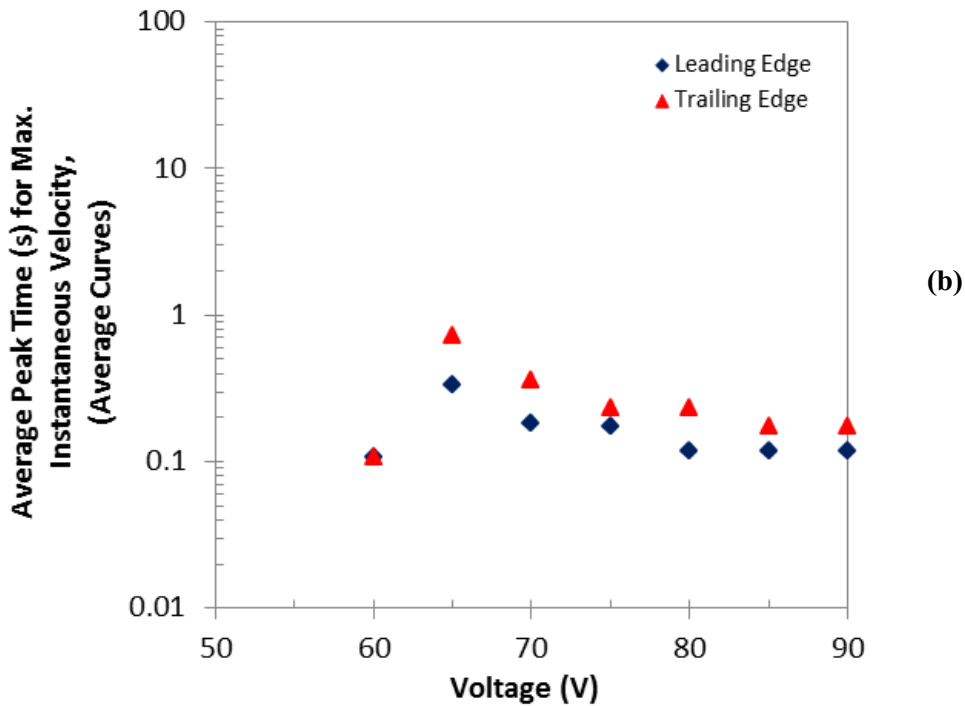
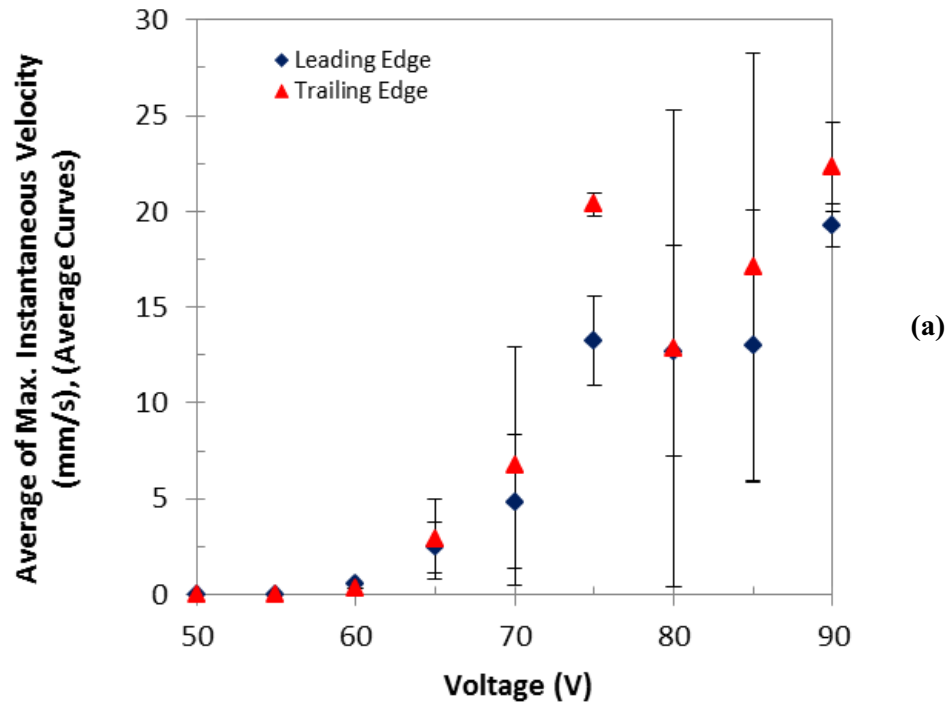


Figure F-45: The average of: (a) max. instantaneous velocity, and (b) peak time for max. instantaneous velocity, as a function of voltage for the leading and trailing edges of the distilled water droplets. The error bars indicate standard deviation.

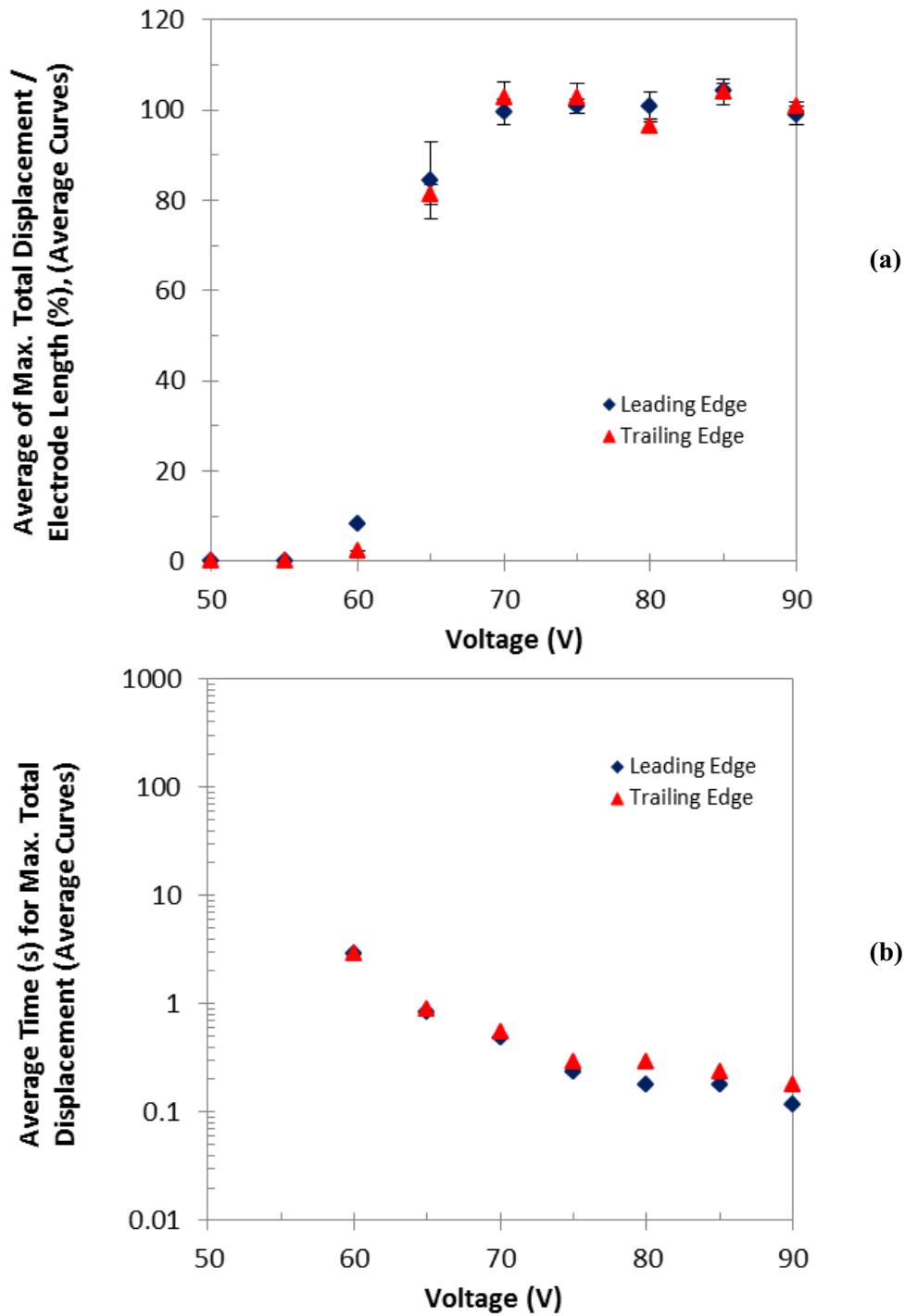


Figure F-46: The average of: (a) max. total displacement, and (b) transition time, as a function of voltage for the leading and trailing edges of the distilled water droplets. The error bars indicate standard deviation.

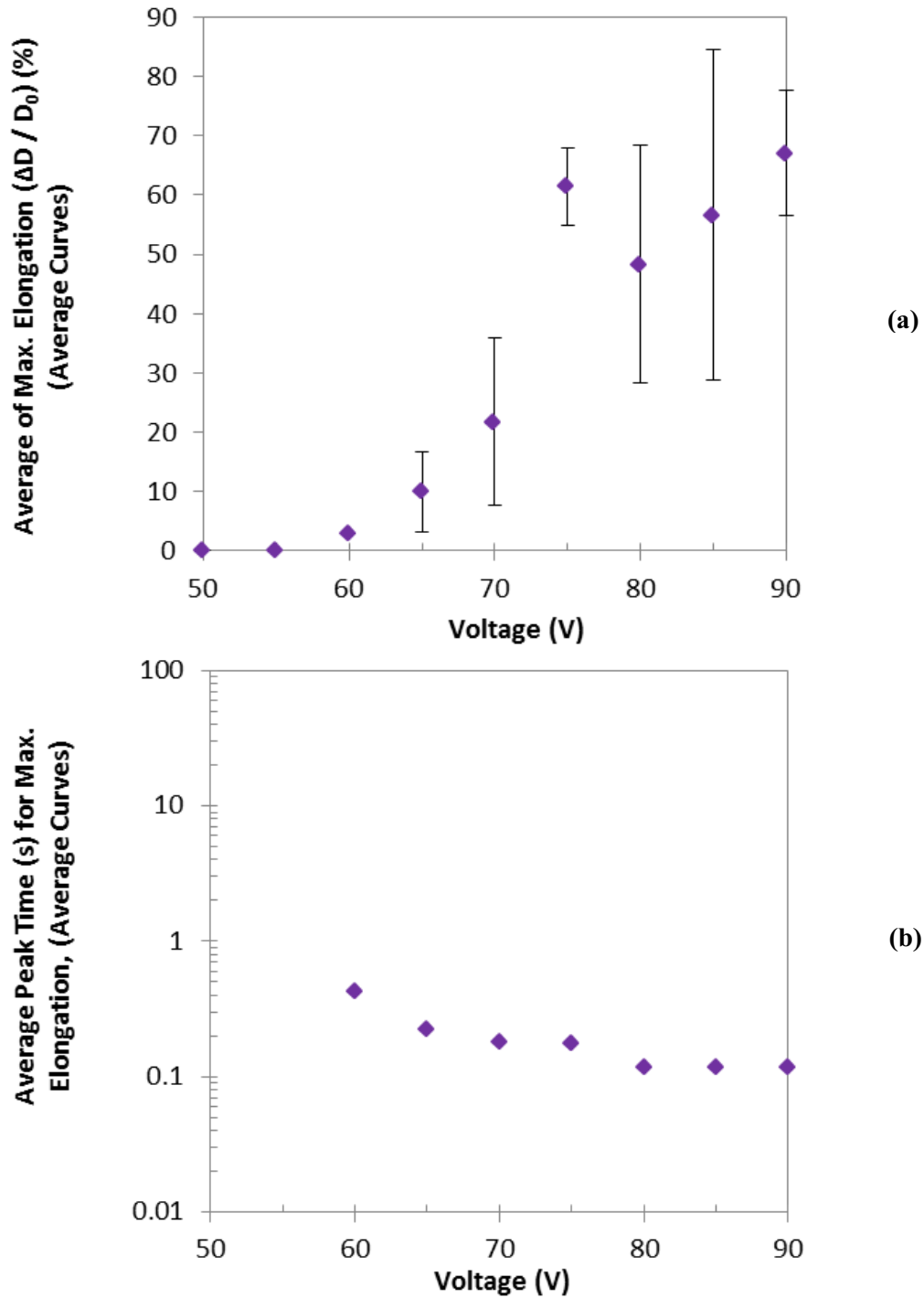
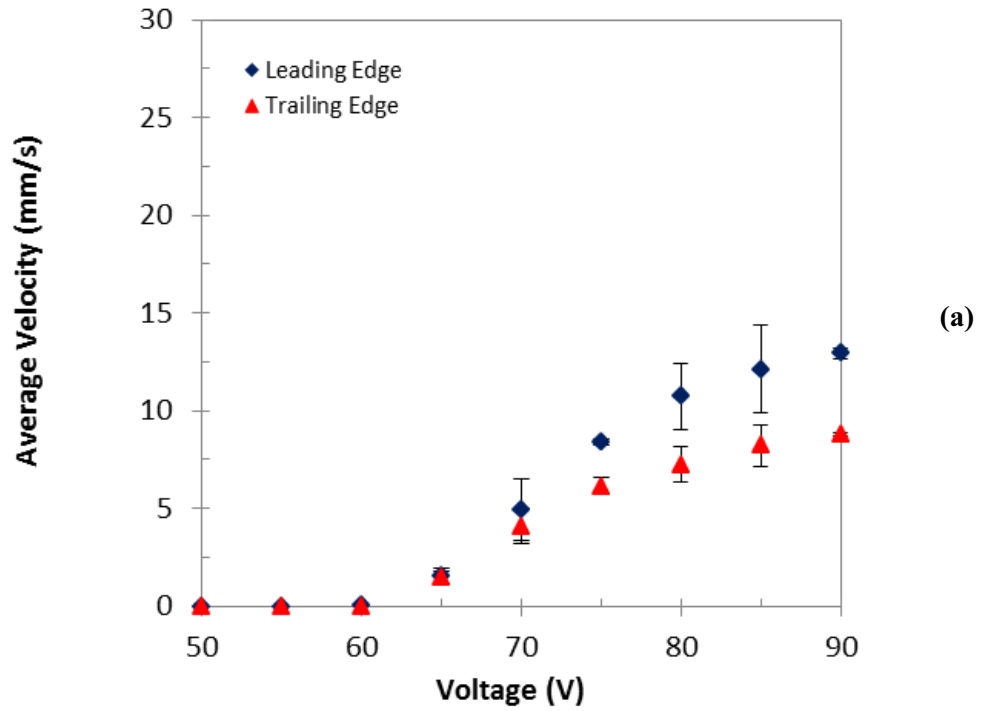
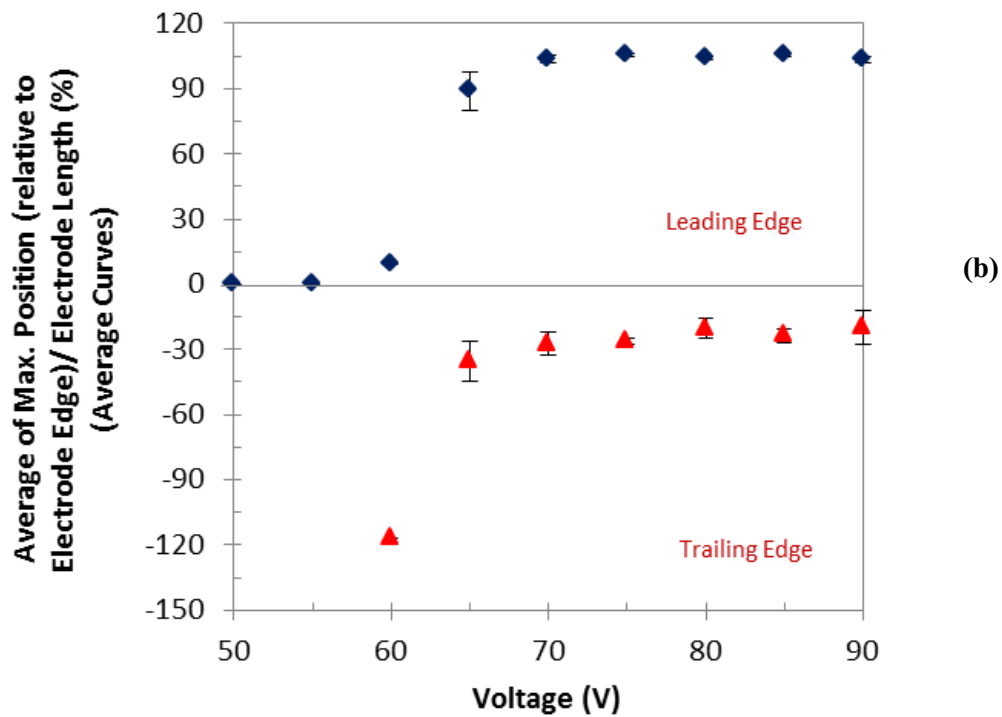


Figure F-47: The average of: (a) max. elongation, and (b) peak time for max. elongation, as a function of voltage for distilled water droplets. The error bars indicate standard deviation.



(a)



(b)

Figure F-48: (a) The average velocity, and (b) the average of max. position, as a function of voltage for the leading and trailing edges of the distilled water droplets. The error bars indicate standard deviation.

Appendix G

Tris-HCl Buffer Solution

G-1) Tris-HCl, 90 V

Tris-HCl buffer solution, 90 V, Leading edge,

Accepted experiments and the average curves

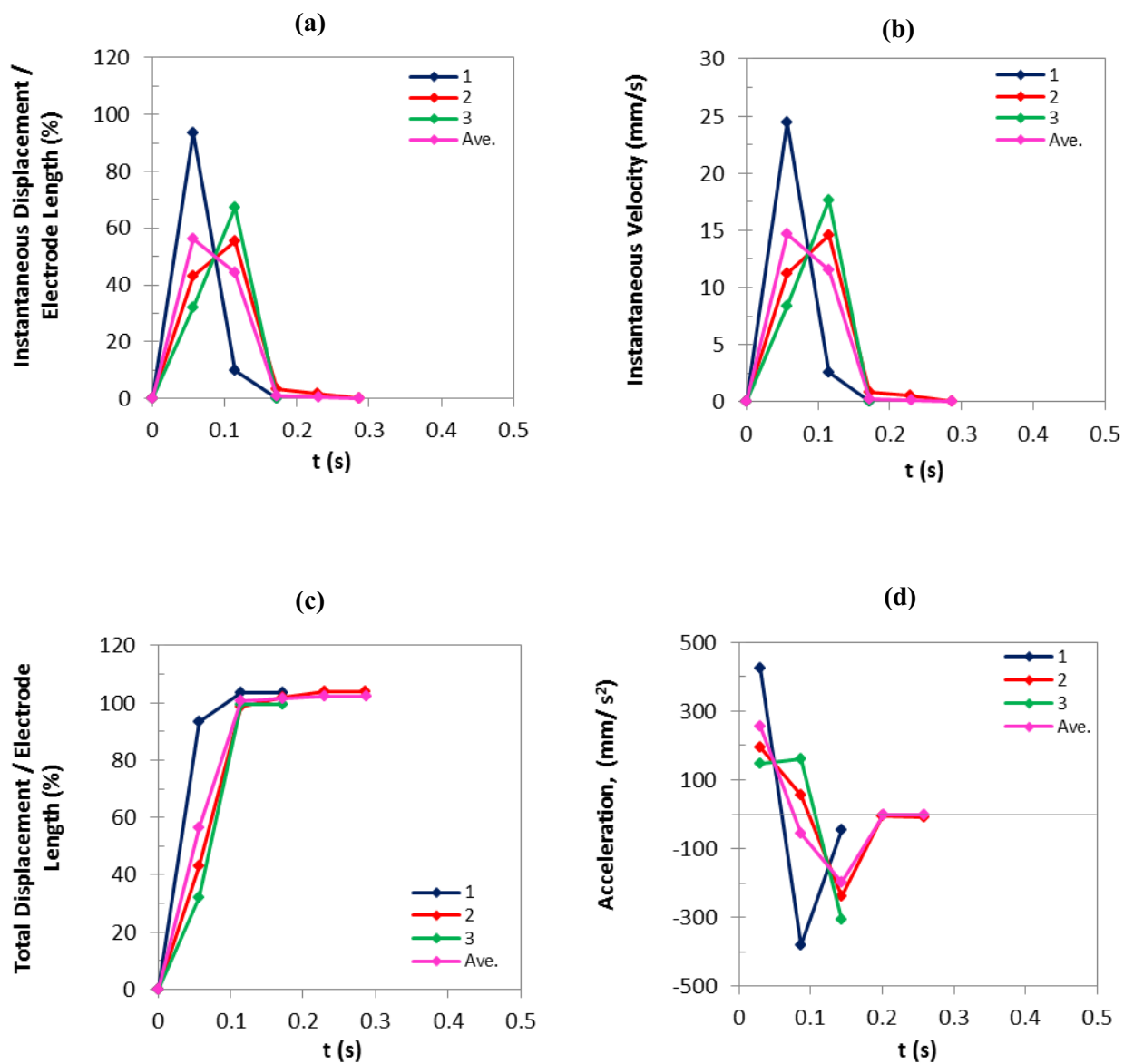


Figure G-1: (a) Instantaneous displacement, (b) instantaneous velocity, (c) total displacement, and (d) acceleration of the leading edges of Tris-HCl buffer droplets as a function of time at 90 V.

Tris-HCl buffer solution, 90 V, Trailing edge,

Accepted experiments and the average curves

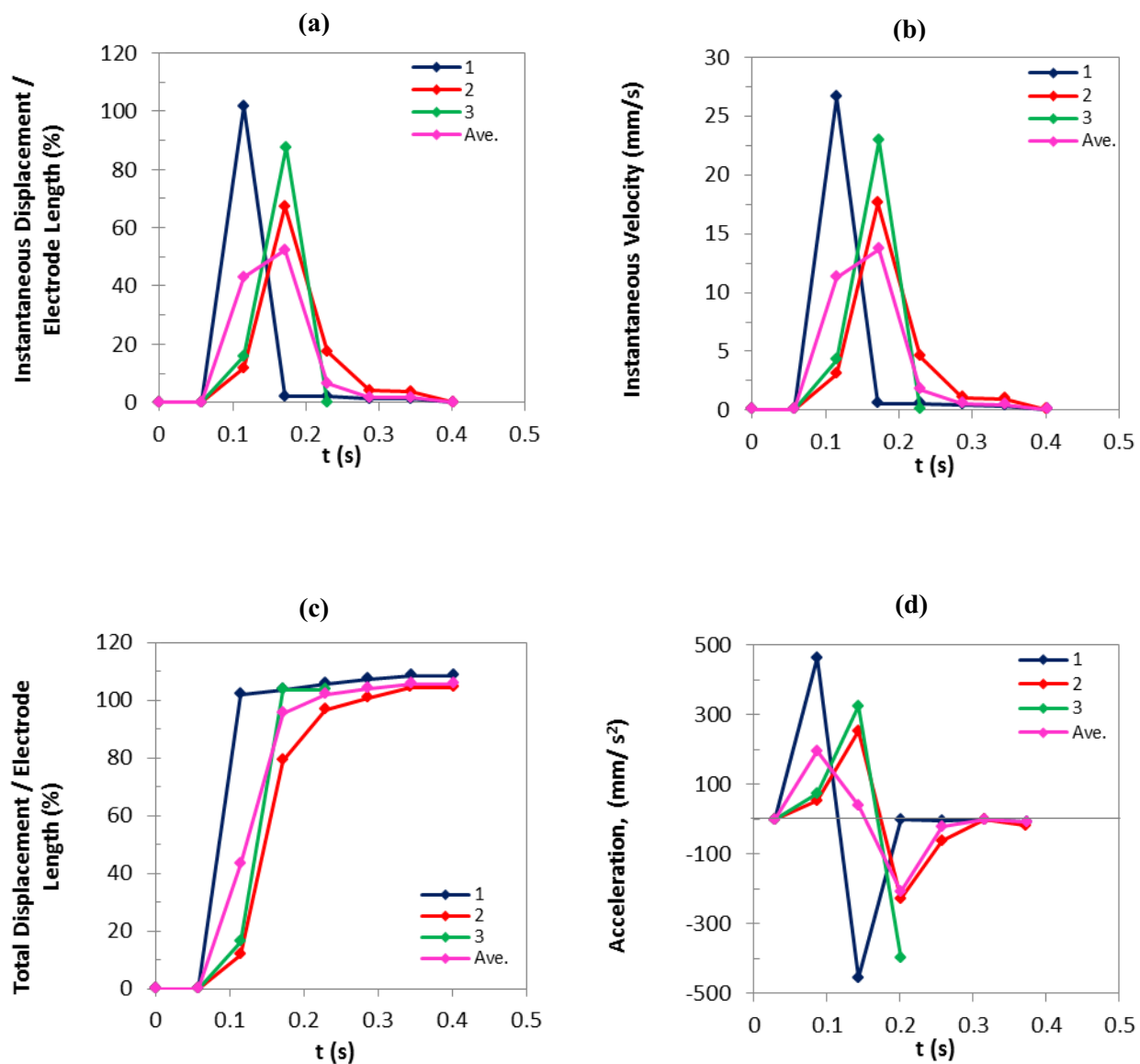


Figure G-2: (a) Instantaneous displacement, (b) instantaneous velocity, (c) total displacement, and (d) acceleration of the trailing edges of Tris-HCl buffer droplets as a function of time at 90 V.

Tris-HCl buffer solution, 90 V

Accepted experiments and the average curves

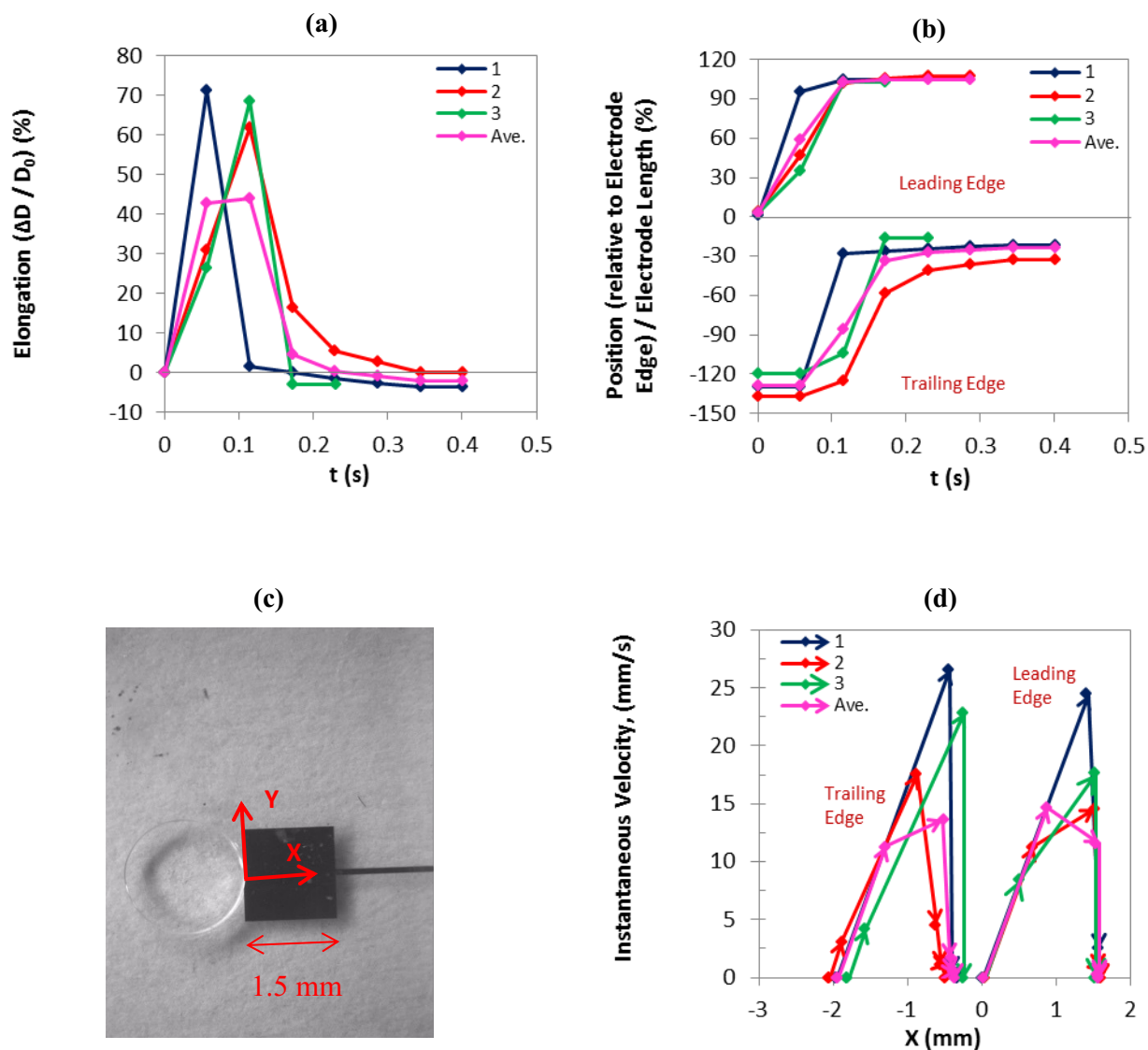


Figure G-3: (a) Droplet elongation and (b) droplet position as a function of time, (d) instantaneous velocity as a function of droplet position as shown in (c) for the leading and trailing edges of Tris-HCl buffer droplets at 90 V. The arrows in graph (d) indicate the changes of velocity along the direction of movement.

Tris-HCl buffer solution, 90 V, Average curves

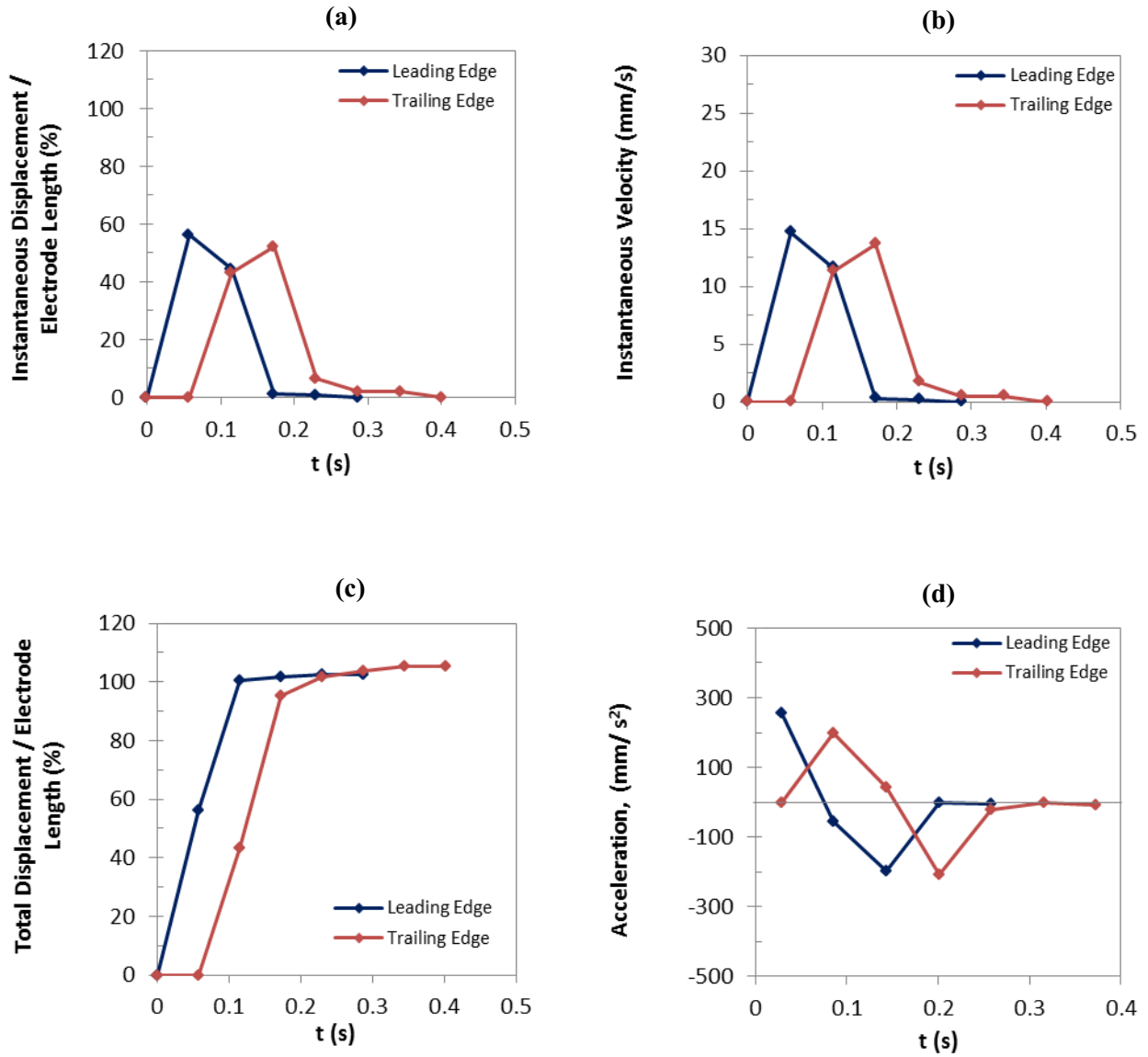


Figure G-4: Comparison of the average curves: (a) instantaneous displacement, (b) instantaneous velocity, (c) total displacement, and (d) acceleration, as a function of time for the leading and trailing edges of Tris-HCl buffer droplets at 90 V.

Tris-HCl buffer solution, 90 V, Average curves

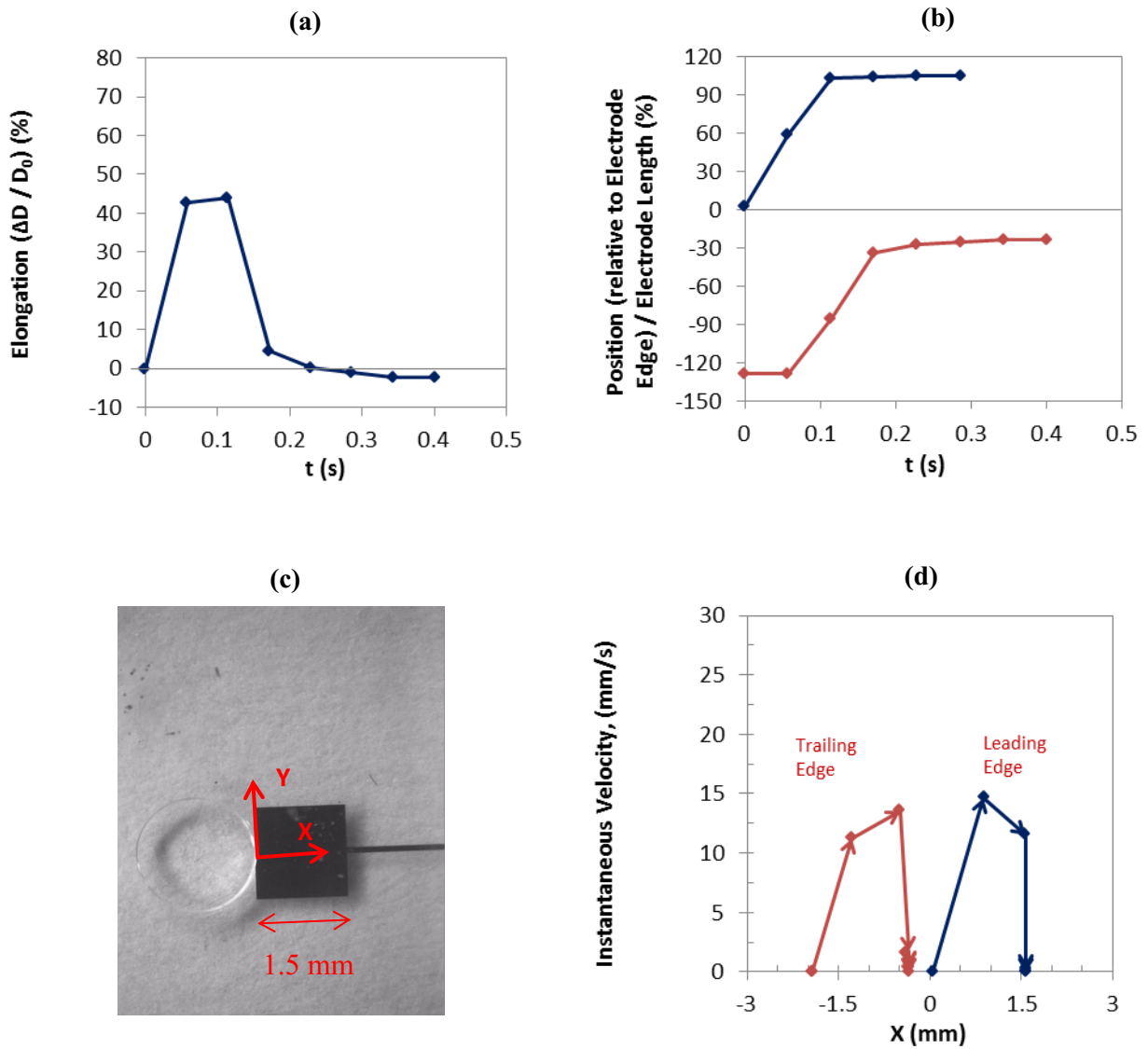


Figure G-5: Comparison of the average curves: (a) droplet elongation and (b) droplet position as a function of time, (d) instantaneous velocity as a function of droplet position as shown in (c) for the leading and trailing edges of Tris-HCl buffer droplets at 90 V. The arrows in graph (d) indicate the changes of velocity along the direction of movement.

G-2) Tris-HCl, 85 V

Tris-HCl buffer solution, 85 V, Leading edge

(all experiments)

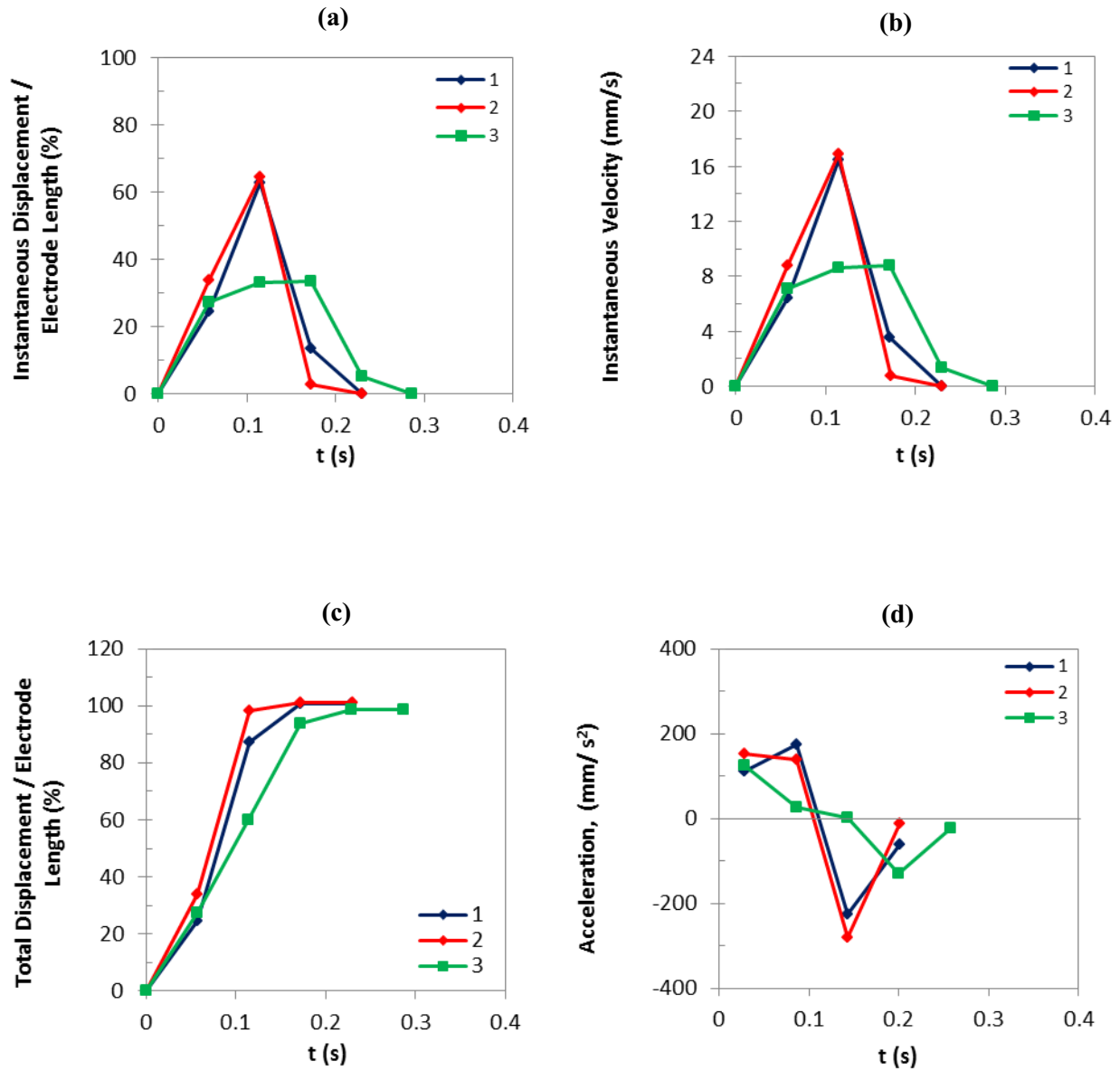


Figure G-6: (a) Instantaneous displacement, (b) instantaneous velocity, (c) total displacement, and (d) acceleration of the leading edges of Tris-HCl buffer droplets as a function of time at 85 V.

Tris-HCl buffer solution, 85 V, Trailing edge

(all experiments)

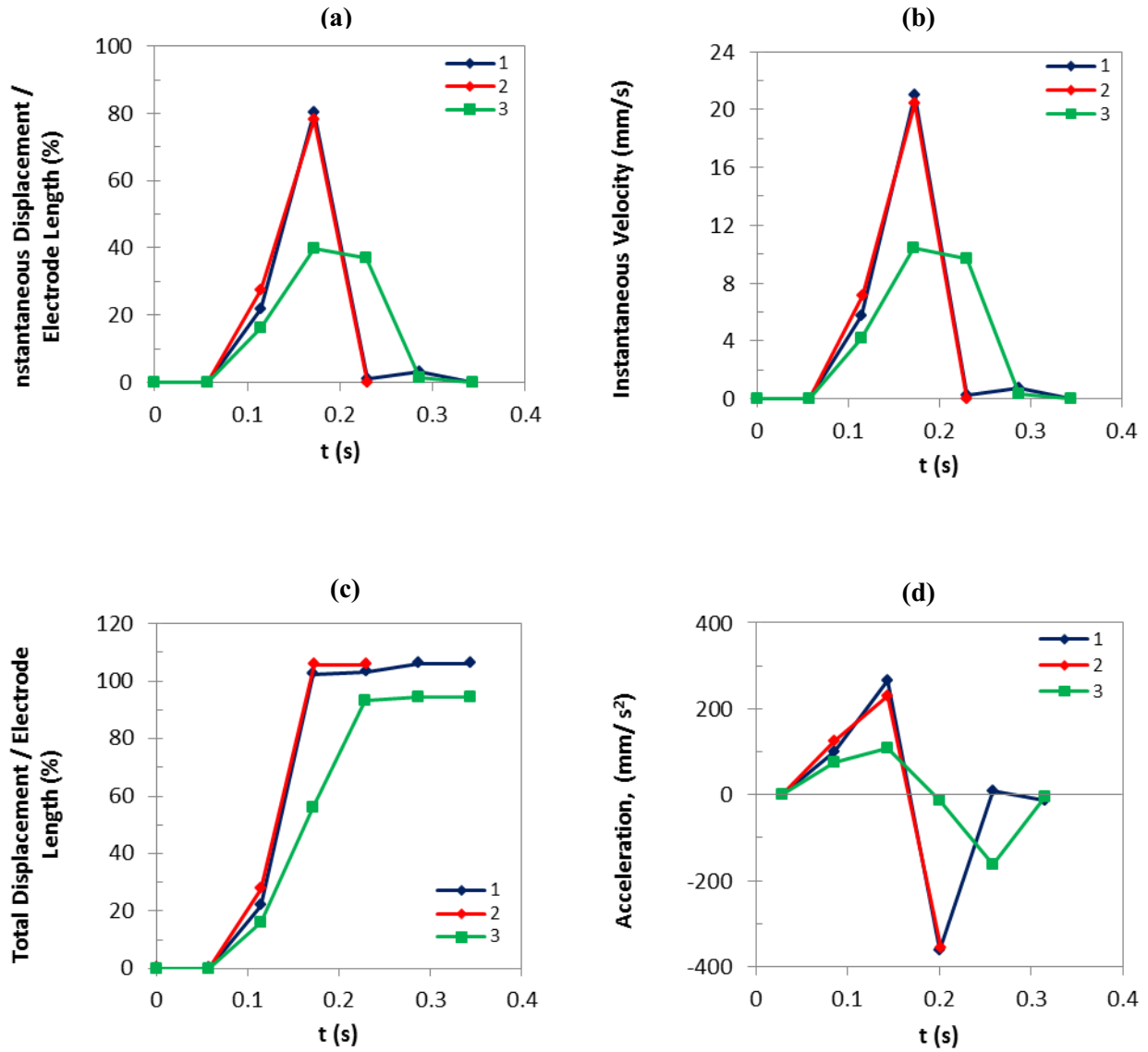


Figure G-7: (a) Instantaneous displacement, (b) instantaneous velocity, (c) total displacement, and (d) acceleration of the trailing edges of Tris-HCl buffer droplets as a function of time at 85 V.

Tris-HCl buffer solution, 85 V

(all experiments)

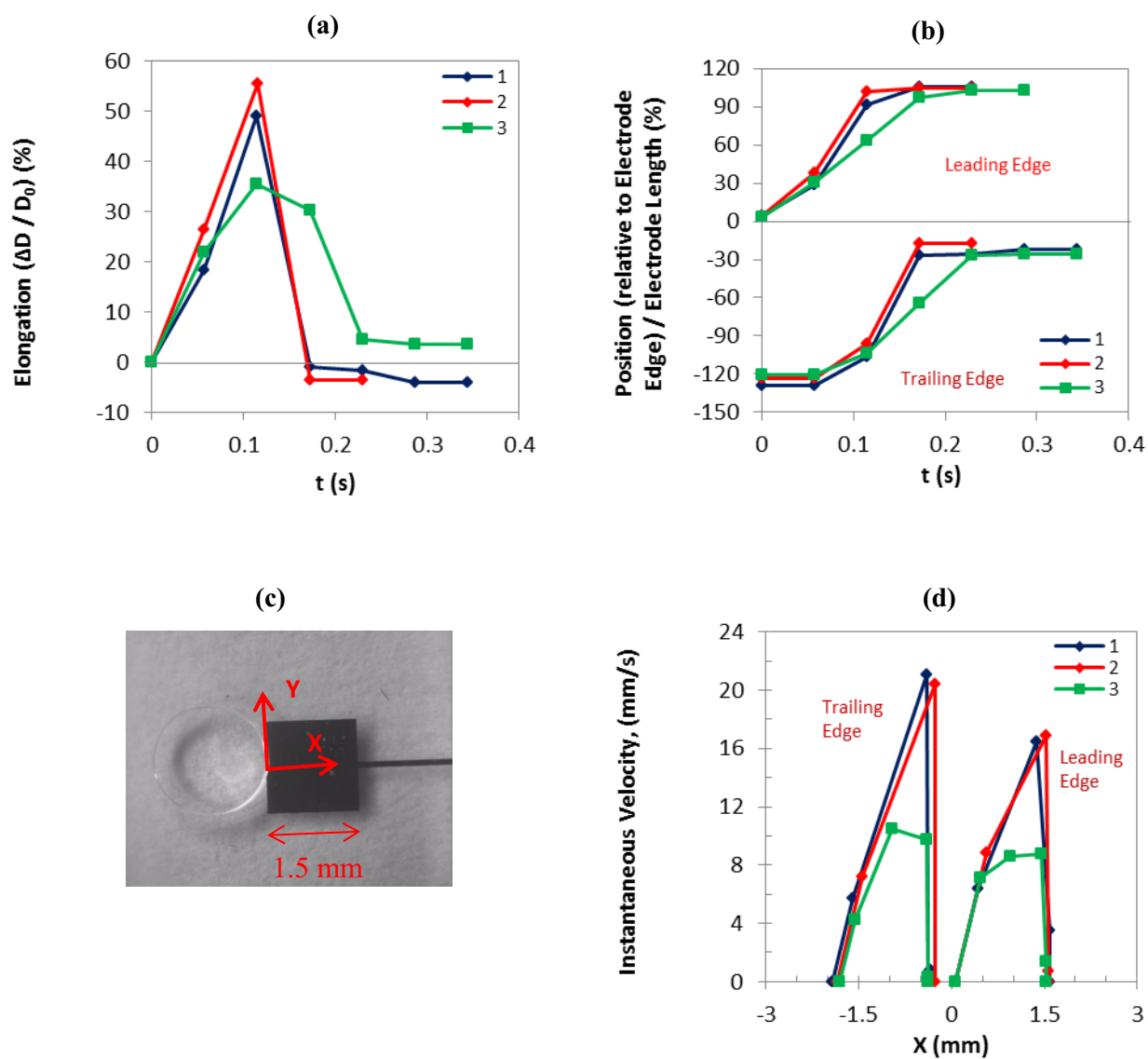


Figure G-8: (a) Droplet elongation and (b) droplet position as a function of time, (d) instantaneous velocity as a function of droplet position as shown in (c) for the leading and trailing edges of Tris-HCl buffer droplets at 85 V.

Tris-HCl buffer solution, 85 V, Leading edge,

Accepted experiments and the average curves

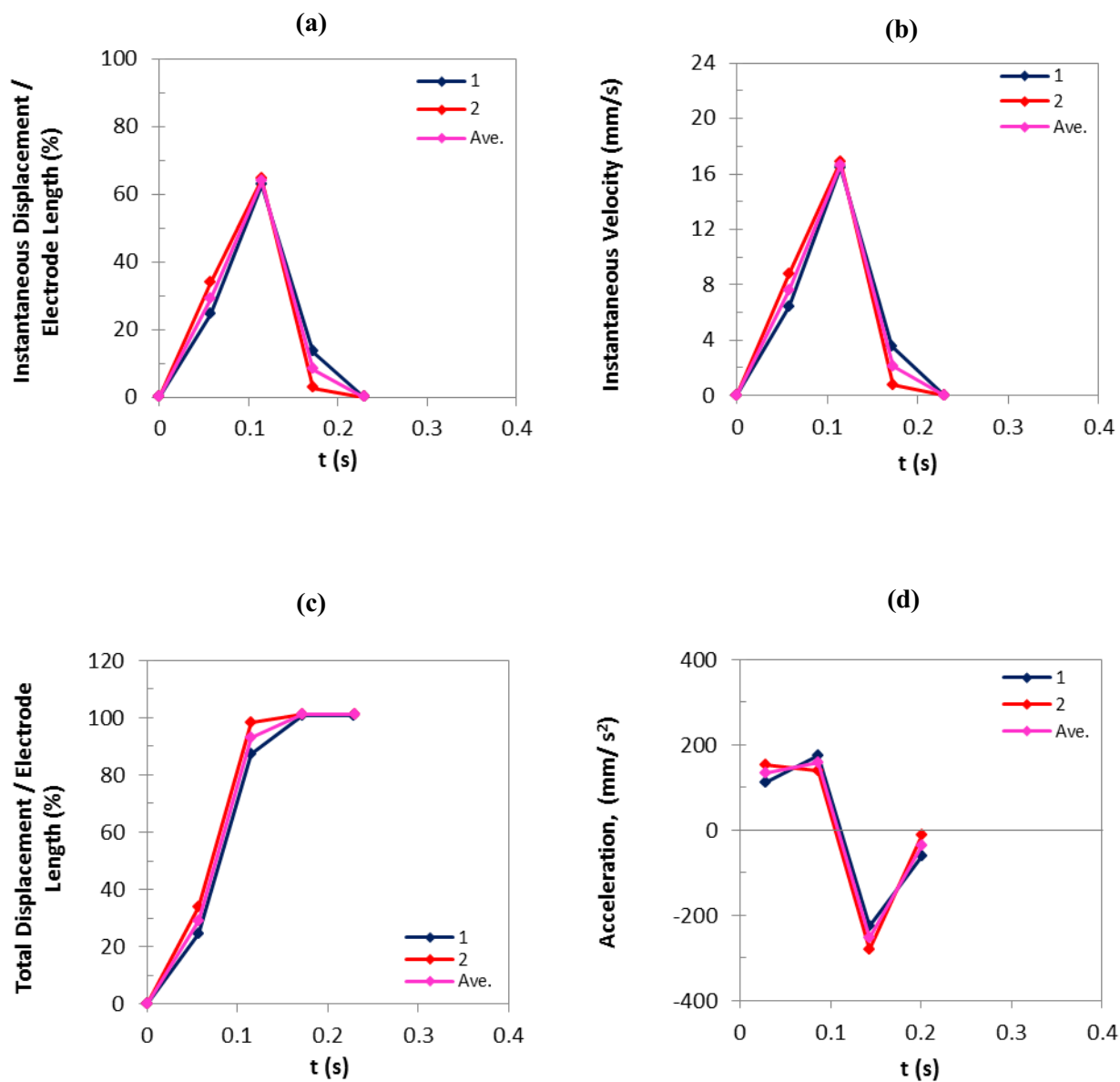


Figure G-9: (a) Instantaneous displacement, (b) instantaneous velocity, (c) total displacement, and (d) acceleration of the leading edges of Tris-HCl buffer droplets as a function of time at 85 V.

Tris-HCl buffer solution, 85 V, Trailing edge,

Accepted experiments and the average curves

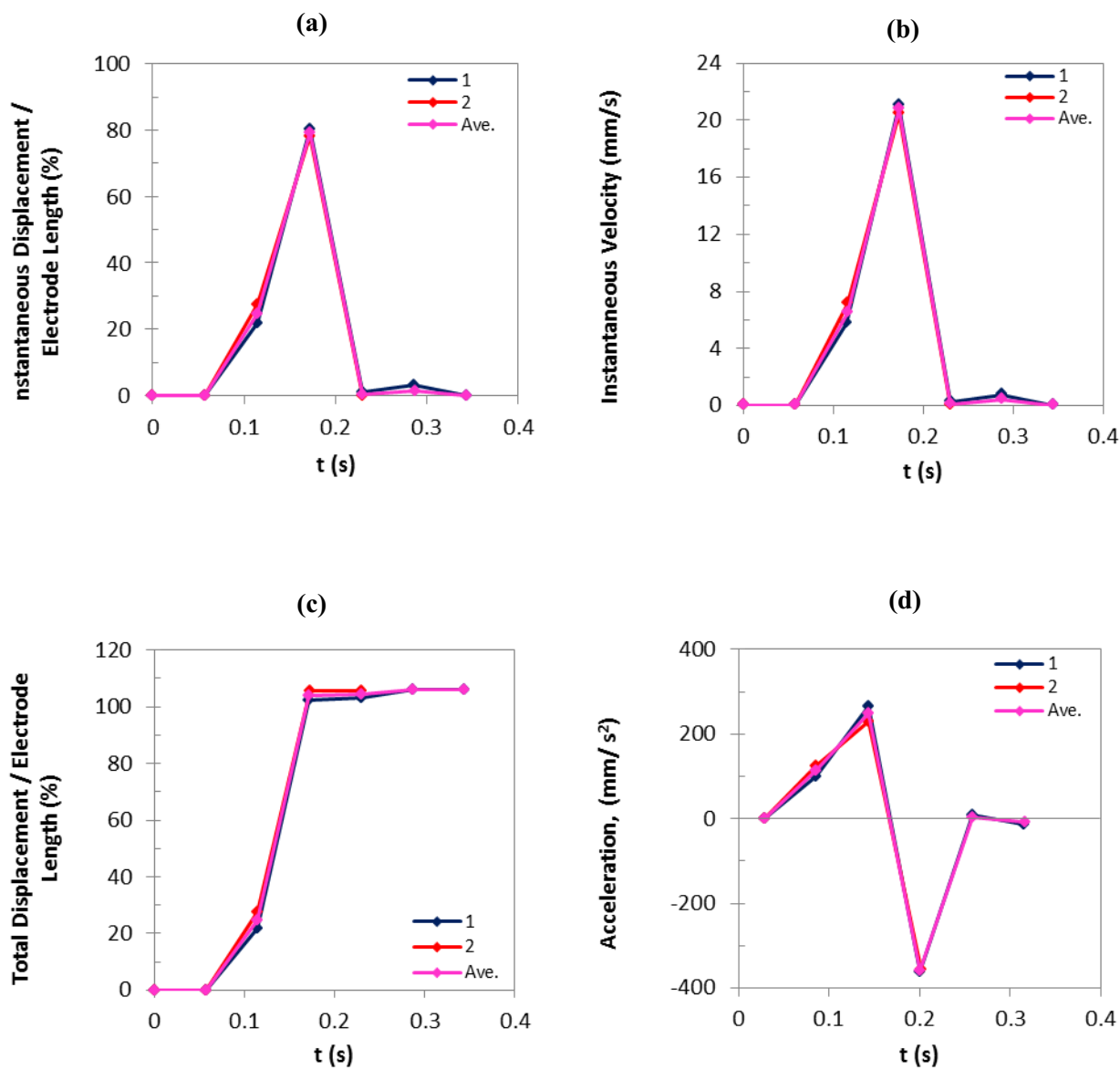


Figure G-10: Time course of the: (a) instantaneous displacement (normalized), (b) instantaneous velocity, (c) total displacement (normalized), and (d) acceleration of the Trailing edges of Tris-HCl buffer solution droplets at 85 V.

Tris-HCl buffer solution, 85 V

Accepted experiments and the average curves

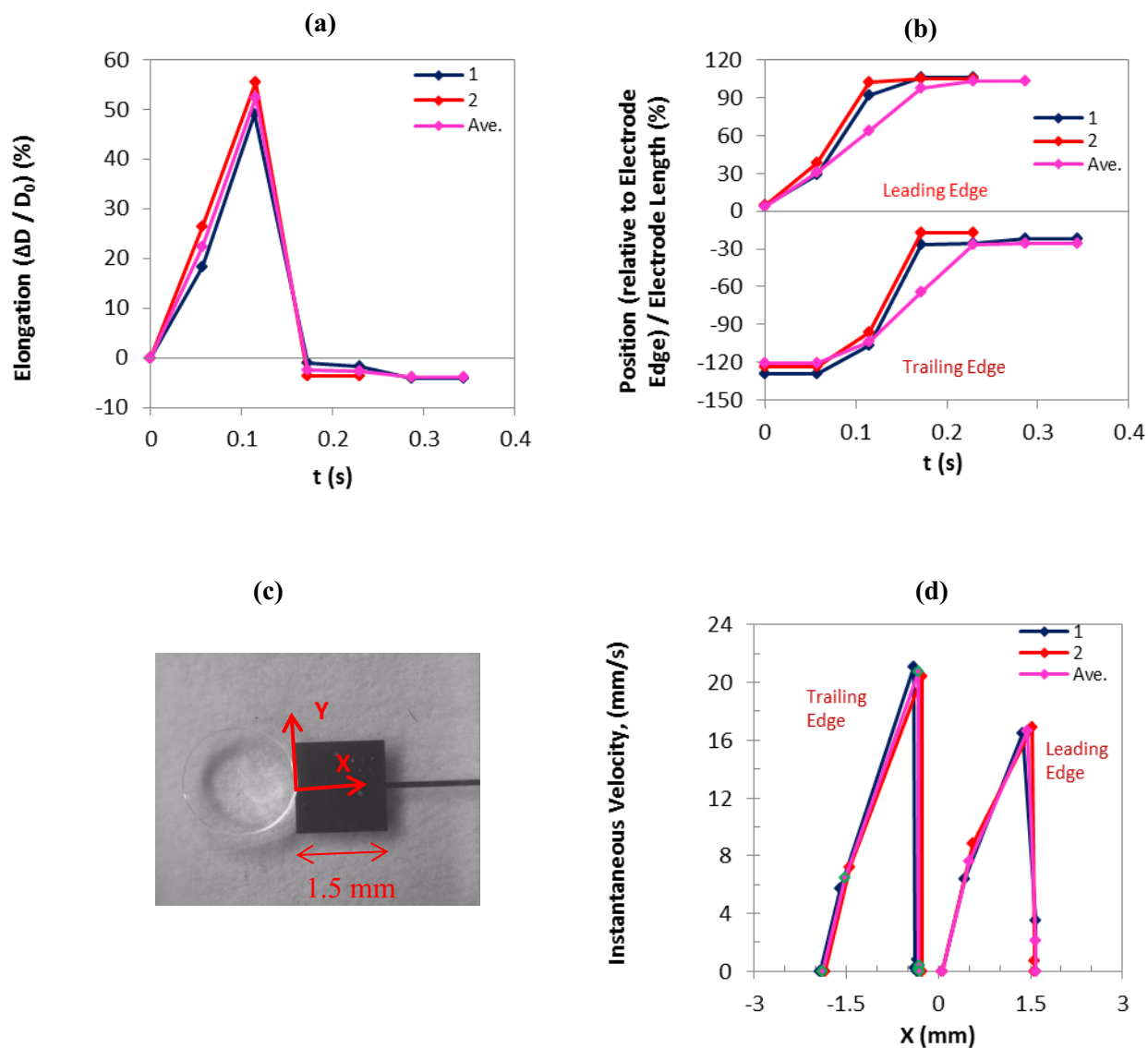


Figure G-11: (a) Droplet elongation and (b) droplet position as a function of time, (d) instantaneous velocity as a function of droplet position as shown in (c) for the leading and trailing edges of Tris-HCl buffer droplets at 85 V.

Tris-HCl buffer solution, 85 V, Average curves

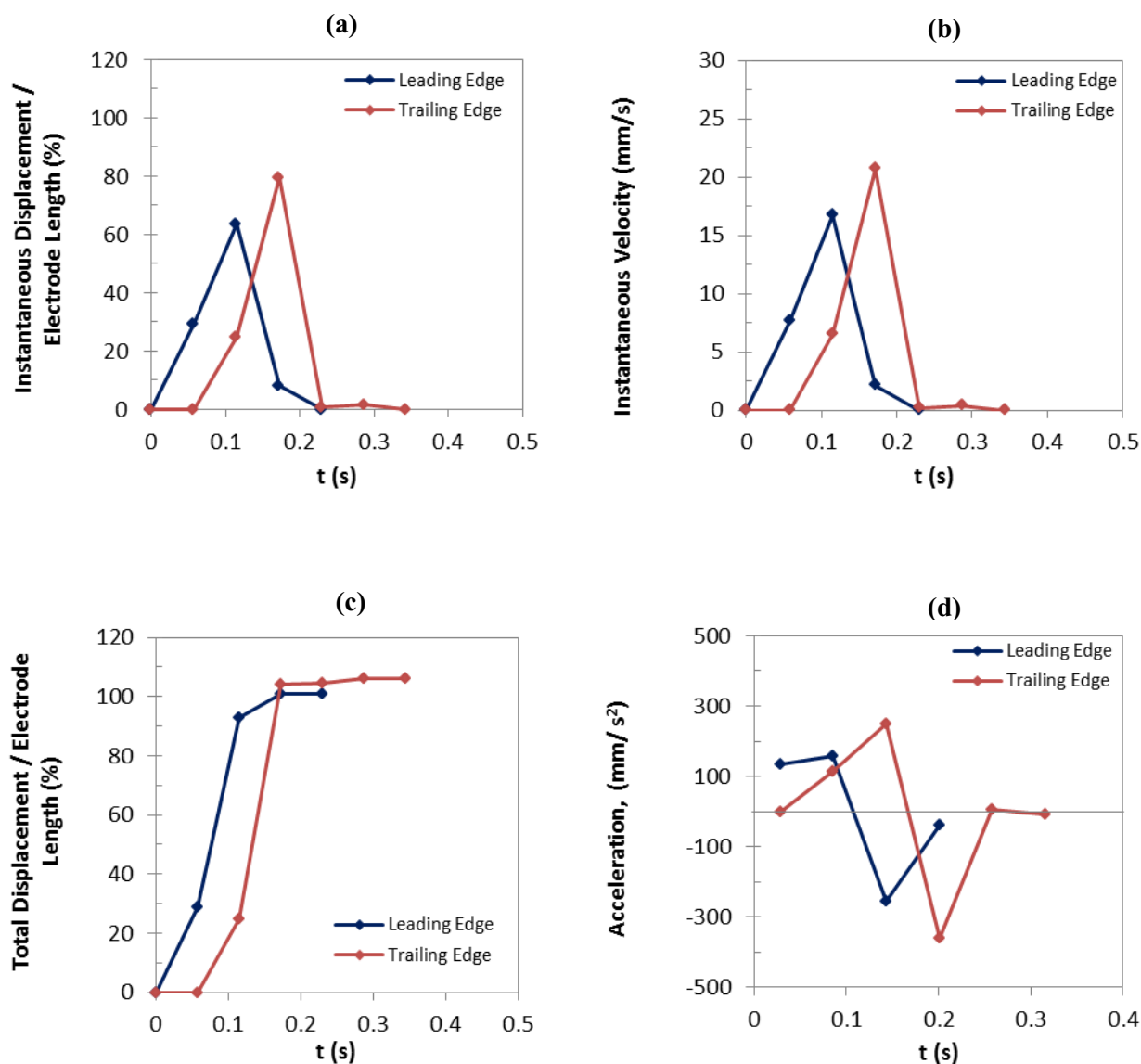


Figure G-12: Comparison of the average curves: (a) instantaneous displacement, (b) instantaneous velocity, (c) total displacement, and (d) acceleration, as a function of time for the leading and trailing edges of Tris-HCl buffer droplets at 85 V.

Tris-HCl buffer solution, 85 V, Average curves

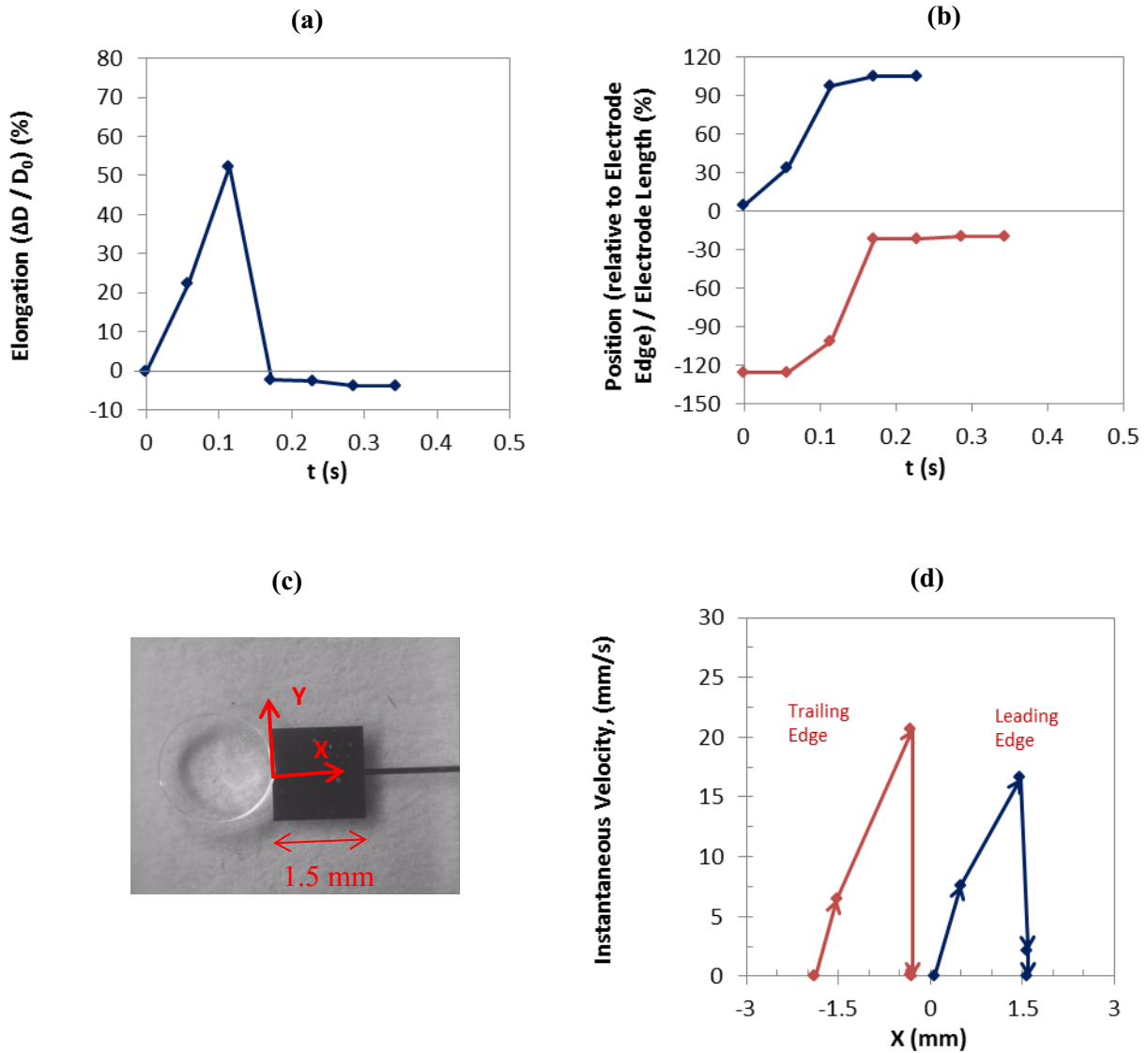


Figure G-13: Comparison of the average curves: (a) droplet elongation and (b) droplet position as a function of time, (d) instantaneous velocity as a function of droplet position as shown in (c) for the leading and trailing edges of Tris-HCl buffer droplets at 85 V. The arrows in graph (d) indicate the changes of velocity along the direction of movement.

G-3) Tris-HCl, 80 V

Tris-HCl buffer solution, 80 V, Leading edge,

Accepted experiments and the average curves

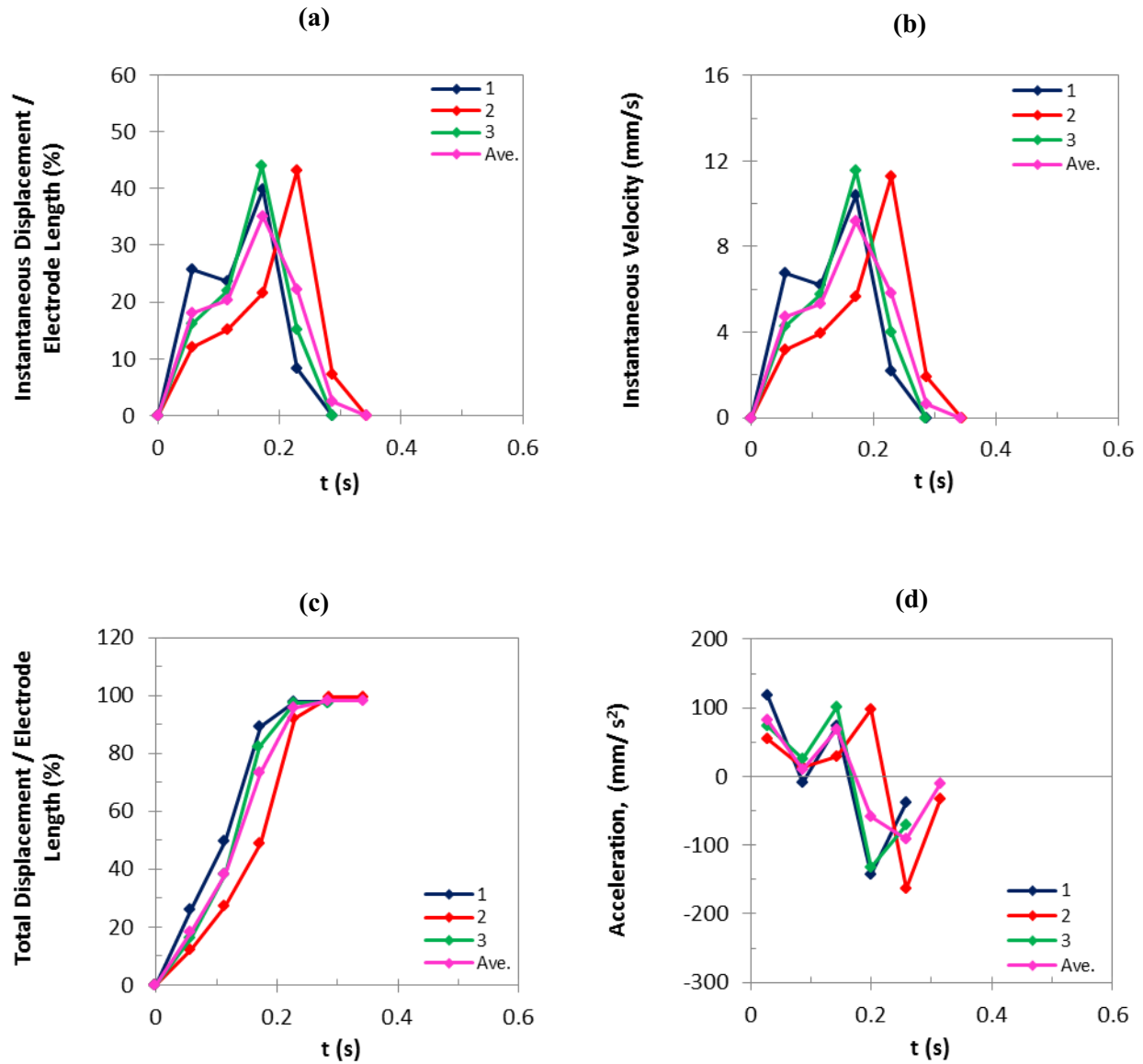


Figure G-14: (a) Instantaneous displacement, (b) instantaneous velocity, (c) total displacement, and (d) acceleration of the leading edges of Tris-HCl buffer droplets as a function of time at 80 V.

Tris-HCl buffer solution, 80 V, Trailing edge,

Accepted experiments and the average curves

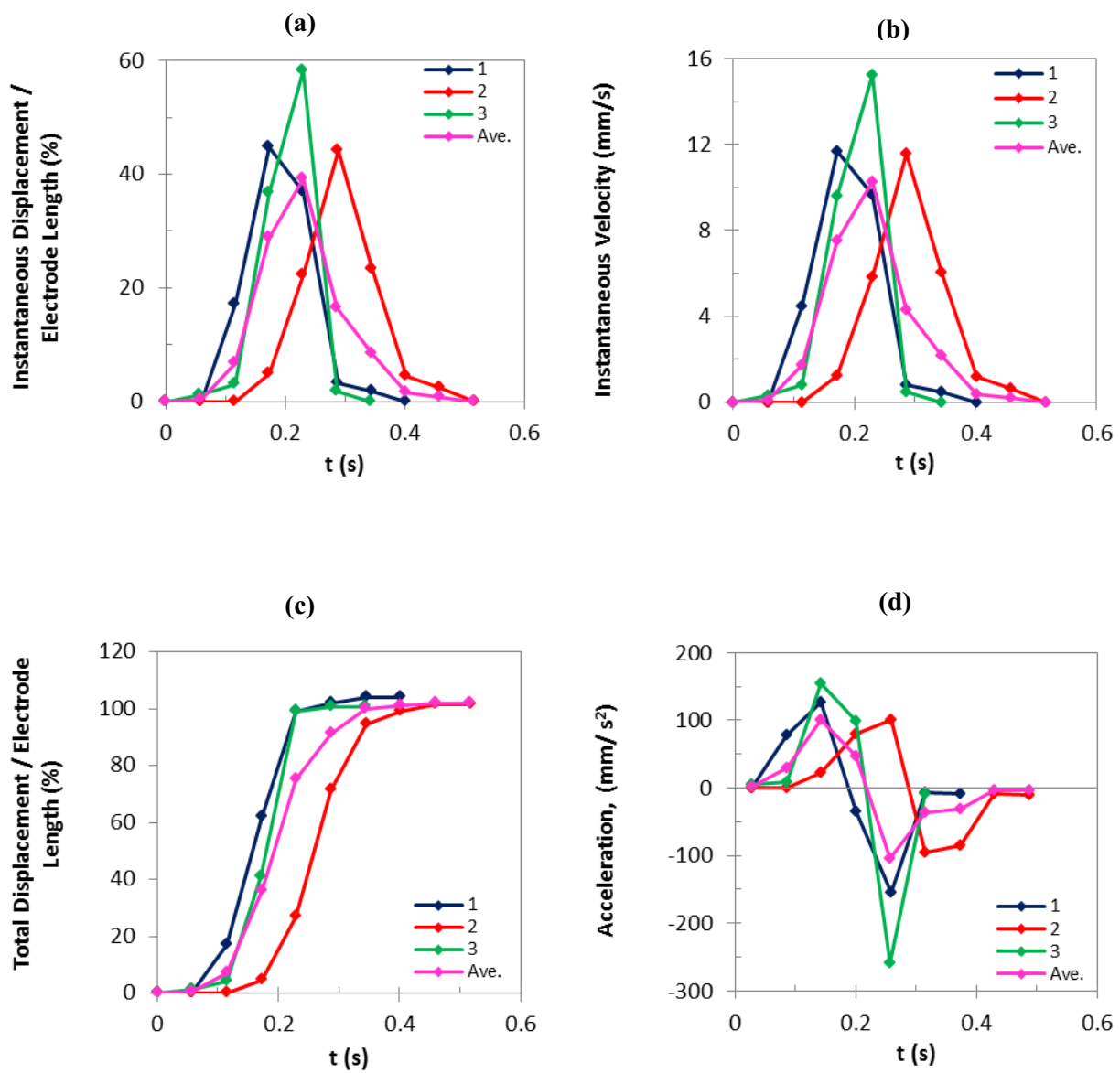


Figure G-15: (a) Instantaneous displacement, (b) instantaneous velocity, (c) total displacement, and (d) acceleration of the trailing edges of Tris-HCl buffer droplets as a function of time at 80 V.

Tris-HCl buffer solution, 80 V

Accepted experiments and the average curves

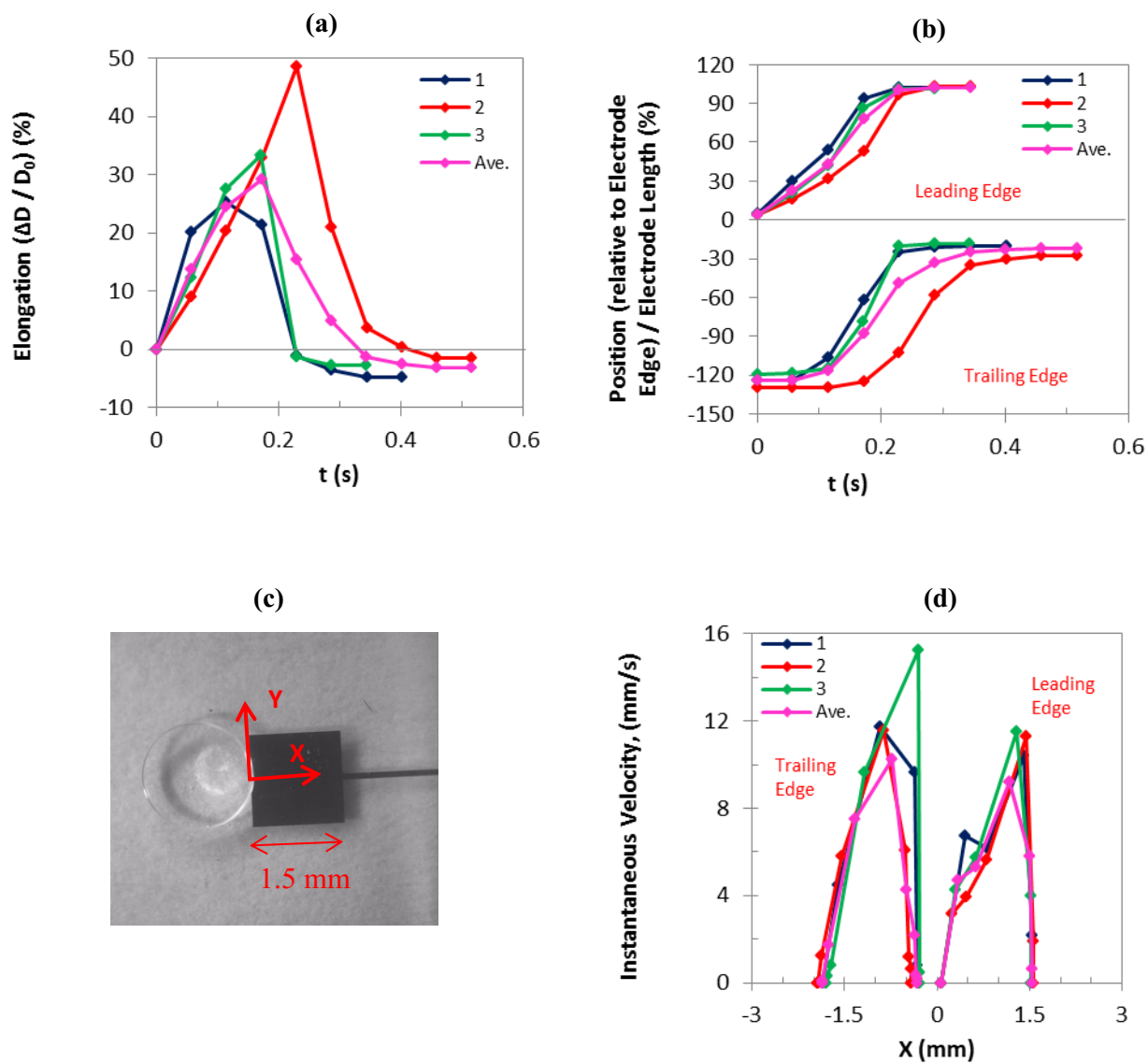


Figure G-16: (a) Droplet elongation and (b) droplet position as a function of time, (d) instantaneous velocity as a function of droplet position as shown in (c) for the leading and trailing edges of Tris-HCl buffer droplets at 80 V.

Tris-HCl buffer solution, 80 V, Average curves

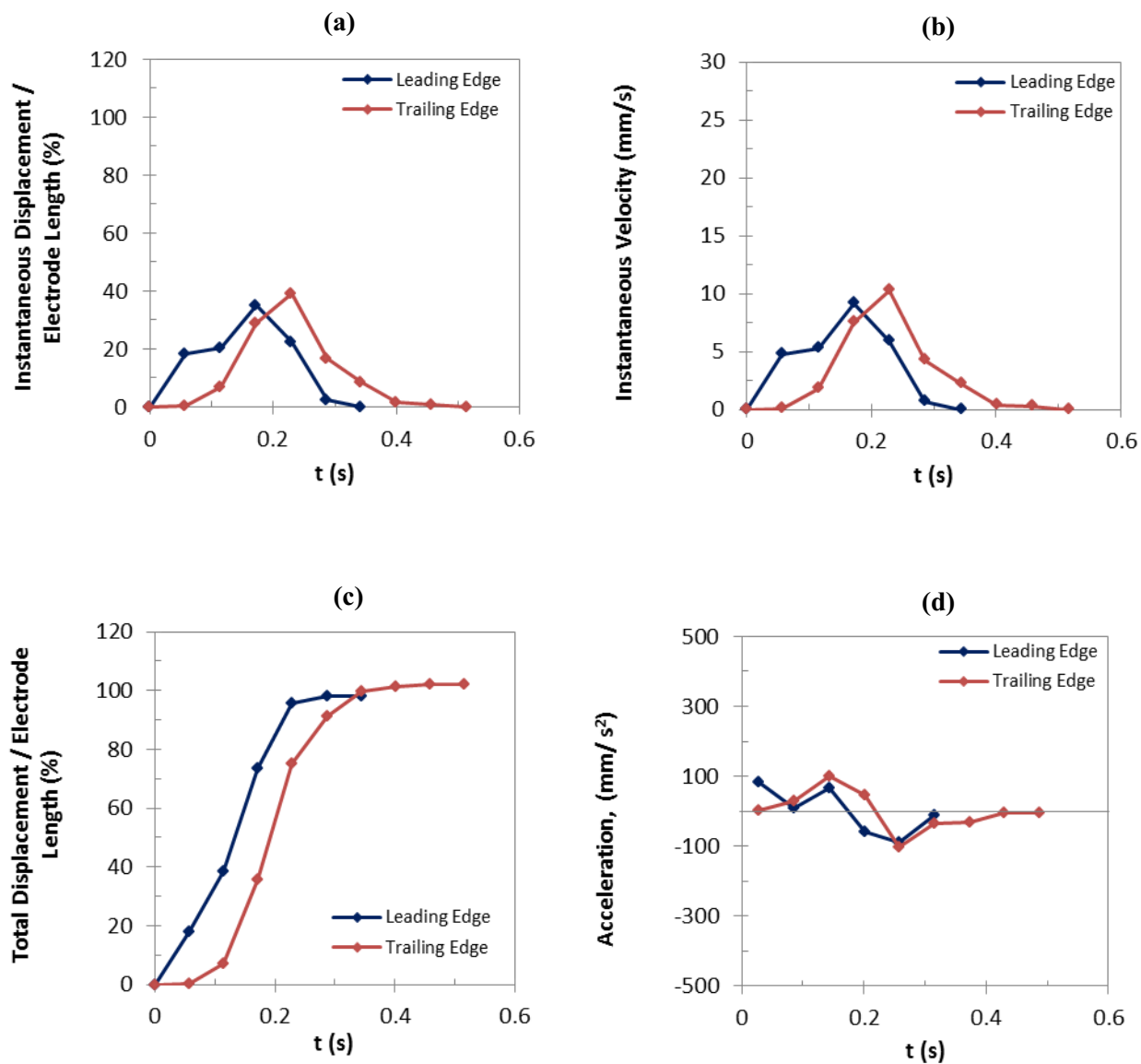


Figure G-17: Comparison of the average curves: (a) instantaneous displacement, (b) instantaneous velocity, (c) total displacement, and (d) acceleration, as a function of time for the leading and trailing edges of Tris-HCl buffer droplets at 80 V.

Tris-HCl buffer solution, 80 V, Average curves

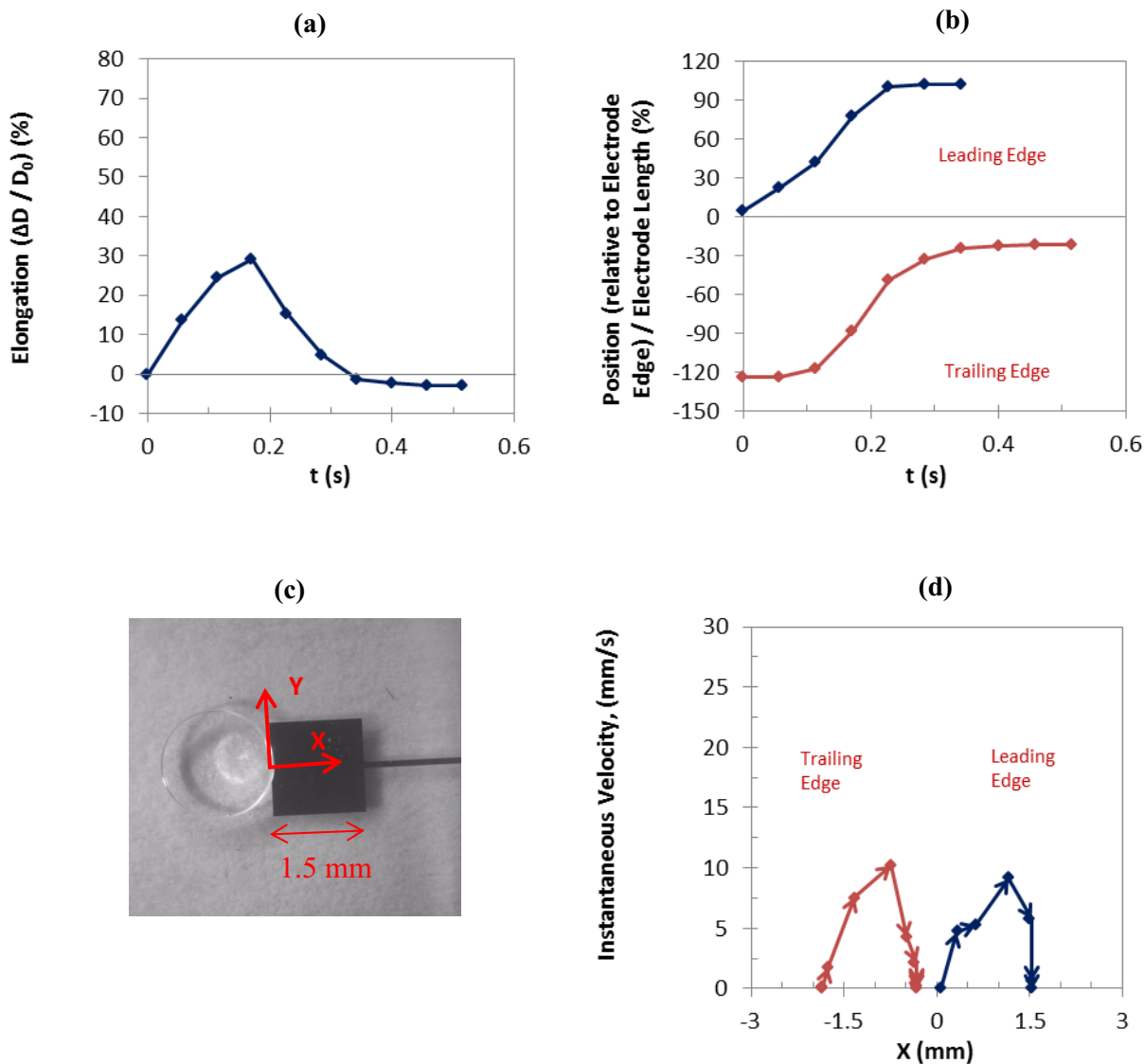


Figure G-18: Comparison of the average curves: (a) droplet elongation and (b) droplet position as a function of time, (d) instantaneous velocity as a function of droplet position as shown in (c) for the leading and trailing edges of Tris-HCl buffer droplets at 80 V. The arrows in graph (d) indicate the changes of velocity along the direction of movement.

G-4) Tris-HCl, 75 V

Tris-HCl buffer solution, 75 V, Leading edge,

Accepted experiments and the average curves

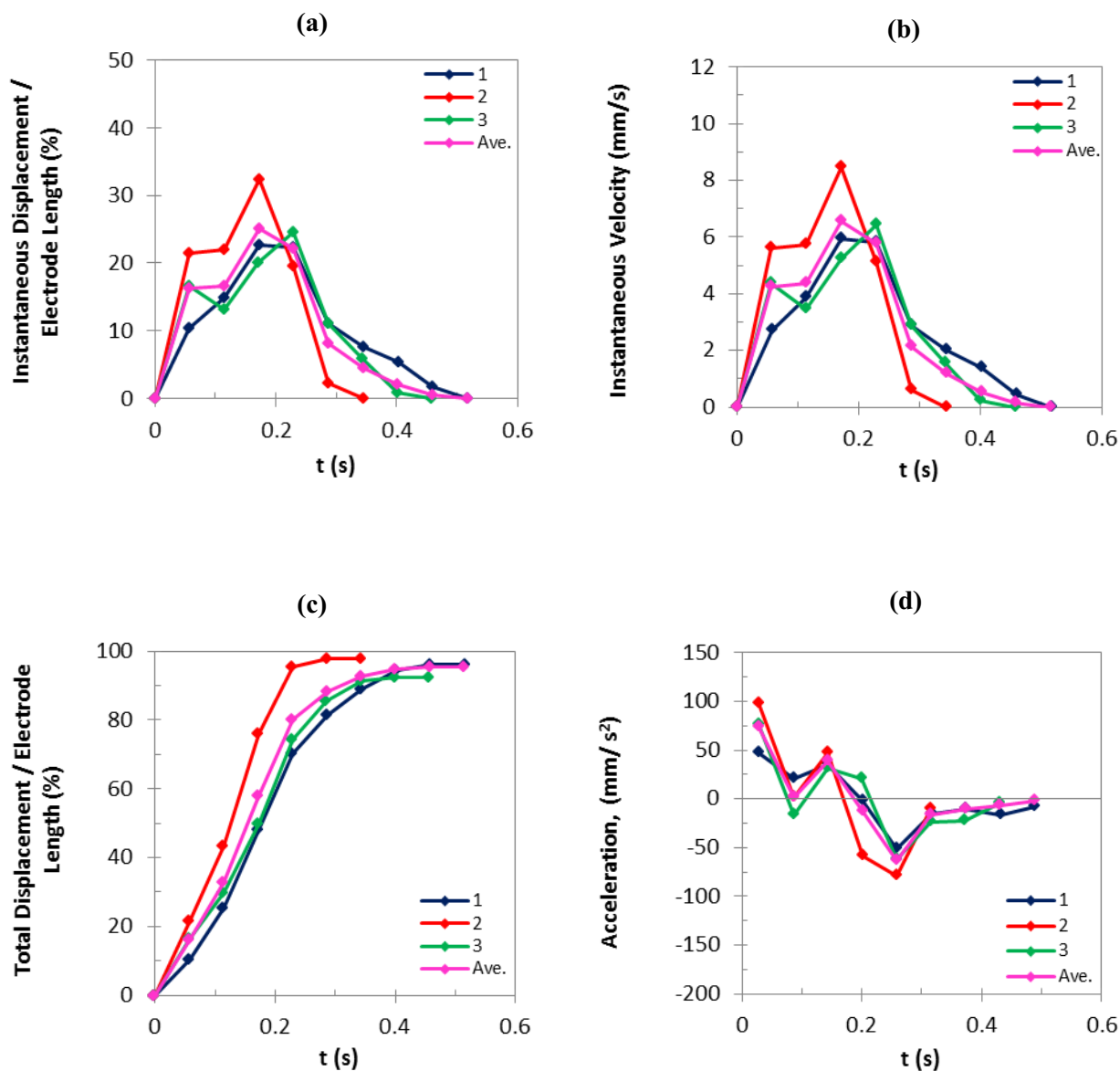


Figure G-19: (a) Instantaneous displacement, (b) instantaneous velocity, (c) total displacement, and (d) acceleration of the leading edges of Tris-HCl buffer droplets as a function of time at 75 V.

Tris-HCl buffer solution, 75 V, Trailing edge,

Accepted experiments and the average curves

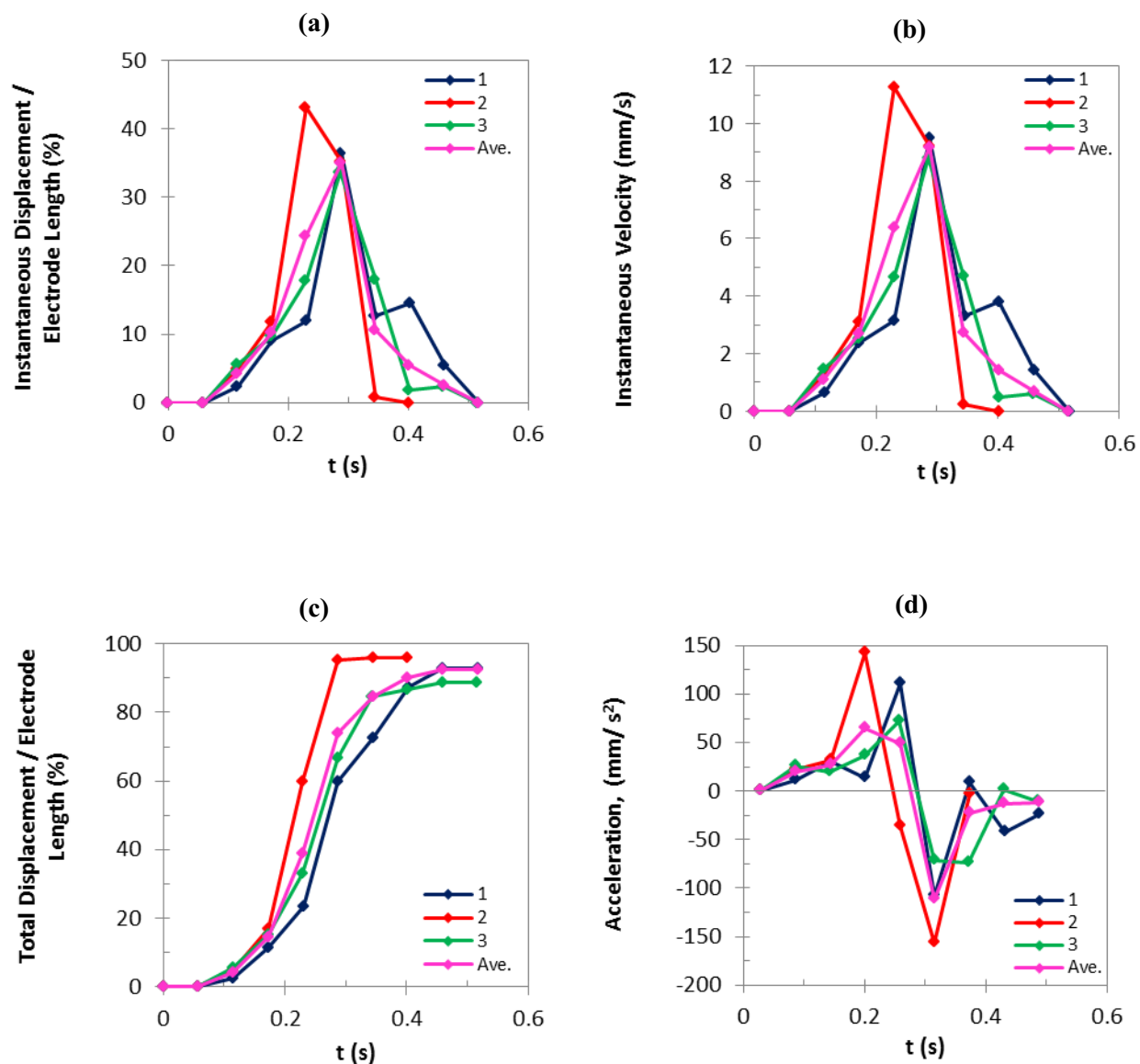


Figure G-20: (a) Instantaneous displacement, (b) instantaneous velocity, (c) total displacement, and (d) acceleration of the trailing edges of Tris-HCl buffer droplets as a function of time at 75 V.

Tris-HCl buffer solution, 75 V

Accepted experiments and the average curves

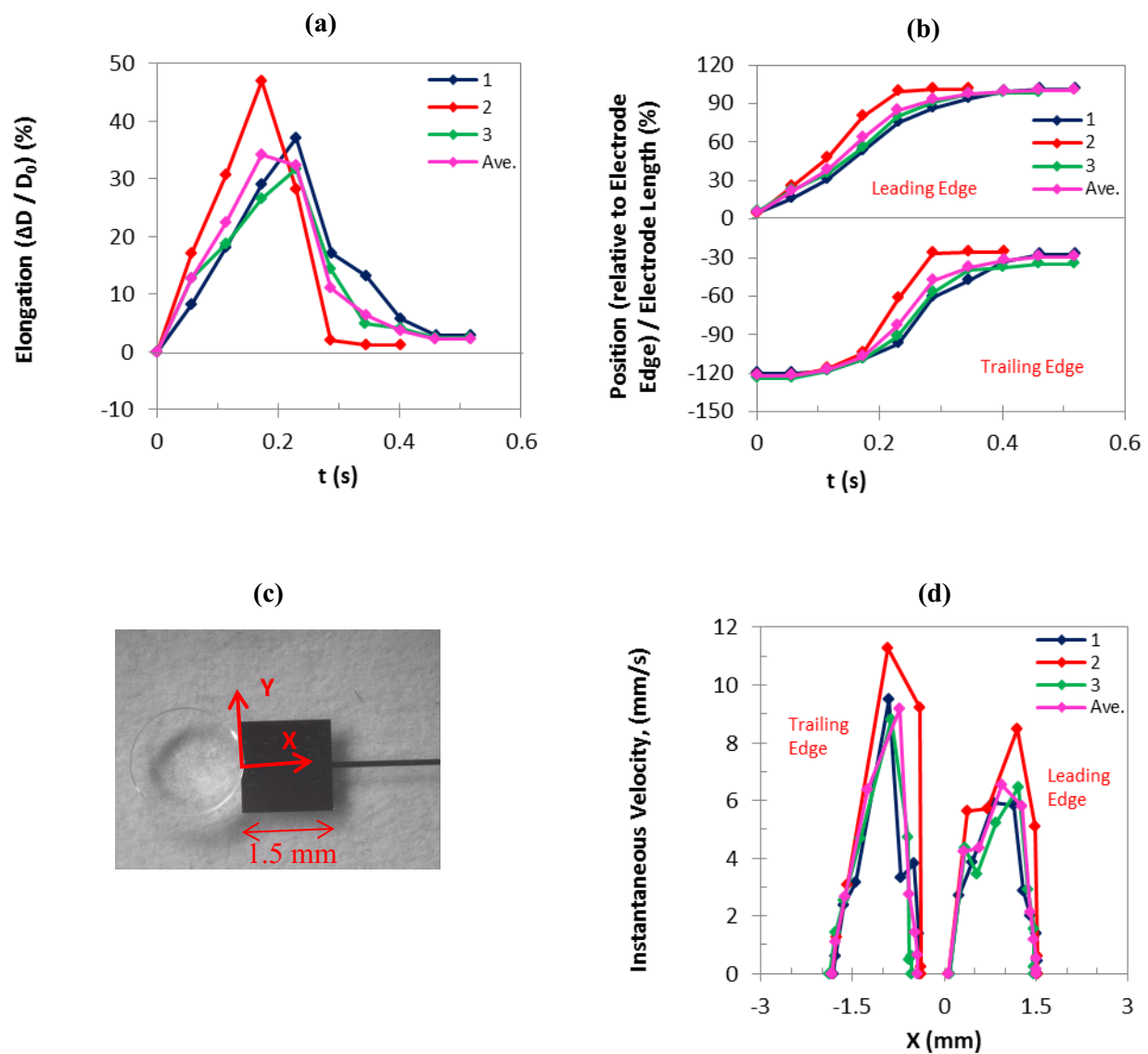


Figure G-21: (a) Droplet elongation and (b) droplet position as a function of time, (d) instantaneous velocity as a function of droplet position as shown in (c) for the leading and trailing edges of Tris-HCl buffer droplets at 75 V.

Tris-HCl buffer solution, 75 V, Average curves

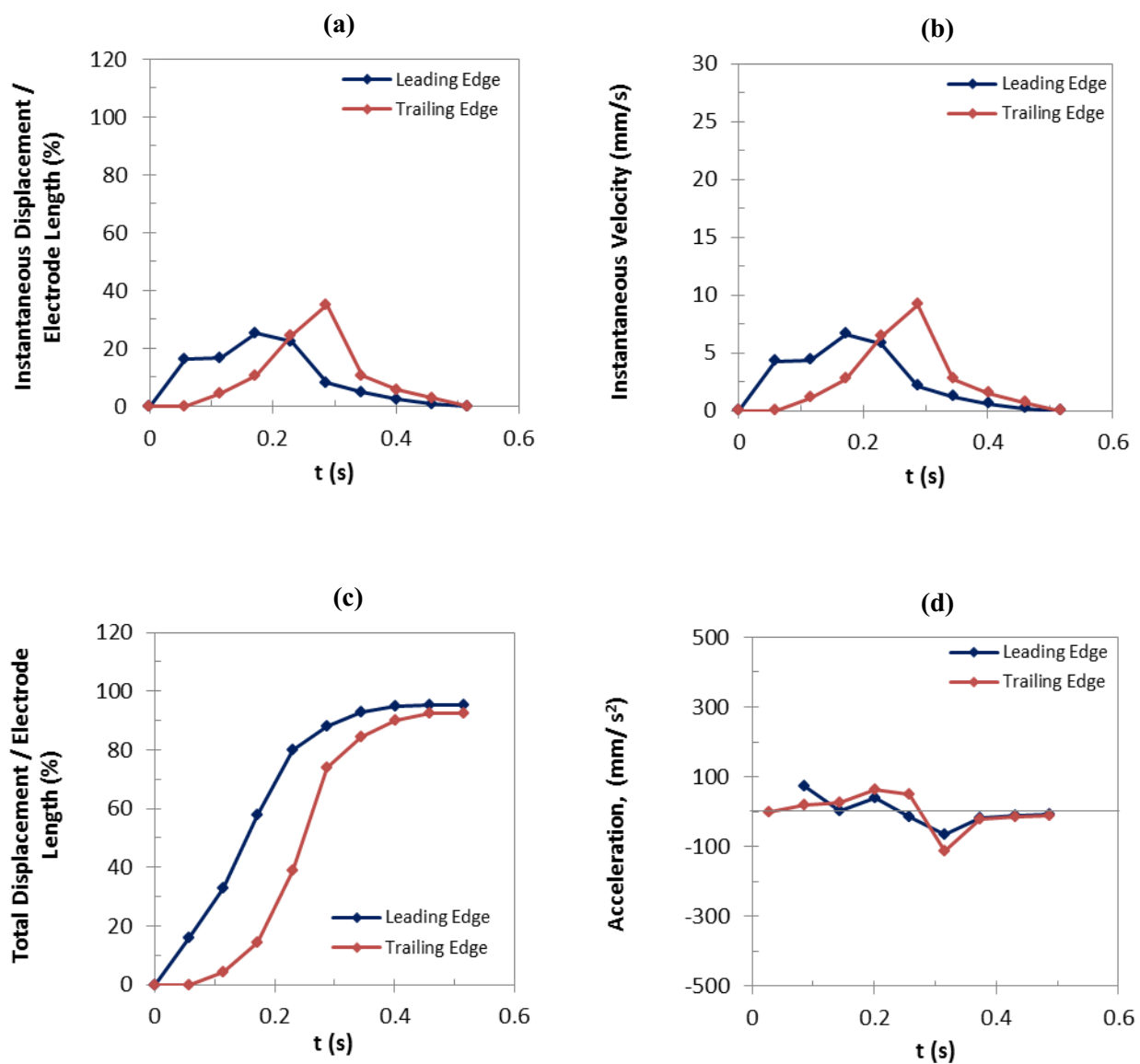


Figure G-22: Comparison of the average curves: (a) instantaneous displacement, (b) instantaneous velocity, (c) total displacement, and (d) acceleration, as a function of time for the leading and trailing edges of Tris-HCl buffer droplets at 75 V.

Tris-HCl buffer solution, 75 V, Average curves

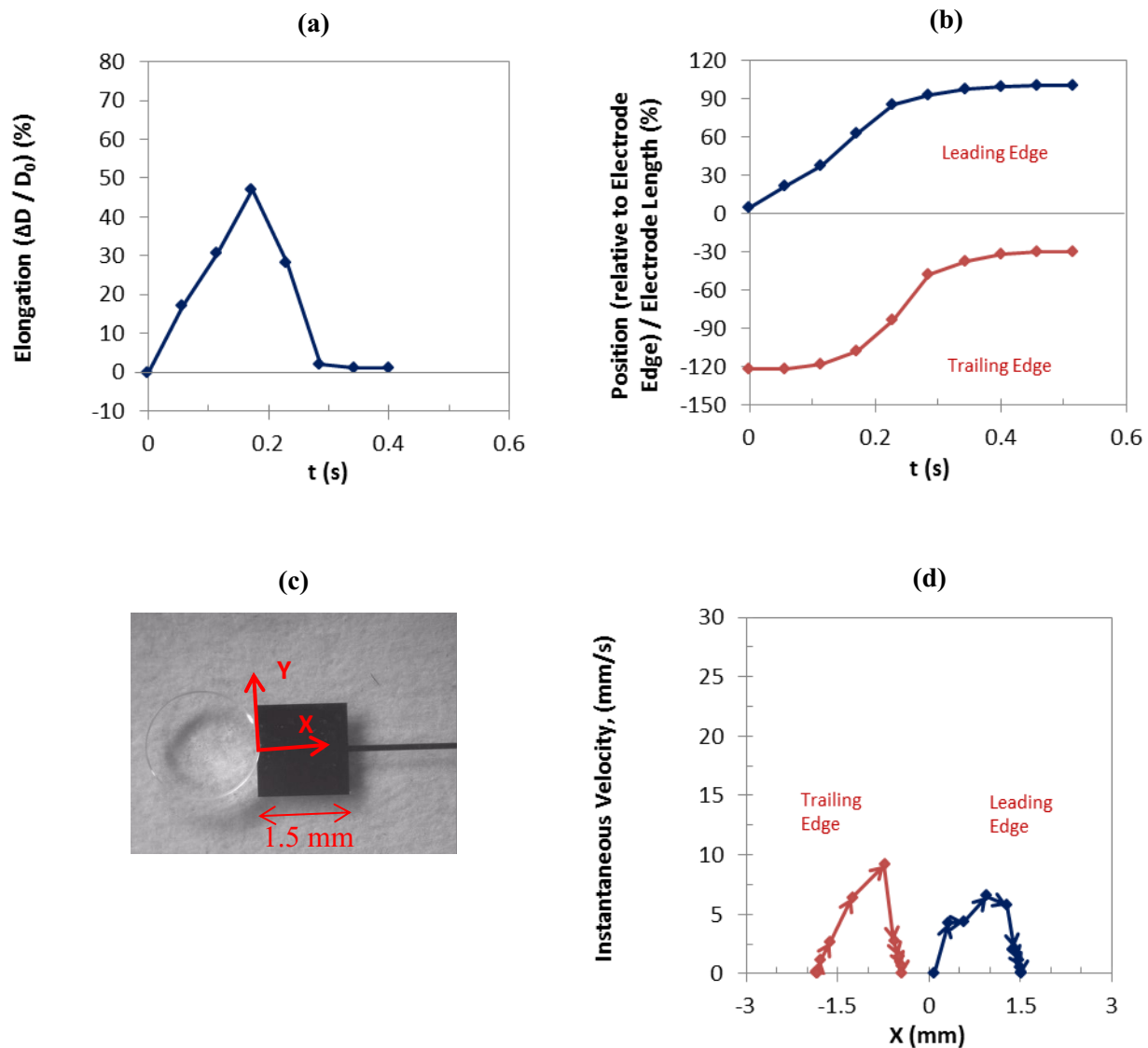


Figure G-23: Comparison of the average curves: (a) droplet elongation and (b) droplet position as a function of time, (d) instantaneous velocity as a function of droplet position as shown in (c) for the leading and trailing edges of Tris-HCl buffer droplets at 75 V. The arrows in graph (d) indicate the changes of velocity along the direction of movement.

G-5) Tris-HCl, 70 V

Tris-HCl buffer solution, 70 V, Leading edge,

Accepted experiments and the average curves

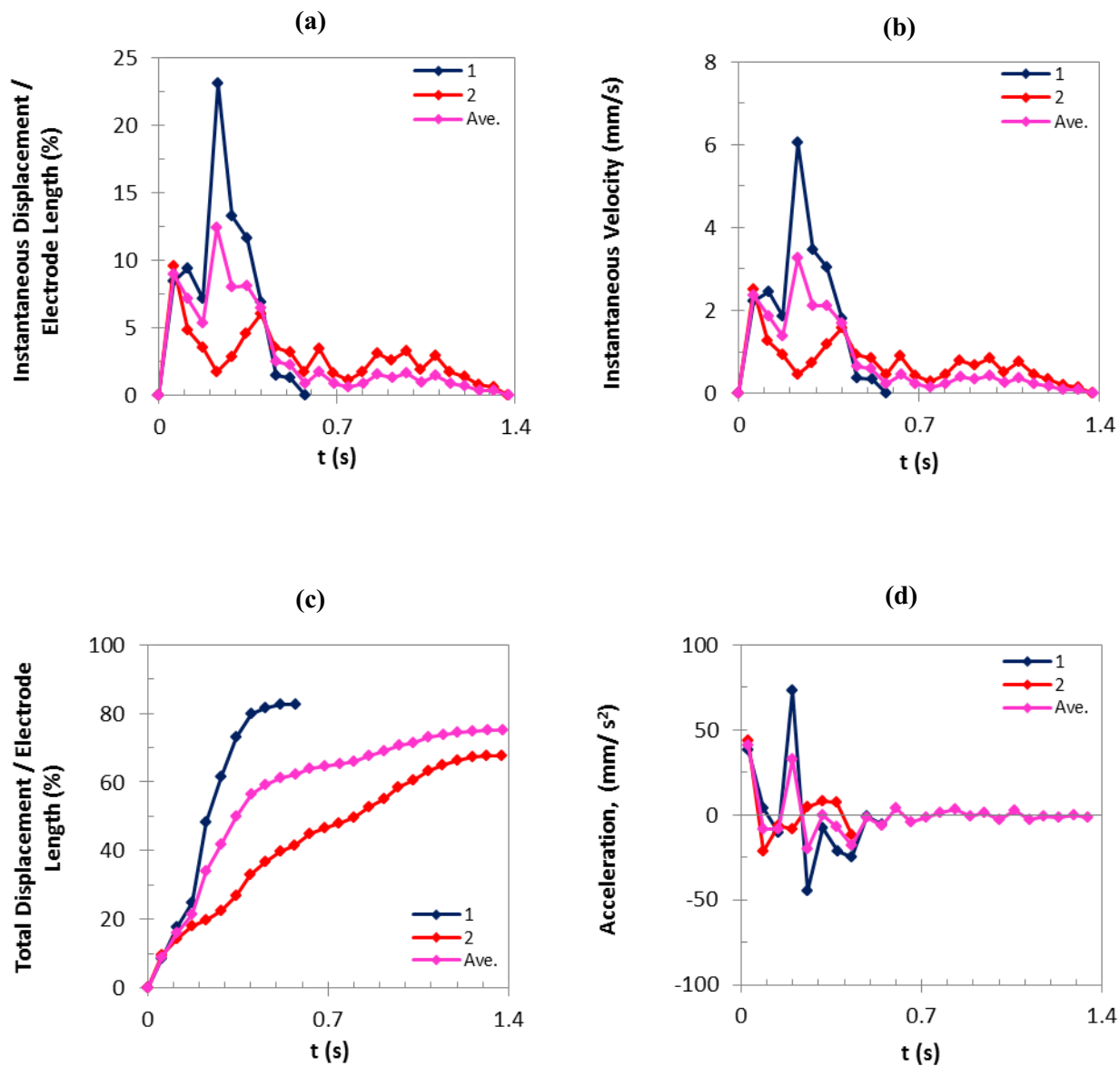


Figure G-24: (a) Instantaneous displacement, (b) instantaneous velocity, (c) total displacement, and (d) acceleration of the leading edges of Tris-HCl buffer droplets as a function of time at 70 V.

Tris-HCl buffer solution, 70 V, Trailing edge,

Accepted experiments and the average curves

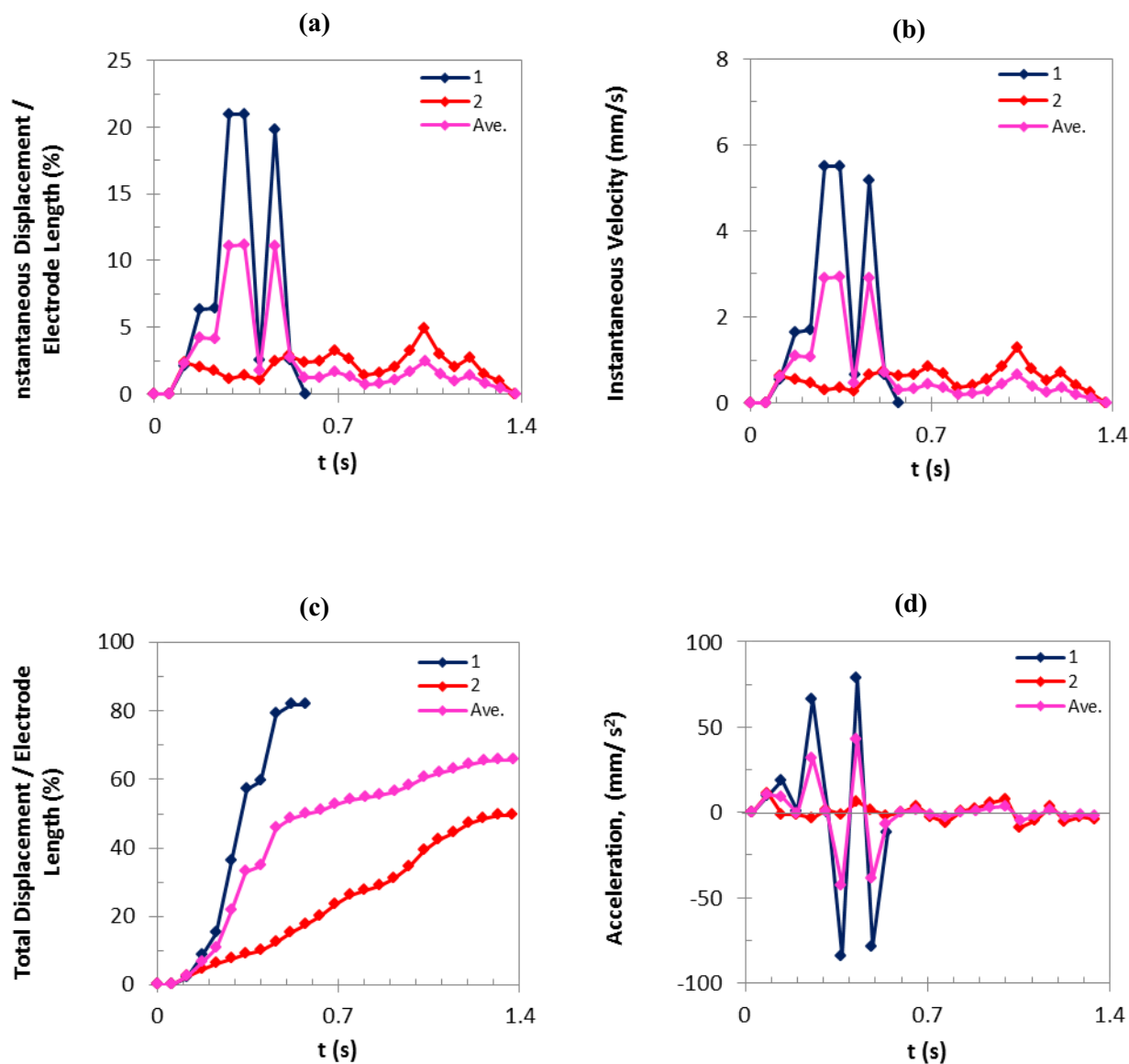


Figure G-25: (a) Instantaneous displacement, (b) instantaneous velocity, (c) total displacement, and (d) acceleration of the trailing edges of Tris-HCl buffer droplets as a function of time at 70 V.

Tris-HCl buffer solution, 70 V

Accepted experiments and the average curves

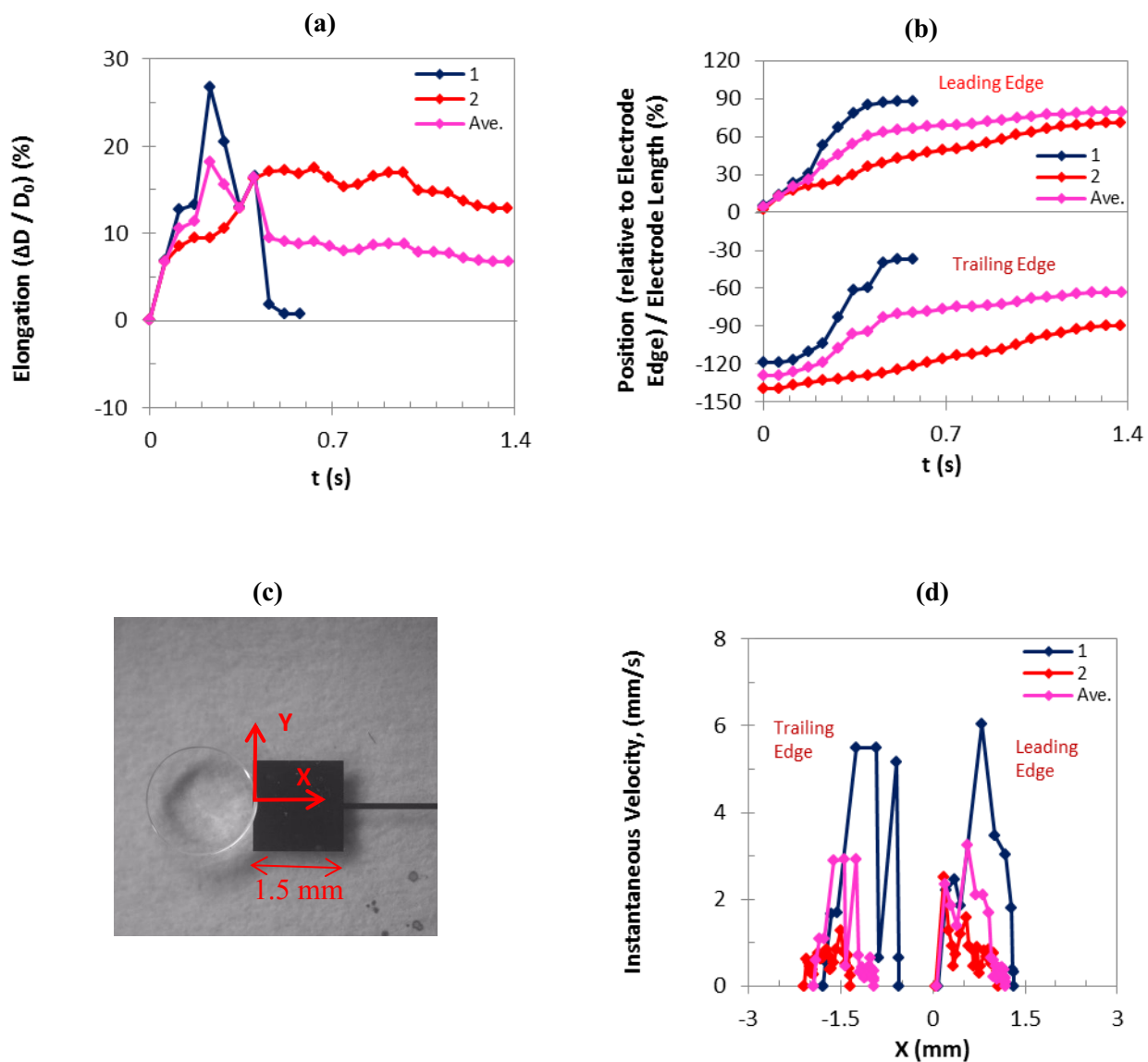


Figure G-26: (a) Droplet elongation and (b) droplet position as a function of time, (d) instantaneous velocity as a function of droplet position as shown in (c) for the leading and trailing edges of Tris-HCl buffer droplets at 70 V.

Tris-HCl buffer solution, 70 V, Average curves

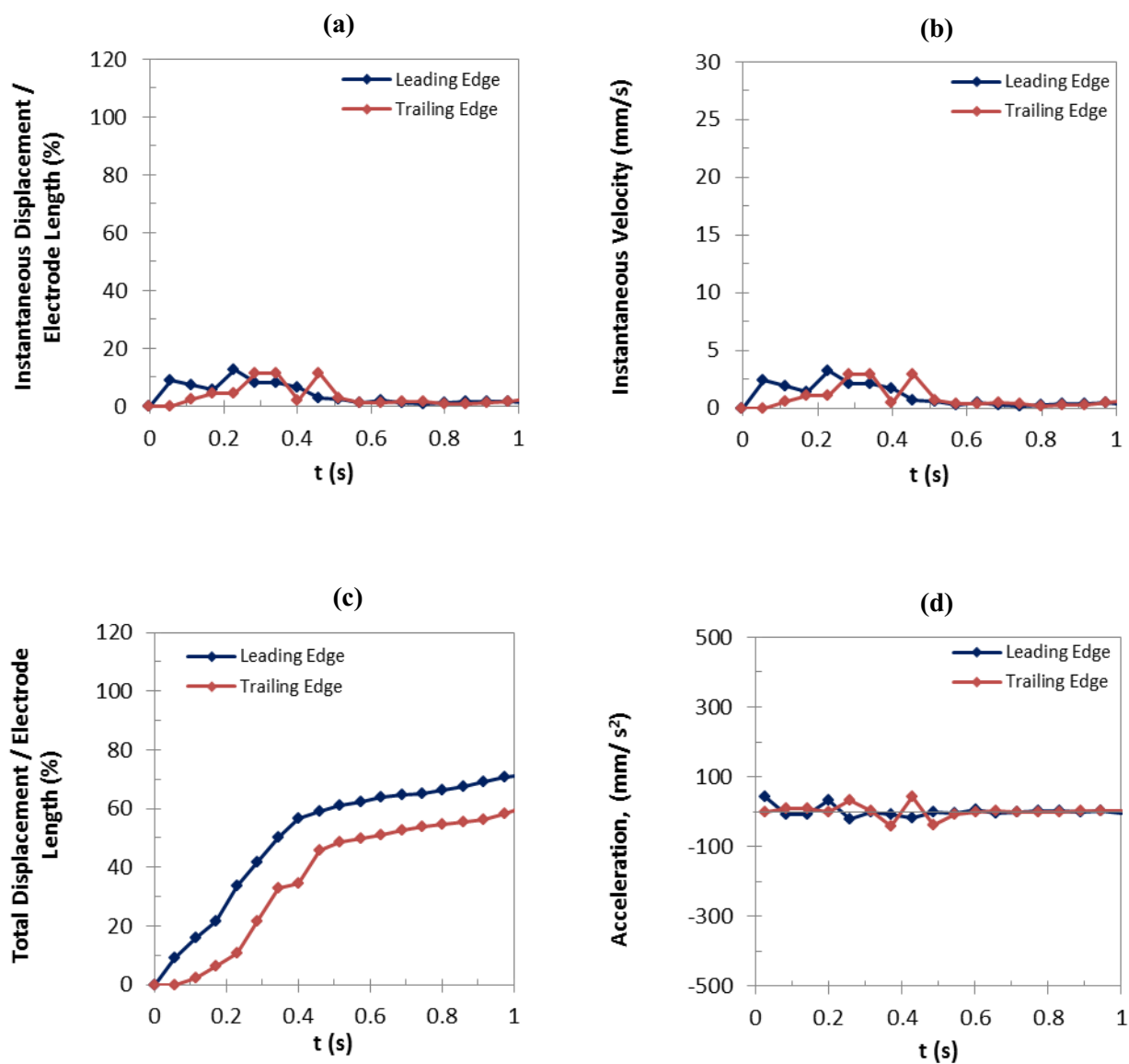


Figure G-27: Comparison of the average curves: (a) instantaneous displacement, (b) instantaneous velocity, (c) total displacement, and (d) acceleration, as a function of time for the leading and trailing edges of Tris-HCl buffer droplets at 70 V.

Tris-HCl buffer solution, 70 V, Average curves

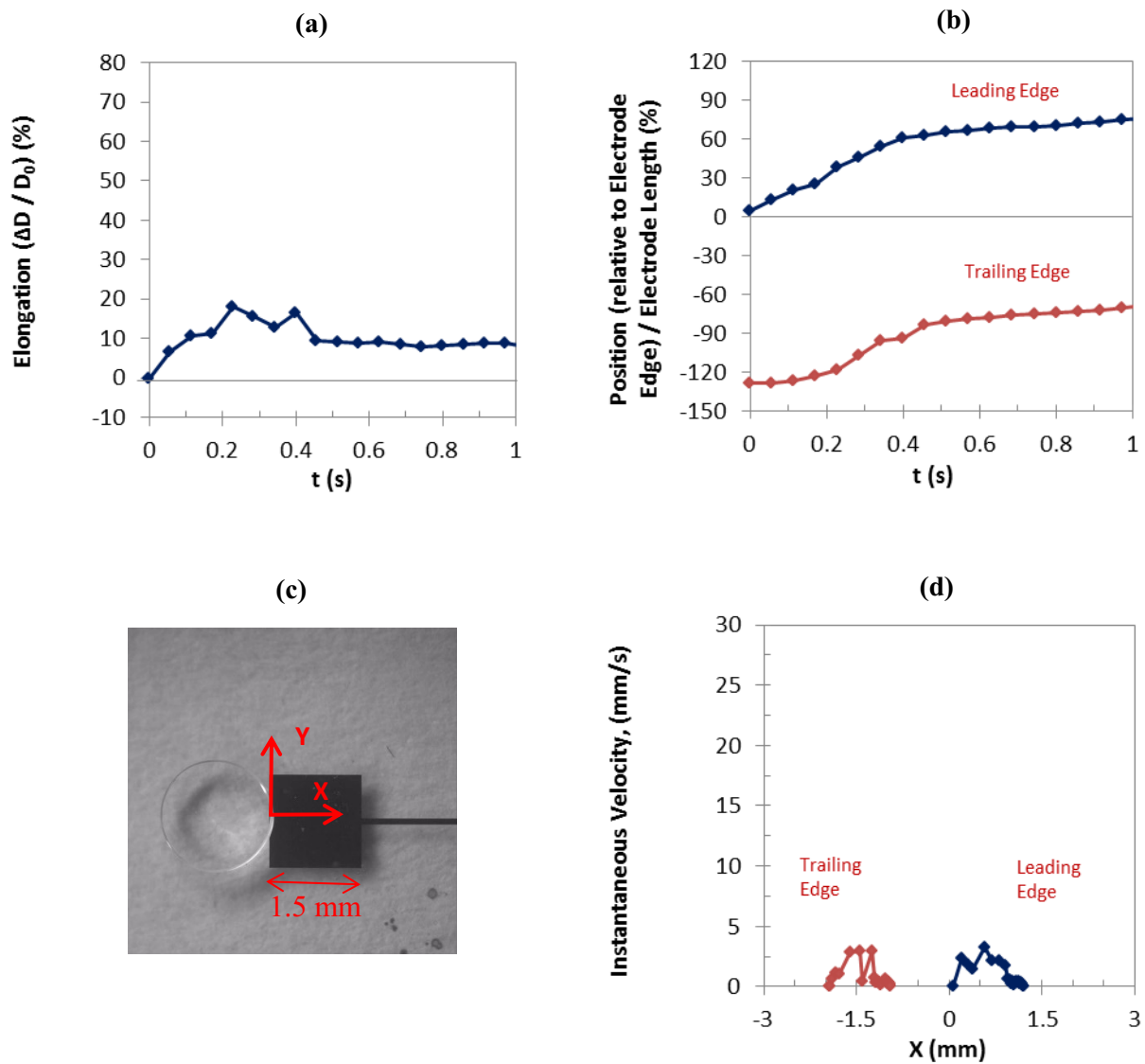


Figure G-28: Comparison of the average curves: (a) droplet elongation and (b) droplet position as a function of time, (d) instantaneous velocity as a function of droplet position as shown in (c) for the leading and trailing edges of Tris-HCl buffer droplets at 70 V.

G-6) Tris-HCl, 65 V

Tris-HCl buffer solution, 65 V, Leading edge,

Accepted experiments and the average curves

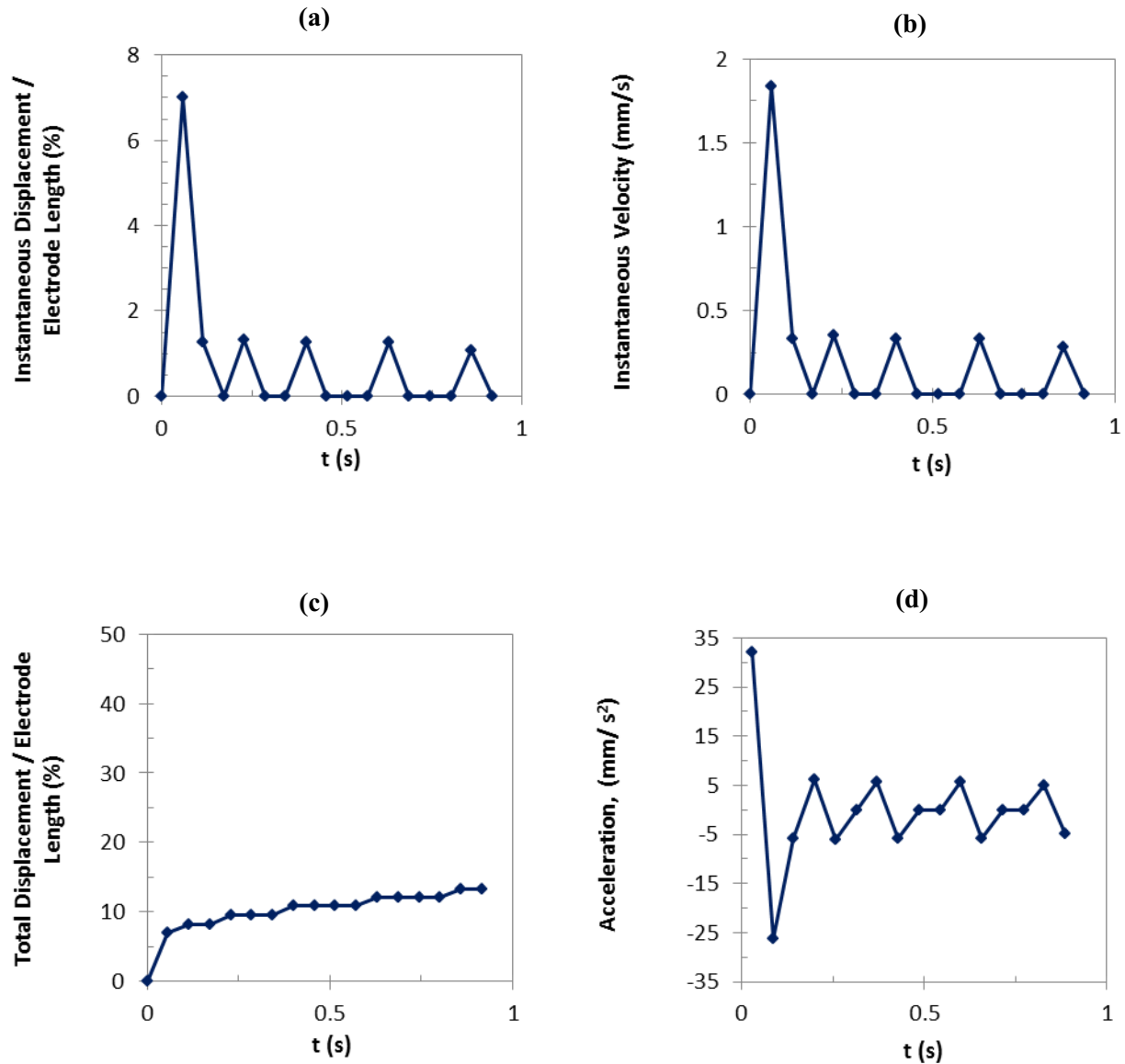


Figure G-29: (a) Instantaneous displacement, (b) instantaneous velocity, (c) total displacement, and (d) acceleration of the leading edges of Tris-HCl buffer droplets as a function of time at 65 V.

Tris-HCl buffer solution, 65 V, Trailing edge,

Accepted experiments and the average curves

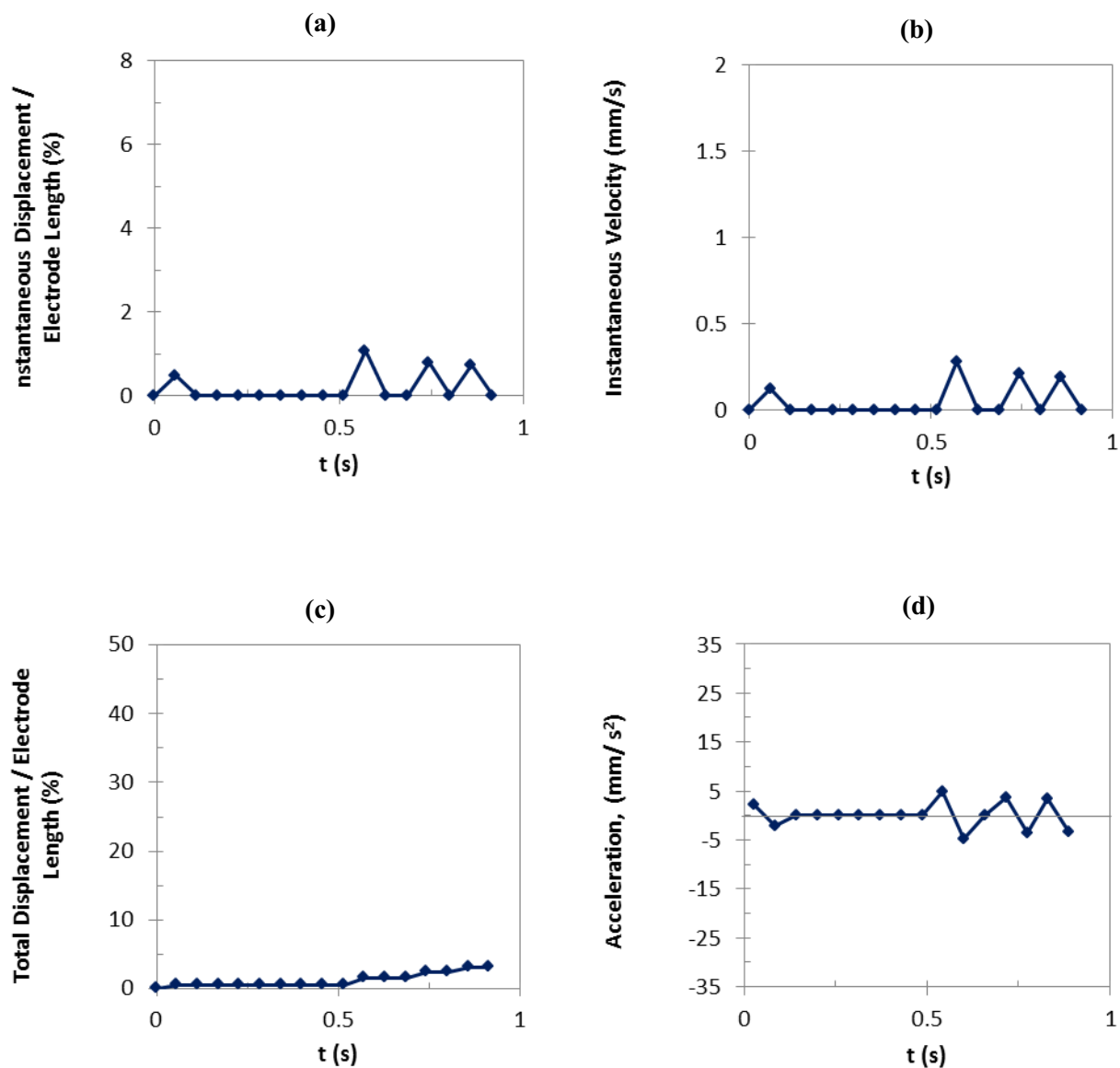


Figure G-30: (a) Instantaneous displacement, (b) instantaneous velocity, (c) total displacement, and (d) acceleration of the trailing edges of Tris-HCl buffer droplets as a function of time at 65 V.

Tris-HCl buffer solution, 65 V

Accepted experiments and the average curves

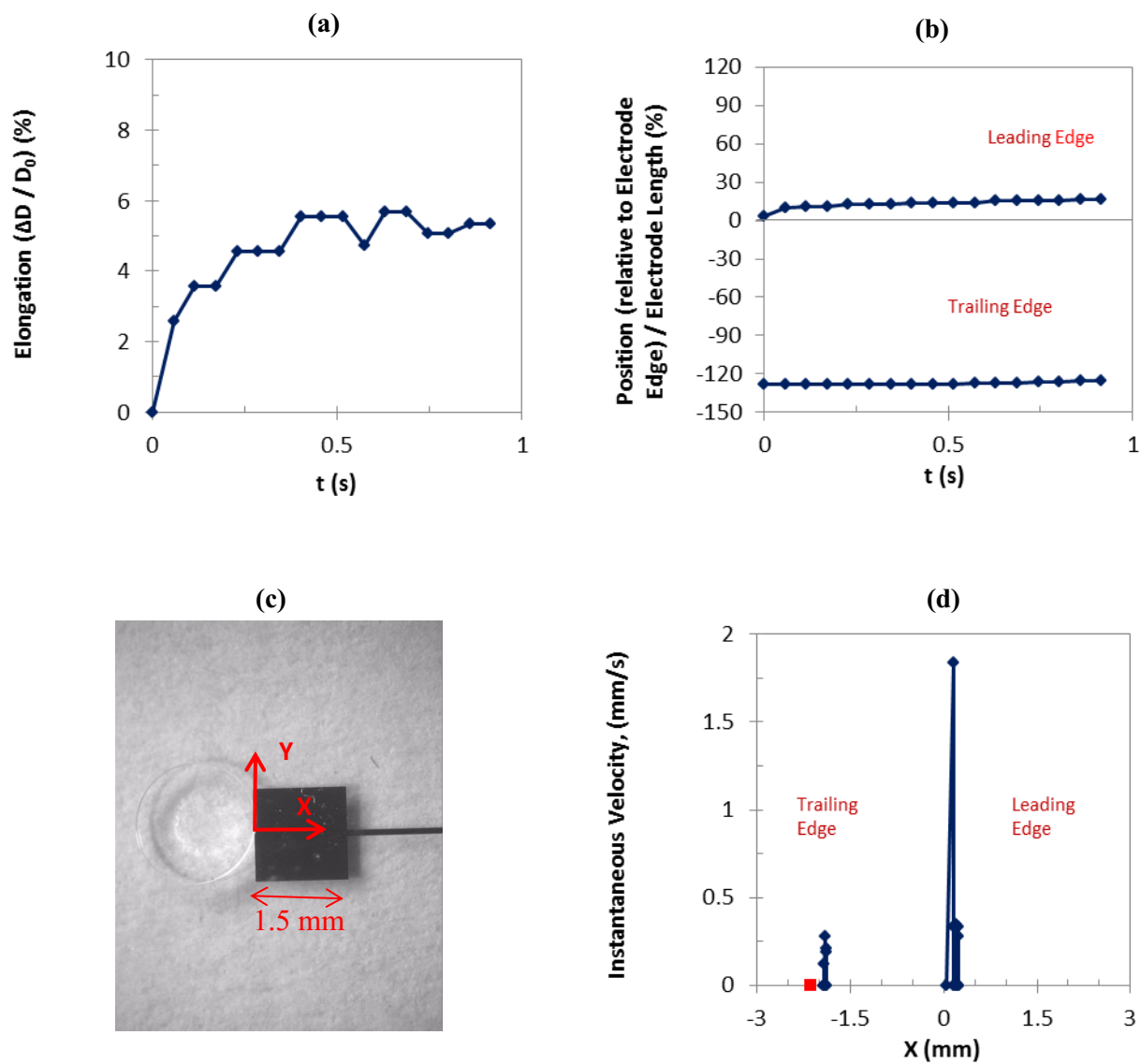


Figure G-31: (a) Droplet elongation and (b) droplet position as a function of time, (d) instantaneous velocity as a function of droplet position as shown in (c) for the leading and trailing edges of Tris-HCl buffer droplets at 65 V.

Tris-HCl buffer solution, 65 V, Average curves

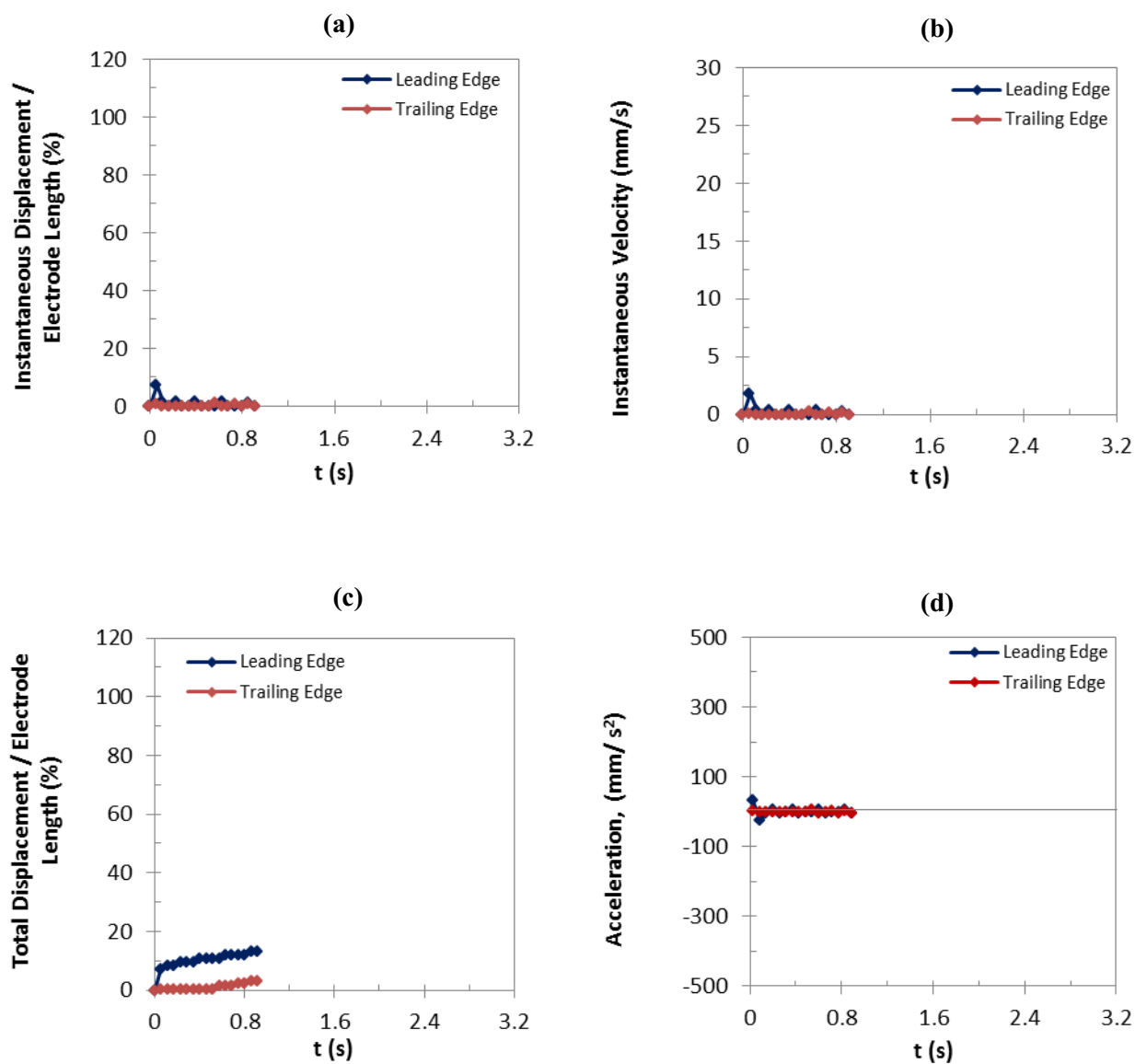


Figure G-32: Comparison of the average curves: (a) instantaneous displacement, (b) instantaneous velocity, (c) total displacement, and (d) acceleration, as a function of time for the leading and trailing edges of Tris-HCl buffer droplets at 65 V.

Tris-HCl buffer solution, 65 V, Average curves

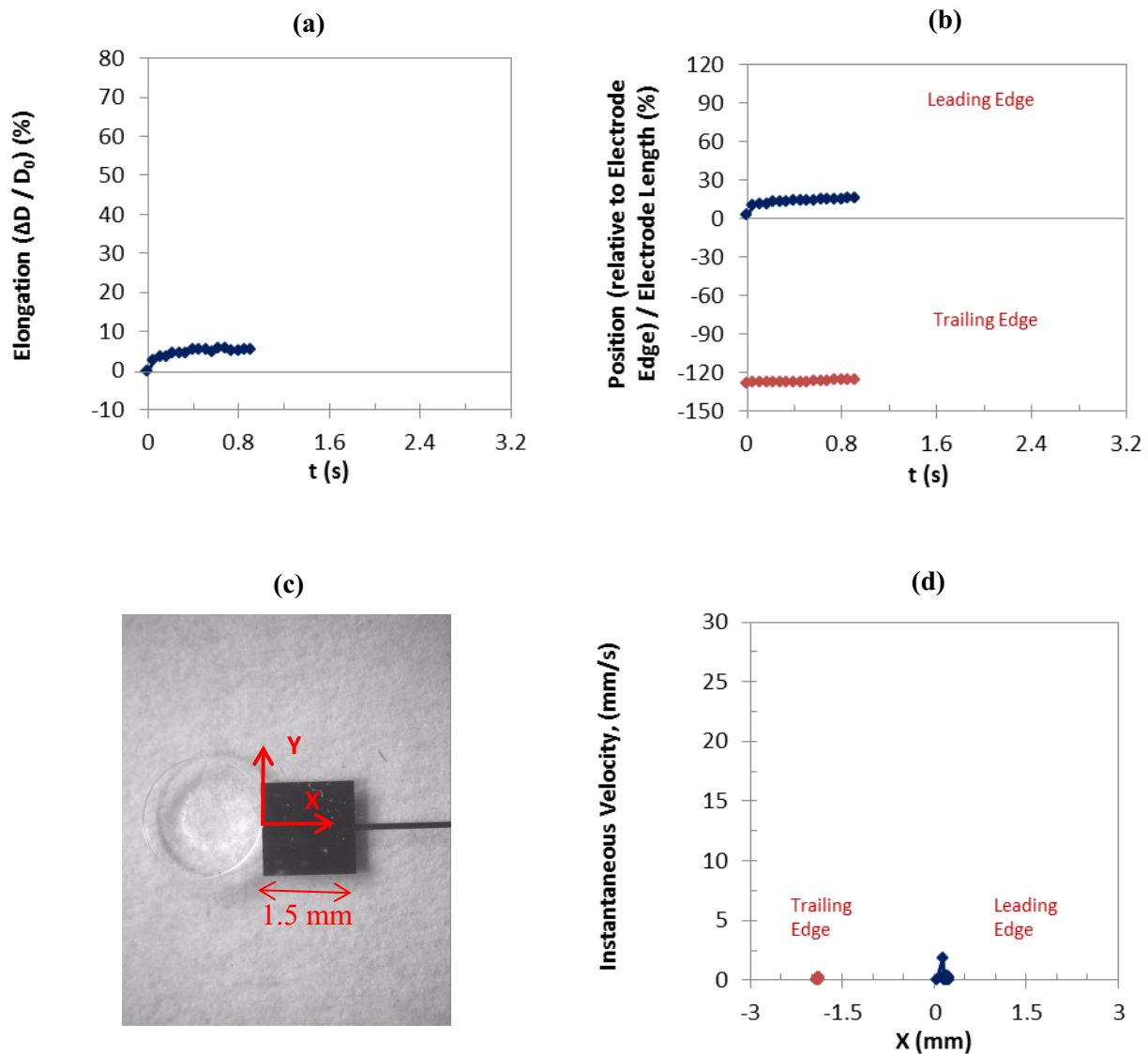


Figure G-33: Comparison of the average curves: (a) droplet elongation and (b) droplet position as a function of time, (d) instantaneous velocity as a function of droplet position as shown in (c) for the leading and trailing edges of Tris-HCl buffer droplets at 65 V.

G-7) Tris-HCl, 60 V

Tris-HCl buffer solution, 60 V, Leading edge,

Accepted experiments and the average curves

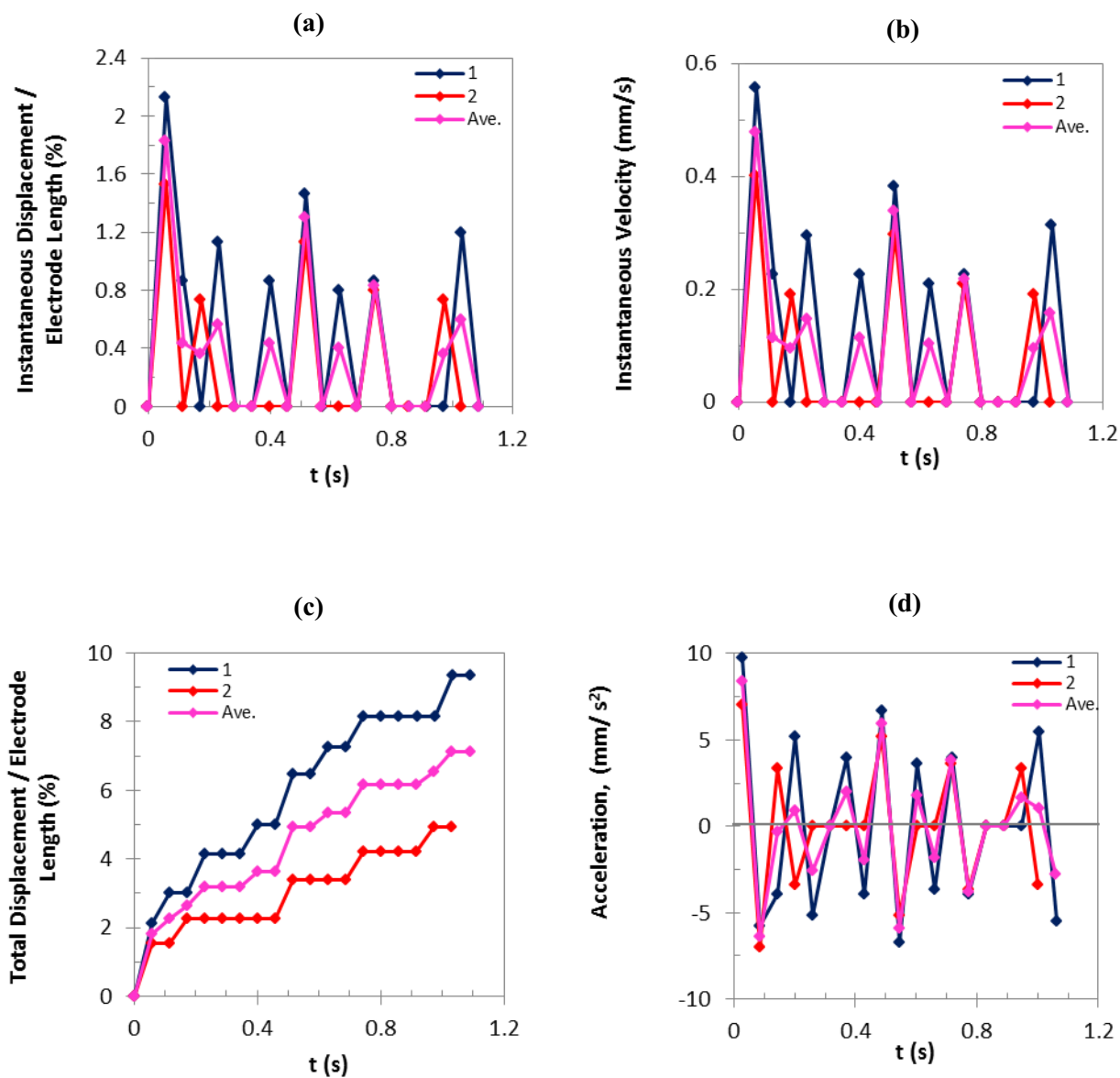


Figure G-34: (a) Instantaneous displacement, (b) instantaneous velocity, (c) total displacement, and (d) acceleration of the leading edges of Tris-HCl buffer droplets as a function of time at 60 V.

Tris-HCl buffer solution, 60 V, Trailing edge,
Accepted experiments and the average curves

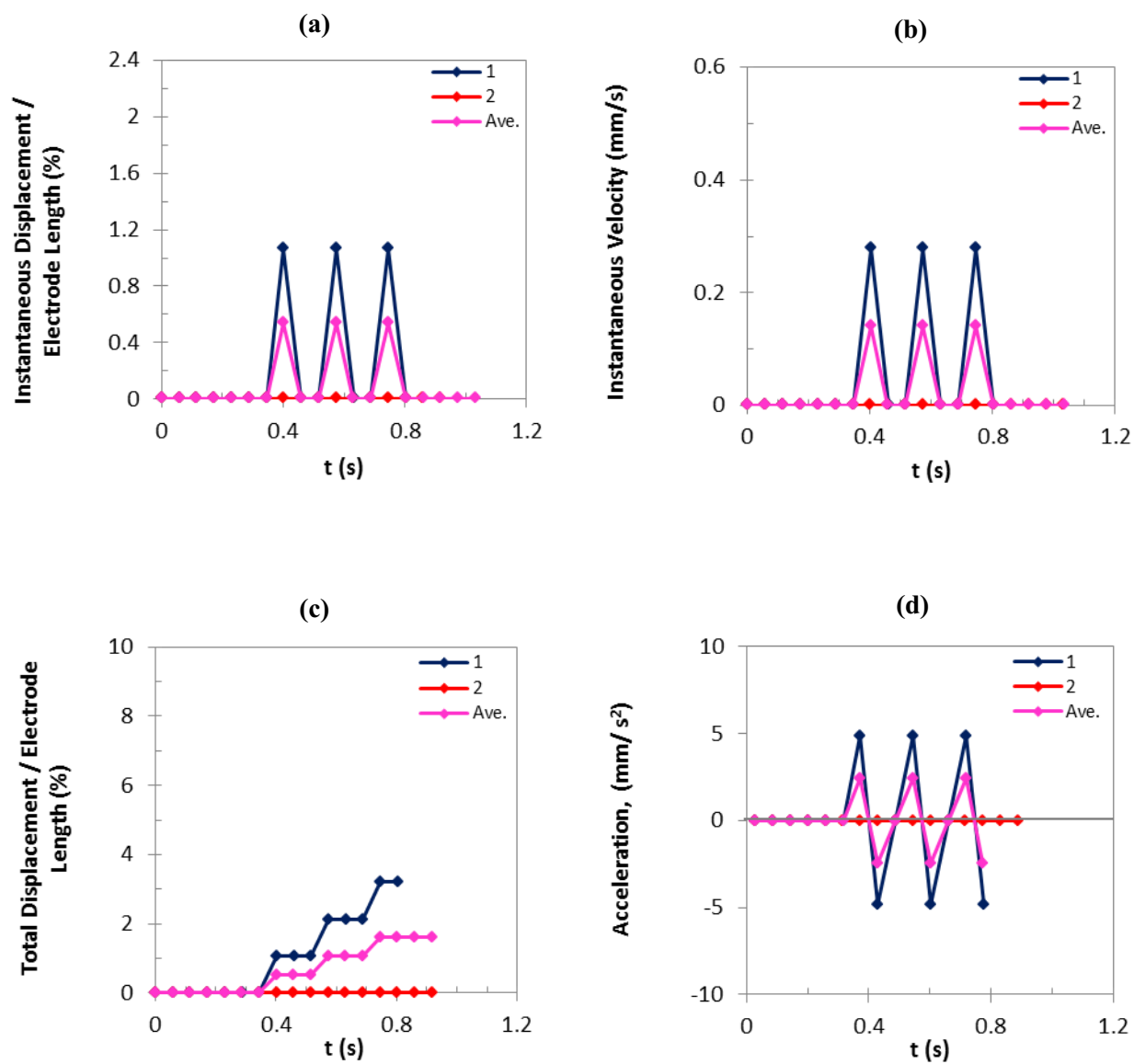


Figure G-35: (a) Instantaneous displacement, (b) instantaneous velocity, (c) total displacement, and (d) acceleration of the trailing edges of Tris-HCl buffer droplets as a function of time at 60 V.

Tris-HCl buffer solution, 60 V

Accepted experiments and the average curves

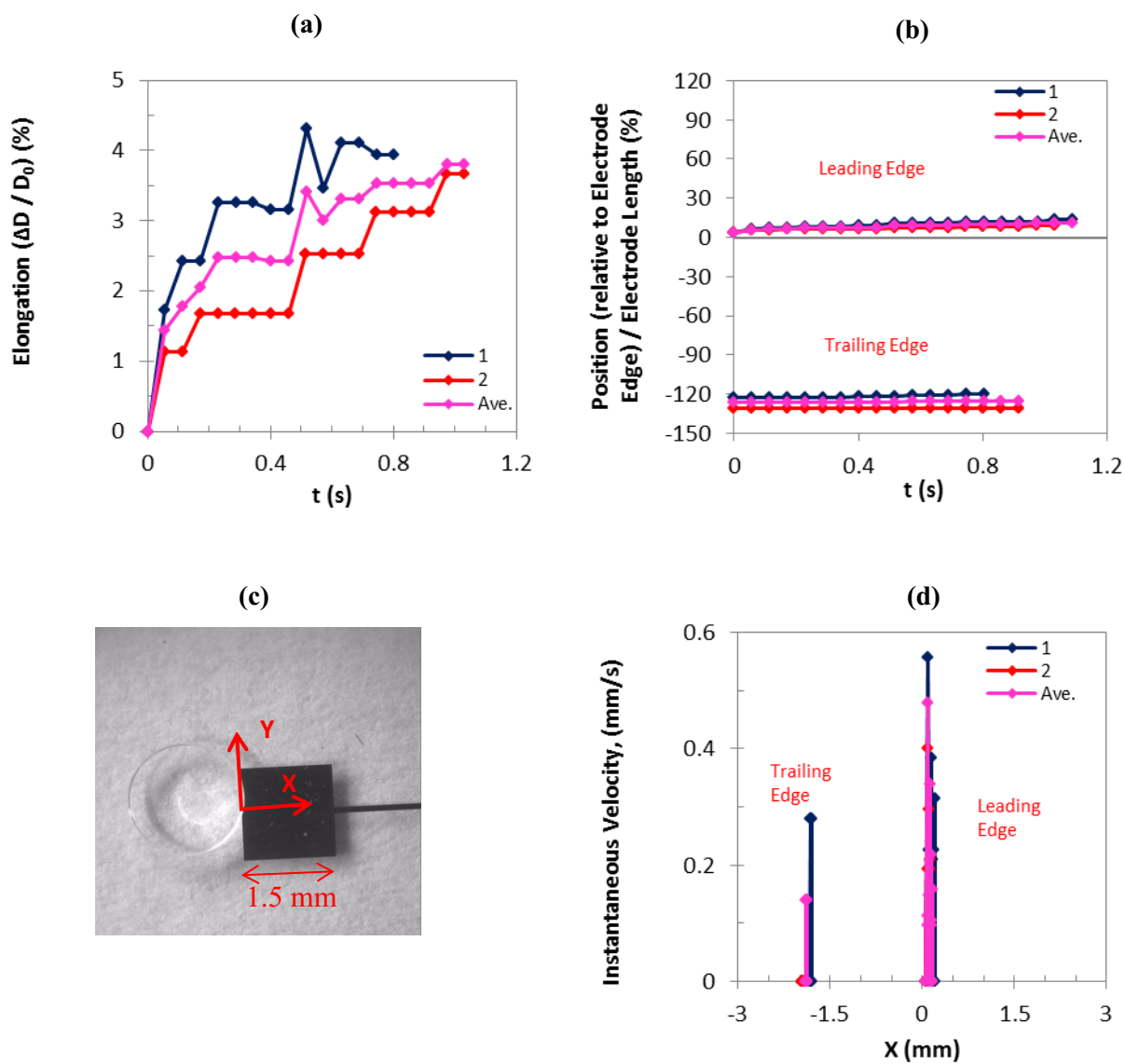


Figure G-36: (a) Droplet elongation and (b) droplet position as a function of time, (d) instantaneous velocity as a function of droplet position as shown in (c) for the leading and trailing edges of Tris-HCl buffer droplets at 60 V.

Tris-HCl buffer solution, 60 V, Average curves

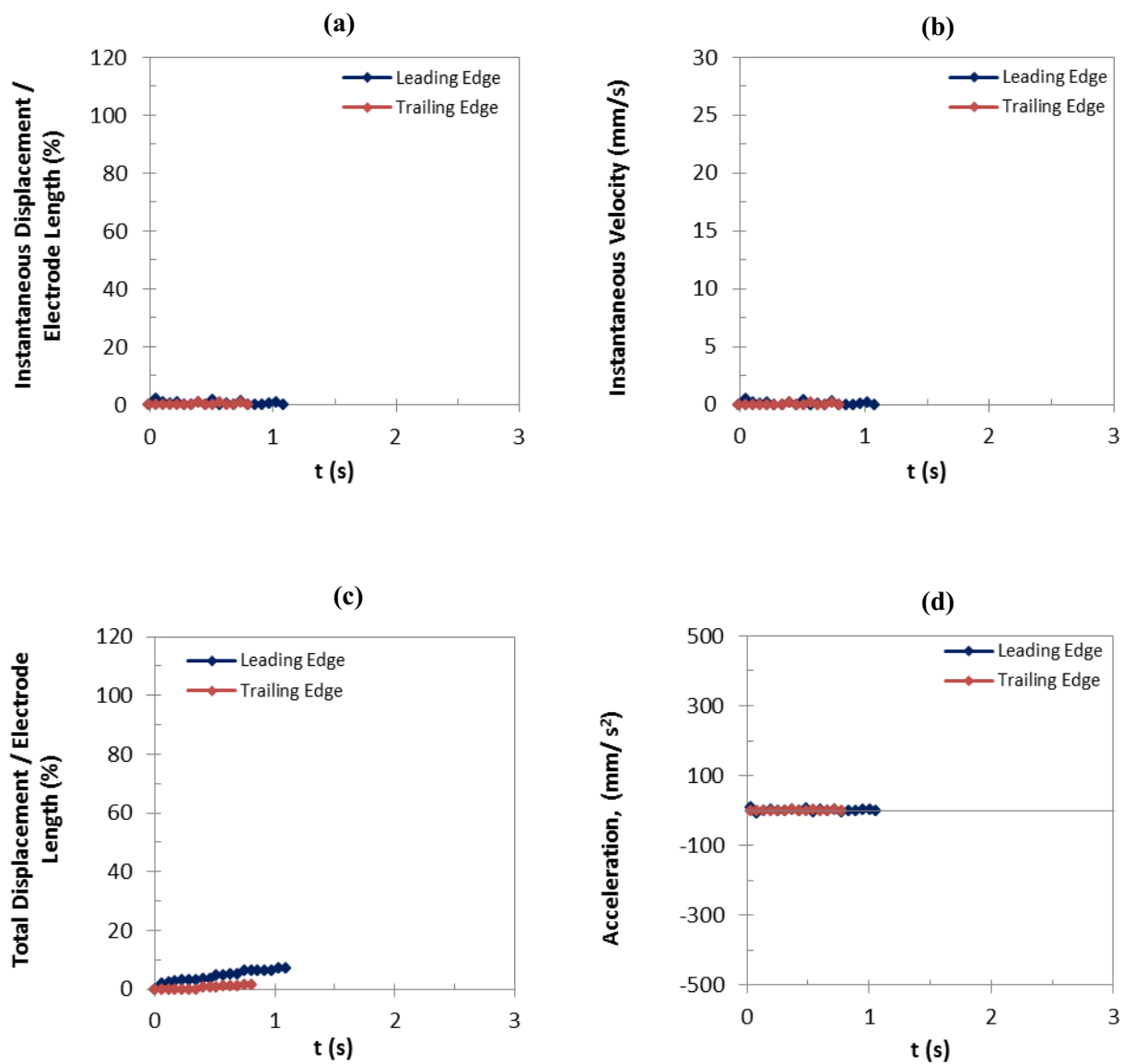


Figure G-37: Comparison of the average curves: (a) instantaneous displacement, (b) instantaneous velocity, (c) total displacement, and (d) acceleration, as a function of time for the leading and trailing edges of Tris-HCl buffer droplets at 60 V.

Tris-HCl buffer solution, 60 V, Average curves

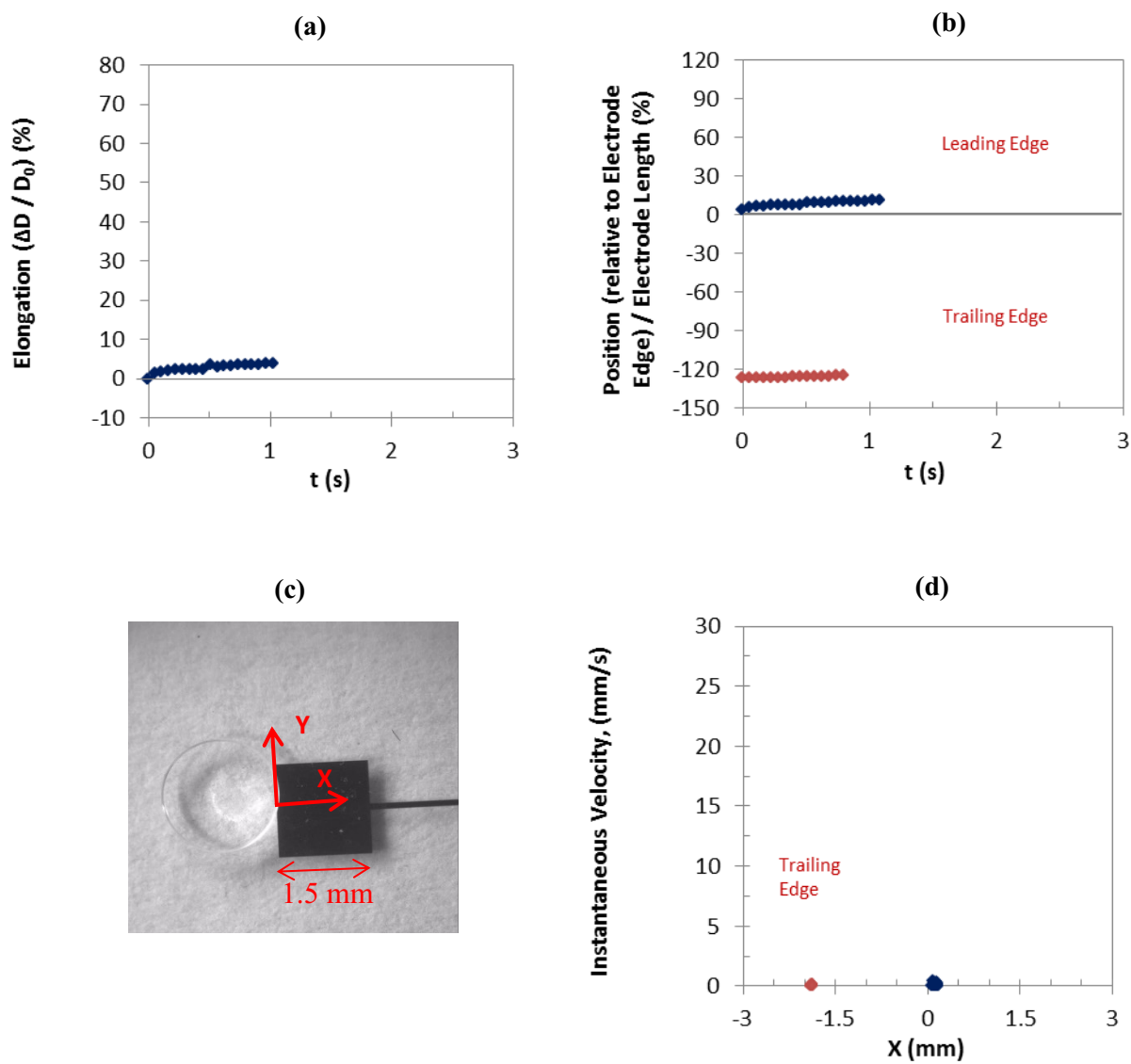


Figure G-38: Comparison of the average curves: (a) droplet elongation and (b) droplet position as a function of time, (d) instantaneous velocity as a function of droplet position as shown in (c) for the leading and trailing edges of Tris-HCl buffer droplets at 60 V.

G-8) Tris-HCl, 55 V

Tris-HCl buffer solution, 55 V, Leading edge,

Accepted experiments and the average curves

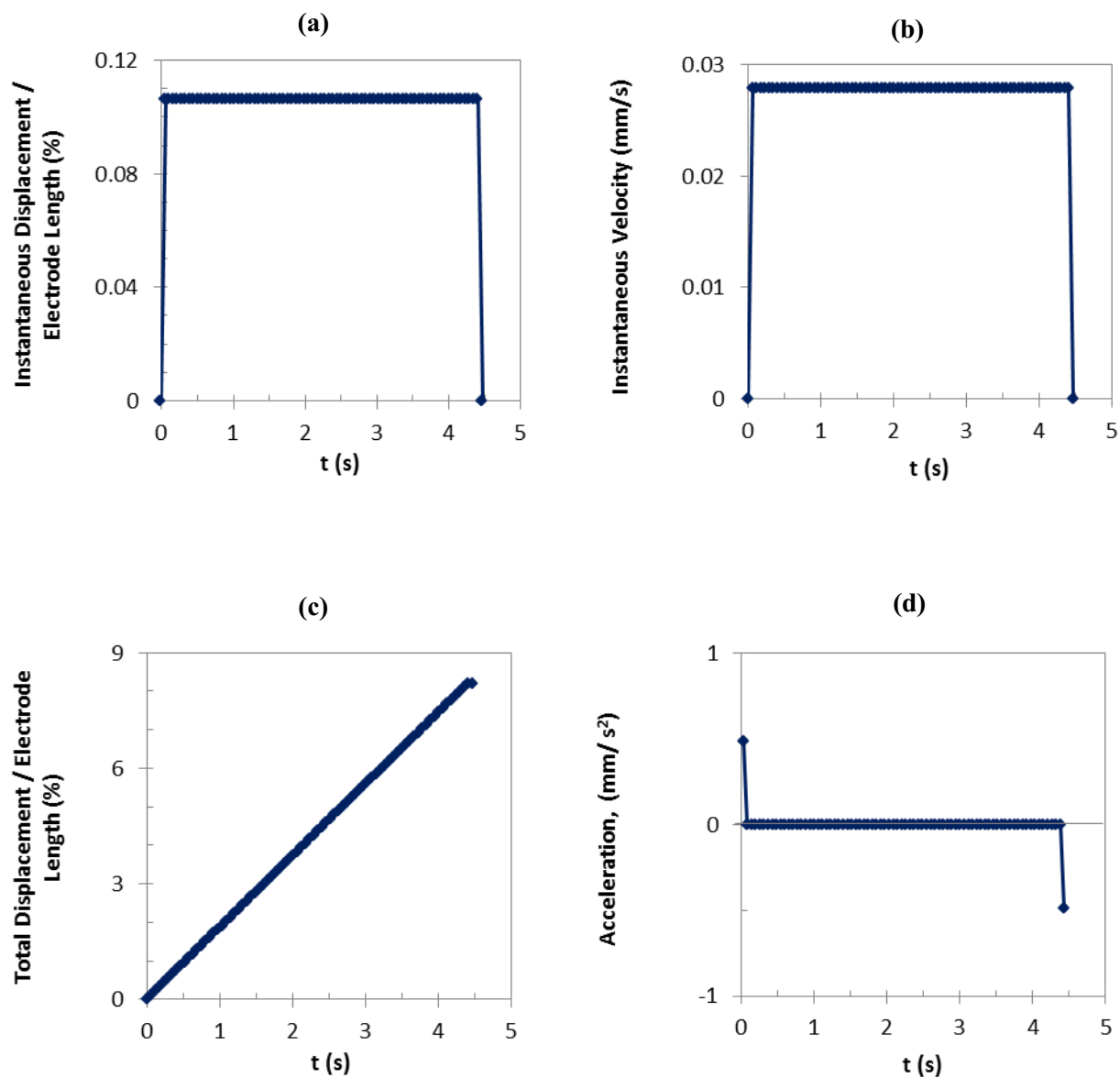


Figure G-39: (a) Instantaneous displacement, (b) instantaneous velocity, (c) total displacement, and (d) acceleration of the leading edges of Tris-HCl buffer droplets as a function of time at 55 V.

Tris-HCl buffer solution, 55 V, Trailing edge,

Accepted experiments and the average curves

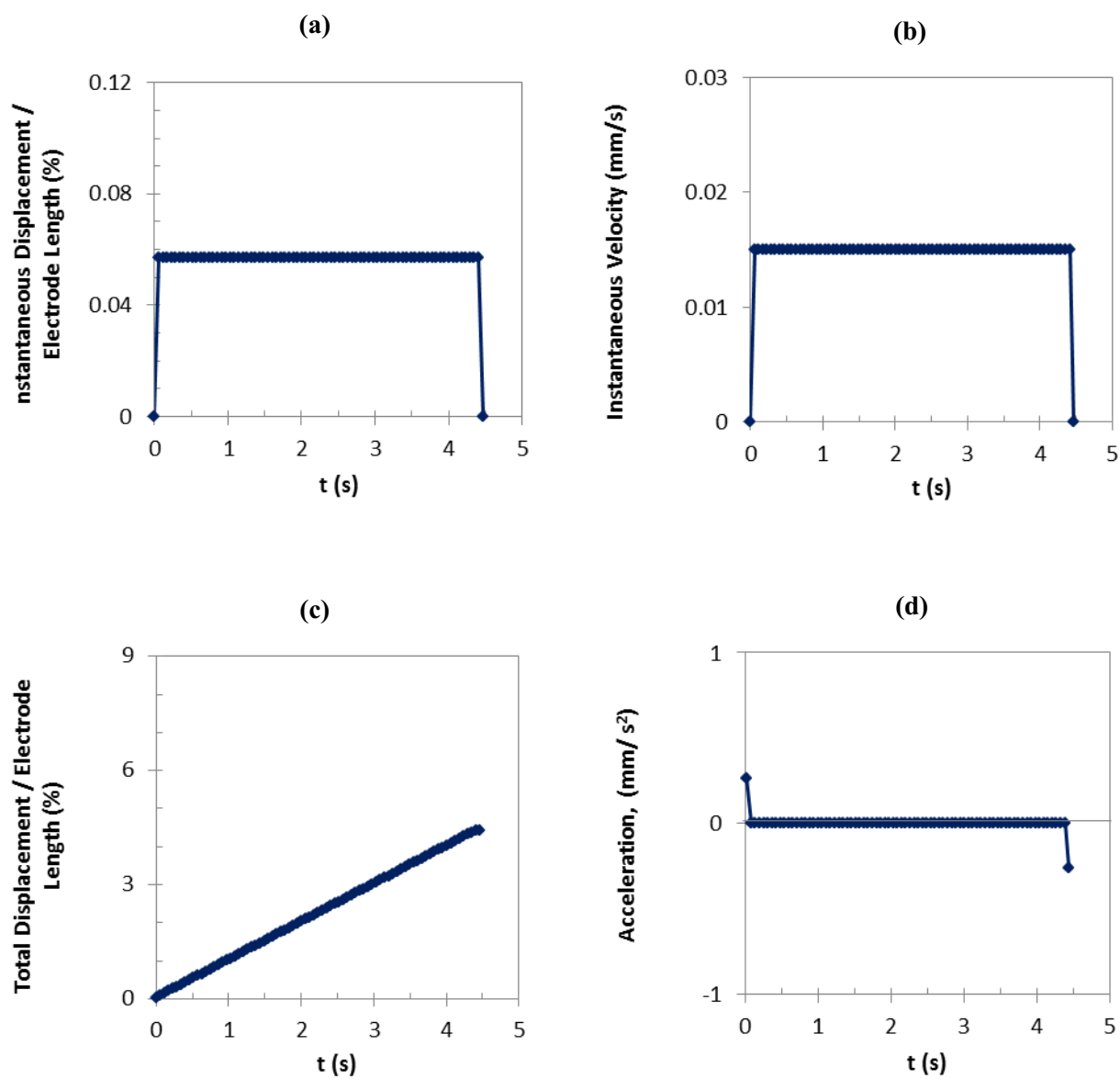


Figure G-40: (a) Instantaneous displacement, (b) instantaneous velocity, (c) total displacement, and (d) acceleration of the trailing edges of Tris-HCl buffer droplets as a function of time at 55 V.

Tris-HCl buffer solution, 55 V

Accepted experiments and the average curves

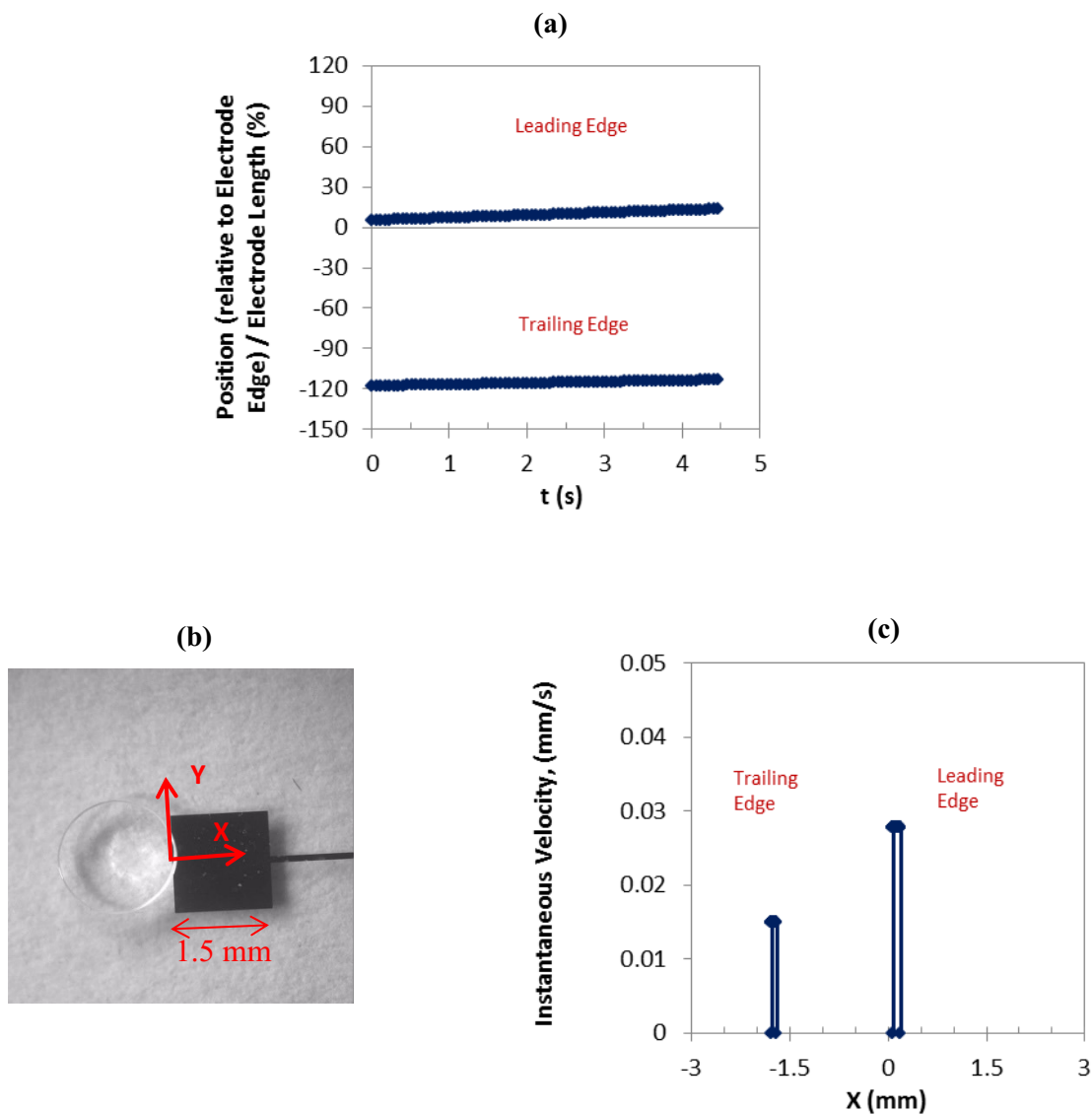


Figure G-41: (a) Droplet elongation and (b) droplet position as a function of time, (d) instantaneous velocity as a function of droplet position as shown in (c) for the leading and trailing edges of Tris-HCl buffer droplets at 55 V.

Tris-HCl buffer solution, 55 V, Average curves

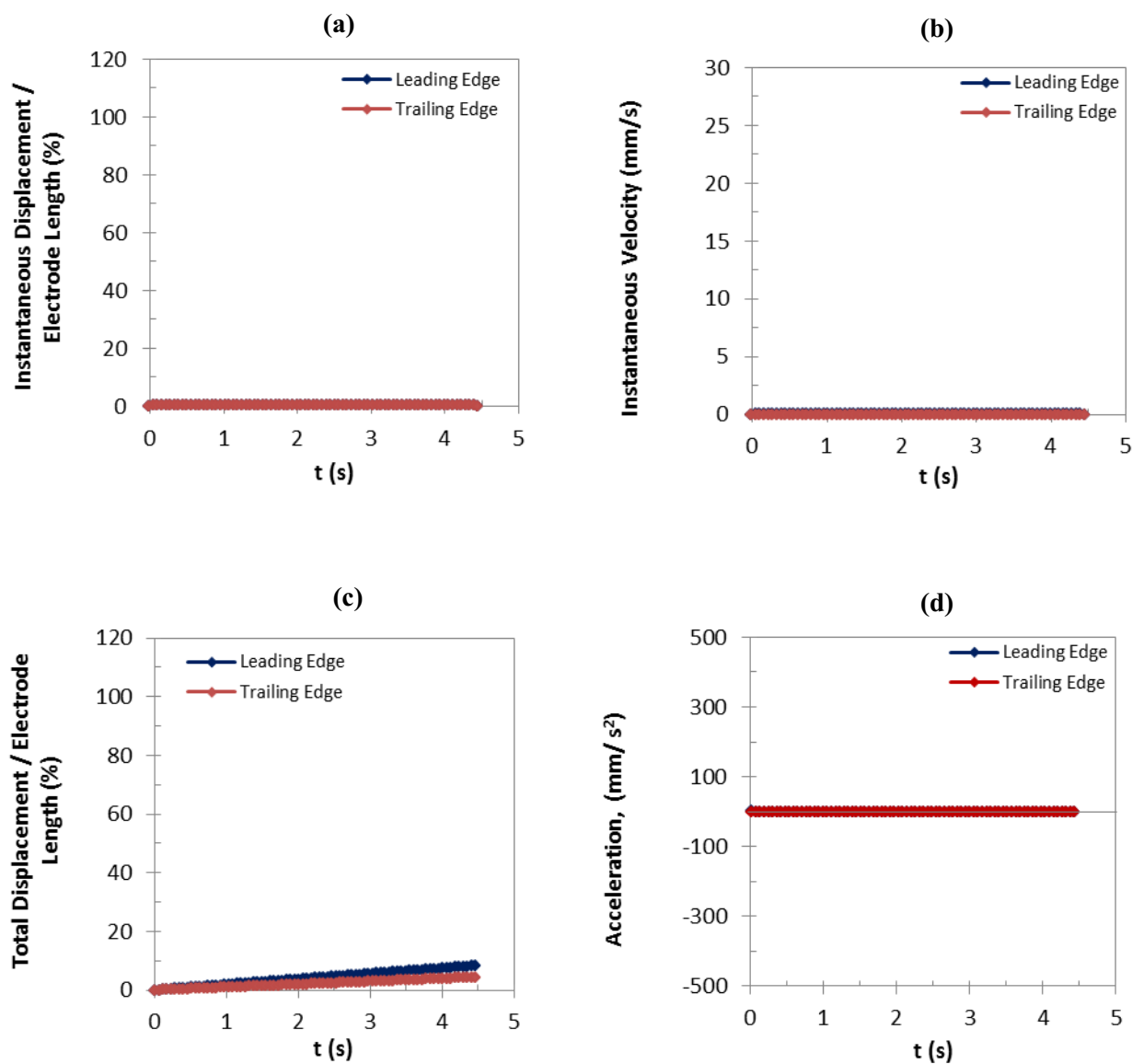


Figure G-42: Comparison of the average curves: (a) instantaneous displacement, (b) instantaneous velocity, (c) total displacement, and (d) acceleration, as a function of time for the leading and trailing edges of Tris-HCl buffer droplets at 55 V.

Tris-HCl buffer solution, 55 V, Average curves

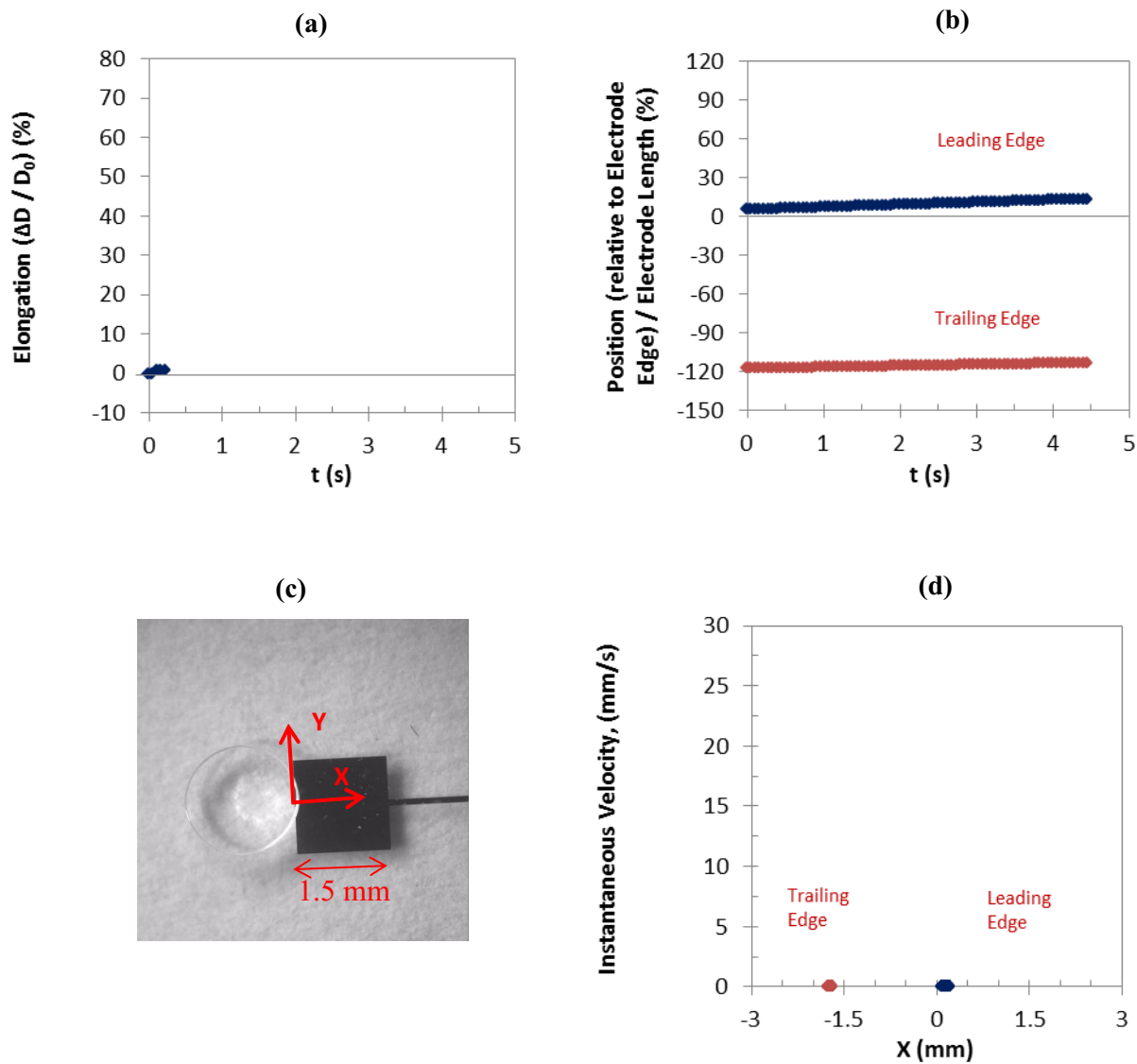


Figure G-43: Comparison of the average curves: (a) droplet elongation and (b) droplet position as a function of time, (d) instantaneous velocity as a function of droplet position as shown in (c) for the leading and trailing edges of Tris-HCl buffer droplets at 55 V.

G-9) Tris-HCl, 50 V

Tris-HCl buffer solution, 50 V, Leading edge,

Accepted experiments and the average curves

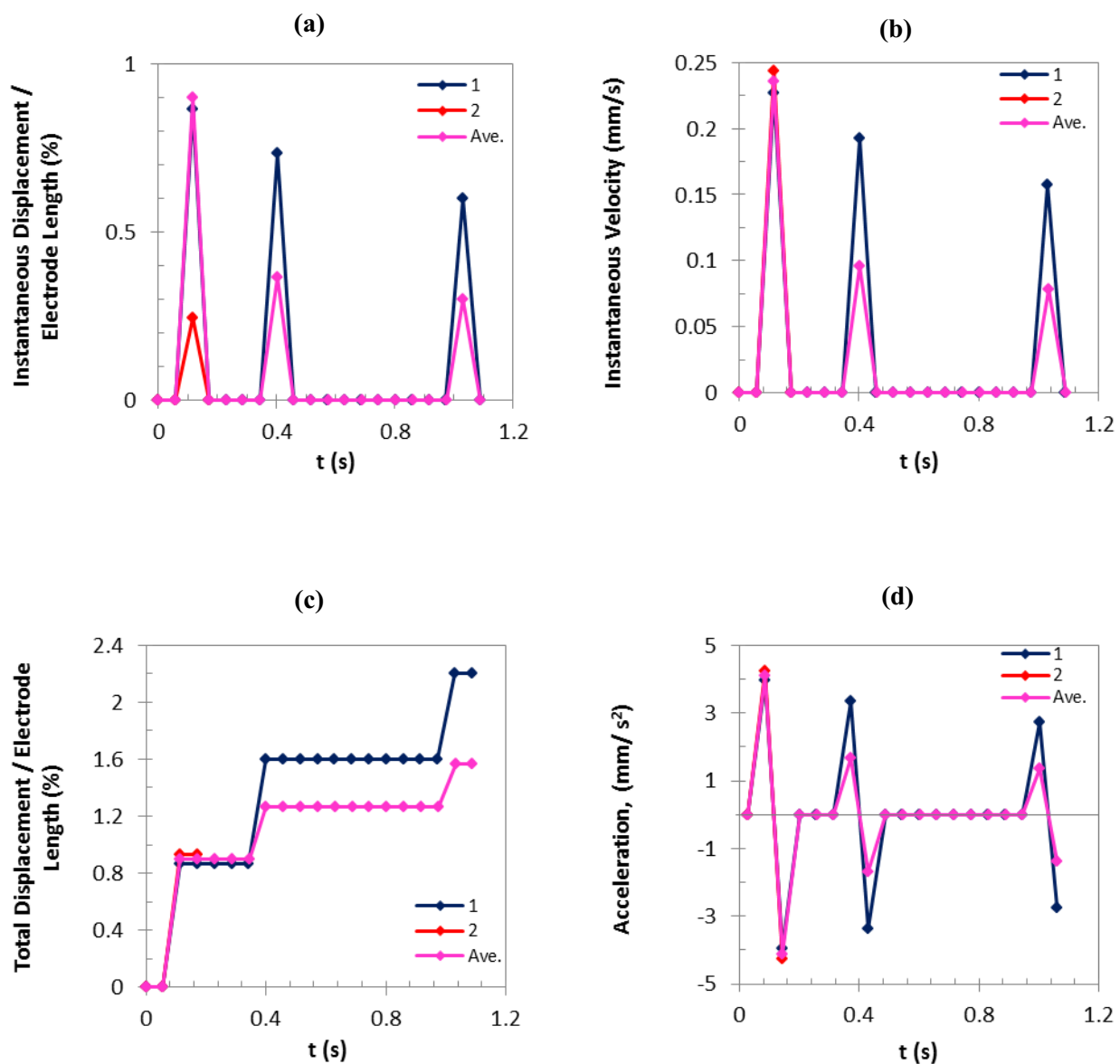


Figure G-44: (a) Instantaneous displacement, (b) instantaneous velocity, (c) total displacement, and (d) acceleration of the leading edges of Tris-HCl buffer droplets as a function of time at 50 V.

Tris-HCl buffer solution, 50 V, Trailing edge,

Accepted experiments and the average curves

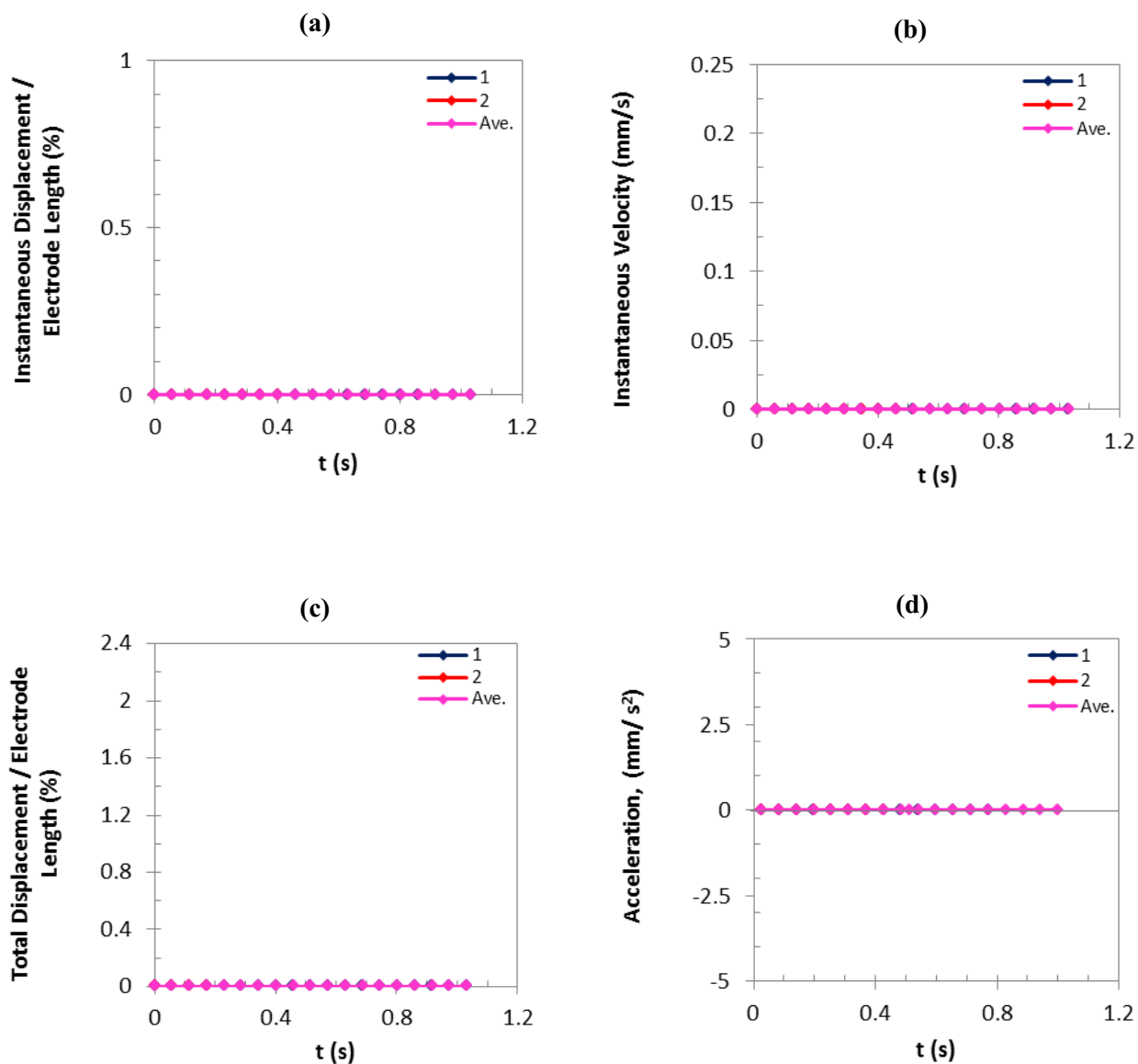


Figure G-45: (a) Instantaneous displacement, (b) instantaneous velocity, (c) total displacement, and (d) acceleration of the trailing edges of Tris-HCl buffer droplets as a function of time at 50 V.

Tris-HCl buffer solution, 50 V

Accepted experiments and the average curves

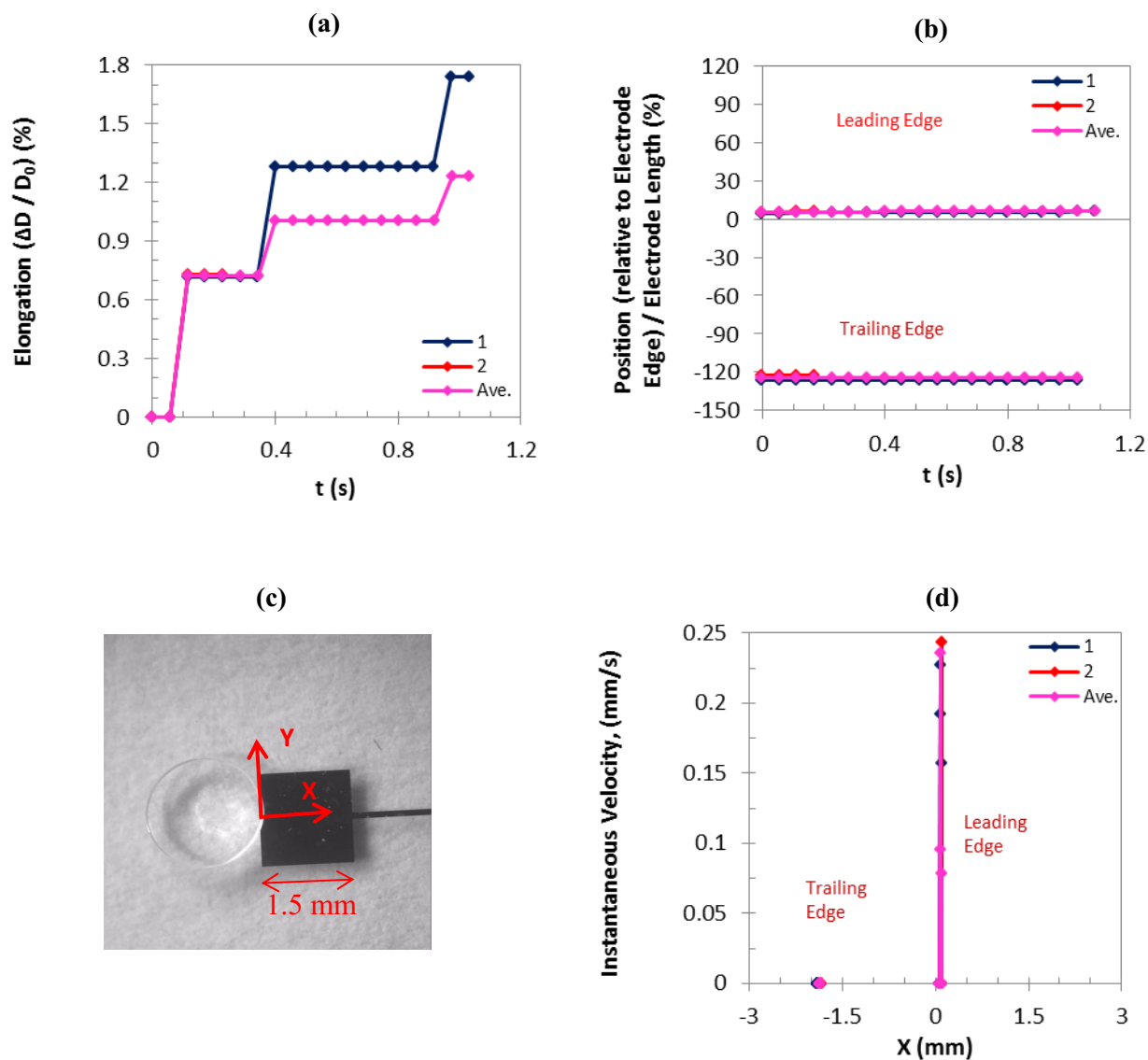


Figure G-46: (a) Droplet elongation and (b) droplet position as a function of time, (d) instantaneous velocity as a function of droplet position as shown in (c) for the leading and trailing edges of Tris-HCl buffer droplets at 50 V.

Tris-HCl buffer solution, 50 V, Average curves

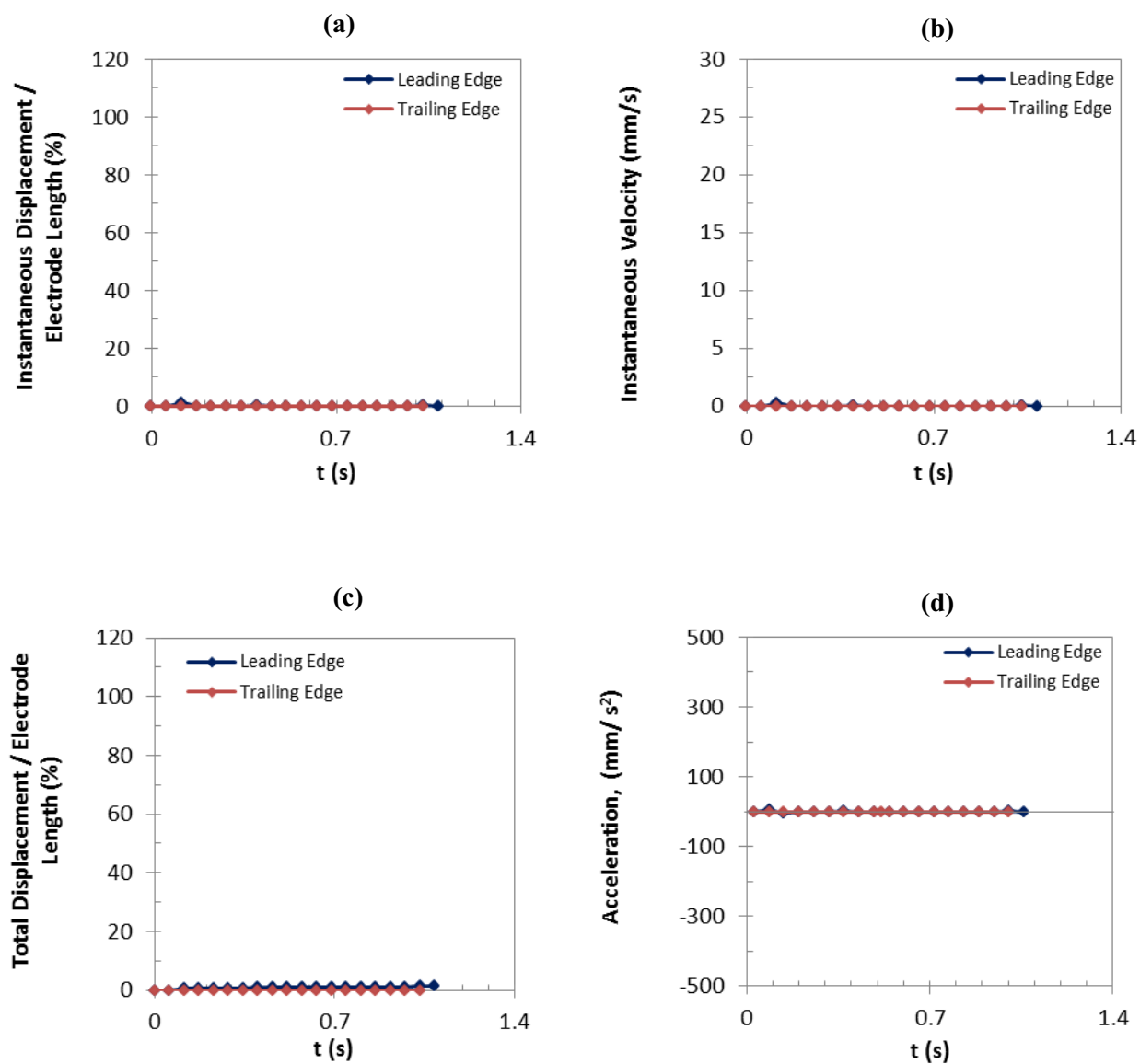


Figure G-47: Comparison of the average curves: (a) instantaneous displacement, (b) instantaneous velocity, (c) total displacement, and (d) acceleration, as a function of time for the leading and trailing edges of Tris-HCl buffer droplets at 50 V.

Tris-HCl buffer solution, 50 V, Average curves

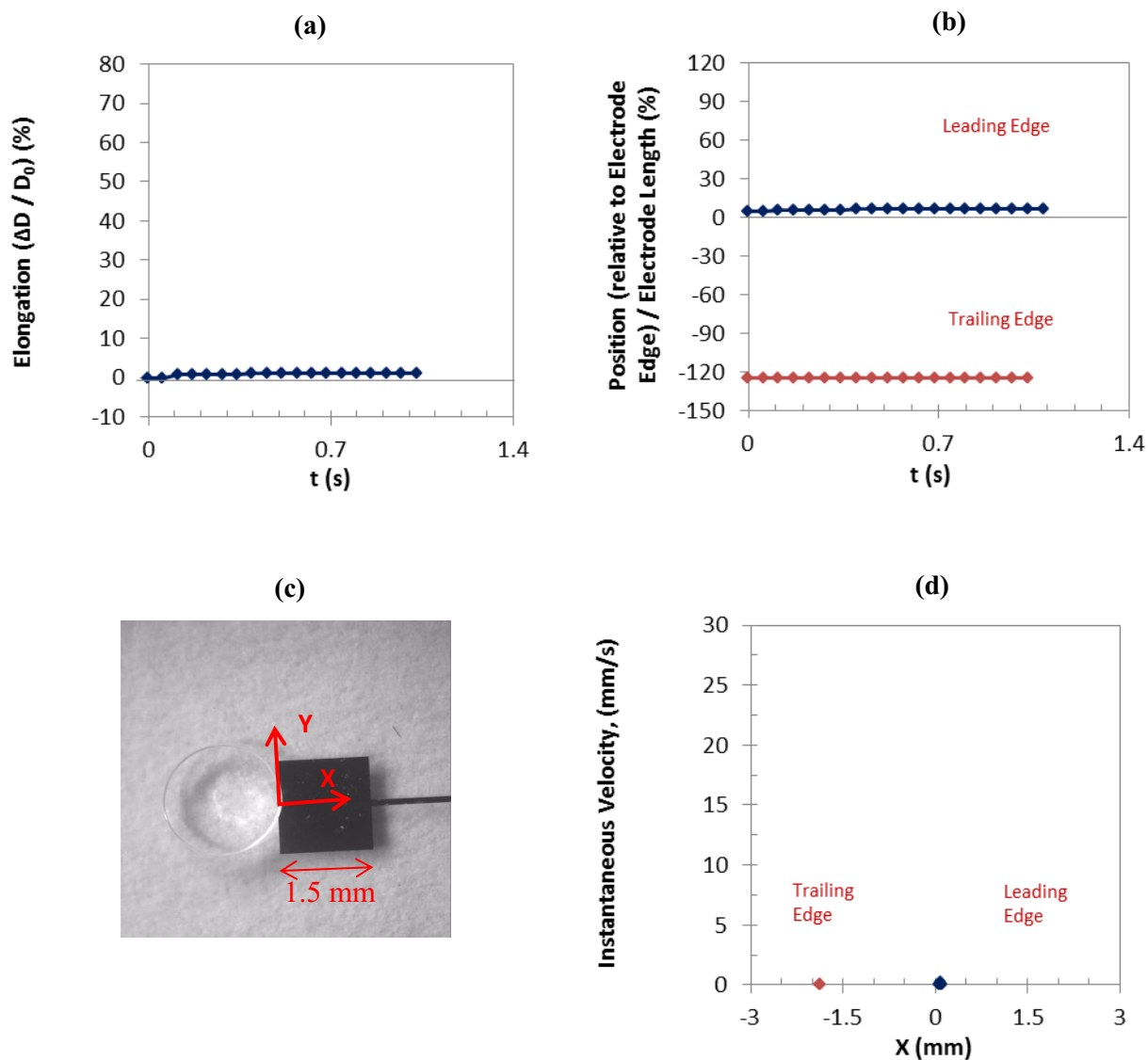


Figure G-48: Comparison of the average curves: (a) droplet elongation and (b) droplet position as a function of time, (d) instantaneous velocity as a function of droplet position as shown in (c) for the leading and trailing edges of Tris-HCl buffer droplets at 50 V.

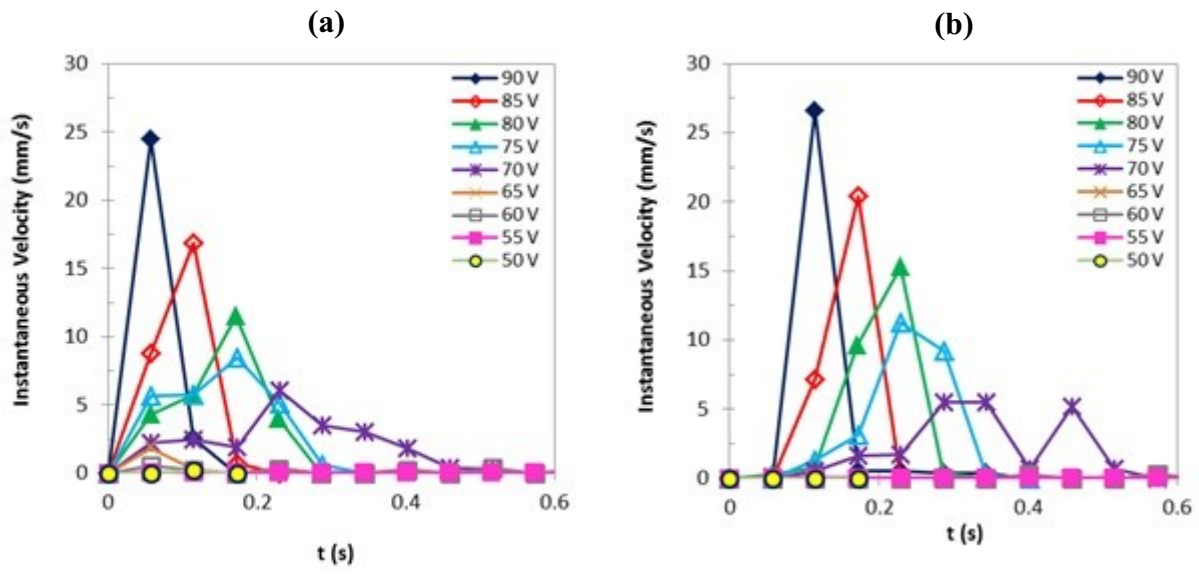


Figure G-49: The instantaneous velocity of Tris-HCl buffer droplets as a function of time for the applied voltages of 50 to 90V. Comparison of results for the experiments with the highest leading edge instantaneous velocity: (a) leading edge, (b) trailing edge.

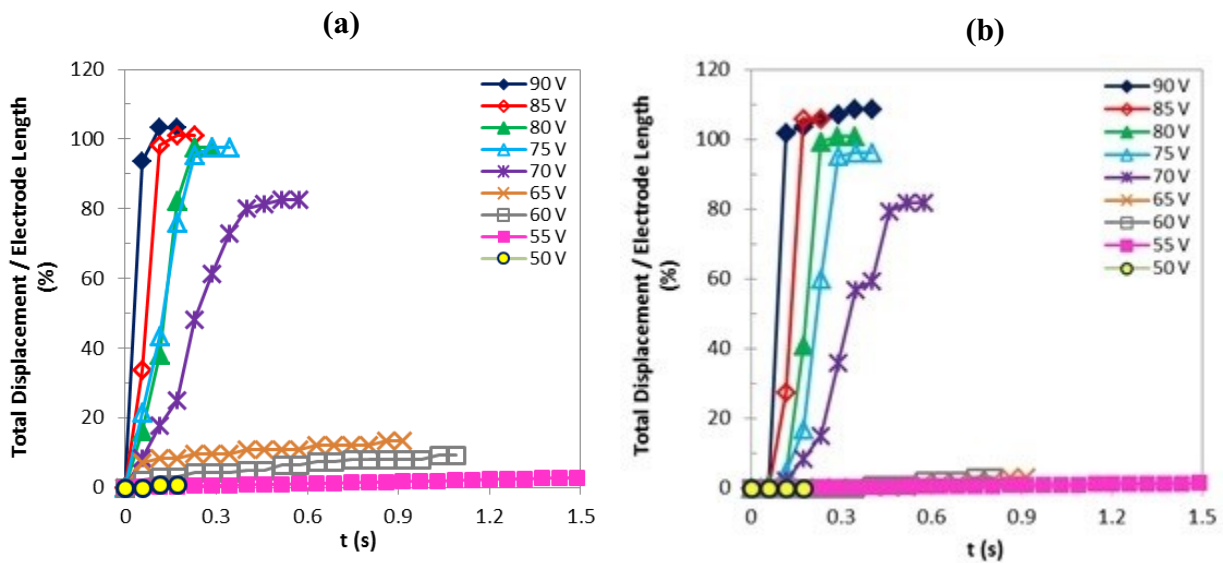


Figure G-50: The total displacement of Tris-HCl buffer droplets as a function of time for the applied voltages of 50 to 90V. Comparison of results for the experiments with the highest leading edge instantaneous velocity: (a) leading edge, (b) trailing edge.

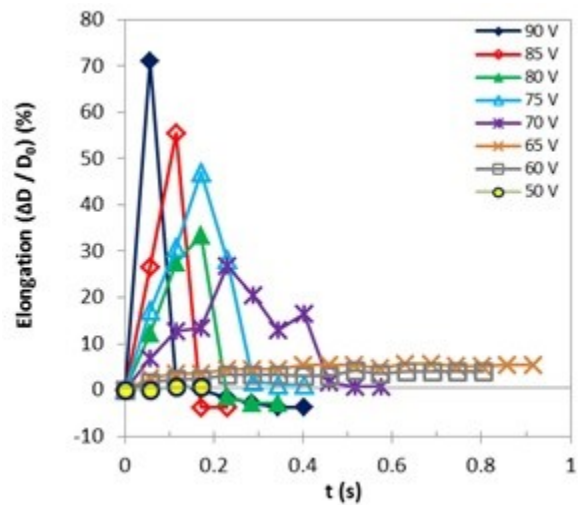


Figure G-51: The comparison of results for the elongation of Tris-HCl buffer droplets as a function of time for the experiments with the highest leading edge instantaneous velocity.

Table G-1: Peaks of the average curves, Tris-HCl buffer solution

Applied Voltage	90 V	85 V	80 V	75 V	70 V	65 V	60 V	55 V	50 V
Leading Edge									
Instantaneous Velocity (mm/s)	14.70	16.7	9.2	6.6	3.3	1.9	0.5	0	0.2
Total Displacement (normalized)	101%	101%	96%	95%	75%	13%	7%	8%	2%
Trailing Edge									
Instantaneous Velocity (mm/s)	13.7	20.8	10.3	9.2	3.0	0.3	0.1	0	0
Total Displacement (normalized)	102%	105%	100%	93%	65%	3%	1.5%	4.5%	0
Elongation (normalized)	44%	52%	29%	34%	18%	6%	4%	-	1.3%

Table G-2: Peaks of the curves for the experiments with the highest leading edge instantaneous velocity, Tris-HCl buffer

Applied Voltage	90 V	85 V	80 V	75 V	70 V	65 V	60 V	55 V	50 V
Leading Edge									
Instantaneous Velocity (mm/s)	24.5	16.9	11.6	8.5	6.1	1.9	0.6	0	0.3
Total Displacement (normalized)	103%	101%	98%	98%	80%	13%	8%	8%	1%
Trailing Edge									
Instantaneous Velocity (mm/s)	26.6	20.5	15.3	11.3	5.5	0.3	0.3	0	0
Total Displacement (normalized)	102%	105%	101%	95%	80%	3%	3%	4.5%	0
Elongation (normalized)	71%	56%	33%	47%	27%	6%	4%	0	0.8%

Table G-3: Average velocity for all experiments, Tris-HCl buffer

Leading Edge									
Average Velocity (mm/s)	16.8	12.2	7.0	4.9	1.9	1.1	0.1	0	0.1
Trailing Edge									
Average Velocity (mm/s)	9.8	9.1	5.7	4.0	1.6	0.1	0	0	0

Table G-4: Average velocity for the experiments with the highest leading edge instantaneous velocity, Tris-HCl buffer

Leading Edge									
Average Velocity (mm/s)	24.5	12.9	7.2	6.3	3.0	1.1	0.2	0	0.1
Trailing Edge									
Average Velocity (mm/s)	13.3	9.2	6.5	5.0	2.6	0.1	0.1	0	0

Tris-HCl buffer solution, Leading edge

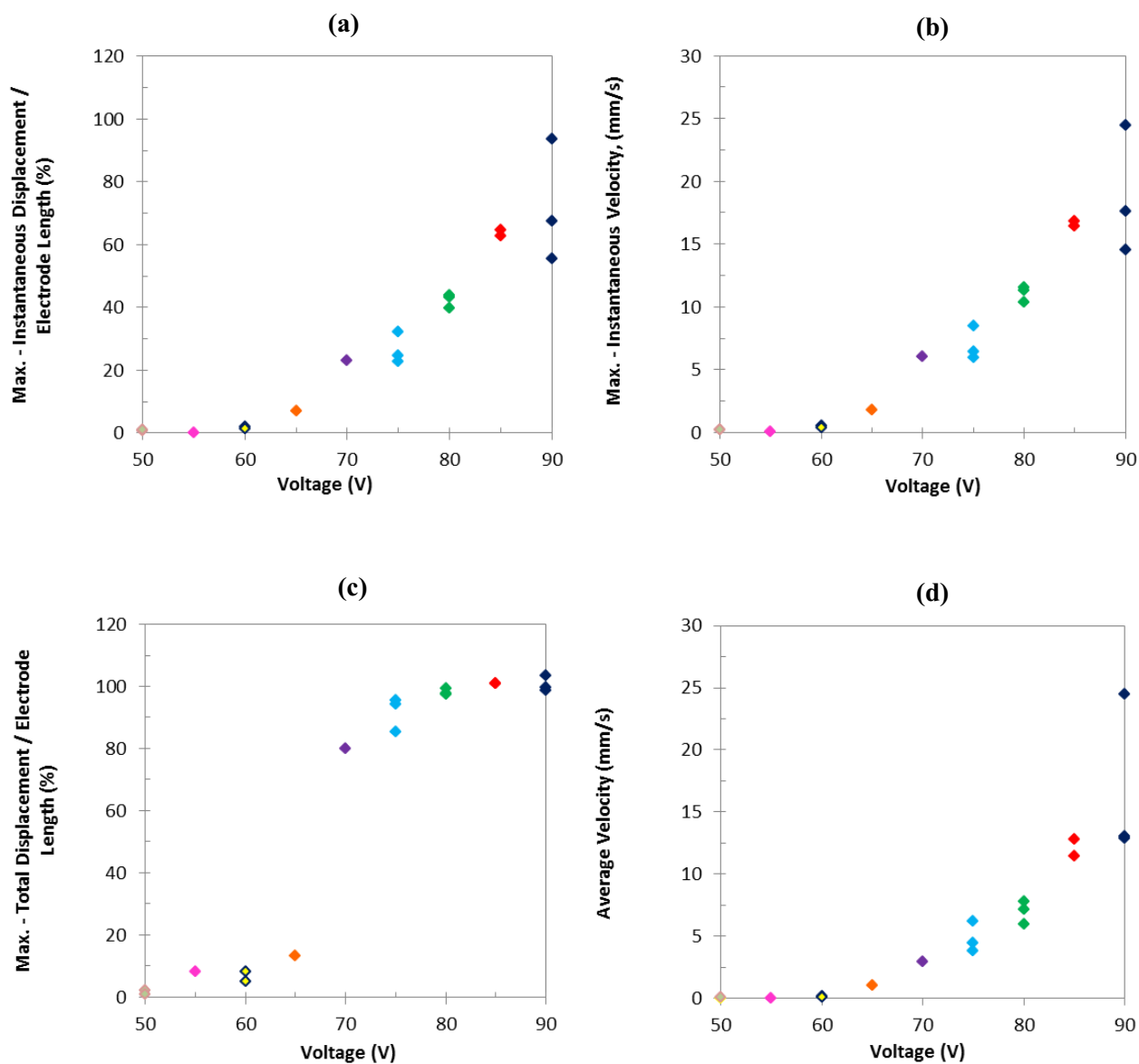


Figure G-52: Changes of the max.: (a) instantaneous displacement, (b) instantaneous velocity, (c) total displacement, and (d) average velocity with the applied voltage for the leading edges of Tris-HCl buffer droplets.

Tris-HCl buffer solution, Trailing edge

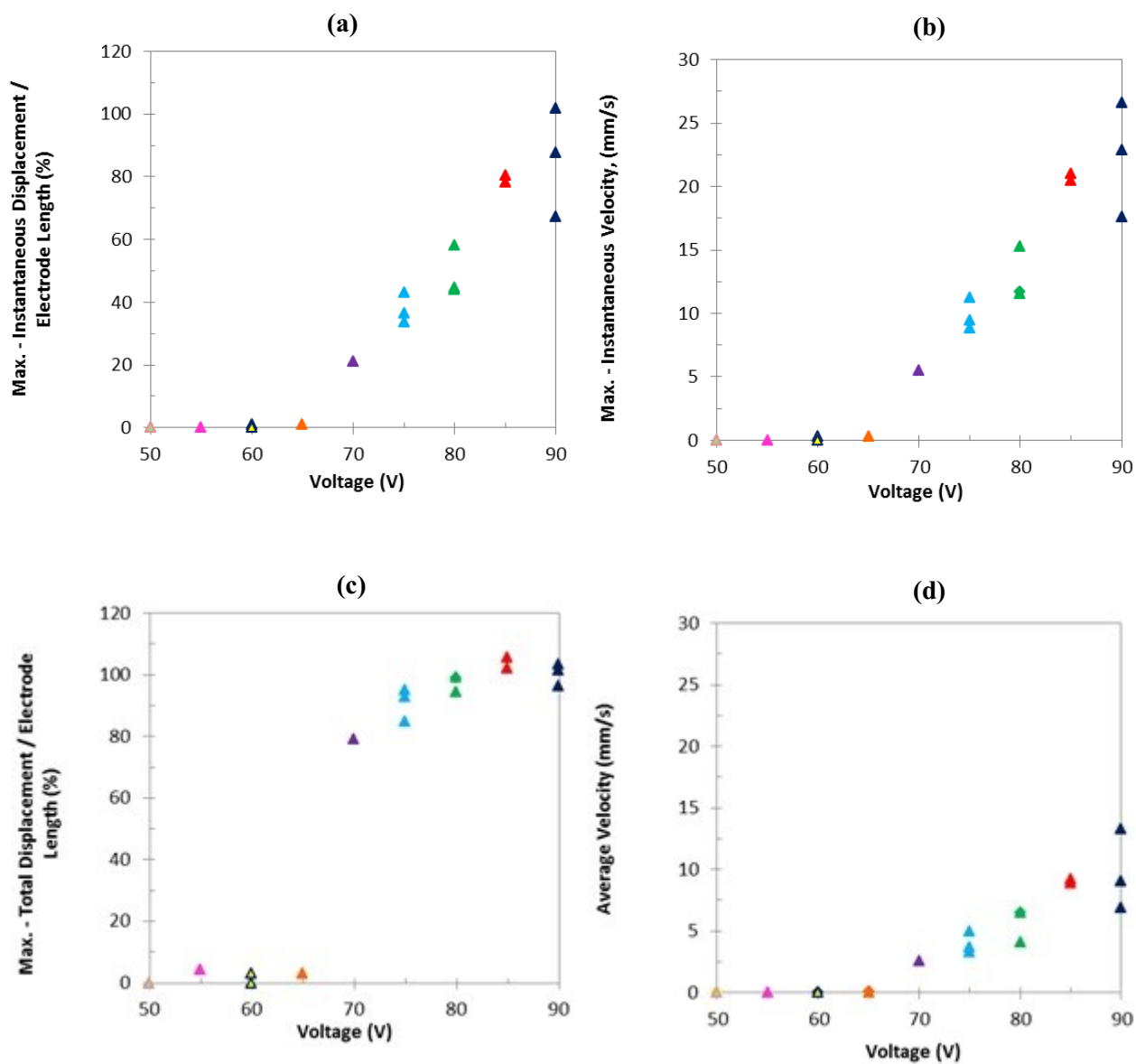


Figure G-53: Changes of the max.: (a) instantaneous displacement, (b) instantaneous velocity, (c) total displacement, and (d) average velocity with the applied voltage for the trailing edges of Tris-HCl buffer droplets.

Tris-HCl buffer solution

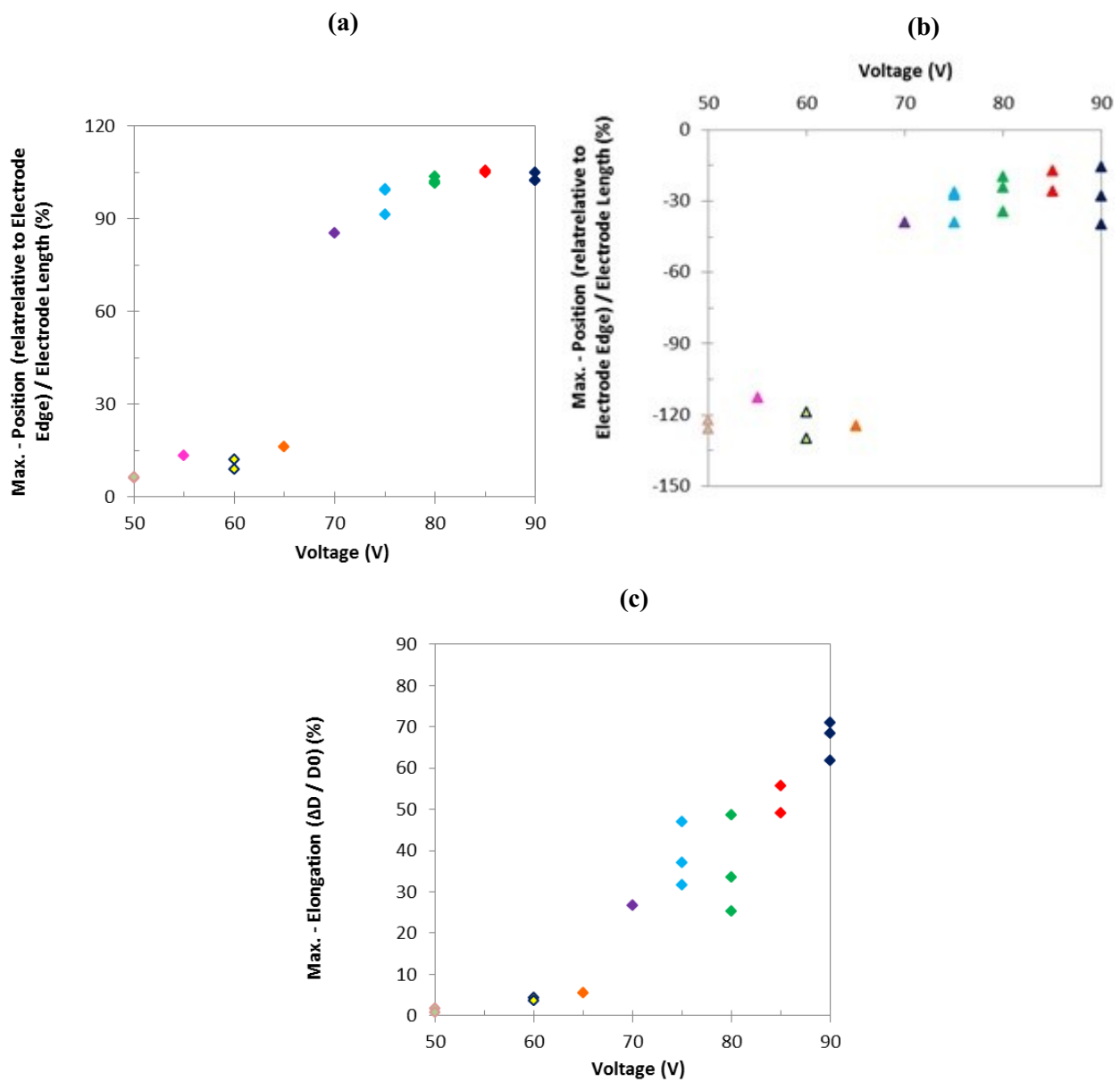


Figure G-54: Changes of the max.: (a) position of the leading edge, (b) position of the trailing edge, (c) elongation, with the applied voltage for Tris-HCl buffer droplets.

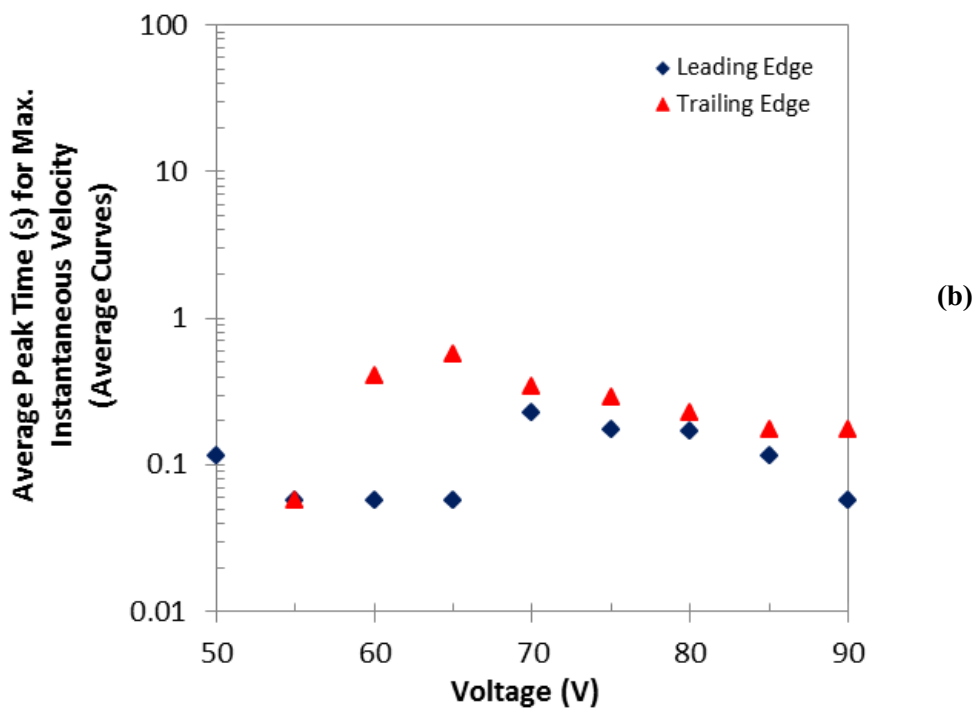
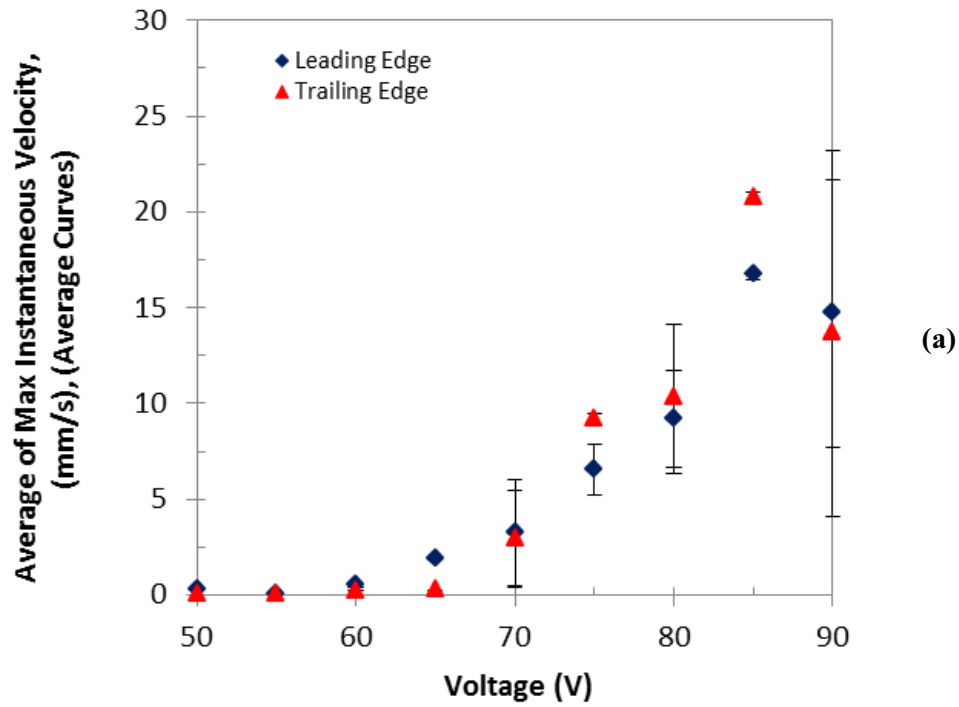


Figure G-55: The average of: (a) max. instantaneous velocity, and (b) peak time for max. instantaneous velocity, as a function of voltage for the leading and trailing edges of Tris-HCl buffer droplets. The error bars indicate standard deviation.

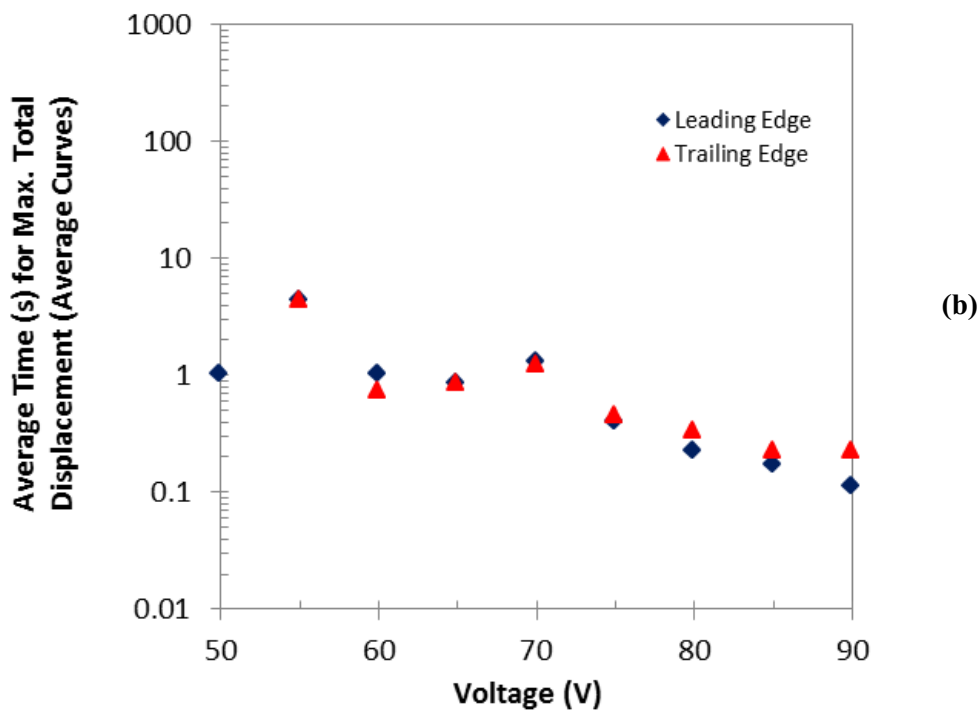
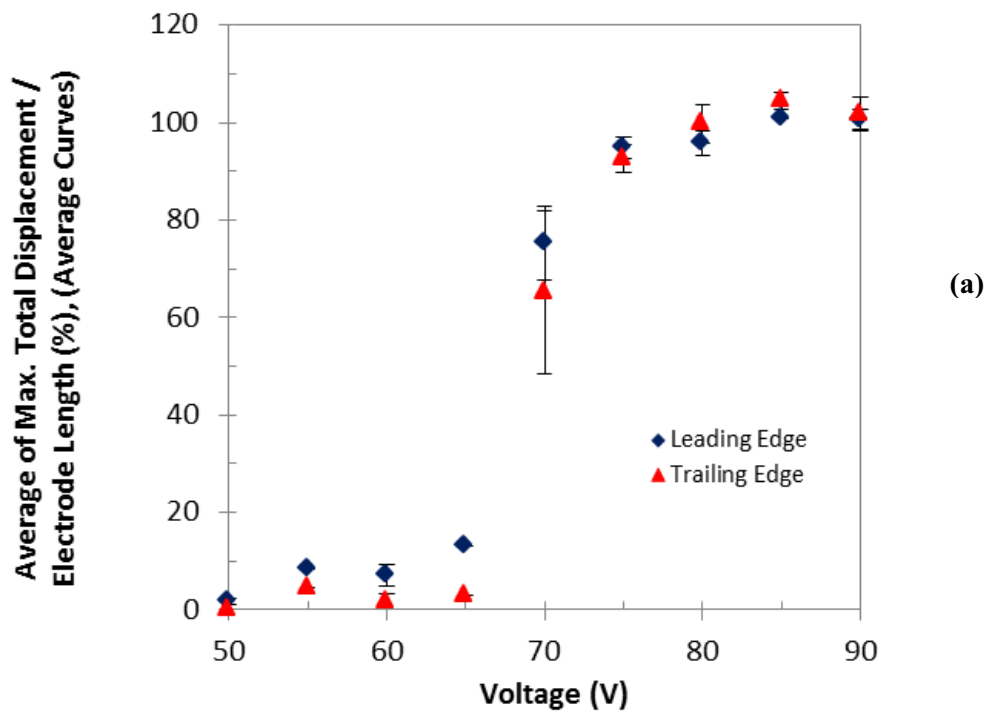


Figure G-56: The average of: (a) max. total displacement, and (b) transition time, as a function of voltage for the leading and trailing edges of Tris-HCl buffer droplets. The error bars indicate standard deviation.

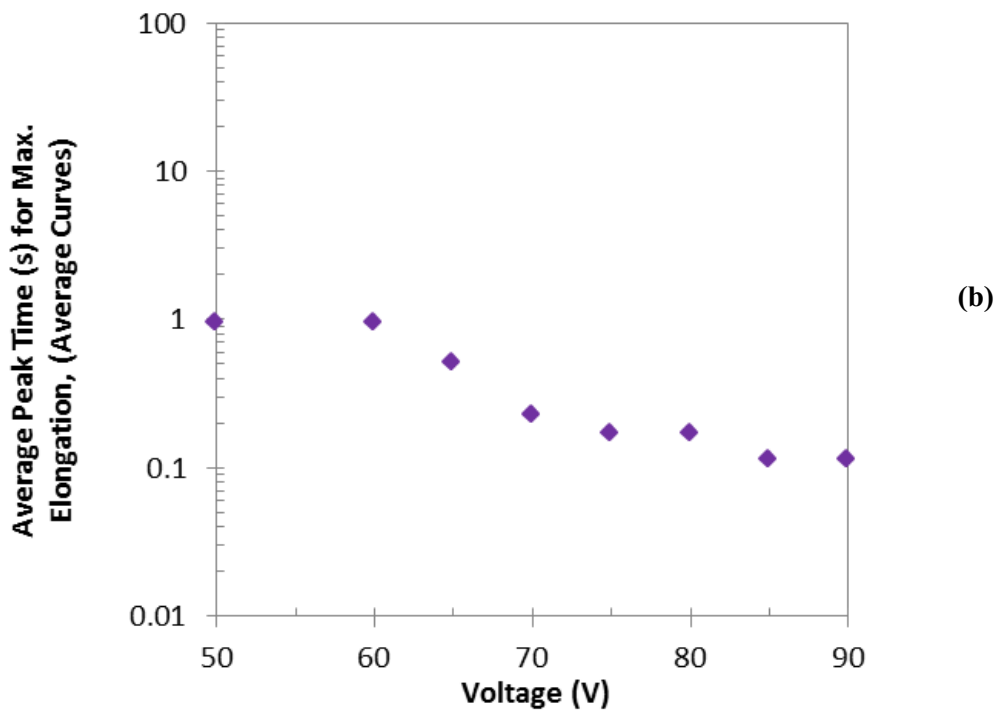
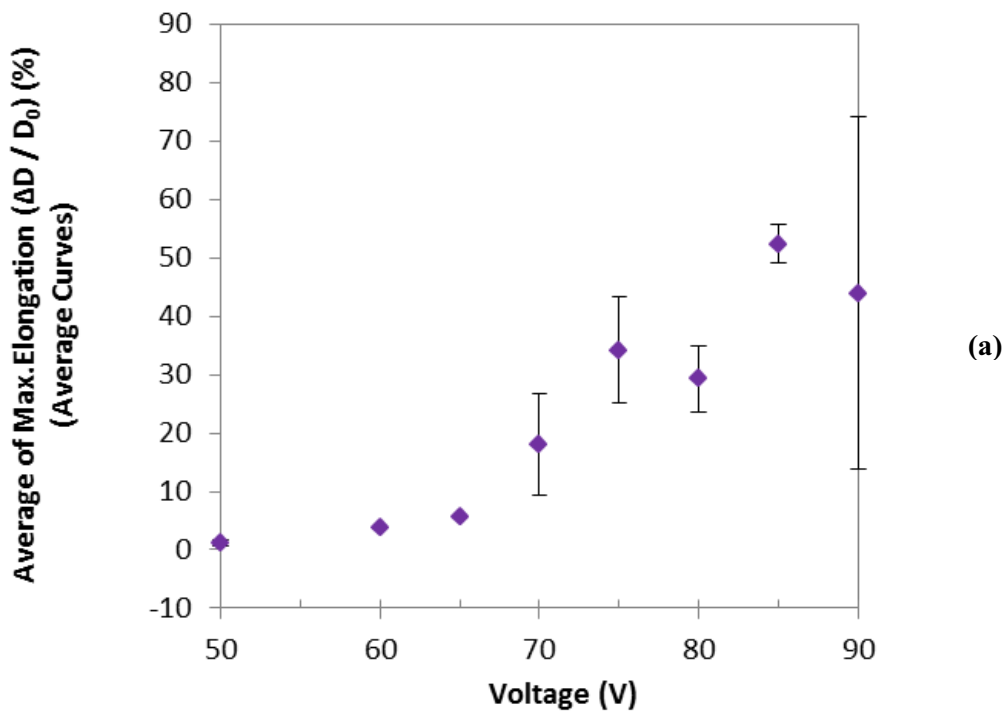


Figure G-57: The average of: (a) max. elongation, and (b) peak time for max. elongation, as a function of voltage for Tris-HCl buffer droplets. The error bars indicate standard deviation.

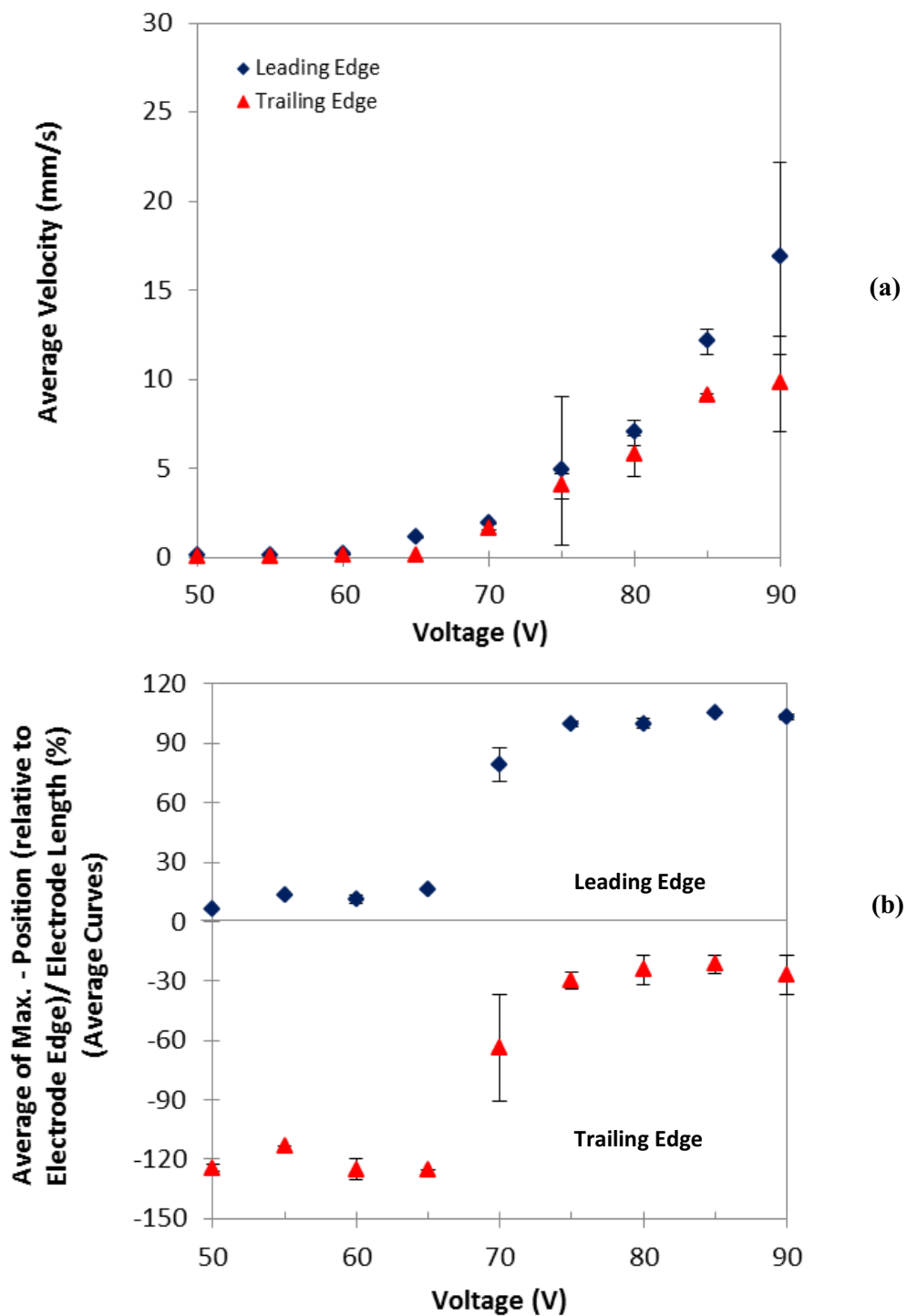


Figure G-58: (a) The average velocity, and (b) the average position, as a function of voltage for the leading and trailing edges of Tris-HCl buffer droplets. The error bars indicate standard deviation.

Appendix H

4 $\mu\text{g}/\text{ml}$ DNA Solution

H-1) 4 $\mu\text{g}/\text{ml}$ DNA solution, 90 V

4 $\mu\text{g}/\text{ml}$ DNA solution, 90 V, Leading edge,

Accepted experiments and the average curves

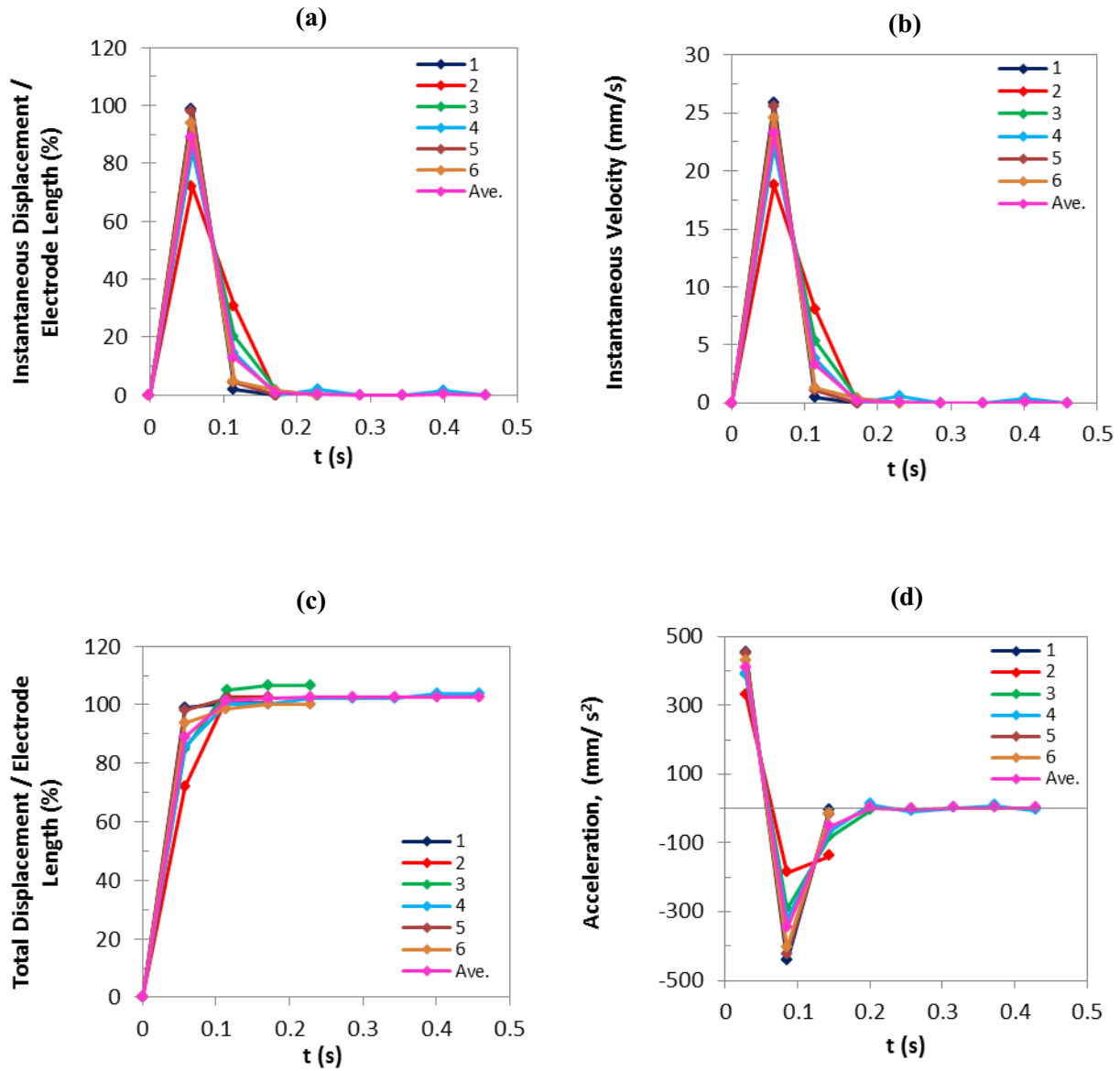


Figure H-1: (a) Instantaneous displacement, (b) instantaneous velocity, (c) total displacement, and (d) acceleration of the leading edges of the droplets of 4 $\mu\text{g}/\text{ml}$ DNA solution as a function of time at 90 V.

4 $\mu\text{g/ml}$ DNA solution, 90 V, Trailing edge,

Accepted experiments and the average curves

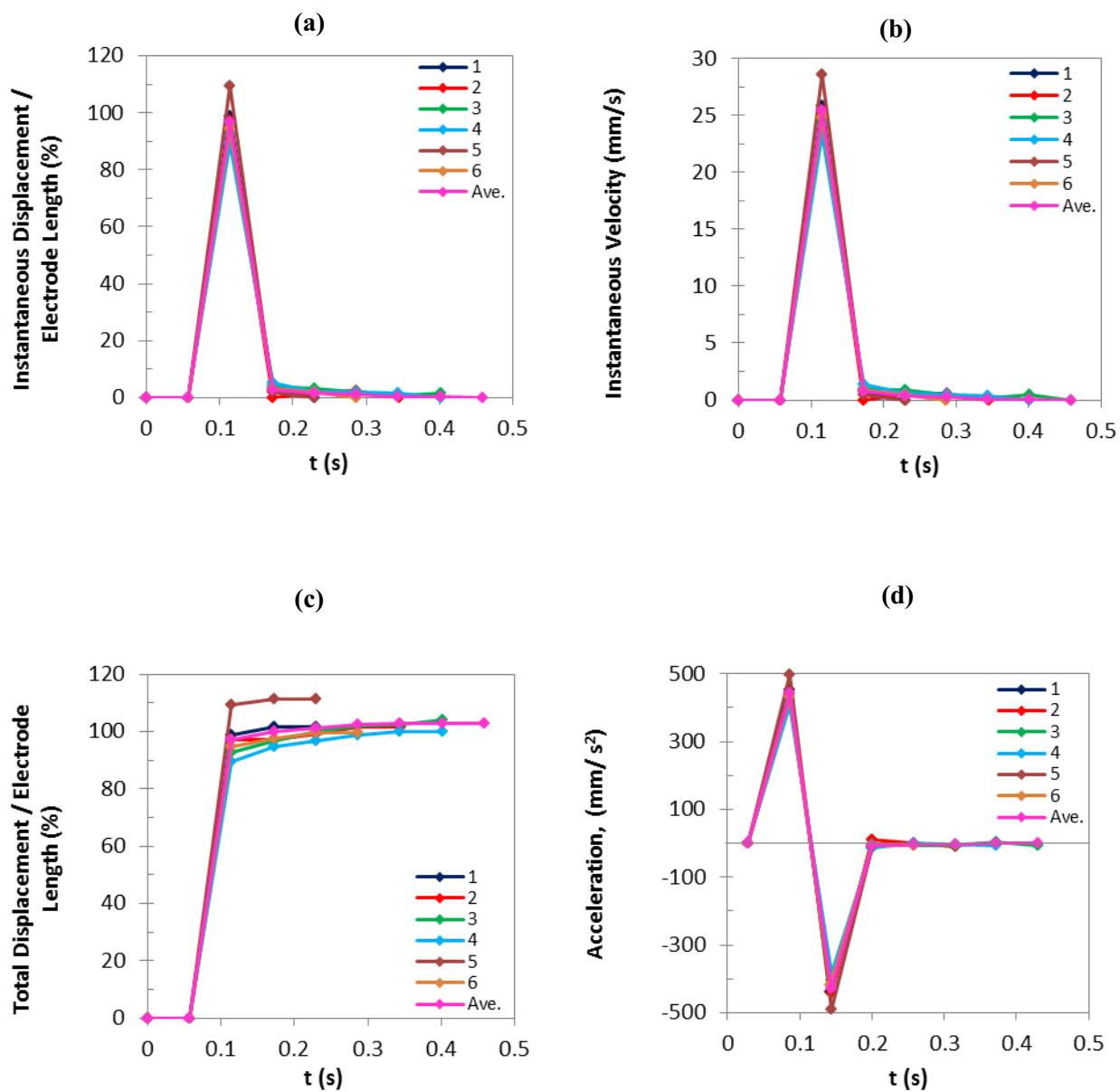


Figure H-2: (a) Instantaneous displacement, (b) instantaneous velocity, (c) total displacement, and (d) acceleration of the trailing edges of the droplets of 4 $\mu\text{g/ml}$ DNA solution as a function of time at 90 V.

4 $\mu\text{g/ml}$ DNA solution, 90 V

Accepted experiments and the average curves

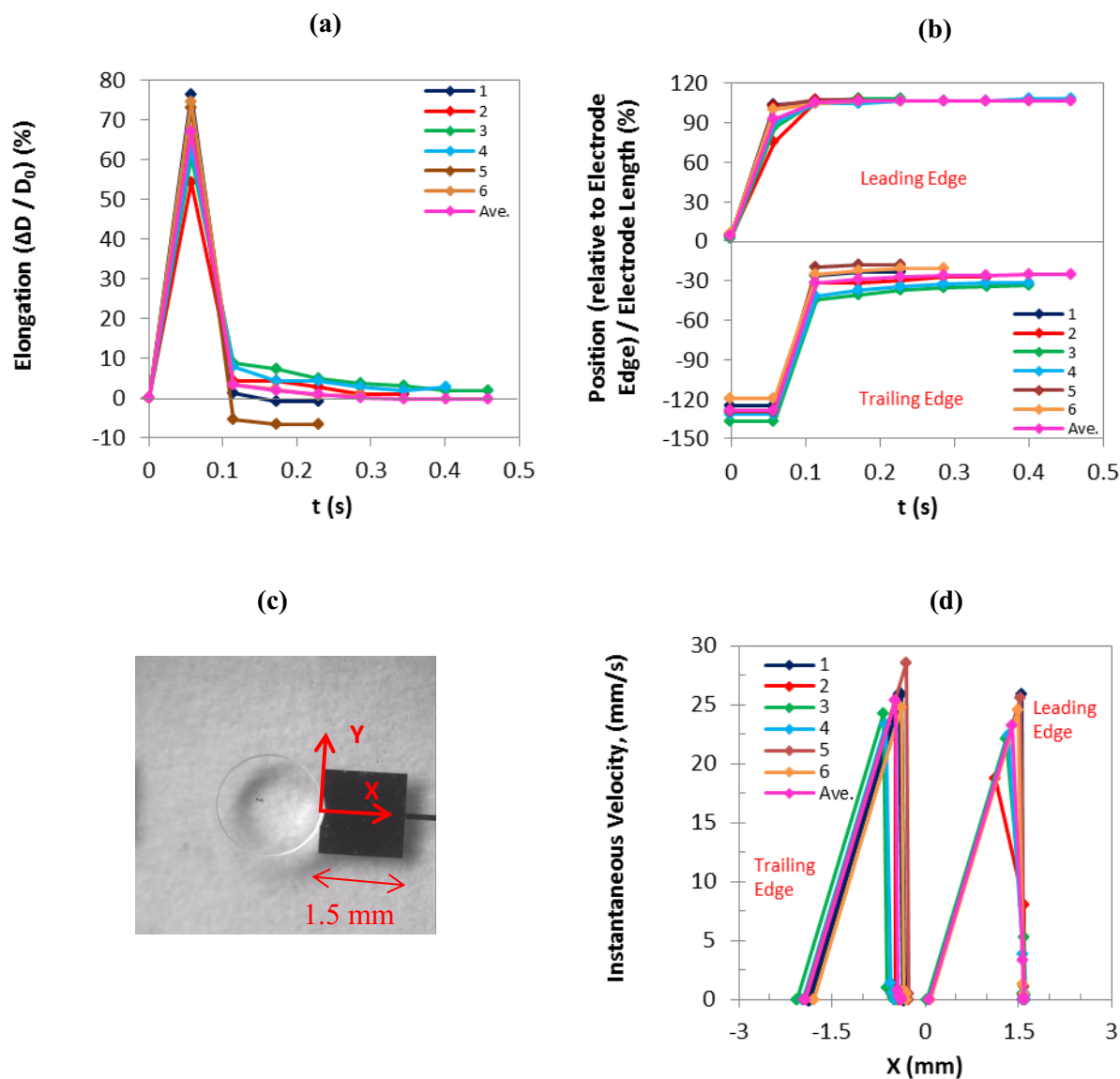


Figure H-3: (a) Droplet elongation, and (b) droplet position as a function of time, (d) instantaneous velocity as a function of droplet position as shown in (c) for the leading and trailing edges of the droplets of 4 $\mu\text{g/ml}$ DNA solution at 90 V.

4 $\mu\text{g/ml}$ solution, 90 V, Average curves

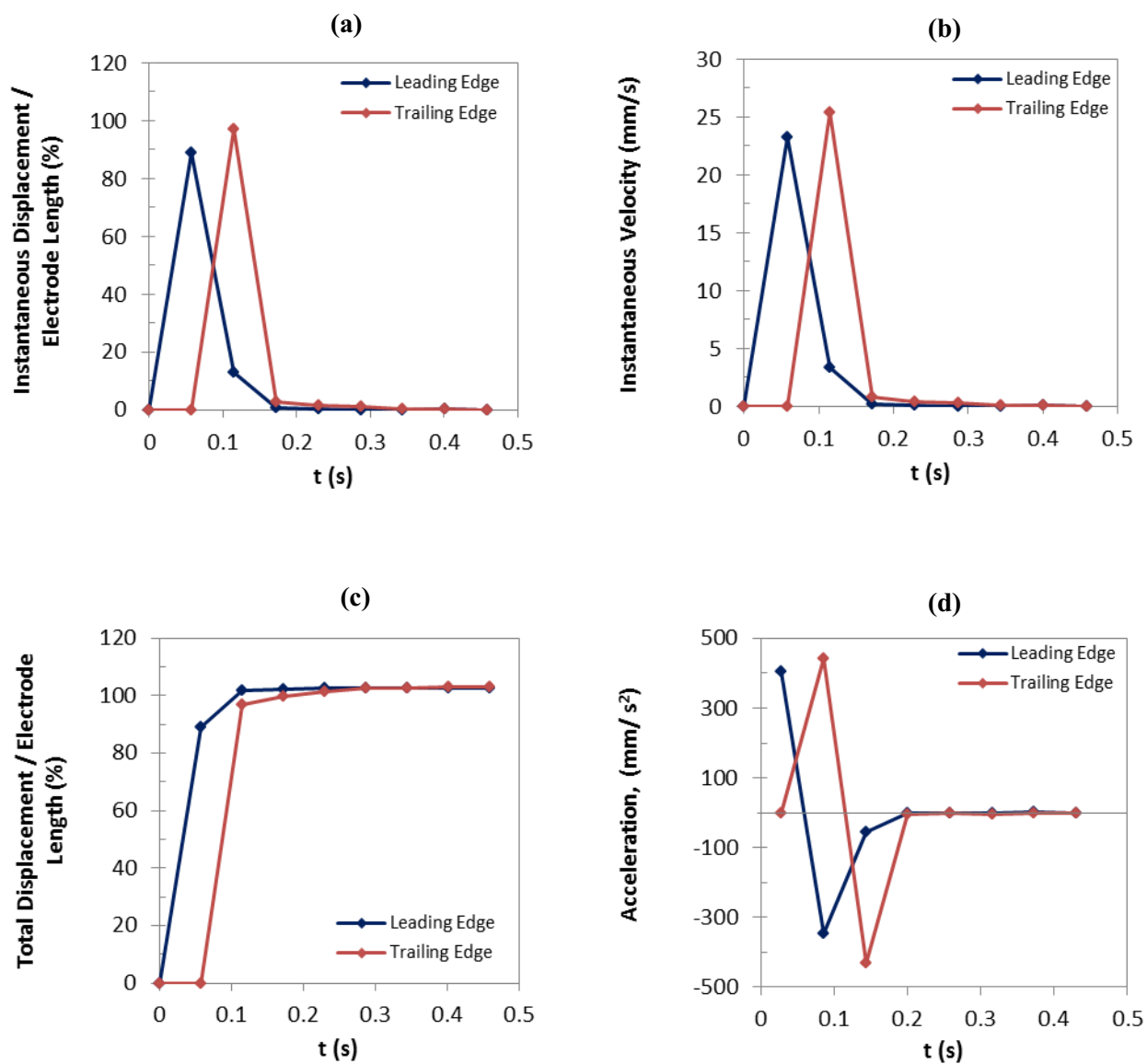


Figure H-4: Comparison of the average curves: (a) instantaneous displacement, (b) instantaneous velocity, (c) total displacement, and (d) acceleration, as a function of time for the leading and trailing edges of the droplets of 4 $\mu\text{g/ml}$ DNA solution at 90 V.

4 $\mu\text{g/ml}$ DNA solution, 90 V, Average curves

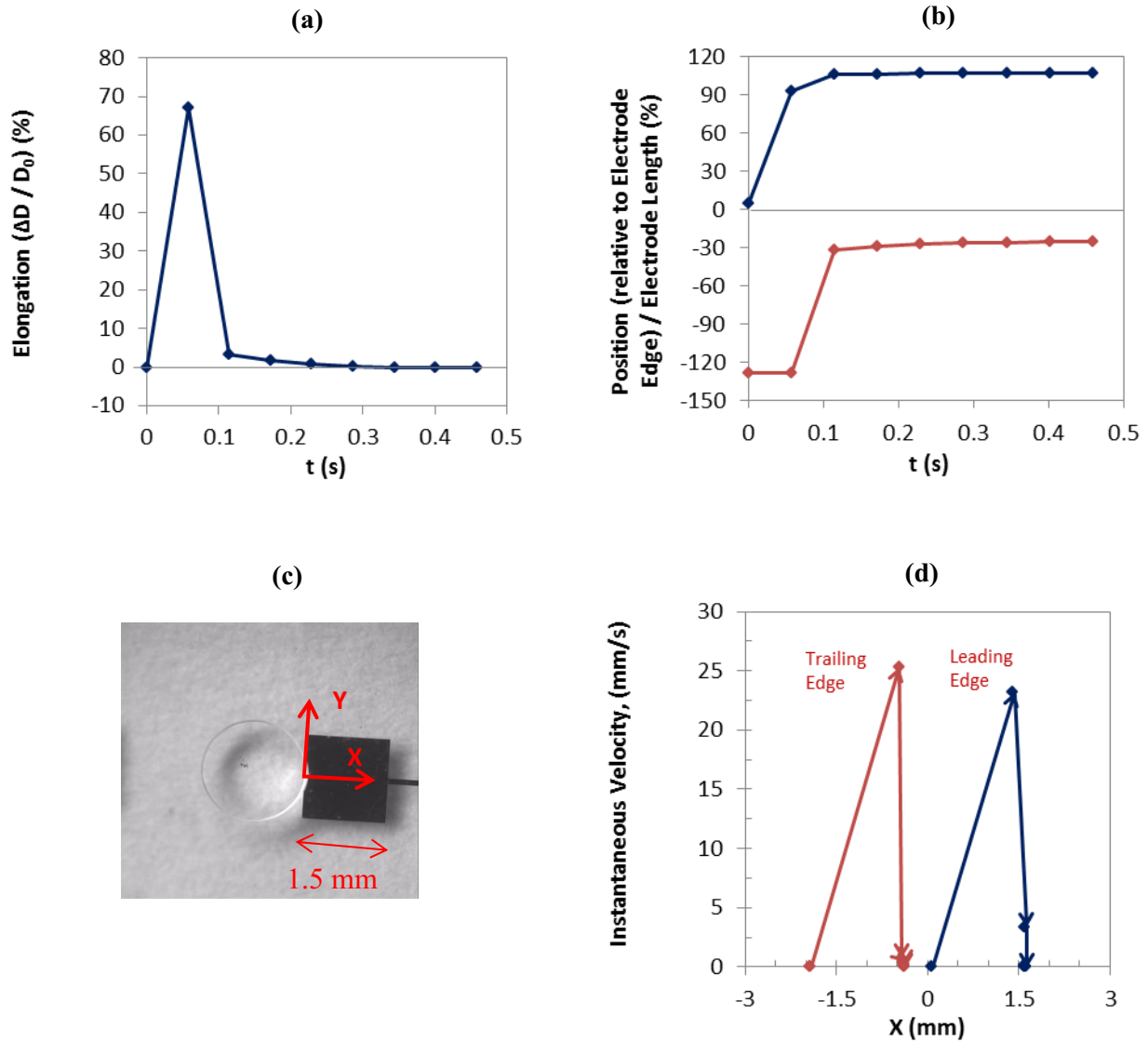


Figure H-5: Comparison of the average curves: (a) droplet elongation and (b) droplet position as a function of time, (d) instantaneous velocity as a function of droplet position as shown in (c) for the leading and trailing edges of the droplets of 4 $\mu\text{g/ml}$ DNA solution at 90 V. The arrows in graph (d) indicate the changes of velocity along the direction of movement.

H-2) 4 $\mu\text{g/ml}$ DNA solution, 85 V

4 $\mu\text{g/ml}$ DNA solution, 85 V, Leading edge,

Accepted experiments and the average curves

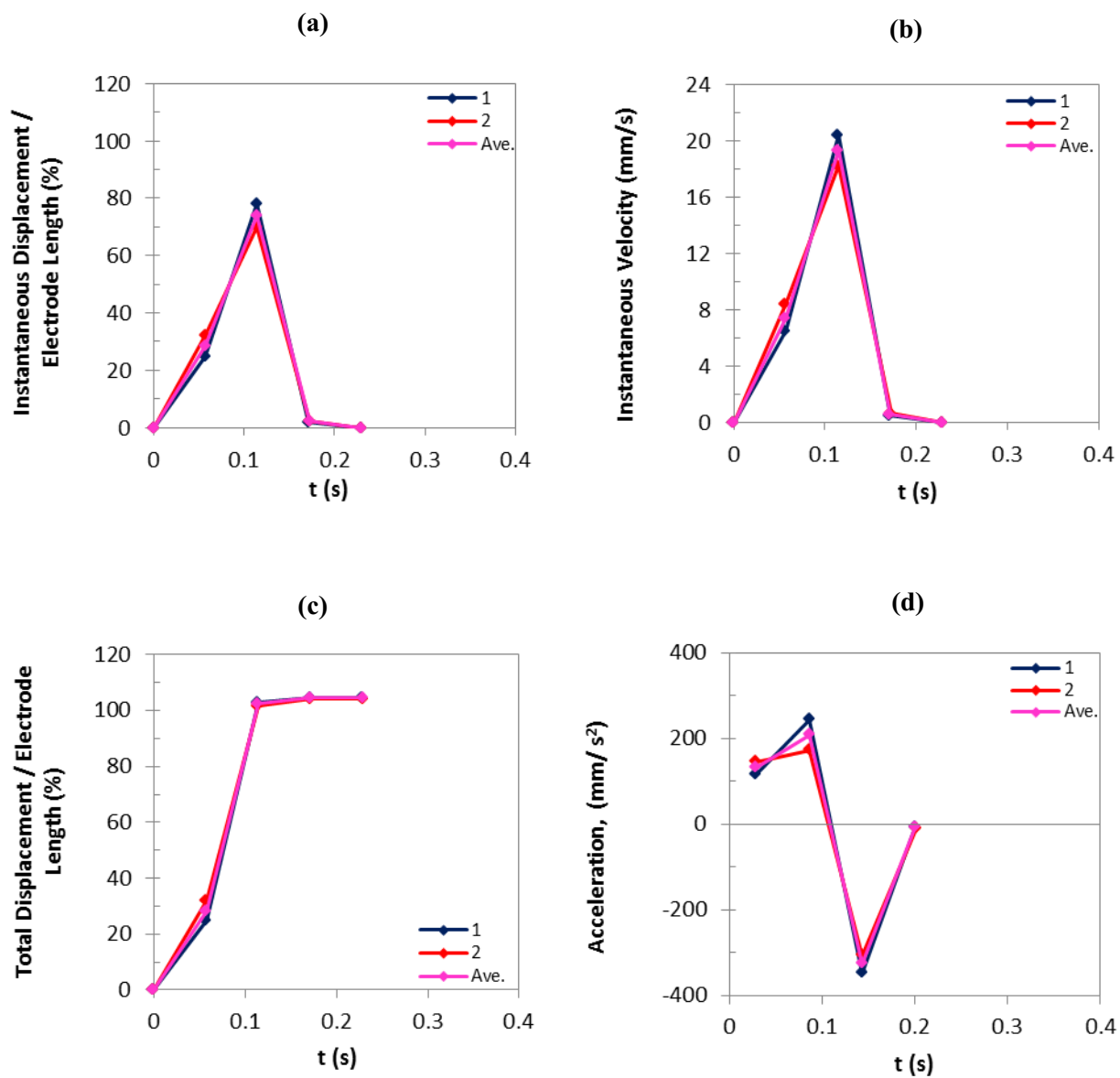


Figure H-6: (a) Instantaneous displacement, (b) instantaneous velocity, (c) total displacement, and (d) acceleration of the leading edges of the droplets of 4 $\mu\text{g/ml}$ DNA solution as a function of time at 85 V.

4 $\mu\text{g/ml}$ DNA solution, 85 V, Trailing edge,

Accepted experiments and the average curves

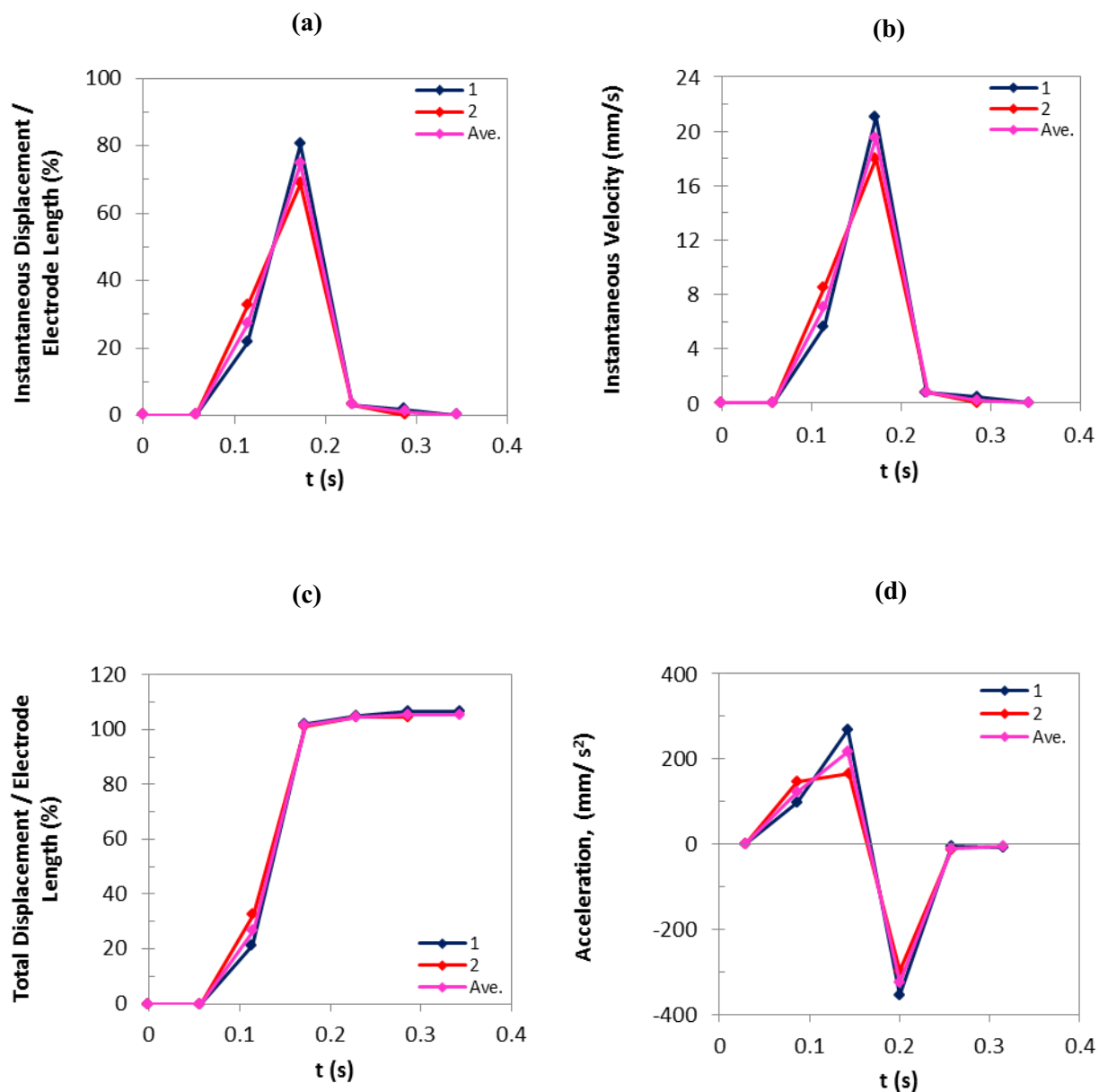


Figure H-7: (a) Instantaneous displacement, (b) instantaneous velocity, (c) total displacement, and (d) acceleration of the trailing edges of the droplets of 4 $\mu\text{g/ml}$ DNA solution as a function of time at 85 V.

4 $\mu\text{g/ml}$ DNA solution, 85 V

Accepted experiments and the average curves

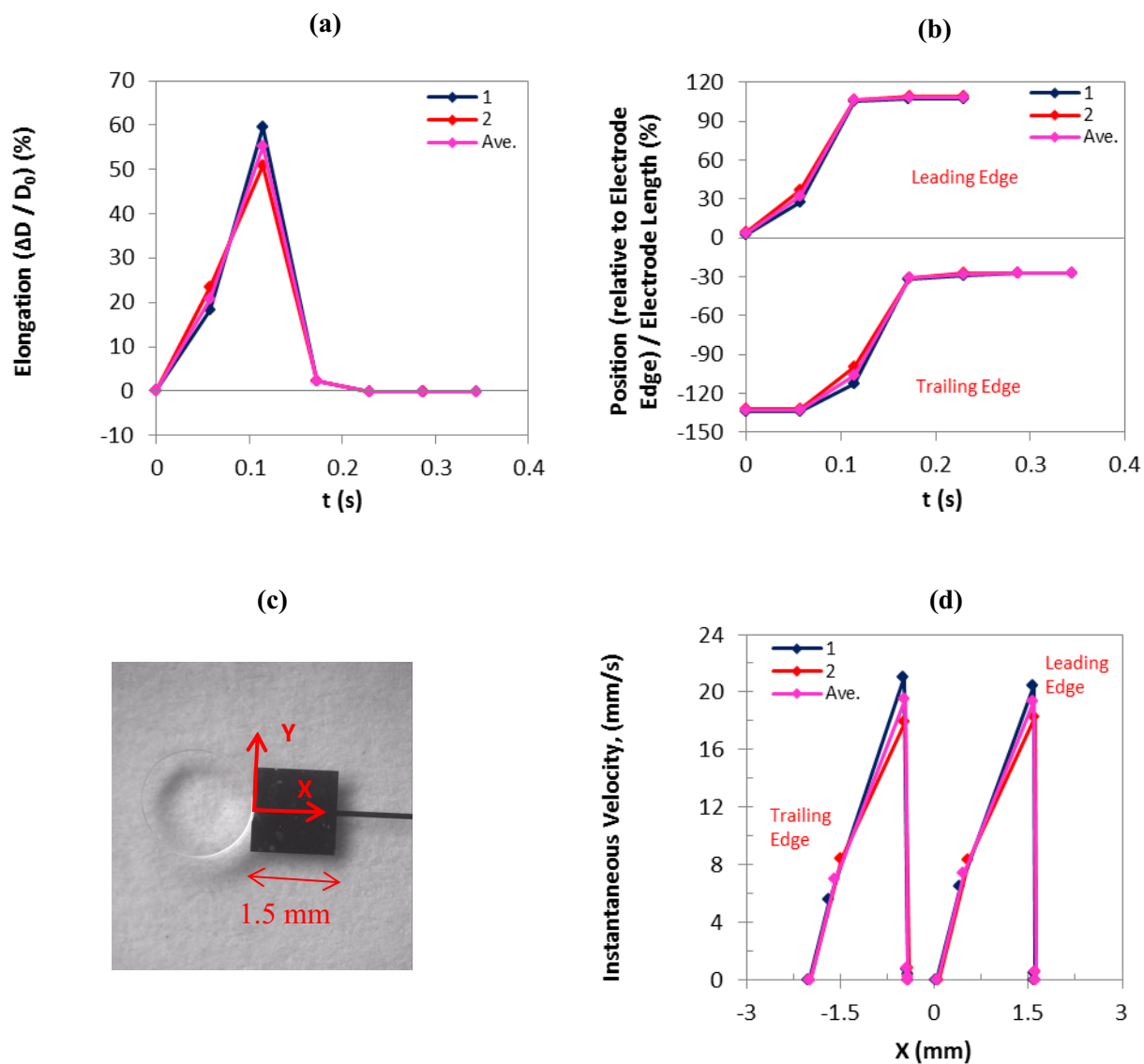


Figure H-8: (a) Droplet elongation, and (b) droplet position as a function of time, (d) instantaneous velocity as a function of droplet position as shown in (c) for the leading and trailing edges of the droplets of 4 $\mu\text{g/ml}$ DNA solution at 85 V.

4 $\mu\text{g/ml}$ DNA solution, 85 V, Average curves

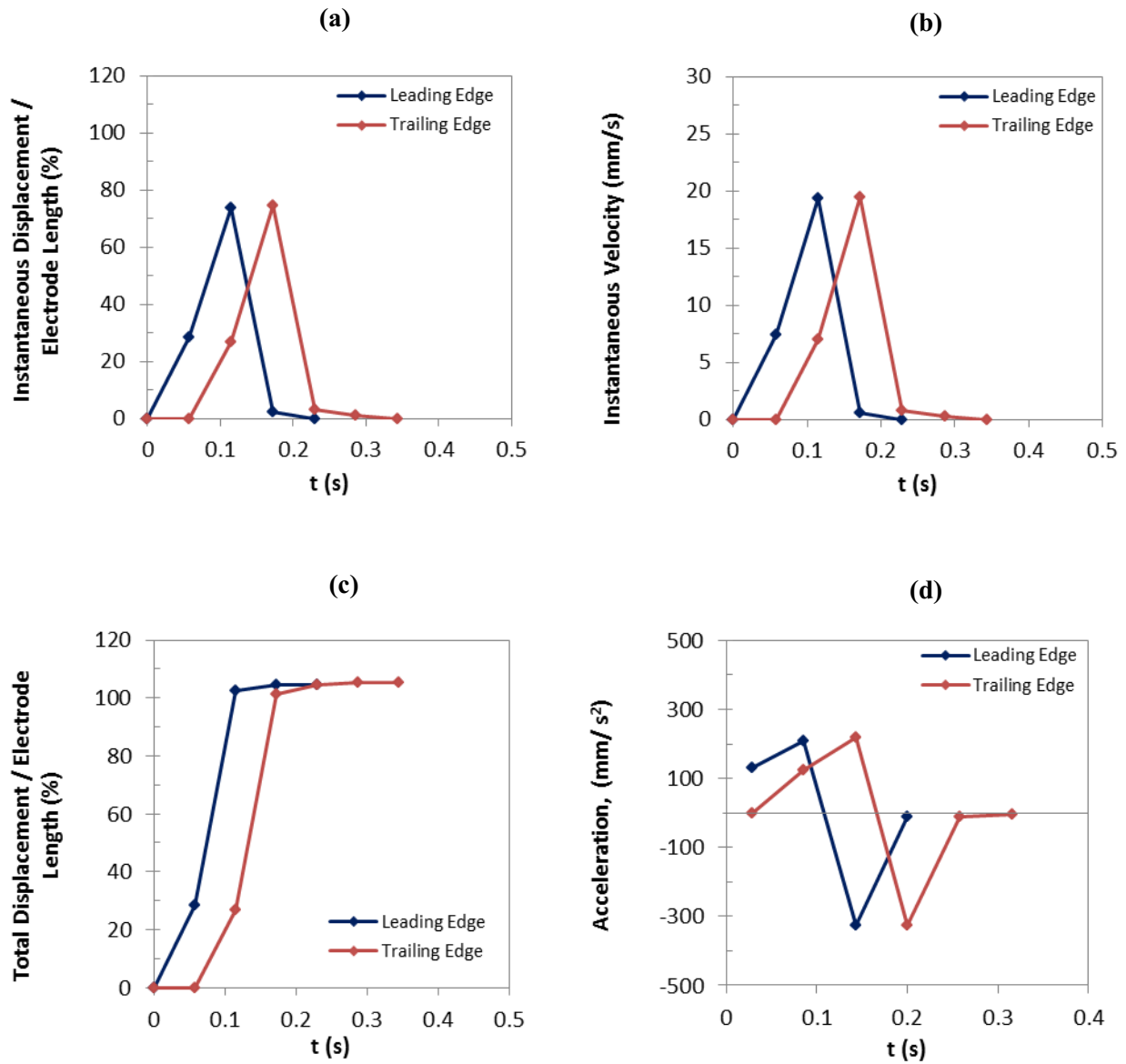


Figure H-9: Comparison of the average curves: (a) instantaneous displacement, (b) instantaneous velocity, (c) total displacement, and (d) acceleration, as a function of time for the leading and trailing edges of the droplets of 4 $\mu\text{g/ml}$ DNA solution at 85 V.

4 $\mu\text{g/ml}$ DNA solution, 85 V, Average curves

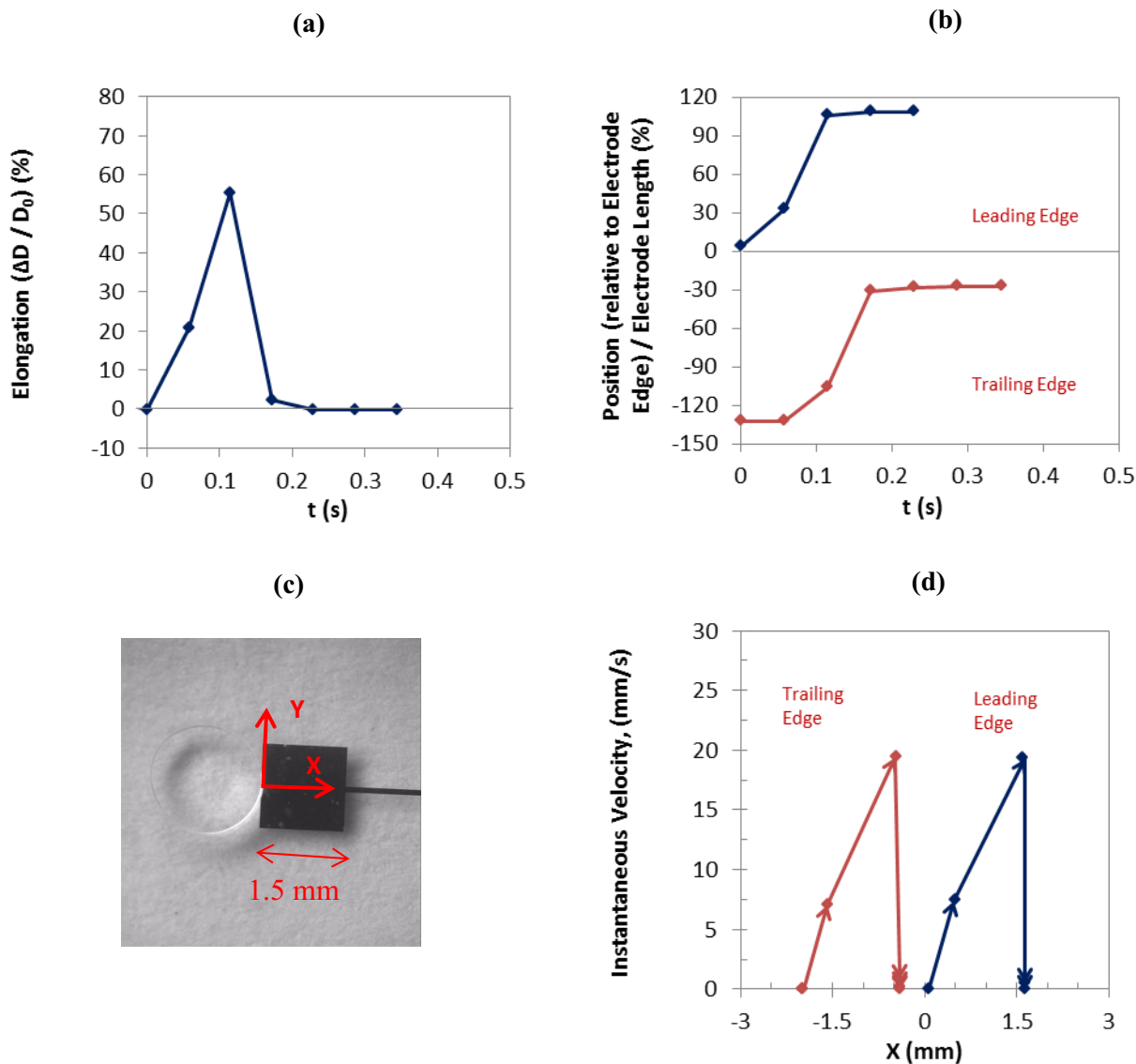


Figure H-10: Comparison of the average curves: (a) droplet elongation and (b) droplet position as a function of time, (d) instantaneous velocity as a function of droplet position as shown in (c) for the leading and trailing edges of the droplets of 4 $\mu\text{g/ml}$ DNA solution at 85 V. The arrows in graph (d) indicate the changes of velocity along the direction of movement.

H-3) 4 $\mu\text{g/ml}$ DNA solution, 80 V

4 $\mu\text{g/ml}$ DNA solution, 80 V, Leading edge,

Accepted experiments and the average curves

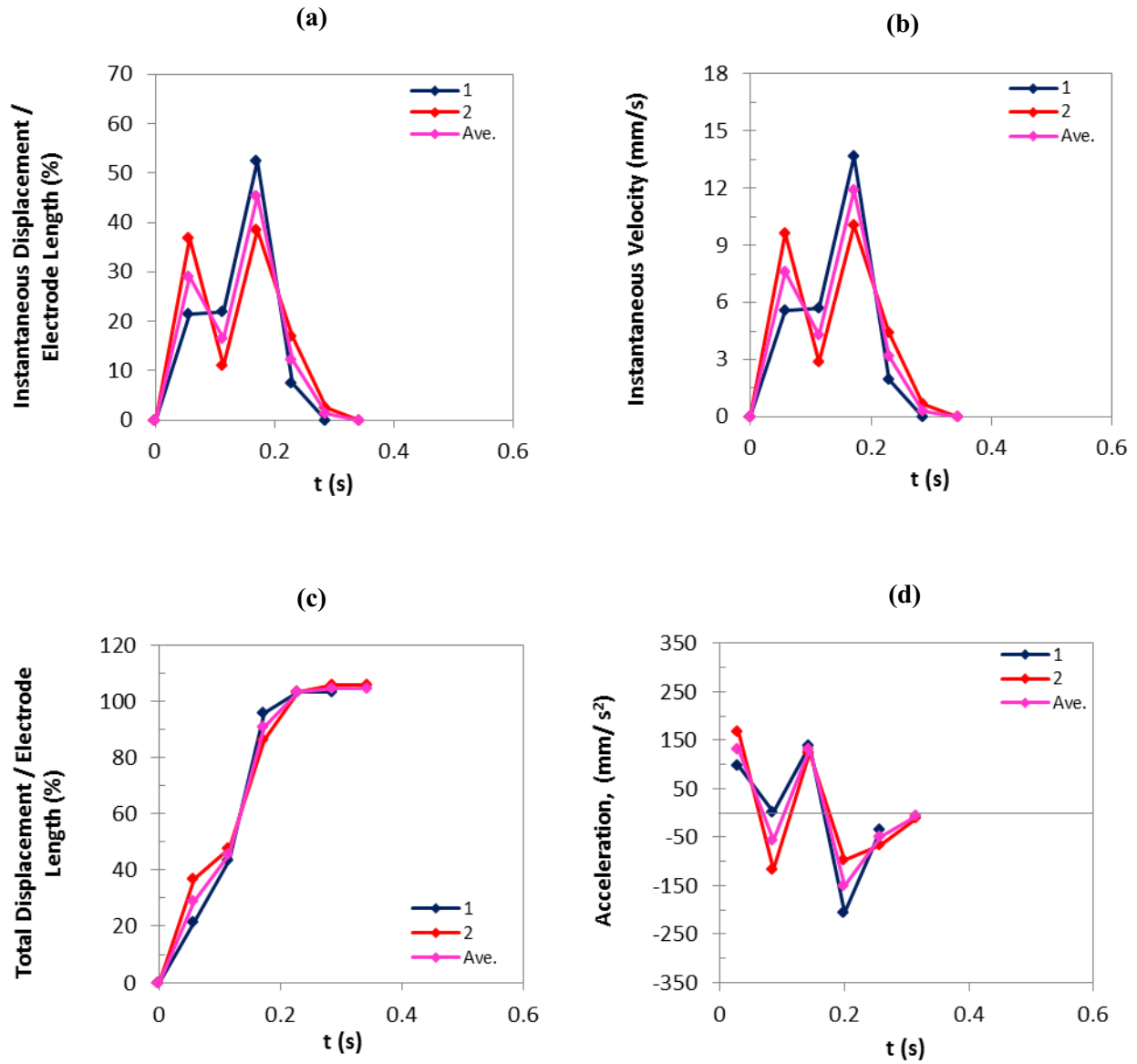


Figure H-11: (a) Instantaneous displacement, (b) instantaneous velocity, (c) total displacement, and (d) acceleration of the leading edges of the droplets of 4 $\mu\text{g/ml}$ DNA solution as a function of time at 80 V.

4 $\mu\text{g/ml}$ DNA solution, 80 V, Trailing edge,

Accepted experiments and the average curves

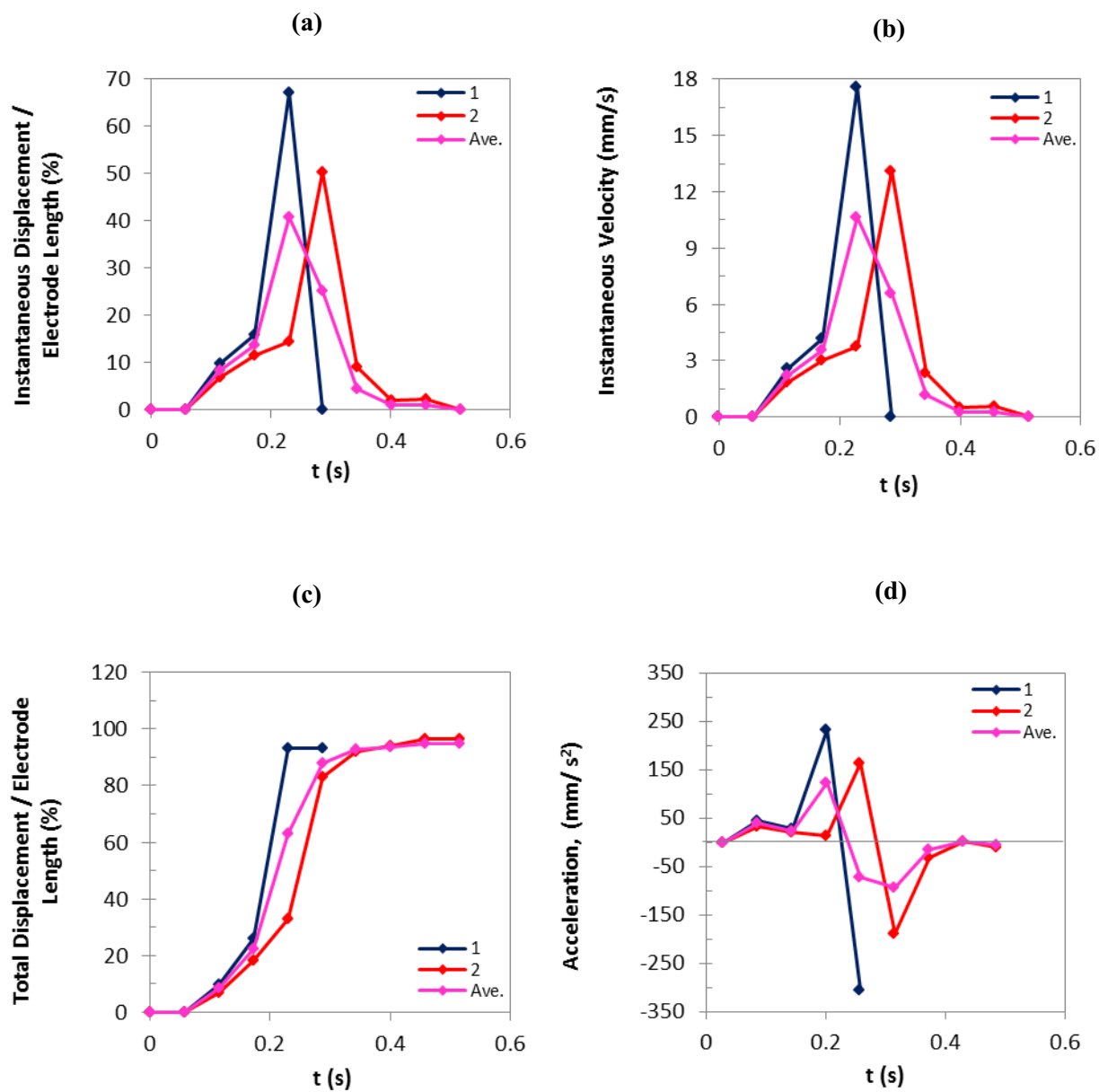


Figure H-12: (a) Instantaneous displacement, (b) instantaneous velocity, (c) total displacement, and (d) acceleration of the trailing edges of the droplets of 4 $\mu\text{g/ml}$ DNA solution as a function of time at 80 V.

4 $\mu\text{g}/\text{ml}$ DNA solution, 80 V

Accepted experiments and the average curves

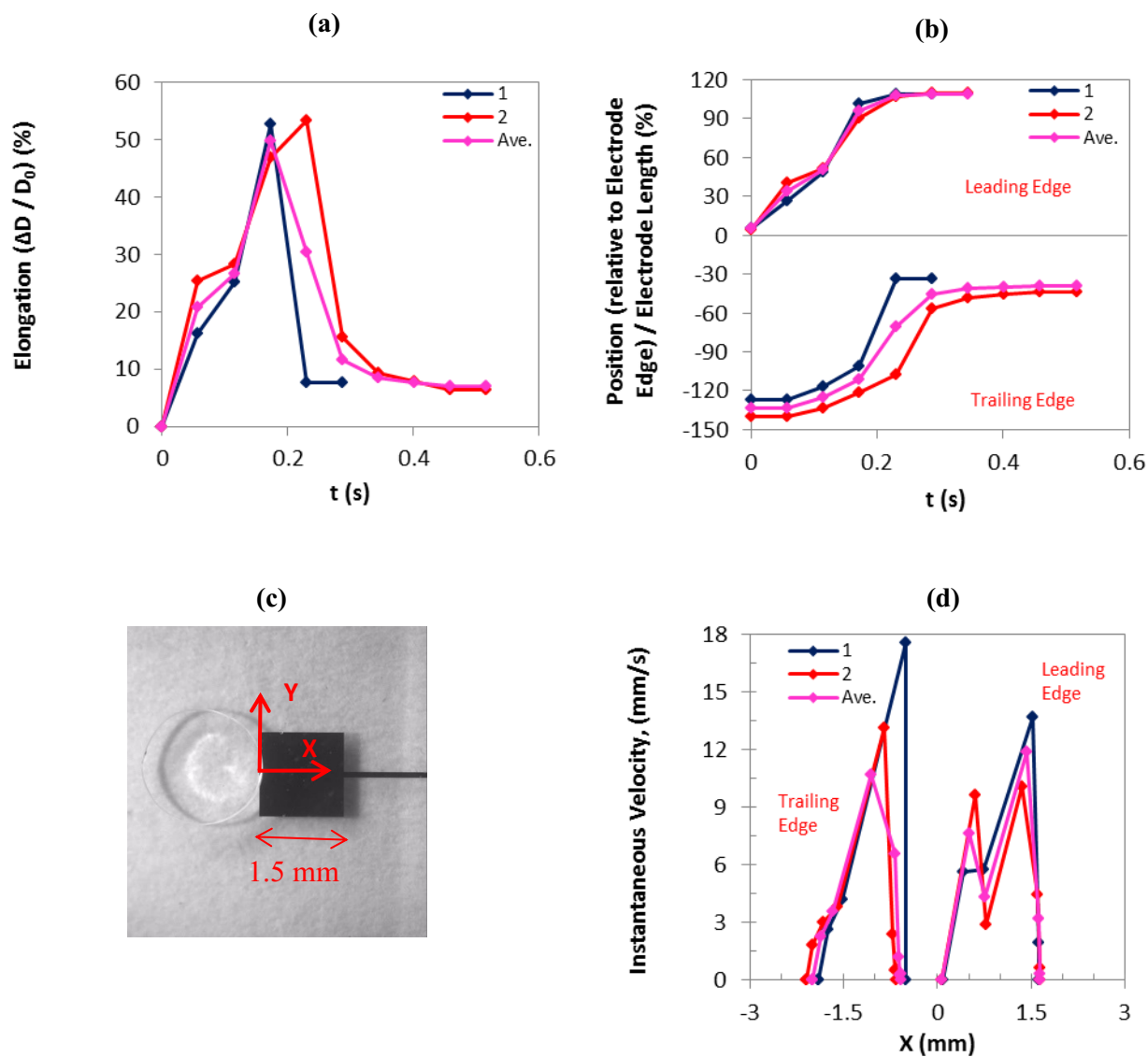


Figure H-13: (a) Droplet elongation, and (b) droplet position as a function of time, (d) instantaneous velocity as a function of droplet position as shown in (c) for the leading and trailing edges of the droplets of 4 $\mu\text{g}/\text{ml}$ DNA solution at 80 V.

4 $\mu\text{g/ml}$ DNA solution, 80 V, Average curves

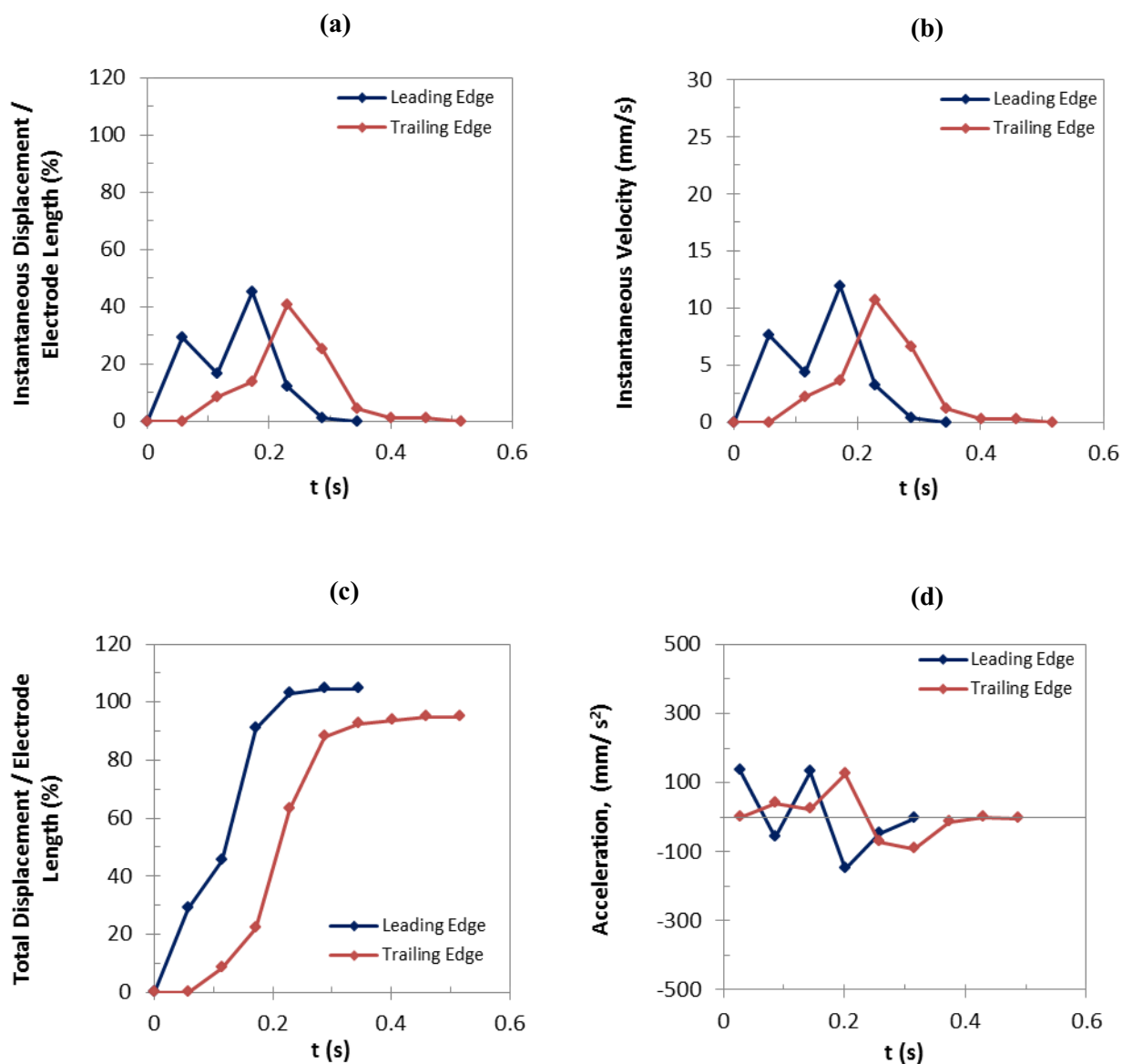


Figure H-14: Comparison of the average curves: (a) instantaneous displacement, (b) instantaneous velocity, (c) total displacement, and (d) acceleration, as a function of time for the leading and trailing edges of the droplets of 4 $\mu\text{g/ml}$ DNA solution at 80 V.

4 $\mu\text{g}/\text{ml}$ DNA solution, 80 V, Average curves

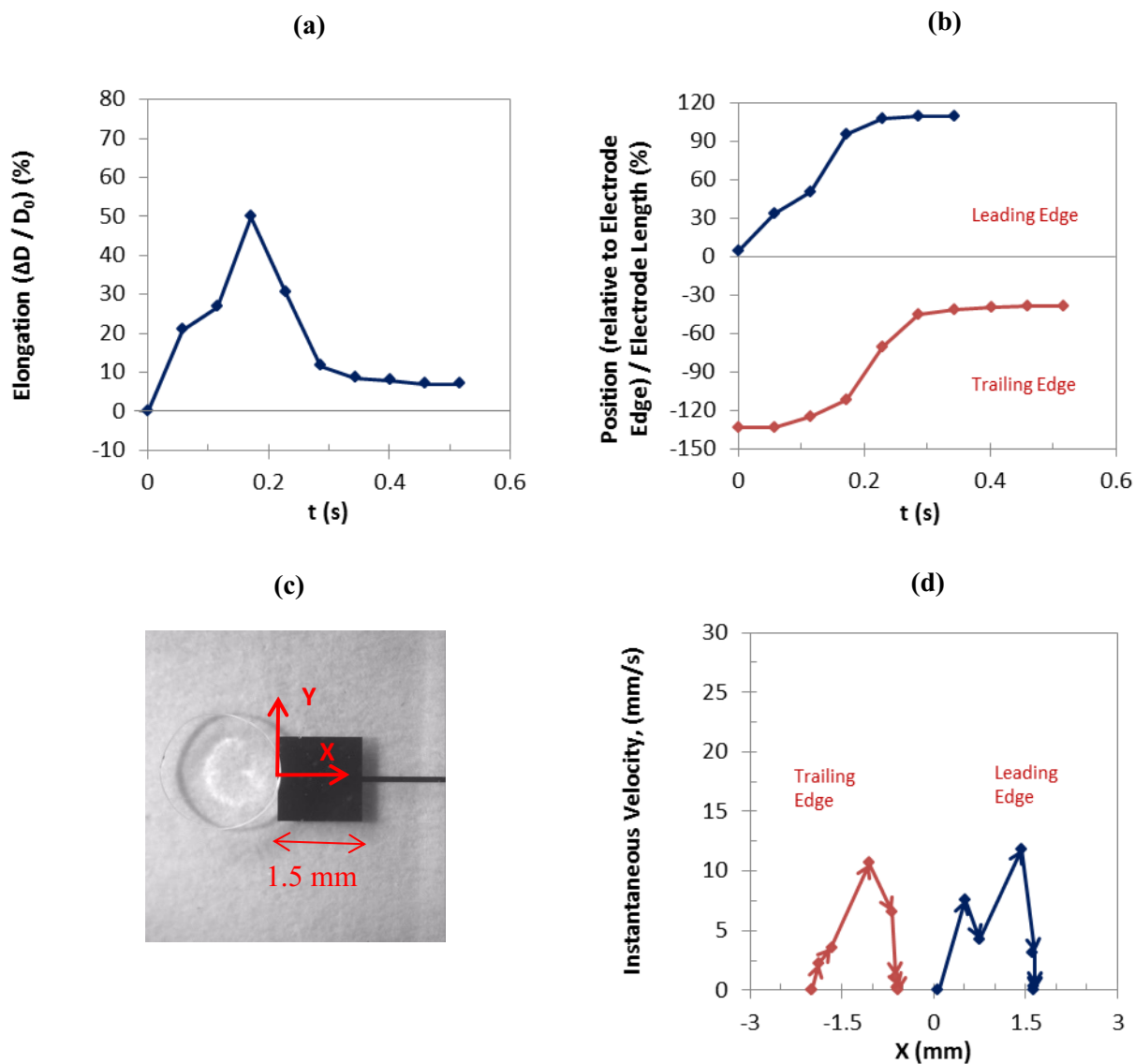


Figure H-15: Comparison of the average curves: (a) droplet elongation and (b) droplet position as a function of time, (d) instantaneous velocity as a function of droplet position as shown in (c) for the leading and trailing edges of the droplets of 4 $\mu\text{g}/\text{ml}$ DNA solution at 80 V. The arrows in graph (d) indicate the changes of velocity along the direction of movement.

H-4) 4 $\mu\text{g/ml}$ DNA Solution, 75 V

4 $\mu\text{g/ml}$ DNA solution, 75 V, Leading edge,

Accepted experiments and the average curves

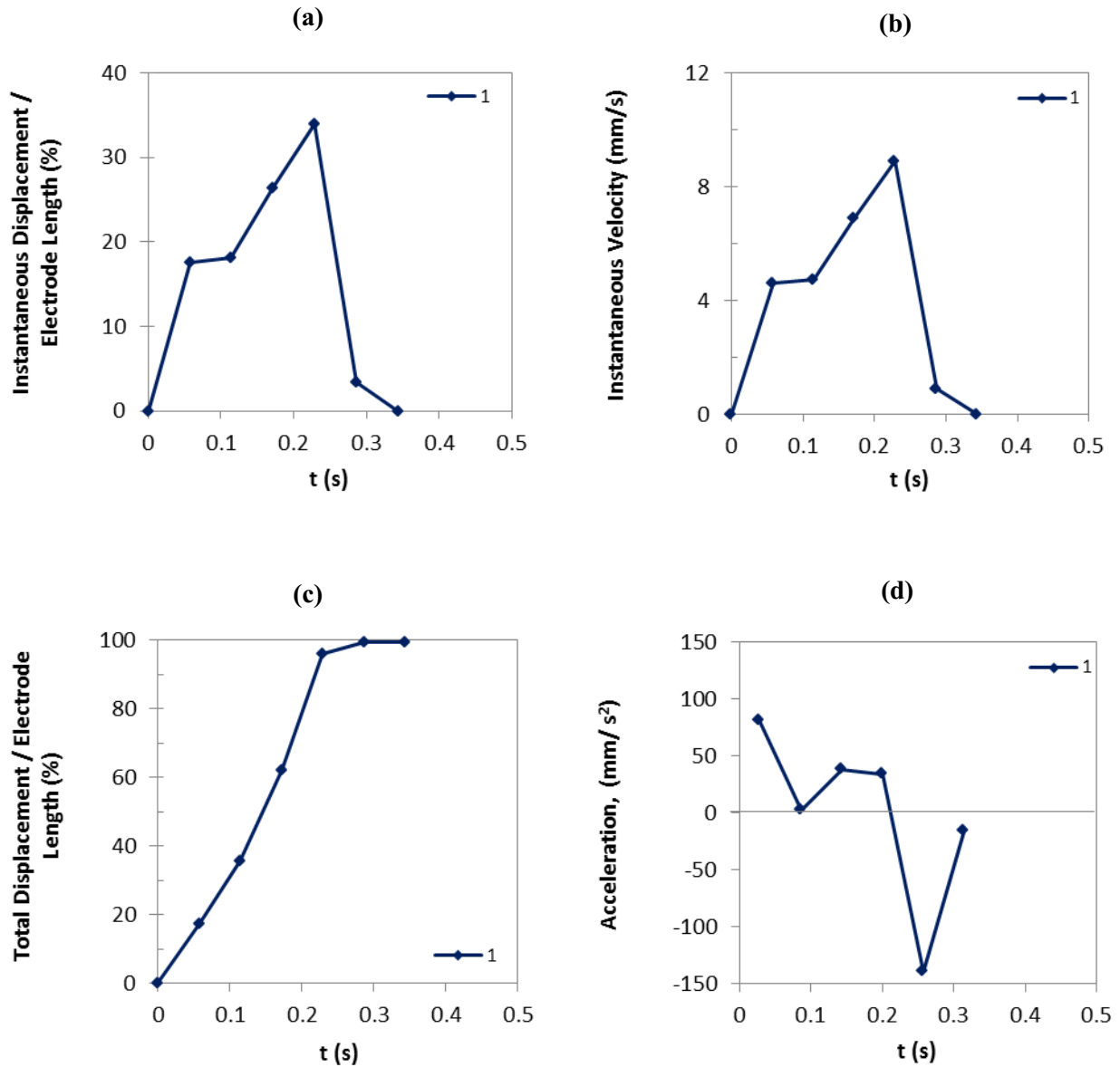


Figure H-16: (a) Instantaneous displacement, (b) instantaneous velocity, (c) total displacement, and (d) acceleration of the leading edges of the droplets of 4 $\mu\text{g/ml}$ DNA solution as a function of time at 75 V.

4 $\mu\text{g/ml}$ DNA solution, 75 V, Trailing edge,

Accepted experiments and the average curves

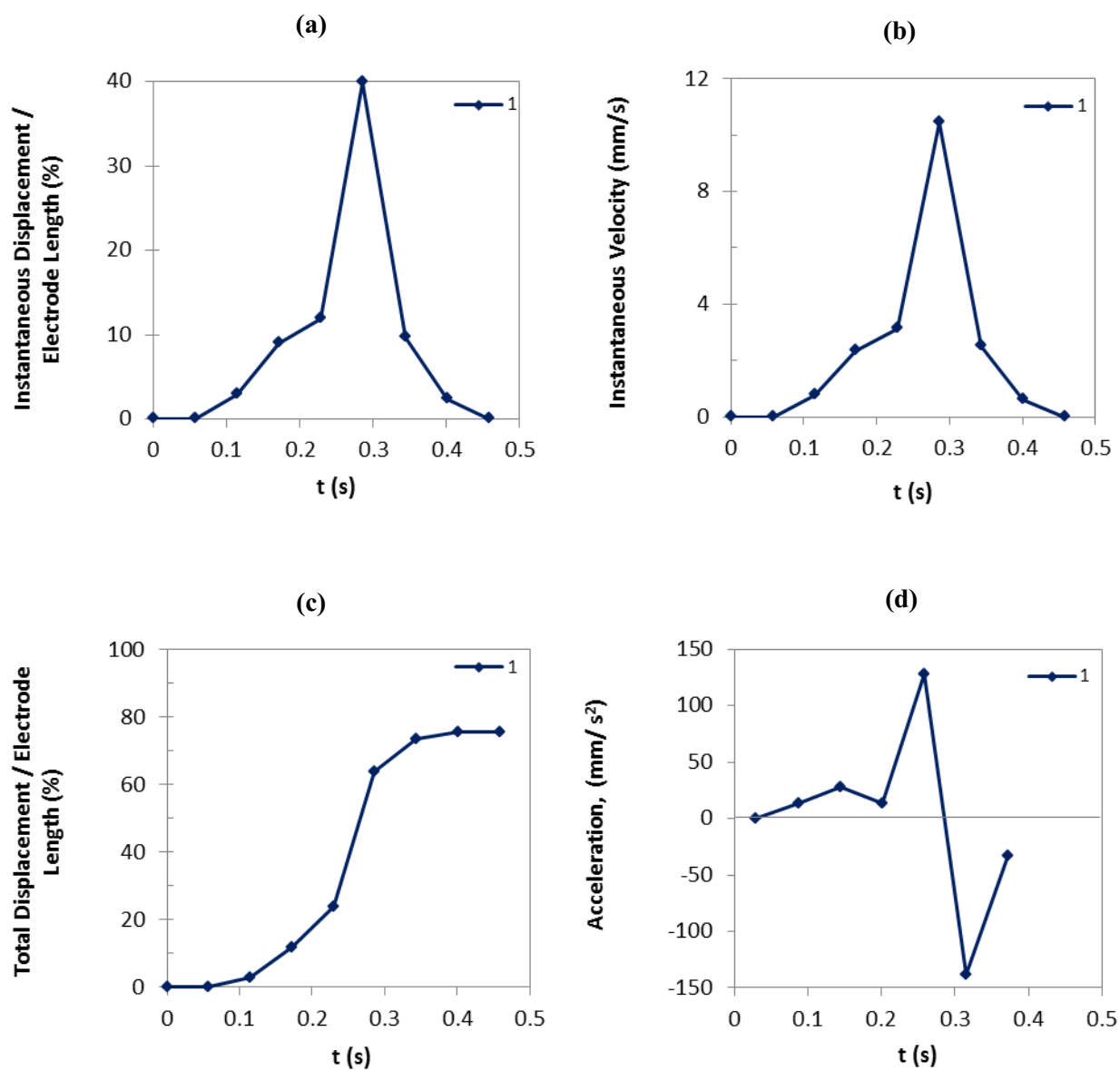


Figure H-17: (a) Instantaneous displacement, (b) instantaneous velocity, (c) total displacement, and (d) acceleration of the trailing edges of the droplets of 4 $\mu\text{g/ml}$ DNA solution as a function of time at 75 V.

4 $\mu\text{g/ml}$ DNA solution, 75 V

Accepted experiments and the average curves

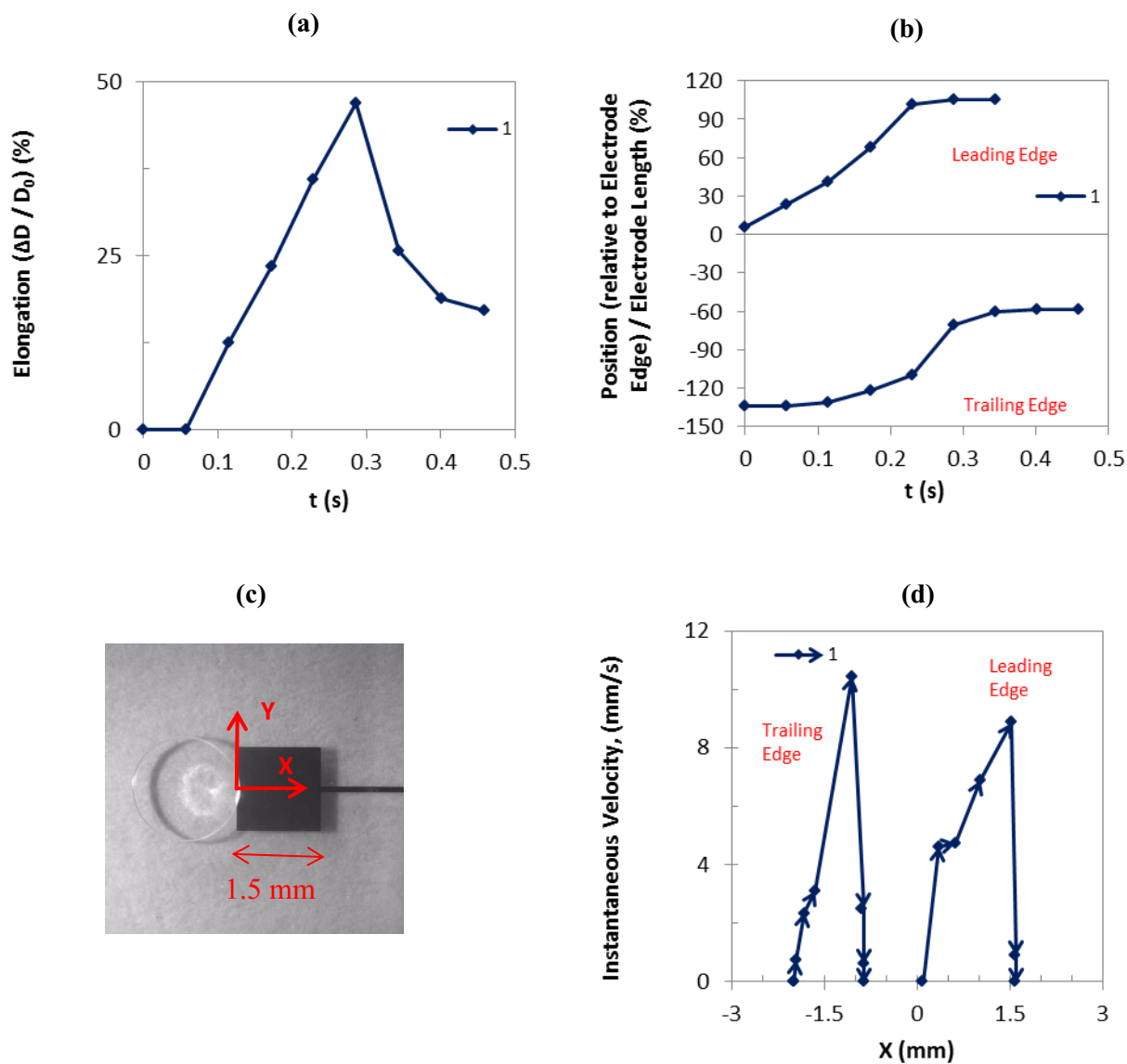


Figure H-18: (a) Droplet elongation, and (b) droplet position as a function of time, (d) instantaneous velocity as a function of droplet position as shown in (c) for the leading and trailing edges of the droplets of 4 $\mu\text{g/ml}$ DNA solution at 75 V. The arrows in graph (d) indicate the changes of velocity along the direction of movement.

4 $\mu\text{g/ml}$ DNA solution, 75 V, Average curves

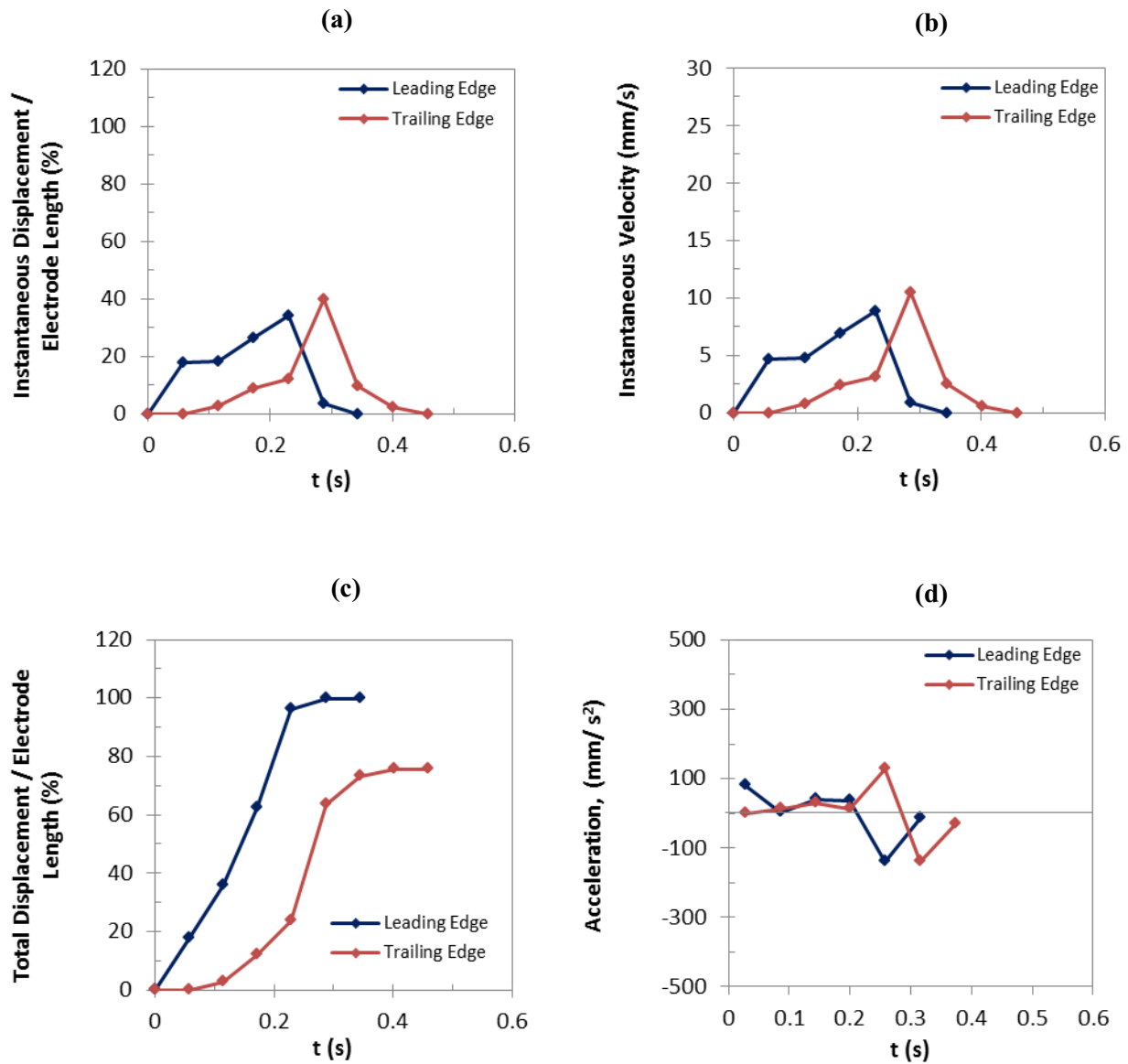


Figure H-19: Comparison of the average curves: (a) instantaneous displacement, (b) instantaneous velocity, (c) total displacement, and (d) acceleration, as a function of time for the leading and trailing edges of the droplets of 4 $\mu\text{g/ml}$ DNA solution at 75 V.

4 $\mu\text{g/ml}$ DNA solution, 75 V, Average curves

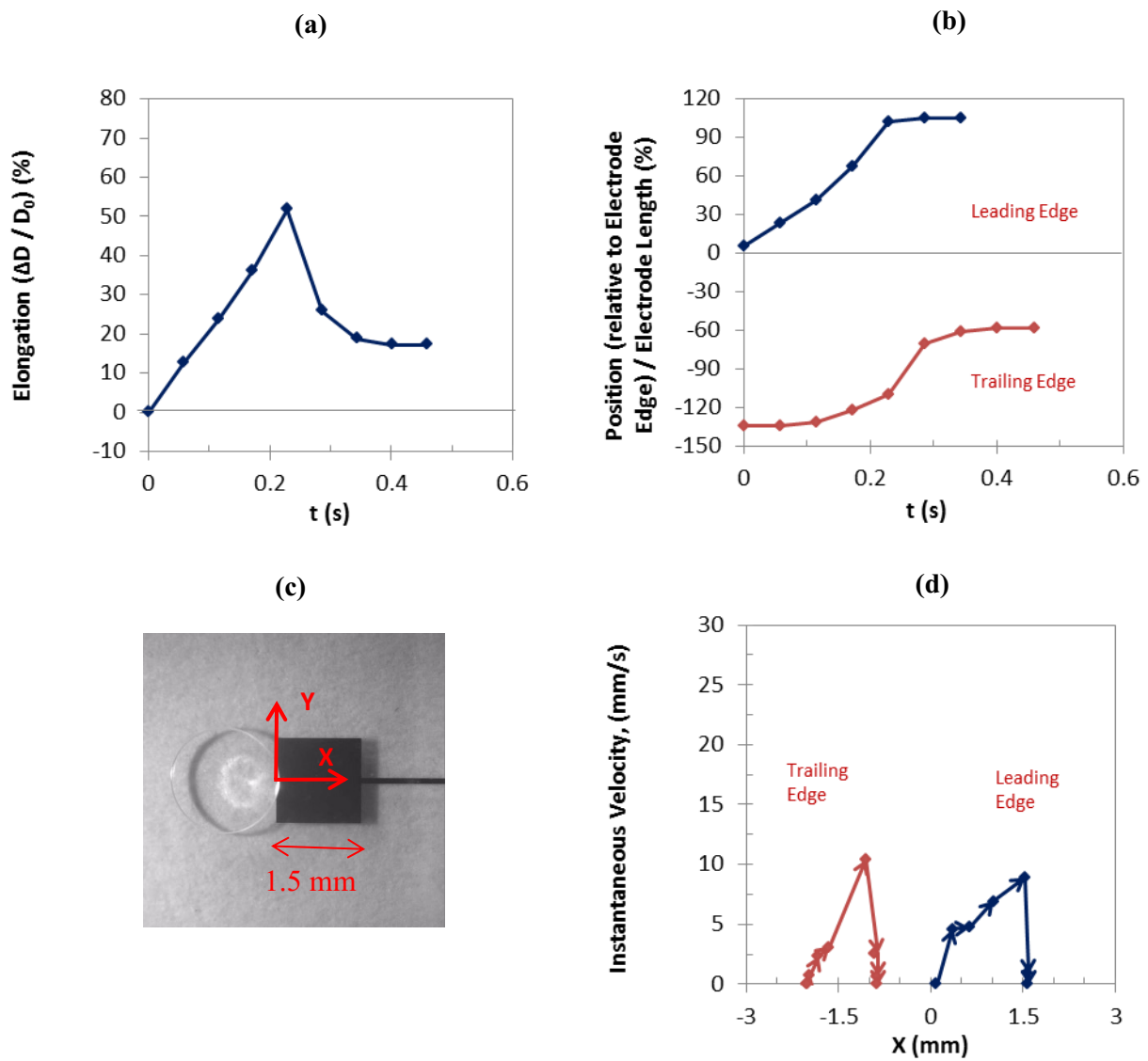


Figure H-20: Comparison of the average curves: (a) droplet elongation and (b) droplet position as a function of time, (d) instantaneous velocity as a function of droplet position as shown in (c) for the leading and trailing edges of the droplets of 4 $\mu\text{g/ml}$ DNA solution at 75 V. The arrows in graph (d) indicate the changes of velocity along the direction of movement.

H-5) 4 $\mu\text{g}/\text{ml}$ DNA Solution, 70 V

4 $\mu\text{g}/\text{ml}$ DNA solution, 70 V, Leading edge,

Accepted experiments and the average curves

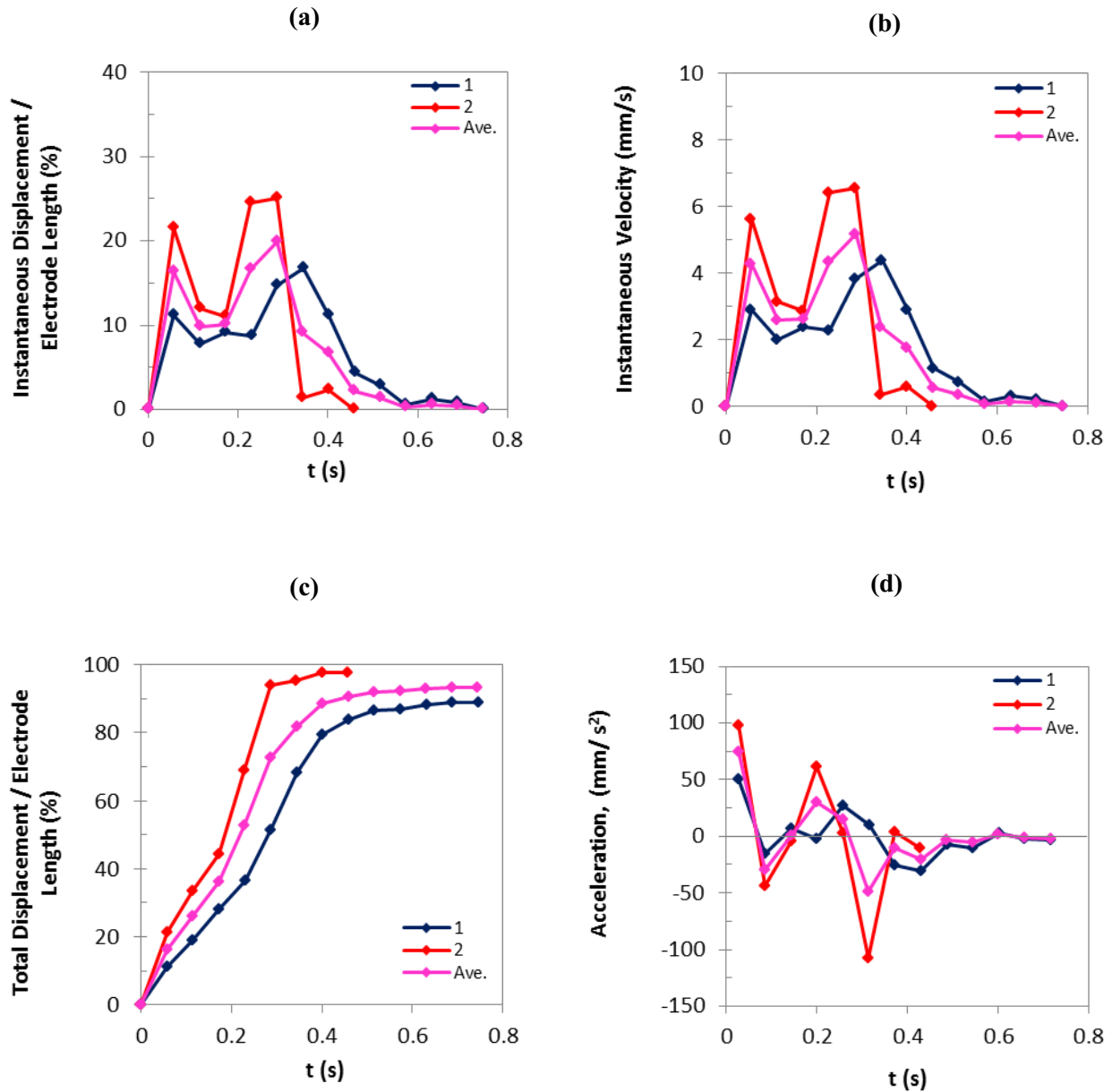


Figure H-21: (a) Instantaneous displacement, (b) instantaneous velocity, (c) total displacement, and (d) acceleration of the leading edges of the droplets of 4 $\mu\text{g}/\text{ml}$ DNA solution as a function of time at 70 V.

4 $\mu\text{g/ml}$ DNA solution, 70 V, Trailing edge,

Accepted experiments and the average curves

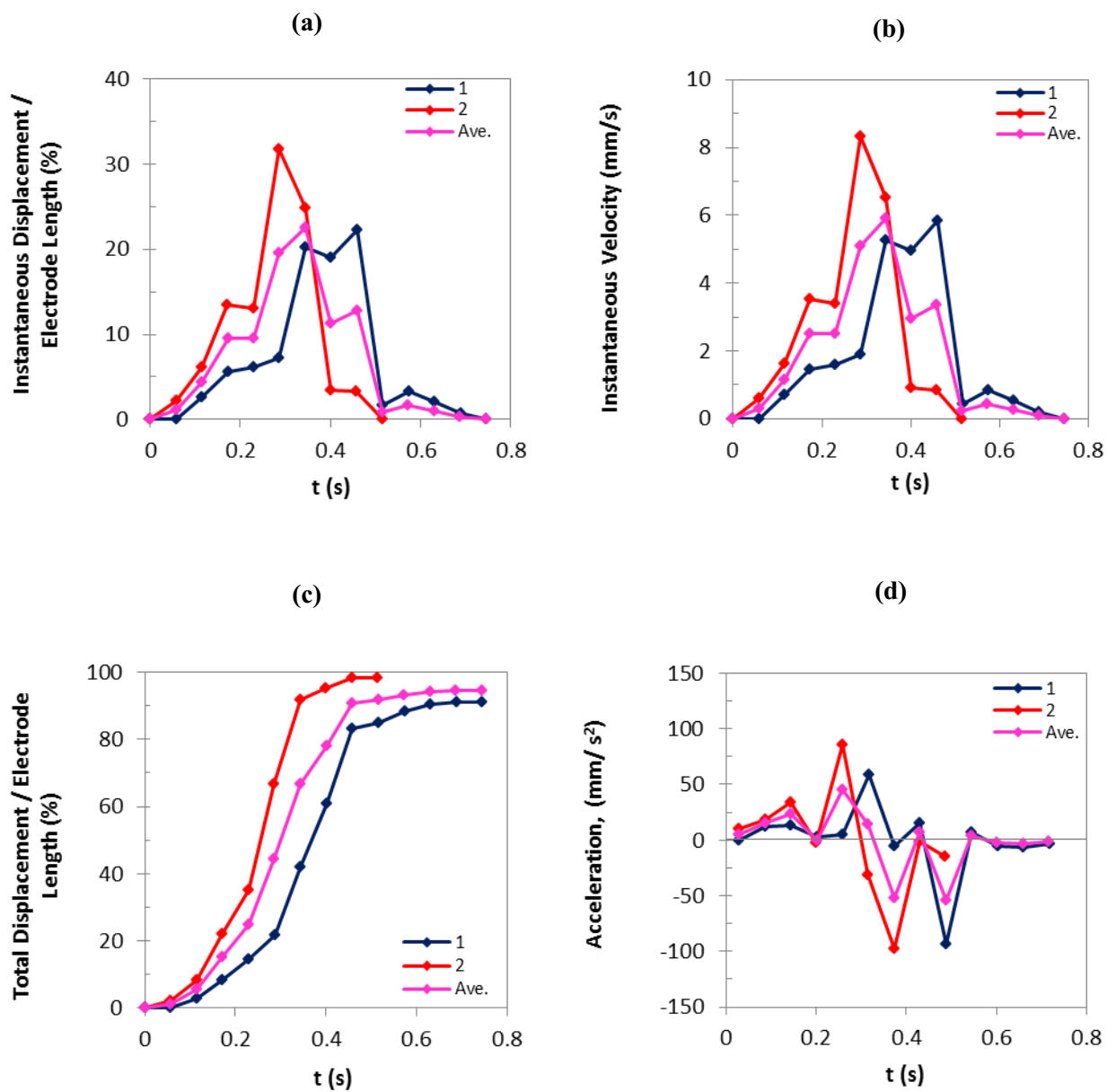


Figure H-22: (a) Instantaneous displacement, (b) instantaneous velocity, (c) total displacement, and (d) acceleration of the trailing edges of the droplets of 4 $\mu\text{g/ml}$ DNA solution as a function of time at 70 V.

4 $\mu\text{g/ml}$ DNA solution, 70 V

Accepted experiments and the average curves

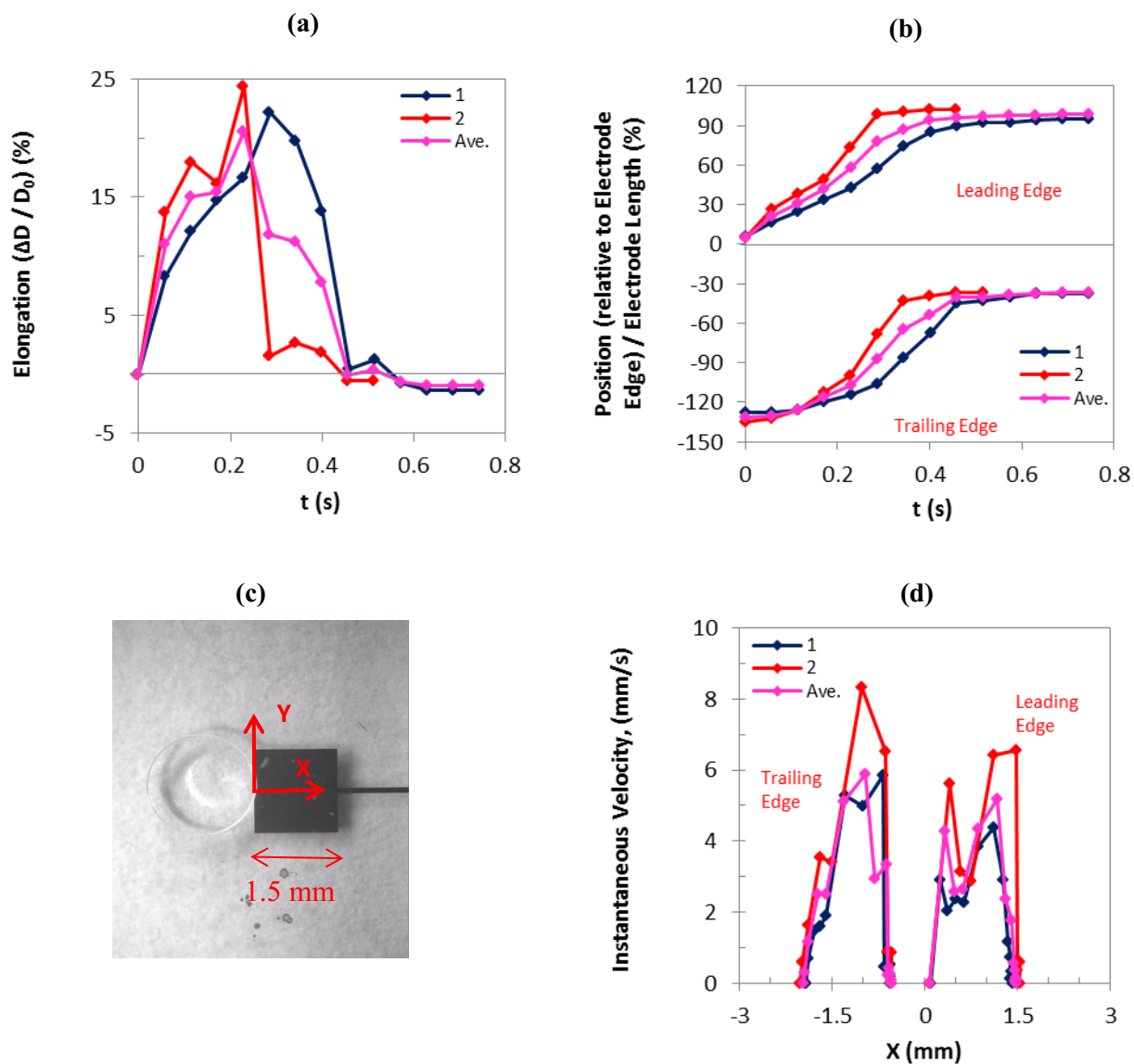


Figure H-23: (a) Droplet elongation, and (b) droplet position as a function of time, (d) instantaneous velocity as a function of droplet position as shown in (c) for the leading and trailing edges of the droplets of 4 $\mu\text{g/ml}$ DNA solution at 70 V.

4 $\mu\text{g/ml}$ DNA solution, 70 V, Average curves

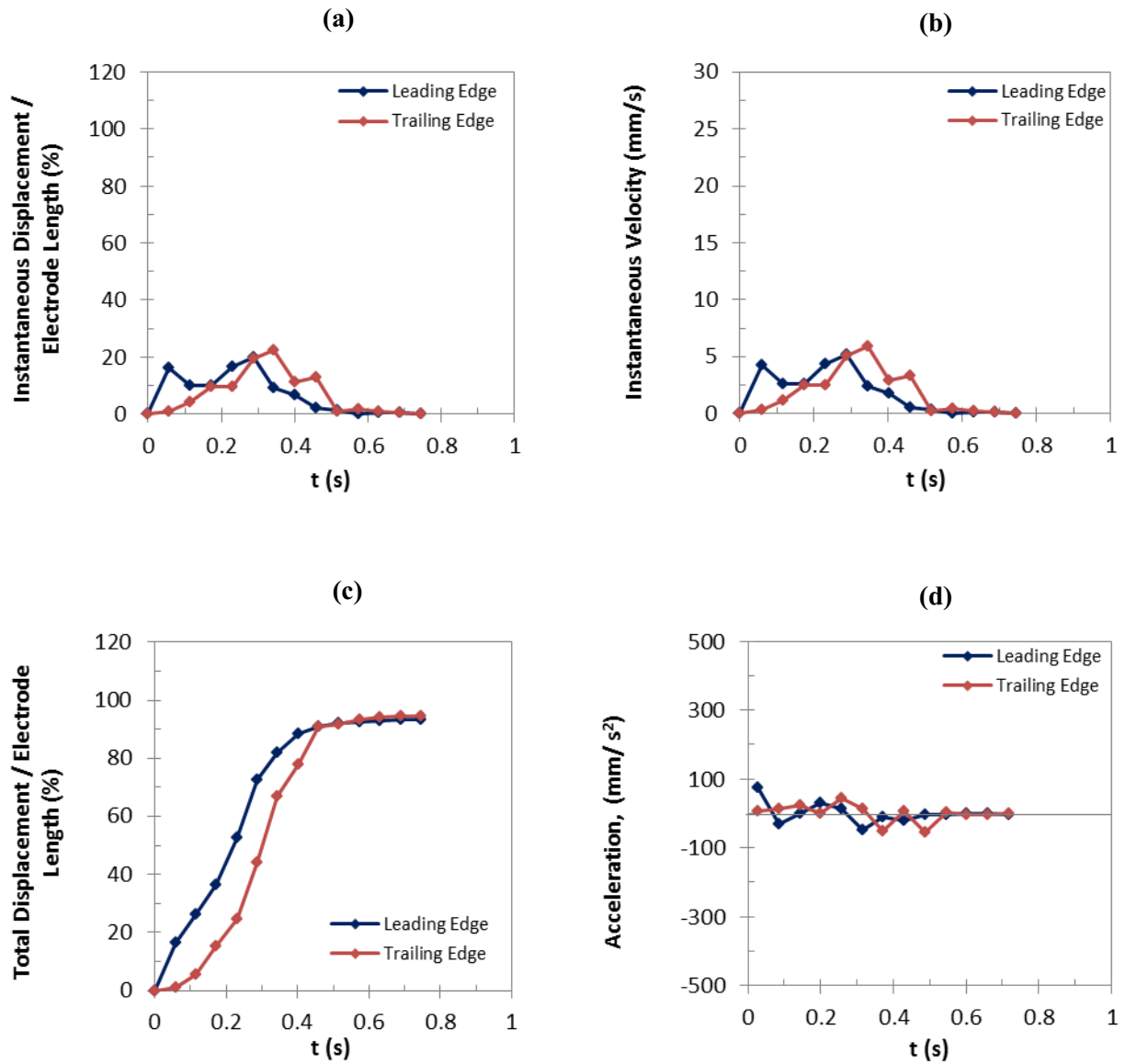


Figure H-24: Comparison of the average curves: (a) instantaneous displacement, (b) instantaneous velocity, (c) total displacement, and (d) acceleration, as a function of time for the leading and trailing edges of the droplets of 4 $\mu\text{g/ml}$ DNA solution at 70 V.

4 $\mu\text{g/ml}$ DNA solution, 70 V, Average curves

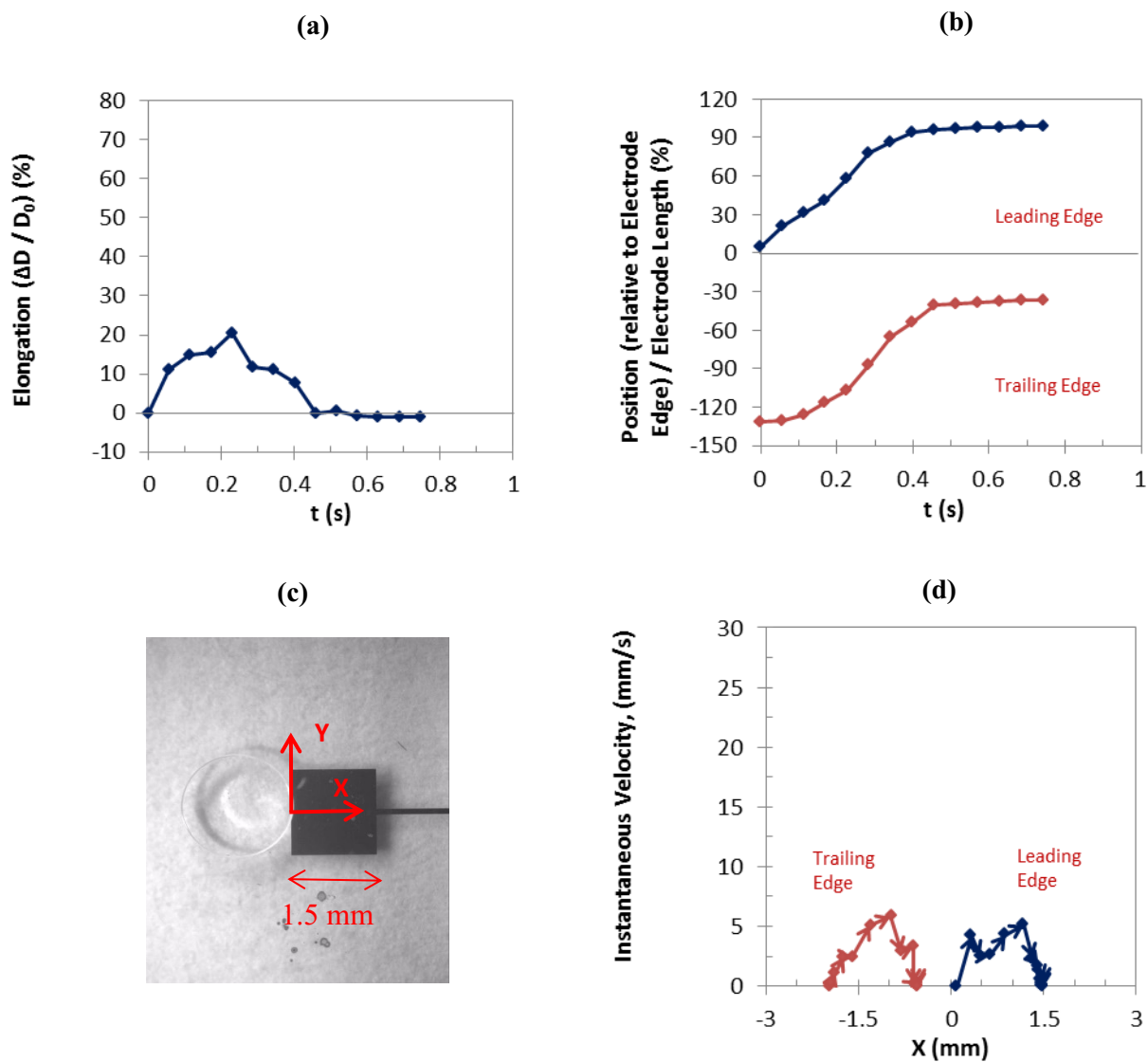


Figure H-25: Comparison of the average curves: (a) droplet elongation and (b) droplet position as a function of time, (d) instantaneous velocity as a function of droplet position as shown in (c) for the leading and trailing edges of the droplets of 4 $\mu\text{g/ml}$ DNA solution at 70 V. The arrows in graph (d) indicate the changes of velocity along the direction of movement.

H-6) 4 $\mu\text{g/ml}$ DNA Solution, 65 V

4 $\mu\text{g/ml}$ DNA solution, 65 V, Leading edge,

Accepted experiments and the average curves

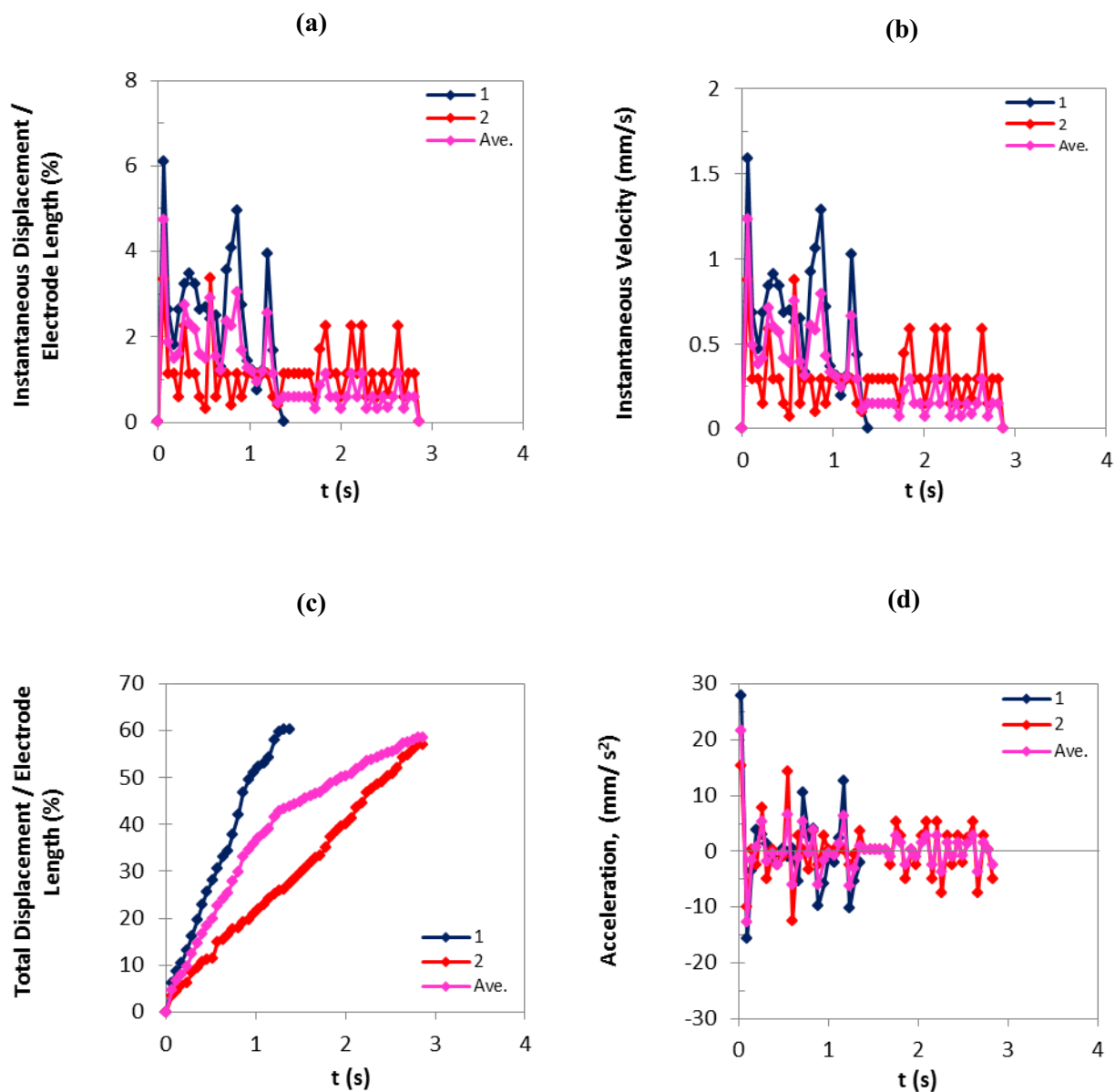


Figure H-26: (a) Instantaneous displacement, (b) instantaneous velocity, (c) total displacement, and (d) acceleration of the leading edges of the droplets of 4 $\mu\text{g/ml}$ DNA solution as a function of time at 65 V.

4 $\mu\text{g/ml}$ DNA solution, 65 V, Trailing edge,

Accepted experiments and the average curves

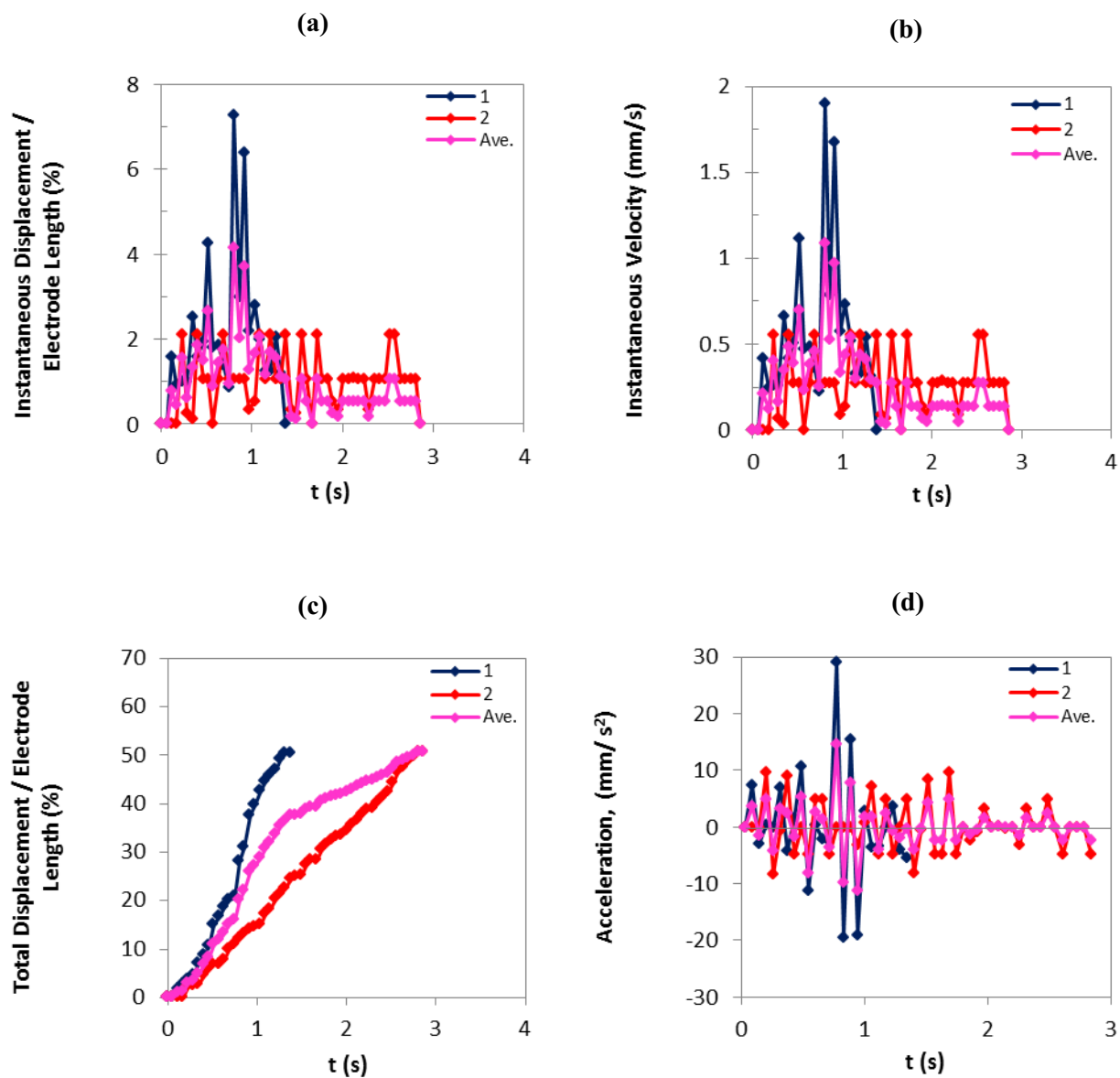


Figure H-27: (a) Instantaneous displacement, (b) instantaneous velocity, (c) total displacement, and (d) acceleration of the trailing edges of the droplets of 4 $\mu\text{g/ml}$ DNA solution as a function of time at 65 V.

4 $\mu\text{g/ml}$ DNA solution, 65 V

Accepted experiments and the average curves

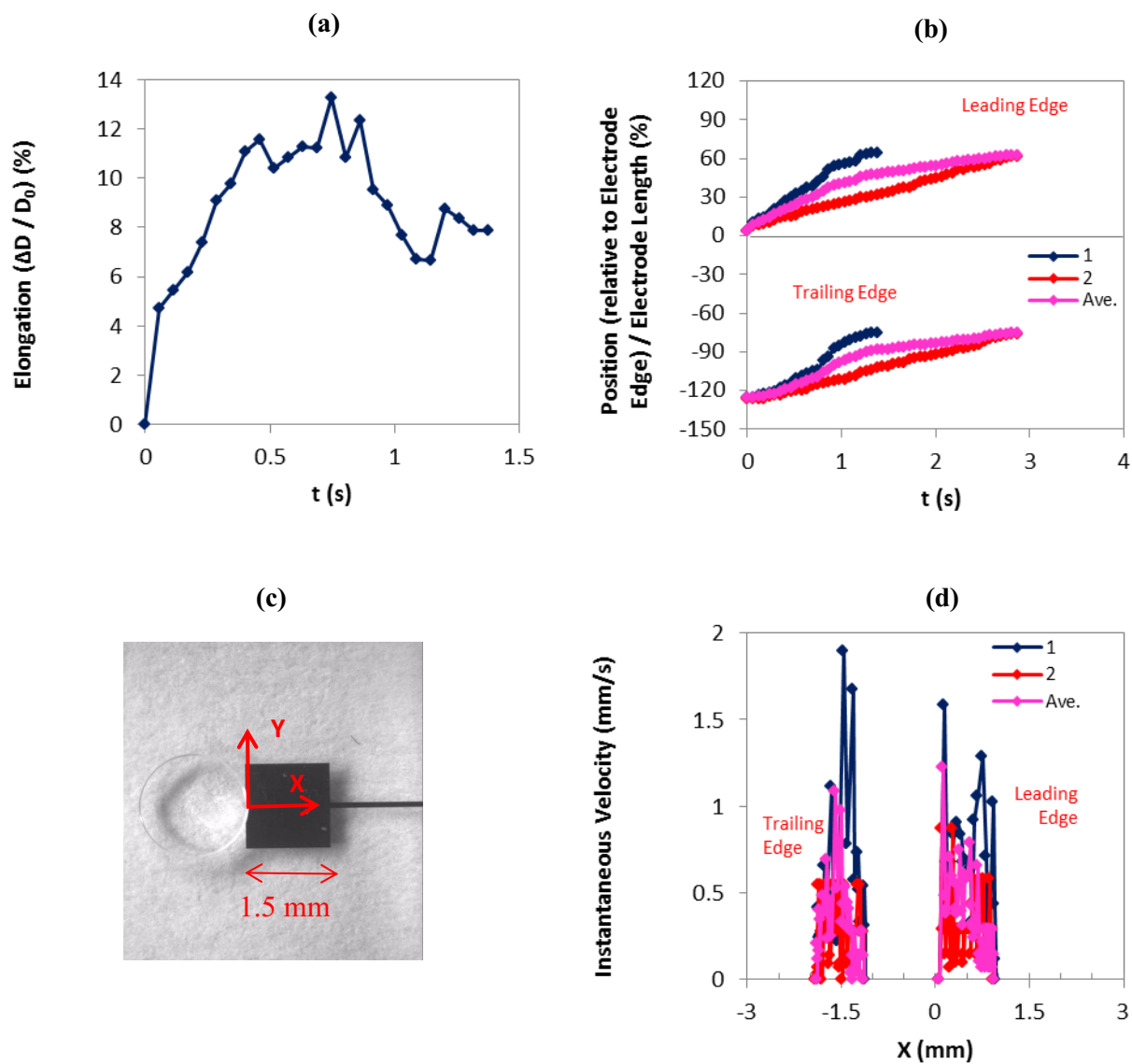


Figure H-28: (a) Droplet elongation, and (b) droplet position as a function of time, (d) instantaneous velocity as a function of droplet position as shown in (c) for the leading and trailing edges of the droplets of 4 $\mu\text{g/ml}$ DNA solution at 65 V.

4 $\mu\text{g/ml}$ DNA solution, 65 V, Average curves

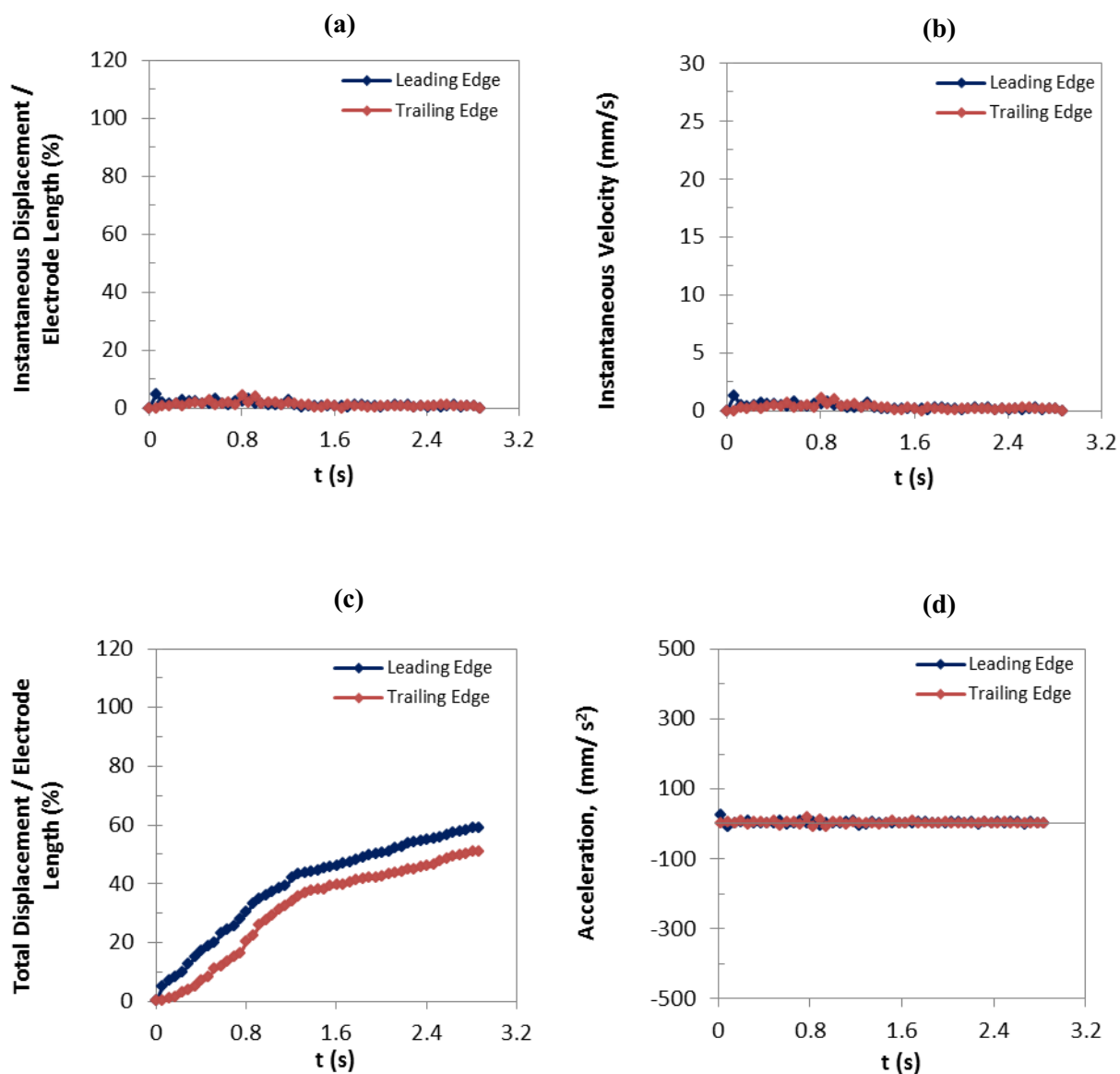


Figure H-29: Comparison of the average curves: (a) instantaneous displacement, (b) instantaneous velocity, (c) total displacement, and (d) acceleration, as a function of time for the leading and trailing edges of the droplets of 4 $\mu\text{g/ml}$ DNA solution at 65 V.

4 $\mu\text{g/ml}$ DNA solution, 65 V, Average curves

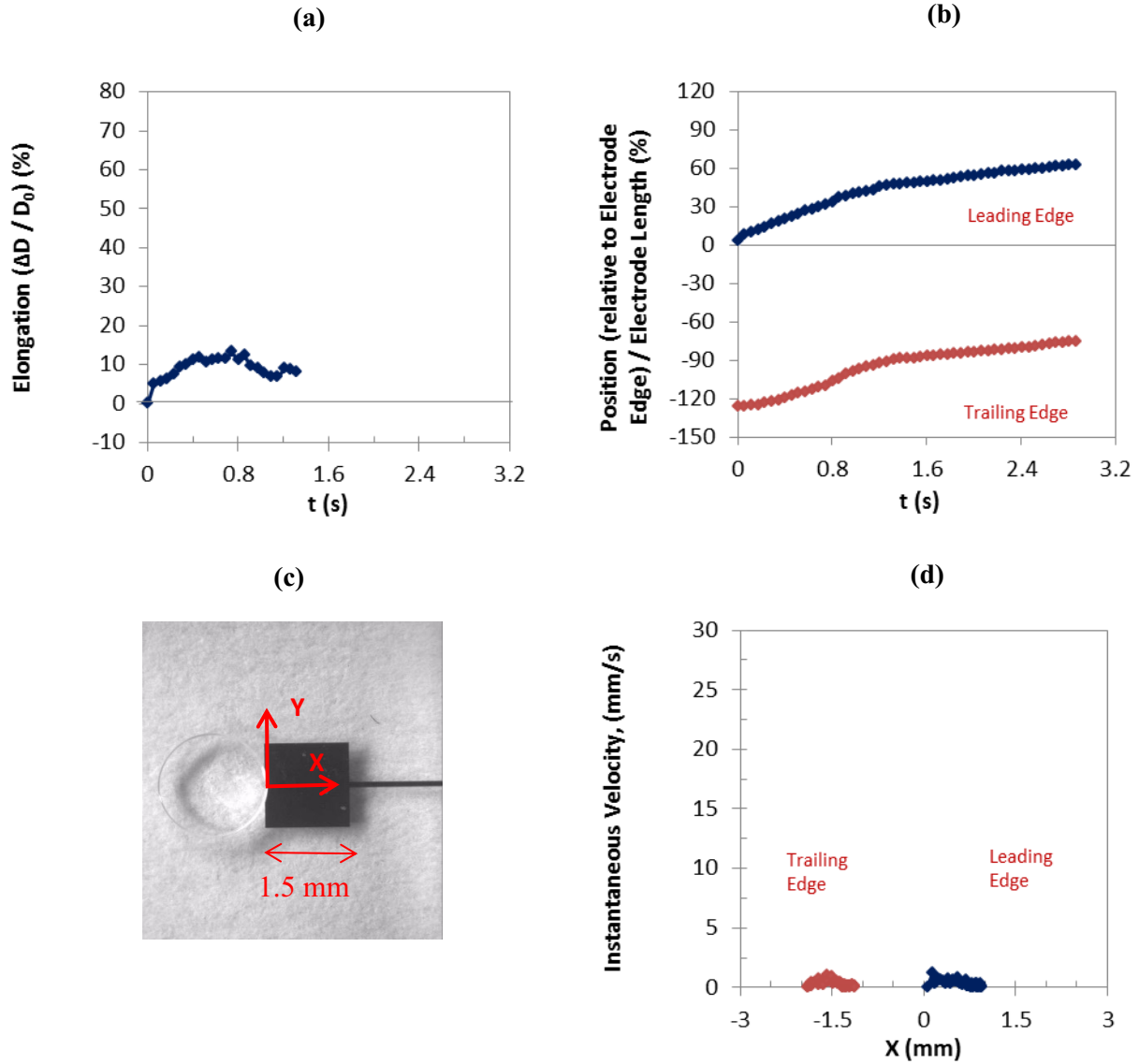


Figure H-30: Comparison of the average curves: (a) droplet elongation and (b) droplet position as a function of time, (d) instantaneous velocity as a function of droplet position as shown in (c) for the leading and trailing edges of the droplets of 4 $\mu\text{g/ml}$ DNA solution at 65 V.

H-6) 4 $\mu\text{g}/\text{ml}$ DNA Solution, 60 V

4 $\mu\text{g}/\text{ml}$ DNA solution, 60 V, Leading edge,

Accepted experiments and the average curves

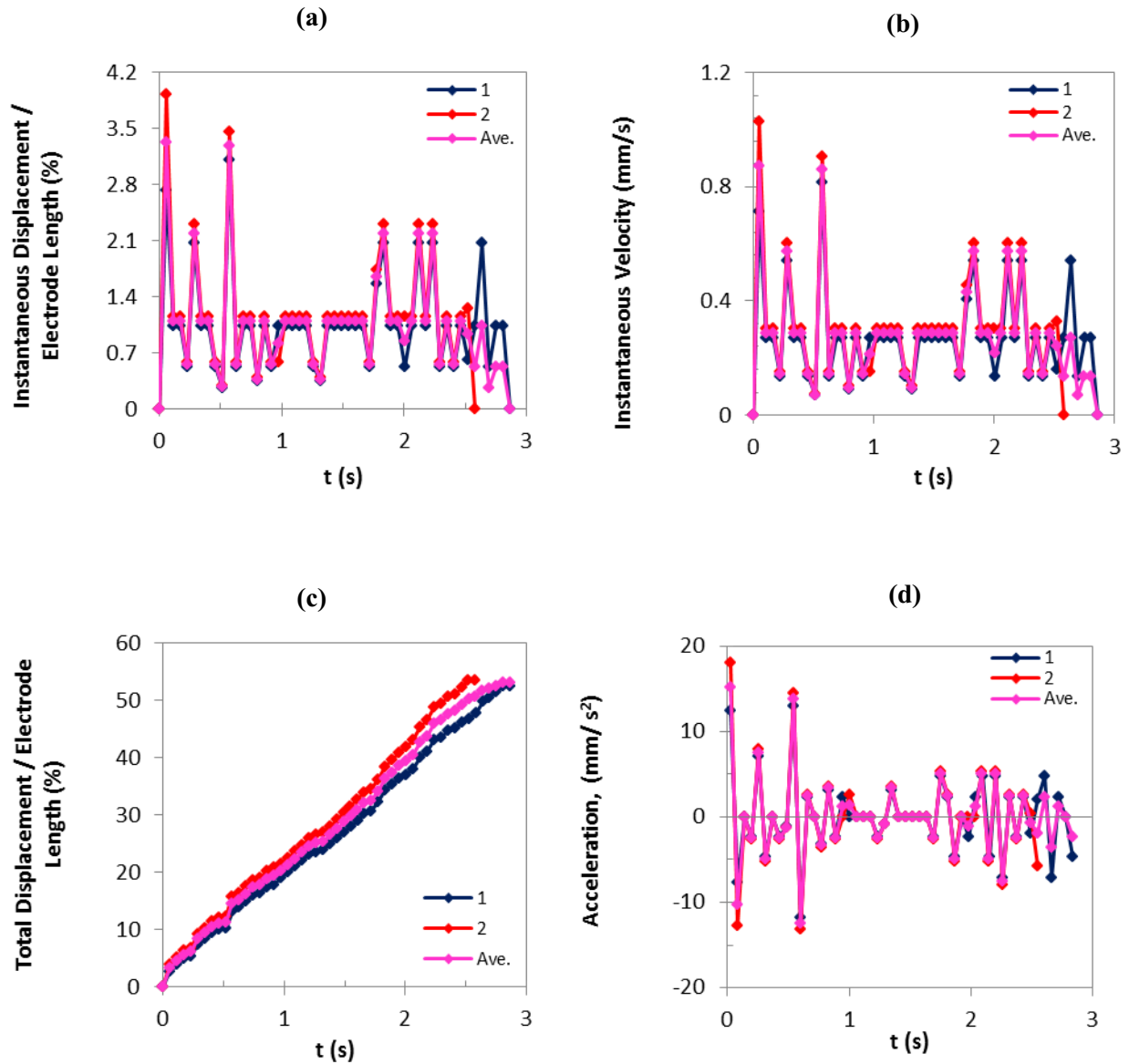


Figure H-31: (a) Instantaneous displacement, (b) instantaneous velocity, (c) total displacement, and (d) acceleration of the leading edges of the droplets of 4 $\mu\text{g}/\text{ml}$ DNA solution as a function of time at 60 V.

4 $\mu\text{g}/\text{ml}$ DNA solution, 60 V, Trailing edge,

Accepted experiments and the average curves

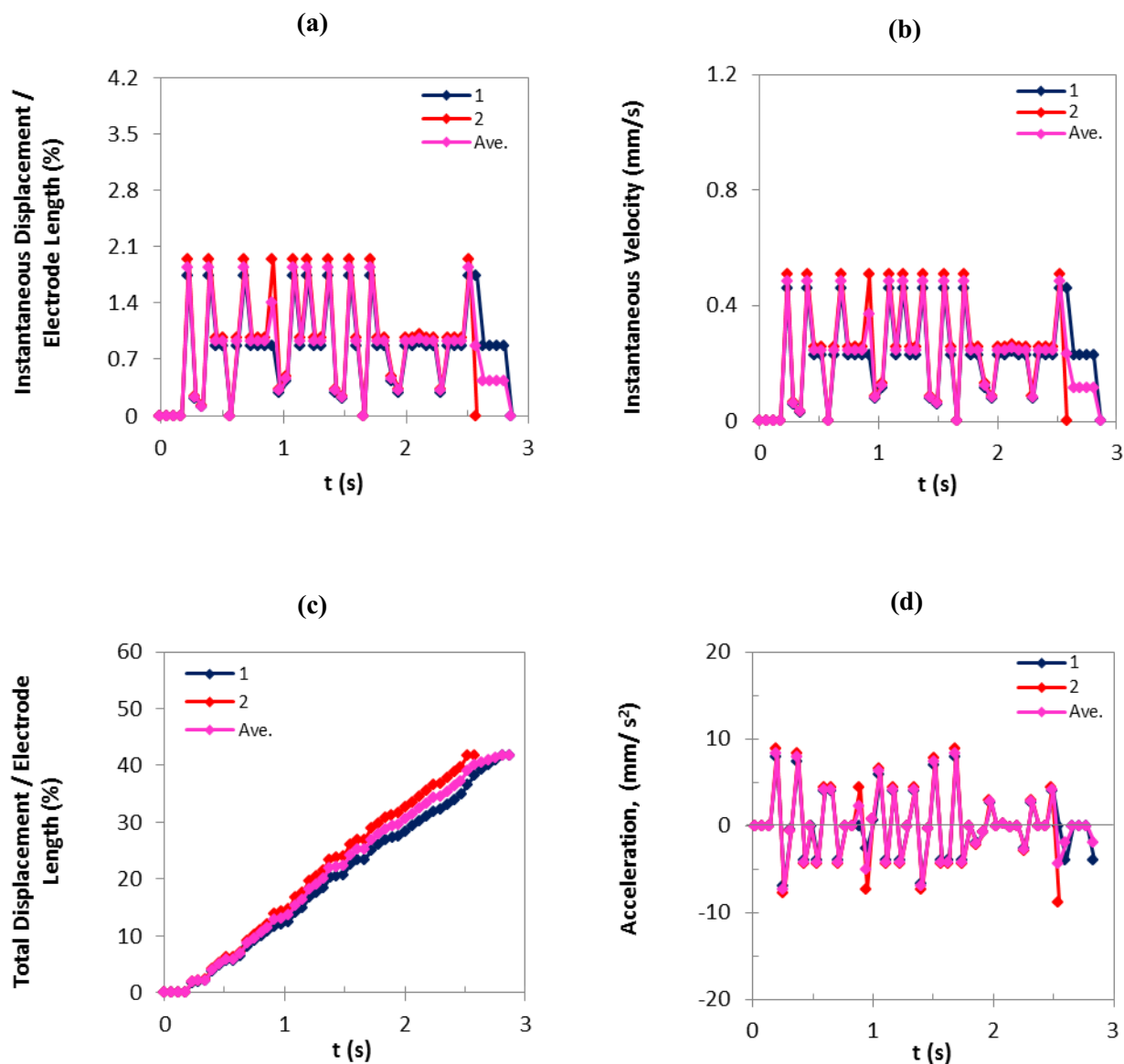


Figure H-32: (a) Instantaneous displacement, (b) instantaneous velocity, (c) total displacement, and (d) acceleration of the trailing edges of the droplets of 4 $\mu\text{g}/\text{ml}$ DNA solution as a function of time at 60 V.

4 $\mu\text{g/ml}$ DNA solution, 60 V

Accepted experiments and the average curves

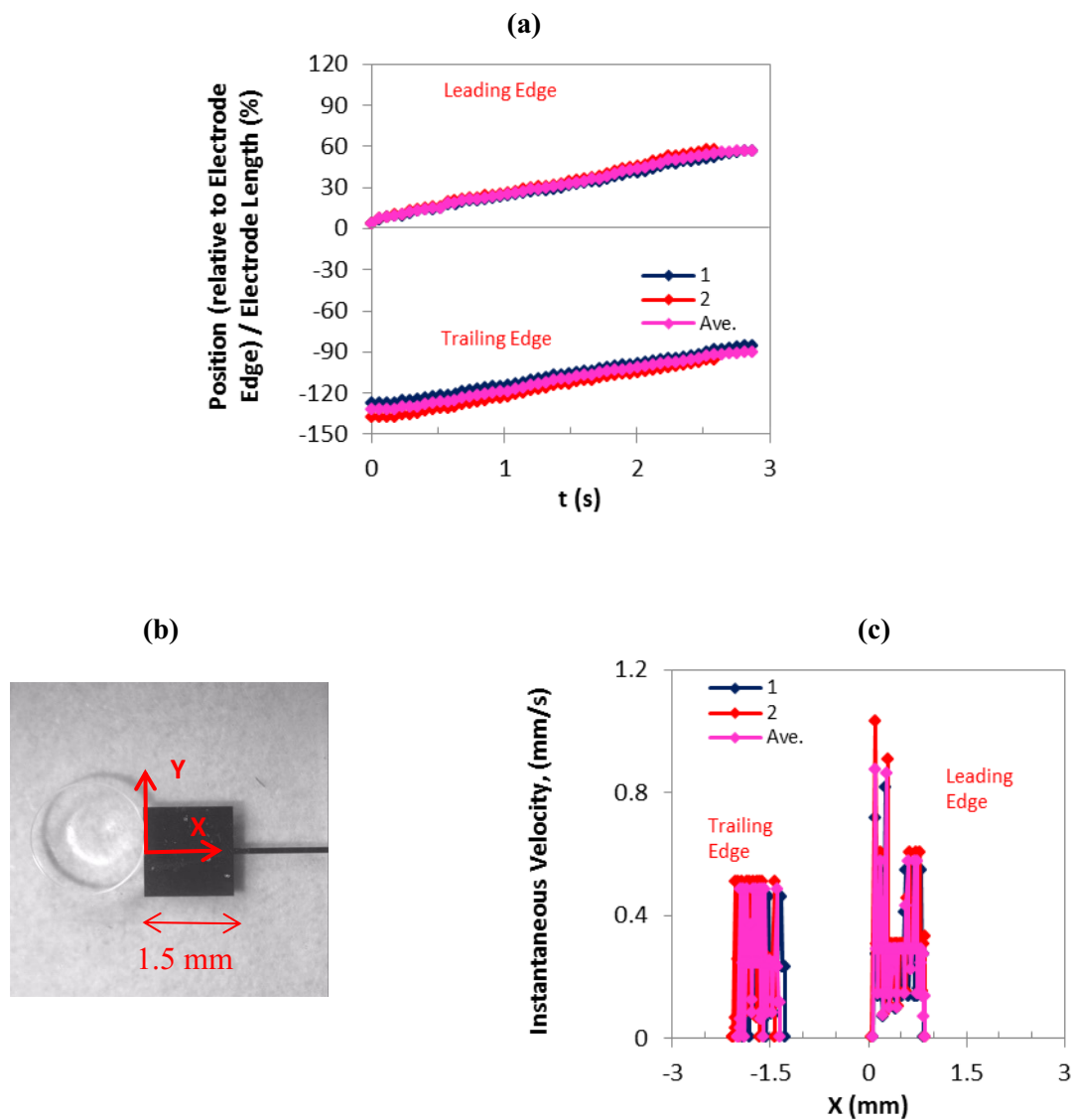


Figure H-33: (a) Droplet elongation, and (b) droplet position as a function of time, (d) instantaneous velocity as a function of droplet position as shown in (c) for the leading and trailing edges of the droplets of 4 $\mu\text{g/ml}$ DNA solution at 60 V.

4 $\mu\text{g/ml}$ DNA solution, 60 V, Average curves

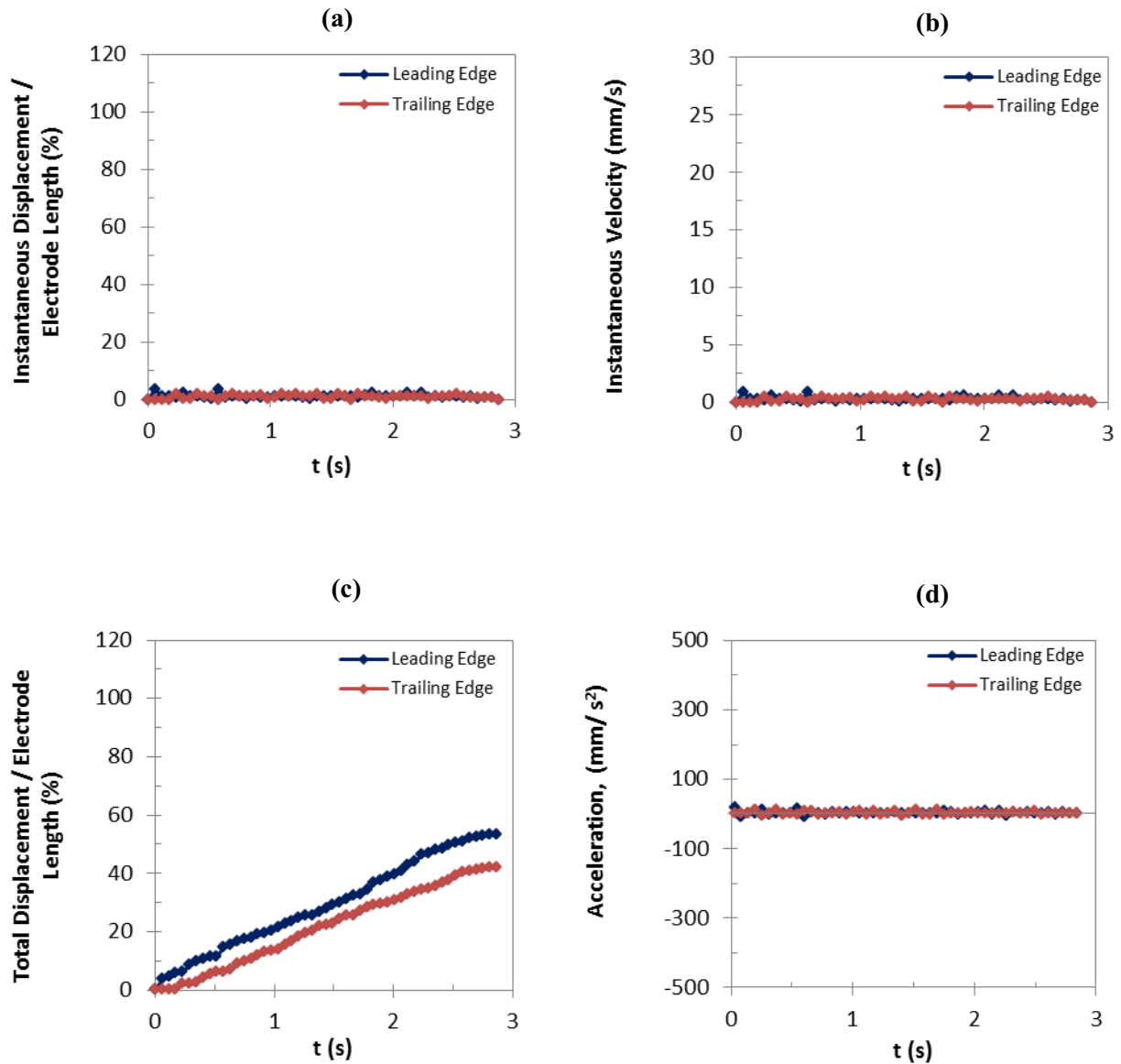


Figure H-34: Comparison of the average curves: (a) instantaneous displacement, (b) instantaneous velocity, (c) total displacement, and (d) acceleration, as a function of time for the leading and trailing edges of the droplets of 4 $\mu\text{g/ml}$ DNA solution at 60 V.

4 $\mu\text{g/ml}$ DNA solution, 60 V, Average curves

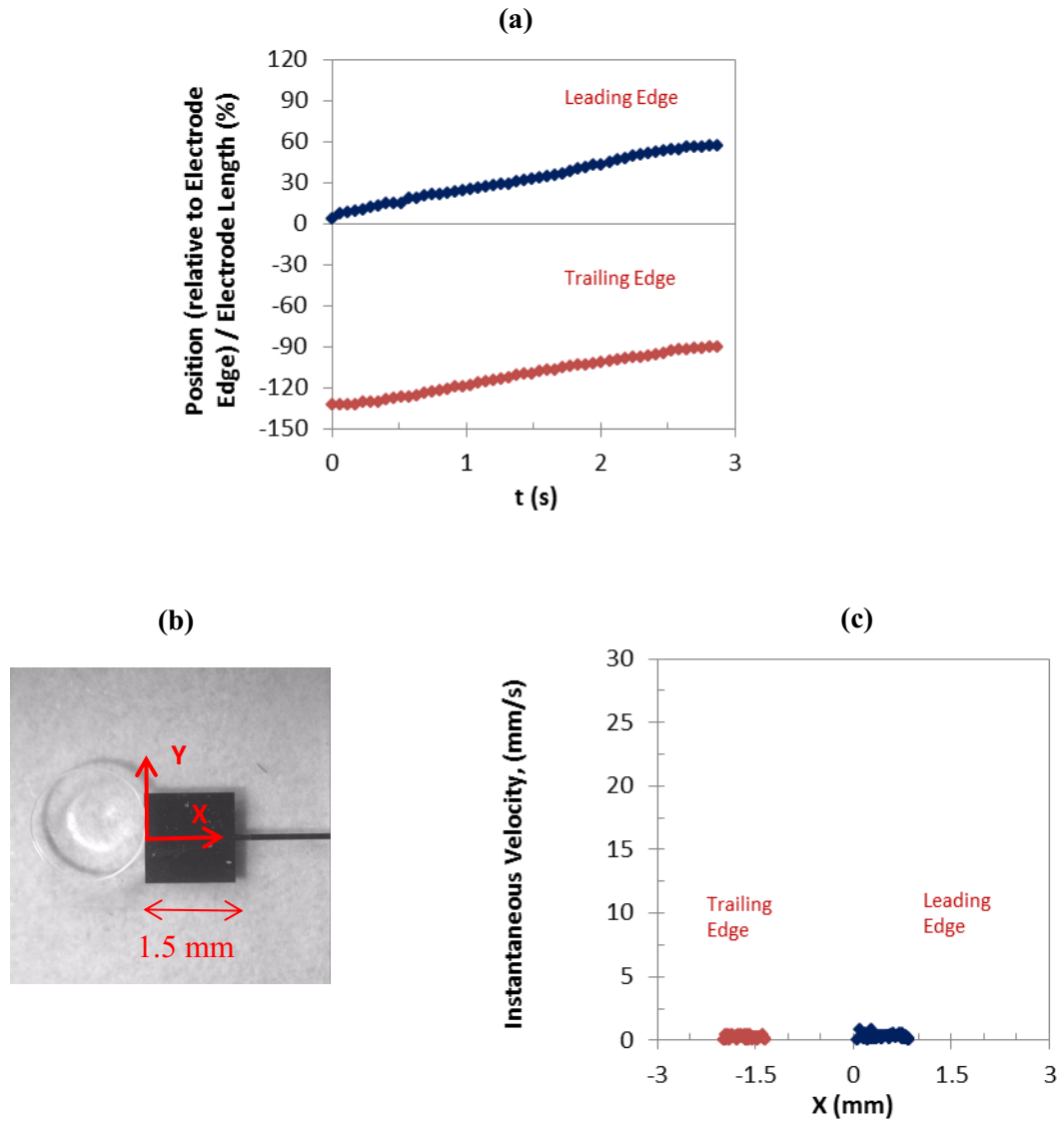


Figure H-35: Comparison of the average curves: (a) droplet elongation and (b) droplet position as a function of time, (d) instantaneous velocity as a function of droplet position as shown in (c) for the leading and trailing edges of the droplets of 4 $\mu\text{g/ml}$ DNA solution at 60 V.

H-8) 4 $\mu\text{g}/\text{ml}$ DNA Solution, 55 V

4 $\mu\text{g}/\text{ml}$ DNA solution, 55 V, Leading edge,

Accepted experiments and the average curves

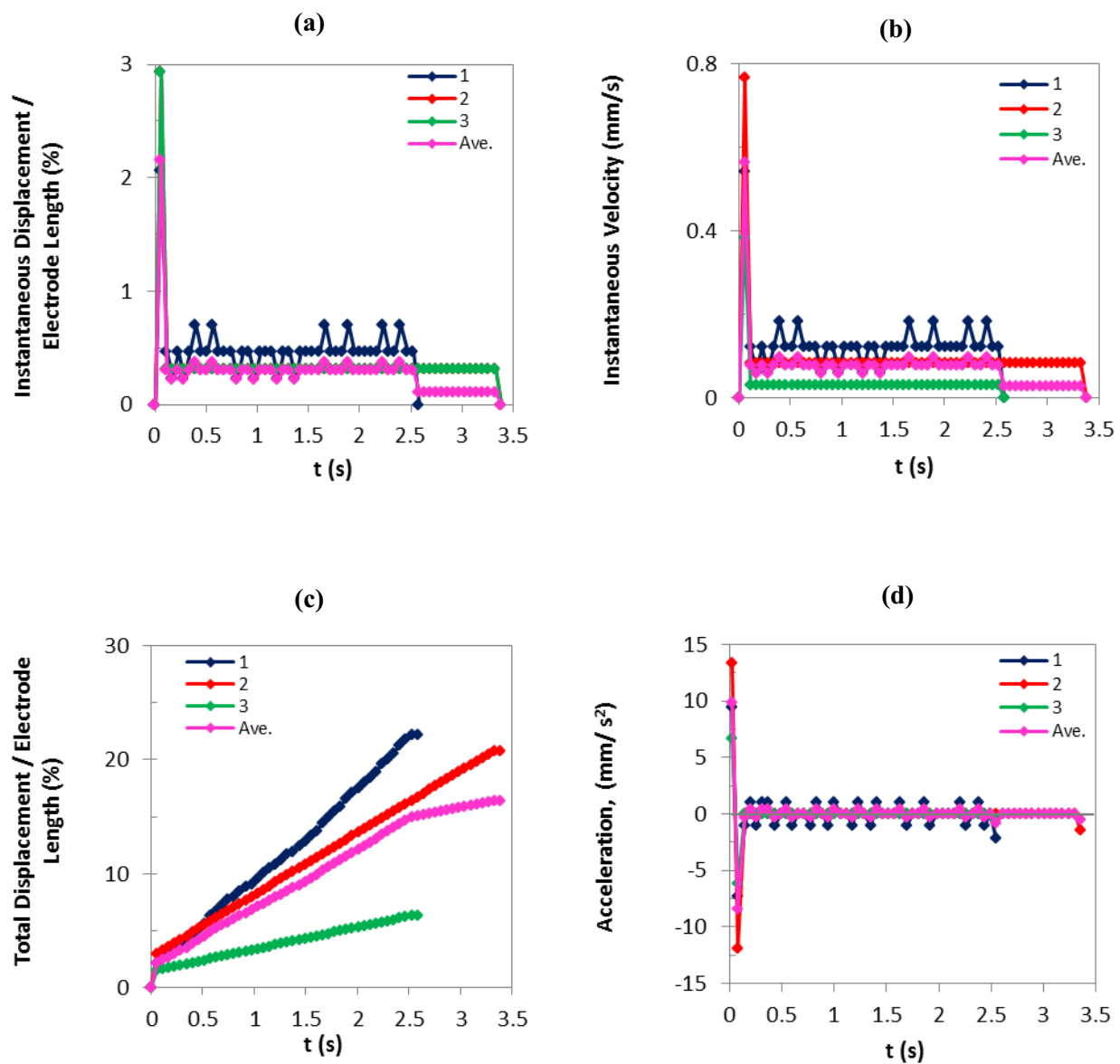


Figure H-36: (a) Instantaneous displacement, (b) instantaneous velocity, (c) total displacement, and (d) acceleration of the leading edges of the droplets of 4 $\mu\text{g}/\text{ml}$ DNA solution as a function of time at 55 V.

4 $\mu\text{g/ml}$ DNA solution, 55 V, Trailing edge,

Accepted experiments and the average curves

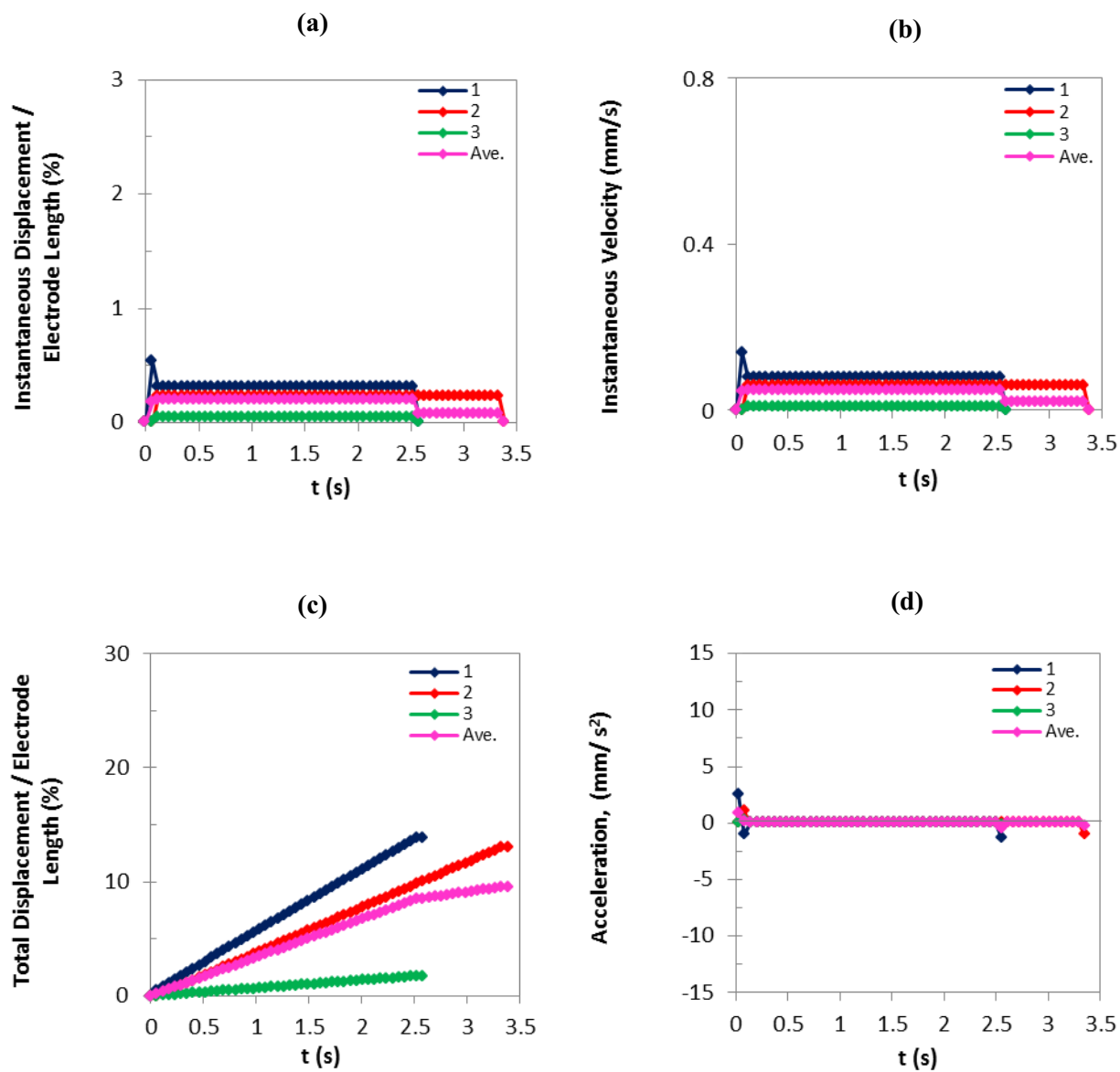


Figure H-37: (a) Instantaneous displacement, (b) instantaneous velocity, (c) total displacement, and (d) acceleration of the trailing edges of the droplets of 4 $\mu\text{g/ml}$ DNA solution as a function of time at 55 V.

4 $\mu\text{g/ml}$ DNA solution, 55 V

Accepted experiments and the average curves

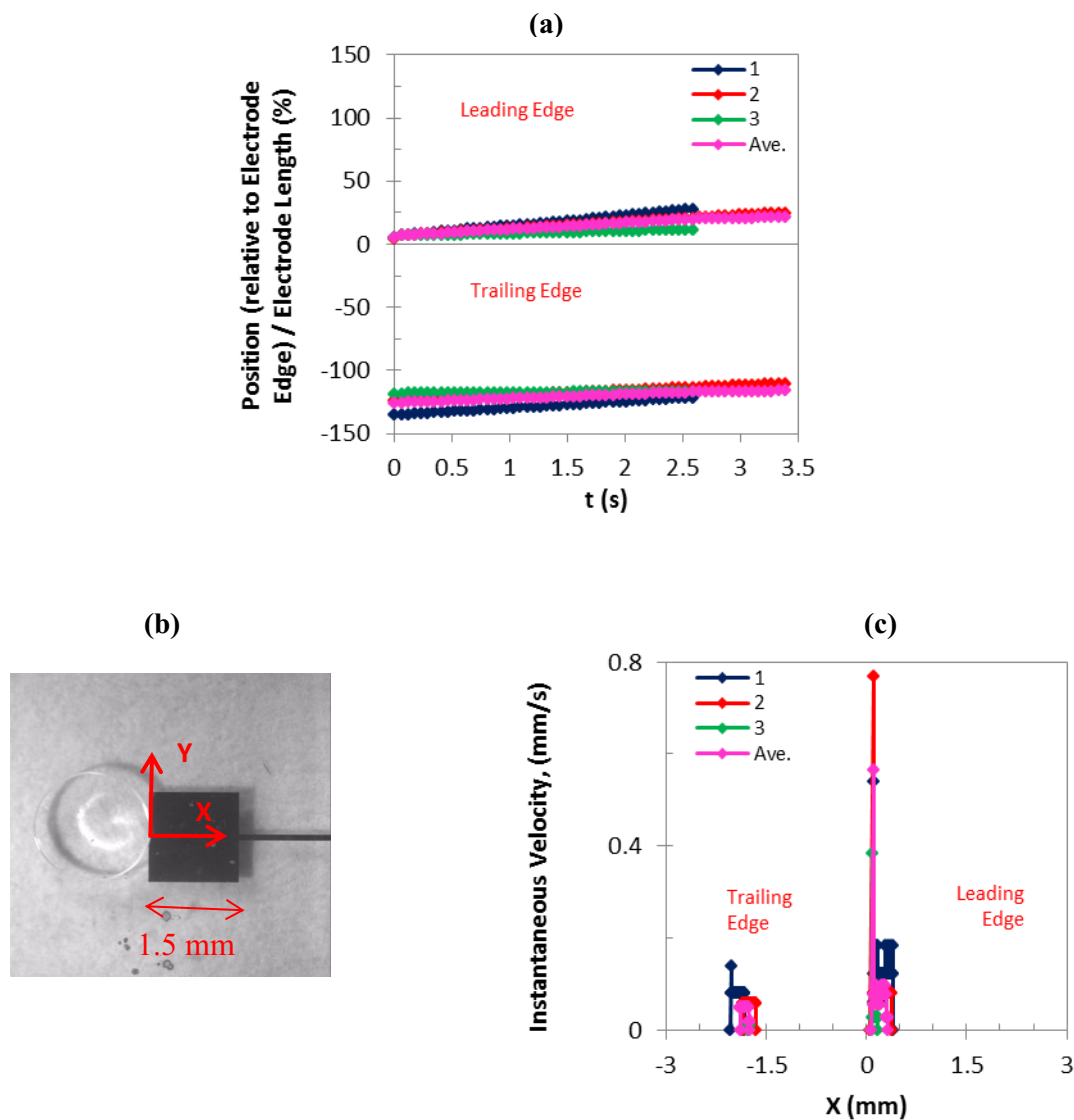


Figure H-38: (a) Droplet elongation, and (b) droplet position as a function of time, (d) instantaneous velocity as a function of droplet position as shown in (c) for the leading and trailing edges of the droplets of 4 $\mu\text{g/ml}$ DNA solution at 55 V.

4 $\mu\text{g}/\text{ml}$ DNA solution, 55 V, Average curves

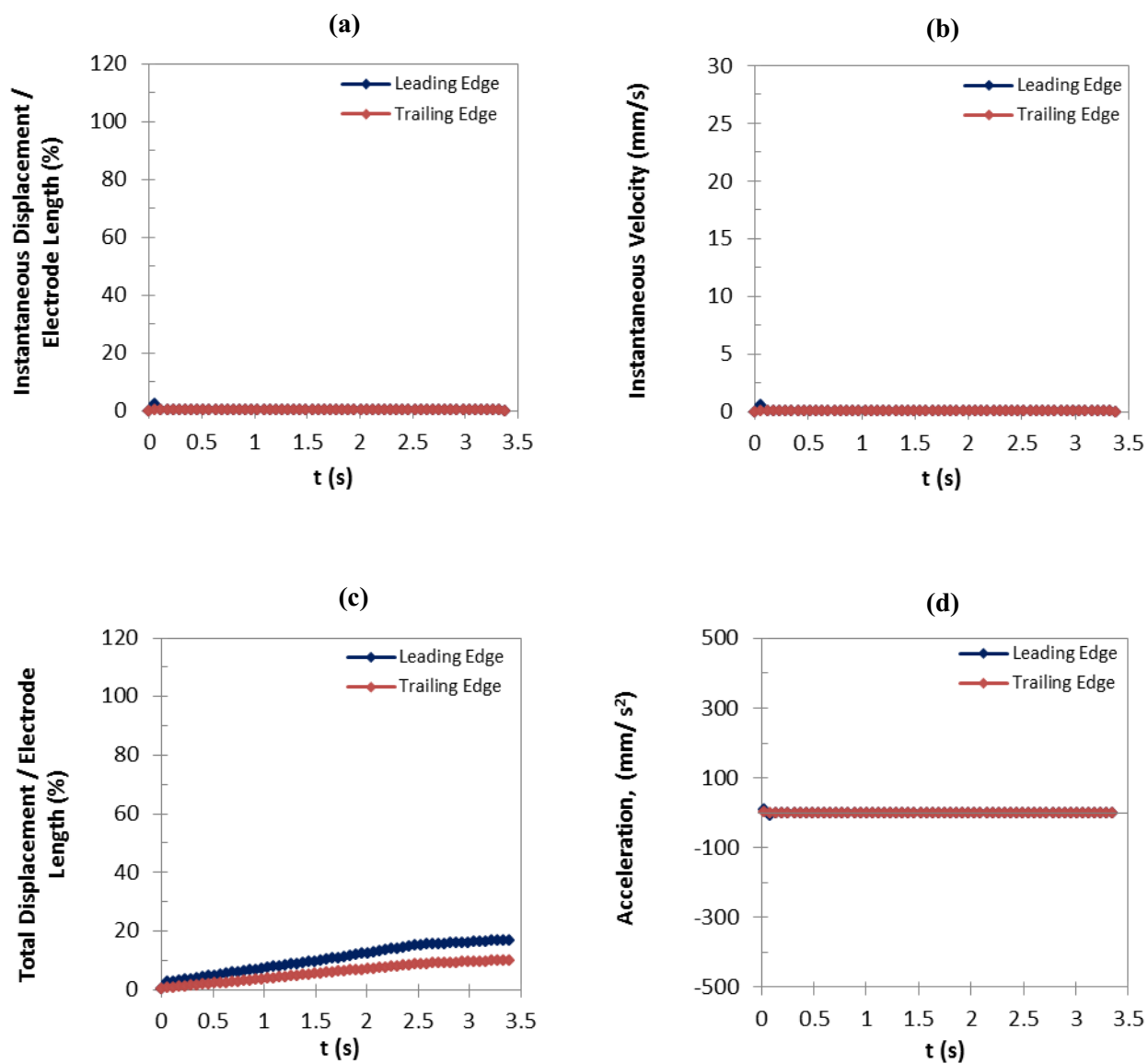


Figure H-39: Comparison of the average curves: (a) instantaneous displacement, (b) instantaneous velocity, (c) total displacement, and (d) acceleration, as a function of time for the leading and trailing edges of the droplets of 4 $\mu\text{g}/\text{ml}$ DNA solution at 55 V.

4 $\mu\text{g/ml}$ DNA solution, 55 V, Average curves

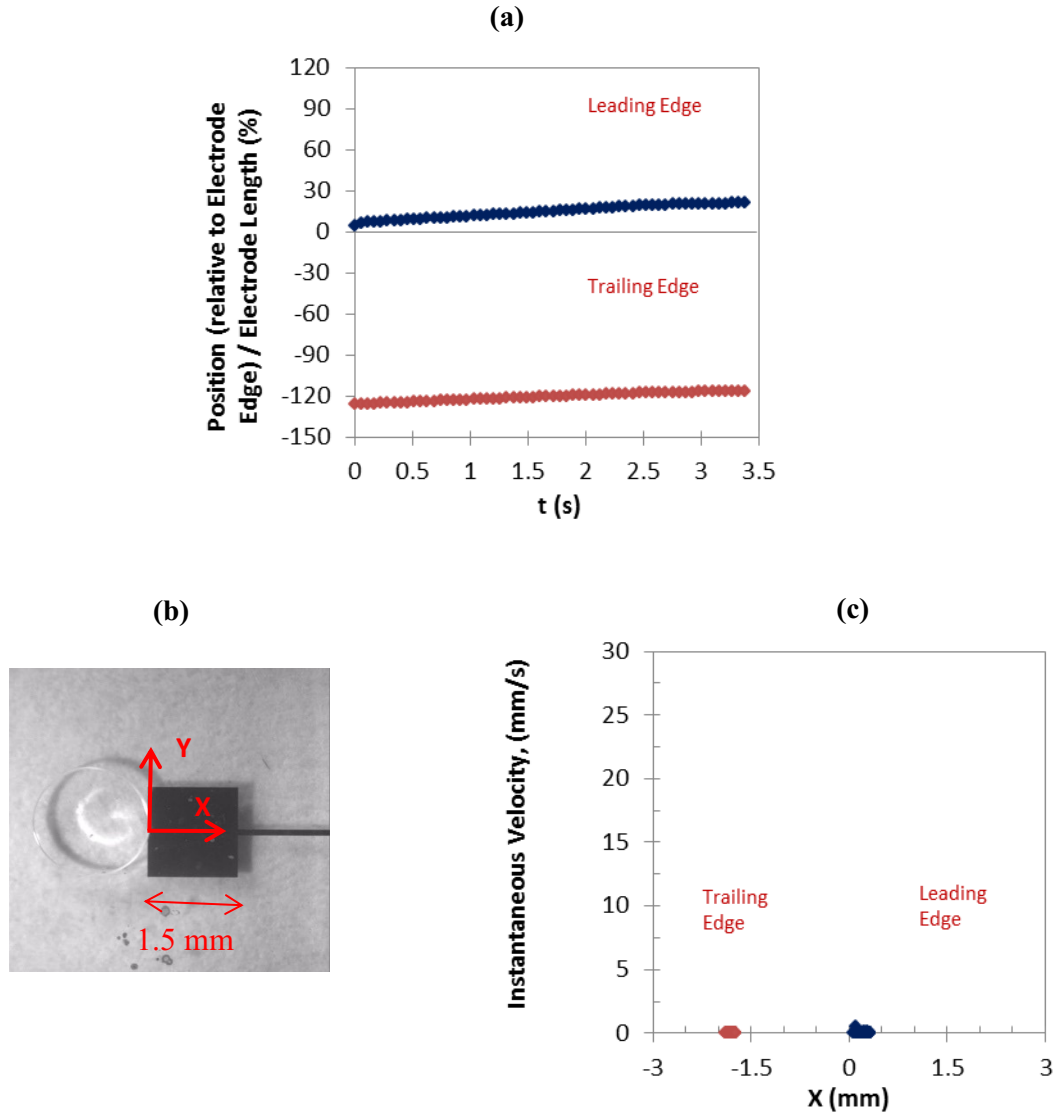


Figure H-40: Comparison of the average curves: (a) droplet elongation and (b) droplet position as a function of time, (d) instantaneous velocity as a function of droplet position as shown in (c) for the leading and trailing edges of the droplets of 4 $\mu\text{g/ml}$ DNA solution at 55 V.

H-9) 4 $\mu\text{g/ml}$ DNA Solution, 50 V

4 $\mu\text{g/ml}$ DNA solution, 50 V, Leading edge,

Accepted experiments and the average curves

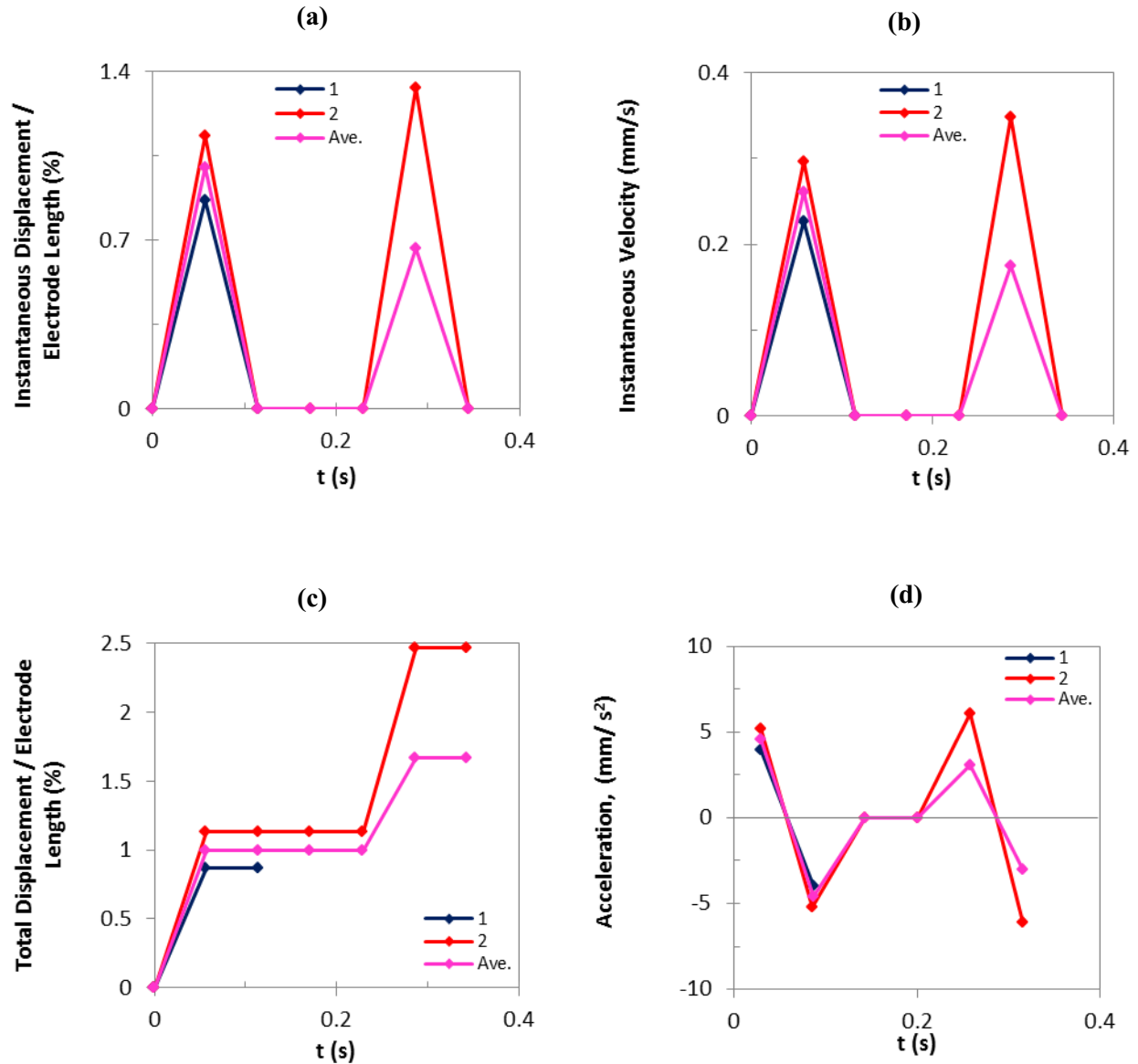


Figure H-41: (a) Instantaneous displacement, (b) instantaneous velocity, (c) total displacement, and (d) acceleration of the leading edges of the droplets of 4 $\mu\text{g/ml}$ DNA solution as a function of time at 50 V.

4 $\mu\text{g/ml}$ DNA solution, 50 V, Trailing edge,

Accepted experiments and the average curves

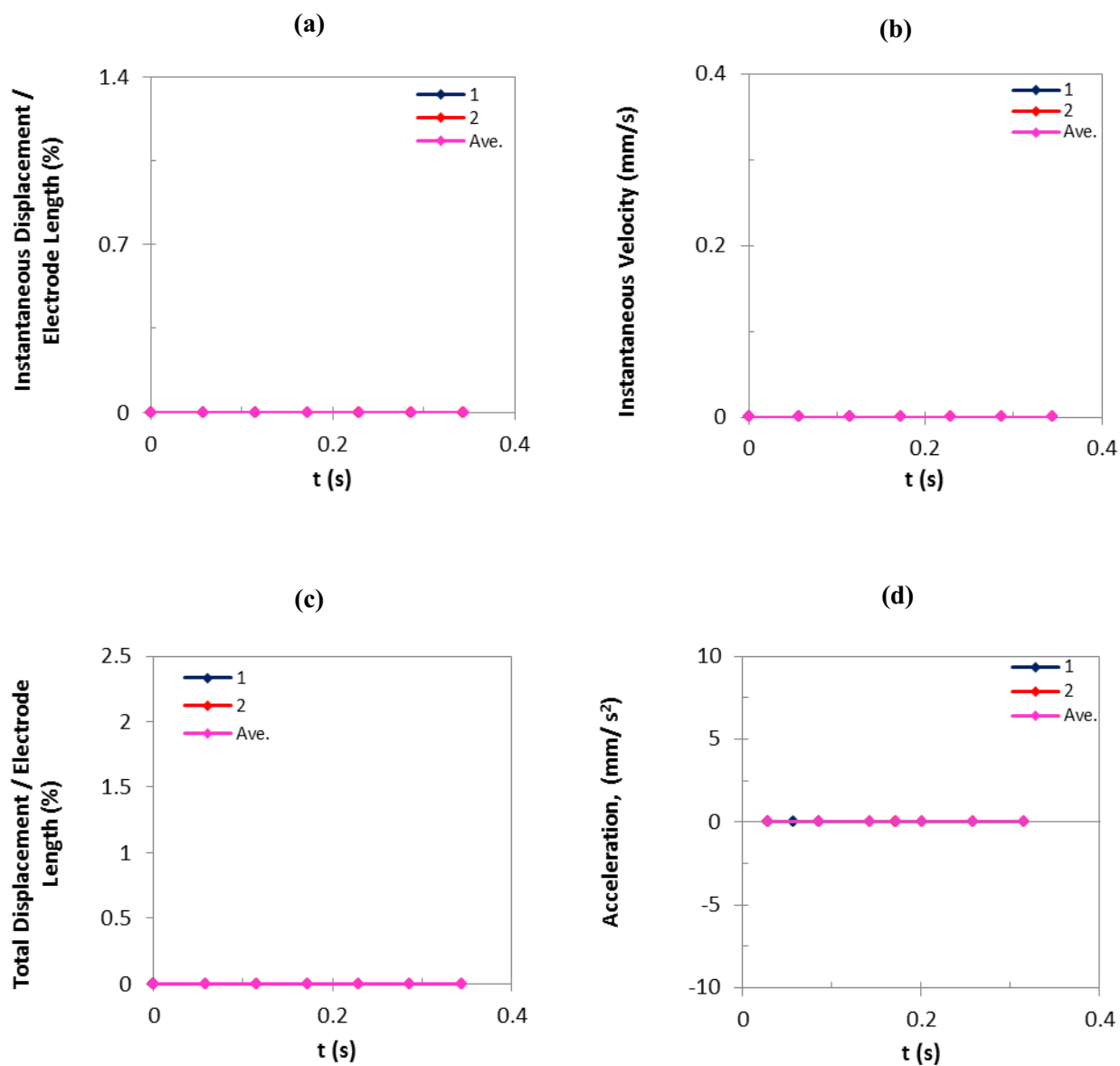


Figure H-42: (a) Instantaneous displacement, (b) instantaneous velocity, (c) total displacement, and (d) acceleration of the trailing edges of the droplets of 4 $\mu\text{g/ml}$ DNA solution as a function of time at 50 V.

4 $\mu\text{g}/\text{ml}$ DNA solution, 50 V

Accepted experiments and the average curves

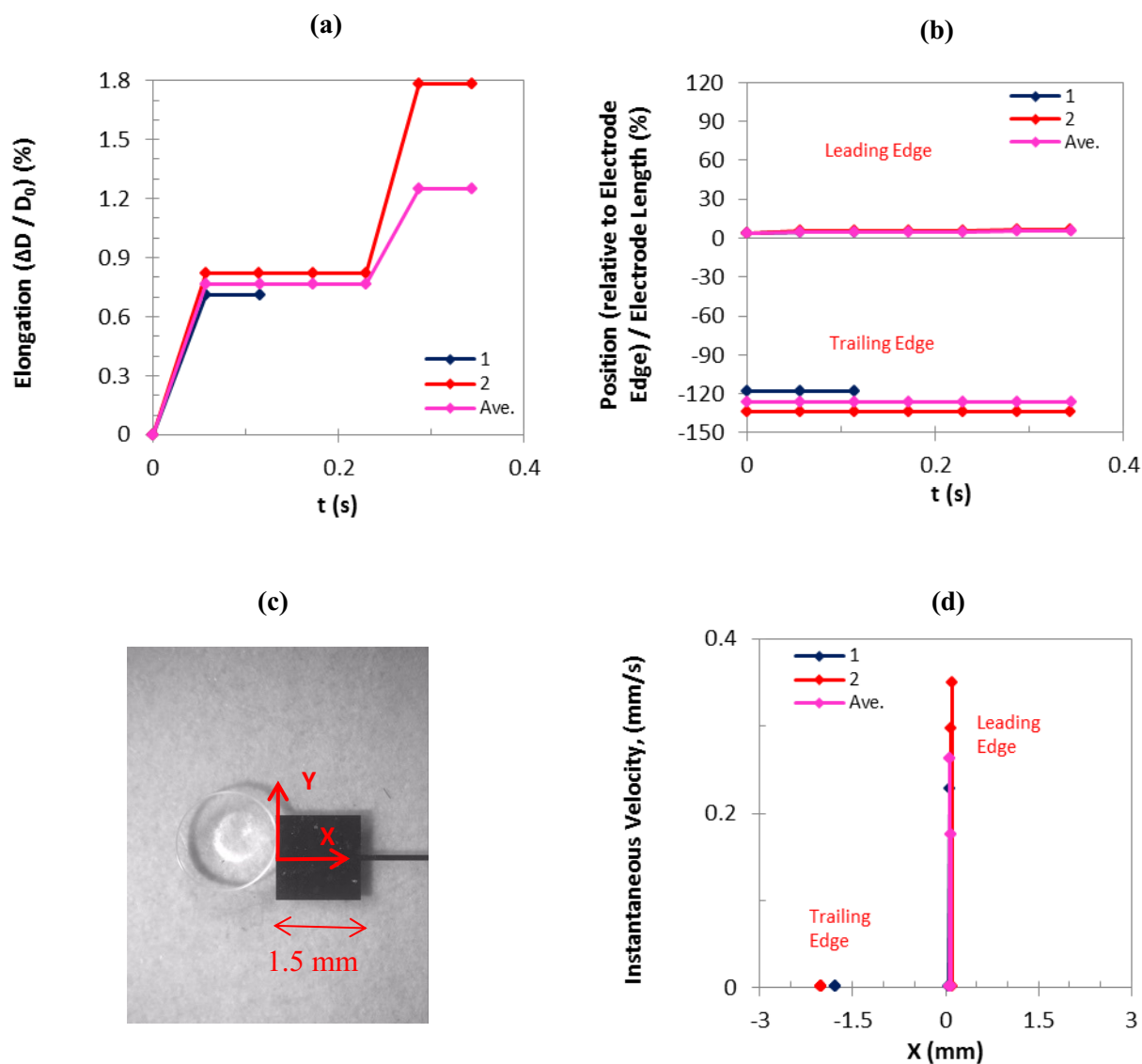


Figure H-43: (a) Droplet elongation, and (b) droplet position as a function of time, (d) instantaneous velocity as a function of droplet position as shown in (c) for the leading and trailing edges of the droplets of 4 $\mu\text{g}/\text{ml}$ DNA solution at 50 V.

4 $\mu\text{g}/\text{ml}$ DNA solution, 50 V, Average curves

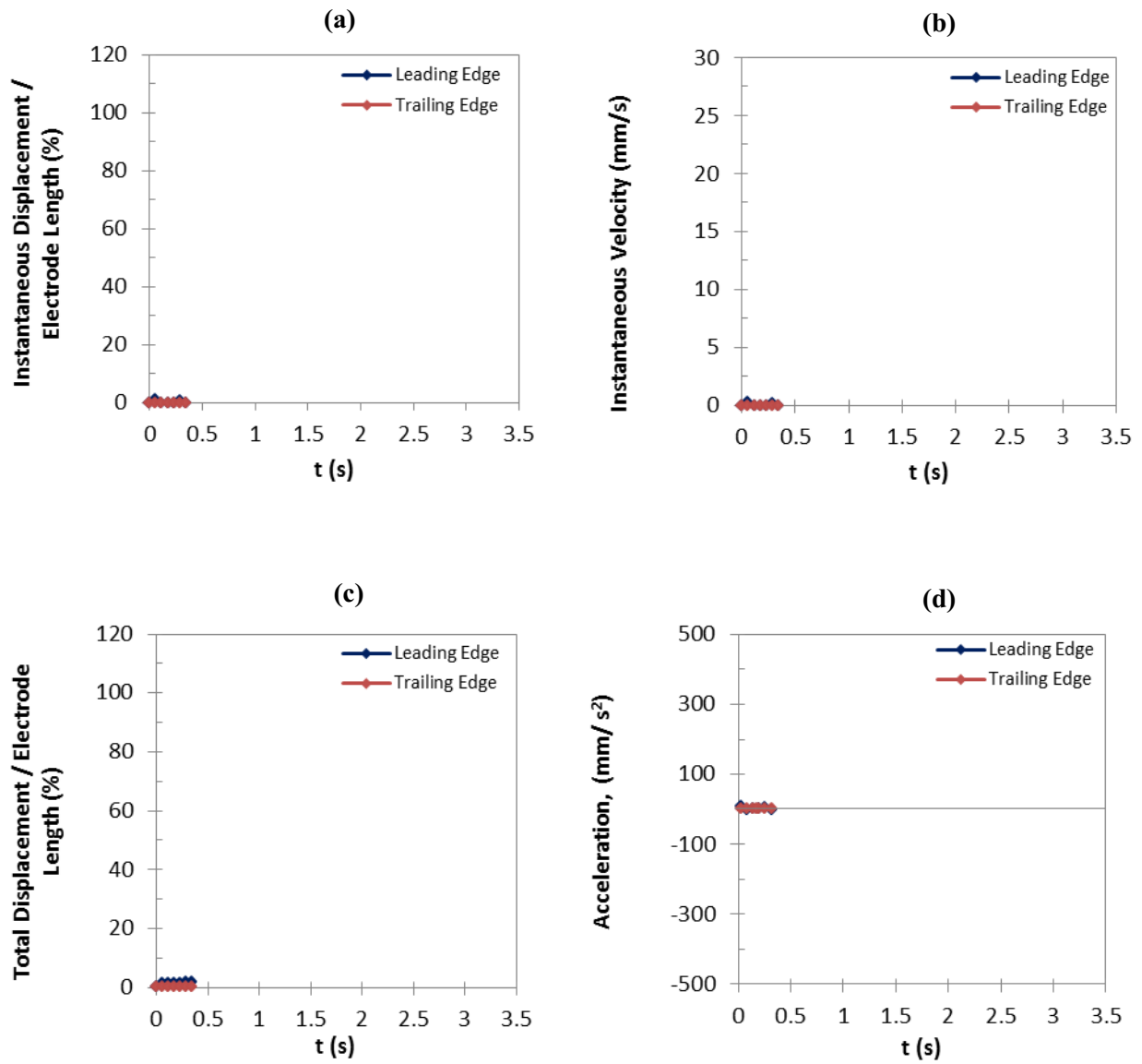


Figure H-44: Comparison of the average curves: (a) instantaneous displacement, (b) instantaneous velocity, (c) total displacement, and (d) acceleration, as a function of time for the leading and trailing edges of the droplets of 4 $\mu\text{g}/\text{ml}$ DNA solution at 50 V.

4 $\mu\text{g}/\text{ml}$ DNA solution, 50 V, Average curves

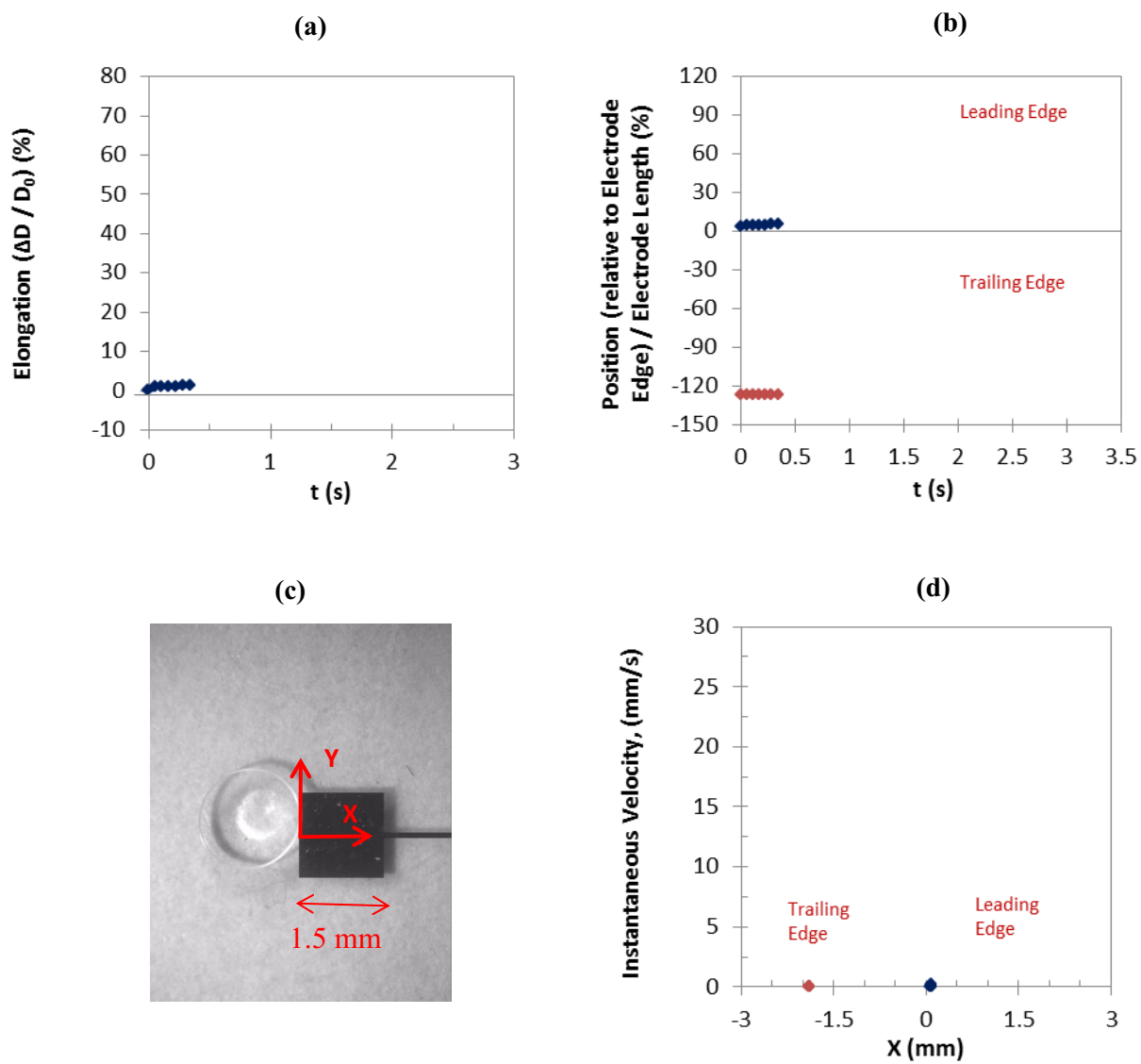


Figure H-45: Comparison of the average curves: (a) droplet elongation and (b) droplet position as a function of time, (d) instantaneous velocity as a function of droplet position as shown in (c) for the leading and trailing edges of the droplets of 4 $\mu\text{g}/\text{ml}$ DNA solution at 50 V.

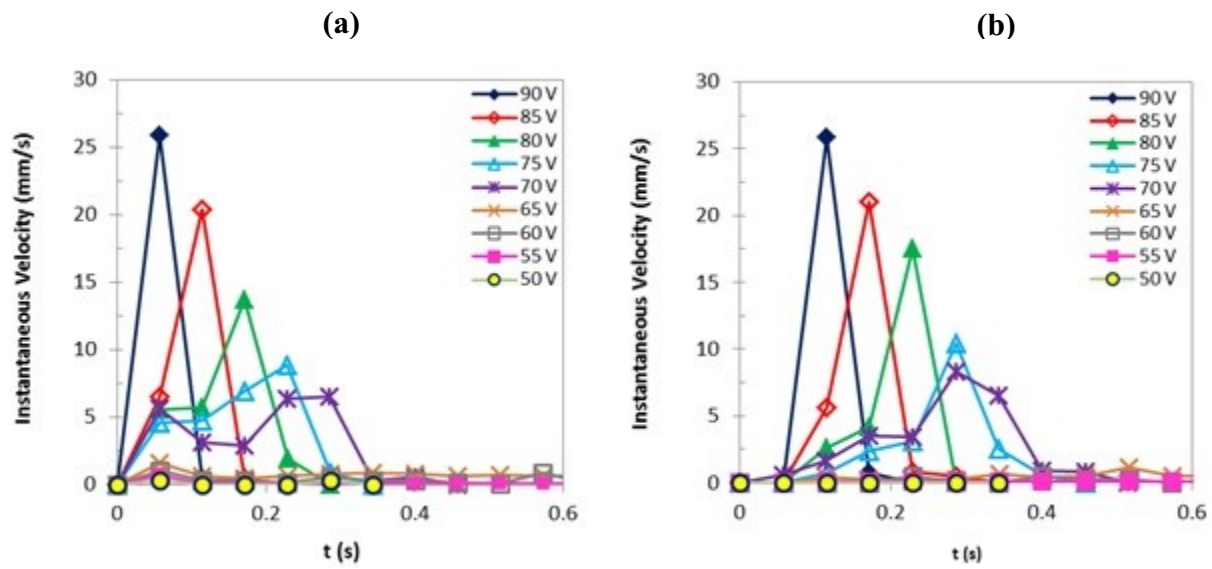


Figure H-46: The instantaneous velocity of the droplets of 4 $\mu\text{g/ml}$ DNA solutions as a function of time for the applied voltages of 50 to 90V. Comparison of results for the experiments with the highest leading edge instantaneous velocity: (a) leading edge, (b) trailing edge.

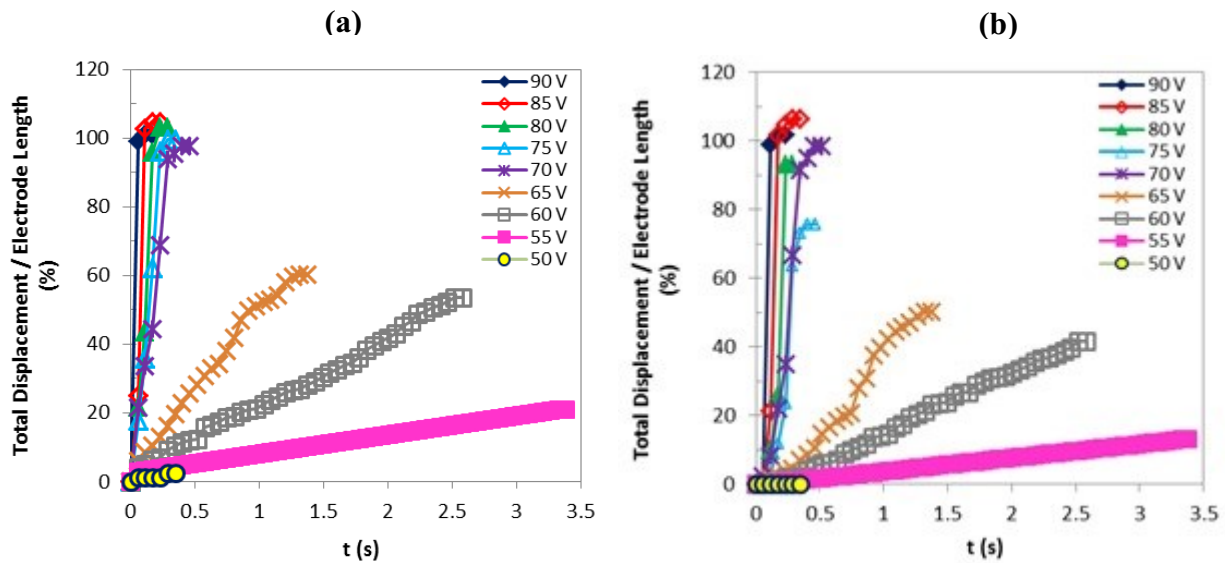


Figure H-47: The total displacement of the droplets of 4 $\mu\text{g/ml}$ DNA solutions as a function of time for the applied voltages of 50 to 90V. Comparison of results for the experiments with the highest leading edge instantaneous velocity: (a) leading edge, (b) trailing edge.

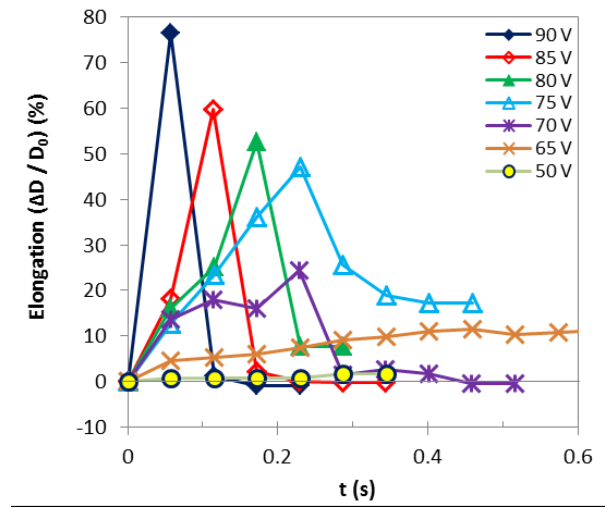


Figure H-48: The comparison of results for the elongation of the droplets of 4 μg/ml DNA solutions as a function of time for the experiments with the highest leading edge instantaneous velocity.

Table H-1: Peaks of the average curves, 4 $\mu\text{g/ml}$ DNA solution

Applied Voltage	90 V	85 V	80 V	75 V	70 V	65 V	60 V	55 V	50 V
Leading Edge									
Instantaneous Velocity (mm/s)	23.3	19.4	11.9	8.9	5.2	0.8	0.9	0.6	0.3
Total Displacement (normalized)	102%	105%	103%	100%	91%	59%	53%	17%	2%
Trailing Edge									
Instantaneous Velocity (mm/s)	25.4	19.5	10.7	10.5	5.9	1.1	0.5	0.1	0
Total Displacement (normalized)	100%	105%	93%	73%	91%	50%	42%	9.5%	0
Elongation (normalized)	67%	55%	50%	52%	21%	13.5%	-	-	0.8%

Table H-2: Peaks of the curves for the experiments with the highest leading edge instantaneous velocity, 4 µg/ml DNA solution

Applied Voltage	90 V	85 V	80 V	75 V	70 V	65 V	60 V	55 V	50 V
Leading Edge									
Instantaneous Velocity (mm/s)	25.9	20.5	13.7	8.9	6.6	1.3	1.1	0.8	0.4
Total Displacement (normalized)	99%	103%	103%	100%	98%	60%	48%	21%	2.5%
Trailing Edge									
Instantaneous Velocity (mm/s)	25.9	21.0	17.6	10.5	8.4	1.9	0.5	0.1	0
Total Displacement (normalized)	99%	105%	93%	73%	92%	50%	42%	13%	0
Elongation (normalized)	76%	60%	53%	52%	24%	13.3%	-	-	1.8%

Table H-3: Average velocity for all experiments, 4 $\mu\text{g/ml}$ DNA solution

Leading Edge									
Average Velocity (mm/s)	23.3	13.4	7.5	5.2	3.3	0.5	0.3	0.1	0.2
Trailing Edge									
Average Velocity (mm/s)	12.7	8.9	5.2	3.4	2.5	0.4	0.2	0.1	0

Table H-4: Average velocity for the experiments with the highest leading edge instantaneous velocity, 4 $\mu\text{g/ml}$ DNA solution

Leading Edge									
Average Velocity (mm/s)	25.5	13.5	8.4	5.2	3.7	0.7	0.3	0.1	0.1
Trailing Edge									
Average Velocity (mm/s)	13.0	8.9	6.1	3.4	2.9	0.6	0.3	0.1	0

4 $\mu\text{g/ml}$ DNA solution, Leading edge

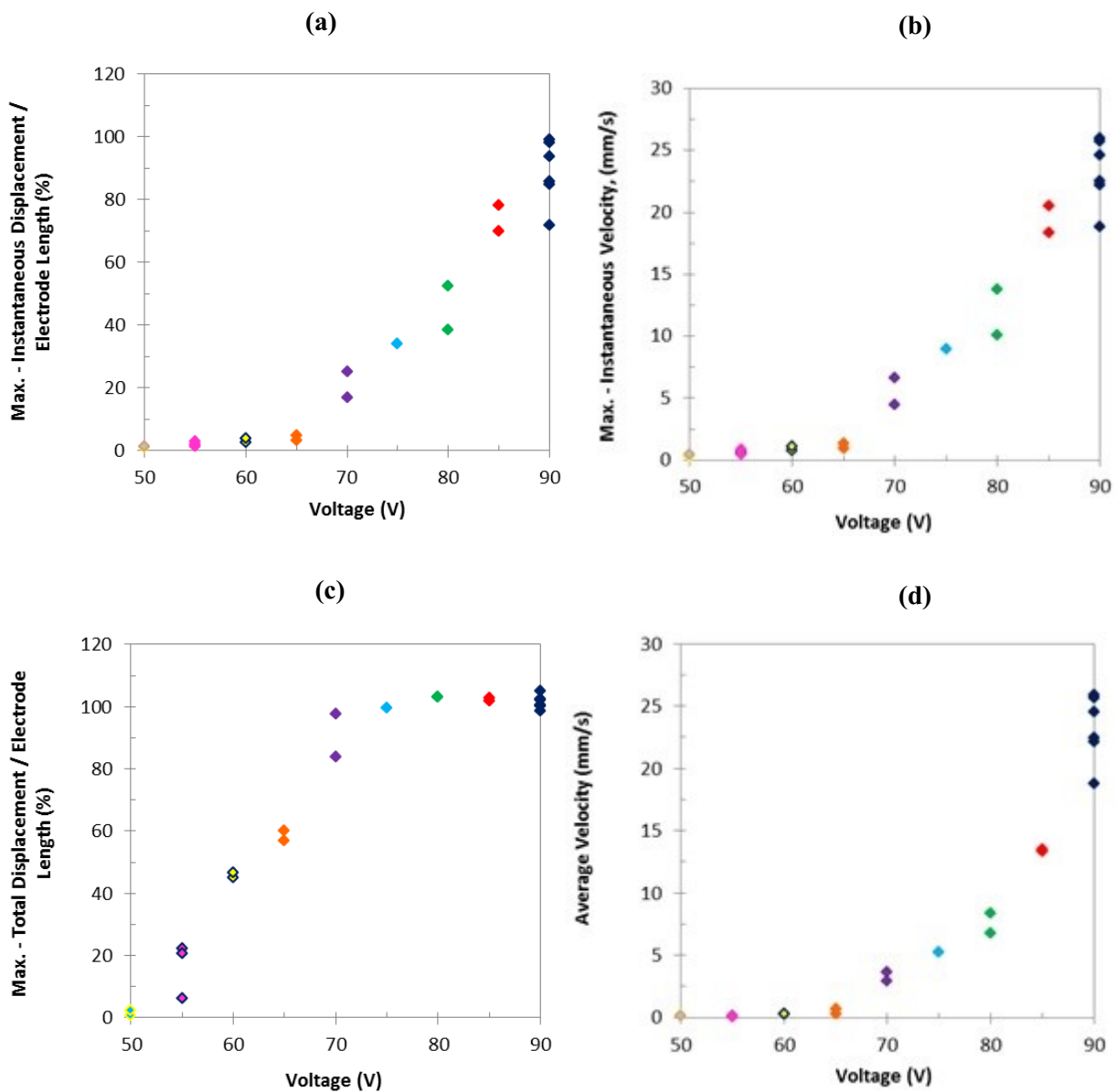


Figure H-49: Changes of the max.: (a) instantaneous displacement, (b) instantaneous velocity, (c) total displacement, and (d) average velocity with the applied voltage for the leading edges of the droplets of 4 $\mu\text{g/ml}$ DNA solution.

4 $\mu\text{g/ml}$ DNA solution, Trailing edge

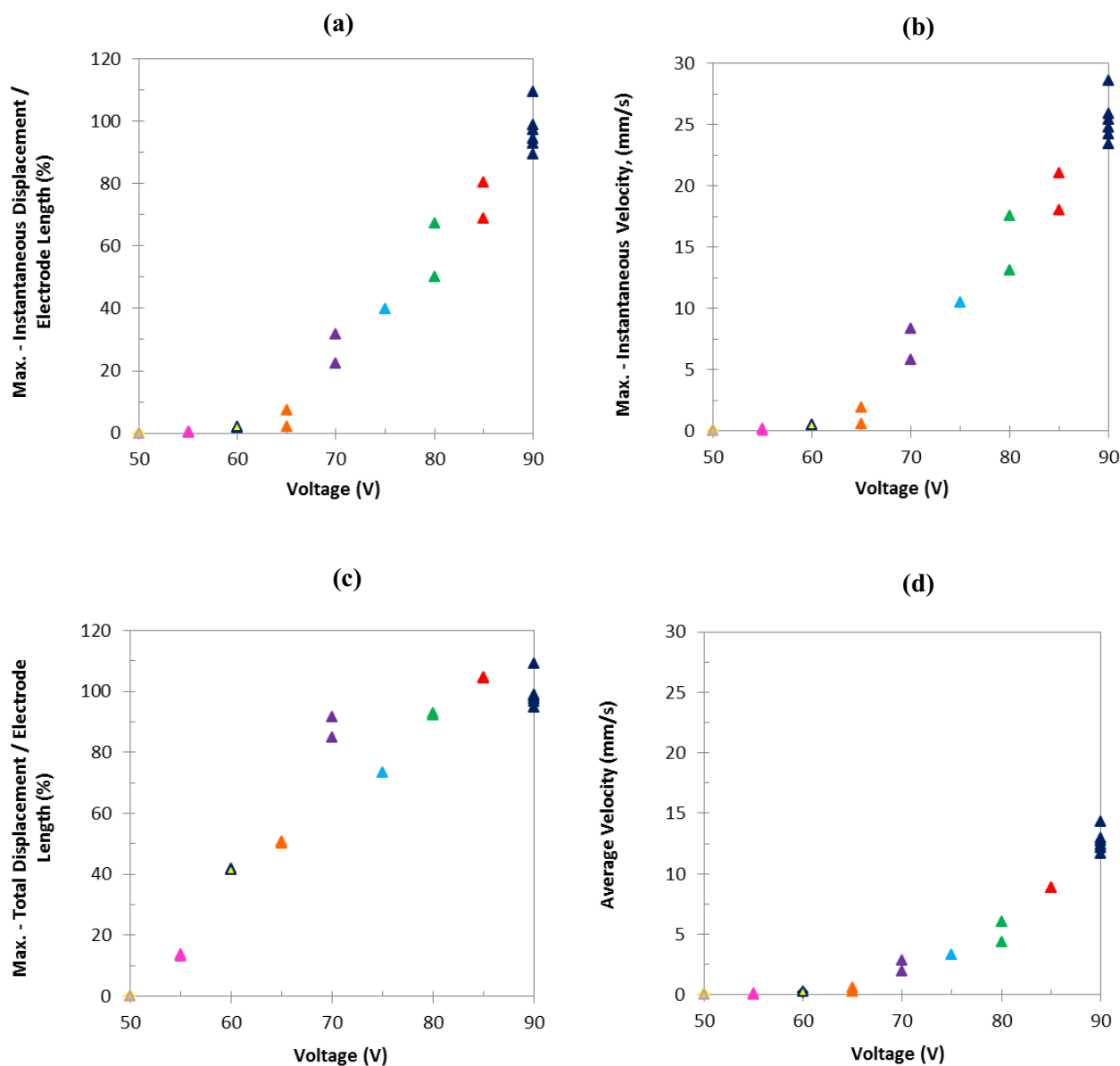


Figure H-50: Changes of the max.: (a) instantaneous displacement, (b) instantaneous velocity, (c) total displacement, and (d) average velocity with the applied voltage for the trailing edges of the droplets of 4 $\mu\text{g/ml}$ DNA solution.

4 $\mu\text{g/ml}$ DNA solution

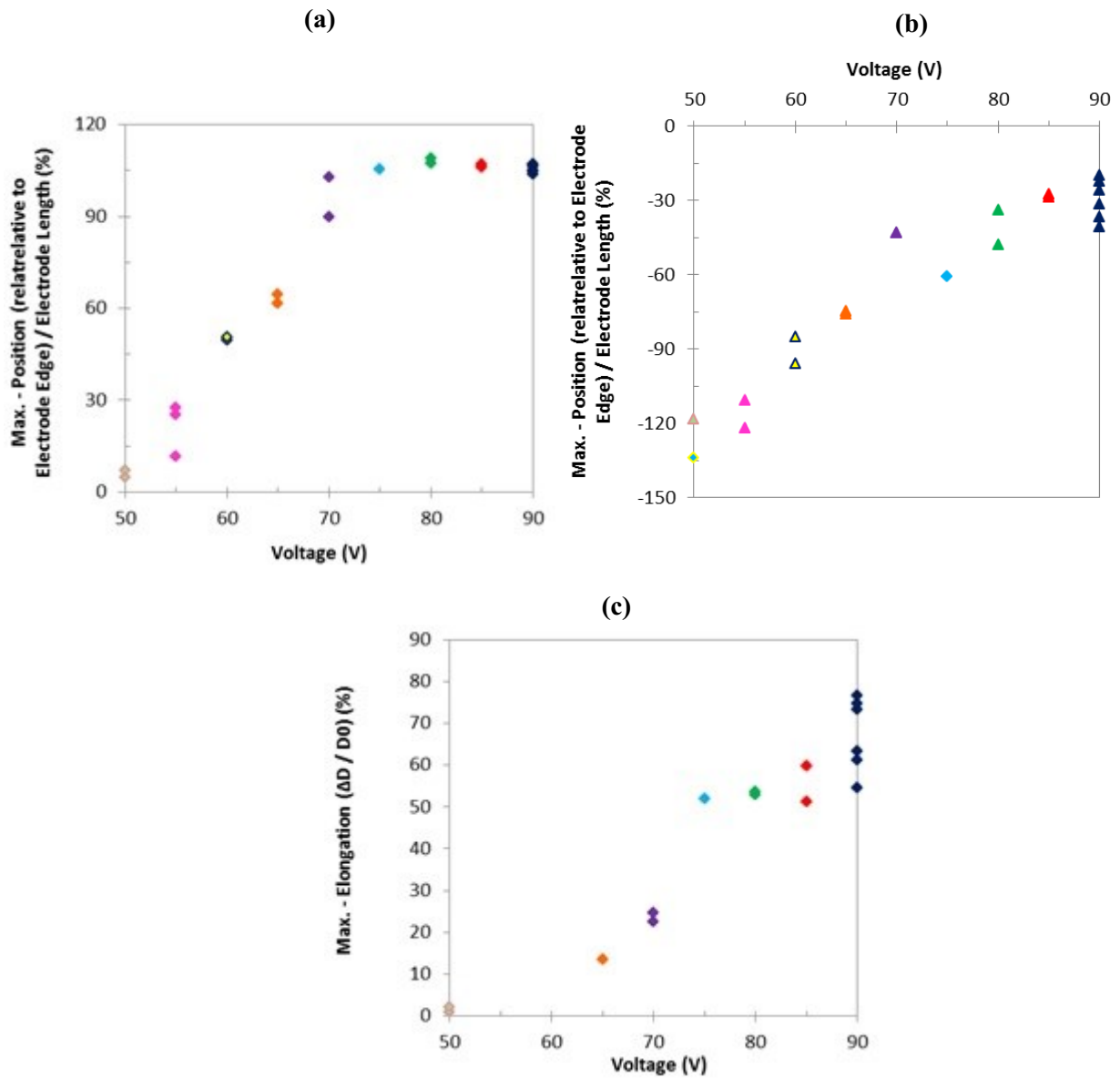
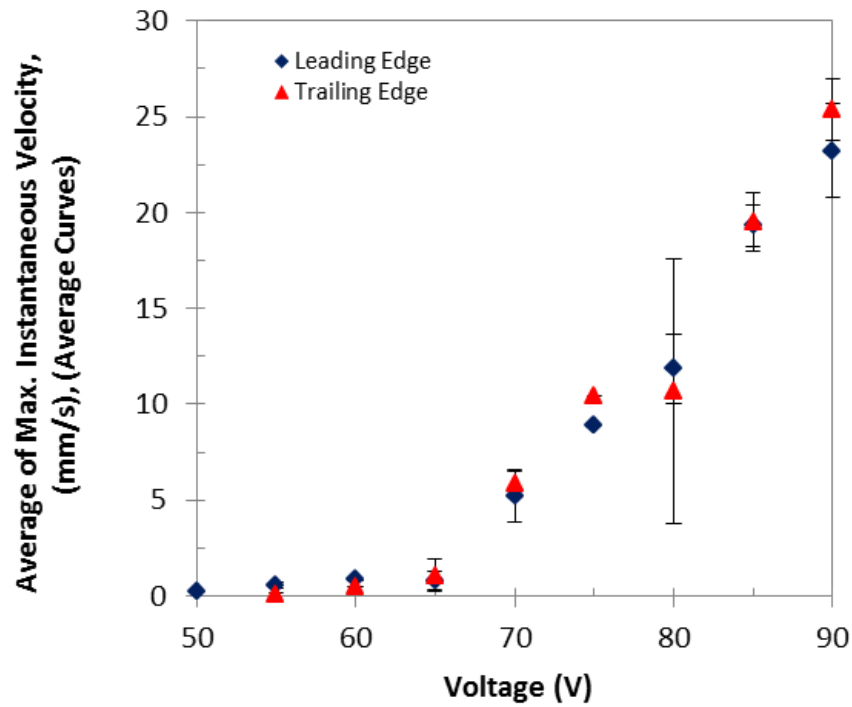
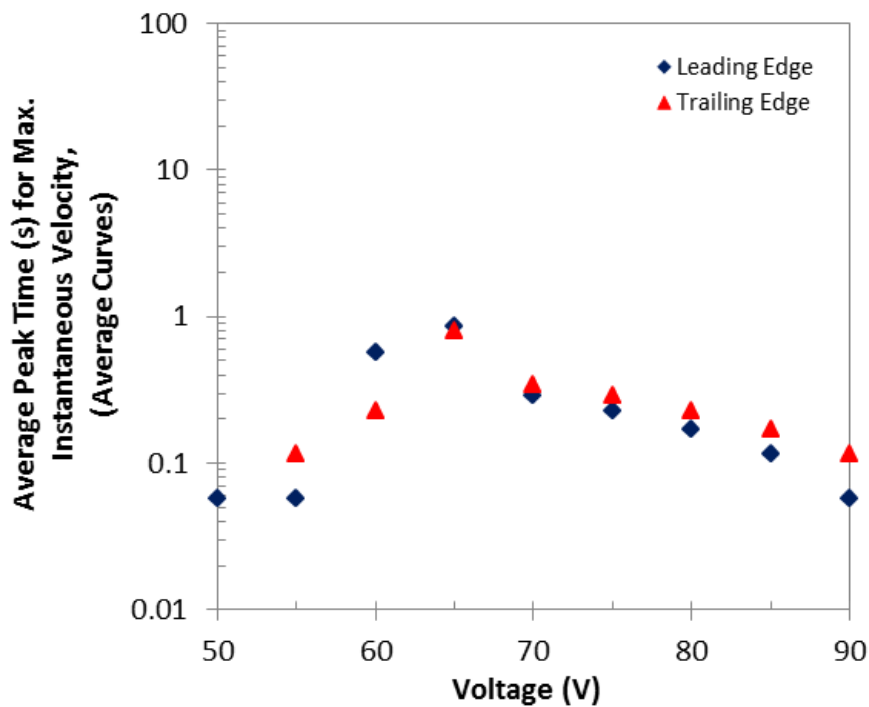


Figure H-51: Changes of the max.: (a) position of the leading edge, (b) position of the trailing edge, (c) elongation, with the applied voltage for the droplets of 4 $\mu\text{g/ml}$ DNA solution.



(a)



(b)

Figure H-52: The average of: (a) max. instantaneous velocity, and (b) peak time for max. instantaneous velocity, as a function of voltage for the leading and trailing edges of the droplets of 4 $\mu\text{g/ml}$ DNA solution. The error bars indicate standard deviation.

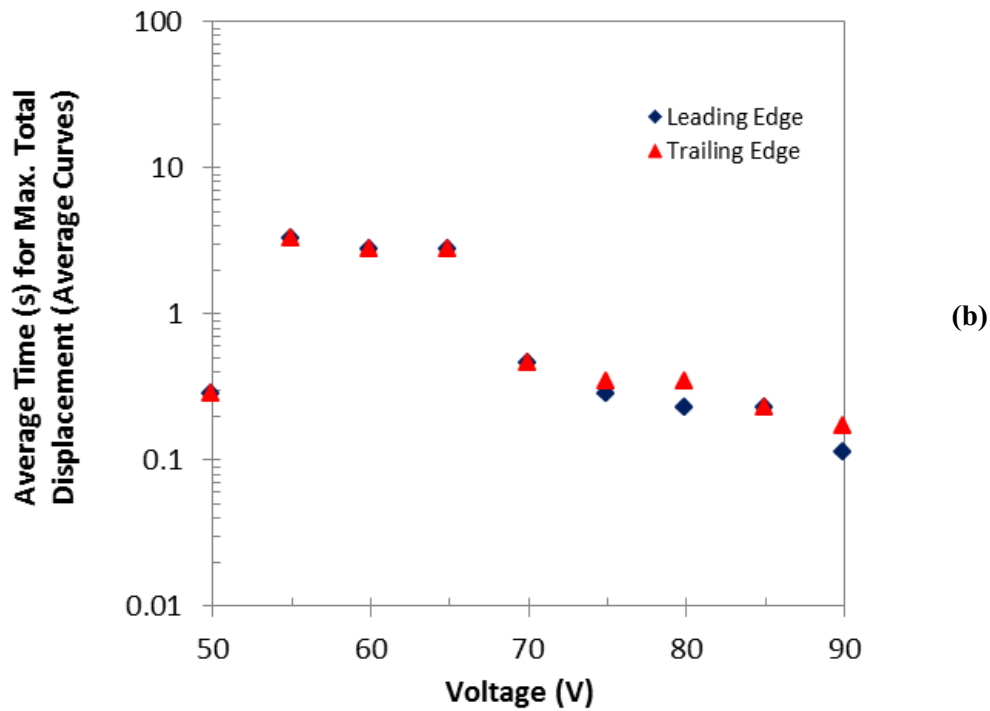
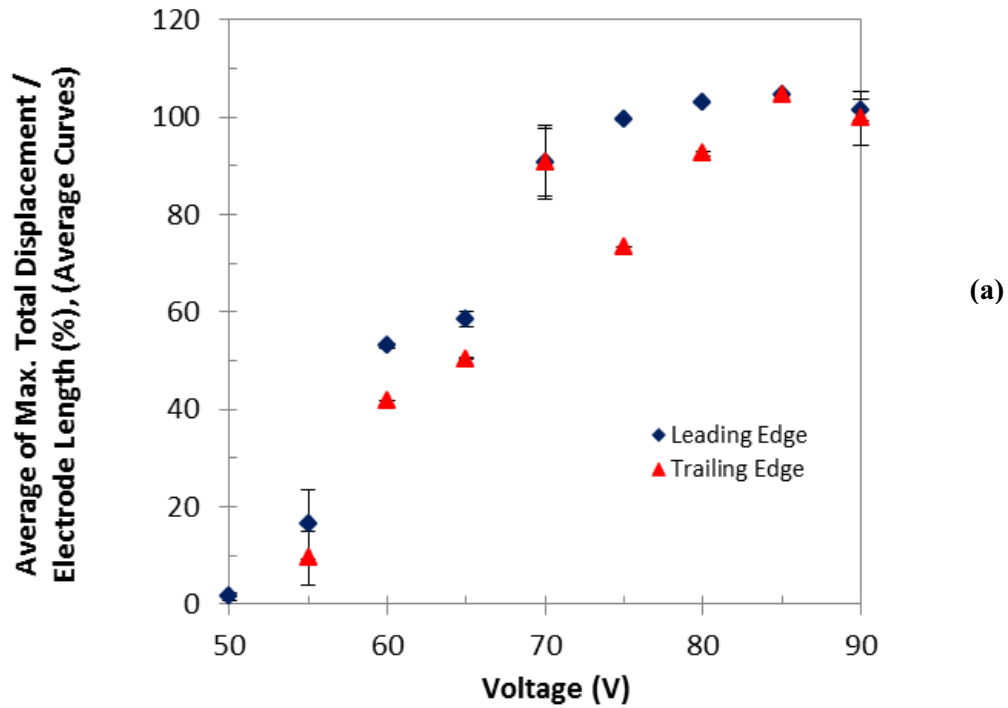


Figure H-53: The average of: (a) max. total displacement, and (b) transition time, as a function of voltage for the leading and trailing edges of the droplets of 4 $\mu\text{g/ml}$ DNA solution. The error bars indicate standard deviation.

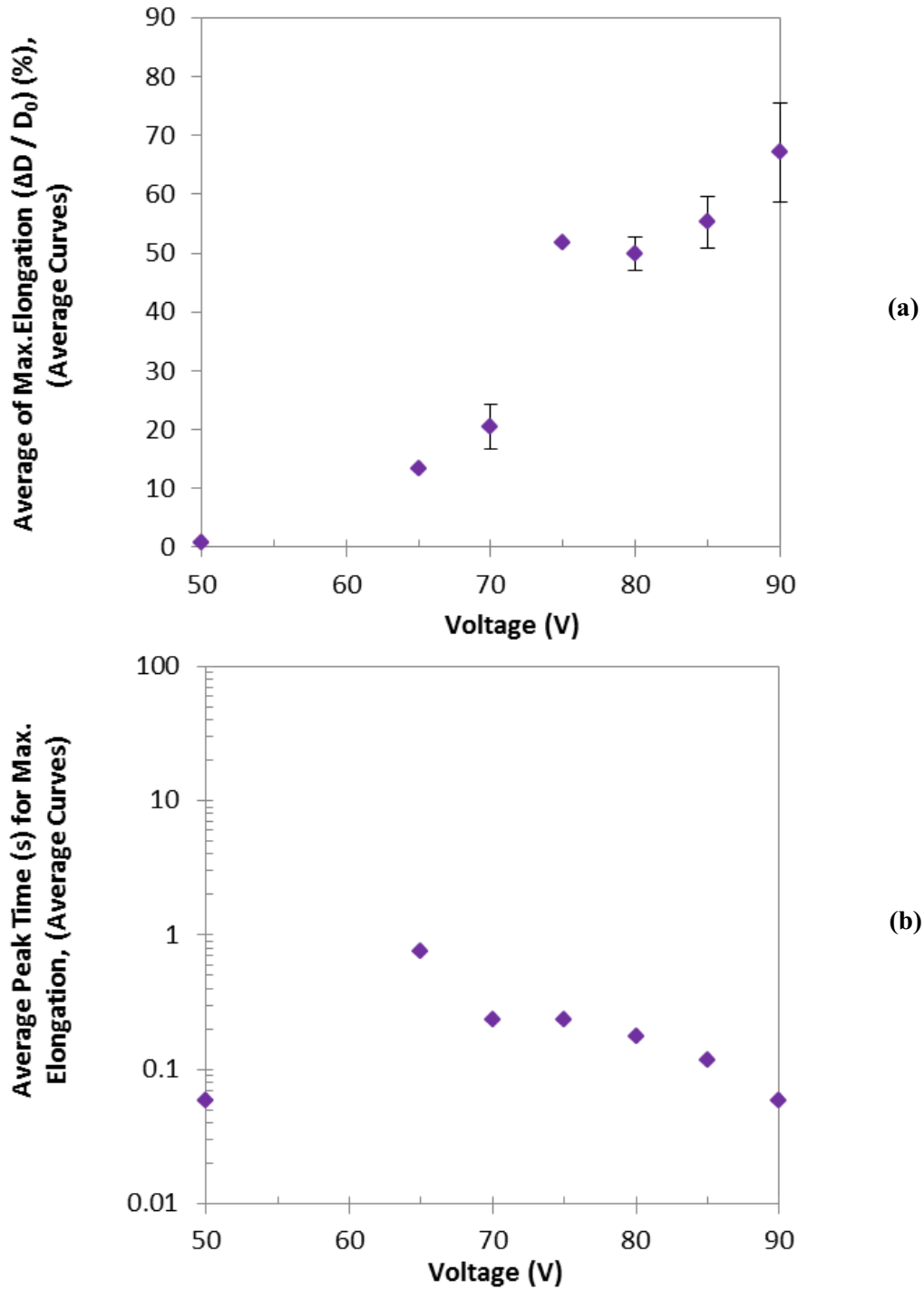


Figure H-54: The average of: (a) max. elongation, and (b) peak time for max. elongation, as a function of voltage for the droplets of 4 $\mu\text{g/ml}$ DNA solution. The error bars indicate standard deviation.

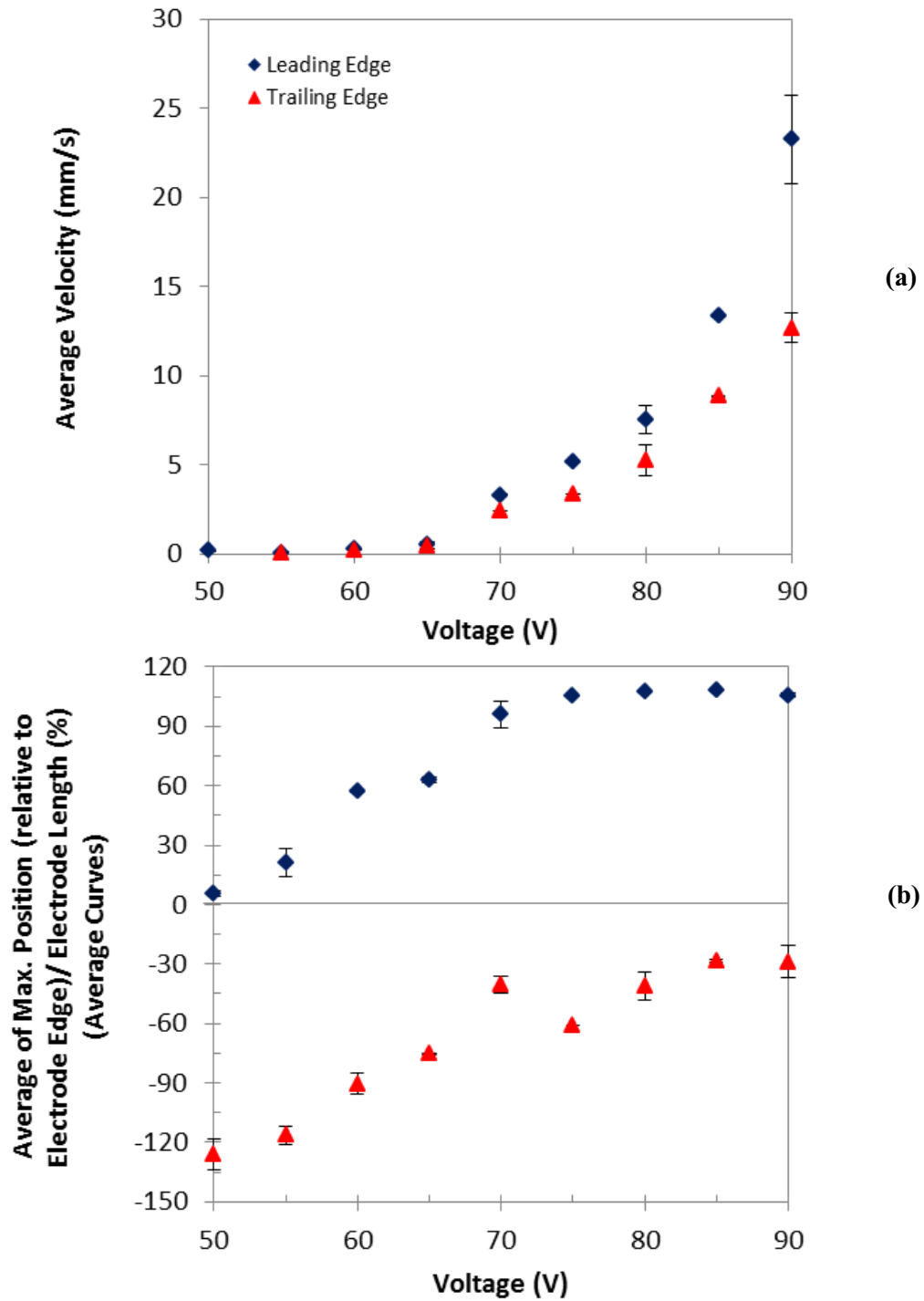


Figure H-55: (a) The average velocity, and (b) the average position, as a function of voltage for the leading and trailing edges of the droplets of 4 $\mu\text{g/ml}$ DNA solution. The error bars indicate standard deviation.

Appendix I

20 $\mu\text{g}/\text{ml}$ DNA Solution

I-1) 20 $\mu\text{g/ml}$ DNA solution, 90 V

20 $\mu\text{g/ml}$ DNA solution, 90 V, Leading edge,

Accepted experiments and the average curves

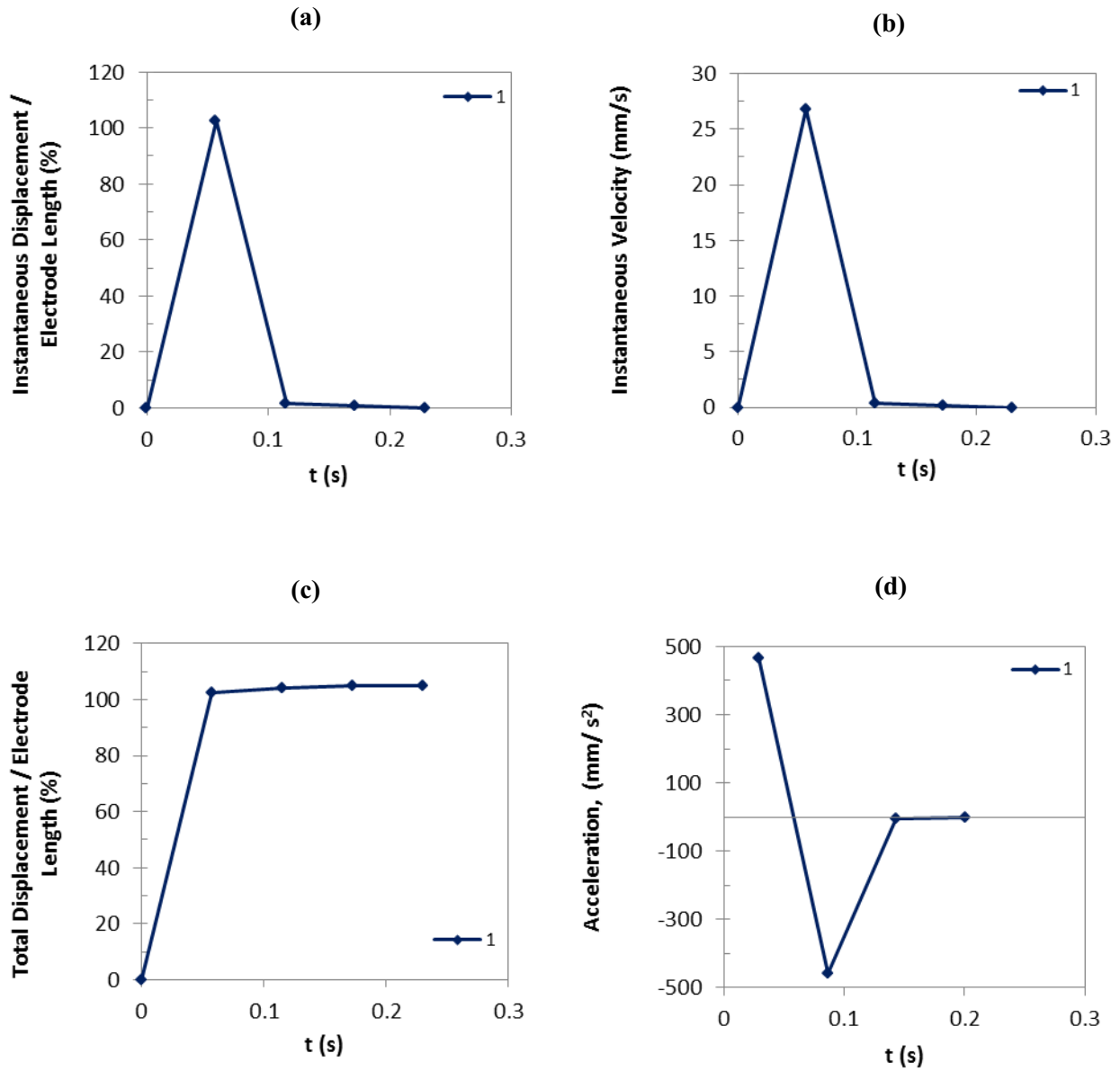


Figure I-1: (a) Instantaneous displacement, (b) instantaneous velocity, (c) total displacement, and (d) acceleration of the leading edges of the droplets of 20 $\mu\text{g/ml}$ DNA solution at 90 V.

20 $\mu\text{g/ml}$ DNA solution, 90 V, Trailing edge,

Accepted experiments and the average curves

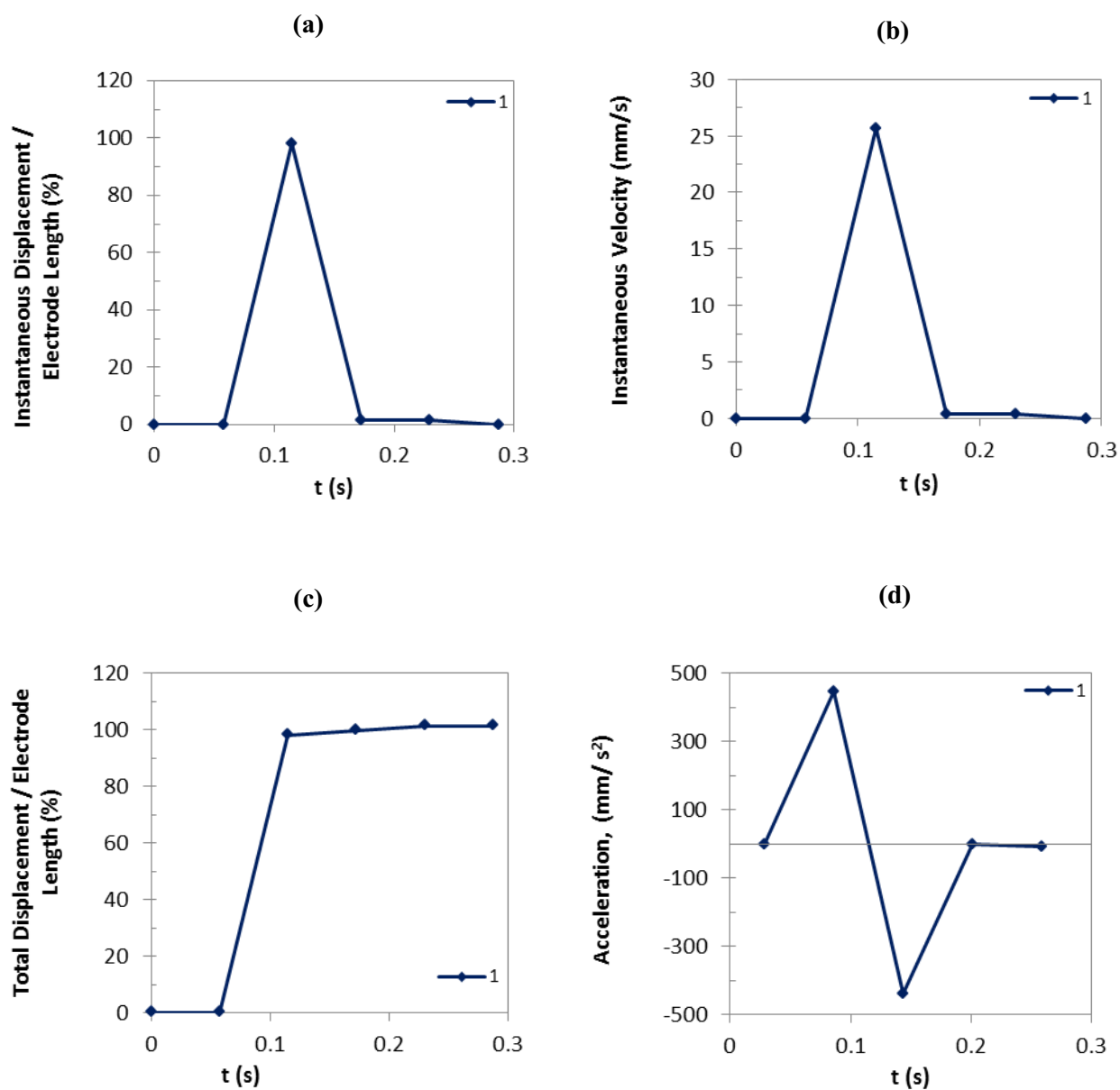


Figure I-2: (a) Instantaneous displacement, (b) instantaneous velocity, (c) total displacement, and (d) acceleration of the trailing edges of the droplets of 20 $\mu\text{g/ml}$ DNA solution at 90 V.

20 $\mu\text{g/ml}$ DNA solution, 90 V

Accepted experiments and the average curves

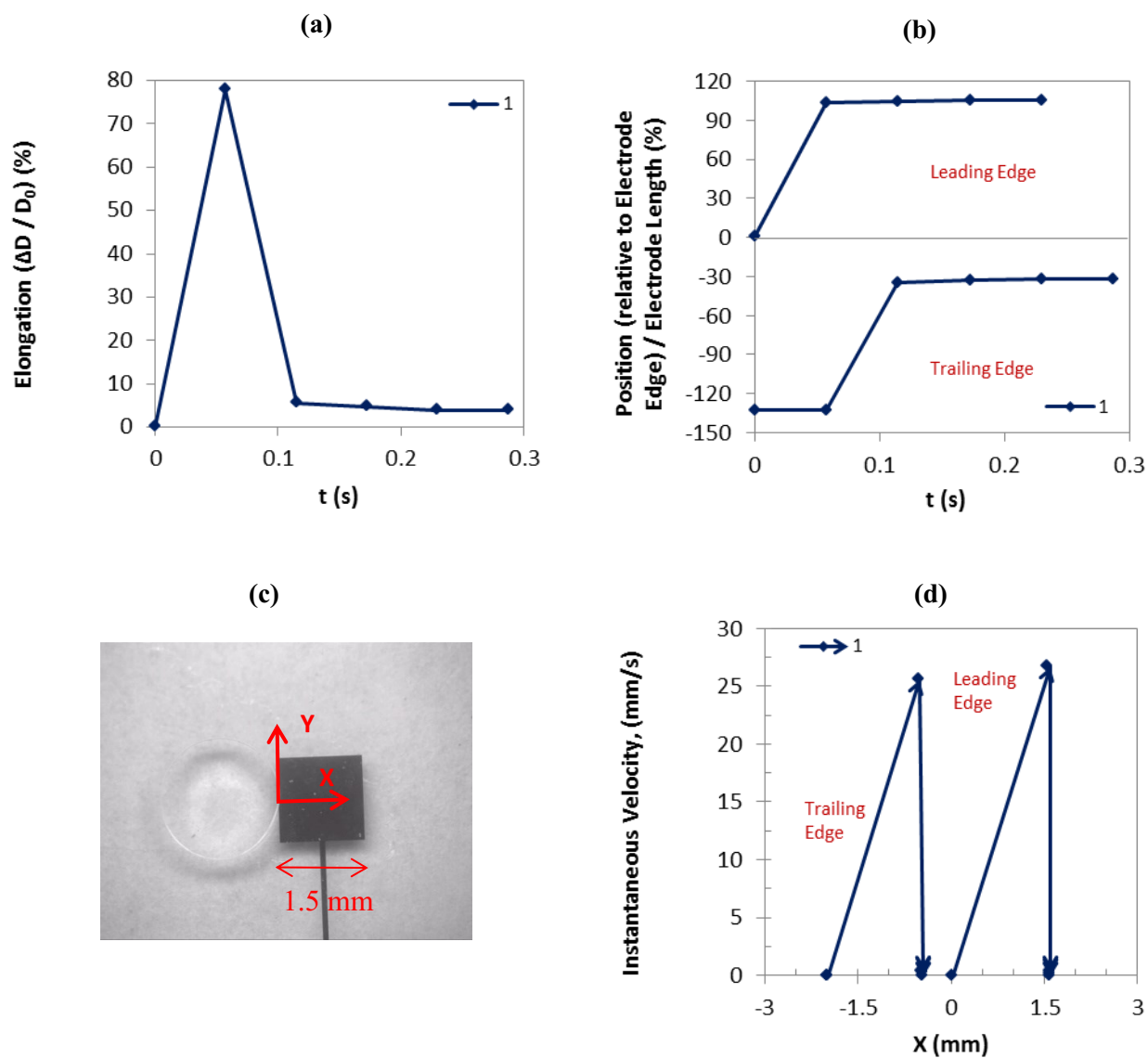


Figure I-3: (a) Droplet elongation, and (b) droplet position as a function of time, (d) instantaneous velocity as a function of droplet position as shown in (c) for the leading and trailing edges of the droplets of 20 $\mu\text{g/ml}$ DNA solution at 90 V. The arrows in graph (d) indicate the changes of velocity along the direction of movement.

20 $\mu\text{g/ml}$ solution, 90 V, Average curves

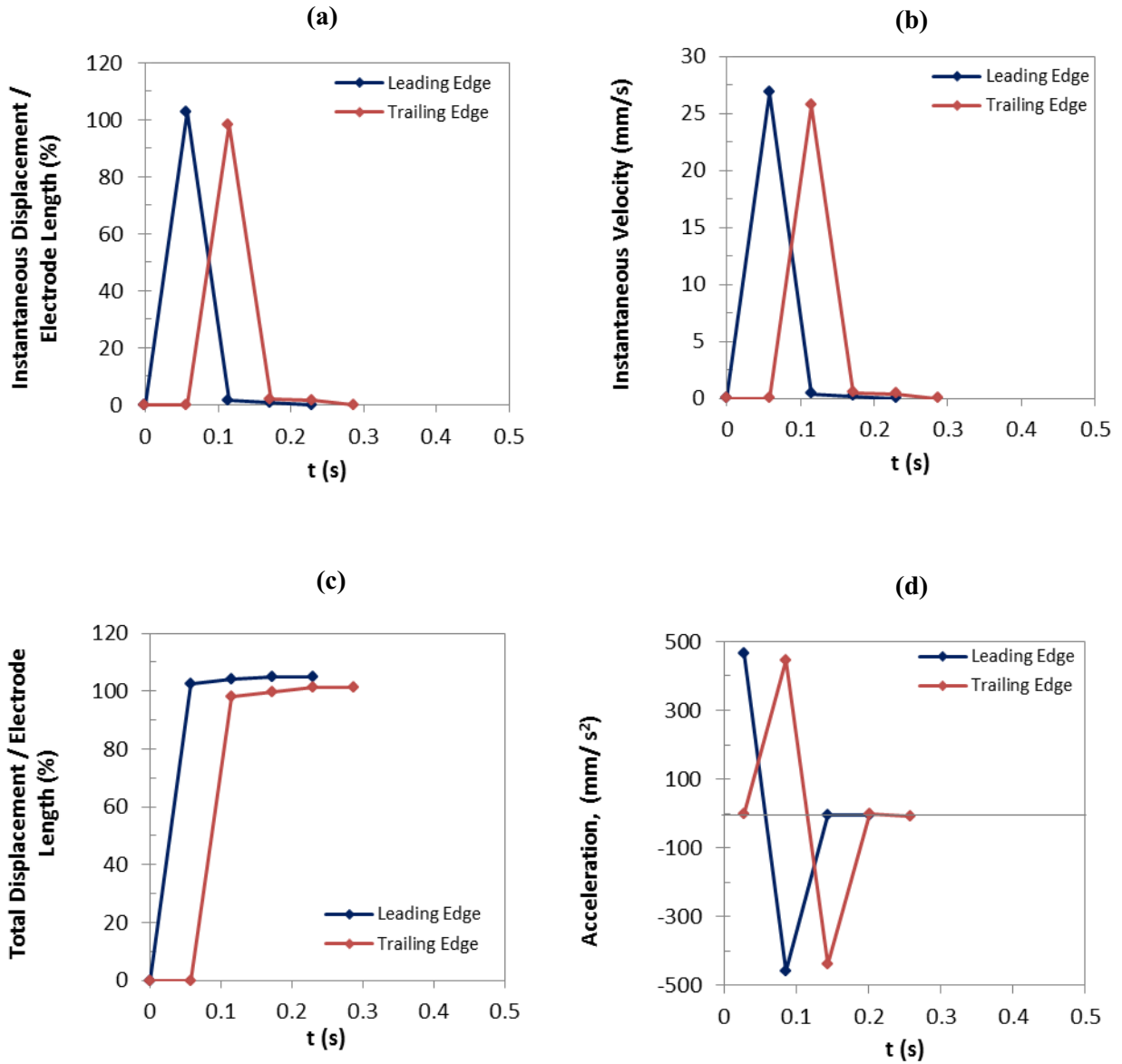


Figure I-4: Comparison of the average curves: (a) instantaneous displacement, (b) instantaneous velocity, (c) total displacement, and (d) acceleration, as a function of time for the leading and trailing edges of the droplets of 20 $\mu\text{g/ml}$ DNA solution at 90 V.

20 $\mu\text{g/ml}$ DNA solution, 90 V, Average curves

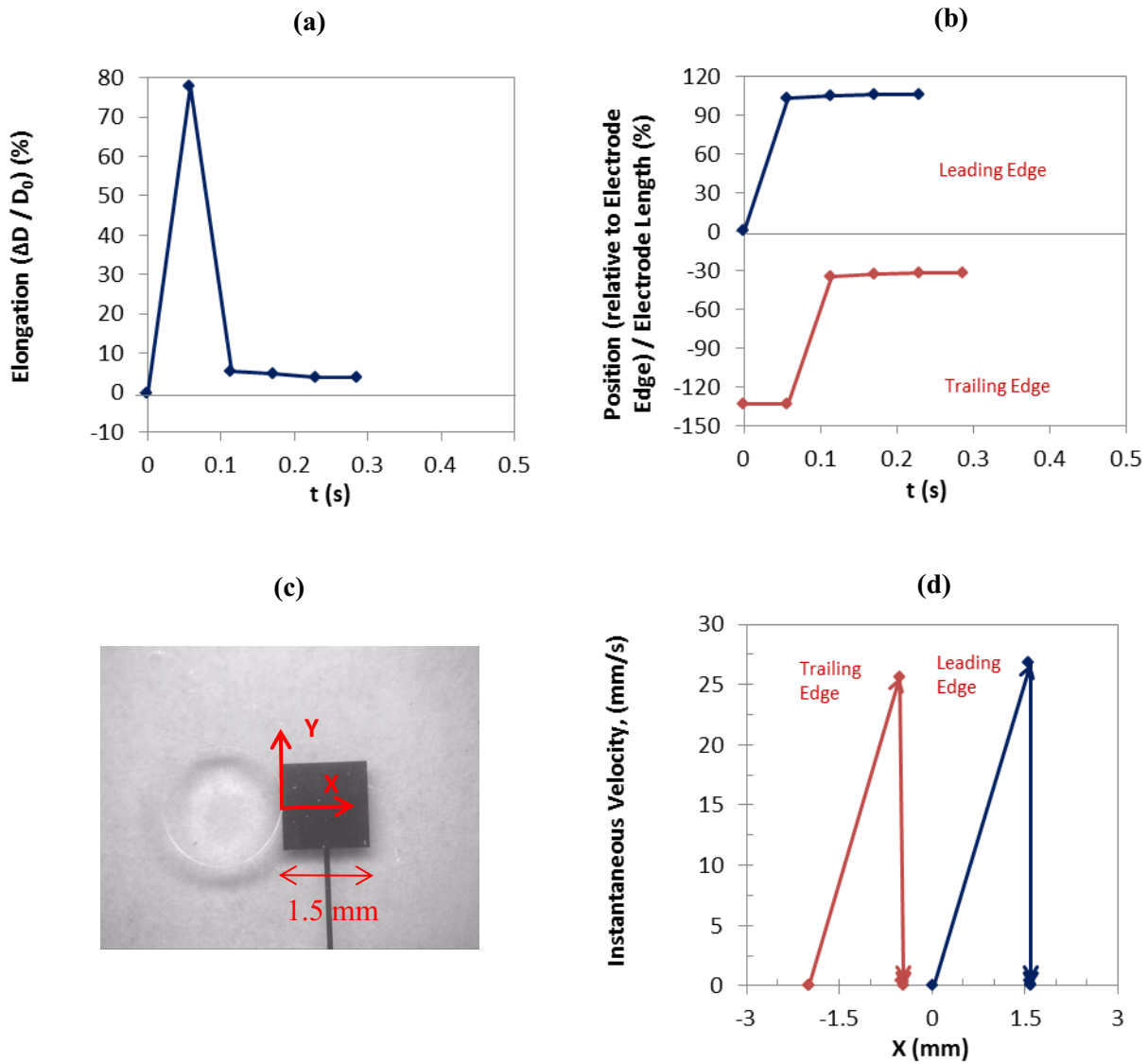


Figure I-5: Comparison of the average curves: (a) droplet elongation and (b) droplet position as a function of time, (d) instantaneous velocity as a function of droplet position as shown in (c) for the leading and trailing edges of the droplets of 20 $\mu\text{g/ml}$ DNA solution at 90 V. The arrows in graph (d) indicate the changes of velocity along the direction of movement.

I-2) 20 $\mu\text{g/ml}$ DNA solution, 85 V

20 $\mu\text{g/ml}$ DNA solution, 85 V, Leading edge,

Accepted experiments and the average curves

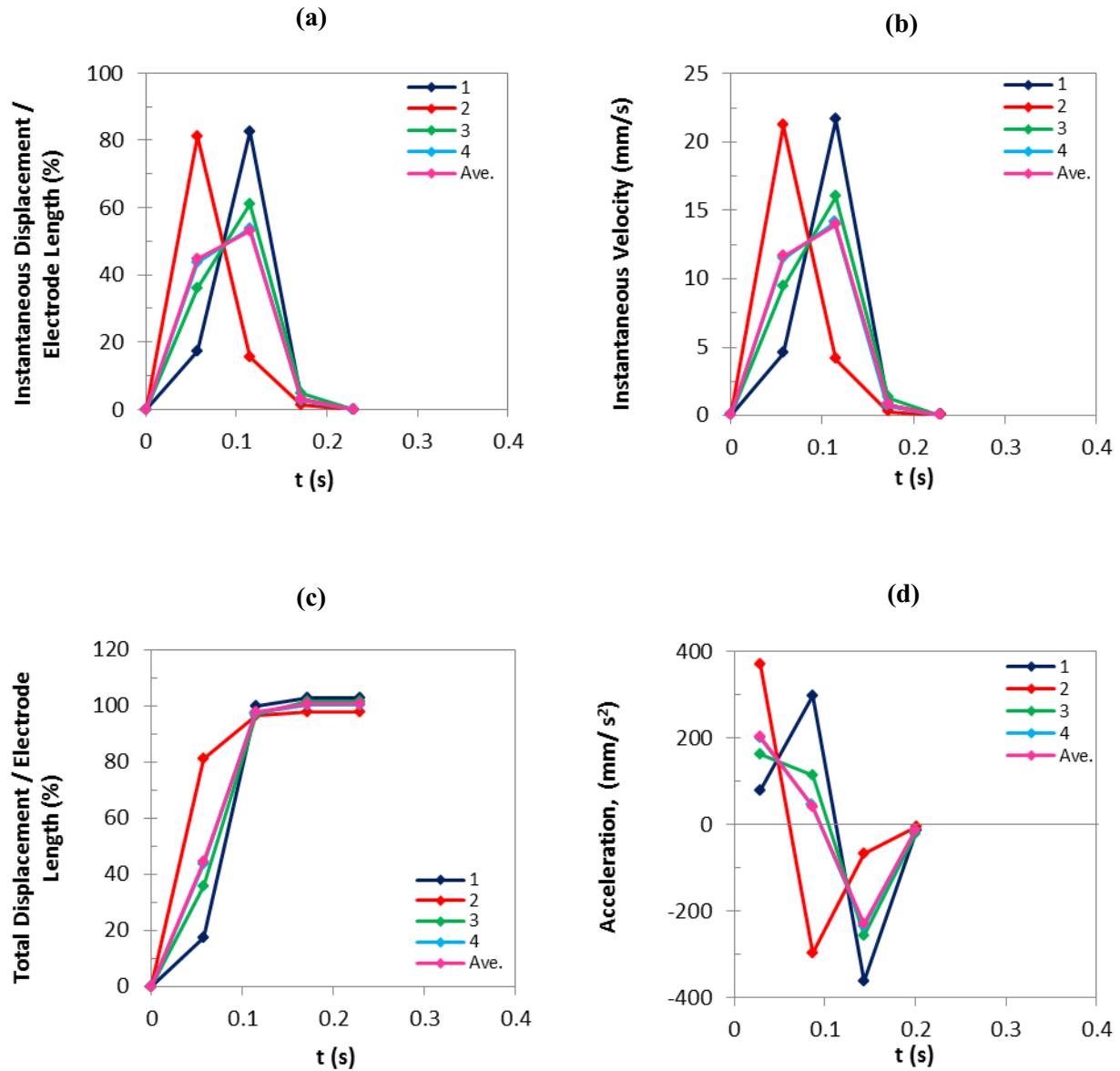


Figure I-6: (a) Instantaneous displacement, (b) instantaneous velocity, (c) total displacement, and (d) acceleration of the leading edges of the droplets of 20 $\mu\text{g/ml}$ DNA solution at 85 V.

20 $\mu\text{g/ml}$ DNA solution, 85 V, Trailing edge,

Accepted experiments and the average curves

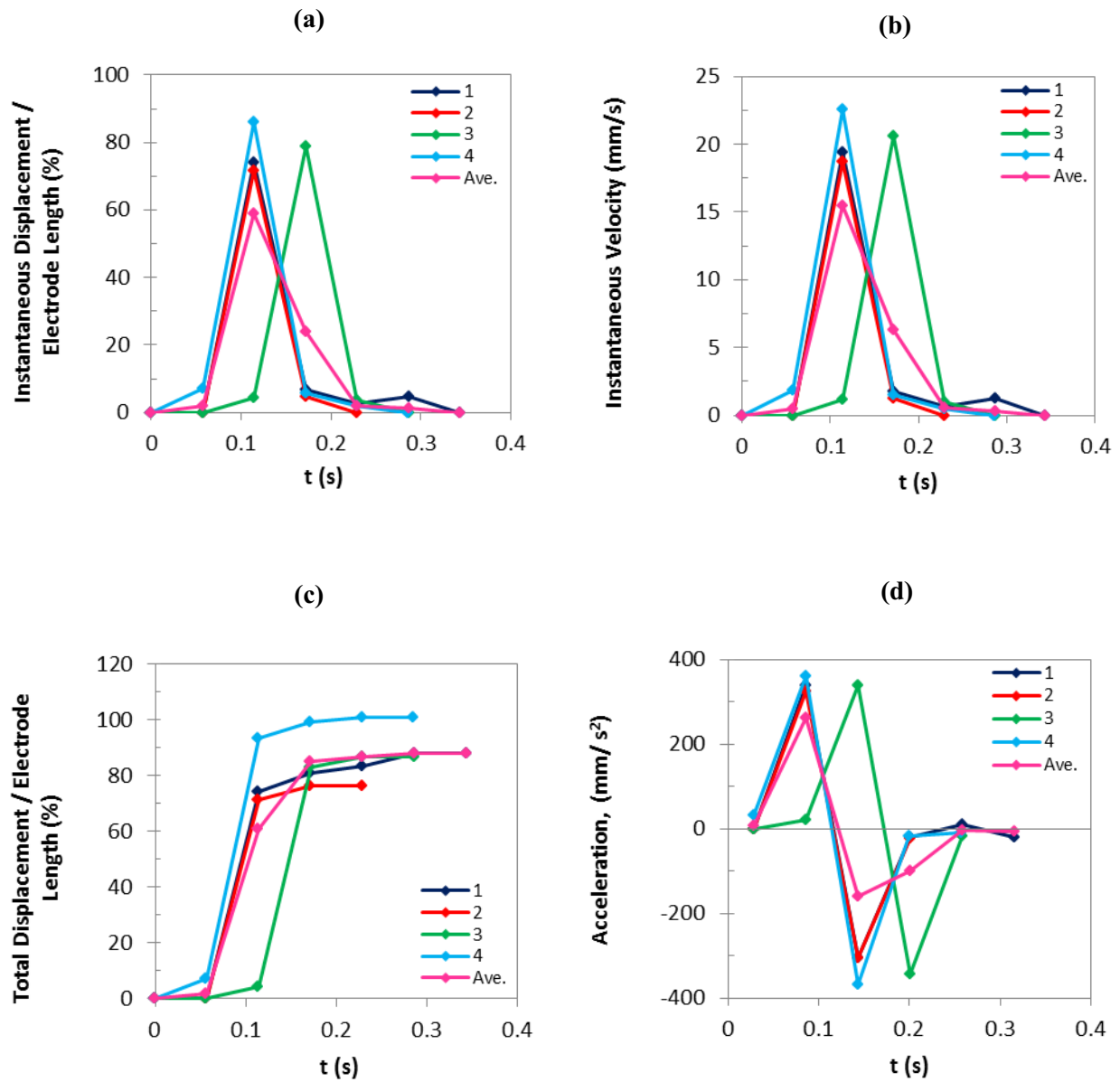


Figure I-7: (a) Instantaneous displacement, (b) instantaneous velocity, (c) total displacement, and (d) acceleration of the trailing edges of the droplets of 20 $\mu\text{g/ml}$ DNA solution at 85 V.

20 $\mu\text{g/ml}$ DNA solution, 85 V

Accepted experiments and the average curves

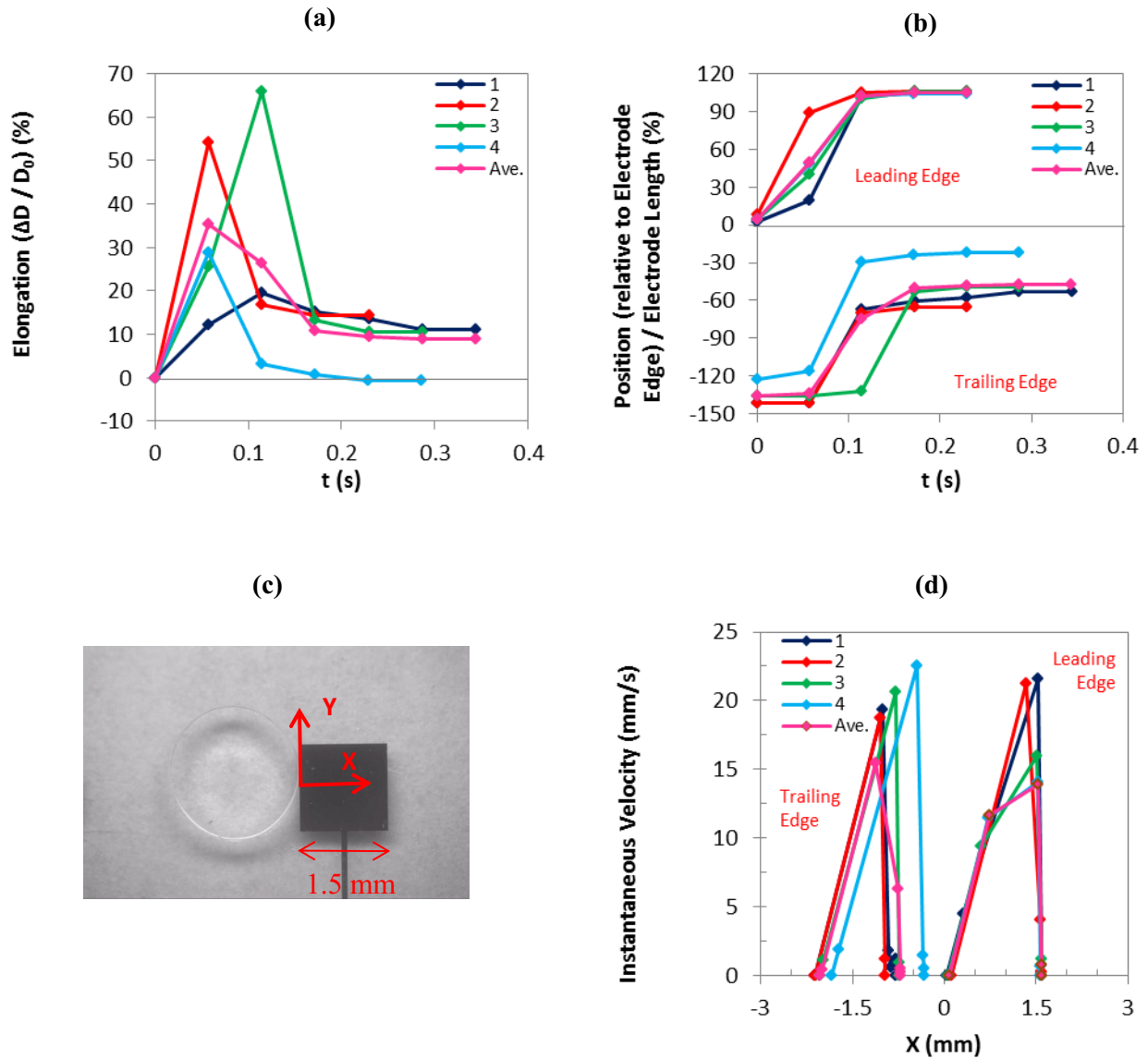


Figure I-8: (a) Droplet elongation, and (b) droplet position as a function of time, (d) instantaneous velocity as a function of droplet position as shown in (c) for the leading and trailing edges of the droplets of 20 $\mu\text{g/ml}$ DNA solution at 85 V.

20 $\mu\text{g/ml}$ DNA solution, 85 V, Average curves

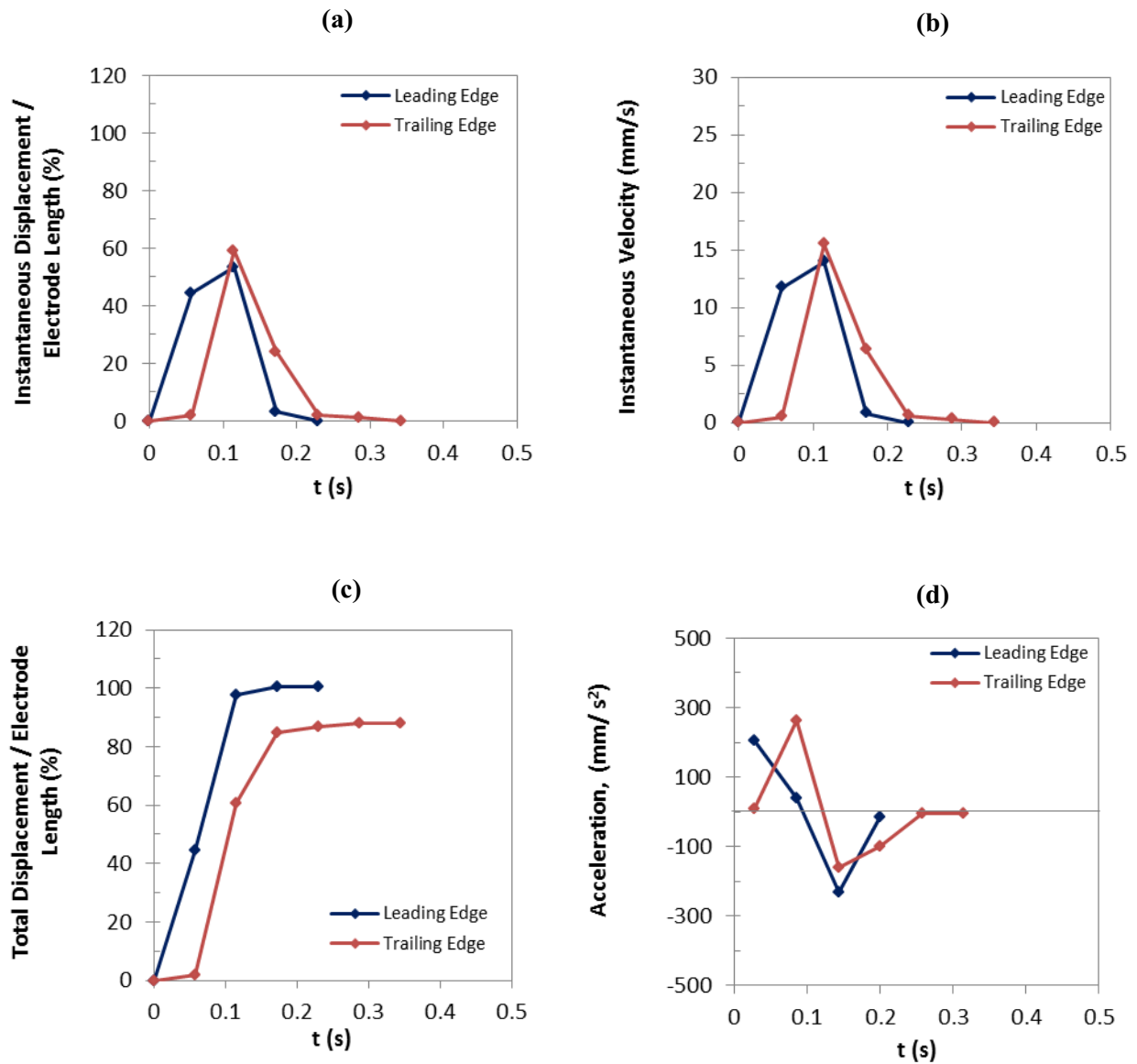


Figure I-9: Comparison of the average curves: (a) instantaneous displacement, (b) instantaneous velocity, (c) total displacement, and (d) acceleration, as a function of time for the leading and trailing edges of the droplets of 20 $\mu\text{g/ml}$ DNA solution at 85 V.

20 $\mu\text{g/ml}$ DNA solution, 85 V, Average curves

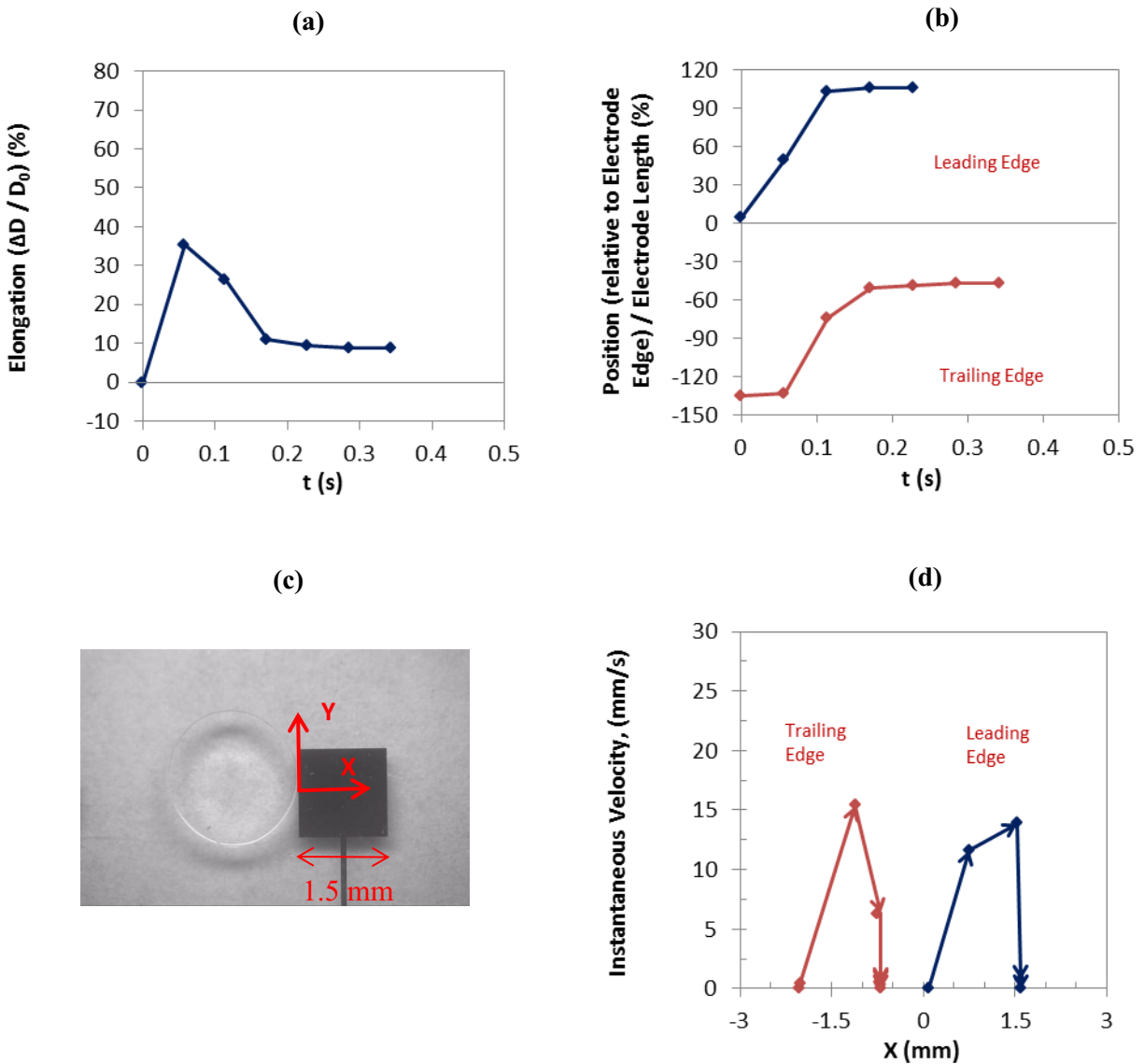


Figure I-10: Comparison of the average curves: (a) droplet elongation and (b) droplet position as a function of time, (d) instantaneous velocity as a function of droplet position as shown in (c) for the leading and trailing edges of the droplets of 20 $\mu\text{g/ml}$ DNA solution at 85 V. The arrows in graph (d) indicate the changes of velocity along the direction of movement.

I-3) 20 $\mu\text{g/ml}$ DNA solution, 80 V

20 $\mu\text{g/ml}$ DNA solution, 80 V, Leading edge,

Accepted experiments and the average curves

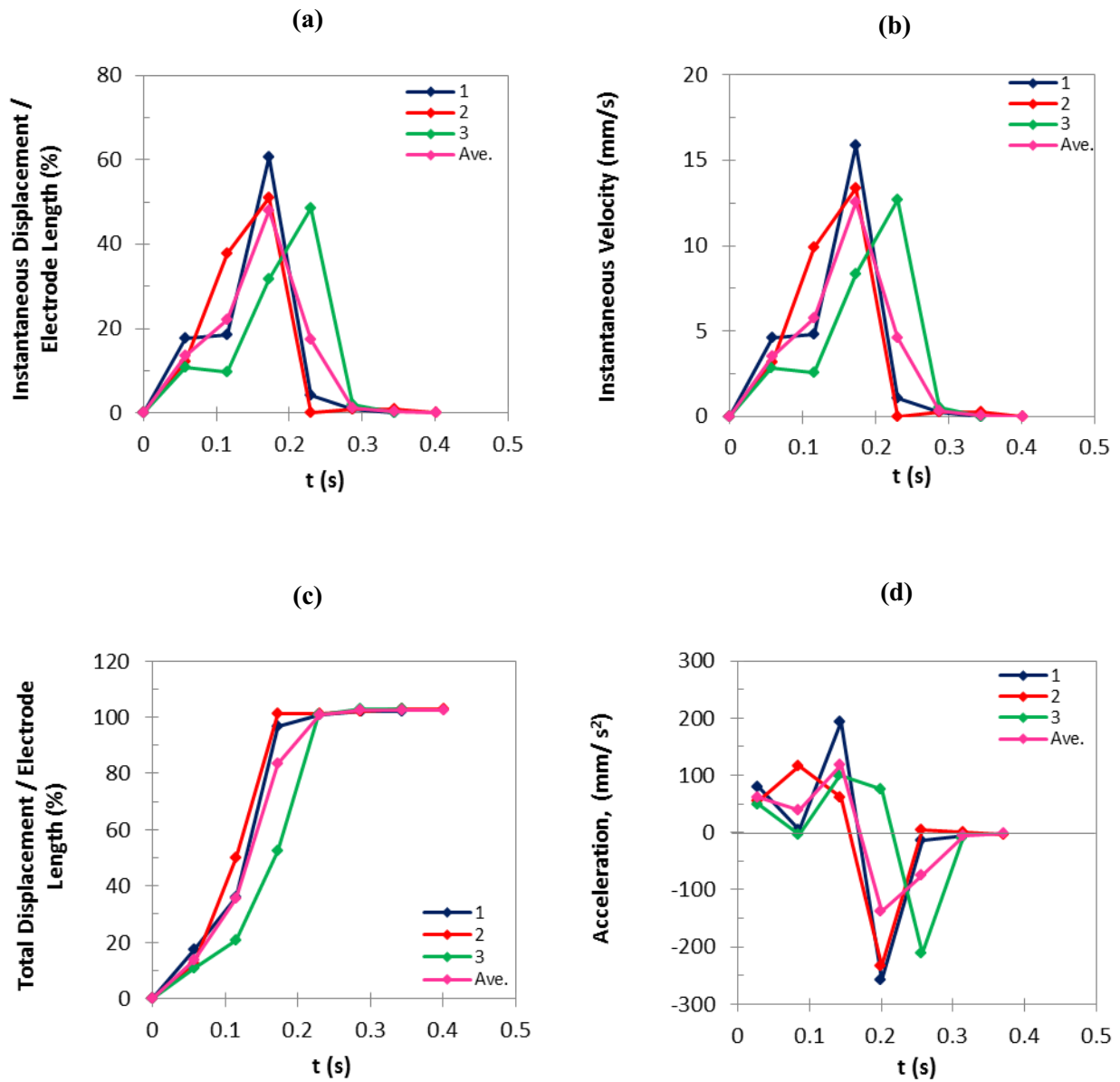


Figure I-11: (a) Instantaneous displacement, (b) instantaneous velocity, (c) total displacement, and (d) acceleration of the leading edges of the droplets of 20 $\mu\text{g/ml}$ DNA solution at 80 V.

20 $\mu\text{g/ml}$ DNA solution, 80 V, Trailing edge,

Accepted experiments and the average curves

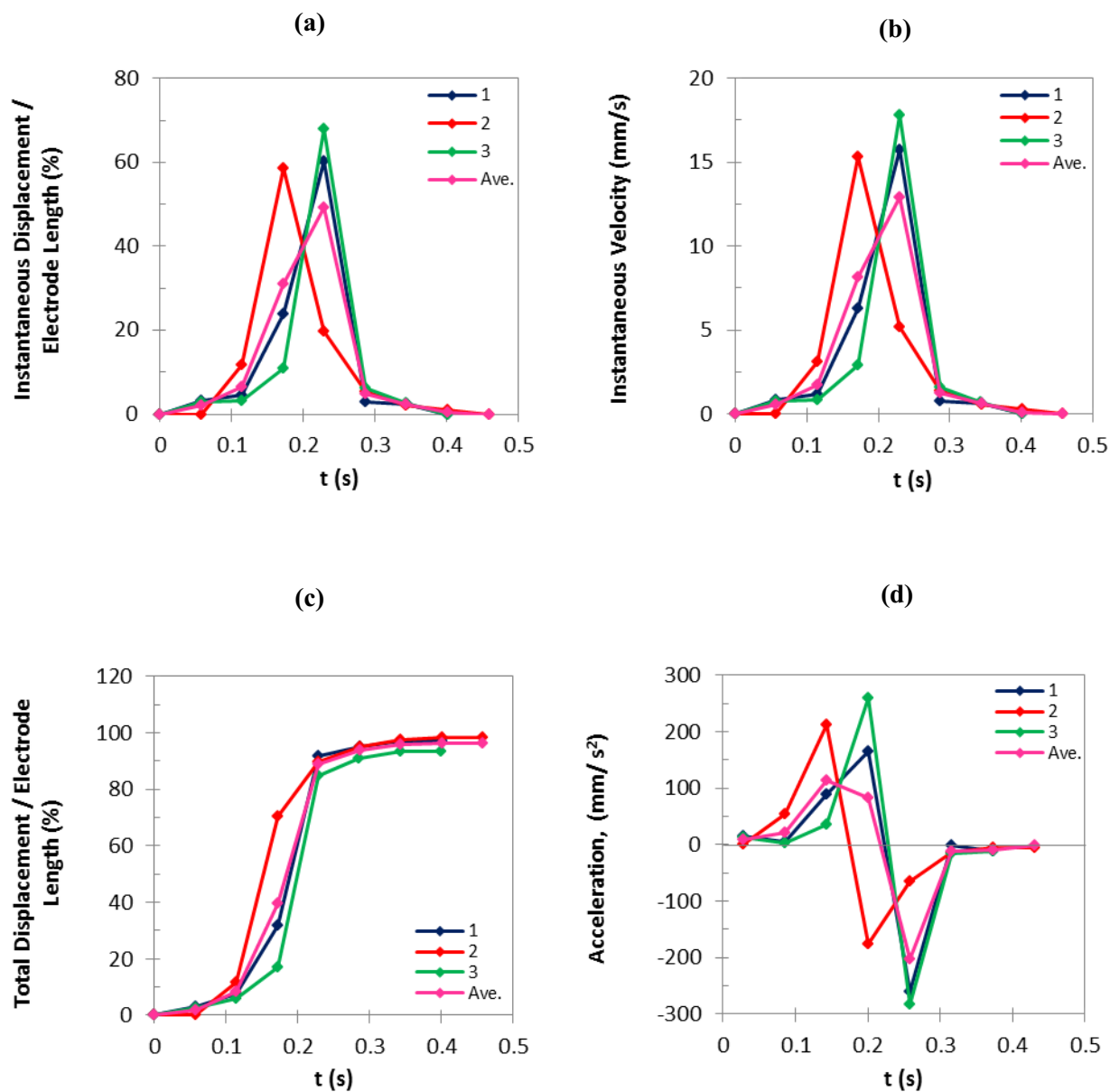


Figure I-12: (a) Instantaneous displacement, (b) instantaneous velocity, (c) total displacement, and (d) acceleration of the trailing edges of the droplets of 20 $\mu\text{g/ml}$ DNA solution at 80 V.

20 $\mu\text{g/ml}$ DNA solution, 80 V

Accepted experiments and the average curves

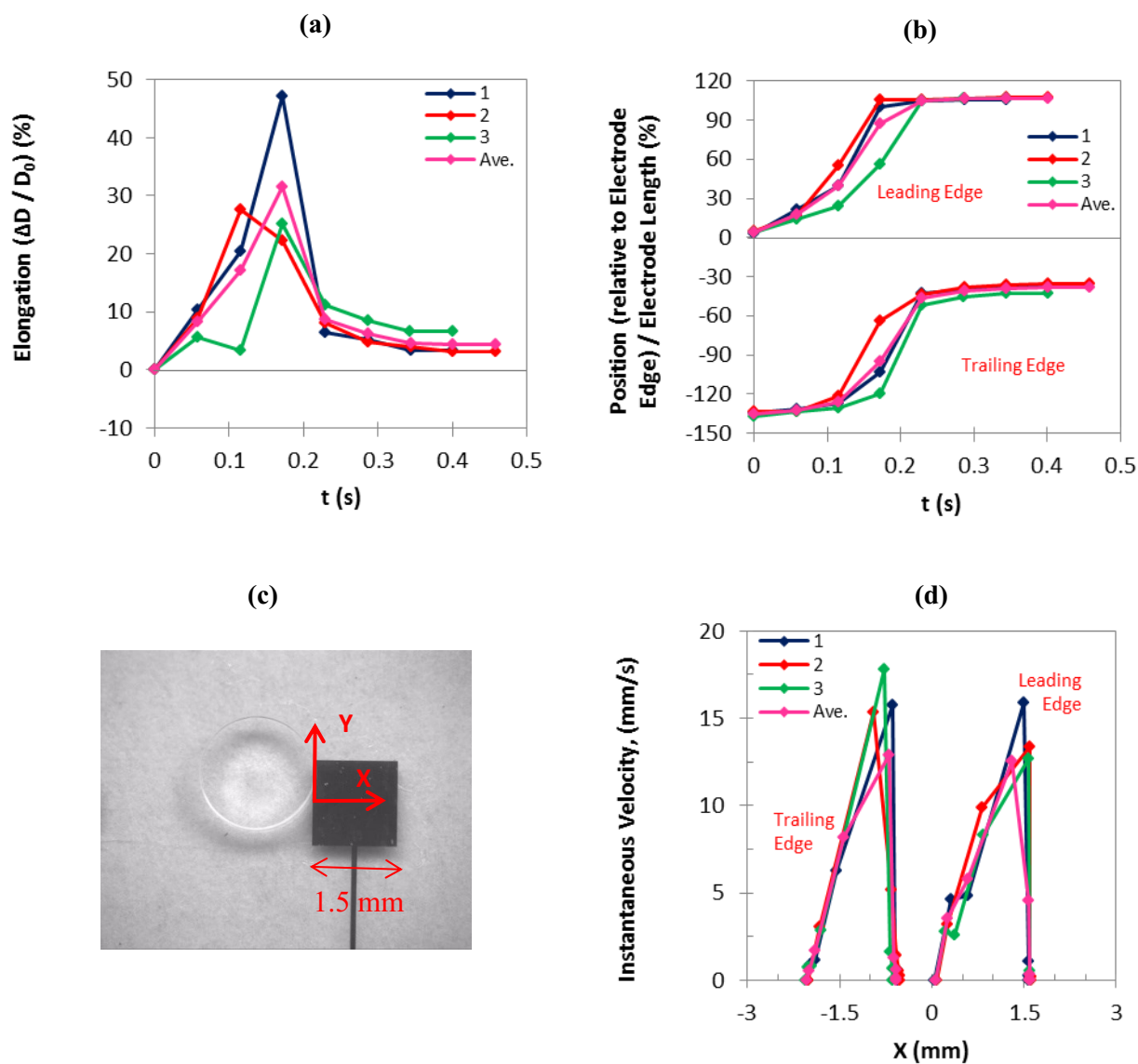


Figure I-13: (a) Droplet elongation, and (b) droplet position as a function of time, (d) instantaneous velocity as a function of droplet position as shown in (c) for the leading and trailing edges of the droplets of 20 $\mu\text{g/ml}$ DNA solution at 80 V.

20 $\mu\text{g/ml}$ DNA solution, 80 V, Average curves

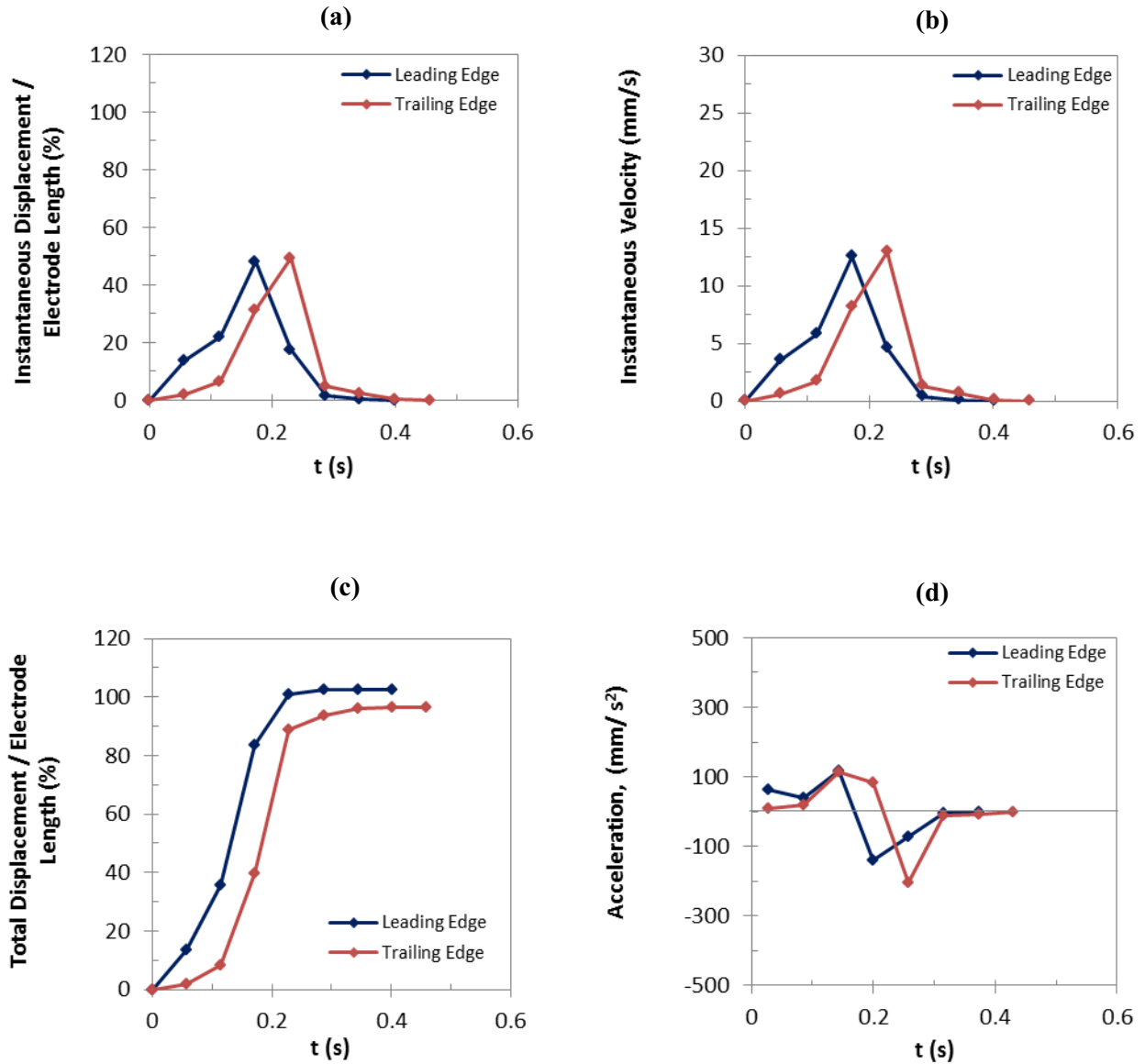


Figure I-14: Comparison of the average curves: (a) instantaneous displacement, (b) instantaneous velocity, (c) total displacement, and (d) acceleration, as a function of time for the leading and trailing edges of the droplets of 20 $\mu\text{g/ml}$ DNA solution at 80 V.

20 $\mu\text{g}/\text{ml}$ DNA solution, 80 V, Average curves

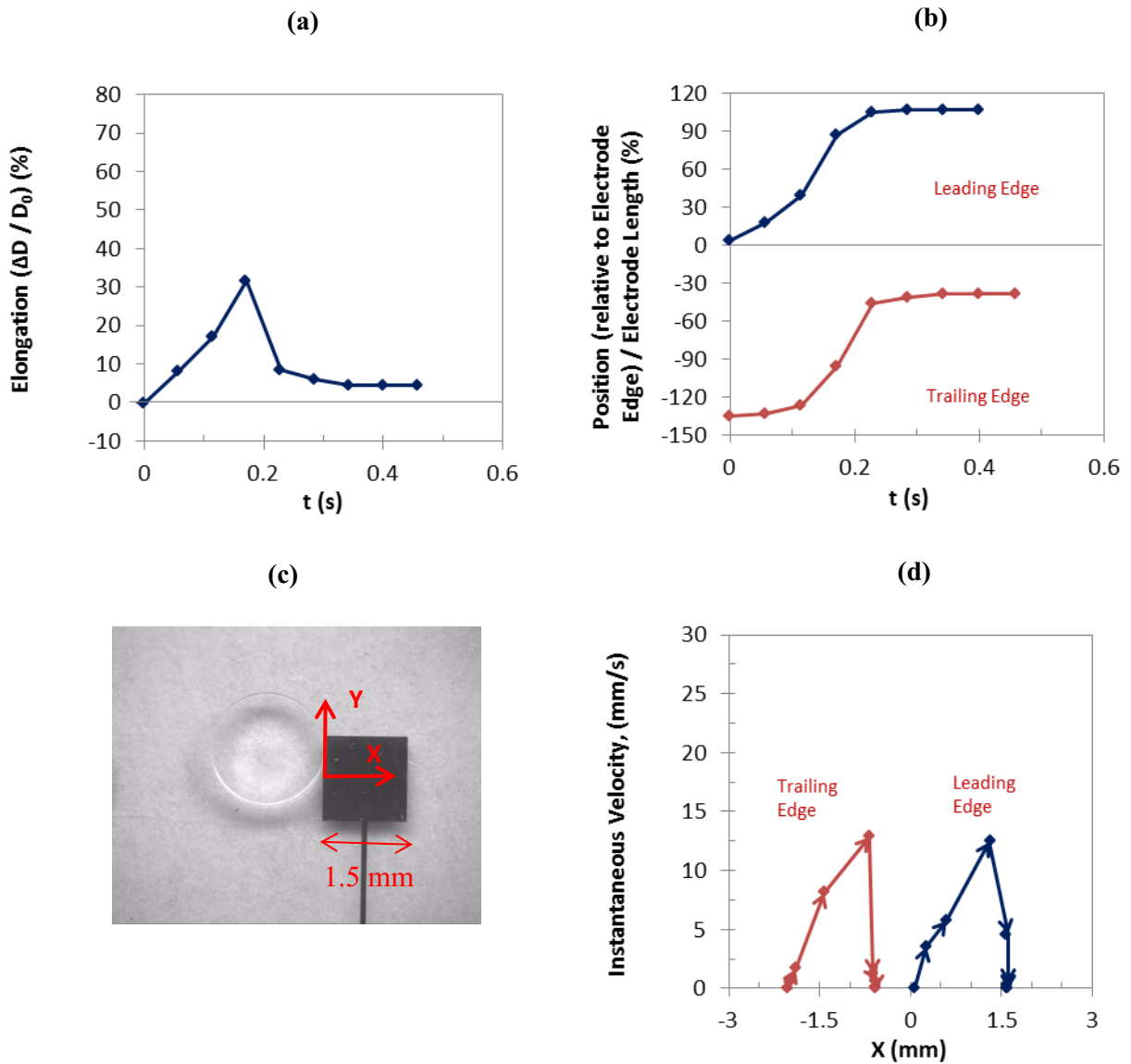


Figure I-15: Comparison of the average curves: (a) droplet elongation and (b) droplet position as a function of time, (d) instantaneous velocity as a function of droplet position as shown in (c) for the leading and trailing edges of the droplets of 20 $\mu\text{g}/\text{ml}$ DNA solution at 80 V. The arrows in graph (d) indicate the changes of velocity along the direction of movement.

I-4) 20 $\mu\text{g/ml}$ DNA Solution, 75 V

20 $\mu\text{g/ml}$ DNA solution, 75 V, Leading edge,

Accepted experiments and the average curves

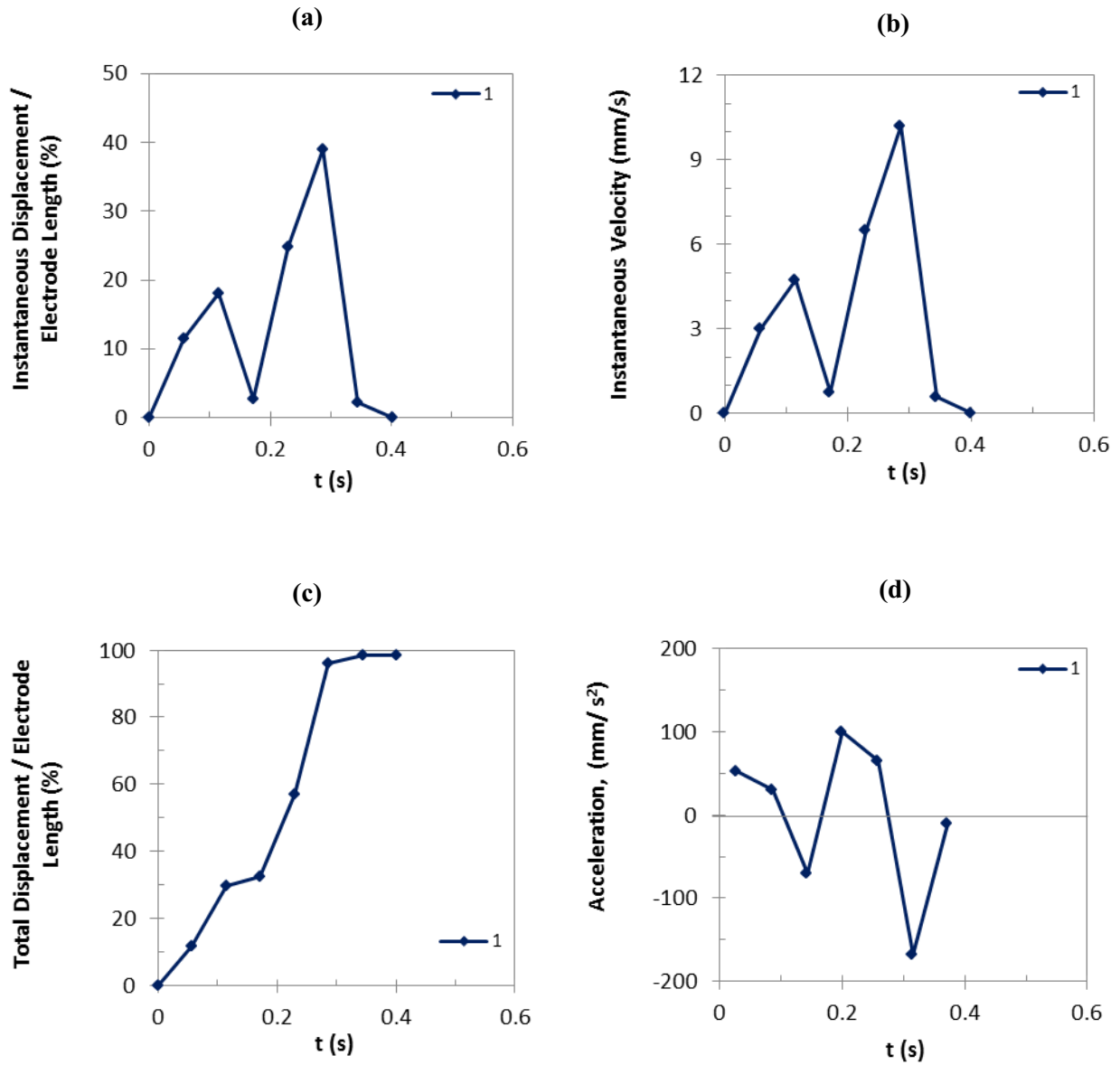


Figure I-16: (a) Instantaneous displacement, (b) instantaneous velocity, (c) total displacement, and (d) acceleration of the leading edges of the droplets of 20 $\mu\text{g/ml}$ DNA solution at 75 V.

20 $\mu\text{g/ml}$ DNA solution, 75 V, Trailing edge,

Accepted experiments and the average curves

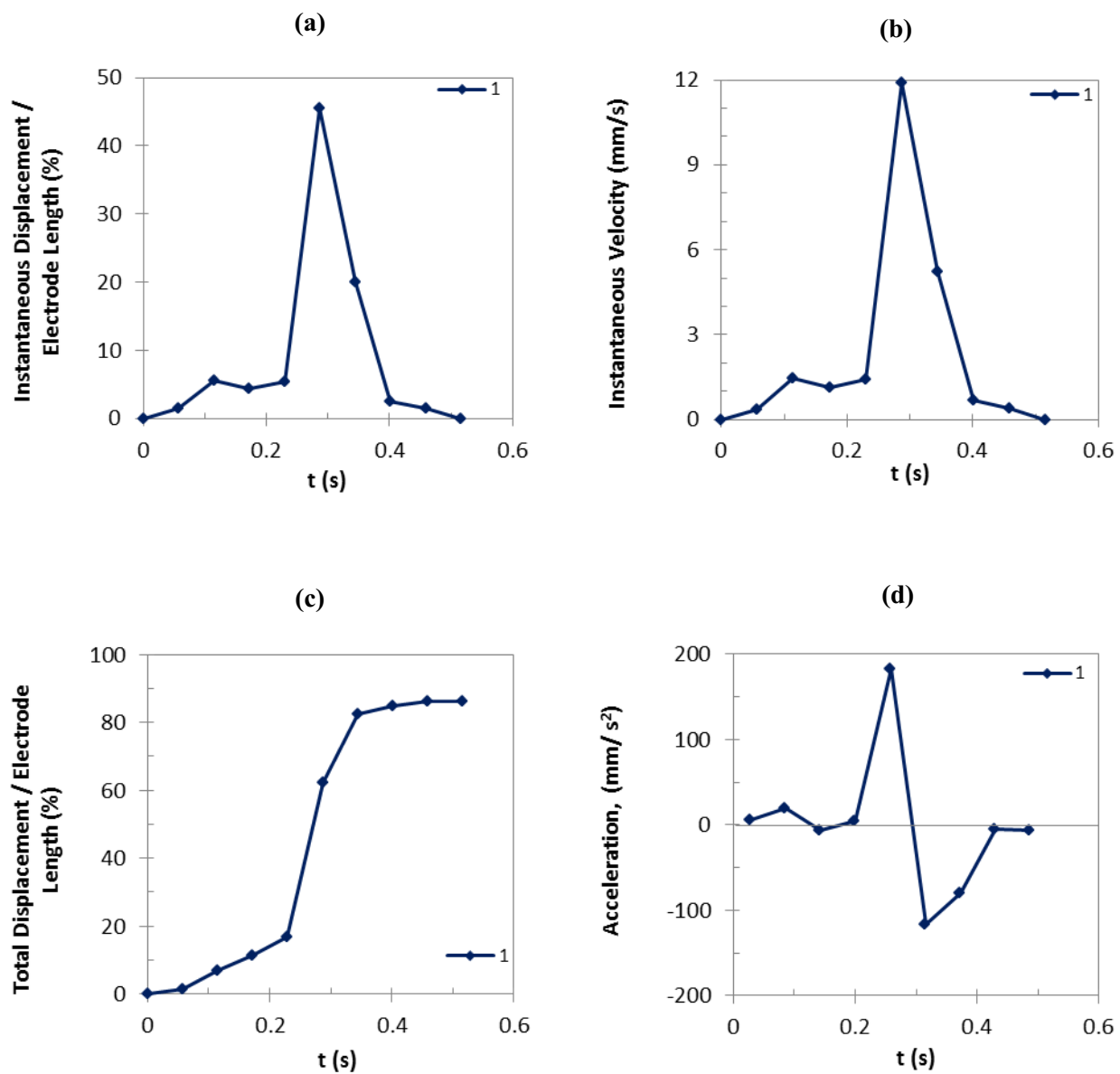


Figure I-17: (a) Instantaneous displacement, (b) instantaneous velocity, (c) total displacement, and (d) acceleration of the trailing edges of the droplets of 20 $\mu\text{g/ml}$ DNA solution at 75 V.

20 $\mu\text{g/ml}$ DNA solution, 75 V

Accepted experiments and the average curves

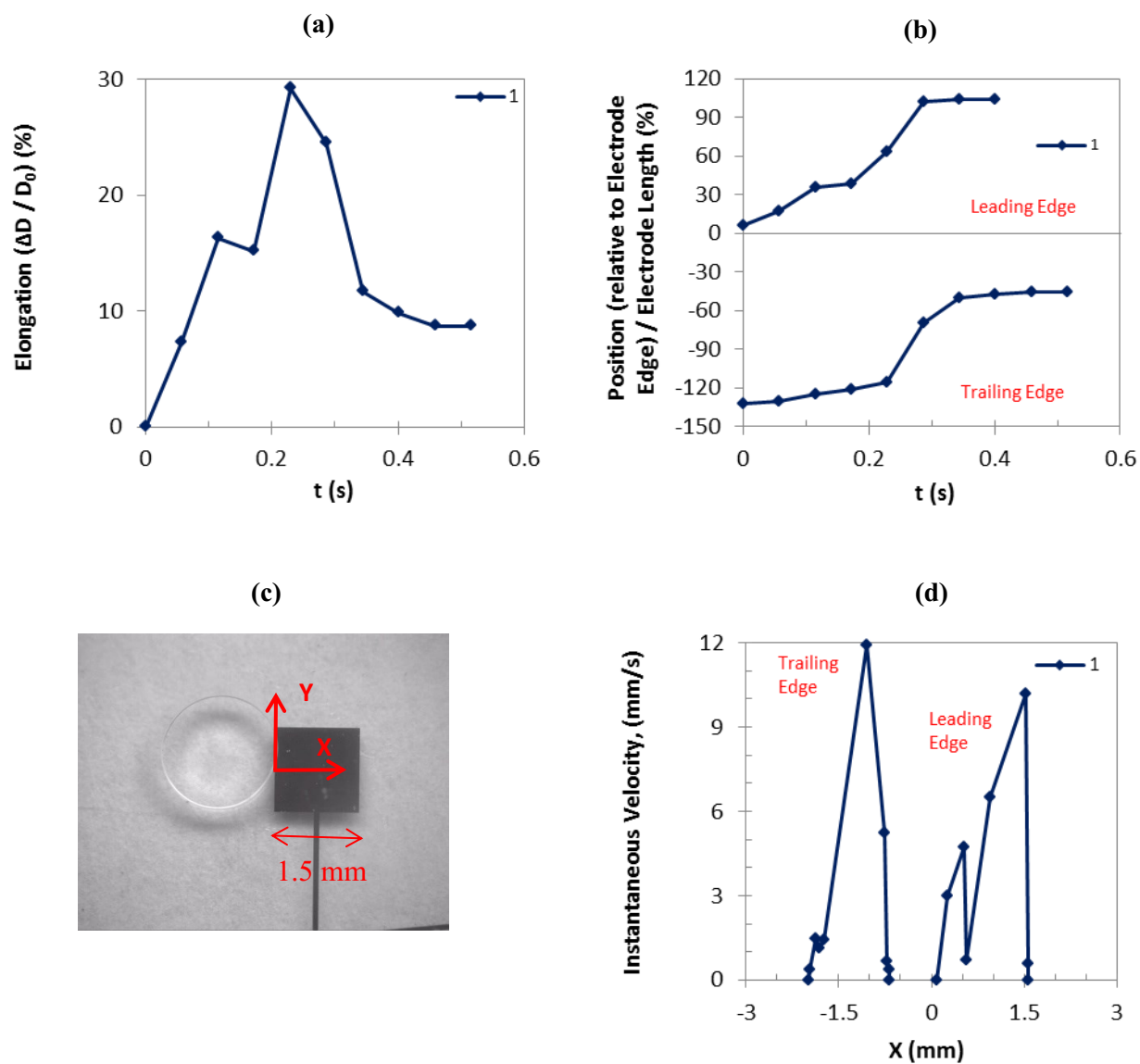


Figure I-18: (a) Droplet elongation, and (b) droplet position as a function of time, (d) instantaneous velocity as a function of droplet position as shown in (c) for the leading and trailing edges of the droplets of 20 $\mu\text{g/ml}$ DNA solution at 75 V.

20 $\mu\text{g/ml}$ DNA solution, 75 V, Average curves

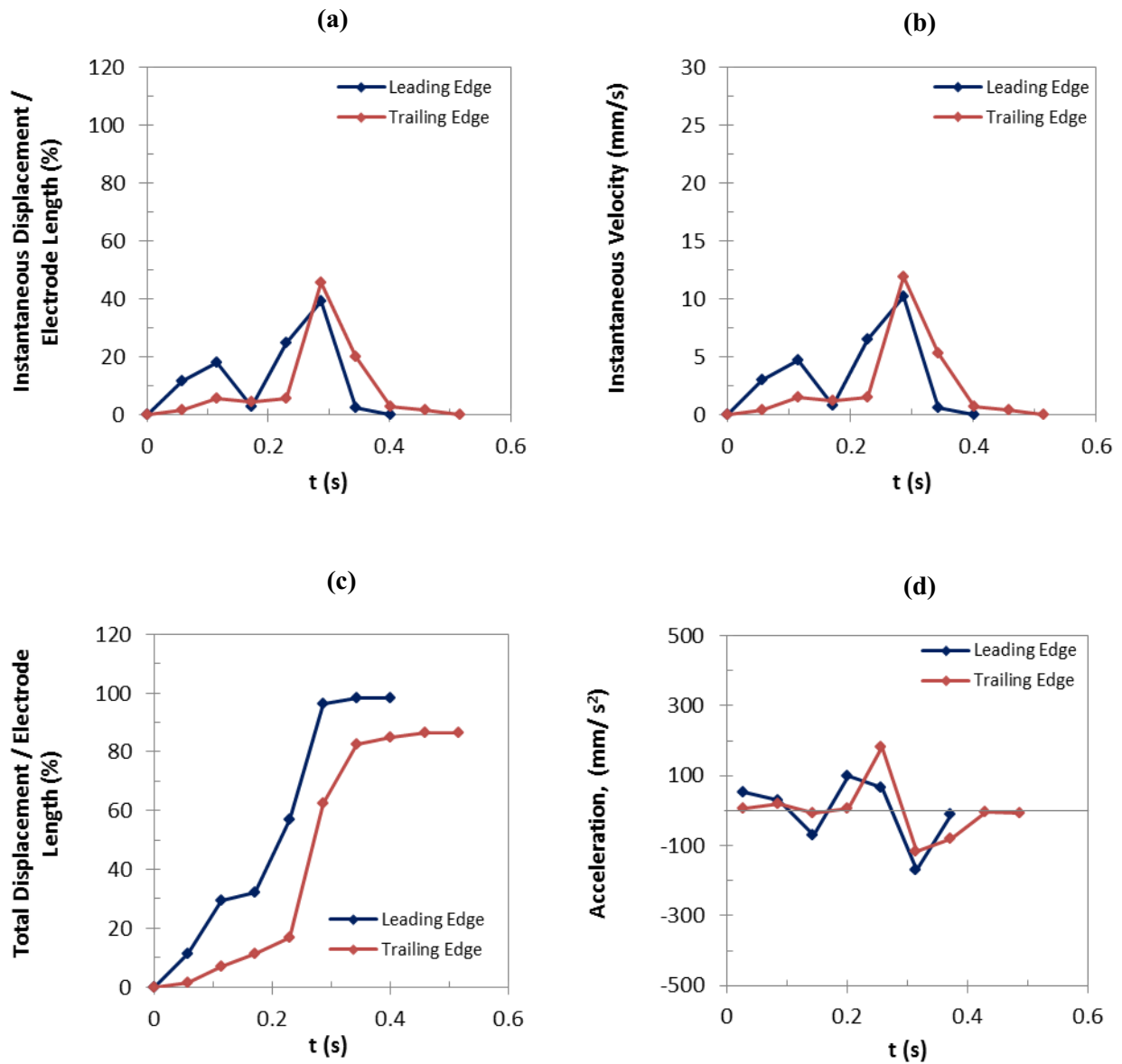


Figure I-19: Comparison of the average curves: (a) instantaneous displacement, (b) instantaneous velocity, (c) total displacement, and (d) acceleration, as a function of time for the leading and trailing edges of the droplets of 20 $\mu\text{g/ml}$ DNA solution at 75 V.

20 $\mu\text{g/ml}$ DNA solution, 75 V, Average curves

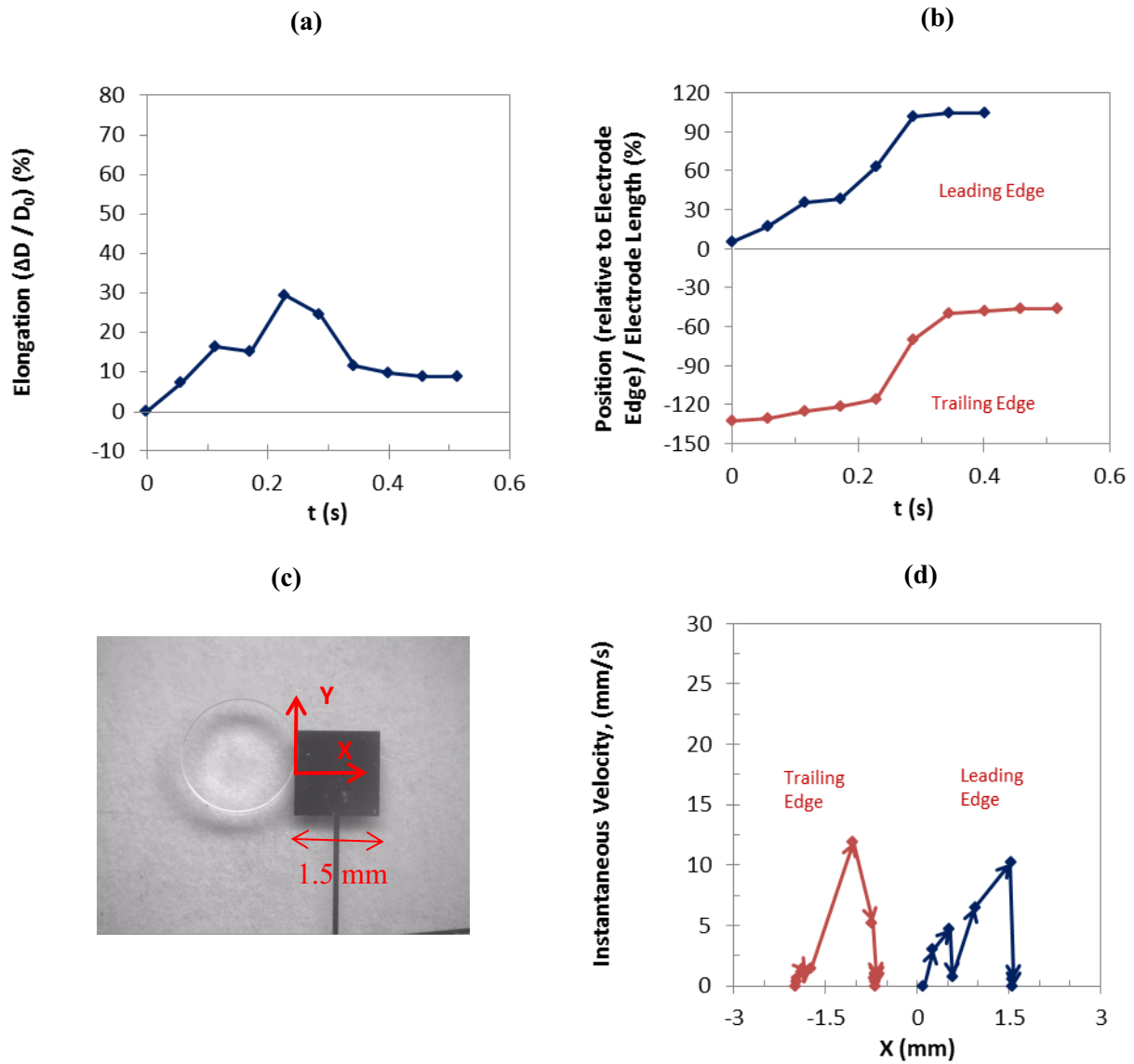


Figure I-20: Comparison of the average curves: (a) droplet elongation and (b) droplet position as a function of time, (d) instantaneous velocity as a function of droplet position as shown in (c) for the leading and trailing edges of the droplets of 20 $\mu\text{g/ml}$ DNA solution at 75 V. The arrows in graph (d) indicate the changes of velocity along the direction of movement.

I-5) 20 $\mu\text{g/ml}$ DNA solution, 70 V

20 $\mu\text{g/ml}$ DNA solution, 70 V, Leading edge,

Accepted experiments and the average curves

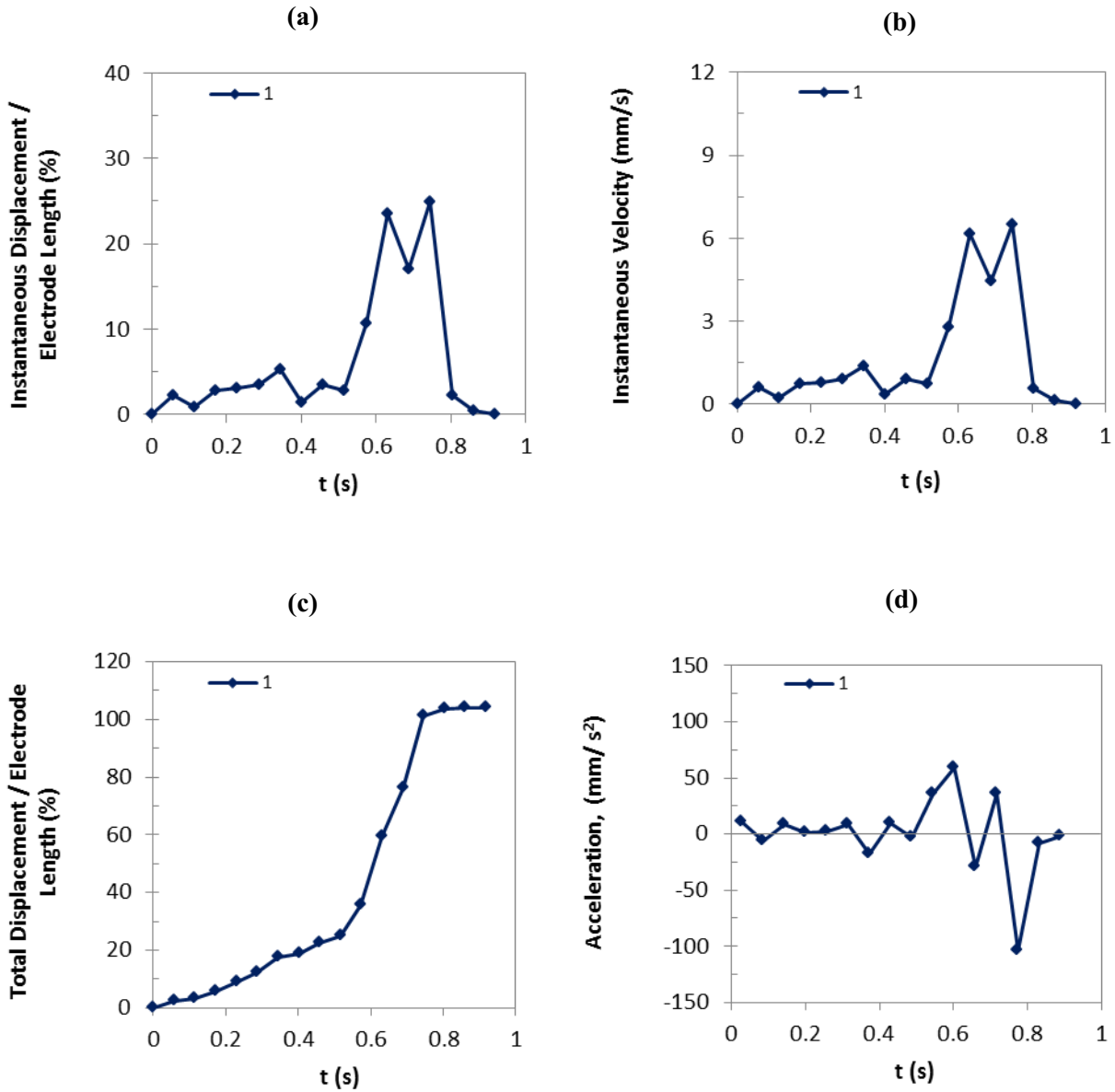


Figure I-21: (a) Instantaneous displacement, (b) instantaneous velocity, (c) total displacement, and (d) acceleration of the leading edges of the droplets of 20 $\mu\text{g/ml}$ DNA solution at 70 V.

20 $\mu\text{g/ml}$ DNA solution, 70 V, Trailing edge,

Accepted experiments and the average curves

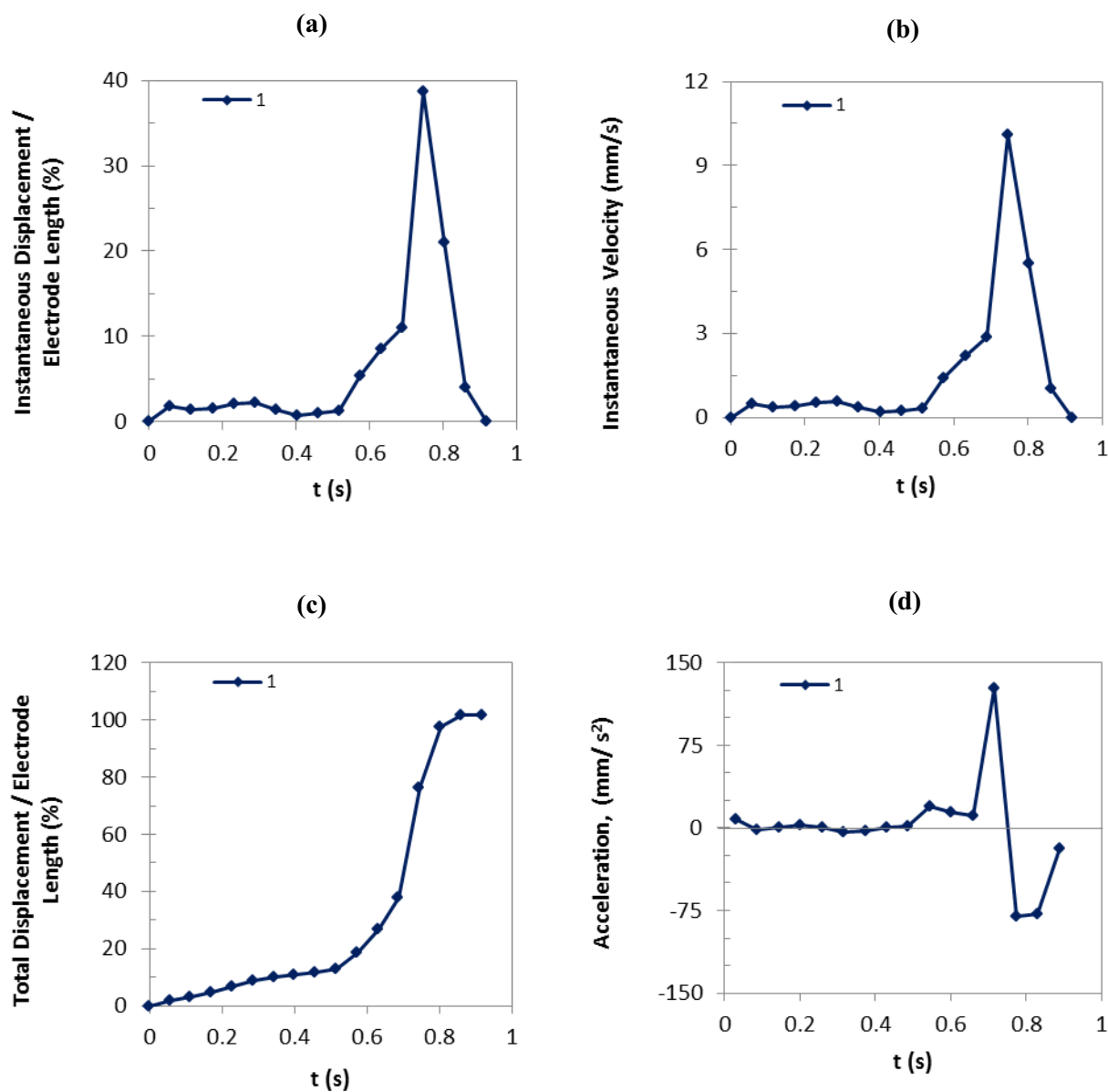


Figure I-22: (a) Instantaneous displacement, (b) instantaneous velocity, (c) total displacement, and (d) acceleration of the trailing edges of the droplets of 20 $\mu\text{g/ml}$ DNA solution at 70 V.

20 $\mu\text{g/ml}$ DNA solution, 70 V

Accepted experiments and the average curves

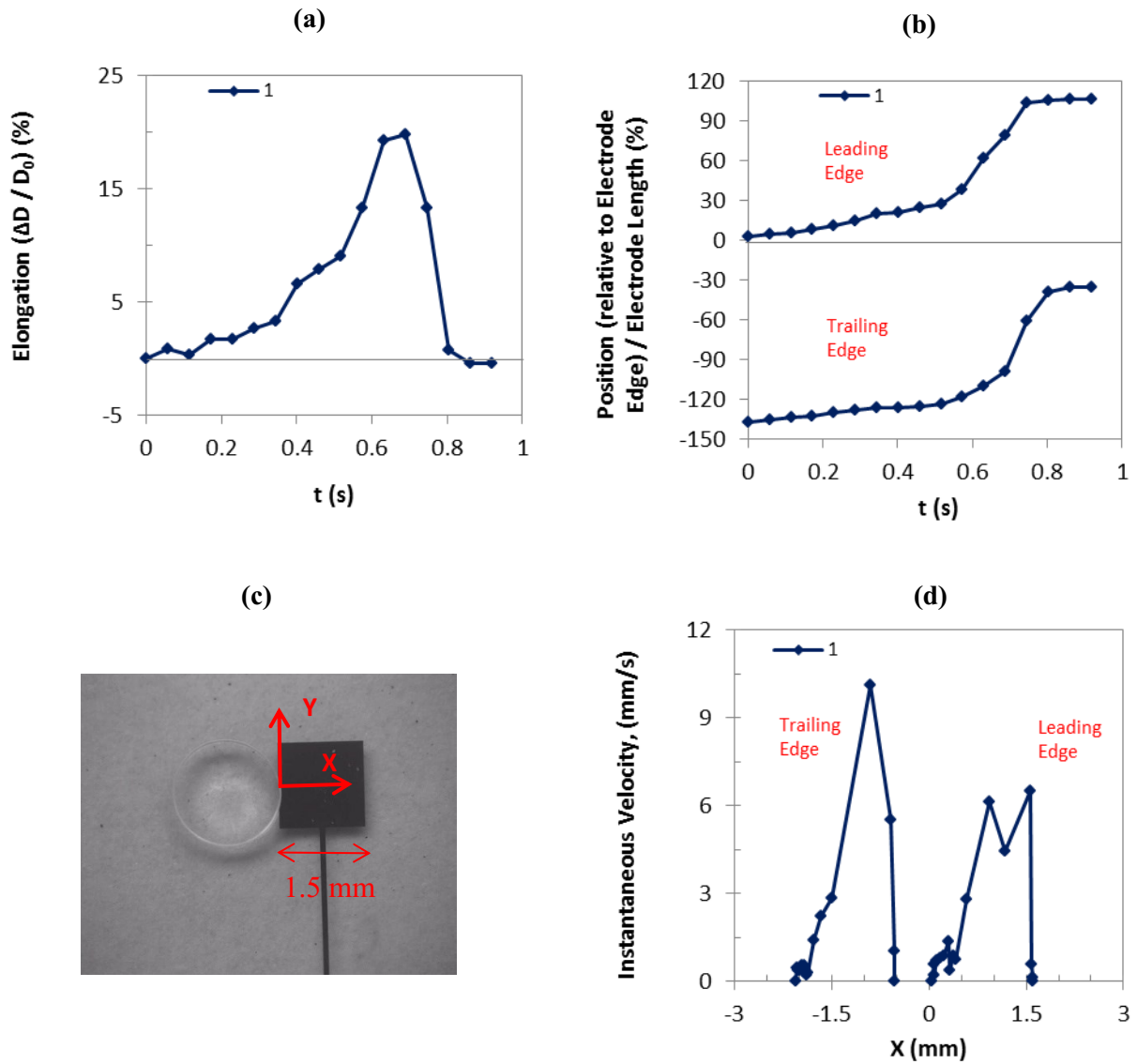


Figure I-23: (a) Droplet elongation, and (b) droplet position as a function of time, (d) instantaneous velocity as a function of droplet position as shown in (c) for the leading and trailing edges of the droplets of 20 $\mu\text{g/ml}$ DNA solution at 70 V.

20 $\mu\text{g/ml}$ DNA solution, 70 V, Average curves

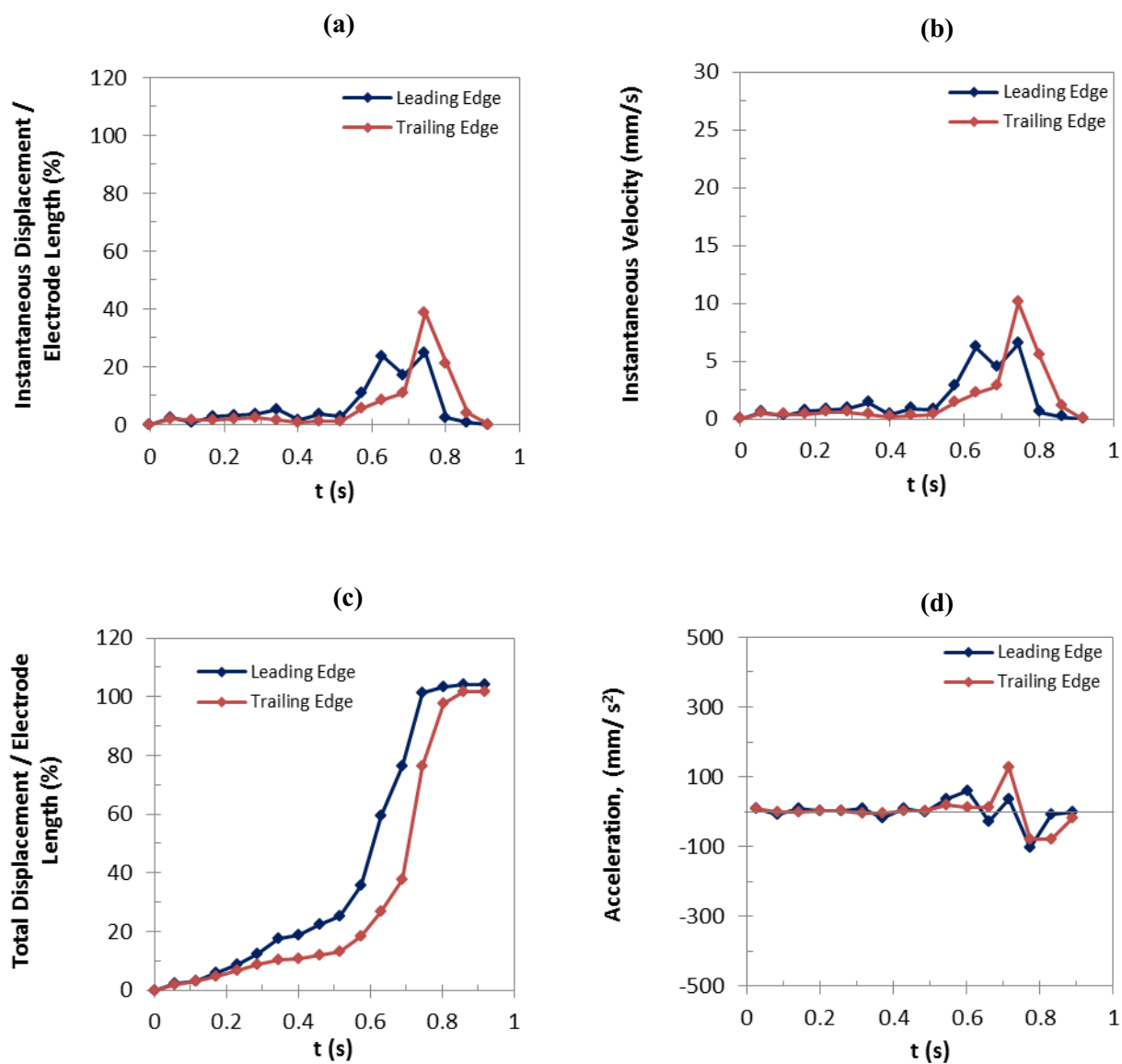


Figure I-24: Comparison of the average curves: (a) instantaneous displacement, (b) instantaneous velocity, (c) total displacement, and (d) acceleration, as a function of time for the leading and trailing edges of the droplets of 20 $\mu\text{g/ml}$ DNA solution at 70 V.

20 $\mu\text{g/ml}$ DNA solution, 70 V, Average curves

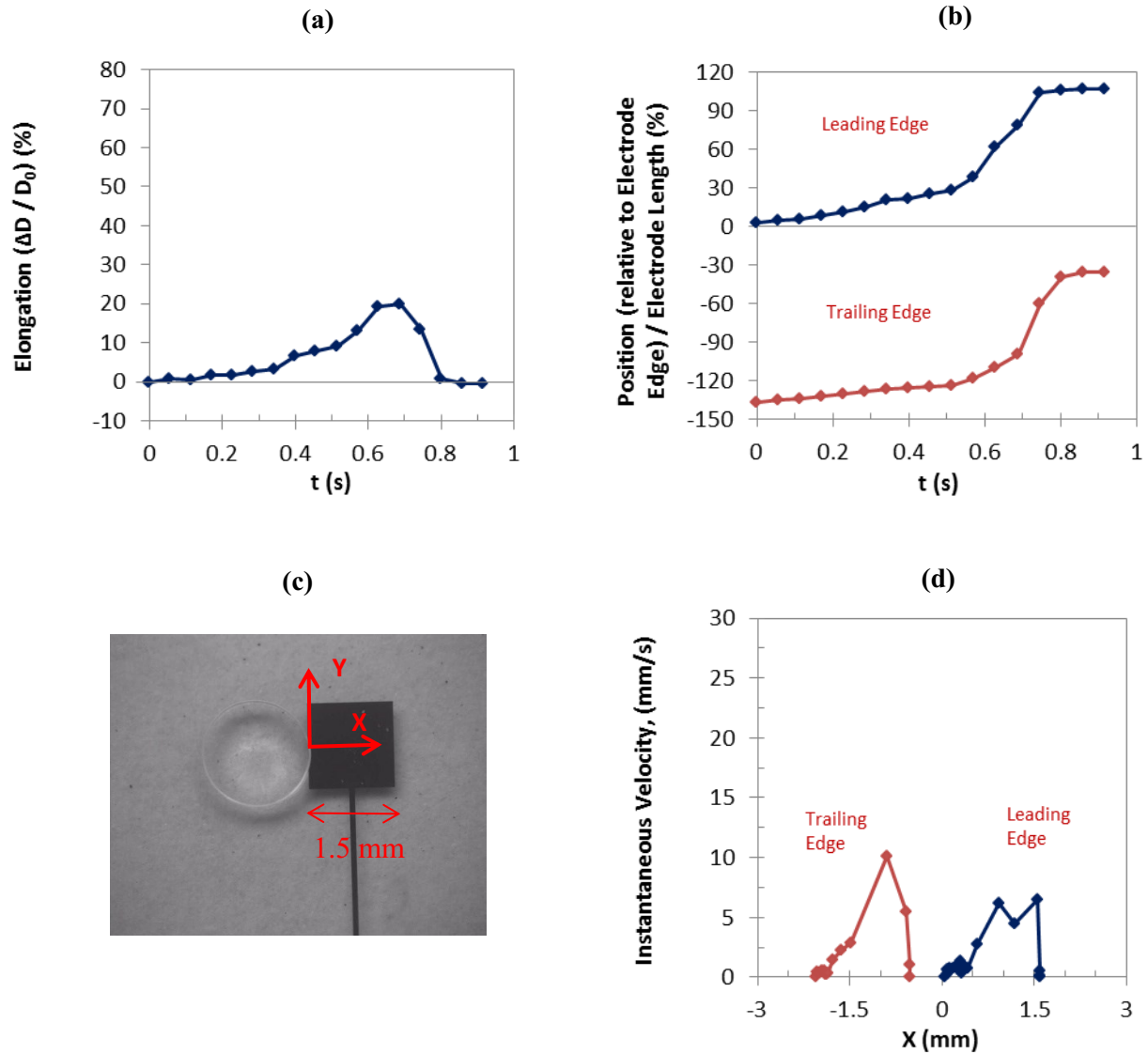


Figure I-25: Comparison of the average curves: (a) droplet elongation and (b) droplet position as a function of time, (d) instantaneous velocity as a function of droplet position as shown in (c) for the leading and trailing edges of the droplets of 20 $\mu\text{g/ml}$ DNA solution at 70 V.

I-6) 20 $\mu\text{g/ml}$ DNA Solution, 65 V

20 $\mu\text{g/ml}$ DNA solution, 65 V, Average curves

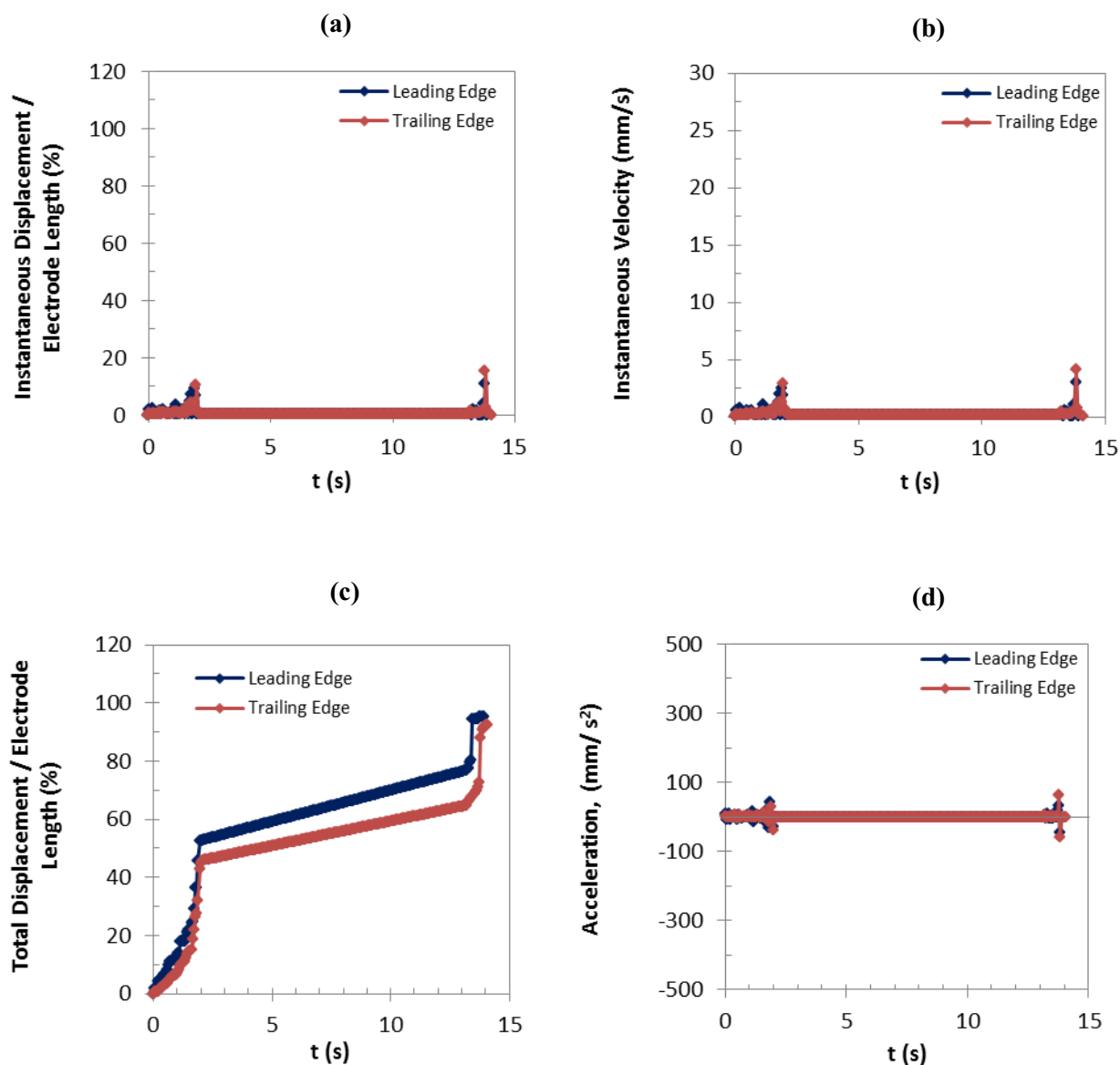


Figure I-26: Comparison of the average curves: (a) instantaneous displacement, (b) instantaneous velocity, (c) total displacement, and (d) acceleration, as a function of time for the leading and trailing edges of the droplets of 20 $\mu\text{g/ml}$ DNA solution at 65 V.

20 $\mu\text{g/ml}$ DNA solution, 65 V, Average curves

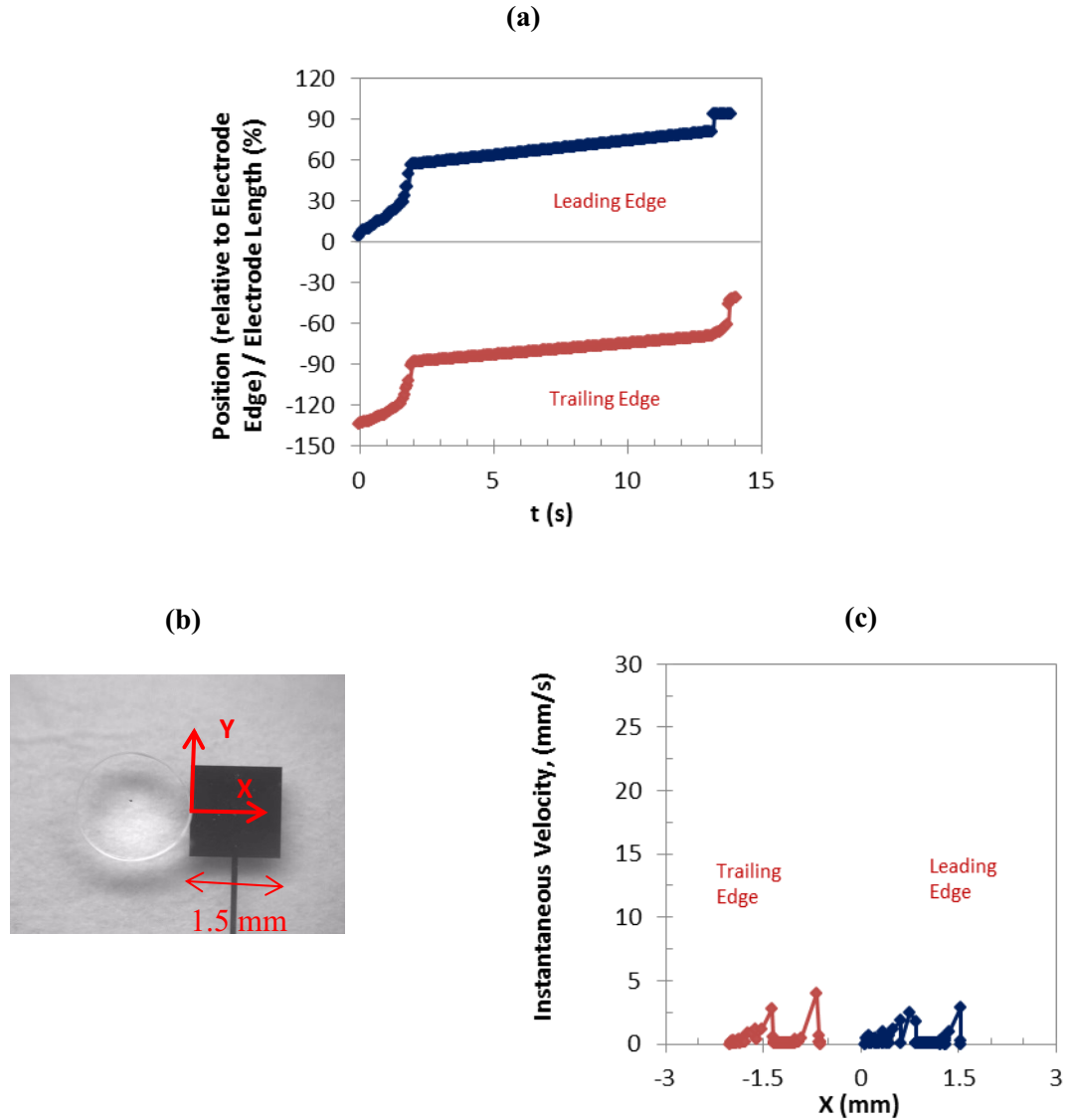


Figure I-27: Comparison of the average curves: (a) droplet elongation and (b) droplet position as a function of time, (d) instantaneous velocity as a function of droplet position as shown in (c) for the leading and trailing edges of the droplets of 20 $\mu\text{g/ml}$ DNA solution at 65 V.

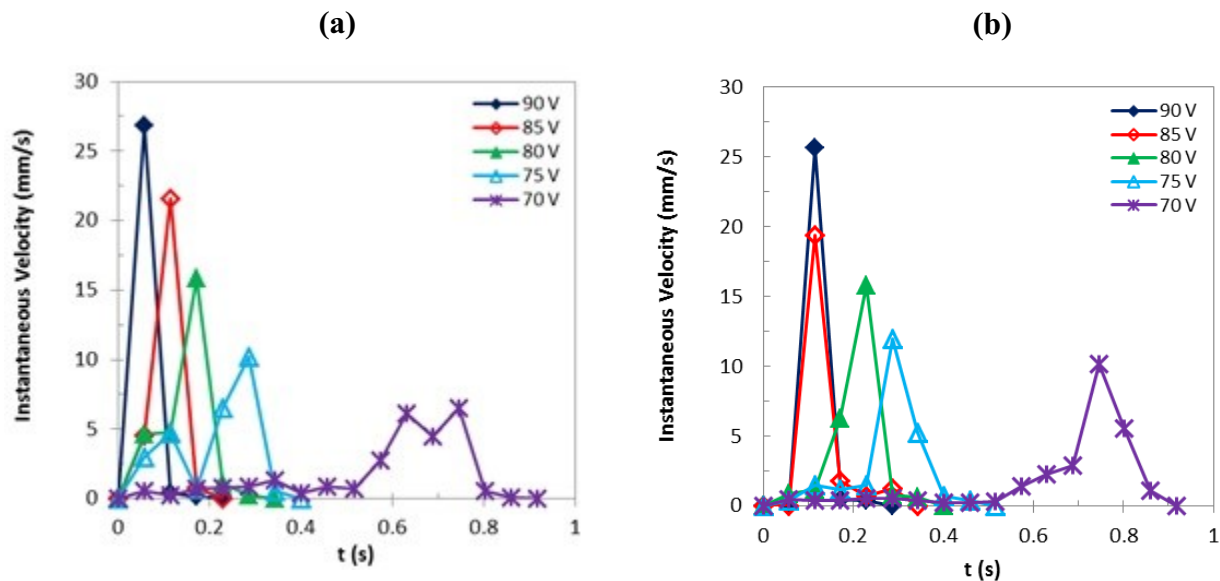


Figure I-28: The instantaneous velocity of the droplets of 20 $\mu\text{g/ml}$ DNA solutions as a function of time for the applied voltages of 70 to 90V. Comparison of results for the experiments with the highest leading edge instantaneous velocity: (a) leading edge, (b) trailing edge.

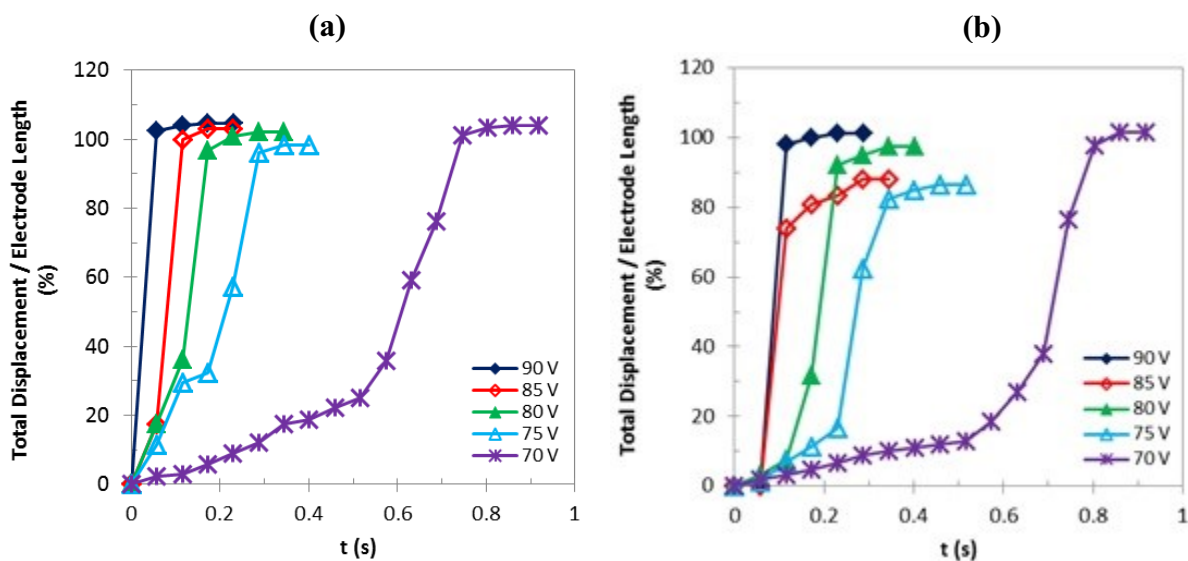


Figure I-29: The total displacement of the droplets of 20 $\mu\text{g/ml}$ DNA solutions as a function of time for the applied voltages of 70 to 90V. Comparison of results for the experiments with the highest leading edge instantaneous velocity: (a) leading edge, (b) trailing edge.

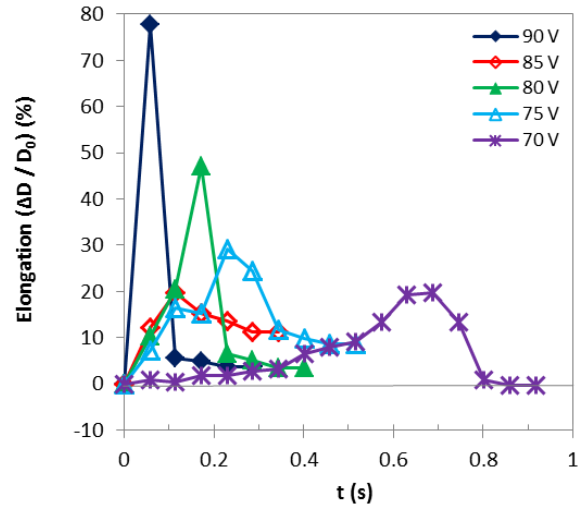


Figure I-30: The comparison of results for the elongation of the droplets of 20 $\mu\text{g/ml}$ DNA solutions as a function of time for the experiments with the highest leading edge instantaneous velocity.

Table I-1: Peaks of the average curves, 20 µg/ml DNA solution

Leading Edge									
Applied Voltage	90 V	85 V	80 V	75 V	70 V	65 V	60 V	55 V	50 V
Instantaneous Velocity (mm/s)	26.8	14.0	12.5	10.2	6.5	2.9	1.6	0.4	0
Total Displacement (normalized)	103%	101%	101%	98%	101%	95%	39%	27%	7%
Trailing Edge									
Applied Voltage	90 V	85 V	80 V	75 V	70 V	65 V	60 V	55 V	50 V
Instantaneous Velocity (mm/s)	25.7	15.5	12.9	11.9	10.1	4.0	0.7	0.2	0
Total Displacement (normalized)	98%	87%	94%	85%	98%	91%	40%	10%	1%
Elongation (normalized)	78%	35%	32%	29%	20%	-	-	-	-

Table I-2: Peaks of the curves for the experiments with the highest leading edge instantaneous velocity, 20 µg/ml DNA solution

Leading Edge										
Applied Voltage	90 V	85 V	80 V	75 V	70 V	65 V	60 V	55 V	50 V	
Instantaneous Velocity (mm/s)	26.8	21.6	15.9	10.2	6.5	5.8	1.6	0.4	0	
Total Displacement (normalized)	103%	100%	101%	98%	97%	98%	39%	30%	7%	

Trailing Edge										
Applied Voltage	90 V	85 V	80 V	75 V	70 V	65 V	60 V	55 V	50 V	
Instantaneous Velocity (mm/s)	25.7	19.4	15.8	11.9	10.1	8.1	0.7	0.2	0	
Total Displacement (normalized)	98%	88%	92%	85%	98%	100%	40%	10%	0.8	

Elongation (normalized)	78%	20%	47%	29%	20%	15%	-	13%	2%	
--------------------------------	-----	-----	-----	-----	-----	-----	---	-----	----	--

Table I-3: Average velocity for all experiments, 20 $\mu\text{g/ml}$ DNA solution

Leading Edge									
Average Velocity (mm/s)	26.8	15.0	8.0	5.0	2.0	0.4	0.1	0	0.1
Trailing Edge									
Average Velocity (mm/s)	12.8	9.75	5.6	3.3	1.8	0.4	0	0	0

Table I-4: Average velocity for the experiments with the highest leading edge instantaneous velocity, 20 $\mu\text{g/ml}$ DNA solution

Leading Edge									
Average Velocity (mm/s)	26.8	13.1	8.5	5.0	2.1	0.1	0.1	0.1	0
Trailing Edge									
Average Velocity (mm/s)	12.8	9.7	6.0	3.3	1.8	0.1	0	0	0

20 $\mu\text{g/ml}$ DNA solution, Leading edge

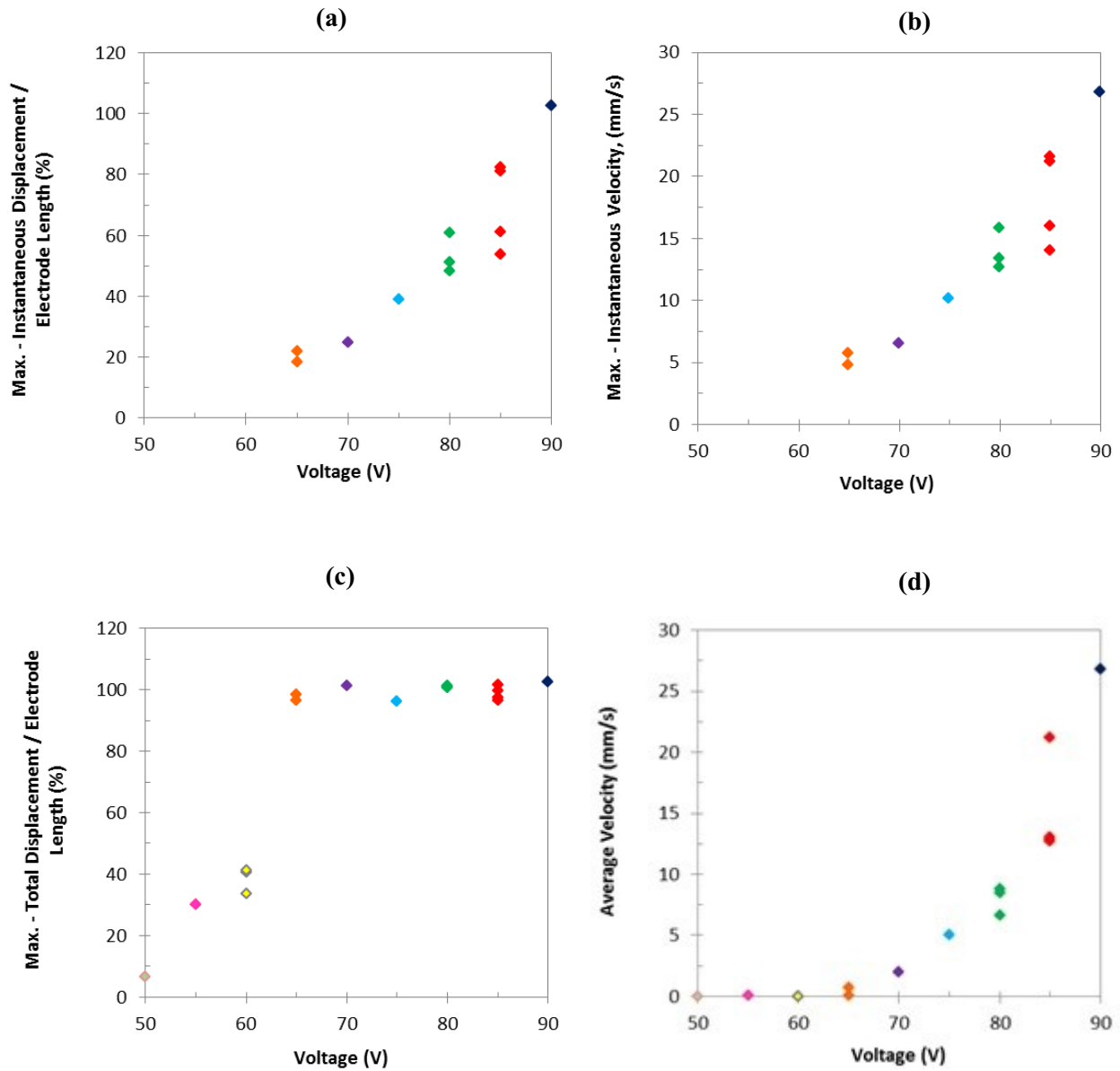


Figure I-31: Changes of the max.: (a) instantaneous displacement, (b) instantaneous velocity, (c) total displacement, and (d) average velocity with the applied voltage for the leading edges of the droplets of 20 $\mu\text{g/ml}$ DNA solution.

20 $\mu\text{g/ml}$ DNA solution, Trailing edge

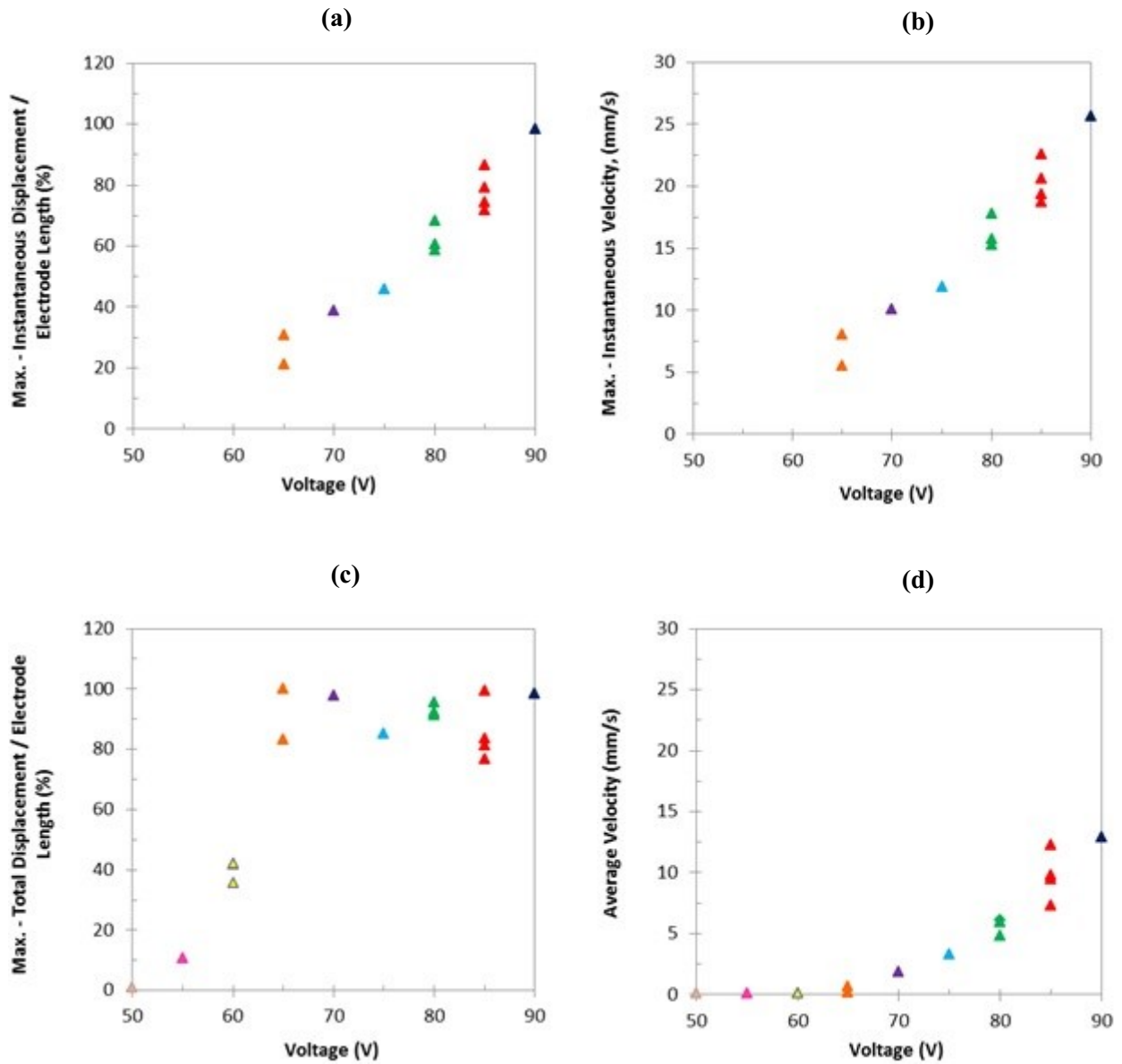


Figure I-32: Changes of the max.: (a) instantaneous displacement, (b) instantaneous velocity, (c) total displacement, and (d) average velocity with the applied voltage for the trailing edges of the droplets of 20 $\mu\text{g/ml}$ DNA solution.

20 $\mu\text{g/ml}$ DNA solution

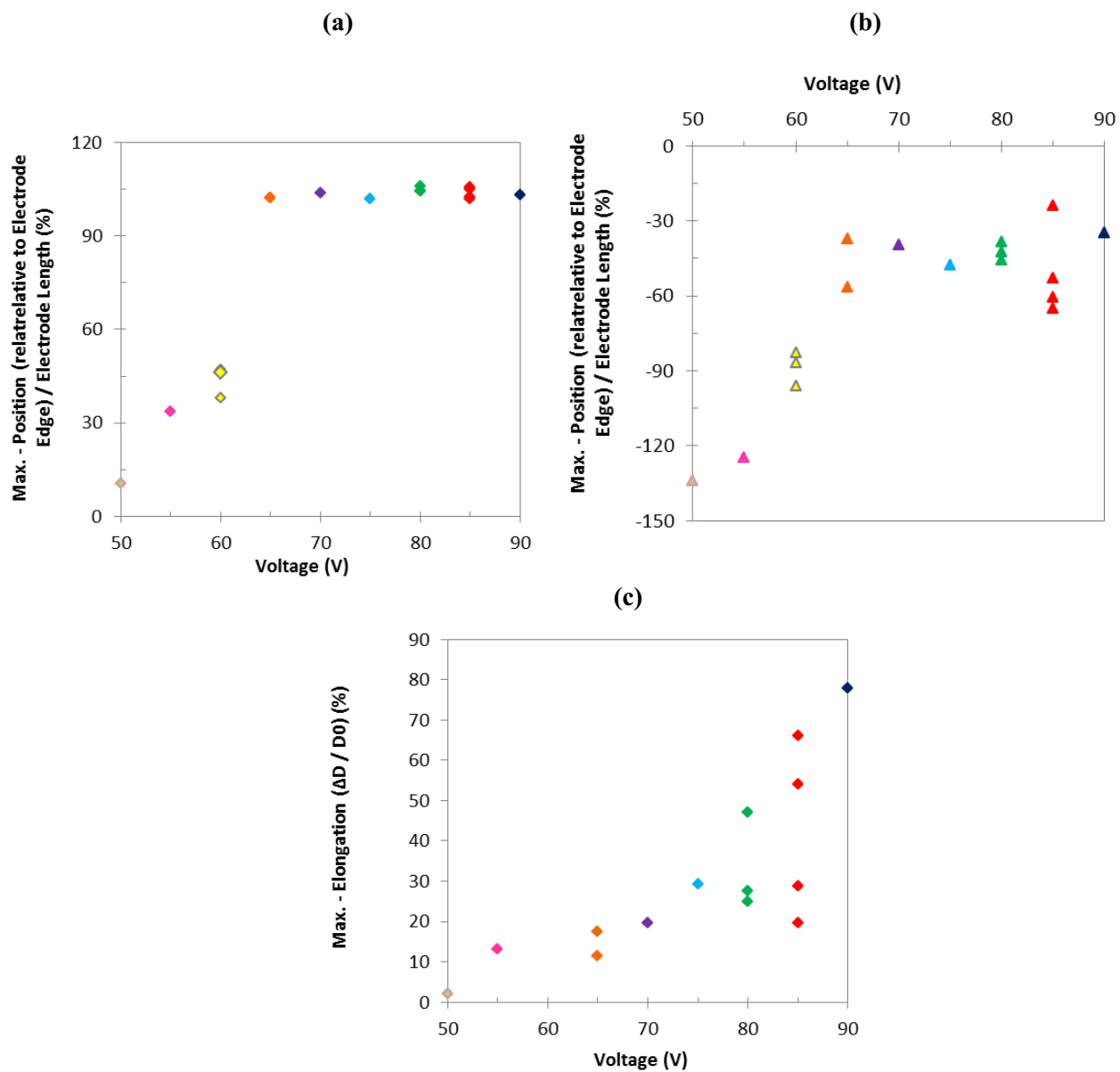
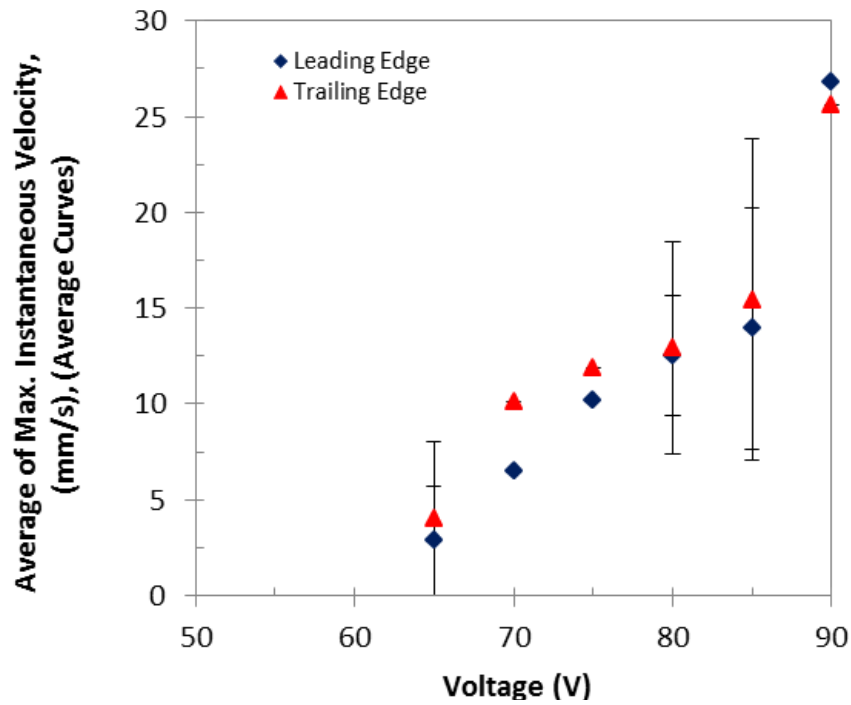
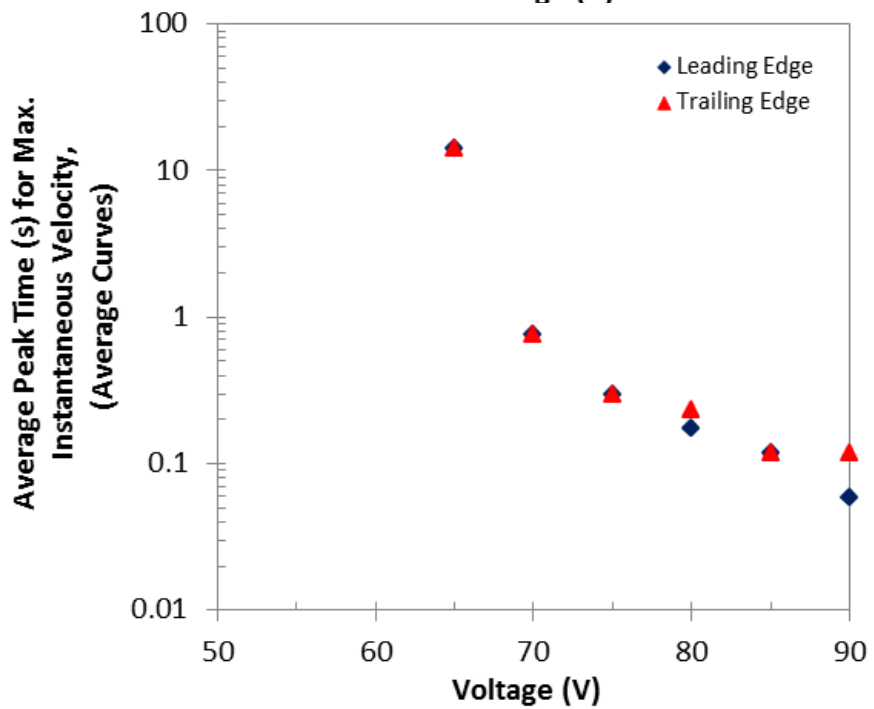


Figure I-33: Changes of the max.: (a) position of the leading edge, (b) position of the trailing edge, (c) elongation, with the applied voltage for the droplets of 20 $\mu\text{g/ml}$ DNA solution.



(a)



(b)

Figure I-34: The average of: (a) max. instantaneous velocity, and (b) peak time for max. instantaneous velocity, as a function of voltage for the leading and trailing edges of the droplets of 20 $\mu\text{g/ml}$ DNA solution. The error bars indicate standard deviation.

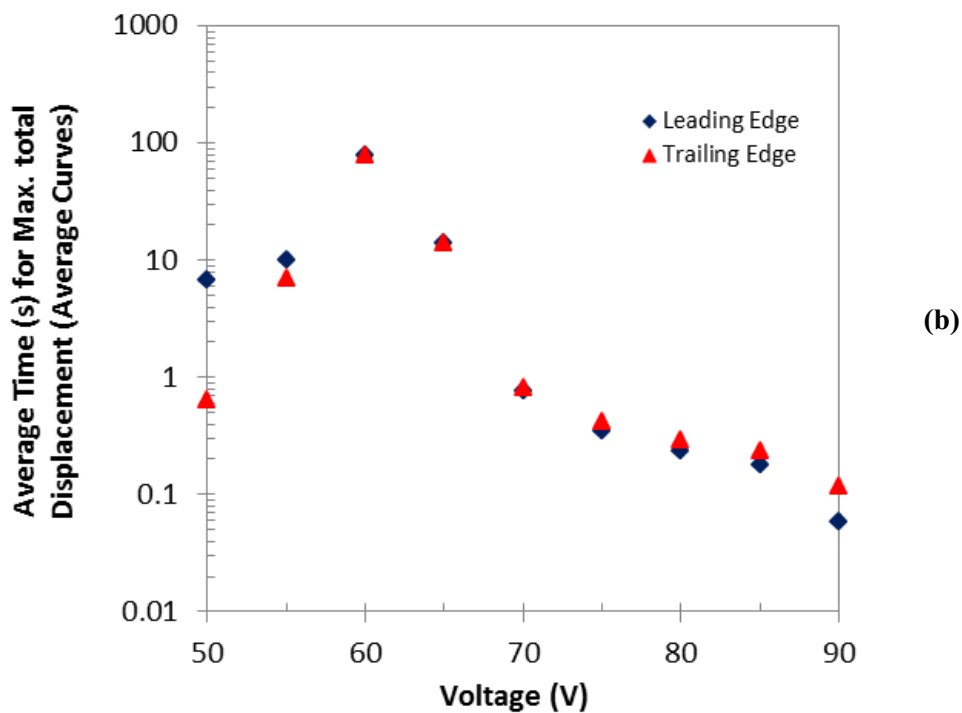
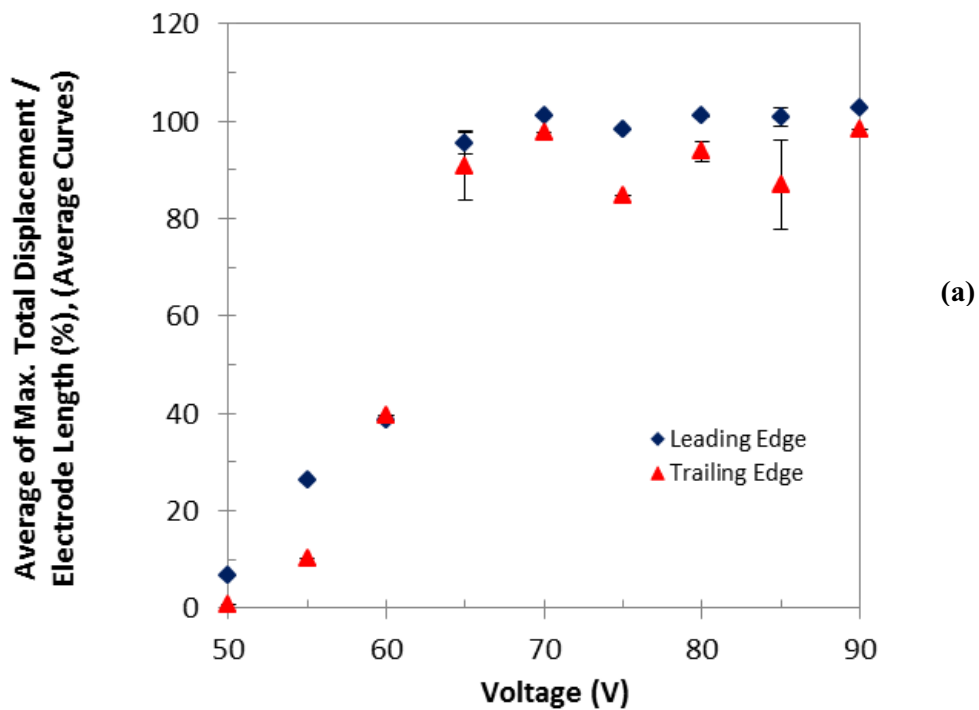


Figure I-35: The average of: (a) max. total displacement, and (b) transition time, as a function of voltage for the leading and trailing edges of the droplets of 20 $\mu\text{g/ml}$ DNA solution. The error bars indicate standard deviation.

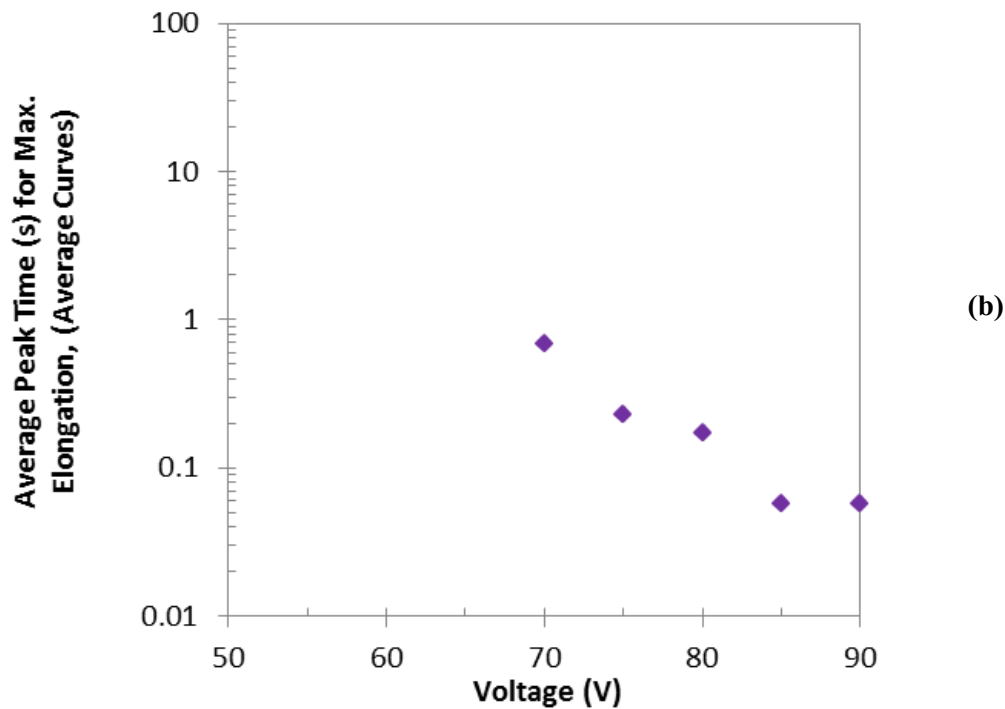
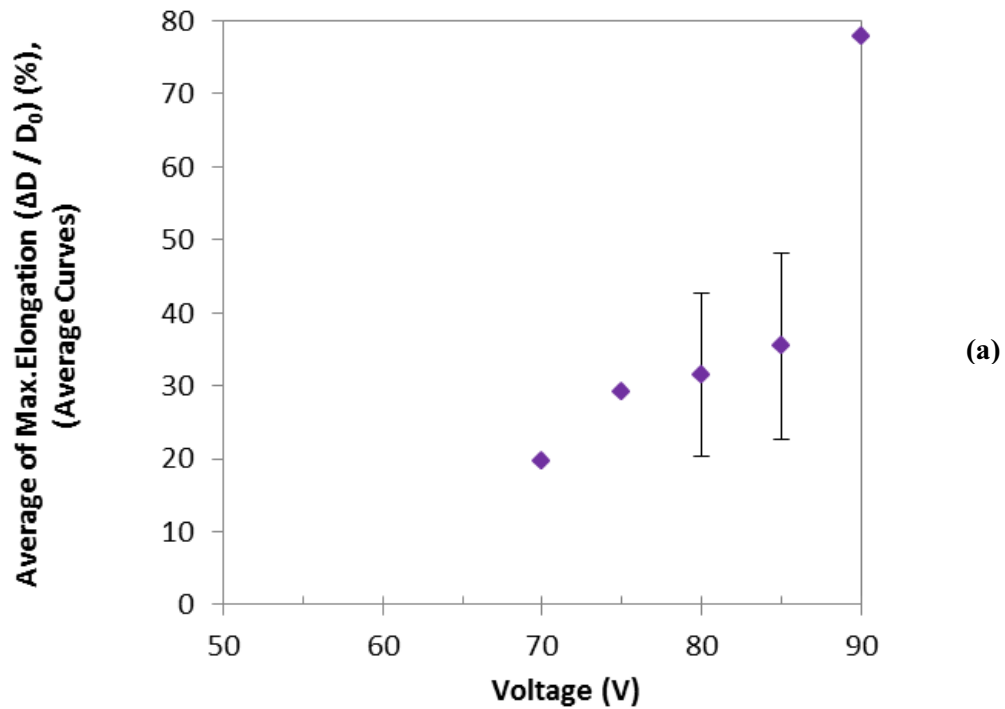


Figure I-36: The average of: (a) max. elongation, and (b) peak time for max. elongation, as a function of voltage of the droplets of 20 $\mu\text{g/ml}$ DNA solution. The error bars indicate standard deviation.

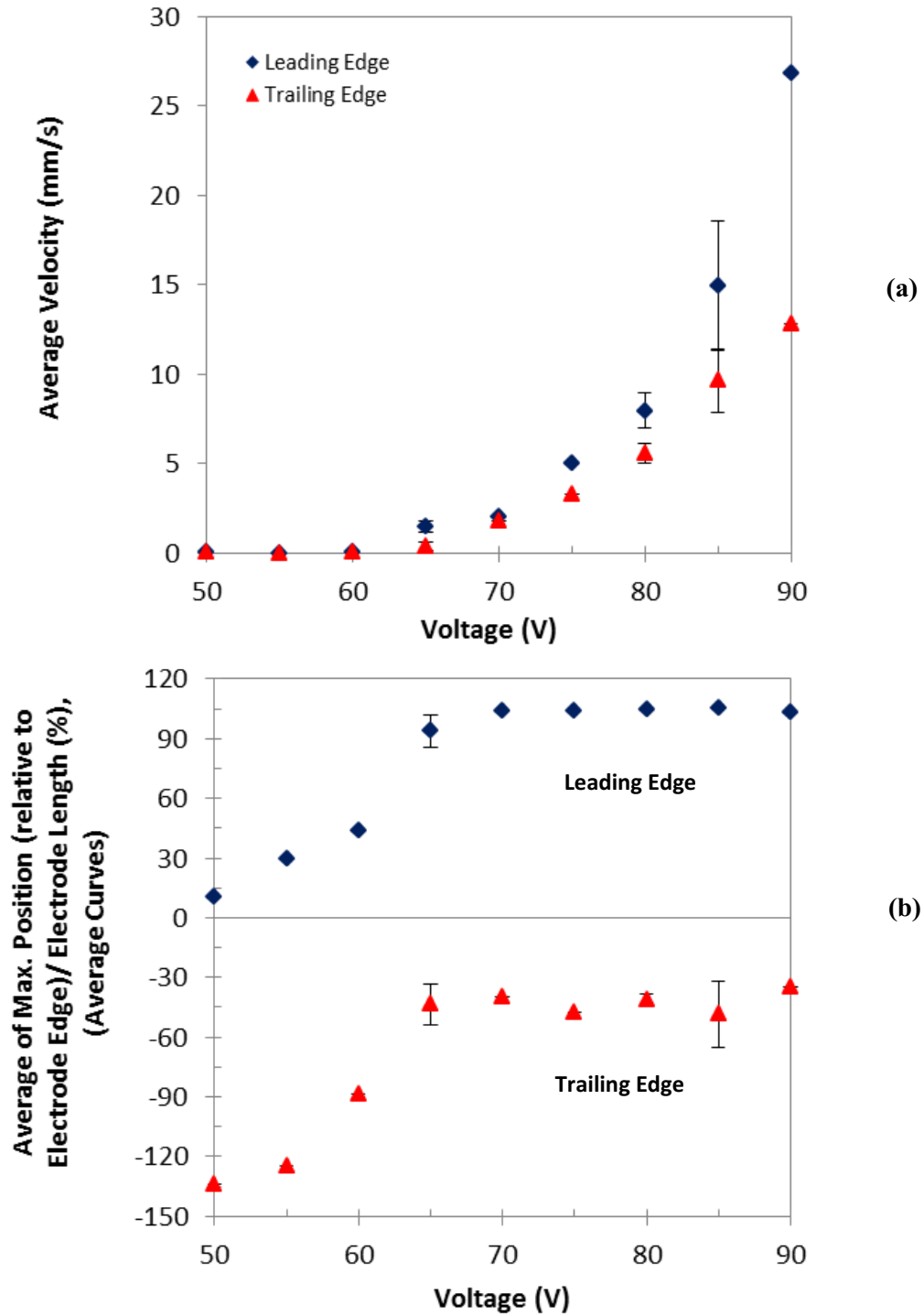


Figure I-37: (a) The average velocity, and (b) the average position, as a function of voltage for the leading and trailing edges of the droplets of 20 $\mu\text{g/ml}$ DNA solution. The error bars indicate standard deviation.

Appendix J

Material Limitations

J-1) Electrolysis and dielectric failure

Despite the fact that numerous numerical models and microfluidic prototypes based on the electrowetting technique have been proposed and developed, the number of commercially available electrowetting based devices is still very limited^{a,b}. Rather complicated systems of dispensing droplets, short term stability of hydrophobic surfaces due to contamination, contact angle hysteresis, contact angle saturation, and dielectric failures are the most important and longstanding fundamental problems of the EWOD platform^{c,d}. In EWOD, where the dielectric layers are used to prevent electrolysis (*i.e.* a chemical decomposition of water produced by passing an electric current through a solution containing ions), a primary commercial challenge is overcoming short or long term dielectric breakdown^{b,c}. Early breakdown usually occurs at material defects such as pinholes in the coating layers (the hydrophobic and the dielectric layer) where the small molecules from the conducting liquid such as hydroxyl and hydronium ions (that function as charge carriers and the source of hydrogen generation) and the additive ionic molecules such as alkali metal ions (that carry a major charge) can breakdown the dielectric coating layers initiating electrolysis^{b,e}. The dielectric layers may also breakdown due to time dependent effects: electrical fatigue, aging and long term interaction with aqueous solutions^b. Besides the dielectric failure, defects such as short circuits between adjacent electrodes and electrode degradations are also fatal problems and if they occur in an EWOD system, the device will be permanently inoperative^{f,g}. Parylene C, the insulation layer frequently used in EWOD, is expected to be pinhole free by nature of the deposition process and at the thicknesses of $\geq 1 \mu\text{m}$ has a breakdown voltage greater than 500 V^{h,i}; however, dielectric failure and consequently electrolysis have been repeatedly observed in this research. Two instances of the water electrolysis are shown in (Figure J-1).

The objective of this chapter is to further study the breakdown spots on the substrates which exhibited electrolysis by means of optical microscopy and EDS elemental mapping (more detail in section J.1.1 in order to better understand the failure mechanism).

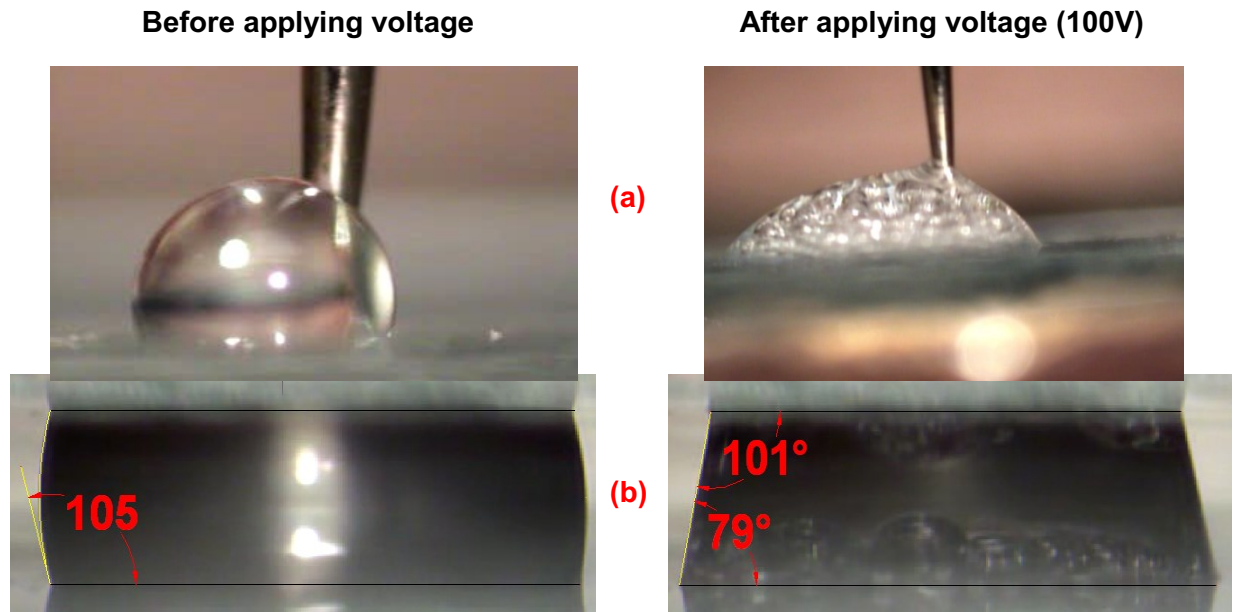
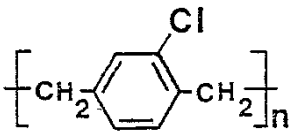


Figure J-1: The actuation of 1.6 μl droplets of deionized water: (a) sessile droplet (b) sandwiched droplet in a microchannel gap of 600 μm . Hydrogen bubbles are clearly observed in the right hand images due to electrolysis.

J.1.1) Breakdown Spots

As demonstrated in Figure 2-4, in this research, the bottom plates are glass substrates coated with: a thin layer of Chromium electrode, Parylene C insulation layer, and finally the hydrophobic layer of Teflon AF. Our goal is to recognize the presence of key elements of the coating layers after the occurrence of electrolysis by means of EDS^j elemental mapping technique in order to understand the mechanism of breakdown failure accordingly. An elemental map which is produced by progressively raster scanning the electron beam point by point over an

area of interest is a 2D image showing the distribution of elements on a surface^k. The coating layers have key elements as shown in Table J-1.

Table J-1: Key elements for the: hydrophobic coating layer (Teflon AF), dielectric layer (Parylene C), control electrode (Chromium), and glass substrate			
Teflon AF (Fluorine: F)	Parylene C (Chlorine: Cl)	control electrode (Chromium: Cr)	glass substrate (Si, O, Ca, Na, Mg)
$\left(\begin{array}{c} \text{F} \quad \text{F} \\ \quad \\ \text{---C---C---} \\ \quad \\ \text{F} \quad \text{F} \end{array} \right)_n$		Cr	SiO₂ CaO Na₂O MgO

J.1.1.1) Two-way array of crescent electrodes

As mentioned in section 1.5, a two-way crescent array of electrodes was introduced by Rajabi^l which is expected to mitigate the movement irreversibility. A detailed schematic of this array of electrodes is shown in Figure J-2. In an instance, while trying to move a 1.6 μl droplet of deionized water on this array in a microchannel gap of 580 μm , electrolysis happened.

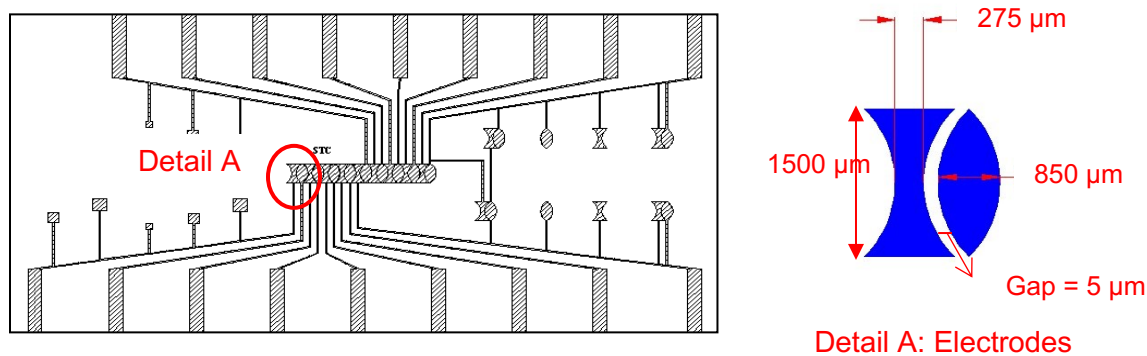


Figure J-2: Detail schematic of a substrate with a two-way array of crescent electrodes.

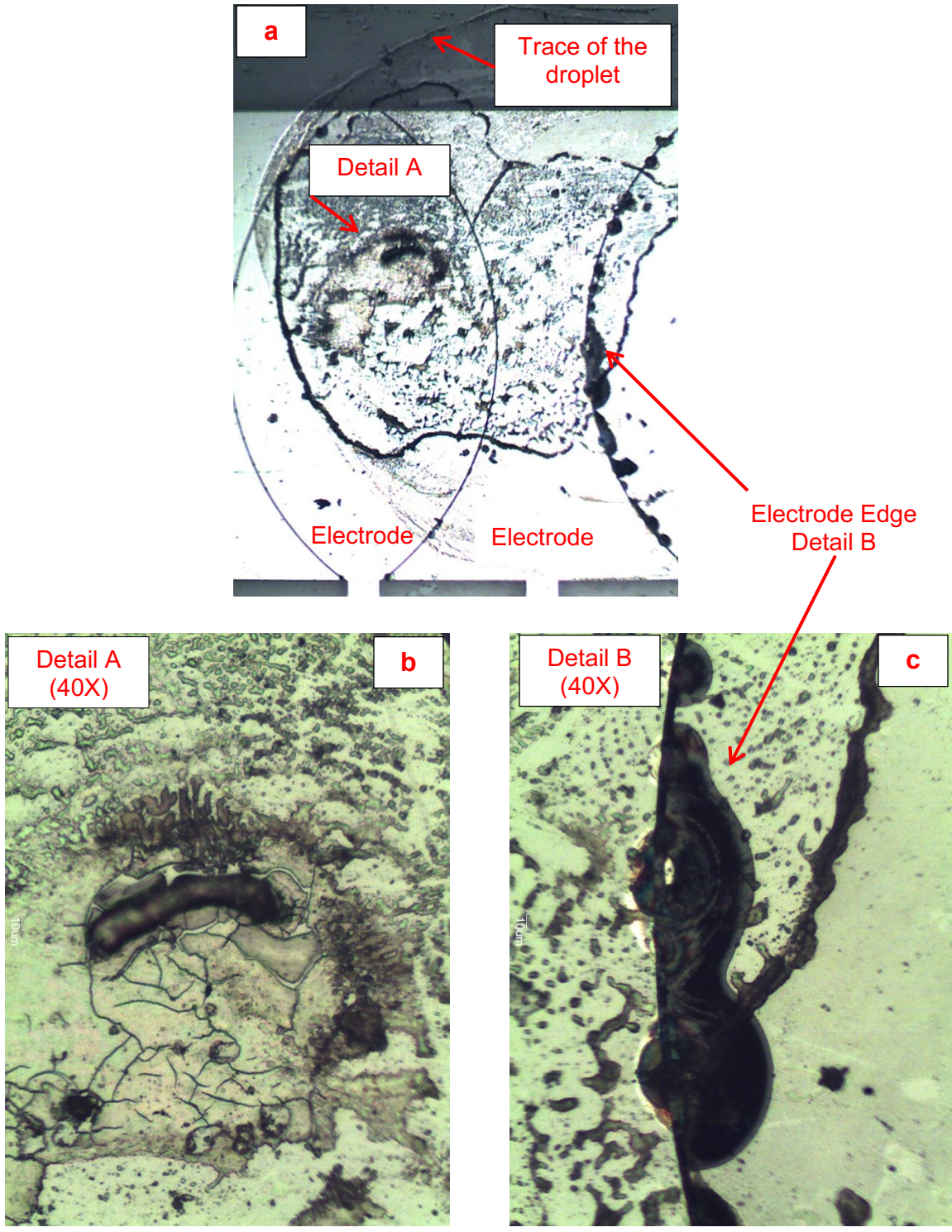


Figure J-3: (a) Optical image of the dielectric breakdown spot on a two-way crescent electrode. (b) and (c) magnified images of Details A and B (40X).

In order to investigate the dielectric breakdown mechanism at the spot where electrolysis happened, several images were taken using an optical microscope (Figure J-3). As shown, the surface beneath the droplet is clearly damaged.

In Figure J-4, a global view of the breakdown spot is shown. This image, which shows a zoomed out preview of the same spot presented in Figure J-3 (a), is taken by scanning electron microscopy (SEM)^m; however, the electrodes edges cannot be clearly seen in this scale, as the gaps between the electrodes are small (5 μm).

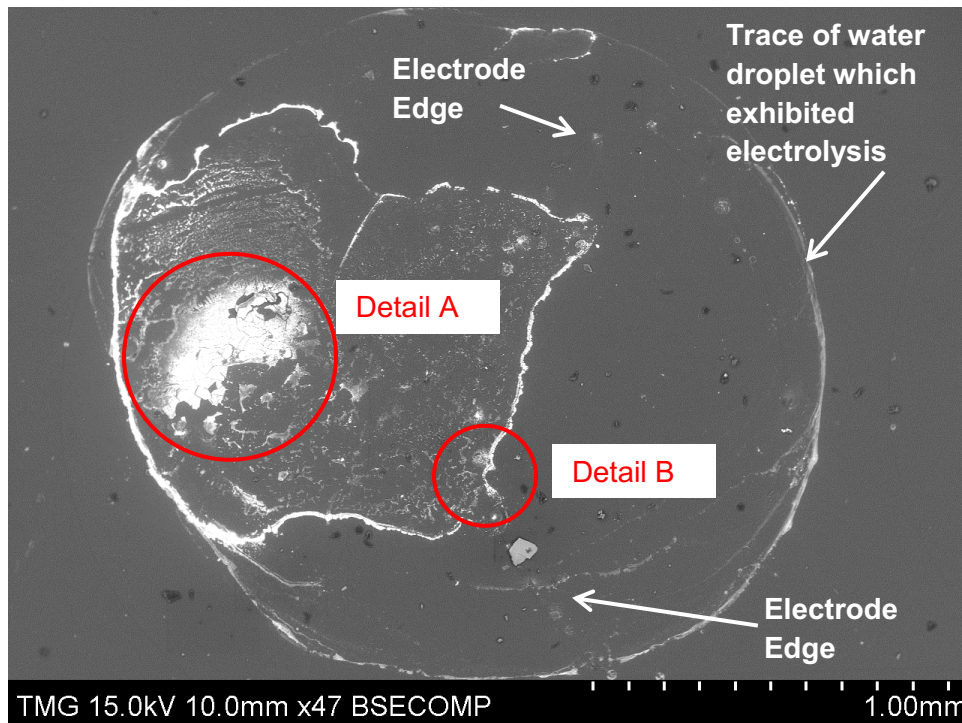


Figure J-4: SEM micrograph showing a global view of the breakdown spot

To further study these two particular locations of Detail A and B, EDS elemental mapping was used. The results are shown Figure J-5 and Figure J-6 where the distributions of key elements in the glass substrate and the coating layers are illustrated. In this section, only two glass elements, silicon (Si) and oxygen (O), are studied; however, in the following section (interdigitated electrodes), the presence of the other glass elements (Mg, Ca, Na) will be also verified.

In the SEM micrograph of Detail A (Figure J-5), the observable cracks and the large dark area, where pieces of coating are missing, are good indications of complete dielectric layer breakdown (Teflon AF and Parylene C coating layers), as according to the EDS elemental maps of F, Cl, and Cr, the concentration of fluorine and chlorine are the lowest in these regions, contrary to chromium which is the highest. It reveals that the cracks and the dark area in the SEM image are basically the surface of chromium electrodes indicating that the net dielectric coating has been entirely eroded. In addition, the zones with the lowest concentration of chromium (darker areas in the EDS elemental map of Cr) show higher concentrations of Si and O in their related EDS elemental maps indicating that localised corrosion of chromium metal has also happened exposing the bare surface of glass substrate.

In Figure J-6, a more generalised form of chromium corrosion can be seen at the gap between the electrodes. By exploring the optical image taken from the electrode edge (Figure J-3 (a)), it can be observed that the chromium electrode has mostly corroded at this gap (in several locations), where the bare surface of glass is exposed. The reason behind this matter will be discussed more in detail in section J.1.2.

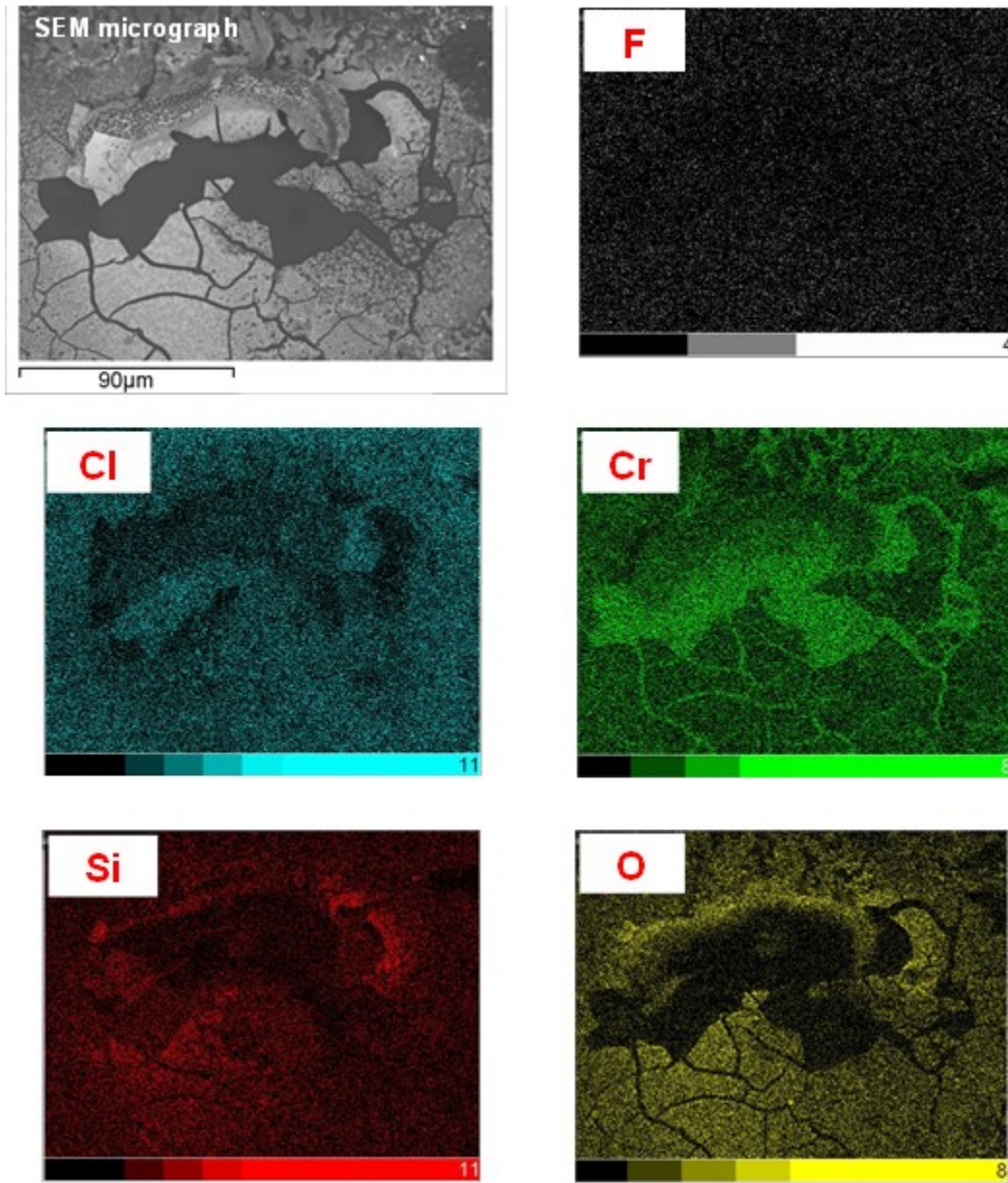


Figure J-5: Detail A in Figure J-3 and Figure J-4 showing the distribution of key elements in coating layers at the breakdown spot; F (Fluorine - Teflon coating), Cl (Chlorine - Parylene C layer), Si and O (for Silicon and Oxygen in SiO_2 - glass wafer), Cr (Chromium – electrode).

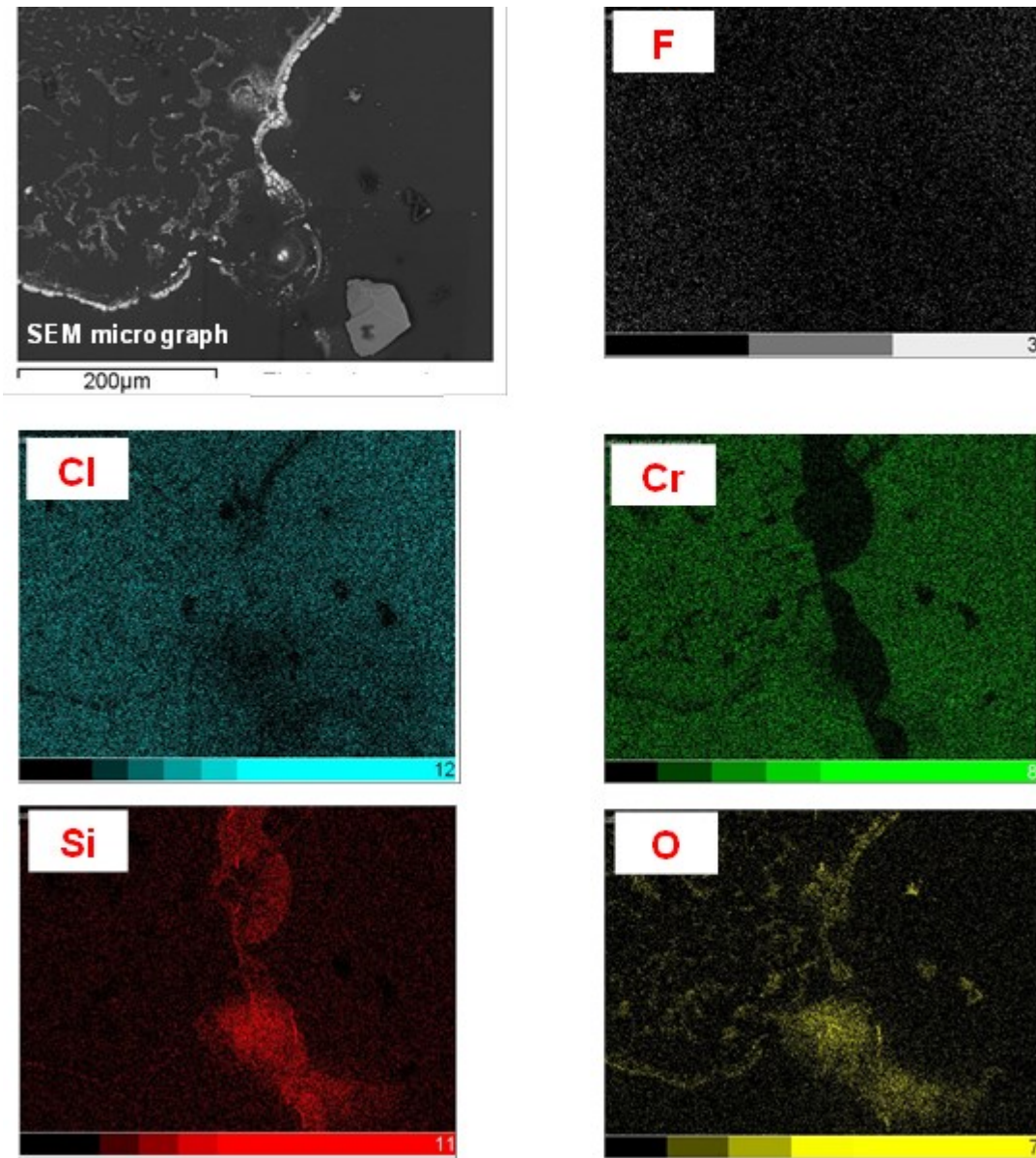


Figure J-6: Detail B in Figure J-3 and Figure J-4 showing the distribution of key elements in coating layers at the breakdown spot; F (Fluorine - Teflon coating), Cl (Chlorine - Parylene C layer), Si and O (for Silicon and Oxygen in SiO_2 – glass wafer), Cr (Chromium – electrode).

J.1.1.2) Interdigitated Electrodes

As discussed before, digital microfluidics is a mechanism which is being used for transporting, cutting, and merging of liquid droplets. This can be done by switching the electrodes on and off sequentially (Figure 2-4). Several experiments were carried out to merge droplets of deionized water on a single interdigitated electrode (with the dimensions of a single electrode as shown in Figure 2-13 and a microchannel gap of 630 μm). A series of these experiments is shown in Figure J-7.

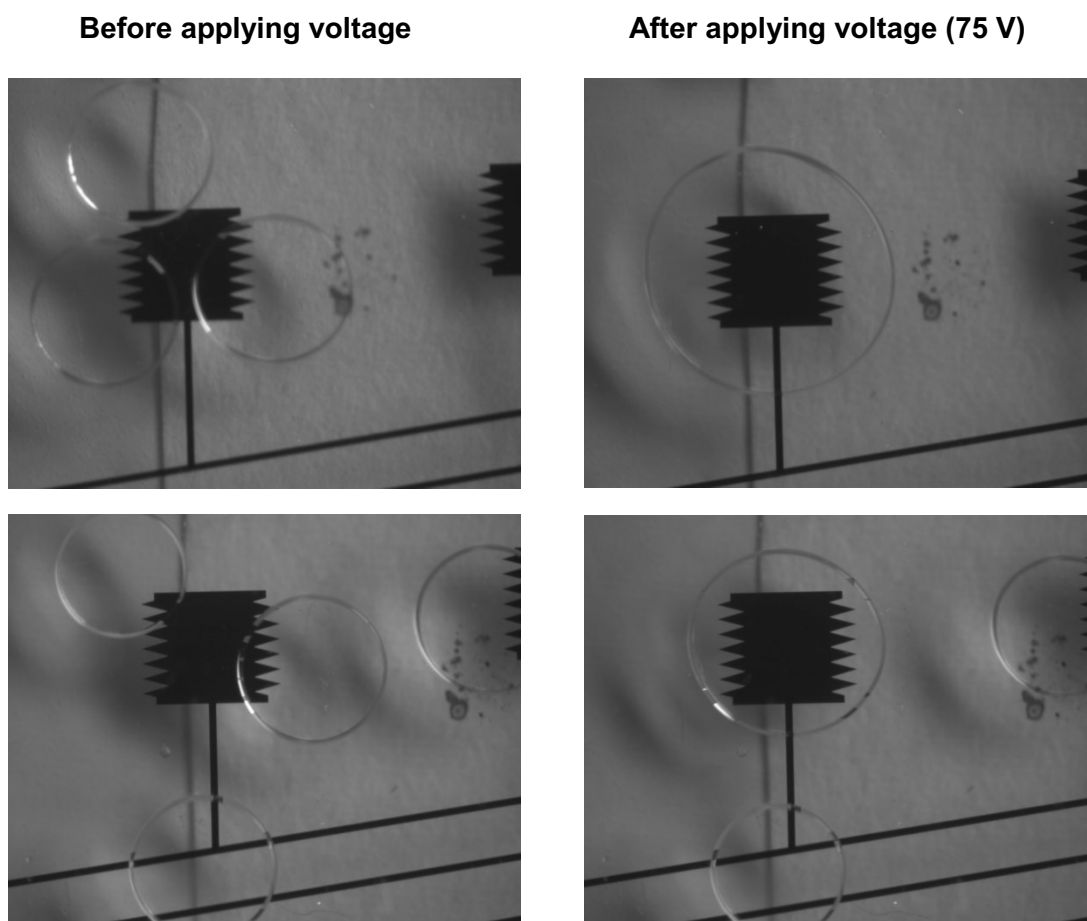


Figure J-7: Merging of deionized water droplets on a single interdigitated electrode.

It was one of the interests of this research to move droplets of aqueous solutions on arrays of interdigitated electrodes (the schematic of this array is shown in Figure 2-13). Despite being

successful in moving the droplets, in many circumstances, electrolysis happened mid-way preventing the droplet to reach the end of the array. It is due to the fact that the insulator between the gaps of the electrodes is easily subject to voltage breakdown as a result of short circuit between adjacent electrodes^f or a locally increased concentration of electric fieldⁿ. Figure J-8 shows an array of 8 interdigitated electrodes marked with A, B, and C; the locations where electrolysis happened after the actuation of three individual droplets of deionized water at 80 V. Among the droplets shown (D₁, D₂, and D₃), we were able to transport D₂ on 3 electrodes before the corner of the last electrode undergoes dielectric breakdown and the subsequent occurrence of electrolysis. Details of A, B, and C are shown in Figure J-9, Figure J-10, and Figure J-11 respectively. These figures present the distributions of key elements at the breakdown spot. The elemental maps of Na, Ca, and Mg (three additional key elements in the glass substrate), are also shown besides those of Si and O (regrettably, the elemental map of O is missing in Figure J-9). The same pattern is observed in the elemental maps of these elements where the areas with higher concentrations of Si, O, Na, Ca, and Mg indicate the exposure of glass substrate due to the chromium corrosion which is in section J.1.2).

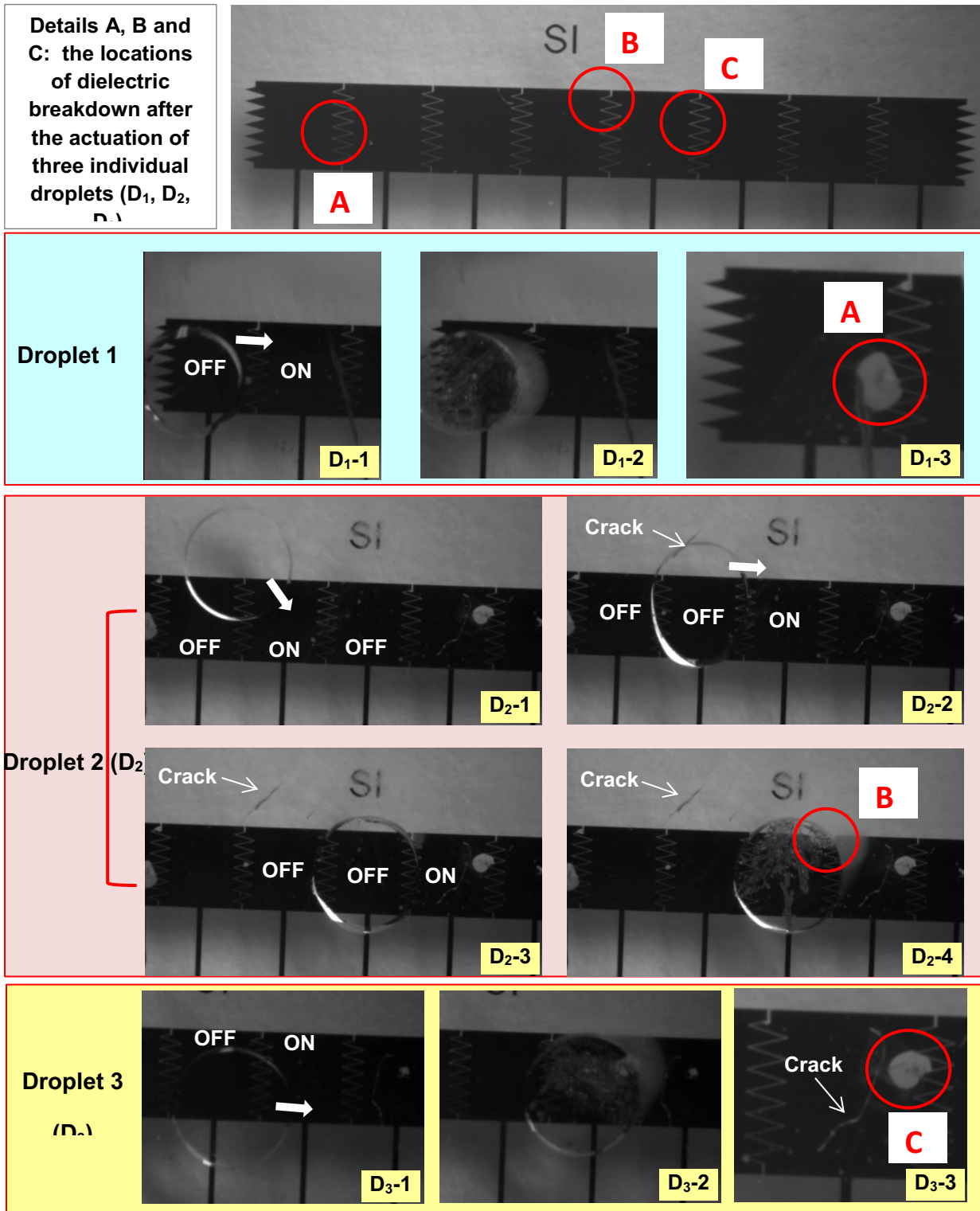


Figure J-8: An array of interdigitated electrodes, the actuation of three individual droplets (D_1 , D_2 , D_3) at 80 V, and the subsequent dielectric breakdown at the locations of A, B, and C.

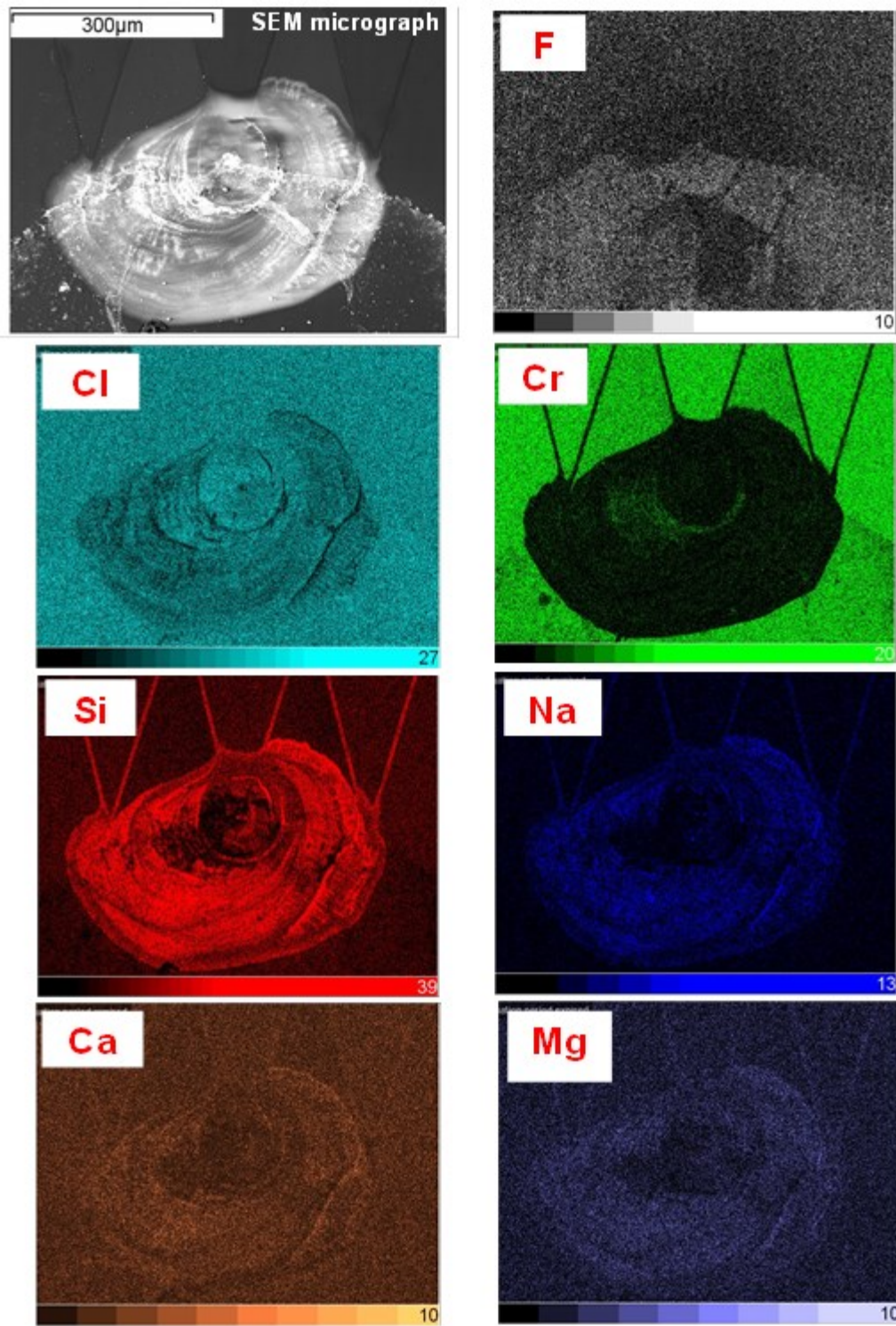


Figure J-9: Detail A, the distributions of key chemical elements present in the coating layers at the breakdown spot.

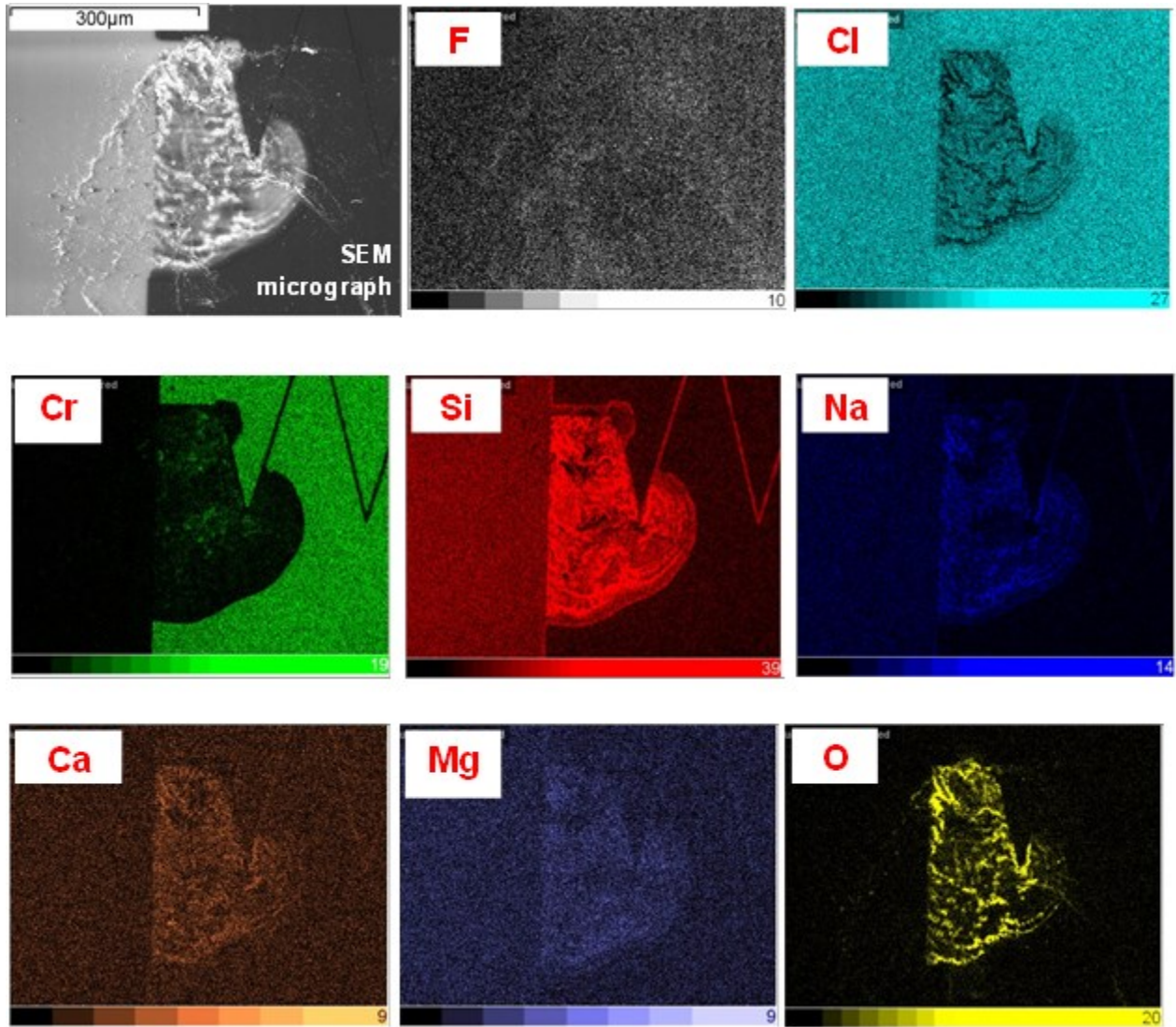


Figure J-10: Detail B, the distributions of key chemical elements present in the coating layers at the breakdown spot.

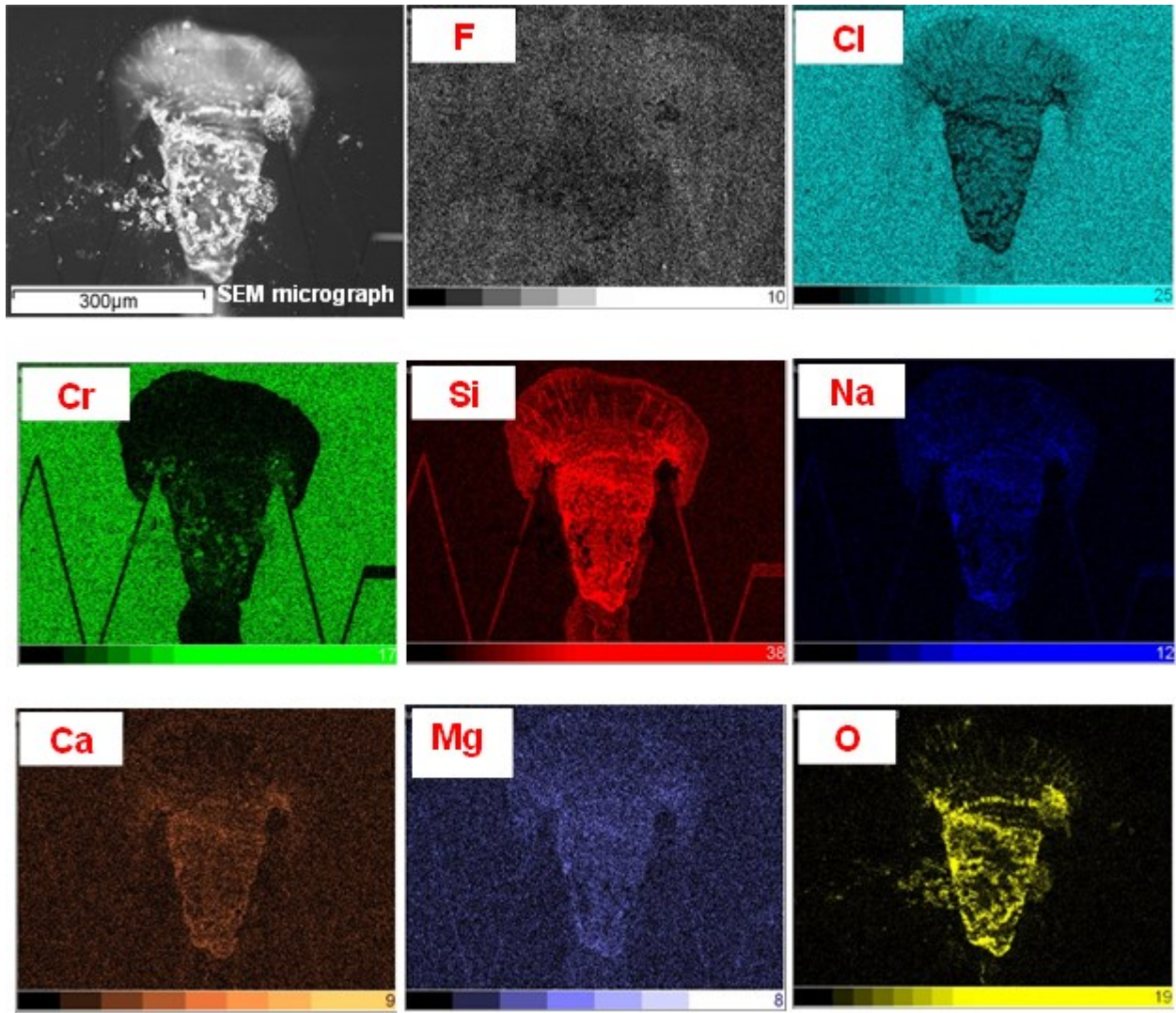


Figure J-11: Detail C, the distributions of key chemical elements present in the coating layers at the breakdown spot.

J.1.2) Discussion

Primarily, breakdown occurs at pinholes in the coating layers where the small molecules from the conducting liquid such as hydroxyl and hydronium ions and the additive ionic molecules such as alkali metal ions can breakdown the dielectric coating layers initiating electrolysis^{b,e}. Pinholes are harmful and unwanted material defects usually made during manufacturing process; however, pinholes may be unintentionally made for various reasons; for instance, while dispensing the droplets, it is possible to damage the dielectric surface with the syringe tip as the insulators with the thicknesses of 1000-2000 μm are still very fragile.

The cracks formed on the surface of the dielectric layer while applying voltage could be another reason for electrolysis. For example, the cracks marked in Figure J-8 were created during the experiment when compared with the image taken from the array of electrodes before applying voltage. The following hypothesis is proposed to explain the cracking: when an electric current passes through a conductor, it releases heat proportional to the current travelling through and the voltage drop across a resistance (*i.e.* in this research, the resistance is the chromium electrode). This heat is known as Joule heating (or ohmic heating). The current from a short circuit between adjacent electrodes may cause ohmic heating producing a high amount of heat. Once the temperature increases, the high thermal conductivity of chromium electrode (93.9 W/(m.k)) allows a faster thermal expansion in the metal electrode. As Parylene C has a slow response to the temperature change^o (thermal conductivity of 0.084 W/(m.k)), it does not expand as fast as the metal electrode; consequently, it breaks, the cracks are created, the metal electrodes are exposed to the solution, and electrolysis occurs. After the initiation of dielectric breakdown, the cracks grow larger. This is the reason that similar patterns of damage are observed over the gaps between the adjacent electrodes (Figure J-3, and Figure J-9 through Figure J-11).

The other hypothesis is that if the local Joule heating exceeds the Parylene C melting point (290 °C), the coating will melt accelerating the electrochemical reactions at the defected areas causing chromium corrosionⁿ.

The items listed below may well be the reasons behind breakdown failure and electrolysis:

- outgassing from the substrate causing a rupture in the Parylene C coating while curing the samples (*e.g.*, the release of adsorbed water vapour from the surface of glass substrate usually by heating in a vacuum oven),
- exceeding Parylene C melting point (290 °C) while curing the samples,
- overshoots and/or hot spots in the oven (uneven temperature distribution),
- if there is any vulnerable location with poor adhesion of the Parylene C to the chromium metal substrate, the aqueous solution can easily penetrate below the dielectric layer to the surface of the metal and consequently cause electrolysis.

Therefore, it is recommended to stay under vacuum with an elevated temperature, as the elevated temperature might accelerate oxidation^p; also, allow the samples which are being cured in the oven to cool to a temperature below 100 °C before venting to the atmosphere. Following, we will discuss how electrolysis initiates the metal corrosion:

Considering the microchannel shown in Figure 2-4 as an electrolytic cell^q (*i.e.* an electrochemical cell that undergoes an electron transfer when electrical energy is applied) with the chromium and ITO electrodes acting as the anode (LHE, left hand electrode) and the cathode (RHE, right hand electrode) respectively as shown in Figure J-12, it is believed that the following reactions (Equation J-1 through Equation J-4) are occurring^r. As the ITO electrodes are coated with Teflon (assuming an intact Teflon coating which has high resistance to chemical attack^s), they will not be in direct contact with the solution; therefore, they will act as a sink for electrons without playing any chemical role in the electrode reaction.

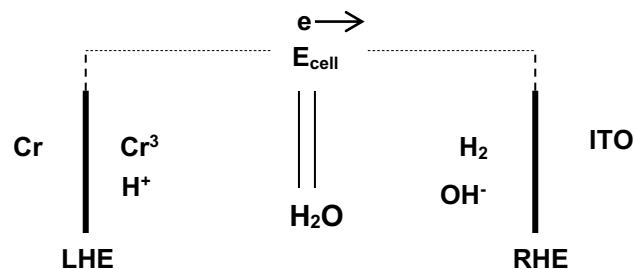


Figure J-12: Abbreviated cell representation showing E_{cell} , LHE (left hand electrode) and RHE (right hand electrode), (Adapted from reference: Stansbury and Buchanan^q).

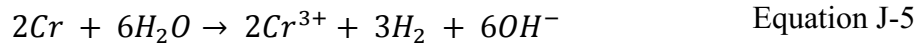
- (a) oxidation half-reaction: at the anode, the oxidation of chromium and re-oxidation of hydrogen takes place (*i.e.* oxidation is the loss of electrons):



- (b) reduction half-reaction: at the cathode, the reduction of water and hydrogen takes place (*i.e.* reduction is the gain of electrons):



by combining the above half reactions:



Equation J-1 to Equation J-5 elucidate the cause of chromium corrosion the same as shown in the elemental maps of Figure J-6 and Figure J-9 through Figure J-11. The presence of hydroxyl ions (OH^{-}) in Equation J-3 will cause: accelerated dielectric breakdown, creating larger cracks, and further exposure of the metal electrode to the solution inducing the chromium corrosion. The same as aluminum, chromium is a very active metal which readily creates an oxide outer-layer on its surface against corrosion (*i.e.* so-called passivation which involves a shielding outer-layer of corrosion)^{b,r}; however, the presence of the adsorbed hydrogen appears to promote the dissolution of Cr as Cr^{3+} preventing the creation of oxide layer on the chromium electrode.

The experiments discussed in this chapter were done on microliter droplets of deionized water. As known, deionized water, when exposed to air, can easily adsorb carbon dioxide and form carbonic acid (H_2CO_3); consequently, the pH drops from 7.0 (neutral for deionized water) to an acidic range of 5.6-5.7 which is a large change in chemistry as pH scale is logarithmic^t. Although, carbonic acid is a weak acid, it can create an acidic medium prompting corrosion to some extent. The electrolysis of carbonic acid (H_2CO_3) is the same as regular water (H_2O); however, when the decomposition happens, it breaks down into water and carbon dioxide.

Therefore, in addition to the electrolysis of water, the anode and cathode electrodes will be contaminated with traces of CO₂ which is soluble in water.

As mentioned before, dielectric failure is one of the most important and longstanding fundamental problems of the EWOD platform. In this chapter, we were able to investigate the breakdown spots on the substrates which exhibited electrolysis by means of optical microscopy and EDS elemental mapping, and the material failure mechanism was analyzed and characterized.

-
- ^a R. Bavière, J. Boutet, Y. Fouillet, “Dynamics of droplet transport induced by electrowetting actuation”, *Microfluid Nanofluid*, vol. 4 (4), pp. 287–294, 2008.
- ^b M. Dhindsa, J. Heikenfeld, W. Weekamp, S. Kuiper, “Electrowetting without electrolysis on self-healing dielectrics”, *Langmuir*, vol. 27 (9), pp. 5665-5670, 2011.
- ^c F. Mugele, “Fundamental challenges in electrowetting: from equilibrium shapes to contact angle saturation and drop dynamics”, *Soft Matter*, vol. 5 (18), pp. 3377-3384, 2009.
- ^d R. Zengerle, C. Cupelli, “Droplet based microfluidics - electrowetting driven devices”, *Microfluidics 2*, *University of Freiburg, Germany*.
- ^e S. Choi, Y. [Kwon](#), Y-S. [Choi](#), E. S. [Kim](#), J. [Bae](#), J. [Lee](#), “Improvement in the breakdown properties of electrowetting using polyelectrolyte ionic solution”, *Langmuir*, vol. 29 (1), pp. 501-509, 2013.
- ^f E. Seyrat, R. A. Hayes, “Amorphous fluoropolymer as insulators for reversible low-voltage electrowetting”, *Journal of Applied Physics*, vol. 90 (3), pp. 1383-1386, 2001.
- ^g K. [Chakrabarty](#), F. [Su](#), “Design Automation Challenges for Microfluidics-Based Biochips”, *DTIP of MEMS & MOEMS*, Montreux, Switzerland, 01-03 June 2005.
- ^h http://scscoatings.com/what_is_parylene/parylene_properties.aspx
- ⁱ <http://scscoatings.com/corporate/library.aspx>
- ^j W. Jansen, M. Slaughter, “["Elemental mapping of minerals by electron microprobe"](#)”, *American Mineralogist*, vol. 67 (5–6), pp. 521–533, 1982.
- ^k http://serc.carleton.edu/research_education/geochemsheets/elementmapping.html
- ^l N. Rajabi, "Droplet actuation on various electrode shapes in electrowetting-based microfluidics" *M.A.Sc. thesis*, Concordia University, Montreal, 2009.

-
- ^m D. [McMullan](#), “Scanning electron microscopy 1928-1965”, *Scanning*, vol. 17(3), pp. 175-185, 1995.
- ⁿ W. Li, D. C. Rodger, P. R. Menon, Y. C. Tai, “Corrosion behavior of Parylene-metal-Parylene thin films in saline”, *ECS Transactions*, vol. 11(18), pp. 1-6, 2008.
- ^o J.-M. Hsu, “Investigation of a-SiC_x:H and Parylene-C thin films as encapsulation materials for neural interface devices”, *Ph.D. thesis*, The University of Utah, 2008.
- ^p J. H. DeVan, “Catastrophic oxidation of high-temperature alloys”, *Oak Ridge National Laboratory*, 1961.
- ^q E. E. Stansbury, R. A. Buchanan, “Fundamentals of electrochemical corrosion”, *ASM International*, 2000.
- ^r Patent: EP 2640873 A1, “Electrolytic dissolution of chromium from chromium electrodes”, 2013.
- ^s http://www2.dupont.com/Teflon_Industrial/en_US/assets/downloads/h44587.pdf
- ^t www.puretecwater.com